

Heft 73

Neubiberg, 2001

T. Schüler

On Ground-Based GPS Tropospheric Delay Estimation

SCHRIFTENREIHE

STUDIENGANG GEODÄSIE UND GEOINFORMATION
UNIVERSITÄT DER BUNDESWEHR MÜNCHEN



T. Schüler

On Ground-Based GPS Tropospheric Delay Estimation

SCHRIFTENREIHE

STUDIENGANG GEODÄSIE UND GEOINFORMATION
UNIVERSITÄT DER BUNDESWEHR MÜNCHEN



Der Druck dieses Heftes wurde aus Haushaltsmitteln der Universität der Bundeswehr München gefördert.

Auflagenhöhe: 150

Herausgeber der Schriftenreihe:

Der Prodekan des Studiengang Geodäsie und Geoinformation der Universität der Bundeswehr München

Bezugsnachweis:

Universität der Bundeswehr München
Fakultät für Bauingenieur- und Vermessungswesen
Studiengang Geodäsie und Geoinformation
Werner-Heisenberg-Weg 39
D - 85577 Neubiberg

ISSN 0173 - 1009

On Ground-Based GPS

Tropospheric Delay Estimation

eingereicht von

Dipl.-Ing. Torben Schüler

Vollständiger Abdruck der an der Fakultät für Bauingenieur- und Vermessungswesen der Universität der Bundeswehr München zur Erlangung des akademischen Grades eines Doktors der Ingenieurwissenschaften (Dr.-Ing.) eingereichten Dissertation.

Vorsitzender: Univ.-Prof. Dr.-Ing. B. Eissfeller

1. Berichterstatter: Univ.-Prof. Dr.-Ing. G. W. Hein

2. Berichterstatter: Univ.-Prof. Dr.-Ing. G. Seeber

Die Dissertation wurde am 18. Oktober 2000 bei der Universität der Bundeswehr München, Werner-Heisenberg-Weg 39, D-85577 Neubiberg eingereicht.

Tag der mündlichen Prüfung: 1. Februar 2001

Abstract

NAVSTAR GPS has become an important aid in navigation and precise space geodesy. Permanent tracking networks like the global IGS net of the International GPS Service for Geodynamics and regional densifications like the German Reference Frame GREF have become very valuable for many scientific applications. For parameter estimation in large-scale networks, two major error sources have to be reduced, namely the orbit error of the GPS space vehicles and the propagation delay in the troposphere. In 1992, the IGS started to produce precise GPS orbits which became a standard product of high precision that virtually eliminated orbit uncertainties from the list of significant contributors to the overall error budget. The remaining problem is that of modeling wet delays with high precision. All conventional models have to fail in this task due to the impossibility of modeling wet delays solely from surface measurements like temperature and relative humidity. Actually, the non-hydrostatic component of the tropospheric propagation delay is highly influenced by the distribution of water vapor in the lower troposphere which cannot be sufficiently predicted with sole help of surface measurements. A work-around is to include atmospheric parameters as additional unknowns in the analysis of GPS data from permanent monitor stations that turns out to improve the quality of position estimates. Moreover, knowledge of zenith wet delays allows to obtain a highly interesting value for climatology and meteorology: integrated or precipitable water vapor being important for the energy balance of the atmosphere and holds share of more than 60% of the natural greenhouse effect. GPS can thereby contribute to the improvement of climate models and weather forecasting.

This work outlines the application of ground-based GPS to climate research and meteorology without omitting the fact that precise GPS positioning can also highly benefit from using numerical weather models for tropospheric delay determination for applications where GPS troposphere estimation is not possible, for example kinematic and rapid static surveys. In this sense, the technique of GPS-derived tropospheric delays is seen as mutually improving both disciplines, precise positioning as well as meteorology and climatology.

Chapters 1 to 4 constitute the theoretical part of this study with first introducing the reader to the importance of water vapor and tropospheric delays (Chapter 1) and outlining the principles of GPS data processing (Chapter 2) with special emphasis on tropospheric delay modeling (Chapter 3). Furthermore, a brief introduction to numerical weather models and extraction methods for needed data is given (Chapter 4) and approaches to combine both data sets - tropospheric delays from numerical weather fields and GPS delays - are described.

Chapters 5 to 7 describe several experiments to validate and assess the quality of numerical weather model data (Chapter 5), GPS-derived troposphere propagation delays (Chapter 6) and combined solutions (Chapter 7). Finally, a summary of the application of ground-based GNSS for tropospheric delay estimation is given (Chapter 8).

Zusammenfassung

NAVSTAR GPS ist inzwischen zu einer wichtigen Hilfe für die Navigation und präzise geodätische Raumverfahren herangewachsen. Permanente Netzwerke wie das IGS Netz des Internationalen GPS Service für Geodynamik und regionale Verdichtung wie beispielsweise das Deutsche Referenznetz DREF haben sich für viele wissenschaftliche Aufgaben als ausgesprochen wertvoll erwiesen. Zwei wesentliche Fehlerquellen müssen zum Zwecke genauer Parameterschätzung in großen Netzen jedoch reduziert werden: die Orbitfehler der GPS-Satelliten und die Laufzeitverzögerungen in der Troposphäre. 1992 begann der IGS mit der Produktion genauer GPS Bahnen und verschiedene Verbesserungen führten dazu, dass dieses Standardprodukt Orbit-Unsicherheiten in der praktischen Nutzung des GPS fast vollständig von der Liste der bedeutenden Fehlereinflüsse eliminiert hat. Es verbleibt das Problem, die feuchte Komponente der troposphärischen Laufzeitverzögerung mit hoher Genauigkeit zu modellieren. Alle konventionellen Modelle müssen in dieser Hinsicht zwangsläufig versagen, denn in der Tat wird die nicht-hydrostatische Komponente der troposphärischen Laufzeitverzögerung maßgeblich von der Verteilung des Wasserdampfes in der unteren Troposphäre beeinflusst, die nicht auf Grund der alleinigen Kenntnis von Oberflächen-Messungen wie Temperatur und relativer Luftfeuchtigkeit prädictiert werden kann. Aus diesem Grunde wird versucht, die feuchte Laufzeitverzögerung als zusätzliche Unbekannte in die Analyse der GPS-Daten von Permanentstationen aufzunehmen und die so erzielten Ergebnisse verbessern zweifelsohne die Qualität der Positionsbestimmung. Weiterhin erlaubt die Kenntnis der feuchten Laufzeitverzögerung aber auch die Ableitung einer für Klimatologie und Meteorologie interessanten Größe, nämlich der des integrierten Wasserdampf-Gehaltes, die für den Energiehaushalt der Atmosphäre von großer Bedeutung und verursacht mehr als 60% des natürlichen Treibhaus-Effektes. GPS kann damit zur Verbesserung von Klima- und Wettervorhersage-Modellen beitragen.

Diese Arbeit stellt die Anwendung des bodengestützten GPS für Klimaforschung und Meteorologie dar, ohne dabei die Tatsache zu vernachlässigen, dass die präzise GPS Positionierung ebenfalls stark von der Nutzung numerischer Wettermodelle zum Zwecke der Bestimmung des Troposphären-Fehlers profitieren kann, nämlich bei Anwendungen, welche die Mitschätzung dieses Fehlers nicht erlauben, beispielsweise im Bereich des kinematischen GPS. In diesem Sinne wird die Technik der GPS-basierten Bestimmung troposphärischer Laufzeitverzögerungen als für beide Disziplinen gewinnbringend betrachtet, für die präzise Positionsbestimmung genauso wie für Meteorologie und Klimatologie.

Kapitel 1 bis 4 bilden den theoretischen Teil dieser Arbeit. Zunächst wird der Leser in die Thematik eingeführt (Kapitel 1) und anschließend werden die Grundlagen der GPS Daten-Prozessierung beschrieben (Kapitel 2), wobei besonderer Wert auf die Modellierung der troposphärischen Laufzeitverzögerung gelegt wird (Kapitel 3). Weiterhin wird eine kurze Einführung in numerische Wettermodelle sowie in die Methoden zur Extraktion der benötigten Daten gegeben (Kapitel 4) und Ansätze zur Kombination beider Datensätze - troposphärischer Verzögerungen aus numerischen Wetterfeldern und GPS Verzögerungen - werden beschrieben.

Kapitel 5 bis 7 beschreiben verschiedene Experimente zur Validierung und Qualitätsabschätzung von numerischen Wettermodell-Daten (Kapitel 5), GPS-basierten troposphärischen Laufzeitverzögerungen (Kapitel 6) und kombinierten Lösungen (Kapitel 7). Schließlich wird eine Zusammenfassung der Anwendung von GNSS für bodengestützte Bestimmung troposphärischer Parameter gegeben (Kapitel 8).

Table of Contents

1. Introduction.....	37
1.1 Importance of Atmospheric Water Vapor for the Climate System	37
1.1.1 Hydrological Cycle and Greenhouse Effect.....	37
1.1.2 Trends.....	38
1.2 The Role of Water Vapor in GPS Geodesy and Navigation	38
1.2.1 NAVSTAR GPS	38
1.2.2 Tropospheric Delays and GPS	39
1.3 Water Vapor Observing Systems.....	39
1.3.1 Description of Selected Sensors	39
1.3.2 Synopsis	43
1.4 Objectives and Structure of this Thesis.....	43
1.4.1 Objectives of this Thesis.....	43
1.4.2 Structure of this Thesis	44
2. Principles of GPS Data Processing	47
2.1 Processing Overview.....	47
2.1.1 Pre-Processing.....	47
2.1.2 Network Filtering	48
2.1.3 Post-Filter Processing	48
2.1.4 Realization	49
2.2 Observations and Observation Equations	50
2.2.1 Pseudo-Ranges	50
2.2.2 Carrier Phase Measurements.....	51
2.2.2.1 Double Differences	53
2.2.2.2 Synchronization Problem.....	54
2.2.2.3 Degradation due to Selective Availability	55
2.2.2.4 Antenna Orientation Problem	57
2.2.2.5 Hardware Biases	58
2.2.2.6 Relativistic Effects.....	59
2.2.3 Linear Combinations	60
2.2.4 Ionospheric Error	62
2.2.4.1 First Order Effect	63
2.2.4.2 Second Order Effect.....	64
2.2.4.3 Interpolation in IONEX Files	65
2.2.4.3.1 Computation of Ionospheric Points	66
2.2.4.3.2 Horizontal Interpolation.....	66
2.2.4.3.3 Temporal Interpolation	66
2.2.5 Cycle Slip Detection and Repair	67
2.2.6 Multipath Detection	68
2.3 Site Displacements and Corrections	69
2.3.1 Velocity Correction.....	70
2.3.2 Solid Earth Tides.....	71
2.3.3 Pole Tide	73
2.3.4 Ocean Loading	73
2.3.5 Antenna Eccentricity	74
2.3.6 Antenna Phase Center Corrections	74
2.3.6.1 Antenna Phase Center Offset	75
2.3.6.2 Elevation-Dependent Phase Center Variations	76
2.4 Handling Precise Orbits	76
2.4.1 Format Conversion of Broadcast Orbits	77
2.4.2 Orbit Interpolation.....	79
2.4.3 Epoch of Signal Transmission and Receiver Clock Check.....	81
2.4.3.1 Epoch of Signal Transmission	81

2.4.3.2 Check of Receiver Clock Error Behavior	85
2.4.4 Antenna Phase Center Eccentricity Correction	86
2.4.5 Eclipsing Season	88
2.5 Parameter Estimation Techniques	91
2.5.1 Least-Squares Adjustment	91
2.5.1.1 Observation Vector, Design Matrix and Stochastic Model	92
2.5.1.2 Adjustment Algorithm	93
2.5.1.3 Iterating on a Previous Solution	95
2.5.1.4 Blunder Detection	95
2.5.1.4.1 Global Test	95
2.5.1.4.2 Blunder Detector of Residual-Type	96
2.5.1.4.3 Blunder Detector of Baarda- or Pope-Type	96
2.5.2 Kalman Filtering	98
2.5.2.1 Observations and Covariance Matrix	98
2.5.2.2 State Vector, Transition and Prediction of State	101
2.5.2.3 Design Matrix	103
2.5.2.4 Filter Update	105
2.5.2.8 Tuning of Stochastic Model	106
2.5.2.7 Backward Filtering	107
2.5.2.7.1 Optimal Estimation	107
2.5.2.7.2 Sub-Optimal Estimation	107
2.5.2.8 Blunder Detection	108
2.5.2.8.1 Level-D: Check of Innovations	109
2.5.2.8.2 Level-U: Check of Stochastic Model of the State Vector	110
2.5.2.8.3 Analysis of Post-Fit Residuals	111
2.5.2.9 Summarizing Coordinates	111
2.5.2.9.1 Arithmetic Weighted Mean	112
2.5.2.9.2 Median	112
2.5.2.9.3 Jump Detection	112
2.6 Ambiguities	113
2.6.1 Direct Fixing	113
2.6.2 Indirect Fixing of the Ionosphere-Free Signal	115
2.6.2.1 Wide Lane Fixing	115
2.6.2.1.1 Code-Carrier-Combination	115
2.6.2.1.2 IONEX-Supported Carrier Solution	117
2.6.2.2 Narrow Lane Fixing	117
2.6.2.3 Nominal L_C -Ambiguity	118
2.6.3 Ambiguity Back-Tracing	118
2.7 Geodetic Datum	119
2.7.1 Datum Transformation	120
2.7.2 Similarity Transformation	121
2.8 Network Composition	123
2.8.1 Centered Networks	123
2.8.2 Shortest Baseline Networks	123
2.8.3 Site Isolation Logic	124
2.9 Network Partitioning	126
 3. Modeling and Estimating Tropospheric Propagation Delays	 129
3.1 Brief Overview of the Lower Atmosphere	129
3.1.1 Pressure	129
3.1.2 Temperature	131
3.1.3 Water Vapor	131
3.2 Modeling of Tropospheric Delays	131
3.2.1 Generalized Functional Description	132
3.2.1 Modeling Zenith Delays	133
3.2.1.1 Zenith Hydrostatic Delay	136
3.2.1.1.1 Hopfield Hydrostatic Delay Model	136

3.2.1.1.2 Saastamoinen Hydrostatic Delay Model	140
3.2.1.1.3 MOPS Hydrostatic Delay Model	142
3.2.1.1.4 Comparison of Hydrostatic Models	144
3.2.1.2 Zenith Wet Delay	145
3.2.1.2.1 Hopfield Wet Delay Model	146
3.2.1.2.2 Ifadis Wet Delay Model	147
3.2.1.2.3 Mendes Wet Delay Model	147
3.2.1.2.4 MOPS Wet Delay Model	147
3.2.1.2.5 Comparison of Wet Delay Models	149
3.2.2 Projecting Zenith Delays into Slant Direction	149
3.2.2.1 Hydrostatic Mapping Functions	151
3.2.2.1.1 Saastamoinen Mapping Function	152
3.2.2.1.2 Chao Hydrostatic Mapping Function	153
3.2.2.1.3 Black Hydrostatic Mapping Function	153
3.2.2.1.4 Davis Hydrostatic Mapping Function	154
3.2.2.1.5 Ifadis Hydrostatic Mapping Function	155
3.2.2.1.6 Herring Hydrostatic Mapping Function	156
3.2.2.1.7 Niell Hydrostatic Mapping Function	157
3.2.2.2 Wet Mapping Functions	158
3.2.2.2.1 Chao Wet Mapping Function	158
3.2.2.2.2 Black Wet Mapping Function	158
3.2.2.2.3 Ifadis Wet Mapping Function	159
3.2.2.2.4 Herring Wet Mapping Function	159
3.2.2.2.5 Niell Wet Mapping Function	160
3.2.2.3 Gradient Mapping Functions	160
3.3 Estimation of Tropospheric Parameters	161
3.3.1 Zenith Wet Delays	161
3.3.2 Horizontal Gradients	162
3.3.3 Mapping Function Coefficients	163
3.3.4 Error Budget and Stochastic Modeling	164
3.3.4.1 Position Error	164
3.3.4.2 Orbit Error	165
3.3.4.3 Convergence Error	165
3.3.4.3.1 Network Considerations for Absolute Delay Estimation	166
3.3.4.3.2 Relative Tropospheric Delay Estimation	167
3.3.4.4 Multipath	169
3.3.4.5 Hydrostatic Delay	169
3.3.4.6 Mapping Function	170
3.3.4.7 Measurement Noise	172
3.4 Stochastic Properties of Zenith Wet Delays	172
3.4.1 Stochastic Filtering	173
3.4.2 Stochastic Processes	174
3.4.2.1 First Order Gauss-Markov Process	175
3.4.2.2 Random Walk	176
3.4.3 Mean Process Noise Parameters from Time Series Analysis	177
3.4.3.1 Results for the IGS Tracking Network	177
3.4.3.2 Process Noise Values	178
3.4.4 Dynamic Tuning and Maximum Tuning	180
3.4.4.1 Methods of Dynamic and Maximum Process Noise Definition	182
3.4.4.2 Validation Study	182
3.5 Conversion of Wet Delays into Precipitable Water	184
3.5.1 Relation between Integrated Water Vapor and Zenith Wet Delay	184
3.5.2 Relation between Precipitable Water and Zenith Wet Delay	185
3.5.3 Mean Temperature and Conversion Factor Q	186
3.5.3.1 Global Functions	187
3.5.3.2 Regional Functions	187
3.5.3.3 Individual Functions	188
3.5.3.4 Height Dependency	188

3.5.4 Conversion Uncertainty	189
4. Application of Numerical Weather Models	193
4.1 Contents of Numerical Weather Fields	193
4.1.1 Contents and Resolution of GDAS-Fields	194
4.1.2 Height Systems	194
4.1.3 Horizontal Coordinates	196
4.2 Surface Data Extraction	197
4.2.1 Surface Pressure	197
4.2.1.1 Interpolation Sequences	197
4.2.1.2 Vertical Interpolation	199
4.2.1.3 Horizontal Interpolation	201
4.2.1.4 Temporal Interpolation	203
4.2.2 Surface Temperature	203
4.2.3 Surface Humidity	204
4.3 Mapping Function Coefficients and Horizontal Gradients	205
4.3.1 Ray-Tracing Algorithm	205
4.3.1.1 Ray-Tracing	205
4.3.1.2 Alternative Ray-Tracing Algorithm	207
4.3.1.3 Horizontal Resolution	208
4.3.1.4 Vertical Resolution	208
4.3.2 Ray-Tracing Analysis	208
4.4 Gridded Tropospheric Correction Files (TROPEX)	209
4.4.1 Contents and Structure of TROPEX Files	211
4.4.2 Zenith Hydrostatic Delay	211
4.4.2.1 Surface Pressure	211
4.4.2.2 Vertical Profile Modeling	212
4.4.3 Zenith Wet Delay	212
4.4.3.1 Integral Evaluation	212
4.4.3.2 Vertical Profile Modeling	213
4.4.4 Other Atmospheric Properties	213
4.4.4.1 Mean Temperature of Troposphere	213
4.4.4.2 Temperature Lapse Rate	214
4.4.4.3 Height of the Tropopause	214
4.4.5 Horizontal Interpolation in TROPEX Files	218
4.4.5.1 Distance Weighting	219
4.4.5.2 Gauss-Markov Weighting	219
4.4.5.3 Best Linear Unbiased Estimator (BLUE)	220
4.5 Combination of NWM Data and GPS Estimates	221
4.5.1 Observations, Parameters and Stochastic Model	222
4.5.2 Functional Model	223
4.5.4 Stochastic Optimization	225
4.5.4.1 Sensing Inconsistencies (Outlier Detection)	225
4.5.4.2 Variance Component Estimation	225
4.5.4.3 Pre-Weighting Approach	227
5. Validation of Numerical Weather Model Data	229
5.1 Surface Meteorological Data	229
5.1.1 Surface Pressure	230
5.1.1.1 Impact of Vertical Interpolation	232
5.1.1.2 Long-Term Comparison	232
5.1.2 Surface Temperature	232
5.1.3 Relative Humidity	234
5.1.4 Results for High-Resolution Weather Fields	238
5.2 Temperature Lapse Rate	240
5.3 Mean Temperature of the Troposphere	241

5.4 NWM-derived Mapping Functions	241
6. GPS Validation Experiments.....	247
6.1 Long-term Experiment.....	248
6.1.1 Availability Statistics	248
6.1.2 Outlier Statistics.....	251
6.1.3 Comparison with IGS Neutral Delays	251
6.1.4 Systematic Effects	256
6.2 Experiment OBER-I	256
6.2.1 Availability and Reliability	256
6.2.2 Comparison with IGS Zenith Neutral Delays.....	257
6.2.3 Evaluation of Tropospheric Mapping Functions	262
6.2.4 Horizontal Gradients.....	262
6.2.5 Ionospheric Impact.....	263
6.2.6 Elevation Masking.....	266
6.2.7 Comparison with Radiosonde Data	266
6.3 Experiment OBER-II	267
6.3.1 Impact of Orbit Accuracy	267
6.3.2 Comparison with Radiosonde Data	269
6.4 EUREF/GREF Experiment	269
6.4.1 Comparison with IGS Delays.....	269
6.4.2 Conversion into Integrated Water Vapor.....	271
6.4.3 Comparison of Integrated Water Vapor Results	272
6.4.4 Comparison with Integrated Water Vapor from Numerical Weather Fields	276
6.5 Multipath Experiment/Receiver Comparison	276
6.6 WVR Validation Experiment	280
6.6.1 Integrated Water Vapor	281
6.6.1.1 Comparison of Results	281
6.6.1.2 Comparison of Different Configuration Settings.....	281
6.6.2 Mapping Function Coefficients.....	285
6.6.3 Horizontal Gradients.....	285
6.6.4 Process Noise Definition.....	287
7. Quality Assessment of TROPEX Data.....	291
7.1 Vertical Reduction	291
7.1.1 Pressure Scale Height.....	291
7.1.1.1 Impact of Scale Height on Hydrostatic Delay.....	291
7.1.1.2 Internal Consistency of Numerical Weather Model.....	296
7.1.2 Water Vapor Scale Height	297
7.1.3 Summary.....	297
7.2 Zenith Neutral Delays from GDAS Weather Fields	299
7.3 Combined GDAS/GPS Solution Fields	312
8. Résumé	315
8.1 GPS Tropospheric Delay Estimation	315
8.1.1 Error Budget	315
8.1.2 Meteorological Inputs	317
8.2 Gridded Tropospheric Correction Data.....	318
8.2.1 NWM-derived Zenith Neutral Delays	318
8.2.2 Combination of NWM and GPS Data Sets	319
8.3 Economical and Technical Aspects	319
8.4 Summary and Outlook	320
9. References	323

Appendices..... 333

 Appendix I: Process Noise Parameters..... 333

 Appendix II: Conversion Coefficients for Mean Temperature..... 336

 Appendix III: Comparison of IWV Conversion Uncertainties 339

 Appendix IV: Mean Values for Water Vapor 342

 Appendix IV: Mean Values for Water Vapor Scale Heights..... 353

 Appendix V: TROPEX Format Description..... 355

Index of Keywords 361

List of Figures

- Figure 1-1** - Overview of water vapor measuring platforms and sensors following CARTER [1997]. Water vapor sensors are carried on a variety of platforms including ground stations, weather balloons, aircraft and satellites. NAVSTAR GPS consists of a minimum of 21 MEO satellites at an orbit altitude of 20,000 km. Atmospheric monitoring with GPS is possible in two ways: by probing the atmosphere with help of GPS receivers on LEO (low-earth orbiting) satellites, the so-called radio occultation technique, or by using networks of ground-based GPS receivers. According to GABOR [1997], remotely piloted vehicles have yet to come of age, but offer a potentially long loiter time and high altitude ceiling. 40
- Figure 1-2** - Structure of this thesis. Chapters 2 to 4 can be considered as the theoretical part describing the modeling methods and algorithms of GPS tropospheric delay estimation and data extraction from numerical weather fields. Practical results are presented in chapters 5 to 7 and a summary is given in chapter 8. 45
- Figure 2-1** - Major modules of the TropAC permanent array filter software and their interrelations. The pre-processor for the GPS data is called PAF_PREP and prepares all needed data for Kalman filtering. Network filtering is carried out with the modules PAF_FILT, PAF_TROP or PAF_RANG. Program PAF_MEO serves as interface to the numerical weather models and PAF_COMB is able to combine regularly gridded tropospheric data sets from the weather fields and the irregularly distributed GPS estimates. 48
- Figure 2-2** - Zenith angle z_A^i from ground station A to satellite i and ionospheric zenith angle z_{IP}^i from the mean ionosphere to the satellite following HOFFMANN-WELLENHOF [1993]. The projection of the ionospheric point IP to the surface yields the horizontal coordinates needed for interpolation in TEC maps like IONEX files. 63
- Figure 2-3** - Comparison of the radial site displacements for IGS tracking station Potsdam (POTS) using the approximation presented by LANDAU [1988] and the IERS model documented by MCCARTHY [1996]. The difference between both models is dominated by a systematic error with a magnitude of about 5 cm. Generally speaking, the diagram shows that site displacements due to solid earth tides cannot be omitted as they cause diurnal variations of more than 2 dm in the radial coordinate channel. 72
- Figure 2-4** - Resulting interpolation error for 1998/11/20 at 12 h GPS time. The data record for this epoch has been cleaned in the original SP3-file and was interpolated with a 18-point-polynomial, i. e. a data gap of 30 minutes was bridged. In operational use, only 15 minutes need to be bridged. The average RMS error is about 2.5 mm; the RMS for a 17-point-interpolator is identical. The satellite ID corresponds to the PRN number given in RINEX measurement and SP3 orbit files. 80
- Figure 2-5** - Possible problems of the use of high-order polynomials for the approximation of functions. Especially high order polynomials tend to 'swing out' at the boundary regions defined by the given points. This is why extrapolation may turn out to be very critical. Moreover, 'oscillations' between given points may degrade the overall accuracy of polynomial approximations. 80
- Figure 2-6** - Principle of symmetric and non-symmetric interpolation. Results showed that non-symmetric interpolation suffers from boundary problems related to swing-out effects and is therefore not recommended. Symmetric interpolation, however, requires that orbit data from both the previous and the following day are needed. (Example: The diurnal data batch starts at midnight, so that symmetric interpolation can only be carried out if orbit data starting at approximately 22 h GPS time of the previous day are available). 81
- Figure 2-7** - Time indices for GPS signal transmission and receipt. The true GPS time of signal transmission is denoted as t_{OT} . This epoch is offset by the satellite clock error δt^i and yields t'_{OT} . The same is true for the receipt time: The true epoch of receipt t_{OR} is offset by the receiver clock error δt_A at station A and the error-corrupted epoch is denoted as t'_{OR} . This is the time recorded by the GPS receiver. As a consequence, the true time of signal transmission τ_A^i between satellite i and receiver A is not equal to the recorded signal transmission time PR_A^i/c 82
- Figure 2-8** - GPS space vehicle body coordinate system after FLIEGEL et al. [1992]. The z-axis points towards the earth center. The z- and x-axis as well as the sun are within one and the same plane (the x-z-plane) and the y-axis points along one of the solar panels so that x-, y- and z-axis constitute a right-handed coordinate system having its origin in the satellite's mass center. The

- drawing shows a NAVSTAR Block I spacecraft. For all newer satellite types, the body-fixed coordinate system has been maintained as described, but the phase center offsets can be different.⁸⁶
- Figure 2-9** - Umbra and penumbra scenarios for GPS satellites following MITTON [1977]. The eclipsing season is difficult to model due to the fact that the satellite tries to adjust the solar panels towards the sun, but cannot find it and therefore begins to rotate around the yaw-axis. 88
- Figure 2-10** - Ray-tracing of umbra and penumbra events. Point P_s shows the center of the sun, P_{s1} an upper and P_{s2} a lower surface point of the solar body. P_E is the center of the earth and P_{E1} an upper surface point of it. P_{SV} shows the GPS space vehicle and P_U is the point of maximum umbra extend. 89
- Figure 2-11** - Transformation of the space vehicle position into the ray-tracing coordinate system with help of triangle P_s - P_E - P_{SV} 90
- Figure 2-12** - Kalman filtering chain illustrating where blunder detection takes place. The level-D check is intended to reveal poor observations by testing the vector of innovations, whereas the level-U check is to reveal problems with the stochastic model of the parameter vector (not the measurements), e. g. due to the fact that the process noise of a particular state has been chosen much too small. 109
- Figure 2-13** - Algorithm to find the optimal and independent set of shortest baselines after MERVART et al. [1994]. The criterion chosen here is the baseline length which is minimized. It is also possible to select the number of measurements as criterion to compose the network. 122
- Figure 2-14** - Centered network. In this example, monitoring station Oberpfaffenhofen (OBER) is of primary interest and therefore, all other network points are centered on this station. 123
- Figure 2-15** - Network composed of a set of shortest independent baselines. For n sites, all those $n-1$ independent baselines are used that have shortest baseline length. This may reduce remaining uncertainties that are proportional to the distance between two stations. 124
- Figure 2-16** - Identification of poorly performing network stations. The values connected to each baseline are the numbers of double difference observations (linearly combined phase measurements) that could be built for the particular baseline. Clearly, site Wettzell (WTZR) can be isolated as mal-functioning. 124
- Figure 2-17** - Exclusion of bad tracking site. Monitor station Wettzell (WTZR) has been excluded from the network and the remaining network is composed of a new set of shortest independent baselines. 125
- Figure 2-18** - Re-connection of bad tracking site. Station Wettzell (WTZR) is relinked to the network, but in contrast to the original network setup it is connected as an isolated site that cannot destabilize the network any longer. 125
- Figure 2-19** - Outline of algorithm for detection and isolation of bad receivers. The criterion for the test is the number of double difference (dd) observations in comparison to the maximum number of dd-observations reached in the network (about 12000 to 15000 linearly combined double differences for diurnal data batches with 30 second data sampling). The total number of stations is denoted with symbol ' n ', so there are exactly ' $n-1$ ' baselines to check. The detection threshold usually lies in the range of 0.6 (60%). 126
- Figure 3-1** - Schematic of the tropospheric and stratospheric layers and the tropopause after MOCKLER [1995]. The mean vertical distribution of temperature and water vapor mixing ratio (logarithmic scale) are shown. 129
- Figure 3-2** - Typical vertical profiles for IGS tracking station Oberpfaffenhofen (OBER) near Munich, Germany on 10 April 2000. The data were extracted from the NOAA/NCEP GDAS numerical weather model (\rightarrow chapter 4). Note that the height axis is expressed by pressure because all vertically distributed data stored in weather models are referenced to pre-defined pressure levels and not to height. Geopotential height corresponds to what is known in geodesy by the term "dynamic height". 130
- Figure 3-3** - Comparison of Hopfield and Saastamoinen hydrostatic models in zenith direction. The Saastamoinen model is assumed to be the most accurate hydrostatic model and is therefore treated as reference. Each dot marks the RMS precision of the Hopfield model with respect to the chosen reference for a particular site of the IGS tracking network. Data were collected and processed from June 1999 up to March 2000. 144
- Figure 3-4** - Accuracy assessment of the MOPS hydrostatic model in zenith direction with the Saastamoinen model as reference. 145

- Figure 3-5** - RMS diagrams for accuracy assessments of the Hopfield, Mendes and MOPS zenith wet delay models. A linear latitude-dependent trend function is indicated by dashed lines. Each dot represents the average RMS for a particular station of the IGS tracking network..... 148
- Figure 3-6** - Curved path of microwave rays in an atmosphere being composed of spherical shells, from SAASTAMOINEN [1972]. 150
- Figure 3-7** - Results of simulated filter run demonstrating the convergence problem. Apparently, absolute zenith wet delay parameters show a faster convergence if they are derived via long baselines. 166
- Figure 3-8** - Typical network structure for absolute zenith wet delay estimation. This example illustrates the two basic belts, the belt of remote stations and the core network. The latter can be further divided into the region of interest (ROI) and a belt of peripheral stations that will be necessary if 2-D interpolation of the results shall be performed..... 168
- Figure 3-9** - Comparison of selected hydrostatic mapping functions with the Niell model serving as reference. The left diagram shows mapping functions of high precision and the figure on the right deals with the most simple approach, the cosecant model which is insufficiently weak for lower elevations. The models are computed for a virtual point at 48° latitude, a geopotential height of 550 m and a radial distance of 6855 km with a surface pressure of 985 hPa, a temperature of 15 °C, a relative humidity of 60%, a temperature lapse rate of -6.81 K/km and a tropopause height of 11 km. The differences in mapping function value were scaled by 2200 mm of zenith hydrostatic delay in order to obtain quantities in units of slant path delay. 171
- Figure 3-10** - Empirical auto-covariance function for IGS tracking station Potsdam (POTS, Germany). The function is given for the first day in a zoom-window on the upper right of the diagram. 179
- Figure 3-11** - Auto-covariance function for IGS tracking station Bahrain (BAHR). The upper zoom-window shows the function during the first 24 hours. Moreover, colored noise components are shown in the zoom-window on the middle, right part of the diagram. 179
- Figure 3-12** - Spatial distribution of the process noise parameters for selected tracking stations of the IGS network. A slight latitudinal dependency can be stated where highest process noise lies in the tropics and smallest values can be found pole-wards. This corresponds to the amplitude of zenith wet delays which are highest near the equator and smallest at the poles as well. See Appendix I for a complete table of the process noise values determined with help of the TropAC database. 180
- Figure 3-13** - Residuals of the least-squares fit of the process noise values to the approximation function..... 180
- Figure 3-14** - Zenith wet delay variability from analysis with help of numerical weather fields. The left y-axis shows the group-variability, e. g. hourly differences of 1 up to 2 mm occur in about 25% of the cases. The right y-axis gives the integrated, cumulative probability, e. g. in 60% of the cases, the variability is equal to or less than 3 mm. The diagram presents the mean ZWD distribution for the sites Oberpfaffenhofen (OBER, Germany), Zimmerwald (ZIMM, Switzerland) and Seychelles (SEY1). 181
- Figure 3-15** - Comparison of zenith wet delays filtered from GPS phase measurements, vertically integrated delays from global numerical weather fields of medium resolution (NOAA/NCEP GDAS 1° x 1°) and predictions using the well-known Hopfield troposphere model. 183
- Figure 3-16** - Differentiated ZWD time series of the different estimates shown before. The values numerically correspond to the (signed) \sqrt{q} -factors..... 183
- Figure 3-17** - Linear regression analysis results for two tracking stations representing the tropics and sub-tropics. Mauna Kea (MKEA, Hawaii) lies in the tropical belt and does not show any linear trends. Bahrain (BAHR) as an example for the sub-tropics obtains clear linear trend properties, but has a higher scatter than sites in the temperate zone. [scales may differ] 190
- Figure 3-18** - Linear regression analysis results for two tracking stations representing the temperate and the polar zone. Oberpfaffenhofen (OBER, temperate zone) and Fairbanks (FAIR, Alaska/polar region) show clear linear relations. Fairbanks reveals an outlying cluster in the range of 4 to 20 °C of surface temperature. This site is meteorologically problematic as it often suffers from inversion scenarios in the very lower troposphere, see HERRING [1992]. [scales may differ] 191
- Figure 4-1** - Data representation in global numerical weather fields of type GRIB 3 (NOAA NCEP GDAS 1° x 1°). The data in the output fields are organized in 26 vertical layers containing geopotential heights for the corresponding pressure levels as well as temperature. Relative humidity is given for 21 layers. In horizontal direction, the data are stored in matrix layout (i. e. an equi-rectangular projection is used) with 181 rows and 360 columns corresponding to a resolution of 1° x 1°. 194

- Figure 4-2** - Vertical and horizontal interpolation sequences illustrated for surface pressure determination. The 1-pillar-method performs horizontal interpolation for the pressure layers first and thereby interpolates the geopotential height for the horizontal position of the target point at the corresponding pressure level. Afterwards, vertical interpolation is performed using the two nearest vertical neighbors. The 4-pillar-method follows a different strategy: First, vertical interpolation is performed for all 4 neighboring pillars. This yields pressure values which are already referenced to the height of the target point. After this, horizontal interpolation takes place. 198
- Figure 4-3** - Nearest horizontal neighbors for point ϕ^*, λ . The spherical distances between the grid points P_{ij} and the target point are indicated by $r \cdot \psi_{ij}$ with r being the earth radius. 202
- Figure 4-4** - TROPEX troposphere correction files contain all gridded information necessary to compute tropospheric delays in zenith direction. These files are created from 3-D numerical weather fields, but in contrast to the NWM-data, TROPEX uses a 2-D data representation and models vertical dependencies with help of reduction coefficients. Moreover, tropospheric delays from numerical weather models and those derived from GPS measurements can be combined. 210
- Figure 4-5** - Total pressure over Germany on 11 March 2000 at 12 h UTC. All pressure data are given in units of [hPa] and referenced to a common geopotential height of 500 m in order to reduce topographic effects. The model output grid with a resolution of $1^\circ \times 1^\circ$ has been projected into the image and is indicated by dots. 215
- Figure 4-6** - Pressure scale heights q_p over Germany on 11 March 2000 at 12 h UTC in units of [km]. The theoretical value of 8 km derived in section 4.2.1.2 marks the very lowest range of those scale heights actually occurring that also show a considerable variability of 2 km and particularly high horizontal gradients over northern Germany. 215
- Figure 4-7** - Zenith wet delays over Germany on 11 March 2000 at 12 h UTC. All delay data are given in units of [mm] and referenced to a common geopotential height of 2000 m in order to reduce topographic effects. For this reason, the zenith delay values are rather small in comparison to those at usual heights of 100 to 500 m. 216
- Figure 4-8** - Water vapor/zenith wet delay scale heights over Germany on 11 March 2000 at 12 h UTC in units of [km]. The plot shows that actual scale heights may reasonably deviate from the average value of about 2.0 km. 216
- Figure 4-9** - Mean atmospheric temperature between the surface and the tropopause height over Germany on 11 March 2000 at 12 h UTC in units of [$^\circ\text{C}$]. 217
- Figure 4-10** - Temperature lapse rates over Germany on 11 March 2000 at 12 h UTC in units of [K/km]. Smallest lapse rates of about -6 K/km occur at the German North Sea coast, steeper temperature gradients can be seen at Germany's north-eastern part. 217
- Figure 4-11** - Tropopause heights over Germany on 11 March 2000 at 12 h UTC in units of [km]. It becomes evident that variations of more than 4 km may occur over distances as small as the north-south extension of Germany and - what is even more important - anomalies of regional extend are apparently possible as shown over the eastern part of the German North Sea coast. 218
- Figure 4-12** - Relating model grid points and irregularly distributed GPS-sites to each other. Following the procedures of interpolation already discussed in the preceding sections, only the 4 nearest model grid points are related to a particular GPS tracking station. This means that certain grid points may remain totally unaffected by the combination algorithm and can be excluded from processing. 224
- Figure 5-1** - Diagram of diurnal pressure biases and standard deviations (σ) for IGS monitor station Potsdam (POTS, Germany) in July 1999. 231
- Figure 5-2** - Diagram of diurnal pressure biases and standard deviations (σ) for IGS monitor station Oberpfaffenhofen (OBER, Germany) in July 1999. 231
- Figure 5-3** - Diagram of diurnal temperature biases and standard deviations (σ) for IGS monitor station Potsdam (POTS, Germany) in July 1999. 233
- Figure 5-4** - Diagram of diurnal temperature biases and standard deviations (σ) for IGS monitor station Oberpfaffenhofen (OBER, Germany) in July 1999. 233
- Figure 5-5** - Diagram of diurnal relative humidity biases and standard deviations (σ) for IGS monitor station Potsdam (POTS, Germany) in July 1999. 235
- Figure 5-6** - Diagram of diurnal relative humidity biases and standard deviations (σ) for IGS monitor station Oberpfaffenhofen (OBER, Germany) in July 1999. 235

Figure 5-7 - Differences between the temperature lapse rates from radiosonde launches at site 10304 and those derived from the vertical temperature profiles of the GDAS weather fields.	236
Figure 5-8 - Differences between the temperature lapse rates from radiosonde launches at site 10437 and those derived from the vertical temperature profiles of the GDAS weather fields.	236
Figure 5-9 - Differences between the temperature lapse rates from radiosonde launches at site 10828 and those derived from the vertical temperature profiles of the GDAS weather fields.	237
Figure 5-10 - Differences between the temperature lapse rates from radiosonde launches at site 10868 and those derived from the vertical temperature profiles of the GDAS weather fields.	237
Figure 5-11 - Comparison of pressure data from the DWD weather model with in situ measurements. Diurnal pressure biases and standard deviations (sigma) for IGS monitor station Potsdam (POTS, Germany) in July 1999 are shown.	239
Figure 5-12 - Comparison of pressure data from the DWD weather model with in situ measurements. Diurnal pressure biases and standard deviations (sigma) for IGS monitor station Wettzell (WTZR, Germany) in July 1999 are shown.	239
Figure 5-13 - Differences between the mean temperatures from radiosonde launches at site 10304 and those derived from the wet refractivity profiles of the GDAS weather fields.	242
Figure 5-14 - Differences between the mean temperatures from radiosonde launches at site 10437 and those derived from the wet refractivity profiles of the GDAS weather fields.	242
Figure 5-15 - Differences between the mean temperatures from radiosonde launches at site 10828 and those derived from the wet refractivity profiles of the GDAS weather fields.	243
Figure 5-16 - Differences between the mean temperatures from radiosonde launches at site 10868 and those derived from the wet refractivity profiles of the GDAS weather fields.	243
Figure 5-17 - Comparison of the Chao mapping function and obliquity factors derived from the GDAS numerical weather fields interpolated for IGS tracking station Oberpfaffenhofen. The reference model is the mapping function of Niell. The differences in hydrostatic delay were scaled by 2.2 m and the wet delay differences by 2 dm, so that the resulting difference can be compared to the error in slant hydrostatic/wet delay at an elevation angle of 15°.....	244
Figure 6-1 - Network stations and baseline setup for the long-term experiment from October 1998 to April 1999. Long baselines are those from ZWEN to BAHN (3460 km) and from HERS to REYK (1970 km).	249
Figure 6-2 - Diagram of the ratio of rejected observations for each day of the long-term experiment. This percentage is defined by dividing the number of outliers per baseline by the total number of double difference observations. The average ratio is around 0.3% what corresponds to about 30 detected blunders per baseline and day.	250
Figure 6-3 - Diagram of diurnal RMS values during the long-term experiment for tracking station Potsdam (POTS, Germany).	252
Figure 6-4 - Diagram of diurnal RMS values during the long-term experiment for tracking station Oberpfaffenhofen (OBER, Germany).	252
Figure 6-5 - Diagram of diurnal RMS values during the long-term experiment for tracking station Wettzell (WTZR, Germany).	253
Figure 6-6 - Diagram of diurnal RMS values during the long-term experiment for tracking station Bahrain (BAHR).	253
Figure 6-7 - Diagram of diurnal biases during the long-term experiment for tracking station Oberpfaffenhofen (OBER, Germany).	254
Figure 6-8 - Diagram of diurnal biases during the long-term experiment for tracking station Bahrain (BAHR).	254
Figure 6-9 - Network plot illustrating the mean systematic errors during the long-term experiment for all network stations. Largest biases can be seen at the network periphery, i. e. at stations connected to the network via long baselines.	255
Figure 6-10 - Network stations and baseline setup for the experiments OBER-I and OBER-II. The network is centered on Oberpfaffenhofen (OBER, Germany).	257
Figure 6-11 - Diagram of the ratio of rejected observations for each day of the OBER-I experiment. This percentage is defined by dividing the mean number of outliers per baseline by the total number of double difference observations. The average ratio is around 0.2% what corresponds to less than 25 detected blunders per baseline and day.	259

Figure 6-12 - Comparison of mean biases for different tropospheric mapping functions. (HERR: Herring mapping function, → 3.2.2.1.6 and → 3.2.2.2.4; SAAS: Saastamoinen mapping function, → 3.2.2.1.1)	260
Figure 6-13 - Comparison of mean RMS values for different tropospheric mapping functions. (HERR: Herring mapping function, SAAS: Saastamoinen mapping function)	260
Figure 6-14 - Diurnal biases and RMS values that occurred during the OBER-I experiment with the Chao tropospheric mapping functions in use.	261
Figure 6-15 - Diurnal biases and RMS values that occurred during the OBER-I experiment with the Niell tropospheric mapping functions in use.	261
Figure 6-16 - Comparison of mean biases introduced through residual ionospheric errors in the linear combinations of the GPS measurements. IGS zenith neutral delays were used as reference data.	264
Figure 6-17 - Comparison of the mean RMS values for the different linear combinations of the GPS measurements without and with ionospheric propagation delay modeling using IONEX files.	264
Figure 6-18 - Comparison of mean biases depending of the elevation cutoff. IGS zenith neutral delays were used as reference data.	265
Figure 6-19 - Comparison of the mean RMS values depending of the elevation cutoff. IGS zenith neutral delays were used as reference data.	265
Figure 6-20 - Comparison of mean biases using different GPS orbit products. IGS zenith neutral delays were used as reference data.	268
Figure 6-21 - Comparison of mean RMS values using different GPS orbit products. IGS zenith neutral delays were used as reference data.	268
Figure 6-22 - Network stations and baseline setup for the EUREF/GREF experiment (October 1997). The experiment discussed here only makes use of the sub-network shown in this plot. The full GREF network is not shown.	270
Figure 6-23 - Uncertainty of the IWV conversion for POTS. The reference data were computed with help of NWM-derived Q-factors and compared with the following models: Emardson (top, see → 3.5.3.2), Bevis (middle, see → 3.5.3.1) and TropAC/GDAS (bottom, see → 3.5.3.3).	273
Figure 6-24 - Integrated water vapor time series for Potsdam (POTS, Germany) analyzed by TropAC (black) and IGS (grey). The differences between both water vapor curves are plotted as well.	274
Figure 6-25 - Integrated water vapor time series for Wettzell (WTZR, Germany) analyzed by TropAC (black) and IGS (grey). The differences between both water vapor curves are plotted as well.	274
Figure 6-26 - Integrated water vapor time series for Potsdam (POTS, Germany) analyzed by TropAC (black) and CODE (grey). The differences between both water vapor curves are plotted as well.	275
Figure 6-27 - Integrated water vapor time series for Wettzell (WTZR, Germany) analyzed by TropAC (black) and CODE (gray). The differences between both water vapor curves are plotted as well.	275
Figure 6-28 - Site-specific mean biases from the comparison of GPS-derived IWV (3 different analysis centers) and IWV from high-resolution numerical weather models.	277
Figure 6-29 - Site-specific mean RMS values from the comparison of GPS-derived IWV (3 different analysis centers) and IWV from high-resolution numerical weather models.	277
Figure 6-30 - Network stations and baseline setup for the multipath experiment during October 1997. The network was centered either on WTZR (shown here) or WTZT.	278
Figure 6-31 - Comparison of hourly zenith neutral delays estimated at tracking station WTZR and at WTZT on 29 October 1997.	279
Figure 6-32 - Comparison of hourly zenith neutral delays estimated at tracking station WTZR and at WTZT on 30 October 1997.	279
Figure 6-33 - Network stations and baseline setup for the water vapor radiometer validation experiment. The network was centered IGS tracking station Potsdam (POTS, Germany).	280
Figure 6-34 - Water vapor time series from WVR (gray) and GPS (black) at tracking station Potsdam (POTS, Germany) starting on 3 January 1999. The difference between both curves is plotted at the bottom of the diagram.	283
Figure 6-35 - Water vapor time series from WVR (gray) and GPS (black) at tracking station Potsdam (POTS, Germany) starting on 12 February 1999. The difference between both curves is plotted at the bottom of the diagram.	283
Figure 6-36 - Estimated mapping function coefficients at tracking station Potsdam (POTS, Germany) during the WVR experiment. The values of the y-axis need to be divided by a factor of 1000 in order to yield the mapping function coefficient.	285

Figure 6-37 - Estimated northward horizontal gradients at tracking station Potsdam (POTS, Germany) during the WVR experiment. The band of standard deviations is plotted as well in order to allow an assessment of the significance of the gradients.	286
Figure 6-38 - Estimated eastward horizontal gradients at tracking station Potsdam (POTS, Germany) during the WVR experiment. The band of standard deviations is plotted as well in order to allow an assessment of the significance of the gradients.	286
Figure 6-39 - Zenith wet delays from water vapor radiometer in comparison to GPS Kalman filter estimates with a process noise of $q = 1 \text{ mm}^2/\text{h}$	288
Figure 6-40 - Zenith wet delays from water vapor radiometer in comparison to GPS Kalman filter estimates with a process noise of $q = 8.4 \text{ mm}^2/\text{h}$	288
Figure 6-41 - Zenith wet delays from water vapor radiometer in comparison to GPS Kalman filter estimates; q was defined dynamically and doubly amplified ($q_{\text{AMP}} = 2.0$).	289
Figure 6-42 - Zenith wet delays from water vapor radiometer in comparison to GPS Kalman filter estimates; q was chosen to be the maximum of all dynamically determined q -factors for the entire data batch resulting in $q = 100 \text{ mm}^2/\text{h}$	289
Figure 7-1 - Differences between the pressure scale heights from radiosonde launches at site 10304 and those derived from the vertical pressure profiles of the GDAS weather fields.	292
Figure 7-2 - Differences between the pressure scale heights from radiosonde launches at site 10437 and those derived from the vertical pressure profiles of the GDAS weather fields.	292
Figure 7-3 - Differences between the pressure scale heights from radiosonde launches at site 10828 and those derived from the vertical pressure profiles of the GDAS weather fields.	293
Figure 7-4 - Differences between the pressure scale heights from radiosonde launches at site 10868 and those derived from the vertical pressure profiles of the GDAS weather fields.	293
Figure 7-5 - Differences between the water vapor scale heights from radiosonde launches at site 10304 and those derived from the vertical ZWD profiles of the GDAS weather fields.	294
Figure 7-6 - Differences between the water vapor scale heights from radiosonde launches at site 10437 and those derived from the vertical ZWD profiles of the GDAS weather fields.	294
Figure 7-7 - Differences between the water vapor scale heights from radiosonde launches at site 10828 and those derived from the vertical ZWD profiles of the GDAS weather fields.	295
Figure 7-8 - Differences between the water vapor scale heights from radiosonde launches at site 10868 and those derived from the vertical ZWD profiles of the GDAS weather fields.	295
Figure 7-9 - Precision of the pressure profile fits over Germany on 1 July 1999 at 12 h UTC in units of [hPa]. The standard deviations plotted in the map are the standard deviations of the weight unit resulting from the fit of the vertical pressure profiles to the TROPEX pressure reduction model (\rightarrow 4.4.2.2, formula 4-54).	298
Figure 7-10 - Precision of the zenith wet delay profile fits over Germany on 1 July 1999 at 12 h UTC in units of [mm]. The standard deviations plotted in the map are the standard deviations of the weight unit resulting from the fit of the vertical zenith wet delay profiles to the TROPEX ZWD reduction model (\rightarrow 4.4.3.2, formula 4-56).	298
Figure 7-11 - Diurnal biases between zenith total delays from TROPEX files (GDAS-derived) and GPS total delays for IGS tracking station Potsdam (POTS, Germany).	300
Figure 7-12 - Diurnal biases between zenith total delays from TROPEX files (GDAS-derived) and GPS total delays for IGS tracking station Oberpfaffenhofen (OBER, Germany).	300
Figure 7-13 - Diurnal biases between zenith total delays from TROPEX files (GDAS-derived) and GPS total delays for IGS tracking station Wettzell (WTZR, Germany).	301
Figure 7-14 - Diurnal biases between zenith total delays from TROPEX files (GDAS-derived) and GPS total delays for IGS tracking station Cocos Island (COCO).	301
Figure 7-15 - Diurnal RMS values between zenith total delays from TROPEX files (GDAS-derived) and GPS total delays for IGS tracking station Potsdam (POTS, Germany).	302
Figure 7-16 - Diurnal RMS values between zenith total delays from TROPEX files (GDAS-derived) and GPS total delays for IGS tracking station Oberpfaffenhofen (OBER, Germany).	302
Figure 7-17 - Diurnal RMS values between zenith total delays from combined TROPEX solution fields and GPS total delays for IGS tracking station Potsdam (POTS, Germany).	303
Figure 7-18 - Diurnal RMS values between zenith total delays from combined TROPEX solution fields and GPS total delays for IGS tracking station Oberpfaffenhofen (OBER, Germany).	303
Figure 7-19 - Diurnal RMS values between zenith total delays from TROPEX files (GDAS-derived) and GPS total delays for IGS tracking station Wettzell (WTZR, Germany).	304

Figure 7-20 - Diurnal RMS values between zenith total delays from TROPEX files (GDAS-derived) and GPS total delays for IGS tracking station Cocos Island (COCO).....	304
Figure 7-21 - Diurnal RMS values between zenith total delays from combined TROPEX solution fields and GPS total delays for IGS tracking station Wettzell (WTZR, Germany).....	305
Figure 7-22 - Diurnal RMS values between zenith total delays from combined TROPEX solution fields and GPS total delays for IGS tracking station Cocos Island (COCO).....	305
Figure 7-23 - Assimilated GPS stations of the IGS tracking network (European part) and affected grid points of the GDAS/TROPEX file (symbol "+").....	307
Figure 7-24 - Comparison of ZND from GPS and GDAS/TROPEX files for tracking station Potsdam (POTS, Germany).	310
Figure 7-25 - Comparison of ZND from GPS and GDAS/TROPEX files for tracking station Oberpfaffenhofen (OBER, Germany).....	310
Figure 7-26 - Comparison of ZND from GPS and combined GDAS & GPS TROPEX files for tracking station Potsdam (POTS, Germany).	311
Figure 7-27 - Comparison of ZND from GPS and combined GDAS & GPS TROPEX files for tracking station Oberpfaffenhofen (OBER, Germany).	311
Figure A-1 - Classification of climate zones of the earth from HOHL [1981, p. 142].	342
Figure A-2 - Global chart of the monitor stations of the IGS tracking network. A zoomed map for those sites located at the European continent is given on the following page.	343
Figure A-3 - Chart of the monitor stations of the IGS tracking network located in Europe.	344
Figure A-4 - IWV samples (gray) and the harmonic function (black) for tracking station AOML at a latitude of 25.73°.	348
Figure A-5 - IWV samples (gray) and the harmonic function (black) for tracking station OBER at a latitude of 48.09°.	348
Figure A-6 - IWV samples (gray) and the harmonic function (black) for tracking station OBER at a latitude of 52.38°.	349
Figure A-7 - IWV samples (gray) and the harmonic function (black) for tracking station OBER at a latitude of 64.98°.	349
Figure A-8 - Sequence of zenith wet delay images for area of the Mediterranean Sea. The legend for the zenith wet delay values is given on the preceding page in units of millimeters. Blue colors indicate wet areas with a huge amount of humidity, red colors represent dry regions. The delays have been reduced to real topography using the standard 5' x 5' digital elevation model of the institute's tropospheric analysis system. The boundaries of the maps are 36° ... 45° (latitude) and -6° ... 16° (longitude). Time is given in UTC.....	357

List of Tables

Table 1-1 - Characteristics of water vapor observing systems following MOCKLER [1995]. It should be noted that GPS provides several ways to explore the atmosphere. The space segment only provides the signal emitters and it depends on the environment where the receivers are operated on how atmospheric sounding is possible. In this way, the GPS radio occultation technique can be classified as satellite-to-satellite technique and the ground-based GPS approach uses receivers of tracking networks located at or near the earth's surface.	42
Table 2-1 - Major modules of TropAC TRIDENT and their purpose within the processing package.	49
Table 2-2 - Characteristic properties of the original signals (1 st section), typical linear L_1 - L_2 -combinations which reduce the ionospheric propagation delay (2 nd section) and additional signals for special purposes like the wide and the narrow lane signal (3 rd section). The widely used L_C signal is free of the 1 st order ionospheric effect, but has the disadvantage of floating ambiguities which complicates ambiguity fixing whereas $L_{77,60}$ has integer ambiguities and is ionosphere-free as well, but is practically unusable for ambiguity fixing due to its tiny wavelength. The wavelength $\lambda_{a1,a2}$ as well as the noise level σ_ϕ are given in units of millimeters	61
Table 2-3 - Amplitude scaling factors f and phase angle offsets u for the required partial tides according to DOODSON [1928, pp. 274-275, tables 25, 26 and 27].	72
Table 2-4 - Center of mass to antenna phase center offsets for GPS spacecraft in use after KING [2000]. The replenishment satellites Block IIR are designed differently from their predecessors Block II/IIA and have a negligibly small offset, although there is still some dispute about which values to use. For the TropAC analysis system, the values above have been adopted. The GAMIT software uses the following offsets: $\Delta x = -3.1$ mm, $\Delta y = -1.2$ mm, $\Delta z = 0.0$ m after KING [2000].	87
Table 2-5 - GPS satellite PRN numbers and corresponding satellite types (Block). The entries are valid from the date of inauguration and were updated in December 2000 by KING [2000].	88
Table 2-6 - Datum defects of 3-D space-geodetic networks. The parameter index defines the order in which the datum parameters are handled by the analysis software. Example: If - for any reason - only 4 datum defects are to be compensated, then module PAF_TRAN will choose the 3 datum shift constants (translations) and a rotation around the X-axis.	120
Table 3-1 - Primary constituents of dry air after DAVIS et al. [1985]. It should be pointed out that none of these primary constituents possesses a permanent dipole moment; this characteristic property is almost solely devoted to the nature of water molecules.	131
Table 3-2 - Average values for the meteorological parameters used for tropospheric delay prediction. The formulas given in the following paragraph for interpolation are identical for all values. For this reason, the corresponding symbols will be substituted by ξ_0 . Note that the sign of the temperature lapse rate is naturally negative what is accounted for directly in the formulas of this model. λ describes the dimensionless lapse rate of water vapor and is needed for computation of the wet component only.	142
Table 3-3 - Seasonal variations of the meteorological parameters used for tropospheric delay estimation. The formulas given in the following paragraph for interpolation are identical for all values. For this reason, the corresponding symbols will be substituted by $\Delta\xi$	143
Table 3-4 - Correction terms for the Saastamoinen neutral delay model from SPILKER [1996]. A slightly different table for the B-values can be found in SAASTAMOINEN [1972]. H_0 is the station height above the mean sea level.	152
Table 3-5 - Coefficients of the Niell hydrostatic mapping function (average values).	157
Table 3-6 - Seasonal variations/ amplitudes of the Niell hydrostatic mapping function.	157
Table 3-7 - Coefficients of the Niell hydrostatic mapping function (height correction).	157
Table 3-8 - Coefficients of the Niell wet mapping function. This table contains average values in dependency of latitude. Seasonal variations are not modeled for the wet component.	160
Table 3-9 - Impact of 1.0/0.3 cm position error for each coordinate component at site A on the zenith wet delay estimates. δ -values denote the actual error whereas σ -values represent the standard deviations; ρ is the correlation coefficient between ZWD on site A and B.	164
Table 3-10 - Impact of 0.1/1.0 m satellite position error for each coordinate component of PRN 6 on the zenith wet delay estimates. δ -values denote the error whereas σ -values represent the standard deviations; ρ is the correlation coefficient between ZWD on site A and B.	165

Table 3-11 - Mean regional values for the coefficients of the polynomial Q-model taking surface temperature into account; from EMARDSON [1998, paper F].....	188
Table 3-12 - Regression coefficients and mean regional conversion coefficients sorted by major climatic regions. The tropics are assumed to range from 0° to 20° latitude and the temperate zone from 40° to 60°	188
Table 4-1 - Characteristics of the numerical weather fields available from the U. S. National Center for Environmental Prediction (NCEP, NOAA). The abbreviations given are only used to provide a simple identification within the text and do not necessarily represent official names. The GRID IDs specifying the contents are given in the very right column.	193
Table 4-2 - Contents of TROPEX troposphere correction files (typical data layers from the analysis of GDAS numerical weather fields). Note that the geo-reference layers are only given once as they are no time-varying data and latitude/longitude are only given for the special case of irregular data (i. e. GPS only). Data belonging to the category "other atmospheric properties" are optional data that may be included, but are not necessary in order to compute zenith neutral delays.	210
Table 5-1 - Result table of surface meteorological data comparison for July 1999. The first column gives the name of the IGS tracking station (refer to Appendix III for the location of these stations), the second contains the number of samples used for the comparison followed by the biases and standard deviations ("sigma") of the particular quantities. The results printed here belong to configuration I (→ 5.1.1.1).....	229
Table 5-2 - Mean biases and standard deviations (sigma) for the three different configurations applied to the vertical pressure interpolation.	232
Table 5-3 - Result table of surface meteorological data comparison with high-resolution numerical weather fields for October 1997. The first column gives the name of the IGS tracking station (refer to Appendix III for the location of these stations), the second contains the number of samples used for the comparison followed by the biases and standard deviations ("sigma") of the particular quantities. The stations inside Germany (POTS, WTZR) are covered by the Germany-model (14 km horizontal resolution) of the German Weather Service (DWD), and the Europe-model (55 km horizontal resolution) was applied for the stations outside Germany.....	238
Table 5-4 - Location of those radiosonde launch sites used for the comparison of temperature lapse rates and mean atmospheric temperatures.	240
Table 5-5 - Mean accuracy quantities for the temperature lapse rate. The radiosonde launch site identifier is given in the first column followed by the bias (systematic offset), the standard deviation (bias-reduced precision) and the RMS (bias inclusive).	240
Table 5-6 - Mean accuracy quantities for the mean temperature of the troposphere. The radiosonde launch site identifier is given in the first column followed by the bias (systematic offset), the standard deviation (bias-reduced precision) and the RMS (bias inclusive).	241
Table 5-7 - Mean accuracy quantities for the hydrostatic and wet delay mapping functions plotted in Figure 5-17.	244
Table 6-1 - Characteristics and objectives of the long-term experiment. The standard configuration was used for this analysis. Ambiguity fixing was disabled, the Chao hydrostatic and wet mapping functions were used and the elevation mask was set to 15°. See → Appendix VI for the full configuration file.	248
Table 6-2 - Overview of the availability of the network stations. Oberpfaffenhofen (OBER, Germany) is the station with maximum availability. REYK and ZWEN were intentionally not continually present and the observation data for GRAZ became available at the beginning of 1999.	249
Table 6-3 - Overview of the diurnal data availability for the network stations. Each diurnal data batch comprises dual-frequency carrier phase measurements and pseudo-ranges with a sampling interval of 30 seconds, i. e. 2779 epochs. This table lists the total number of epochs that were missing inside these diurnal data batches - it does not account for total receiver failures (see preceding table for this statistic). Example: WTZR had 3028 missing epochs and was available for 170 days, so 17.8 epochs (= "ratio") were missing per day in average. This corresponds to a data gap of about 9 minutes per day.	250
Table 6-4 - Mean biases, standard deviations ("sigma") and RMS values for the network stations of the long-term experiment. The column labeled "samples" is identical to the number of days compared. Each day comprises 24 hourly zenith neutral and wet delays.....	251

Table 6-5 - Characteristics and objectives of experiment OBER-I. See → Appendix VI for the full configuration file.....	257
Table 6-6 - Overview of the availability of the network stations. OBER, GRAZ, ONSA and ZWEN were continually present, data from POTS were only used for half of the month.	258
Table 6-7 - Overview of the diurnal data availability of the network stations. This table lists the total number of epochs that were missing inside these diurnal data batches and the number of missing epoch per day ("ratio") - it does not account for total receiver failures (see preceding table for this statistic).	258
Table 6-8 - Mean biases, standard deviations ("sigma") and RMS values for the network stations of the OBER-I experiment in comparison to the IGS combined tropospheric product (= reference data). The column labeled "samples" is identical to the number of days compared. Each day comprises 24 hourly zenith neutral and wet delays.	258
Table 6-9 - Extract from the information file of the TropAC TRIDENT software for 30 July 1999 (experiment OBER-I). All baselines are well-performing expect for baseline OBER-POTS. Obviously, the measurement data for Potsdam (POTS, Germany) were corrupted from 0 h to 4 h GPS time.	259
Table 6-10 - Result tables for the default run without horizontal gradients (left) and the run with horizontal gradients from GDAS numerical weather fields (right). Reference data: IGS zenith neutral delays.....	263
Table 6-11 - Result tables for the run without (left) and with (right) 2 nd order ionospheric corrections applied. Reference data: IGS zenith neutral delays.....	263
Table 6-12 - Comparison of GPS-derived zenith neutral and wet delays with integrated quantities from radiosonde profiles for Oberschleißheim near Oberpfaffenhofen (OBER, Germany). The entry "IGS" means that the comparison is based on the IGS combined zenith total delay product whereas "TropAC" stands for the results from the TropAC analysis software.....	266
Table 6-13 - Characteristics and objectives of experiment OBER-II. See Appendix VI for the full configuration file.....	267
Table 6-14 - Results of the OBER-II experiment. The IGS combined troposphere product was used as reference data set. The results of the tropospheric analysis software TropAC were derived using 4 different orbit products from the IGS, namely predicted (IGP), ultra-rapid (ULT), rapid (IGR) and final orbits (IGS). The accuracy quantities given here are the mean values over the full analysis period of 2 months.....	267
Table 6-15 - Comparison of GPS-derived zenith neutral delays with integrated quantities from radiosonde profiles for Oberschleißheim near Oberpfaffenhofen (OBER, Germany). The entry "IGS" means that the comparison is based on the IGS combined zenith total delays product whereas "TropAC" stands for the results from the tropospheric analysis software.	269
Table 6-16 - Characteristics and objectives of the EUREF/GREF experiment. See Appendix VI for the full configuration file.....	270
Table 6-17 - Mean biases, standard deviations ("sigma") and RMS values for the network stations of the EUREF/GREF experiment in comparison to the IGS combined tropospheric product (= reference data). The column labeled "samples" is identical to the number of days compared. Each day comprises 24 hourly zenith neutral and wet delays.	271
Table 6-18 - Different approaches to derive the mean temperature of the atmospheric and/or the conversion factor to transform zenith wet delays into precipitable water.....	271
Table 6-19 - Table of mean biases, standard deviations and RMS values for the IWV comparison in units of [kg/m ²]. The columns labeled "IGS" show the results from the comparison of the TropAC and the IGS data whereas the columns labeled "CODE" refer to the data of the CODE analysis center. Station ZECK is not included due to obvious inconsistencies of the CODE results.	272
Table 6-20 - Characteristics and objectives of the multipath experiment. See Appendix VI for the full configuration file.....	278
Table 6-21 - Characteristics and objectives of the water vapor radiometer validation experiment.	280
Table 6-22 - Distribution of the difference between the reference data (IWV measured by WVR) and the GPS filter estimated. The column in the middle gives the number of samples belonging to the designated class and the very right column expresses this amount as relative percentage. Less than 4% of the discrepancies exceed a level of 2 kg/m ² and more than 68% of all samples agreed at a level of better than 1 kg/m ²	282

Table 6-23 - Diurnal biases, standard deviations ("sigma", bias-reduced) and RMS values (not bias-reduced) as well as minimum and maximum of the absolute difference between the GPS and the WVR integrated water vapor measurements in units of [kg/m ²].	282
Table 6-24 - Agreement between GPS and WVR results using different processing settings. Some of the configuration options are explained in the text more detailed.	284
Table 7-1 - Comparison of the TROPEX pressure scale heights (derived from GDAS weather fields) and those derived from radiosonde launches (→ 5.2) for July 1999. See footnote below.	296
Table 7-2 - Comparison of the TROPEX zenith wet delay/water vapor scale heights (derived from GDAS weather fields) and those derived from radiosonde launches (→ 5.2) for July 1999.	297
Table 7-3 - Mean biases, standard deviations ("sigma") and RMS values in [mm] for the stations involved in the TROPEX/GDAS validation experiment. IGS ZPD estimates served as reference data. Please refer to → Appendix IV for information about the location of the particular sites.	306
Table 7-4 - Mean biases, standard deviations ("sigma") and RMS values in [mm] after the combination of NWM and GPS delays using blunder detection and variance component estimation.	308
Table 7-5 - Mean biases, standard deviations ("sigma") and RMS values in [mm] after the combination of NWM and GPS delays using pre-weighting and variance component estimation.	309
Table 8-1 - Error budget for ground-based GPS zenith wet delay and integrated water vapor estimation. The components contributing to the total standard deviation of the ZWD (σ_{ZWD}) and integrated water vapor (σ_{IWV}) are assessed for average situations.	316
Table A-1 - Mean zenith wet delays (MEAN), their variability (SIGMA, standard deviation) and random walk parameters (PRO.-NOISE) with precision of fit in unit of [mm/√h]. The ZWD time series is treated as random walk stochastic process. The position of the IGS tracking stations is given by latitude, longitude [°, decimal] and orthometric height [m]. The number of original samples as well as the effective number are given. The effective number of samples takes auto-correlation into account. The smaller this number is in comparison to the original number, the higher the time series is auto-correlated. (last update: 2000/03/15)	335
Table A-2 - Analysis of the TropAC database for linear conversion coefficients of surface into mean atmospheric temperature separated into 4 major climatic zones. The function coefficients are denoted as a and b, respectively, and require the surface temperature to be input in units of degrees centigrade. The number of statistical degrees of freedom of the linear fit is given by "f" and the regression coefficient is denoted as "r". The last three columns give the minimum and maximum surface temperature that were present in the analyzed data set as well as the mean surface temperature of the ensemble. (last update: 2000/03/15)	338
Table A-3 - Description of the columns of the following result tables.	344
Table A-4 - Harmonic IWV analysis of the TropAC database separated into 4 major climatic zones and referenced to the station/antenna height. Last day analyzed: 2000/03/15	347
Table A-5 - Harmonic IWV analysis of the TropAC database separated into 4 major climatic zones and referenced to the mean sea level (0 m). Last day analyzed: 2000/03/15	352
Table A-6 - Mean zenith wet delays/water vapor scale heights for 188 stations of the IGS tracking network. The row "SITE" contains the 4-characters station ID, the number of samples denotes the number of days that were used for the derivation of the mean scale height and the scale height q_{ZWD} is given in meters as well as the associated empirical standard deviation "SIG". Only values obtained using a sufficiently large number of samples should be used. Some scale heights included in this table are based on very few observations. In such cases, it is recommended to use the mean scale height of about 2 km. Last day analyzed: 2000/03/15.	354

List of Symbols

The symbols used in this work and their preferred units are listed in the table below. Note that certain symbols can have several meanings depending on the particular context. In many cases, the symbols are explained separately under each formula where they appear. Units given in the table denote the most commonly used way to express the mentioned quantity. The symbols are not always ordered alphabetically in a rigorous manner. Instead, it was tried to form groups of symbols belonging together. Symbols not listed here might be included in the subsequently printed *List of Acronyms*.

$x > y$	x is higher than y
$x \gg y$	x is much higher than y
$x < y$	x is smaller than y
$x \ll y$	x is much smaller than y
$x = y$	x is equal to y
$x \approx y$	x is approximately equal to y
$x \neq y$	x is unequal to y
$x \equiv y$	x is identical with y
$x \stackrel{!}{=} y$	x is expected to be equal to y (expresses a condition), or x should be equal to y
$x \sim y$	x is proportional to y
$x \rightarrow \infty$	x converges to infinity
$\dots \wedge \dots$	\dots and \dots
$\dots \vee \dots$	\dots or \dots
$\dots \Rightarrow \dots$	from \dots follows that \dots
$\dots \Leftrightarrow \dots$	\dots is equivalent to \dots
$\underline{a} \cdot \underline{b}$	dot product of vectors \underline{a} and \underline{b}
$\underline{a} \times \underline{b}$	cross product of vectors \underline{a} and \underline{b}
\underline{A}^{-1}	inverse of matrix \underline{A}
$ x $	absolute value of x ; $ -5 = 5$, $ 5 = 5$
atan2	special arctan function of the C programming language; computes the heading angle ψ with a range of $-\pi$ to $+\pi$ given the inputs in form of $\sin \psi$ and $\cos \psi$ (arctan only has a range of $-\frac{1}{2}\pi$ to $+\frac{1}{2}\pi$)
arccos	arcus cosine, reverse cosine function
arctan	arcus tangent, reverse tangent function
cos	cosine
csc	cosecants
exp(x)	exponential function e^x with e being the Euler number $e = 2.71 \dots$
int	integer function; $\text{int } -6.55 = -6$; $\text{int } 6.55 = 6$
lim	limes, limit
ln	logarithmus naturalis; natural logarithm
sgn	signum function; $\text{sgn } x = 0$ for $x=0$, -1 for $x<0$ and $+1$ for $x>0$
sin	sine
tan	tangent

trace	sum of all diagonal elements of a (quadratic) matrix
[mm]	millimeters; 1000 mm = 1 m
[cm]	centimeters; 100 cm = 1 m
[dm]	decimeters; 10 dm = 1 m
[m]	meters
[gpm]	geopotential meters; same as meters, but indicates that the corresponding height is a <i>geopotential</i> height
[km]	kilometers; 1000 m = 1 km
[Mm]	megameters; 1000 km = 1 Mm
[m ³]	cubic meters
[s]	second
[ss]	second
[sec]	second
[min]	minute
[h]	hour
[hh]	hour
[d]	day
[dd]	day
[mon]	month
[y]	year
[yyyy]	year (4 digits)
[Pa]	pascal
[hPa]	hectopascal
[mbar]	numerically equal to hectopascal
[psia]	1 psia = 68.94745 hPa
[K]	kelvin
[°C]	degrees centigrade
[°R]	degrees reaumur (absolute temperature)
[%]	percent
[kg]	kilogram
[J]	joule
[N]	newton
[cyc]	cycles
[rad]	radians ($2\pi = 1$ cycle)
[°]	degrees ($360^\circ = 1$ cycle)
[deg]	degrees
[']	arc-minutes
["]	arc-seconds
[arcsec]	arc-seconds
a	semi-major axis of GPS satellite trajectory
a_0, a_1, a_2	polynomial clock error coefficients for offset (a_0), drift (a_1) and aging (a_2)

a_1, a_2	linear combination factors for the original L_1 and L_2 carrier phases
a, b, c	mapping function coefficients
α	probability defining the significance level $p = 1 - \alpha$ or $p = 1 - \alpha/2$
α	geodetic azimuth
α_M	geomagnetic azimuth
\underline{A}	design matrix or functional matrix
b	baseline length
β	temperature lapse rate in [K/km]
β	reciprocal period $1/T$ of a Gauss-Markov process
c	speed of light (in vacuum, $c = 299\,792\,458$ m/s)
c_2, c_3, c_4	coefficients of series expansion of ionospheric refraction n_{ION}
C	constant of first order ionospheric delay ($C = 40.3$ m ³ /s ²)
C	auto-covariance function
$\chi^2_{f,p}$	quantile of the χ^2 -distribution for f degrees of freedom and probability p
C/N	signal-to-noise ratio
D	day of year elapsed since January 1 st of year Y
	(computation of ocean loading displacements)
D	gravity acceleration correction factor for SAASTAMOINEN model
\underline{d}	vector of innovations
d_i	innovation linked to measurement i
\underline{d}_A	effective dipole vector of the receiving antenna
	at site A referring to satellite i
\underline{d}^i	effective dipole vector of the transmitting antenna
	of satellite i referring to site A
d_{AB}	length of baseline AB
d_{MAX}	threshold for maximum baseline length accepted (ambiguity fixing)
db	error in baseline length
Δb	bending correction
δb^i	satellite/transmitter hardware bias
$\delta b_A^{\text{ch}\{i\}}$	receiver hardware bias for channel $\text{ch}\{i\}$ that is tracking satellite i
Δ_i	outlier associated with observation i
DoY	Day of Year (start: 1 = January, 1 st)
DoY_0	day of "maximum winter",
	28 for northern and 211 for southern hemisphere
ΔE_{AE}	eastward component of the antenna eccentricity correction
Δf	difference of the values of the function that is to be differenced
δf_s	GPS satellite broadcast frequency error invoked by S/A
$\delta \Delta \Phi^i$	error of single difference carrier phase due to S/A clock dithering
$\Delta \Phi^i_{\text{A(ORI)}}$	orientation correction for phase measurement at station A to satellite i
dh	differential increment in height
dH	differential change in height (H : height above sea level, geopotential height)
δi	correction term for inclination of GPS satellite trajectory
di/dt	change of inclination of GPS satellite trajectory
Δm	absolute height correction for NIELL hydrostatic mapping function
Δn	filter length for receiver clock error check
ΔN_{AE}	northward component of the antenna eccentricity correction
$\delta \nabla \Delta N$	triple-difference ambiguity for cycle-slip detection

$d\Omega/dt$	change in ascending node of GPS satellite trajectory
dp	differential change in pressure
$\Delta\Theta^{\text{PCV}}$	elevation-dependent antenna phase center correction term in meters
dr	orbit error
δr	correction term for radius of GPS satellite trajectory
ΔR_{AE}	radial (upward) component of the antenna eccentricity correction
ds	differential increment in distance (line of sight)
$\delta S_{\text{A[CLK]}}^i$	combined receiver and satellite clock error term
$\delta S_{\text{A[HYD]}}^i$	hydrostatic slant path delay
$\delta S_{\text{A[HWB]}}^i$	error due to receiver/transmitter hardware biases
$\delta S_{\text{A[ION]}}^i$	ionospheric propagation delay
$\delta S_{\text{A[NEU]}}^i$	total/neutral slant path delay from receiver antenna A to satellite i
$\delta S_{\text{A[ORI]}}^i$	receiver/transmitter antenna orientation correction
$\delta S_{\text{A[PCV]}}^i$	antenna phase center variation error
$\delta S_{\text{A[RDE]}}^i$	relativistic radar delay effect
$\delta S_{\text{A[REL]}}^i$	correction term due to relativistic effects
$\delta S_{\text{[RPE]}}^i$	relativistic periodic effect for satellite i
$\delta S_{\text{A[SYNC]}}^i$	synchronization error induced by receiver clock error δt_A
$\delta S_{\text{A[TROP]}}^i$	tropospheric propagation delay (total slant path delay)
$\delta S_{\text{A[WET]}}^i$	non-hydrostatic or wet slant path delay
δt	satellite clock error
δt_A	receiver clock error
δt^i	satellite clock error
δt_A^i	receiver clock error at station A determined via satellite i
δt_A^*	moving average receiver clock error estimate at station A
$\delta t_{\text{A[TOTAL]}}^i$	combined satellite/receiver clock error
δt_{MAX}	maximum residual of receiver clock error allowed
Δt	difference of sampling times between both receivers
$\Delta \tau$	difference of signal propagation times
$\delta \tau$	increment in elevation, correction due to refraction
δu	correction term for latitude argument of GPS satellite trajectory
Δx	differentiation spacing (for numerical differentiation)
$\Delta \xi$	seasonal variation of meteorological value (MOPS model)
$\Delta \underline{X}_{\text{CORR}}$	vector of coordinate corrections
ΔX_{MAX}	point jump detection threshold
$\Delta \underline{X}_{\text{PCV}}^{\text{L1} \rightarrow \text{L2}}$	relative antenna phase center offset vector between L_1 and L_2
$\Delta \underline{X}_{\text{SV}}^{\text{SUN}}$	distance vector between the sun and the GPS space vehicle
$\Delta \underline{X}_{\text{PCV}}$	GPS satellite phase center correction vector in the ECEF system
$\Delta \underline{X}_{\text{PCV}}$	receiver antenna phase center offset vector
$\Delta \underline{X}(t)_{\text{VEL}}$	velocity correction vector at epoch t
$\Delta \underline{X}(t)_{\text{SET}}$	solid earth tide correction vector at epoch t
$\Delta \underline{X}(t)_{\text{PT}}$	pole tide correction vector at epoch t
$\Delta \underline{X}(t)_{\text{OL}}$	ocean loading correction vector at epoch t
$\Delta \underline{X}_{\text{AE}}$	antenna eccentricity vector
δX	error of coordinate component X
ΔX	translation in direction of X -axis (datum shift)

ΔY	translation in direction of Y-axis (datum shift)
ΔZ	translation in direction of Z-axis (datum shift)
Δz	difference between geometric and apparent ("actual ") zenith angle
δZWD_A	error of zenith wet delay
ΔZWD_{AB}	zenith wet delay difference between station <i>A</i> and <i>B</i>
E	eccentric anomaly of GPS satellite trajectory
e	eccentricity of GPS satellite trajectory
e	partial water vapor pressure [hPa]; $e = f(T, RH)$
e_0	surface (antenna) partial water vapor pressure in [hPa]
\underline{E}	identity matrix
$E\{\dots\}$	expectation value
\underline{e}_i	unit vector (all cells are zero, but row <i>i</i> is 1)
\underline{e}_A^i	unit vector from receiving to transmitting antenna (LOS-vector)
\underline{e}_x	unit vector in direction of the x-dipole element of the receiving antenna
\underline{e}_x^i	unit vector in direction of the x-dipole element of the transmitting antenna
\underline{e}_y	unit vector in direction of the y-dipole element of the receiving antenna
\underline{e}_y^i	unit vector in direction of the y-dipole element of the transmitting antenna
\underline{e}_x	unit vector along the GPS satellite-fixed x-axis, expressed in ECEF system
\underline{e}_y	unit vector along the GPS satellite-fixed y-axis, expressed in ECEF system
\underline{e}_z	unit vector along the GPS satellite-fixed z-axis, expressed in ECEF system
ε_A^i	geodetic (ellipsoidal) elevation angle between station <i>A</i> and satellite <i>i</i>
ε_{MIN}	threshold for minimum elevation accepted (ambiguity fixing)
ε	residual or difference between two values
ε_M	geomagnetic elevation angle
ε_Φ	noise term of carrier phase measurements
ε_{PR}	noise term of pseudo-ranges
ε_{MAX}	maximum difference between two ambiguity estimates allowed, threshold for cycle slip detection
ε_x	rotation around X-axis
ε_y	rotation around Y-axis
ε_z	rotation around Z-axis
\underline{F}	functional matrix (e. g. for error propagation)
f	number of statistical degrees of freedom
f	function
f	frequency of carrier wave
f_{L1}, f_{L2}	frequency of carrier signal L_1 and L_2 , respectively
f_s	satellite broadcast frequency
f_{WGS}	flattening of WGS84 ellipsoid ($f_{\text{WGS}} = 1/298.257224$)
f_i	difference angle between tangent to atmospheric shell and parallel line to surface
Φ	carrier phase measurement in units of cycles; $\Phi_{L1} = \Theta_{L1}/\lambda_{L1}$
Φ_0	initial carrier phase
Φ_A^i	carrier phase measurement, carrier beat phase in cycles
Φ_{REC}	received carrier phase from satellite <i>i</i> in cycles
Φ^i	carrier phase of satellite <i>i</i> in cycles
Φ_{REF}	phase of reference signal generated by the receiver <i>A</i> in cycles
GM	geocentric gravitational constant (WGS84: $GM = 3,986005 \cdot 10^{14} \text{ m}^3/\text{s}^2$)

g	gravity acceleration in m/s^2
g	surface gravity of the normal gravity field at 45° latitude, $g = 9.80665 \text{ m/s}^2$
g_m	weighted mean gravity acceleration
g_m	effective gravity
$\mathbf{g}: y_U$	straight line defining the umbra ray
$\mathbf{g}: y_{PU}$	straight line defining the penumbra ray
$C_{[N]}$	gradient in northward direction
$C_{[E]}$	gradient in eastward direction
$C_{A[N]}$	horizontal gradient at site A in northward direction
$C_{A[E]}$	horizontal gradient at site A in eastward direction
h_2	LOVE number ($h_2 = 0.6090$)
h_s	surface height
h_c	height of the center of the atmospheric column above the ellipsoid in [km]
h	height of the antenna site above the ellipsoid in [km]
H	height above sea level
H	orthometric height of station in [m]
H_0	height of site above sea level in [km]
H_d	effective height of the dry atmosphere above the surface in [km]
H_{d0}	effective height of the dry atmosphere for a temperature of 0°C in [km]
H_T	height of the tropopause
H_w	effective height for the wet component (identical with H_T)
i	inclination of GPS satellite trajectory
I_{WV}	integrated water vapor in kg/m^2
\mathbf{J}	transformation matrix (similarity transformation)
φ	ellipsoidal latitude
φ^*	geocentric latitude
\underline{K}	Kalman filter gain matrix
$\underline{K}_{k \leftrightarrow}$	gain matrix for smoothing computations at epoch k (backward in time)
k	current epoch
$k-1$	previous epoch
k_1, k_2, k_3	refraction constants
\underline{L}	vector of observations
\underline{L}_0	vector of approximated observations
\underline{L}'	vector of adjusted observations
\underline{l}	vector of reduced observations, vector of pre-fit residuals
l_2	SHIDA number ($l_2 = 0.0852$)
l_c	scale factor for Black mapping function
λ	geodetic (ellipsoidal) longitude
λ_M	geomagnetic longitude
λ	wavelength of carrier wave
λ_{L1}	wavelength of the L_1 carrier signal ($\lambda_{L1} = 19.02 \text{ cm}$)
$\lambda_{a1,a2}$	virtual wavelength of linear combination with coefficients a_1 and a_2
λ_W	virtual wavelength of the wide lane linear combination
M	mean anomaly of GPS satellite trajectory
M_0	mean anomaly of GPS satellite trajectory at reference epoch t_{OE}
m_{MOON}/m_E	mass ratio of moon to earth ($m_{\text{MOON}}/m_E = 0.012300034$)
m_{SUN}/m_E	mass ratio of sun to earth ($m_{\text{SUN}}/m_E = 332945.94$)

m	scaling of network; $q = (1 + m)$
m	tropospheric mapping function
m	mass
M_i	molar mass of gas i
M_d	molar weight of dry air ($M_d = 28.9644$ kg/kmol)
M_w	molar weight of wet air ($M_w = 18.0152$ kg/kmol)
MP	multipath signal (code-minus-carrier)
μ	mean (true) value of ensemble
N	time argument for computation of scale factor and phase angle offsets (ocean loading displacements)
N_A^i	ambiguity term (phase bias) of measurements from antenna A to satellite i
N_e	electron density in electrons/m ³
n_{ION}	index of ionospheric refraction
n	index of atmospheric refraction
$n(s)$	index of refraction as function of distance s
N	reduced index of (tropospheric) refraction, refractivity
$N_{[\text{HYD}]}$	hydrostatic refractivity
$N_{[\text{WET}]}$	wet refractivity
n_0	computed, uncorrected mean motion
n	number of observations
n	number of epochs
n	number of realizations of a process
\underline{N}	normal equation matrix
Ω	argument of ascending node of GPS satellite trajectory
Ω_0	ascending node at reference epoch t_{OE} of GPS satellite trajectory
Ω_A^i	rotation angle elapsed during time of signal travel τ_A^i
ω_E	angular velocity of the earth (WGS84: $\omega_E = 7.2921151467 \cdot 10^{-5}$ rad/s)
\underline{P}	weight matrix of the observations
p_{ii}	weight associated with observation i , diagonal element of matrix \underline{P}
p	probability, significance level; $p = 1 - \alpha$ (one-sided) or $p = 1 - \alpha$ (two-sided)
p_i	pressure of ideal gas i
p	total pressure in hPa
p_d	dry pressure; $p_d = p - e$
p_s	surface (total) pressure or pressure at antenna site in hPa
p_0	surface/antenna pressure in [hPa]
PR_A^i	measured pseudo-ranges between satellite i and receiver A
PW	precipitable water in mm; $\text{IWV} = \text{PW}/\rho$ with ρ : density of liquid water
PWV	precipitable water vapor in mm; alternative term for PW used by some authors
θ	geodetic (ellipsoidal) pole distance (co-latitude, $\theta = \frac{1}{2}\pi - \phi$)
θ_M	geomagnetic pole distance (co-latitude)
q	scaling factor of network (datum parameter)
q	process noise parameter, often called q -factor
q_{AMP}	amplifier for q -factor
Q	factor for conversion of ZWD into PW; $Q = f(T_M) = \text{ZWD}/\text{PW} \approx 6.2$
$\underline{Q}_{\text{LL}}$	cofactor matrix of the observations
$\underline{Q}_{\text{LL}'}$	cofactor matrix of the adjusted observations

Q_{VV}	cofactor matrix of the residuals
Q_{XX}	cofactor matrix of the adjusted parameters
q_{Vii}	element of cofactor matrix Q_{VV} associated with observation i
q_{AB}	scaling factor
q_x	amplifier
q_z	zenith angle scaling factor
q	scaling factor of network; $q = (1+m)$
Θ	carrier phase measurement in units of meters; $\Theta_{L1} = \Phi_{L1} \cdot \lambda_{L1}$
θ	angle between ray and tangent to the spherical shell passing through the slant profile point
r	orbit altitude ($r = 20000$ km for GPS satellites)
r	radius of GPS satellite trajectory
r	radial distance from earth center to GPS antenna
r_E	radius of the earth ($r_E = 6\,371$ km)
r_S	radius of the sun ($r_S \approx 696\,000$ km)
\underline{R}	matrix of redundancies
\underline{R}	rotation and scaling matrix (datum transformation)
r_i	redundancy associated with measurement i
R_i	specific gas constant
R_0	universal gas constant; $R_0 = 8.31434$ [J mol ⁻¹ K ⁻¹]
RH	relative humidity in %
$\rho_{i,j}$	correlation coefficient between observation i and j
ρ_i	density of gas i
ρ_{LW}	density of liquid water
$\rho_{ZWD[A,B]}$	correlation coefficients between zenith wet delay at station A and B
S_A^i	geometric distance between receiver antenna A and satellite i
s_0^2	empirical variance of the weight unit a posteriori, global value
s_0^{2*}	empirical variance of the weight unit, individual value for each observation (outlier)
s_W	empirical standard deviation of the mean wide lane ambiguity
σ^2	variance
σ_0	standard deviation of the weight unit a priori (theoretical value)
σ_i	theoretical standard deviation of observation i
$\sigma_0^{A\,POST}$	theoretical value of the empirical standard deviation of the weight unit
σ_{di}	(theoretical) standard deviation of innovation linked to observation i
$\sigma_{\Delta i}$	standard deviation of the outlier associated with observation i
σ_Φ	standard deviation of the undifferenced phase observation
σ_O	original standard deviation of the phase measurement
σ_θ	scaling factor for elevation-dependent weighting
$\sigma_{ZWD[A]}$	standard deviation of zenith wet delay at station A
\underline{S}	similarity matrix (similarity transformation)
$\underline{\Sigma}_{dd}$	covariance matrix of the innovations
$\underline{\Sigma}_{LL}$	covariance matrix of the observations
$\underline{\Sigma}_{LL}$	"tuned" covariance matrix of the observations
$\underline{\Sigma}_{XX}$	theoretical covariance matrix of the adjusted parameters
\underline{S}_{XX}	empirical covariance matrix of the adjusted parameters
$\underline{\Sigma}_{XX}$	predicted covariance matrix of the states

$\underline{\Sigma}_{XX}^*$	updated covariance matrix of the states
$\underline{\Sigma}_{XX \rightarrow}$	predicted covariance matrix (forward run)
$\underline{\Sigma}_{XX \rightarrow}^*$	updated covariance matrix (forward run)
$\underline{\Sigma}_{XX \leftarrow}^*$	covariance matrix of updated state vector (backward run)
$\underline{\Sigma}_{XX \leftrightarrow}$	smoothed/combined covariance matrix
$\underline{\Sigma}_{SS}$	process noise matrix
SND	slant neutral delay
STD	slant total delay (identical with SND)
SHD	slant hydrostatic delay
SWD	slant wet delay
t	epoch (time)
t	observation epoch in years
t_{REF}	reference epoch in years
t	true GPS time at the measurement epoch
t'	receiver time at the measurement epoch
t_k	time elapsed since the reference epoch of the GPS satellite orbits
t_{OC}	time of clock, reference epoch of clock error coefficients
t_{OE}	time of ephemeris, reference epoch of the orbit elements
t_{OR}	time of receipt
t_{OT}^i	time of signal transmission by satellite i
τ_A^i	time of signal travel between satellite i and ground station A
T	period of a Gauss-Markov process
\underline{T}	transition matrix
T	temperature in K
t	temperature in [°C]
T_C	temperature in [°C]
T_M	(weighted) mean temperature of the atmosphere in [K]
t_M	(weighted) mean temperature of the atmosphere in [°C]
T_0	surface/antenna temperature in [K]
t_0	surface/antenna temperature in [°C]
T_s	surface temperature or temperature at antenna site in [K]
TEC	total electron content
τ	signal propagation time
τ	increment in time
u	argument of latitude in the GPS satellite system
u_0	uncorrected argument of latitude in the GPS satellite system
u	number of unknowns
v	true anomaly of GPS satellite trajectory
v_i	residual associated with observation i
$\underline{v}_X(t_{\text{REF}})$	velocity vector of station at reference epoch in meters per year
V_{ION}	ionospheric amplification factor
VTEC	vertical total electron content
\underline{v}	vector of post-fit residuals
V	volume
ϖ	factor for conversion of zenith wet delays into integrated water vapor
w	white noise
w_i	test quantity associated with the blunder in observation i

w_{MAX}	maximum outlier
\underline{X}	vector of adjusted parameters
\underline{X}_0	vector of approximated unknowns
\underline{x}	reduced vector of adjusted parameters
$\underline{\hat{X}}$	predicted state vector
$\underline{X}_{\text{COO}}$	sub-vector containing the ground station coordinates
$\underline{X}_{\text{ZWD}}$	sub-vector containing the tropospheric parameters
$\underline{X}_{\text{SAT}}$	sub-vector containing the satellite orbit biases
$\underline{X}_{\text{AMB}}$	sub-vector containing the ambiguities
\underline{X}^*	updated state vector
$\underline{X}_{\leftrightarrow}$	combined/smoothed state vector matrix
$\underline{X}_{\rightarrow}^*$	updated state vector matrix (forward run)
$\underline{X}_{\rightarrow}$	predicted state vector matrix (forward run)
$\underline{X}_{\leftarrow}^*$	updated state vector (backward run)
X^i	weighted mean coordinate component
X_i	filtered coordinate component at epoch i
\underline{x}	local coordinate vector consisting of the northward (x), eastward (y) and radial component (z)
$\underline{X}_{\text{AE}}$	vector of antenna eccentricity corrections in the local level system
$\underline{X}_{\text{OL}}$	vector of ocean loading corrections in the local level system
$\underline{X}_{\text{PT}}$	vector of pole tide corrections in the local level system
\underline{X}	geodetic position vector, global, Cartesian, ECEF
\underline{X}	coordinate vector of the point monument
$\underline{X}(t)$	antenna phase center position vector at epoch t
\underline{X}_0	global geocentric coordinate vector of the origin of the local topocentric system
\underline{X}_{M}	geomagnetic position vector
\underline{X}_{S}	position vector of the sun, expressed in the ECEF system
$\underline{X}_{\text{SV}}$	position vector of the GPS space vehicle, expressed in ECEF system
ξ_0	average meteorological value of MOPS troposphere model
x_{POLE}	x -component of the pole in arc-seconds
y_{POLE}	y -component of the pole in arc-seconds
Y	year, 4 digits, e. g. 1999
Y_p	quantile of normal (Gauss) distribution at a significance level of p
Y_{MIN}	minimum quantile of the Gauss distribution to be exceeded by the test quantity
Y_{MAX}	maximum quantile of the Gauss distribution not to be exceeded by the test quantity
Ψ_i	observation equation i (function of the unknowns \underline{X}_0)
$\underline{\Psi}(\underline{X})$	vector of observation equations as functions of the unknowns in vector \underline{X}
Ψ_{L_1}	observation equation for the L_1 carrier phase measurement
z	zenith angle in radians or degrees, "geometric" zenith angle
z^*	apparent ("actual") zenith angle
ZHD	zenith hydrostatic delay in mm
ZND	zenith neutral delay in mm
ZTD	zenith total delay in mm; note that ZND is identical to ZTD
ZWD	zenith wet delay in mm

ZWD_A	zenith wet delay at site A
Z_i	compressibility factor of gas i
$Z_{d/w}^{-1}$	inverse compressibility factors for dry $_{(d)}$ and wet $_{(w)}$ air

List of Acronyms

A/S	anti-spoofing
atan2	see list of symbols
BLUE	best linear unbiased estimator
CODE	GPS analysis center of the IGS at the Astronomical Institute of the University of Berne, Switzerland
C/N	see list of symbols
CRINEX	Compact RINEX, → RINEX
DEM	digital elevation model
DoY	day of year (range: 1 ... 365/366; start: 1 = January, 1 st)
DoW	day of week (range: 0 ... 6, start: 0 = Sunday)
DWD	Deutscher Wetterdienst, German Weather Service
ECEF	earth-centered earth-fixed coordinate system
EUREF	European Reference Frame
exp	see list of symbols
GDAS	Global Data Assimilation System
GFZ	GeoForschungsZentrum Potsdam
GREF	German Reference Frame
IERS	International Earth Rotation Service
IGP	IGS predicted orbits, predicted for 24 up to 48 hours
IGR	IGS rapid orbits, delivered with a latency of 2 days
IGS	International GPS Service for Geodynamics
IGS	IGS final orbits, delivered with a latency of 2 weeks
IGU	IGS ultra-rapid orbits, see also → ULT
int	see list of symbols
ILW	integrated liquid water
ITRF	International Terrestrial Reference Frame
IWV	see list of symbols
LEO	low-earth orbiter, satellite with small orbit altitude ($\approx 500 \dots 1000$ km)
LIDAR	light detection and ranging
LOS	line of sight
MEO	medium-earth orbiter, satellite with medium orbit altitude ($\approx 20,000$ km)
NCEP	National Centers for Environmental Prediction, USA
NGS	National Geodetic Survey, USA
NOAA	National Oceanic and Atmospheric Administration, USA
NWF	numerical weather field
NWM	numerical weather model
PAF	Permanent Array Filter
PCV	phase center variation, filename suffix of antenna calibration tables
PW	see list of symbols
PWV	see list of symbols
RH	see list of symbols
RINEX	receiver-independent exchange format
RMS	root mean square
ROI	region of interest
S/A	selective availability

SAGE II	Stratospheric Aerosol and Gas Experiment
sgn	see list of symbols
SMMR	Scanning Multi-channel Microwave Radiometer
SRIF	square root information filter, numerically highly stable Kalman filter
SSM/I	Special Sensor Microwave Imager
TDT	Temps Dynamique Terrestrique
TEC	see list of symbols
TOVS	TIROS operational vertical sounder
trace	see list of symbols
TROPAC	Tropospheric Analysis Center
ULT	ultra-rapid orbits, can be used in real-time, higher accuracy than IGP
VLBI	very long baseline interferometry
VTEC	see list of symbols
WVR	water vapor radiometer
ZHD	see list of symbols
ZND	see list of symbols
ZTD	see list of symbols
ZWD	see list of symbols

1. Introduction

1.1 Importance of Atmospheric Water Vapor for the Climate System

Water vapor¹ is constantly cycling through the atmosphere, evaporating from the surface, condensing to form clouds and subsequently returning to the earth as precipitation. Heat from the sun evaporates water and this heat is released into the air when the water condenses into clouds and when it precipitates. The evaporation-condensation cycle is an important mechanism for transferring heat energy from the earth's surface to its atmosphere and in moving heat around the earth. Hence, MOCKLER [1995] states that atmospheric water vapor is important for the climate system and a key to understand the hydrological cycle.

1.1.1 Hydrological Cycle and Greenhouse Effect

The hydrological cycle describes the transfer of water in solid, liquid and gaseous form through these phases as well as the physical movement of water within the ecosystem of the earth and between its atmosphere, oceans and continents (see GABOR [1997] and MOCKLER [1995]). In the vapor phase, water moves quickly through the atmosphere and redistributes energy associated with its evaporation and re-condensation. The movement of water vapor through the hydrological cycle is strongly coupled to precipitation and soil moisture that have important practical implications. Not all details of the hydrologic cycle are well understood, mainly due to a lack of sufficiently good observations of water vapor.

BEVIS [1992] also stresses the role of water vapor for the atmospheric energy balance and considers the distribution of water vapor to be of high importance for the vertical stability of the atmosphere and the structure and evolution of storm systems. Limitations in the analysis of water vapor are treated as dominant error source for short-term forecasts of precipitation.

With a total amount of 62%, water vapor contributes more than any other component of the atmosphere to the greenhouse effect. Carbon dioxide only holds share of about 22% according to the UMWELTBUNDESAMT [1998]. Greenhouse gases allow much of the sun's short-wave radiation to pass through them, but absorb or trap the long-wave, infrared radiation emitted by the surface. Without water vapor and other greenhouse gases in the air, the surface air temperatures would be well below the freezing point.

¹ Water vapor is water in the gaseous phase. Following MOCKLER [1995], several definitions exist to express the amount of water vapor in the air: One can refer to the actual concentration of water vapor in the air or relate the actual amount to the amount that would saturate the air. Air is saturated when it contains the maximum possible amount of water vapor without bringing on condensation. At that point, the rate at which water molecules enter the air by evaporation exactly balances the rate at which they leave by condensation. Ground-based GPS allows to measure the total amount of water vapor above the antenna site. Following the definitions given by BEVIS [1992], two terms are to be distinguished: IWV (*integrated water vapor*) is the quantity of atmospheric water vapor overlying a certain point (in our case it is the GPS antenna) and describes the mass of vapor in units of kg/m². Alternatively, the term PW (*precipitable water*) expresses the height of an equivalent column of liquid water in units of [mm]. The relation between both quantities is given by $PW = IWV/\rho$ with ρ being the density of liquid water ($\rho = 1 \text{ kg/dm}^3$).

However, it should be pointed out that water vapor is the major source of the *natural* greenhouse effect. The amount of water vapor released into the atmosphere due to human activities is negligible compared to the amount of vapor available from natural sources, but the natural effects are going to be amplified by an increased emission of carbon dioxide, methane and nitrogen dioxide. It is not yet clearly understood how these changes may affect the climate system. GPS-derived time series of water vapor are expected to improve this situation.

1.1.2 Trends

Recent global estimates of long-term tropospheric water vapor changes show an increase in precipitable water during the period from 1973 to 1990 that is mentioned by MOCKLER [1995]. Largest trends can be observed in the tropics with an increase of about 13% per decade. An analysis of water vapor trends above North America based on radiosonde measurements from 1973 to 1993 reveals increases in precipitable water over all regions except northern and eastern Canada where it fell slightly. Regions of moisture increase are associated with regions of rising temperatures over the same period, and the regions of decreased moisture are associated with falling temperatures.

One major hindrance for an improved knowledge of the role of water vapor in the climate system is linked to observational gaps that currently exist. Most studies primarily rely on radiosonde data. They have a reasonably good vertical, but a poor horizontal resolution.

1.2 The Role of Water Vapor in GPS Geodesy and Navigation

1.2.1 NAVSTAR GPS

NAVSTAR GPS is funded and controlled by the U. S. Department of Defense (DOD) and consists of three segments, the space, the control and the user segment. The space and the user segment are briefly explained here. For a more detailed overview of GPS please refer to DANA [1995], HOFFMANN-WELLENHOF et al. [1993] and SEEGER [1989, 1993].

The GPS constellation consists of a minimum of 21 satellites arranged in 6 orbital planes with 55° inclination and an altitude of 20,200 km above the earth's surface. The orbital period is about 12 hours, so a GPS satellite is continuously visible above the horizon for about 5 hours.

Several types of GPS satellites have been launched so far. Most of the satellites currently in use are Block II and Block IIA satellites. The latter are just a small modification of the original design. Block II satellites have a weight of 930 kg and a velocity of 4 km/s. They transmit signals using two frequencies, namely L_1 ($f_{L_1} = 1575.42$ MHz) and L_2 ($f_{L_2} = 1227.60$ MHz) and receive signals on a frequency of 1783.74 MHz. Block II satellites carry 4 atomic clocks - 2 rubidium and 2 cesium clocks - and have a design-lifetime of 7.5 years. The replenishment satellites of type Block IIR have a higher lifetime of 10 years.

The user segment comprises the GPS receivers needed to decode the transmitted signals. For tropospheric delay estimation, high-quality two-frequency receivers are necessary in order to eliminate ionospheric propagation delays properly.

1.2.2 Tropospheric Delays and GPS

Precise GPS applications are complicated by atmospheric effects, namely propagation delays in the ionosphere and troposphere. As far as the ionosphere is concerned, it is possible to compensate the first order effect given measurements on two different frequencies. For the delay caused by the troposphere, no dispersion effects are present and elimination is not possible. The tropospheric delay can be separated into a hydrostatic and a wet component. The hydrostatic component in zenith direction is called ZHD (*zenith hydrostatic delay*). It can be precisely determined by surface pressure measurements. The ZWD (*zenith wet delay*), however, cannot be sufficiently modeled by surface measurements due to the irregular distribution of water vapor in the atmosphere. Chapter 3 will deal with the details of tropospheric delay modeling.

The ZHD amounts to about 2.3 m, whereas the ZWD is only in the range of 0.15 m in global average. Although it is much smaller than the hydrostatic component, the uncertainties in wet tropospheric delay modeling do place a great burden on high-precision GPS applications if we recall that carrier phase measurements themselves have an accuracy of a few millimeters and certain receiver manufacturers even claim that they have reached noise levels in the sub-millimeter range.

Among many examples in geodesy and navigation, NAITO [1998] reports about a Japanese network that has been established for deformation analysis and earth-quake detection. The analysis of the measurements showed drifts in the coordinate solutions that apparently were not due to plate motions, but related to an insufficient compensation of tropospheric delays. Additional estimation of wet delays within the routine analysis should improve the situation.

1.3 Water Vapor Observing Systems

A variety of platforms and sensors is available to measure atmospheric water vapor. Each system has certain advantages and disadvantages. The following synopsis is based on MOCKLER [1995] and GABOR [1997]. Figure 1-1 shows some of these sensors and their characteristics are summarized in Table 1-1.

1.3.1 Description of Selected Sensors

Ground-based direct sensors, weather balloons and aircraft were the only tools available to measure precipitable water vapor in the past. The radiosonde has been one of the most important devices and will certainly continue to be a valuable water vapor sensor in the future. Radiosondes are balloon-borne instruments with radio transmitting capabilities. They contain instruments capable of making direct in-situ measurements of air temperature, humidity and pressure with height, typically to altitudes of approximately 30 km. These observed data are transmitted immediately to the ground station by a radio transmitter. Ground-based radio direction finding antenna equipment tracks the motion of the radiosonde during its ascent through the

air. The recorded elevation and azimuth information are converted to wind speed and direction at various levels by triangulation techniques.

Today, many more remote sensors capable of taking water vapor measurements over large areas are available. Substantial progress has been made using satellite observations to obtain total column water vapor and low-resolution vertical profiles from infrared and microwave sensors, but these satellite observations do not provide data under all weather conditions nor above all surfaces. Generally speaking, they measure absorption lines in the radiation from the hot background provided by the earth. Consequently, clouds may cause problems as well as the surface of land masses. Best results are obtained over oceanic regions.

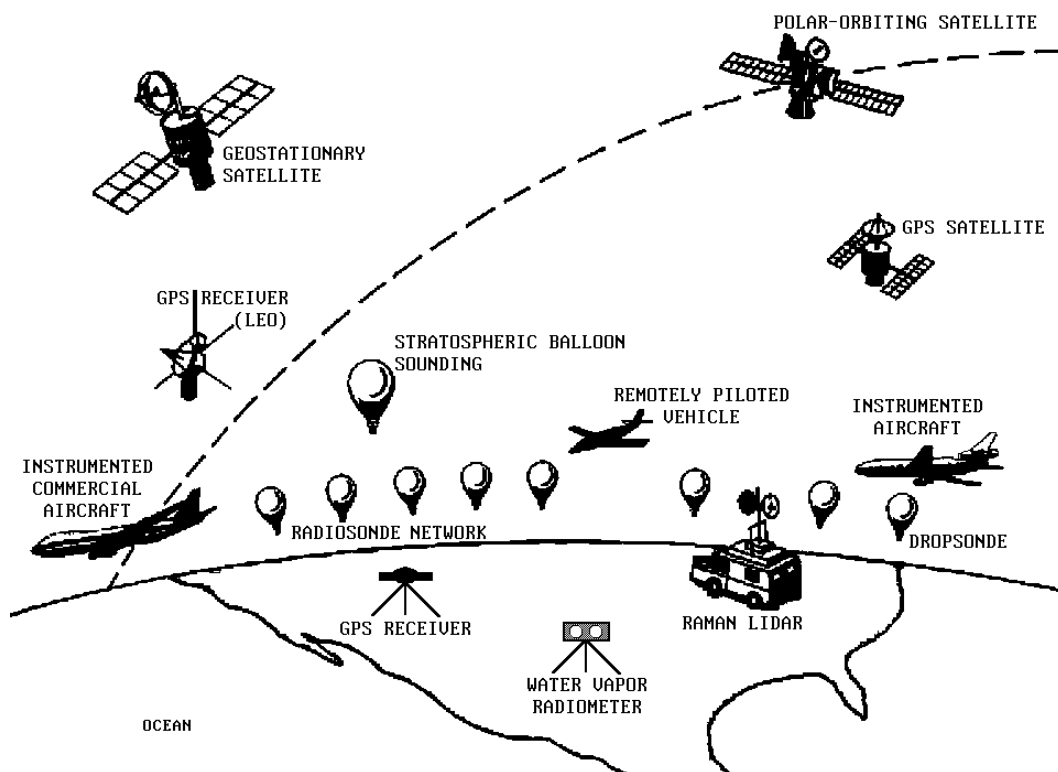


Figure 1-1 - Overview of water vapor measuring platforms and sensors following CARTER [1997]. Water vapor sensors are carried on a variety of platforms including ground stations, weather balloons, aircraft and satellites. NAVSTAR GPS consists of a minimum of 21 MEO satellites at an orbit altitude of 20,000 km. Atmospheric monitoring with GPS is possible in two ways: by probing the atmosphere with help of GPS receivers on LEO (low-earth orbiting) satellites, the so-called radio occultation technique, or by using networks of ground-based GPS receivers. According to GABOR [1997], remotely piloted vehicles have yet to come of age, but offer a potentially long loiter time and high altitude ceiling.

Hygrometers and LIDARs can be useful for detailed local studies. LIDAR is an acronym for *light detection and ranging*, an active remote sensing technique that operates in a similar way as sonar systems: A pulse of laser light is emitted into the sky and the amount of return due to backscatter from the atmosphere is measured versus time. With knowledge of the speed of light, the time is converted into altitude. The number of photons counted for each altitude bin is proportional to the atmospheric density.

Observing Platform	Measurement System	Advantages	Disadvantages
Satellites	Infrared sensors (e. g. TOVS) SUSSKIND et al. [1984]	Sensors provide total column water vapor and some vertical profile information over large areas.	Data are limited to cloud-free regions and can exhibit regional biases. Vertical resolution is poor.
	Microwave sensors (e. g. SMMR, SSM/I) PRABHAKARA et al. [1985]	Sensors provide total column water vapor data over large regions and are not highly influenced by clouds.	Data are limited to ice-free ocean regions, vertical resolution is poor.
	Solar occultation methods (e. g. SAGE II) RIND et al. [1993]	Global humidity data at very high altitudes in the stratosphere and above. High accuracy and vertical resolution.	Coverage is limited by clouds. Sampling is poor in tropical regions.
	GPS radio occultation (GPS satellites in conjunction with GPS receivers on LEO satellites) MELBOURNE et al. [1994]	Limb sounding technique can provide pressure, temperature and humidity/ water vapor with relatively good vertical resolution in the higher troposphere.	Methods are in research and development stage.
Aircraft STARR and MELFI [1991]; KELLY et al. [1991]	Instruments mounted on special research airplanes or commercial aircraft. The research instruments include dew point and lyman alpha hygrometers, differential absorption LIDARs and capacitive sensors	Research aircraft can make measurements at almost any location at any time desired. Measurements with commercial aircraft could provide good data coverage over much of the globe.	Research missions are expensive, so data collection is limited. Programs involving commercial aircraft have not been widely implemented.
Balloons	Routine radiosonde (weather balloon) observations. Humidity sensors include carbon and lithium chloride hygristors, capacitive sensors, goldbeater's skin, and human hair. ELLIOTT and GAFFEN [1991]	Instruments are expendable, observations are relatively inexpensive. Method is in use since 1930s, so long data records are available. Global network of about 800 stations making 1 to 4 observations per day at each station. Data have relatively good vertical resolution in lower troposphere.	Data quality is variable in the upper troposphere and poor in the stratosphere. Quality of observations is poor at very high and low humidities. Differences in instruments and practices between countries, and changes over time, make data interpretation difficult. Spatial coverage is limited.
	Research soundings (using, e. g., frost point hygrometers) OLTMANS and HOFMANN [1995]	Quality of humidity observations is high. Data extend beyond altitude limits of radiosondes.	Instruments are expensive, so soundings are made infrequently at limited locations.
	Reference radiosondes DABBERDT et al. [1995]	High-quality observations could be used for comparison with operational measurement systems and for field experiments.	In development. Instruments are more expensive than expendable radiosondes.

Observing Platform	Measurement System	Advantages	Disadvantages
Ground-based sensors (earth surface)	Routine surface meteorological observations. Instruments include wet- and dry-bulb psychrometer and dew point hygrometer MIDDLETON and SPILHAUS [1953]	Long records of reasonably high quality global data are available. Observations are made at least daily and often more frequently.	Spatial coverage is nonuniform. Data are at the earth's surface only.
	Ground-based water vapor radiometers BEVIS et al. [1992]	Integrated water vapor measurements with high precision.	Expensive devices, poor horizontal resolution, weather conditions limit the use of radiometers (no measurements during rainfall).
	Raman LIDAR, differential absorption LIDAR ENGLAND et al. [1992]	Sensors provide high-quality data with high vertical and temporal resolution.	The systems are expensive and require highly skilled operators. Usefulness is limited in daytime and in cloudy conditions.
	Ground-based GPS receivers in conjunction with GPS satellites - THE FOLLOWING CHAPTERS -	Global soundings of integrated water vapor using existing and planned navigation satellites and tracking networks with high precision and excellent temporal resolution.	Horizontal resolution depends on tracking network infrastructure: good resolution in industrialized countries, but poor resolution in non-developed regions; poor vertical resolution

Table 1-1 - Characteristics of water vapor observing systems following MOCKLER [1995]. It should be noted that GPS provides several ways to explore the atmosphere. The space segment only provides the signal emitters and it depends on the environment where the receivers are operated on how atmospheric sounding is possible. In this way, the GPS radio occultation technique can be classified as satellite-to-satellite technique and the ground-based GPS approach uses receivers of tracking networks located at or near the earth's surface.

Ground-based water vapor radiometers (WVR) are upward-looking instruments and can estimate the integrated water vapor contents (IWV) along a given line of sight as well as the integrated liquid water (ILW). The background microwave radiation due to atmospheric water vapor is measured in terms of sky brightness temperature at two or more frequencies, i. e. the water vapor emission lines against the cold background of space are analyzed. The brightness temperature is frequency-dependent and, consequently, simultaneous measurements of IWV and ILW are possible. Note that, according to BEVIS [1992], the retrieval algorithm needs parameters which show variations with season and geographic location. Therefore, a WVR has to be tuned to the local conditions if highest precision shall be obtained. The reader may refer to ELGERED et al. [1991] and ENGLAND et al. [1992] for further information on water vapor radiometry.

The Global Positioning System NAVSTAR GPS can be used for atmospheric sounding in two ways. It is possible to equip low-earth orbiting satellites (LEO) with GPS

receivers and to analyze occultation events. This satellite-to-satellite mode² yields vertical profiles of pressure, temperature and relative humidity or water vapor. The other principle which is discussed in the following chapters in detail uses ground-based networks of GPS receivers to estimate the total amount of water vapor by a special way of processing the signals received from the Global Positioning System satellites and may provide long-term measurements with high precision.

1.3.2 Synopsis

Table 1-1 compares the characteristic properties of the above-mentioned techniques to measure atmospheric water vapor. The sensors are categorized by the observing platforms. Advantages and disadvantages are roughly outlined.

1.4 Objectives and Structure of this Thesis

The outstanding issues in water vapor research for climatology are outlined by MOCKLER [1995] and divided into theoretical, observational and climate modeling issues. To summarize the first two categories, a lack of knowledge as far as the role of water vapor in influencing the radiation budget of the earth can be stated. The same is true for the processes determining the distribution of water vapor and its changes over time. Retrievals of water vapor shall be improved and extended with special emphasis on long-term, continuous and global observations to aid in the trend analysis.

In GPS geodesy and navigation, the primary goal in modeling the tropospheric propagation delay is to reduce the uncertainties related to the wet component or, equivalently, to water vapor. For permanent GPS arrays, the additional estimation of zenith wet delays reduces the impact of tropospheric modeling errors and supplies valuable estimates of total atmospheric column water vapor for climate models and meteorology. For many other GPS applications, tropospheric delay estimation is not possible or problematic. A typical example for this group are kinematic applications which normally do not allow the determination of such additional parameters and are therefore subject to improvement by precise tropospheric corrections supplied by GPS permanent arrays and/or numerical weather models.

1.4.1 Objectives of this Thesis

In order to exploit the potential of GPS receivers as water vapor sensors, a tropospheric analysis system is to be developed that is able to precisely filter zenith wet delays and integrated water vapor from GPS phase measurements. This platform-independent processing package should be operable in semi-automatic and fully automatic mode including non-interactive data editing. Input data in standard formats must be supported and the analysis results have to be stored in commonly agreed standard formats, too. Special emphasis is to be laid on the reliability of the results, and the network performance is to be automatically analyzed and, if necessary, to be altered (i. e. exclusion of suspicious receivers) and re-analyzed accordingly. The software shall be able to analyze multi-station networks with long baselines (more

² Actually, it is also possible to install GPS receivers on aircraft and to analyze radio occultation events from this platform. Consequently, this technique is not necessarily limited to satellite platforms.

than 1000 km) with sufficient accuracy. The temporal resolution is to be chosen adequately and shall meet possible needs for high-frequency data.

The overall goal is to estimate wet delays and integrated water vapor whereas the standard output of stand-alone GPS data analysis can only consist of neutral (or total) delays. This means that additional meteorological data are needed like surface pressure for modeling the hydrostatic component and temperature for the conversion of wet delays into precipitable/integrated water vapor. Therefore, the analysis system must provide all necessary interfaces to access these additional data. As a matter of fact, the availability of in situ meteorological measurements at GPS monitor stations is very limited. As a consequence, algorithms have to be developed to extract the needed information from numerical weather models. Due to the global size of GPS tracking networks like the IGS net, weather models of global extend are favorable to accomplish this task.

The efforts to extract tropospheric information from numerical weather models shall not be limited to the support of the GPS data analysis with respect to meteorology and climatology, but shall also be assessed in terms of their applicability to GPS navigation and geodesy. An open, memory-efficient and gridded data format shall be developed that carries all data analyzed in the 3-D numerical weather models that are needed to determine hydrostatic, wet and neutral delays at any place on the globe. These gridded tropospheric correction data shall be suited for kinematic GPS processing and should also serve as a carrier for gridded integrated water vapor data. Proper methods for horizontal interpolation and vertical reduction of the delays are to be developed and validated.

Finally, the irregularly distributed tropospheric delays estimated at the GPS sites shall be combined with the gridded data of the tropospheric correction files that are derived from numerical weather models. In this way, the GPS and the less accurate NWM delays will be melted together and the outcome will be an improved, more accurate solution for the gridded data sets. Suitable algorithms for this combination shall be investigated with special focus on stochastic optimization.

All algorithms are to be documented and discussed. This does not only refer to the special tasks of GPS tropospheric delay estimation, but also includes a full overview of the parts that can be called "conventional" GPS data processing, i. e. those algorithms that are essential for GPS data analysis, albeit not primarily related to GPS tropospheric delay estimation. The dominant error sources shall be analyzed and their impact is to be evaluated with help of practical experiments. All three cornerstones, namely (I) the filtering of zenith wet delays and integrated water vapor from GPS measurements, (II) the meteorological data extraction from numerical weather fields and its application to GPS meteorology, and (III) the suitability of the gridded tropospheric correction data from weather fields as well as the combined GPS/NWM solution fields should be validated.

1.4.2 Structure of this Thesis

The issues defined in the preceding section are addressed in the following chapters. Figure 1-2 outlines the structure of this study that can be divided into a theoretical

and a practical part. In the theoretical section, the algorithms of the tropospheric analysis system TropAC that meets all the defined objectives are outlined.

Chapter 2 deals with the principles of GPS data processing without paying special attention on tropospheric delays since the entire chapter 3 is devoted to this issue including tropospheric delay modeling, mapping functions, tropospheric parameter estimation and the conversion of wet delays into precipitable water vapor. Practical results of validation experiments are presented in chapter 5.

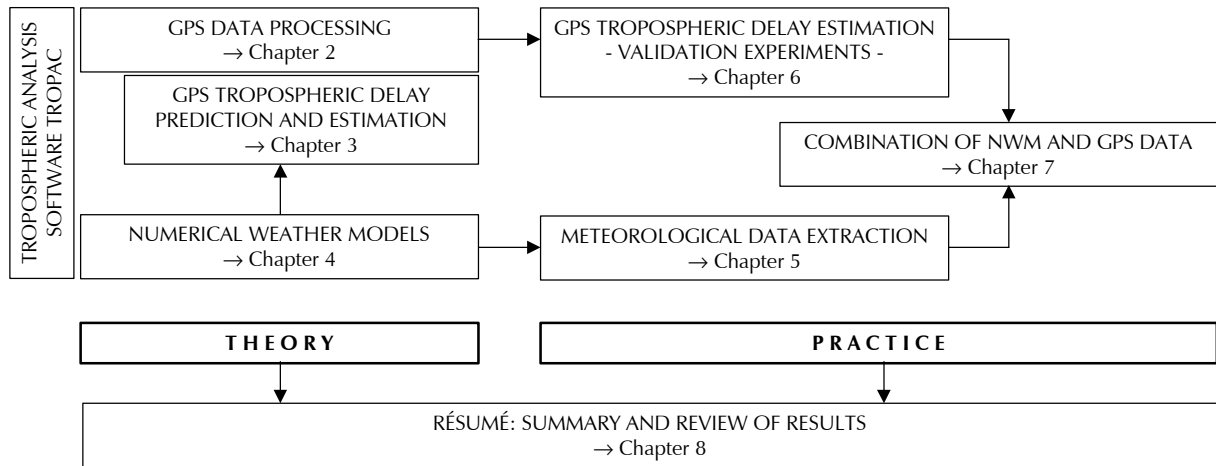


Figure 1-2 - Structure of this thesis. Chapters 2 to 4 can be considered as the theoretical part describing the modeling methods and algorithms of GPS tropospheric delay estimation and data extraction from numerical weather fields. Practical results are presented in chapters 5 to 7 and a summary is given in chapter 8.

The analysis software is able to extract data from numerical weather models. Chapter 4 describes the methods to do so and emphasizes the added value of this approach because experiences actually proved that the task of GPS meteorology cannot be fulfilled with the meteorological data supplied by GPS tracking networks in a satisfactory way. Some of the results for surface meteorological data and other atmospheric quantities are summarized in chapter 5. Moreover, chapter 4 has a central function since the concept and realization of global gridded tropospheric correction data are discussed. These so-called TROPEX files also allow to combine GPS-derived tropospheric propagation delays and those integrated in numerical weather fields in a relatively convenient way. The entire chapter 7 is devoted to the validation studies concerning TROPEX files and the combination of numerical weather model and GPS data sets.

Finally, chapter 8 concludes this thesis by critically summarizing the outcome of the preceding chapters.

2. Principles of GPS Data Processing

Tropospheric delay estimation requires careful modeling of the GPS measurements. For this reason, the principles of GPS data processing are outlined here in the first place before the problem of tropospheric propagation delays is addressed in the chapter 3 in detail. Note that the following sections are not intended as a general introduction into GPS processing, but focus on the methods implemented in the tropospheric analysis software TropAC on which the results presented in chapters 5, 6 and 7 are based. For a general description, the interested reader may refer to SEEGER [1989, 1993] and HOFFMANN-WELLENHOF et al. [1993], for instance.

2.1 Processing Overview

The main processing steps can be divided into *pre-processing*, *network filtering* and *post-filter processing*. These three stages are briefly discussed below. Links to the corresponding sections are given.

2.1.1 Pre-Processing

At the pre-processing stage, the needed data are read, checked and corrected. The *measurements* like code ranges (→ 2.2.1) and carrier phase observations (→ 2.2.2) are read from RINEX files. Carrier phases require some additional corrections, e. g. the synchronization problem (→ 2.2.2.2) has to be addressed if (single or) double differences shall be formed (→ 2.2.2.1), the orientation problem (→ 2.2.2.4) can be relevant for longer baselines, elevation-dependent antenna phase center corrections (→ 2.2.2.1) must be applied. Finally, ionospheric (→ 2.2.4) and tropospheric delays (→ 3.) are predicted. Moreover, typical problems like cycle slip detection and repair (→ 2.2.5) as well as multipath detection (→ 2.2.6) also belong to the tasks of the pre-processor.

The *ground station coordinates* are subject to corrections (→ 2.3), too, since effects like plate tectonics lead to changes in the coordinates (→ 2.3.1) and solid earth tides (→ 2.3.2) cause displacements in the range of a few decimeters, pole tides (→ 2.3.3) can be in the centimeter range and ocean loading effects (→ 2.3.4) can be of relevance for certain sites. Additionally, geometric corrections like the antenna eccentricity (→ 2.3.5) have to be addressed. Finally, the antenna phase center offset correction (→ 2.3.6.1) is taken into account.

Pre-processing also comprises the handling of *precise orbits*. In contrast to broadcast orbits (→ 2.4.1) that are too inaccurate for tropospheric delay filtering, the precise orbits provided by the IGS do not refer to the antenna phase center of the transmitting GPS antenna, but to the mass center of the space vehicle. Consequently, the antenna phase center correction must be computed (→ 2.4.4) that can be complicated during eclipsing seasons (→ 2.4.5). Determination of the satellite positions requires knowledge of the epoch of signal transmission and - as a consequence - of the receiver clock error (→ 2.4.3). The satellite positions are computed with help of polynomial interpolation (→ 2.4.2).

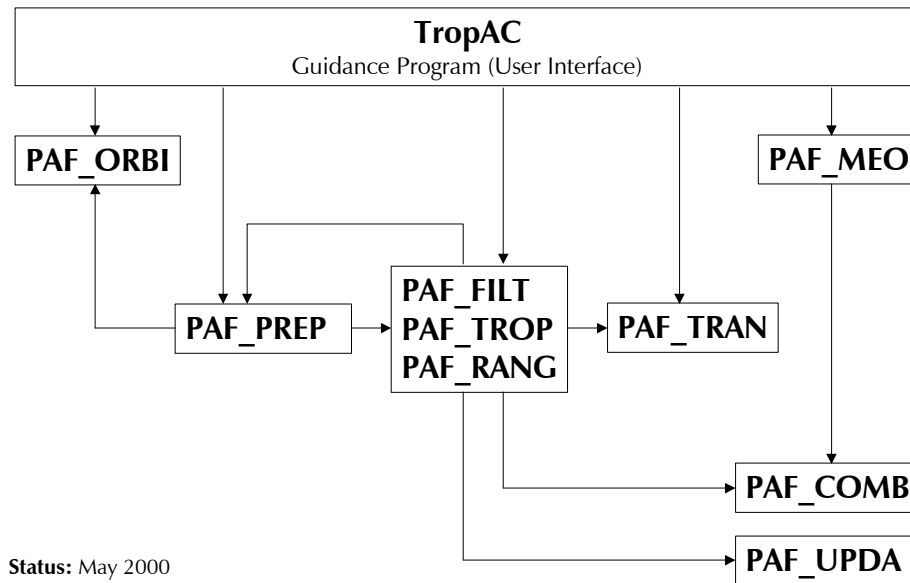


Figure 2-1 - Major modules of the TropAC permanent array filter software and their interrelations. The pre-processor for the GPS data is called PAF_PREP and prepares all needed data for Kalman filtering. Network filtering is carried out with the modules PAF_FILT, PAF_TROP or PAF_RANG. Program PAF_MEO serves as interface to the numerical weather models and PAF_COMB is able to combine regularly gridded tropospheric data sets from the weather fields and the irregularly distributed GPS estimates.

Finally, the pre-processor has the job to compose the baselines of the network to be filtered (\rightarrow 2.8) and to check whether there are poorly performing receivers that either must be excluded or isolated (\rightarrow 2.8.3).

2.1.2 Network Filtering

The pre-processed data are filtered for the unknowns, namely ground station coordinates (and in special cases also satellite orbit biases), zenith wet delays and ambiguities (see also \rightarrow 2.6). For this purpose, a Kalman filter is used (\rightarrow 2.5.2). Although pre-processing should have removed suspicious data, the filter itself is capable of blunder detection (\rightarrow 2.5.2.8) and may even perform a post-fit residual analysis (\rightarrow 2.5.2.8.3) and iterate on the previous solution if necessary. As during the pre-processing steps, the network is checked for poorly performing sites once more (\rightarrow 2.8.3) resulting in a new filter run if such stations are found.

2.1.3 Post-Filter Processing

At the post-filter stage, certain computations are carried out that do not belong directly to the Kalman filter process, e. g. the derivation of mean ground station coordinate estimates (\rightarrow 2.5.2.9), the datum transformation of networks (\rightarrow 2.7.1) as well as the creation of free network solutions by similarity transformation (\rightarrow 2.7.2) and the process of melting network partitions to an overall solution file (\rightarrow 2.9). Certainly, troposphere-related jobs like the conversion of zenith wet delays into integrated water vapor (\rightarrow 3.5) belong to this processing stage, too.

Name of Module	Purpose
TROPAC	Guidance program; user interface to simplify access to the program system; generation of batch-files, scheduling of processes, visualization.
PAF_ORBI	TropAC normally uses precise orbits from the IGS analysis centers which are provided in the SP3-format defined by the National Geodetic Survey (NGS, USA), see REMONDY [1989, 1991] for details on this format. Broadcast orbits are less accurate and given in a different format (RINEX NAV files). This module allows to create SP3-files from one or more RINEX navigation files.
PAF_MEO	The meteorological module of TropAC. It allows to extract meteorological data from numerical weather models provided in GRIB-format. Several data can be extracted like surface pressure, temperature and humidity. TROPEX files can be generated and ray-tracing can be performed (→ 4.).
PAF_COMB	The tropospheric combination module. It allows to combine GPS-derived tropospheric delays with those integrated in numerical weather fields (→ 4.).
PAF_PREP	The GPS pre-processor for static networks. This module prepares all needed data for the filter process: GPS measurements are read and filtered, orbits are interpolated, double differences are formed and synchronized, cycle slips are detected and repaired, tropospheric delays are predicted and, finally, a binary network file is created containing all necessary information for the filter engine.
PAF_FILT	The Kalman filter engine based on double-difference phase measurements. The state vector of this filter consists of 3 coordinate components for each site and - optionally - of one zenith wet delay per site modeled as random walk stochastic process. Moreover, orbit relaxation can be applied. The ambiguity parameters are dynamically allocated in the state vector.
PAF_TROP	This module equals PAF_FILT except for the fact that it does not estimate coordinates. This reduces the number of unknowns and speeds up processing.
PAF_RANG	The filter engine for pseudo-ranges. In contrast to PAF_FILT, this module only uses doubly differenced pseudo-ranges in order to derive approximate positions for those stations which are not well-known in advance.
PAF_TRAN	Network transformation module. Several routines are implemented in this program including datum transformation and combination of several partial networks to one single network solution. The module also allows to transform the Kalman filtered network into a free network solution by application of a similarity transformation.
PAF_UPDA	Network-update module. The core component of this module is a Kalman filter which uses coordinates as input and sequentially updates the network in time. It also allows to filter site velocities related to plate tectonics or other deformations.

Table 2-1 - Major modules of TropAC TRIDENT and their purpose within the processing package.

2.1.4 Realization

The algorithms described in this as well as in the two following chapters were implemented in the software package TropAC TRIDENT¹. This software package is

¹ TropAC: Tropospheric Analysis Center; TRIDENT: Tri-Discipline Enhancement Tools (special modules referring to the 3 disciplines positioning, geophysics and atmospheric research)

platform-independent² and can filter complete networks with a user-defined number of stations³. The modules which are of concern here are shown in Figure 2-1 and were coded in the C++ programming language.

The program is designed as platform-independent software package and can be remote-administered. Besides its capabilities to filter coordinates and tropospheric delays, TropAC provides access to numerical weather models and can extract meteorological information from these weather fields (\rightarrow 4.). Table 2-1 gives a synopsis of the most important modules.

2.2 Observations and Observation Equations

GPS observations⁴ mainly comprise pseudo-range and carrier phase measurements. Phase measurements have a noise level of a few millimeters and are very precise in comparison to code ranges that are only accurate to a few meters or some decimeters at their best. For this reason, carrier phases are the primary and most important type of observation for high-precision parameter estimation. The purpose of pseudo-ranges is primarily related to the pre-processing stages. In contrast to carrier phases, code ranges are not ambiguous and can therefore be easily applied to detect phase breaks, for instance, and serve for many other purposes as will be discussed in the following sections.

2.2.1 Pseudo-Ranges

Pseudo-ranges are non-ambiguous measurements. Although they have a higher noise level than phase measurements, they may serve a good job for the detection of multipath (\rightarrow 2.2.6), the ambiguity resolution process (\rightarrow 2.6.2.1) and the derivation of approximate station coordinates. Moreover, code ranges play a key-role for the determination of the signal transmission epoch (\rightarrow 2.4.3.1) and help to synchronize the baselines⁵ (\rightarrow 2.2.2.2). Following WÜBBENA [1991, p. 21], the simplified observation equation for carrier wave L_1 can be expressed as:

² Current versions exist for MS-DOS, MS Windows 95/98/NT/2000, LINUX, IRIX and HP-UX. Compilation of the modules is possible on any machine with the GNU/EGCS C++ compiler (gcc front end) installed. All modules are coded in C/C++ following the ANSI standard, so most other compilers that are ANSI-compliant should work well, too.

³ There is a logical limit of 428 stations per network. This limit is more than sufficient since the CPU load increases by the 3rd power of the number of network stations and this is what actually limits the size of a network to be analyzed.

⁴ GPS measurement data are exchanged using the receiver-independent exchange format RINEX (version 1.0 to 2.10 are supported, see GURTNER [1998]). In addition to the GPS observations, RINEX data also consist of navigation files containing the broadcast orbit information and meteorological files with pressure, temperature and relative humidity (and possibly water vapor radiometer measurements). All files are stored in ASCII-format and are therefore independent of compiler- or platform-specifics. For the GPS observation files, a special ASCII differential compression algorithm developed by Y. Hatanaka is frequently applied (see IGS [1997, pp. 17-18] for details). Hatanaka-compressed observation files are called *Compact RINEX* (CRINEX) files.

⁵ The desired accuracy level for measurement synchronization is about 1 microsecond which can be reached using pseudo-ranges even in times of activated selective availability (S/A) causing range errors of up to a maximum of 300 meters.

$$PR_{A[L1]}^i = S_{A[L1]}^i + c \cdot (\delta t_A - \delta t^i) + \delta S_{A[ION,L1]}^i + \delta S_{A[TROP]}^i + \epsilon_{PR} \quad (2-1)$$

$S_{A[L1]}^i$: geometric distance between receiver antenna A and satellite i
 c : speed of light (in vacuum, $c = 299\,792\,458$ m/s)
 δt_A : receiver clock error
 δt^i : satellite clock error
 $\delta S_{A[ION]}^i$: ionospheric propagation delay
 $\delta S_{A[TROP]}^i$: tropospheric propagation delay
 ϵ_{PR} : noise term

Please note that a clear distinction is made between measurements on L_1 and L_2 . The equation given here is valid for L_1 . Both measurements mainly differ in terms of the ionospheric delay which is frequency-dependent. The distance between receiver antenna and GPS satellite is defined as

$$S_{A[L1]}^i = \left| \underline{X}^i - \underline{X}_{A[L1]} \right| \quad (2-2)$$

\underline{X}^i : geocentric position vector of GPS satellite i
 $\underline{X}_{A[L1]}$: geocentric position vector of L_1 antenna phase center at site A

and is always referenced to the antenna phase center throughout this disquisition. Since the antenna phase centers are normally different for L_1 and L_2 (\rightarrow 2.3.6), the two distances are different as well.

The accuracy of C/A-code pseudo-ranges lies in the range of 1 to 5 meters for most receivers. P-code ranges may even reach decimeter accuracy. Modern receivers are able to apply techniques like *carrier phase smoothing* internally, i.e. the low noise of the phase measurements is used to smooth the code ranges. Hence the precision of the ranges is improved and multipath effects can be mitigated. It should be pointed out that such a filtered output does no longer represent the original measurements and, in certain cases, might even be disadvantageous for processing (\rightarrow 2.6.2.1).

2.2.2 Carrier Phase Measurements

Precise positioning and filtering of tropospheric delays is carried out using carrier phase measurements. The observation is the so-called *carrier beat phase*

$$\Phi_A^i(t_{OR}) = \Phi_{REC}(t_{OR}) - \Phi_{REF}(t_{OR}) = \Phi^i(t_{OT}) - \Phi_{REF}(t_{OR}) \quad (2-3)$$

t_{OR} : time of signal receipt
 t_{OT} : time of signal transmission
 Φ_A^i : carrier phase measurement, carrier beat phase
 Φ_{REC} : received carrier phase from satellite i at receipt time t_{OR}
 Φ^i : carrier phase of satellite i at signal transmission time t_{OT}
 Φ_{REF} : phase of reference signal generated by the receiver A at receipt time t_{OR}

and results from the comparison of the received, Doppler-shifted carrier signal Φ_{REC} and the reference signal Φ_{REF} generated by the GPS receiver using the nominal base frequency $f_0 = 10.23$ MHz. For L_1 , the corresponding frequency of the carrier wave is

$154 \cdot f_0$ and for L_2 it is $120 \cdot f_0$. The observation equation for carrier phase measurements on L_1 as given in RINEX observation files is always expressed in cycles:

$$\Phi_{A[L1]}^i = \frac{S_{A[L1]}^i + c \cdot (\delta t_A - \delta t^i) - \delta S_{A[ION,L1]}^i + \delta S_{A[TROP]}^i}{\lambda_{L1}} - N_{A[L1]}^i + \epsilon_\Phi \quad (2-4)$$

N_A^i : ambiguity term (phase bias) of measurement from antenna A to satellite i

λ_{L1} : wavelength of carrier signal; here: L_1 ($\lambda_{L1} = 19.02$ cm)

ϵ_Φ : noise term

For clarity, the carrier phases in units of cycles are denoted as Φ . In some cases, it is useful to convert these measurements into metric units which are then denoted as Θ :

$$\Theta_{A[L1]}^i = \lambda_{L1} \cdot \Phi_{A[L1]}^i \quad \wedge \quad \Theta_{A[L2]}^i = \lambda_{L2} \cdot \Phi_{A[L2]}^i \quad (2-5)$$

Carrier phase measurements are precise to a few millimeters on L_1 and modern receivers may even reach sub-millimeter noise levels under ideal circumstances. The signal-to-noise ratio as well as the precision are usually significantly worse on the L_2 carrier signal.

Note that some additional correction terms will be mentioned in the following sections. A more complete observation equation is

$$\begin{aligned} \Theta_{A[L1]}^i = S_{A[L1]}^i - \delta S_{A[AMB,L1]}^i + \delta S_{A[CLK]}^i + \delta S_{A[HWB,L1]}^i + \delta S_{A[SYNC]}^i + \delta S_{A[ORI,L1]}^i \\ + \delta S_{A[PCV,L1]}^i + \delta S_{A[REL]}^i - \delta S_{A[ION,L1]}^i + \delta S_{A[TROP]}^i + \epsilon_\Phi \end{aligned} \quad (2-6)$$

or

$$\begin{aligned} \Theta_{A[L1]}^i = S_{A[L1]}^i - N_{A[L1]}^i \cdot \lambda_{L1} + \delta S_{A[CLK]}^i + \delta S_{A[HWB,L1]}^i + \delta S_{A[SYNC]}^i + \delta S_{A[ORI,L1]}^i \\ + \delta S_{A[PCV,L1]}^i + \delta S_{A[REL]}^i - \delta S_{A[ION,L1]}^i + \delta S_{A[TROP]}^i + \epsilon_\Phi \end{aligned} \quad (2-7)$$

$\delta S_{A[AMB]}^i$: ambiguity term ("carrier phase offset")

$\delta S_{A[CLK]}^i$: combined receiver and satellite clock error term

$\delta S_{A[HWB]}^i$: hardware biases of the receiver and the transmitter
(includes inter-channel and inter-frequency biases)

$\delta S_{A[SYNC]}^i$: synchronization error

$\delta S_{A[ORI]}^i$: receiver/transmitter antenna orientation correction

$\delta S_{A[PCV]}^i$: antenna phase center variation correction

$\delta S_{A[REL]}^i$: relativistic effects

and shows some additional terms like the antenna orientation correction (\rightarrow 2.2.2.4), the transmitter and receiver hardware biases (\rightarrow 2.2.2.5) and relativistic effects (\rightarrow 2.2.2.6). Further correction terms involve the synchronization error (\rightarrow 2.2.2.2) and the elevation-dependent antenna phase center variations (\rightarrow 2.3.6.2). For matters of convenience, the analysis software evaluates these two error terms and uses them to correct the original phase measurements. As a consequence, the observation equation becomes

$$\Theta_{A[L1]}^i - \delta S_{A[SYNC]}^i - \delta S_{A[PCV]}^i = S_{A[L1]}^i - N_{A[L1]}^i \cdot \lambda_{L1} + \delta S_{A[CLK]}^i - \delta S_{A[ION,L1]}^i + \dots + \epsilon_\phi \quad (2-8)$$

with the left side of the equation representing the corrected phase measurement in units of wavelength λ_{L1} (usually meters) and the right side representing the ordinary functional description of the observation equation.

2.2.2.1 Double Differences

The original carrier phases are not used for filtering because these measurements are corrupted by receiver and satellite clock errors. Instead, double differences are derived: In a first step, single differences⁶ are formed, i. e. phase differences between two ground stations *A* and *B* which both have satellite *i* in view. In a second step, the same is done with those measurements to satellite *j*. The difference between the two single differences is computed and yields the doubly differenced phase observation

$$\nabla \Delta \Theta_{AB[L1]}^{ij} = (\Theta_{B[L1]}^j - \Theta_{A[L1]}^j) - (\Theta_{B[L1]}^i - \Theta_{A[L1]}^i) \quad (2-9)$$

and the corresponding simplified observation equation is

$$\begin{aligned} \nabla \Delta \Theta_{AB[L1]}^{ij} = & \nabla \Delta S_{A[L1]}^i - \nabla \Delta N_{A[L1]}^i \cdot \lambda_{L1} + c \cdot (\nabla \Delta \delta t_{AB} - \nabla \Delta \delta t^{ij}) \\ & - \nabla \Delta \delta S_{A[ION,L1]}^i + \nabla \Delta \delta S_{A[TROP]}^i + \nabla \Delta \epsilon_\phi \end{aligned} \quad (2-10)$$

where it becomes clear that the satellite clock errors formally cancel from the equation

$$\nabla \Delta \delta t^{ij} = -\{(\delta t^j - \delta t^i) - (\delta t^i - \delta t^i)\} = 0 \quad (2-11)$$

The same is also true for the receiver clock error, but rigorous receiver clock error elimination will only take place if all measurements strictly refer to the same measurement epoch. This means that a synchronization correction can be necessary (\rightarrow 2.2.2.2). Now, the (simplified) observation equation can be reduced to

$$\nabla \Delta \Theta_{AB[L1]}^{ij} = \nabla \Delta S_{A[L1]}^i - \nabla \Delta N_{A[L1]}^i \cdot \lambda_{L1} - \nabla \Delta \delta S_{A[ION,L1]}^i + \nabla \Delta \delta S_{A[TROP]}^i + \nabla \Delta \epsilon_\phi \quad (2-12)$$

There are several ways to compose double differences. The most common method is to sort the measurements according to their elevation angle and to choose the measurement associated with the satellite at highest elevation as reference. Given a sequence of satellites *i*, *j*, *k*, *l* and the corresponding elevation angles $\epsilon_A^i > \epsilon_A^j > \epsilon_A^k > \epsilon_A^l$, the set of double differences is

$$\begin{aligned} \nabla \Delta \Theta_{AB}^{ij} &= (\Theta_B^j - \Theta_A^j) - (\Theta_B^i - \Theta_A^i) \\ \nabla \Delta \Theta_{AB}^{ik} &= (\Theta_B^k - \Theta_A^k) - (\Theta_B^i - \Theta_A^i) \\ \nabla \Delta \Theta_{AB}^{il} &= (\Theta_B^l - \Theta_A^l) - (\Theta_B^i - \Theta_A^i) \end{aligned} \quad (2-13)$$

⁶ Single differences between measurements at two sites to the same satellite are normally denoted with a leading Δ sign. Differences between two satellites are denoted with a leading ∇ sign.

This *ij*, *ik*, *il* scheme has certain advantages: The measurement to the satellite with highest elevation usually also has the best signal-to-noise ratio and therefore highest accuracy and weight. Consequently, ideal standard deviations for the entire set of double differences can be expected due to the coupling of this observation to all other measurements. On the other hand, this scheme can be disadvantageous for point positioning as far as the influence of tropospheric (and ionospheric) delays is concerned. The atmospheric slant delay to the highest satellite in view will always have the smallest value and the delay to the satellite at lowest elevation angle will be at maximum value. Erroneous modeling of delays will therefore introduce errors in double differences for longer baselines that can be reduced if double differences are formed in a stepwise subsequent manner:

$$\begin{aligned}\nabla\Delta\Theta_{AB}^{ij} &= (\Theta_B^j - \Theta_A^j) - (\Theta_B^i - \Theta_A^i) \\ \nabla\Delta\Theta_{AB}^{jk} &= (\Theta_B^k - \Theta_A^k) - (\Theta_B^j - \Theta_A^j) \\ \nabla\Delta\Theta_{AB}^{kl} &= (\Theta_B^l - \Theta_A^l) - (\Theta_B^k - \Theta_A^k)\end{aligned}\tag{2-14}$$

In this *ij*, *jk*, *kl* scheme, the double differences are composed using neighboring satellite pairs that have similar elevation angles and thus also similar tropospheric slant delays. This means that tropospheric errors are reduced more efficiently than for the *ij*, *ik*, *il* method⁷.

Of course, for GPS tropospheric delay estimation as primary goal, it is highly wanted to obtain measurements containing the tropospheric delay to maximum extend. Therefore, the first method (*ij*, *ik*, *il*) is preferred and applied throughout this study.

2.2.2.2 Synchronization Problem

Due to the presence of receiver clock errors, care must be taken to refer the measurements to the correct epoch. Following the definitions given by WÜBBENA [1991, p. 20], the receiver time t' at the measurement epoch deviates from the true GPS time t by the receiver clock error δt_A in the following way:

$$t'_{OR} = t_{OR} + \delta t_A \quad \Leftrightarrow \quad t_{OR} = t'_{OR} - \delta t_A\tag{2-15}$$

t_{OR} : true GPS time of signal receipt at receiver site A

t'_{OR} : receiver time of signal receipt

δt_A : synchronization error, receiver clock error

The reader may also refer to MANIATIS [1989] and REMONDI [1985] who have a closer look at carrier phase observations. Synchronization problems are always of relevance when data strictly have to refer to the same epoch, e. g. when double differences are formed (\rightarrow 2.2.2.1).

⁷ A third method is implemented in the analysis software: The double differences are composed following the *ij*, *ik*, *il* scheme in the first epoch (where satellite i has the highest elevation) and afterwards, the reference satellite i is not changed as long as possible (i. e. as long as it remains visible) whether it is still the satellite with maximum elevation or not. This method is called "*maximum i scheme*" and only applied for very special purposes like rapid static positioning.

Following ROTHACHER and MERVART [1996, pp. 136-137], the error in slant distance

$$\delta S_{A[\text{SYNC}]}^i = -\frac{dS_A^i}{dt} \cdot \delta t_A \quad (2-16)$$

dS_A^i/dt : time derivative of distance S_A^i , radial velocity of satellite i with respect to station A

$\delta S_{A[\text{SYNC}]}^i$: synchronization error in distance induced by the receiver clock error δt_A

induced by the receiver clock offset δt_A from true GPS time can be computed with knowledge of the radial velocity of the satellite⁸ that may reach maximum values of 900 m/s for elevations near 10°. If the receiver clock error can be determined with an accuracy of about 1 microsecond, synchronization errors will be less than 1 millimeter. This task can be easily performed using pseudo-ranges. Even with S/A being enabled, code ranges are expected to be accurate to at least 300 m. This corresponds to an error in time of 1 microsecond.

For double differences, the synchronization term due to the receiver clock offsets δt_A and δt_B at the two stations involved is significantly reduced and becomes

$$\begin{aligned} -\nabla \Delta S_{AB[\text{SYNC}]}^{ij} &= \left(\frac{dS_B^j}{dt} \cdot \delta t_B - \frac{dS_A^j}{dt} \cdot \delta t_A \right) - \left(\frac{dS_B^i}{dt} \cdot \delta t_B - \frac{dS_A^i}{dt} \cdot \delta t_A \right) \\ &= \left(\frac{dS_B^j}{dt} - \frac{dS_B^i}{dt} \right) \cdot \delta t_B - \left(\frac{dS_A^j}{dt} - \frac{dS_A^i}{dt} \right) \cdot \delta t_A \end{aligned} \quad (2-17)$$

For stations controlled by stable atomic oscillators, there will be no problem in terms of synchronization issues and, moreover, modern receivers provide an automatic clock adjustment mode where the receiver itself performs proper time keeping with help of the GPS satellites. Nevertheless, for many receivers in use, the problem still remains and must be addressed by the processing software. The GPS pre-processor of the tropospheric analysis software takes care of this fact during the interpolation of the satellite orbits where the receiver clock error, the time of signal travel and the signal transmission time are determined (\rightarrow 2.4.3.1).

2.2.2.3 Degradation due to Selective Availability

Selective Availability (S/A) may place an additional burden on precise GPS analysis that is linked to the synchronization problem depicted before. Although, selective availability has been disabled in May 2000, most results presented in this study are based on data collected under S/A-conditions making a closer look at the problem necessary.

The so-called *d-technique* leads to an artificial degradation of the satellite oscillator frequency. FEIGL et al. [1991] show that this dithering directly affects the phase measurements if receivers are sampling their data at separate times which was the case for ancient Minimac and TI4100 receivers (offset of 0.92 s). Modern receivers

⁸ Note that the GPS pre-processor of the TropAC analysis system uses a slightly different approach to determine the synchronization correction (\rightarrow 2.4.3.1, step 7).

have taken the edge of this problem, but a brief look at this issue is useful since some Trimble 4000 SSE/SSI and other receivers still in use show an inability to maintain the nominal sampling epoch. For instance, irregular sampling was observed at the IGS tracking station Zimmerwald (*ZIMM*) in 1999 with an offset of about 30 ms at the end of a day (the nominal sampling epochs are exactly each 0.0 and 30.0 seconds). Worse situations occurred when the German Reference Network GREF was filtered where the monitor station Karlsruhe (*KARL*) showed offsets of as much as 160 ms from the nominal sampling epoch during August 1999.

Recalling the definition of the carrier beat phase, the received phase at receipt time t_{OR} is identical to the phase at signal transmission time $t_{OT} = t_{OR} - \tau$ with τ being the signal propagation time:

$$\Phi_{REC}(t_{OR}) = \Phi^i(t_{OT}) = \Phi^i(t_{OR} - \tau) \quad (2-18)$$

t_{OR} : time of receipt
 t_{OT} : time of transmission
 τ : signal propagation time
 Φ_{REC} : received phase

FEIGL et al. [1991] treat the satellite's phase as a linear function

$$\Phi^i(t) = \Phi_0 + f_s \cdot t \quad (2-19)$$

Φ_0 : initial phase
 f_s : satellite broadcast frequency

and demonstrate the influence of S/A for single differences between two GPS receivers with a frequency offset of δf_s . The corresponding single difference carrier phase shows an error which is proportional to the frequency deviation and the difference in propagation delay:

$$\delta \Delta \Phi^i \sim \delta f_s (\Delta t - \Delta \tau) \quad (2-20)$$

$\delta \Delta \Phi^i$: error of single difference carrier phase
 δf_s : GPS satellite broadcast frequency error invoked by S/A
 Δt : difference of sampling times between both receivers
 $\Delta \tau$: difference of signal propagation times

It is hardly possible to eliminate this error since it would require both receivers to sample the same wave-front. However, for baselines as long as 3000 km and well-synchronized sampling of the data, the term $\Delta t - \Delta \tau$ only reaches about 10 ms which causes an error of about 2 mm (0.01 cycles) when a frequency error of 1 Hz is present, but it will increase if both receivers sample with a spacing of significantly more than 10 ms apart. For the case of the joint Minimac/TI4100 experiment described by Feigl, an error of 2 dm (1 cycle) is to be expected⁹. A possible work-

⁹ The presence of clock dithering is also one major reason why it does not make much sense to interpolate carrier phase measurements which have been collected under S/A-conditions.

around is to measure the frequency deviations with help of receivers connected to stable oscillators.

2.2.2.4 Antenna Orientation Problem

Circularly polarized electromagnetic waves are transmitted from the GPS satellite's antenna to the receiving antenna. Consequently, the observed carrier phase measurements depend on the orientation of the receiver and transmitter antennas and the direction of the line of sight. If the orientation between the transmitting and the receiving antenna changes, a change will also be measured in the observed phase. For static networks, such changes in orientation are caused by the moving GPS satellites. WU et al. [1993] demonstrated that the correction due to antenna orientation is negligible for short baselines, but may reach a magnitude of up to 4 cm for baselines as long as 4000 km.

The algorithm given here allows a general description of the problem and can also be applied for kinematic GPS processing. However, attitude and azimuth information is needed in such cases because the orientation of the antenna dipoles must be known and may certainly vary in the case of moving antennas.

The *effective dipole* of the receiving antenna is found to be

$$\underline{d}_A = \underline{e}_x - \underline{e}_A^i \cdot (\underline{e}_A^i \cdot \underline{e}_x) + \underline{e}_A^i \times \underline{e}_y \quad (2-21)$$

\underline{d}_A : effective dipole vector of the receiving antenna at site A referring to satellite i

\underline{e}_x : ECEF unit vector in direction of the x-dipole element of the receiving antenna

\underline{e}_y : ECEF unit vector in direction of the y-dipole element of the receiving antenna

\underline{e}_A^i : ECEF unit vector from receiving to transmitting antenna

where all vectors are expressed in the global, Cartesian ECEF system. For static networks with the ground antennas being correctly aligned to northward direction, the *local level unit vectors* of the two antenna dipole elements are defined as

$$\underline{e}_x = \begin{bmatrix} 1 \\ 0 \\ 0 \end{bmatrix} \quad \wedge \quad \underline{e}_y = \begin{bmatrix} 0 \\ -1 \\ 0 \end{bmatrix} \quad (2-22)$$

\underline{e}_x : local level orientation vector of x-dipole element

\underline{e}_y : ECEF orientation vector of x-dipole element

with \underline{e}_x describing the orientation of the northward and \underline{e}_y that of the westward dipole element. These local level vectors (\underline{e}_x , \underline{e}_y) must be transformed into the global system (\rightarrow 2.3) yielding \underline{e}_x , \underline{e}_y before they can be used to compute the effective dipole. The next step is to compute the effective dipole of the transmitting antenna

$$\underline{d}^i = \underline{e}_x^i - \underline{e}_A^i \cdot (\underline{e}_A^i \cdot \underline{e}_x^i) - \underline{e}_A^i \times \underline{e}_y^i \quad (2-23)$$

\underline{d}^i : effective dipole vector of the transmitting antenna of satellite i referring to site A

\underline{e}_x^i : ECEF unit vector in direction of the x-dipole element of the transmitting antenna

\underline{e}_y^i : ECEF unit vector in direction of the y-dipole element of the transmitting antenna

\underline{e}_A^i : ECEF unit vector from receiving to transmitting antenna

where the unit vectors in direction of the dipole elements of the transmitting antenna are computed with help the expressions given in section → 2.4.4. Now, the fractional part of a cycle $\Delta\phi$ can be determined with help of

$$\zeta = \underline{e}_A^i \cdot (\underline{d}^i \times \underline{d}_A) \quad (2-24)$$

yielding

$$\Delta\phi_A^i = \frac{\text{sgn } \zeta}{2\pi} \cdot \arccos \left(\frac{\underline{d}^i \cdot \underline{d}_A}{|\underline{d}^i| \cdot |\underline{d}_A|} \right) \quad (2-25)$$

$\Delta\phi_A^i$: fractional part of orientation correction with respect to receiver A and satellite i in units of cycles

and the integer part

$$\Delta N_A^i = \text{int} [\Delta\Phi_{A[\text{ORI},\text{PREV}]}^i - \Delta\phi_A^i + \text{sgn} (\Delta\Phi_{A[\text{ORI},\text{PREV}]}^i - \Delta\phi_A^i)] \quad (2-26)$$

ΔN_A^i : integer part of the orientation correction

$\Delta\Phi_{A[\text{ORI},\text{PREV}]}^i$: orientation correction of the previous epoch, initialized with zero for the first epoch

can be separated with help of the previous correction value $\Delta\Phi_{A[\text{ORI},\text{PREV}]}^i$. So, the new orientation correction of the carrier phase measurements is

$$\Delta\Phi_{A[\text{ORI}]}^i = \Delta N_A^i + \Delta\phi_A^i \quad (2-27)$$

$\Delta\Phi_{A[\text{ORI}]}^i$: orientation correction for phase measurement at station A to satellite i

and must be added to the measured carrier phase. The correction term $\Delta\Phi_{A[\text{ORI}]}^i$ is initialized with zero for the very first epoch and accumulated subsequently. The algorithm assumes that no correction greater than 180° occurs between two successive epochs. This is never the case for static networks as long as no large data gaps occur since the receiving antennas do not move at all and the transmitters only move relatively slowly. The correction term in units of distance becomes

$$\delta S_{A[\text{ORI},L_1]}^i = \Delta\Phi_{A[\text{ORI},L_1]}^i \cdot \lambda_{L_1} \quad (2-28)$$

$\delta S_{A[\text{ORI}]}^i$: orientation correction in units of wavelength λ_{L_1} for phase measurement at station A to satellite i

for carrier wave L_1 and is, of course, different for the two carrier frequencies. It is recommended to apply this correction when long baselines are part of the network to analyze.

2.2.2.5 Hardware Biases

The transmitted signals are delayed in the GPS satellite's electrical circuits as well as in the receiver. Following WÜBBENA [1991, p. 21], the combined receiver/transmitter hardware bias term for carrier wave L_1 becomes

$$\delta S_{A[HWB,L1]}^i = -c \cdot (\delta b_{A[L1]}^{ch\{i\}} + \delta b_{[L1]}^i) \quad (2-29)$$

c : speed of light (in vacuum, $c = 299\,792\,458$ m/s)

δb^i : satellite/transmitter hardware bias

$\delta b_A^{ch\{i\}}$: receiver hardware bias for channel $ch\{i\}$ that is currently tracking satellite i

$\delta S_{A[HWB]}^i$: combined influence of transmitter/receiver hardware bias (receiver at station A to satellite i)

and the double difference error term is

$$\begin{aligned} \nabla \Delta \delta S_{AB[HWB,L1]}^{ij} &= (\delta S_{B[HWB,L1]}^j - \delta S_{A[HWB,L1]}^j) - (\delta S_{B[HWB,L1]}^i - \delta S_{A[HWB,L1]}^i) \\ &= -c \cdot \{(\delta b_{B[L1]}^{ch\{j\}} - \delta b_{A[L1]}^{ch\{j\}}) - (\delta b_{B[L1]}^{ch\{i\}} - \delta b_{A[L1]}^{ch\{i\}})\} \end{aligned} \quad (2-30)$$

that is free from the transmitter hardware biases, but not from the receiver hardware biases. The hardware bias error is only zero if we can assume that the bias for channel $ch\{i\}$ is identical to that of channel $ch\{j\}$. This was true for old receivers like the Texas Instruments TI 4100 that used the multiplex-technique to track up to 4 different satellites. This means that this special receiver type only had one hardware channel for L_1 (and another one for L_2) and tracking of the satellites was performed by quickly switching between them (multiplexing) like a single CPU of a personal computer is able to switch between several applications and threads (multitasking). Hence, only one receiver hardware bias for each carrier wave was present and fully eliminated during double differencing. Modern receivers are disadvantageous in this case because they usually provide 12 (or more) parallel hardware channels for each carrier frequency and, as a consequence, the hardware biases will not necessarily be identical for all these channels. However, the *inter-channel biases* are under control for most receivers currently at the market and remaining uncertainties are soaked up by the ambiguity states of the filter engine (\rightarrow 2.5.2.2) as long as no ambiguity fixing is forced (\rightarrow 2.6). As the *inter-frequency biases* of both the transmitter and the receiver cancel during double differencing, hardware biases are not expected to deteriorate the GPS analysis results.

2.2.2.6 Relativistic Effects

According to WÜBBENA [1991, p. 30], relativistic effects involve the *periodic effect* due to the eccentricity of the GPS satellite trajectory

$$\delta S_{[RPE]}^i = -4.443 \cdot 10^{-10} \left[\frac{s}{\sqrt{m}} \right] \cdot c \cdot e \cdot \sqrt{a} \cdot \sin E \quad (2-31)$$

c : speed of light (in vacuum, $c = 299\,792\,458$ m/s)

e : eccentricity of trajectory of GPS satellite i

a : semi-major axis of GPS satellite trajectory

E : eccentric anomaly of GPS satellite i

$\delta S_{[RPE]}^i$: relativistic periodic effect for satellite i in units of [m]

and the *radar delay effect*

$$\delta S_{A[RDE]}^i = \frac{2 \cdot GM}{c^2} \cdot \ln \left(\frac{|\underline{X}^i| + |\underline{X}_A| + |\underline{X}^i - \underline{X}_A|}{|\underline{X}^i| + |\underline{X}_A| - |\underline{X}^i - \underline{X}_A|} \right) \quad (2-32)$$

GM: geocentric gravitational constant (WGS84: $GM = 3.986005 \cdot 10^{14} \text{ m}^3/\text{s}^2$)

\underline{X}^i : ECEF position vector of GPS satellite i

\underline{X}_A : ECEF position vector of receiver antenna A

$\delta S_{A[RDE]}^i$: relativistic radar delay effect in units of [m]

The total relativistic correction is the sum of both effects,

$$\delta S_{A[REL]}^i = \delta S_{A[RPE]}^i + \delta S_{A[RDE]}^i \quad (2-33)$$

but the periodic effect will cancel out during double differencing and only the radar delay effect will remain. This correction may have a maximum value of about 2 cm for the undifferenced phase observation.

2.2.3 Linear Combinations

Precise GPS network analysis with long baselines always makes use of the dual-band carrier phases provided by GPS. Special linear combinations between these two signals can be formed for special purposes. Generally speaking, a combined double difference phase measurement can be written as

$$\nabla \Delta \Phi_{AB[a1,a2]}^{ij} = a_1 \cdot \nabla \Delta \Phi_{AB[L1]}^{ij} - a_2 \cdot \nabla \Delta \Phi_{AB[L2]}^{ij} \quad (2-34)$$

$a_{1,2}$: combination factors for the original L_1 and L_2 carrier phases

and the ambiguity term associated with the linearly combined phase measurement can be written in analogous form

$$\nabla \Delta N_{AB[a1,a2]}^{ij} = a_1 \cdot \nabla \Delta N_{AB[L1]}^{ij} - a_2 \cdot \nabla \Delta N_{AB[L2]}^{ij} \quad (2-35)$$

Of course, the same can be done for (doubly differenced) pseudo-ranges after the ranges have been converted into units of cycles:

$$\nabla \Delta PR_{AB[a1,a2]}^{ij} = a_1 \cdot \frac{\nabla \Delta PR_{AB[L1]}^{ij}}{\lambda_{L1}} - a_2 \cdot \frac{\nabla \Delta PR_{AB[L2]}^{ij}}{\lambda_{L2}} \quad (2-36)$$

The virtual wavelength of a linearly combined signal is given by SEEGER [1993, p. 257]

$$\lambda_{a1,a2} = \frac{c}{a_1 \cdot f_{L1} - a_2 \cdot f_{L2}} \quad (2-37)$$

c : speed of light in vacuum

f_{L1}, f_{L2} : frequency of carrier signal L_1 and L_2 , respectively

$a_{1,2}$: combination factors

and the frequency is

$$f_{a1,a2} = \frac{c}{\lambda_{a1,a2}} = a_1 \cdot f_{L1} - a_2 \cdot f_{L2} \quad (2-38)$$

The standard deviation σ_Φ ("noise level") of the undifferenced phase observation is

$$\sigma_{\Phi[a1,a2]} = \sqrt{(a_1 \cdot \sigma_{\Phi[L1]})^2 + (a_2 \cdot \sigma_{\Phi[L2]})^2} \quad (2-39)$$

The ionospheric amplification factor

$$V_{ION} = \frac{a_1 \cdot f_{L2} - a_2 \cdot f_{L1}}{f_{a1,a2}} \quad (2-40)$$

is defined by LEINEN [1997, p. 12] and describes the impact of the 1st order ionospheric effect on the linear combination. Special choices for a_1 and a_2 allow to reduce or to eliminate the ionospheric effect. Some important linear combinations are given in Table 2-2:

Symbol	a_1	a_2	$l_{[a1,a2]}$	$ V_{ION} $	$SF_{[a1,a2]}$	Remark
L_1	1	0	190	0.780	3.0	original L_1 signal
L_2	0	-1	244	1.280	4.0	original L_2 signal
L_{43}	4	3	114	0.070	9.2	near ionosphere-free
L_{54}	5	4	101	0.055	10.4	near ionosphere-free
L_{97}	9	7	54	0.004	9.8	almost ionosphere-free
$L_{77;60}$	77	60	6	0.000	9.8	ionosphere-free, integer ambiguities
L_C	1	f_{L2}/f_{L1}	484	0.000	9.8	ionosphere-free, floating ambiguities
L_W	1	1	862	1.000	19.6	wide lane
L_N	1	-1	107	1.000	2.4	narrow lane

Table 2-2 - Characteristic properties of the original signals (1st section), typical linear L_1 - L_2 -combinations which reduce the ionospheric propagation delay (2nd section) and additional signals for special purposes like the wide and the narrow lane signal (3rd section). The widely used L_C signal is free of the 1st order ionospheric effect, but has the disadvantage of floating ambiguities which complicates ambiguity fixing whereas $L_{77;60}$ has integer ambiguities and is ionosphere-free as well, but is practically unusable for ambiguity fixing due to its tiny wavelength. The wavelength $\lambda_{a1,a2}$ as well as the noise level σ_Φ are given in **units of millimeters**.

The most commonly used signal for filtering baselines longer as some tens of kilometers is L_C . Though this signal is called to be *ionosphere-free*, it is stressed here that only the first order effect of the ionospheric propagation delay is eliminated (\rightarrow 2.2.4), but WÜBBENA [1991, pp. 25-26] states that higher order ionospheric effects can be neglected for baselines up to several thousand kilometers if double differences are used (see also section \rightarrow 6.2.5). The problem with L_C is its non-integer nature that complicates ambiguity fixing. Although experience underpins that float solutions are sufficient when diurnal data batches from permanent tracking networks are analyzed, ambiguity fixing is supported by the tropospheric analysis software with help of the following two linear combinations: If the *wide lane* ($a_1 = 1$; $a_2 = 1$) and the *narrow*

lane ($a_1 = 1$; $a_2 = -1$) ambiguities can be fixed, the nominal L_C -ambiguity can be computed and constrained in the filter (\rightarrow 2.6.2).

The network filter software is also able to handle different linear combinations depending on the baseline length. For example, *near ionosphere-free* combinations like L_{54} can be used for shorter baselines up to 100 or 200 km and the L_C -signal will be used for larger ones. The background to offer this opportunity to the analyst is to simplify ambiguity fixing by using combinations with integer nature in situations where the ionospheric effect is either eliminated in double differences to sufficient extend, or properly modeled by external ionospheric information (\rightarrow 2.2.4.3). A disadvantage of near ionospheric-free linear combinations is their relatively short wavelength.

2.2.4 Ionospheric Error

Apart from the tropospheric propagation delay which is the core issue of this disquisition (\rightarrow 3.), the ionospheric delay must be properly addressed either by elimination of most of its effect or by modeling it. In most cases, it is preferable to eliminate the effect with help of dual-frequency data and use of the ionosphere-free linear combination L_C . As already mentioned, it is also possible to use linear combinations with integer nature like L_{54} that only partially eliminate the ionospheric influence. For further reduction, so-called IONEX maps¹⁰ are used which contain the vertical TEC (VTEC) to estimate the first order ionospheric propagation delay. A compensation with help of the Klobuchar-model is not recommended nor supported because SEEGER [1989, p. 50] states that this model only mitigates about 50% of the true propagation delay.

The ionosphere can be divided into several layers starting at an altitude of about 70 km and extends to an upper boundary layer of 1000 km. The propagation of microwave signals transmitted by GPS satellites is influenced by charged particles throughout this part of the atmosphere. Following HOFFMANN-WELLENHOF et al. [1993, p. 91], the ionospheric propagation delay in radial direction over the antenna A at height h_A is the difference between the measured and the geometrical distance in vacuum

$$\delta S_{\text{ION}}^{Z=0} = \int_{\text{ION}} n_{\text{ION}}(h) \cdot dh - \int_{\text{VAC}} dh \quad (2-41)$$

n_{ION} : index of ionospheric refraction

dh : differential increment in height

z : zenith angle

ION : path of a ray passing from GPS antenna in radial direction through the ionosphere

VAC : virtual path of a ray passing from GPS antenna in radial direction through the vacuum

¹⁰ The format of the ionosphere map exchange format *IONEX* is defined by SCHAEER et al. [1998].

where the index of ionospheric refraction n_{ION} can be approximated by a series expansion with reciprocal powers of the signal frequency f and given here for the group delay¹¹

$$n_{\text{ION}} = 1 + \frac{C_2}{f^2} + \frac{C_3}{f^3} + \frac{C_4}{f^4} + \dots \quad (2-42)$$

$C_{2,4}$: coefficients of series expansion

f : frequency of carrier wave

WÜBBENA [1991, p. 25] as well as BASSIRI and HAJJ [1993] mention that the first order ionospheric effect ($O\{1/f^2\}$) is by far the most dominant one with a maximum delay of about 33 m on L_1 and 54 m on L_2 (absolute values) in zenith direction. Under average conditions, zenith path delays in the range of 16 m (L_1) to 27 m (L_2) can be expected. Second order terms ($O\{1/f^3\}$) are in the range of 1 cm with a maximum of less than 3 cm for the linear combination L_C . Finally, third order terms ($O\{1/f^4\}$) of up to 6 mm, but usually below 1 mm may remain in L_C as well. These effects are normally further reduced by double differencing of the observations.

2.2.4.1 First Order Effect

Knowledge of the electron content is sufficient in order to model the first order ionospheric effect. In most cases, only the first order delay is taken into account because it is by far the most dominant part of the ionospheric propagation delay.

$$n_{\text{ION}} \approx 1 + \frac{C_2}{f^2} = 1 + \frac{C \cdot N_e}{f^2}$$

N_e : electron density in [electrons/m³]

C : constant; $C = 40.28$ [m³/s²]

Now, the ionospheric propagation delay in zenith direction can be integrated using the electron density N_e . For carrier phase measurements this correction in zenith direction is

$$\delta S_{\text{ION}}^{Z=0} = \int_{h_A}^{\infty} \frac{C_2}{f^2} = \frac{C}{f^2} \cdot \int_{h_A}^{\infty} N_e(h) \cdot dh = \frac{C}{f^2} \cdot \text{VTEC} \quad (2-44)$$

VTEC: vertical total electron content in [TECU]

1 TECU = 10^{16} electrons/m²

In practice, the zenith ionospheric delay must be mapped into the direction of the line of sight of the particular satellite. This is done by application of a

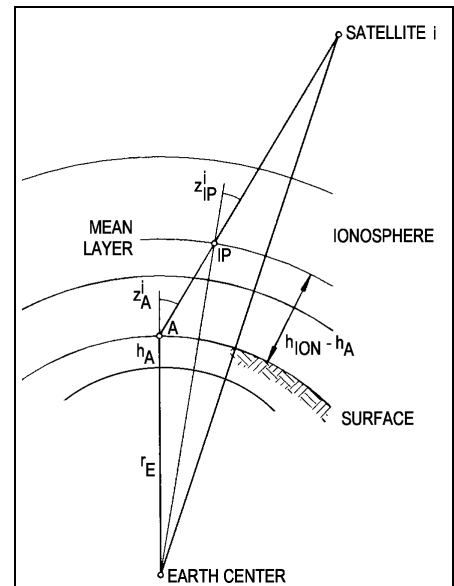


Figure 2-2 - Zenith angle z_A^i from ground station A to satellite i and ionospheric zenith angle z_{IP}^i from the mean ionosphere to the satellite following HOFFMANN-WELLENHOF [1993]. The projection of the ionospheric point IP to the surface yields the horizontal coordinates needed for interpolation in TEC maps like IONEX files.

¹¹ The ionospheric effect for the group delay is to be applied for pseudo-range measurements; the absolute value for the ionospheric delay applied to carrier phase measurements is the same, but the sign is negative. This fact has already been accounted for in the observation equations discussed before.

mapping function. To do so, the zenith angle from the ground antenna at station A to satellite i

$$\cos z_A^i = \frac{\cos \varphi_A \cdot \cos \lambda_A \cdot \Delta X_A^i + \cos \varphi_A \cdot \sin \lambda_A \cdot \Delta Y_A^i + \sin \varphi_A \cdot \Delta Z_A^i}{S_A^i} \quad (2-45)$$

φ_A : ellipsoidal latitude of receiver antenna at station A
 λ_A : ellipsoidal longitude of receiver antenna at station A
 $\Delta X_A^i, \Delta Y_A^i, \Delta Z_A^i$: components of the distance vector between antenna at station A and satellite i
 S_A^i : distance between antenna at station A and satellite i

is commonly corrected by taking the distance between antenna and ionosphere into account as shown in Figure 2-2:

$$\sin z_{IP}^i = \frac{r_E + h_A}{r_E + h_{ION}} \cdot \sin z_A^i \quad (2-46)$$

z_{IP}^i : zenith angle from ionospheric point IP to satellite i
 z_A^i : zenith angle from ground station A to satellite i
 r_E : earth radius ($r_E = 6371$ km)
 h_{ION} : mean height of ionosphere ($h_{ION} = 300 \dots 500$ km)
 h_A : height of ground station A

where the weighted mean height of the ionosphere is normally chosen to be about 450 km. Generally speaking, heights in the range of 300 to 500 km are valid values, see HOFFMANN-WELLENHOF [1993, p. 92]. Uncertainties in h_{ION} mainly affect observations at low elevations, whereas high-elevation measurements remain more or less untouched. The slant delay now becomes

$$\delta S_{A[ION]}^i = m_{ION}(z_{IP}^i) \cdot \delta S_{ION}^{Z=0} = \frac{1}{\cos z_{IP}^i} \cdot \delta S_{ION}^{Z=0} = \frac{C}{f^2} \cdot \frac{1}{\cos z_{IP}^i} \cdot VTEC \quad (2-47)$$

where $1/\cos z$ is the mapping function or *obliquity factor*. Other formulations are, of course, possible. For instance, KLOBUCHAR [1996] uses

$$m_{ION}(\epsilon_A^i) = 1 + 16 \cdot \left(0.53 - \frac{\epsilon_A^i}{\pi} \right)^3 \quad (2-48)$$

ϵ_A^i : elevation angle from ground station A to satellite i in radians ($z_A^i = \pi - \epsilon_A^i$)

and uses the zenith or elevation angle, respectively, from antenna site A to satellite i rather than that from the ionospheric point IP to the satellite.

2.2.4.2 Second Order Effect

For high-precision applications, it might be desirable to model the second order effect to further reduce ionospheric errors. BASSIRI and HAJJ [1993] have developed an approximate method to describe this effect for average conditions. Geomagnetic coordinates are needed for these computations:

$$\begin{aligned}
\cos \theta_M &= \sin \delta \cdot \cos \beta \cdot \sin \theta \cdot \cos \lambda + \sin \delta \cdot \sin \beta \cdot \sin \theta \cdot \sin \lambda + \cos \delta \cdot \cos \theta \\
\tan \lambda_M &= \frac{-\sin \beta \cdot \sin \theta \cdot \cos \lambda + \cos \beta \cdot \sin \theta \cdot \sin \lambda}{\cos \delta \cdot (\cos \beta \cdot \sin \theta \cdot \cos \lambda + \sin \beta \cdot \sin \theta \cdot \sin \lambda) - \sin \delta \cdot \cos \theta} \\
\varepsilon_M &= \varepsilon \\
\alpha_M &= \alpha + \arccos(\sin \lambda \cdot \sin \lambda_M \cdot \cos \delta \cdot \cos \beta + \cos \lambda \cdot \cos \lambda_M \cdot \cos \beta \\
&\quad + \sin \lambda \cdot \cos \lambda_M \cdot \sin \beta - \cos \lambda \cdot \sin \lambda_M \cdot \cos \delta \cdot \sin \beta)
\end{aligned} \tag{2-49}$$

θ_M, θ : geomagnetic and geodetic pole distance (co-latitude, $\theta = 1/2\pi - \varphi$)

λ_M, λ : geomagnetic and geodetic longitude

$\varepsilon_M, \varepsilon$: geomagnetic and geodetic elevation angle

α_M, α : geomagnetic and geodetic azimuth

δ, β : rotation angles ($\beta = 291^\circ, \delta = 11.5^\circ$)

Alternatively, global geocentric position vectors can be transformed into geomagnetic coordinates with help of the transformation equation

$$\underline{X}_M = \begin{pmatrix} \cos \delta \cdot \cos \beta & \cos \delta \cdot \sin \beta & -\sin \delta \\ -\sin \beta & \cos \beta & 0 \\ \sin \delta \cdot \cos \beta & \sin \delta \cdot \sin \beta & \cos \delta \end{pmatrix} \cdot \underline{X} \tag{2-50}$$

$\underline{X}_M, \underline{X}$: geomagnetic and geodetic ECEF position vector

The pole distance is further corrected by

$$\theta'_M \approx \theta_M - \frac{h_{ION}}{r_E} \cdot \frac{\cos \alpha_M}{\tan \varepsilon_M} \tag{2-51}$$

and now, the second order group delay can be computed

$$\begin{aligned}
\delta S_{ION}^{2nd} &\approx \left(1.377 \cdot 10^{-6} \cdot \lambda \cdot \frac{r_E}{r_E + h_{ION}} \right)^3 \cdot \left| \sin \theta'_M \cdot \cos \varepsilon_M \cdot \cos \alpha_M - 2 \cdot \cos \theta'_M \cdot \sin \varepsilon_M \right| \\
&\quad \cdot m_{ION}(Z_{IP}^i) \cdot VTEC
\end{aligned} \tag{2-52}$$

λ : wavelength of carrier wave

that shows a sensitivity of 0.16 and 0.33 mm per TECU for L_1 and L_2 , respectively.

2.2.4.3 Interpolation in IONEX Files

As already stated, needed VTEC values are interpolated in IONEX files which are more accurate than using the Klobuchar-model. Currently, this IGS product contains global VTEC layers with a horizontal resolution of 5° in longitude and 2.5° in latitude and a temporal resolution of 2 hours, i. e. 12 VTEC maps per day and 12 RMS maps describing the accuracy. Several analysis centers take part in the production of these files, but rather different analysis methods are in use. A joint product like the combined IGS orbits has not been established by the IGS community yet. The methods for horizontal and temporal interpolation applied in this study are given here briefly. Further details on the format can be found in SCHAEER et al. [1998].

2.2.4.3.1 Computation of Ionospheric Points

Due to the relatively high altitude of the mean ionosphere, it is not suitable to interpolate VTEC values directly at the coordinates of antenna A . Instead, ionospheric points IP (see Figure 2-2) have to be computed for each line of sight. This also implies that for all satellites i, j, k, \dots in view there will exist individual ionospheric points. The azimuth

$$\tan \alpha_A^i = \frac{-\sin \lambda_A \cdot \Delta X_A^i + \cos \lambda_A \cdot \Delta Y_A^i}{-\sin \varphi_A \cdot \cos \lambda_A \cdot \Delta X_A^i - \sin \varphi_A \cdot \sin \lambda_A \cdot \Delta Y_A^i + \cos \varphi_A \cdot \Delta Z_A^i} \quad (2-53)$$

φ_A, λ_A : ellipsoidal latitude and longitude of receiver antenna A
 $\Delta X_A^i, \Delta Y_A^i, \Delta Z_A^i$: components of the distance vector between antenna A and satellite i

is needed for the derivation of ionospheric points. According to LEINEN [1997], the latitude of the ionospheric point IP shown in Figure 2-2 can be obtained by

$$\sin \varphi_{IP}^i = \sin \varphi_A \cdot \cos z_{IP}^i + \cos \varphi_A \cdot \sin z_{IP}^i \cdot \cos \alpha_A^i \quad (2-54)$$

and the longitude is

$$\lambda_{IP}^i = \lambda_A + \arcsin \left(\frac{\sin z_{IP}^i \cdot \sin \alpha_A^i}{\cos \varphi_{IP}^i} \right) \quad (2-55)$$

Note that the VTEC grid is represented by *geocentric* latitude and longitude, so the ellipsoidal latitude of a particular tracking station must be converted to

$$\tan \varphi_{IP}^{i*} = (1 - f_{WGS})^2 \cdot \tan \varphi_{IP}^i \quad (2-56)$$

φ^* : geocentric latitude
 φ : ellipsoidal latitude
 f_{WGS} : flattening of WGS84 ellipsoid ($f_{WGS} = 1/298.257224$)

2.2.4.3.2 Horizontal Interpolation

The 4 nearest neighbors contained in the VTEC map are looked up and a weighted mean is computed using the reciprocal spherical distance raised to the power of 1.5 as weighting coefficient.

2.2.4.3.3 Temporal Interpolation

A 10-point-polynomial is used for interpolation in time domain. This allows to model the periodical behavior of the VTEC time series, but also requires IONEX maps of the previous and the following day as the analysis system normally processes diurnal data batches.

2.2.5 Cycle Slip Detection and Repair

If it can be assumed that all coordinates are known a priori with reasonable accuracy, the floating ambiguities can be computed by solving the observation equation for the ambiguity term:

$$\begin{aligned}\nabla\Delta N_{AB[L1]}^{ij} &= \frac{\nabla\Delta S_{AB[L1]}^{ij} - \nabla\Delta S_{AB[ION,L1]}^{ij} + \nabla\Delta S_{AB[TROP]}^{ij}}{\lambda_1} - \nabla\Delta\Phi_{AB[L1]}^{ij} \\ \nabla\Delta N_{AB[L2]}^{ij} &= \frac{\nabla\Delta S_{AB[L2]}^{ij} - \nabla\Delta S_{AB[ION,L2]}^{ij} + \nabla\Delta S_{AB[TROP]}^{ij}}{\lambda_2} - \nabla\Delta\Phi_{AB[L2]}^{ij}\end{aligned}\quad (2-57)$$

The analysis software now compares the floating ambiguities of the current with those of a previous epoch

$$\begin{aligned}\delta\nabla\Delta N(t)_{AB[L1]}^{ij} &= \nabla\Delta N(t - \Delta t)_{AB[L1]}^{ij} - \nabla\Delta N(t)_{AB[L1]}^{ij} \\ \delta\nabla\Delta N(t)_{AB[L2]}^{ij} &= \nabla\Delta N(t - \Delta t)_{AB[L2]}^{ij} - \nabla\Delta N(t)_{AB[L2]}^{ij}\end{aligned}\quad (2-58)$$

and if this difference $\delta\nabla\Delta N(t)$ exceeds a pre-defined threshold, e. g. 1 cycle, it is rounded to the nearest integer value

$$\delta\nabla\Delta N(t)_{AB[INT,L1]}^{ij} = \text{int}\left(\delta\nabla\Delta N(t)_{AB[L1]}^{ij} + \frac{1}{2} \cdot \text{sgn}(\delta\nabla\Delta N(t)_{AB[L1]}^{ij})\right)\quad (2-59)$$

The ambiguity of the current epoch t will be updated to become equal to that of the preceding epoch $t - \Delta t$ by

$$\nabla\Delta N(t)_{AB[REPAIRED,L1]}^{ij} = \nabla\Delta N(t)_{AB[L1]}^{ij} + \delta\nabla\Delta N(t)_{AB[INT,L1]}^{ij}\quad (2-60)$$

and the phase measurement is corrected as well

$$\nabla\Delta\Theta(t)_{AB[REPAIRED,L1]}^{ij} = \nabla\Delta\Theta(t)_{AB[L1]}^{ij} - \delta\nabla\Delta N(t)_{AB[INT,L1]}^{ij} \cdot \lambda_{L1}\quad (2-61)$$

In this way, both carrier frequencies can be checked for cycle slips separately. Moreover, no code-carrier combination is necessary which has a high noise-level. So, the detection is rather sensitive and will also reveal phase gaps as small as one cycle. The major disadvantage of this algorithm¹² is the necessity of a reasonably good a priori knowledge of the site coordinates. In the case of new stations with uncertain coordinates being part of the network, the detection threshold must be relaxed or the algorithm must be disabled entirely. In principle, it is not harmful to disable cycle slip detection because the Kalman filter itself (\rightarrow 2.5.2) has several blunder detectors (\rightarrow 2.5.2.8) that will easily *detect* phase gaps, but in contrast to the pre-processing

¹² Actually, the cycle slip detector presented here is quite similar to the use of triple difference phase observations. The major differences are that predicted atmospheric effects and a priori coordinates (satellite-receiver geometry) are incorporated, so the algorithm does not entirely rely on measurements alone.

procedure described here, the filter will not *repair* cycle slips. For other approaches to this problem, the reader may also refer to HOFFMANN-WELLENHOF et al. [1993].

Note that a maximum value for the time lag Δt is defined that usually lies below 3000 s. It defines the history of an ambiguity record maintained by the analysis software. The background for the definition of a maximum history can be explained by the following example: It might happen that a certain ambiguity combination is not present for some few epochs due to bad signal-to-noise ratio¹³ or other reasons. In case of re-occurrence after some epochs, there will be no loss of memory: The pre-processor will look a bit more backward in history, will find a corresponding ambiguity and perform the comparison. If the history covered only one single epoch, a possible phase break could not be repaired. On the other hand, if the history list is enlarged to more than half of the day, there will certainly be a re-occurrence of one and the same satellite (and likely of the same ambiguity combination) because the orbital period is about 12 hours. So, after the disappearance of a certain satellite, it will re-occur during the day, the cycle slip detector will look up the history list, find an entry related to the previous revolution of the satellite and compare it with the measurements of the current revolution. In this case, the difference would be hardly of integer nature.

An additional remark should be devoted to the process of cycle slip fixing: Phase gaps are only closed if the integer difference does not deviate from the float solution for more than a pre-defined threshold which is 0.3 cycles by default. This check guarantees a reliable round-off to the nearest integer. Test-runs showed that there are only very few non-fixable cycle slips on carrier phase L_1 , but a much larger amount of non-fixable gaps may occur on L_2 . This fact is not too unexpected as the C/A-code is missing on L_2 and in many cases, the signal-to-noise ratio of these measurements is significantly worse in comparison to L_1 measurements.

2.2.6 Multipath Detection

The multipath problem is less troublesome for permanent GPS arrays with carefully selected antenna sites than for kinematic surveys and similar applications. As for the case of cycle slips, the blunder detector of the Kalman filter is also able to detect strong multipath affection and can eliminate associated observations (\rightarrow 2.5.2.8). Moreover, a code-carrier combination can be used at the pre-processing stage in order to detect multipath situations. This combined signal is furthermore denoted as multipath signal MP and expressed in doubly differenced form. The following equation shows the multipath signal for carrier wave L_1

$$\begin{aligned}\nabla \Delta \text{MP}_{AB[L1]}^{ij} &= \nabla \Delta \text{PR}_{AB[L1]}^{ij} - \nabla \Delta \Theta_{AB[L1]}^{ij} \\ &= 2 \cdot \nabla \Delta \delta S_{AB[ION,L1]}^{ij} + \nabla \Delta N_{AB[L1]}^{ij} \cdot \lambda_{L1} + \varepsilon_{\nabla \Delta \text{MP}}\end{aligned}\quad (2-62)$$

¹³ The pre-processor will eliminate measurements with poor signal-to-noise ratio. In RINEX files, the signal-to-noise ratio is described by an indicator ranging from 1 to 9 where 9 is best and 1 is poorest signal quality. The threshold to good C/N is about 5. Flags below this value will normally lead to down-weighting of the associated measurements. All measurements flagged with a C/N-indicator of worse than 2 are deleted by the pre-processing module.

MP: multipath signal, code-minus-carrier combination
 ε_{MP} : noise term (will contain noise due to multipath effects)

which does not only incorporate the multipath noise ε_{MP} , but also the ambiguity term N and the double influence of the ionospheric propagation delay $\delta S_{[ION]}$. If this signal is compared with the value of the previous epoch, it can be assumed that the ionospheric delay remained approximately constant

$$\nabla \Delta \delta S_{AB[ION,L]}^{ij}(t - \Delta t) \approx \nabla \Delta \delta S_{AB[ION,L]}^{ij}(t) \quad (2-63)$$

and the same should be true for the ambiguity term. In contrast to the cycle slip detection function, the time lag Δt is limited to exactly one epoch, i. e. $\Delta t = 30$ s for the IGS tracking network, so only subsequent samples are compared with each other. If the difference

$$\delta \nabla \Delta MP_{AB[L]}^{ij}(t) = \left| \nabla \Delta MP_{AB[L]}^{ij}(t - \Delta t) - \nabla \Delta MP_{AB[L]}^{ij}(t) \right| \quad (2-64)$$

exceeds a pre-defined threshold and it is certain that the reason for this discrepancy is not linked to a (non-fixable) cycle slip, the associated measurements of the current epoch as well as those of Δt_{MP} future epochs will be eliminated. Δt_{MP} is typically between 5 to 10 minutes (10 to 20 epochs for the IGS network) and represents typical periods for multipath affection. Further information about the multipath problem can be found in BRAASCH [1996] and RAY and CANNON [1999].

2.3 Site Displacements and Corrections

This section deals with the correction of antenna coordinates due to several effects. *Solid earth tides* cause displacements in the order of up to several decimeters, the *pole tide* may have an impact of up to a few centimeters depending on the pole position and *ocean loading effects* are usually in the range of some millimeters, but can amount to more than 1 cm for certain sites. Moreover, geometric corrections must be applied, the antenna eccentricity offset for instance, and the antenna phase center correction is of relevance.

For several corrections it is necessary to transform coordinates between the global geocentric (ECEF) and the local topocentric reference system (local level system). The transformation of local level coordinates into the global Cartesian ECEF system is given below

$$\underline{X} = \underline{X}_0 + \begin{pmatrix} -\sin \varphi \cdot \cos \lambda & -\sin \lambda & \cos \varphi \cdot \cos \lambda \\ -\sin \varphi \cdot \sin \lambda & \cos \lambda & \cos \varphi \cdot \sin \lambda \\ \cos \varphi & 0 & \sin \varphi \end{pmatrix} \cdot \underline{x} \quad (2-65)$$

φ : ellipsoidal latitude of the origin of the local topocentric system
 λ : ellipsoidal longitude of the origin of the local topocentric system
 \underline{X}_0 : global geocentric coordinate vector of the origin of the local topocentric system
 \underline{X} : global geocentric coordinate vector (X, Y, Z) of the transformed point
 \underline{x} : local coordinate vector consisting of the northward (x), eastward (y) and the radial component (z)

and can be used to transform several corrections, e. g. ocean loading or pole tide deformations which are originally expressed in the local level system: The geocentric coordinate vector \underline{X}_0 and the associated latitude and longitude represent the uncorrected station coordinates, the site displacement is given in form of vector \underline{x} (or $\Delta\underline{x}$) and the transformed point \underline{X} is the corrected station position expressed in the global coordinate system.

The coordinate vector for an arbitrary station for carrier wave L_1 can be denoted in the ECEF system as

$$\underline{X}(t)_{[L_1]} = \underline{X} + \Delta\underline{X}(t)_{\text{VEL}} + \Delta\underline{X}(t)_{\text{SET}} + \Delta\underline{X}(t)_{\text{PT}} + \Delta\underline{X}(t)_{\text{OL}} + \Delta\underline{X}_{\text{AE}} + \Delta\underline{X}_{\text{PCV}[L_1]} \quad (2-66)$$

$\underline{X}(t)$: antenna phase center position vector at epoch t
 \underline{X} : coordinate vector of the point monument
 $\Delta\underline{X}(t)_{\text{VEL}}$: velocity correction vector at epoch t
 $\Delta\underline{X}(t)_{\text{SET}}$: solid earth tide correction vector at epoch t
 $\Delta\underline{X}(t)_{\text{PT}}$: pole tide correction vector at epoch t
 $\Delta\underline{X}(t)_{\text{OL}}$: ocean loading correction vector at epoch t
 $\Delta\underline{X}_{\text{AE}}$: antenna eccentricity vector
 $\Delta\underline{X}_{\text{PCV}}$: antenna phase center offset correction vector

where the velocity correction (\rightarrow 2.3.1), the earth (\rightarrow 2.3.2) and pole tide (\rightarrow 2.3.3) as well as the ocean loading correction (\rightarrow 2.3.4) try to compensate several effects deforming the earth's body. The antenna eccentricity term (\rightarrow 2.3.5) is a pure geometric correction accounting for the fact that the point monument is normally not identical with the antenna reference point. Finally, the antenna phase center offset correction (\rightarrow 2.3.6) models the difference between the antenna reference point and the true GPS antenna phase center which is usually different for L_1 and L_2 . The vector \underline{X} is what we usually try to estimate during network filtering, i. e. the time-invariant components of the ground monuments.

2.3.1 Velocity Correction

The initial positions normally refer to the *ITRF*, *EUREF*, or a similar reference frame. The *ITRF* is a global reference frame. This means that effects like plate tectonics will make the positions of the ground-stations to vary with time. Therefore, the epoch must be explicitly given for any coordinate solution and a position record does not only consist of a coordinate triple, but also of a velocity vector. The reference epoch is expressed in decimal years. The solutions for both the *ITRF96* and *ITRF97* are referenced to the epoch 1997.0, for instance. Assuming a constant velocity, the coordinates of the observation epoch can be obtained by applying the law of linear motion

$$\underline{X}(t) = \begin{pmatrix} X \\ Y \\ Z \end{pmatrix} = \underline{X}(t_{\text{REF}}) + (t - t_{\text{REF}}) \cdot \underline{v}_X(t_{\text{REF}}) \quad \wedge \quad \underline{v}_X(t_{\text{REF}}) \equiv \underline{v}_X(t) \quad (2-67)$$

t : observation epoch in [years, decimal]
 t_{REF} : reference epoch in [years] as given in network solution file

$\underline{X}(t)$: ECEF position vector at observation epoch t in [m]
 $\underline{X}(t_{\text{REF}})$: ECEF position vector at reference epoch t_{REF} in [m]
 $\underline{V}_X(t_{\text{REF}})$: velocity vector of station at reference epoch in [m/year]

Typical site velocities are between 1 and 2 cm per year, e. g. *Oberpfaffenhofen (OBER)* and *Potsdam (POTS)* have a resulting velocity is 2.4 cm/year, and some stations with higher rates can be found, too, for example *Easter Island (EISL)* with 6.9 cm/year.

2.3.2 Solid Earth Tides

The gravitational attraction of moon and sun (and other bodies of the solar system) is responsible for what we call solid earth tides causing site displacements of up to several decimeters¹⁴. LANDAU [1988] approximates the site displacement by the formula

$$\Delta \bar{X}_j = \frac{m_j}{m_E} \cdot \frac{r_E^4}{|\underline{X}_j|^3} \cdot \left[3 \cdot l_2 \cdot \frac{\underline{X}_p \cdot \underline{X}_j}{|\underline{X}_p| \cdot |\underline{X}_j|} \cdot \frac{\underline{X}_j}{|\underline{X}_j|} + \left[3 \cdot \left(\frac{h_2}{2} - l_2 \right) \cdot \left(\frac{\underline{X}_p \cdot \underline{X}_j}{|\underline{X}_p| \cdot |\underline{X}_j|} \right)^2 - \frac{h_2}{2} \right] \cdot \frac{\underline{X}_p}{|\underline{X}_p|} \right] \quad (2-68)$$

r_E : radius of the earth (set equal to $|\underline{X}_p|$)
 \underline{X}_j : ECEF coordinate vector of the disturbing body (moon or sun)
 \underline{X}_p : ECEF coordinate vector of the ground station
 m_j/m_E : mass ratio of disturbing body to earth ($m_{\text{MOON}}/m_E = 0.012300034$, $m_{\text{SUN}}/m_E = 332945.94$)
 h_2, l_2 : Love and Shida number ($h_2 = 0.6090$ and $l_2 = 0.0852$)

that can be easily implemented. Comparative studies with the IERS reference model showed that this approximation is only accurate to some centimeters as it only takes the frequency independent transfer functions (h_2, l_2) of tides of degree and order 2 into account and does not involve any corrections due to the frequency dependency of the transfer functions.

A more precise algorithm was implemented in the analysis software that follows the IERS Conventions 1996¹⁵. This model is significantly more sophisticated and said to have an accuracy in the millimeter range. The reader may refer to MCCARTHY [1996, pp. 55-65] for a full documentation. A concise summary can be given as follows: In a first step, several corrections are computed in the time domain, e. g. the general degree 2 and 3 in phase corrections are processed taking into account elastic and inelastic effects as well as out-of-phase corrections of degree 2 and contributions from the latitude dependence for the diurnal and semi-diurnal tides. In a second step, corrections are computed in the frequency domain for the diurnal, semi-diurnal and long-term tides. Figure 2-3 shows a comparison in radial direction of the models presented by MCCARTHY [1996] and LANDAU [1988].

¹⁴ Computation of solid earth tides requires knowledge of the positions of the disturbing bodies (sun and moon). The TropAC analysis system uses the JPL Planetary Ephemeris DE200. For more information on this issue see http://www.gb.nrao.edu/~rfisher/Ephemerides/ephem_descr.html.

¹⁵ The algorithm was originally coded by V. Dehant, S. Mathews and J. Gipson in the FORTRAN programming language and translated to C++ which is the standard programming language of the TropAC analysis software. The original code can be obtained via <ftp://ftpserver.oma.be/pub/astro/dehant/IERS>.

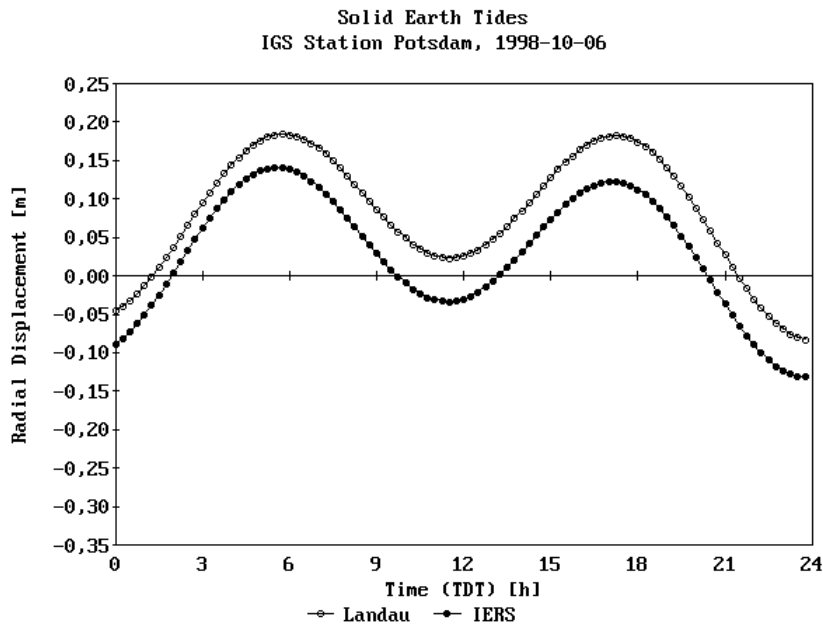


Figure 2-3 - Comparison of the radial site displacements for IGS tracking station Potsdam (POTS) using the approximation presented by LANDAU [1988] and the IERS model documented by MCCARTHY [1996]. The difference between both models is dominated by a systematic error with a magnitude of about 5 cm. Generally speaking, the diagram shows that site displacements due to solid earth tides cannot be omitted as they cause diurnal variations of more than 2 dm in the radial coordinate channel.

Tide	f	u
M_2	$1.0004 - 0.0373 \cos N + 0.0002 \cos (2N)$	$-2.14^\circ \sin N$
S_2	1.0	0.0
N_2	see M_2	see M_2
K_2	$1.0241 + 0.2863 \cos N + 0.0083 \cos (2N) - 0.0015 \cos (3N)$	$-17.74^\circ \sin N + 0.68^\circ \sin (2N) - 0.04^\circ \sin (3N)$
K_1	$1.0060 + 0.1150 \cos N - 0.0088 \cos (2N) + 0.0006 \cos (3N)$	$-8.86^\circ \sin N + 0.68^\circ \sin (2N) - 0.07^\circ \sin (3N)$
O_1	$1.0089 + 0.1871 \cos N - 0.0147 \cos (2N) + 0.0014 \cos (3N)$	$10.80^\circ \sin N - 1.34^\circ \sin (2N) + 0.19^\circ \sin (3N)$
P_1	1.0	0.0
Q_1	see O_1	see O_1
M_f	$1.0429 + 0.4135 \cos N - 0.0040 \cos (2N)$	$-23.74^\circ \sin N + 2.68^\circ \sin (2N) - 0.38^\circ \sin (3N)$
M_m	$1.0000 - 0.1300 \cos N + 0.0013 \cos (2N)$	0.0
S_{sa}	1.0	0.0

Table 2-3 - Amplitude scaling factors f and phase angle offsets u for the required partial tides according to DOODSON [1928, pp. 274-275, tables 25, 26 and 27].

2.3.3 Pole Tide

The site deformation due to polar motion can reach a maximum radial displacement of about 2.5 cm. Following the IERS Conventions 1996, the correction in the local topocentric system is

$$\Delta \vec{x}_{PT} = \begin{pmatrix} \Delta x \\ \Delta y \\ \Delta z \end{pmatrix} = \begin{pmatrix} +0.009 \left[\frac{m}{\text{arc sec}} \right] \cdot \cos 2\theta \cdot (x_{POLE} \cdot \cos \lambda - y_{POLE} \cdot \sin \lambda) \\ +0.009 \left[\frac{m}{\text{arc sec}} \right] \cdot \cos \theta \cdot (x_{POLE} \cdot \sin \lambda + y_{POLE} \cdot \cos \lambda) \\ -0.032 \left[\frac{m}{\text{arc sec}} \right] \cdot \sin 2\theta \cdot (x_{POLE} \cdot \cos \lambda - y_{POLE} \cdot \sin \lambda) \end{pmatrix} \quad (2-69)$$

Δx : northward displacement in the local level system

Δy : eastward displacement in the local level system

Δz : radial (vertical) displacement in the local level system (positive upwards)

θ : pole distance; $\theta = \frac{1}{2}\pi - \phi$ with ϕ being the ellipsoidal latitude

λ : ellipsoidal longitude

x_{POLE} : pole coordinate component x in arc-seconds

y_{POLE} : pole coordinate component y in arc-seconds

where the current pole position is given in seconds of arc. More details are given in MCCARTHY [1996, pp. 65-66].

2.3.4 Ocean Loading

Site displacements due to ocean tide loading can be modeled if the amplitudes and phase angles of the partial tides are known which are made available by SCHERNECK¹⁶. According to MCCARTHY [1996, pp. 51-55], the site correction due to ocean load can be estimated by summing up the influence of all partial tides via the formula

$$\Delta \underline{x}_{OL} = \begin{pmatrix} -\Delta x_3 \\ -\Delta x_2 \\ \Delta x_1 \end{pmatrix} \quad \wedge \quad \Delta x_c = \sum_j f_j \cdot A_{C,j} \cdot \cos(\omega_j \cdot t + \chi_j + u_j - \phi_{C,j}) \quad \wedge \quad c = 1, 2, 3 \quad (2-70)$$

Δx_c : site displacement due to ocean loading for coordinate component $c = 1, 2, 3$

t : time argument

$A_{C,j}$: amplitude of partial tide j for coordinate component c with $j = 1, 2, \dots, 11$

$\phi_{C,j}$: phase angle of partial tide j for coordinate component c

f_j : scale factor for tide j

u_j : phase angle offset for tide j

ω_j : angular period of partial tide j

χ_j : astronomical argument of partial tide j

where the ocean loading tables provide amplitudes $A_{C,j}$ and phase angles $\phi_{C,j}$ for the following 11 tides in ascending order from $j = 1, 2, \dots, 11$: $M_2, S_2, N_2, K_2, K_1, O_1, P_1,$

¹⁶ Ocean loading tables were computed by SCHERNECK [1983] and are available for most IGS sites via <ftp://gere.oso.chalmers.se/~pub/hgs/oload/README>.

Q_1 , M_f , M_m and S_{sa} . The sum of $\omega_j t + \chi_j$ can be computed by the function ARG^{17} as given by MCCARTHY [1996, page 52]. The coordinate components Δx_c are given as radial_(c=1), westward_(c=2) and southward component_(c=3) in the local level system. f_j and u_j are the scale factor and the phase angle offset for tide j and depend on the longitude of the lunar node. These values can be calculated with help of tables XXV, XXVI and XXVII of DOODSON [1928] where the argument N is computed using the formula

$$N = 259.157 [\text{deg}] - 19.32818 [\text{deg/year}] (Y - 1900) - 0.05295 [\text{deg/day}] (D + l) \quad (2-71)$$

Y: year, 4 digits, e. g. 1999

D: day of year elapsed since January 1st of year Y

l: $l = \text{int}[(Y-1901)/4]$

and is needed for the interpolation functions for f and u . The factors and phase angle offsets are given in Table 2-3.

2.3.5 Antenna Eccentricity

The antenna eccentricity correction is a geometric correction due to the fact that the antenna reference point is usually not identical with the point fixing. The eccentricity information is given in the RINEX header in local level coordinates and directly constitutes the displacement vector

$$\Delta \underline{x}_{AE} = \begin{pmatrix} \Delta x \\ \Delta y \\ \Delta z \end{pmatrix} = \begin{pmatrix} \Delta N_{AE} \\ \Delta E_{AE} \\ \Delta R_{AE} \end{pmatrix} \quad (2-72)$$

with ΔN_{AE} , ΔE_{AE} , ΔR_{AE} being the northward, eastward and radial antenna eccentricities as given in the header section of the RINEX observation file.

2.3.6 Antenna Phase Center Corrections

The observation equations were presented in section 2.2 and the reader might have noticed that the geometrical distance between antenna and satellite was denoted in connection with the carrier signal. Usually, it is

$$S_{A[L1]}^i \neq S_{A[L2]}^i \quad (2-73)$$

because the antenna coordinates are unequal on L_1 and L_2 due to difference in antenna phase center which is about 2 cm for *Dorne Margolin* antennas that are widely used within the IGS network.

In addition to this constant offset between the nominal antenna reference point and the actual antenna phase center, elevation-dependent antenna phase center variations may occur. This second term is applied as a correction to the phase measurements.

¹⁷ Note that a year 2000 problem may arise since the function needs a 2-digit-year (99 instead of 1999) as input. However, for 2000 and future dates up to 2999, it is necessary to continue with $100 + Y\%100$ where '%' is the modulo operator and Y the 4-digit-year.

Variations in azimuth are also possible, but are not yet part of the official antenna phase center calibration tables provided by IGS and NGS. For further reading refer to MADER [1999], who also describes the standard format of PCV-files supported by the TropAC analysis system, and KANIUTH et al. [1998].

2.3.6.1 Antenna Phase Center Offset

The antenna phase center offsets are given in the calibration tables for L_1 and L_2 , respectively, in the local topocentric coordinate system

$$\Delta \underline{X}_{PCV[L1]} = \begin{pmatrix} \Delta x \\ \Delta y \\ \Delta z \end{pmatrix} = \begin{pmatrix} \Delta N_{PCV[L1]} \\ \Delta E_{PCV[L1]} \\ \Delta R_{PCV[L1]} \end{pmatrix} \quad (2-74)$$

and can be converted into a global geocentric correction vector $\Delta \underline{X}_{PCV[L1]}$. Now, the distance between the GPS receiver antenna and the GPS satellite can be written as

$$\begin{aligned} S_{A[L1]}^i &= \sqrt{(X_A + \Delta X_{PCV[L1]} - X^i)^2 + (Y_A + \Delta Y_{PCV[L1]} - Y^i)^2 + (Z_A + \Delta Z_{PCV[L1]} - Z^i)^2} \\ S_{A[L2]}^i &= \sqrt{(X_A + \Delta X_{PCV[L2]} - X^i)^2 + (Y_A + \Delta Y_{PCV[L2]} - Y^i)^2 + (Z_A + \Delta Z_{PCV[L2]} - Z^i)^2} \end{aligned} \quad (2-75)$$

X^i, Y^i, Z^i : satellite position

X_A, Y_A, Z_A : coordinates of receiver antenna reference points

$\Delta \underline{X}_{PCV}$: local level vector of antenna phase center offset corrections

$\Delta \underline{X}_{PCV}$: ECEF vector of antenna phase center offset corrections

The coordinates can be referred to the L_1 antenna phase center, too,

$$\Delta \underline{X}_{A[L1]} = \underline{X}_A + \Delta \underline{X}_{PCV[L1]} \quad (2-76)$$

and in this case, only the phase center difference between L_1 and L_2

$$\Delta \underline{X}_{PCV}^{L1 \rightarrow L2} = \Delta \underline{X}_{PCV[L2]} - \Delta \underline{X}_{PCV[L1]} \quad (2-77)$$

is needed for proper modeling of the observations:

$$\begin{aligned} S_{A[L1]}^i &= \sqrt{(X_{A[L1]} - X^i)^2 + (Y_{A[L1]} - Y^i)^2 + (Z_{A[L1]} - Z^i)^2} \\ S_{A[L2]}^i &= \sqrt{(X_{A[L1]} + \Delta X_{PCV}^{L1 \rightarrow L2} - X^i)^2 + (Y_{A[L1]} + \Delta Y_{PCV}^{L1 \rightarrow L2} - Y^i)^2 + (Z_{A[L1]} + \Delta Z_{PCV}^{L1 \rightarrow L2} - Z^i)^2} \end{aligned} \quad (2-78)$$

Note that the phase center offset correction cannot be omitted for precise coordinate solutions nor tropospheric parameter estimation. To recall two antenna types which show rather high L_1/L_2 phase center differences: *Dorne Margolin* antennas have a

radial difference of almost 2 cm and the *Ashtech 700829* antenna shows a difference of 3.2 cm between both phase centers¹⁸.

2.3.6.2 Elevation-Dependent Phase Center Variations

Following MADER [1999], GPS antennas are currently best calibrated in relative mode. At the NGS, the receiver clock error is minimized using a rubidium oscillator. A set of single-difference phase residuals for L_1 and L_2 is fitted to a polynomial function

$$\Delta(\Phi_{\text{OBS}} - \Phi_{\text{CALC}})_i = \tau_i + c_1 \cdot \epsilon_i + c_2 \cdot \epsilon_i^2 + c_3 \cdot \epsilon_i^3 + c_4 \cdot \epsilon_i^4 \quad (2-79)$$

Φ_{OBS} : observed phase measurement

Φ_{CALC} : calculated (fitted) phase measurement

τ_i : relative time delay

$c_{1..4}$: polynomial coefficients

ϵ_i : elevation angle to satellite i

and the adjusted, elevation-dependent calibration function is represented in *PCV* calibration files by discrete values in elevation-increments of 5°. The user can interpolate the values for the requested elevation angle with help of linear interpolation between the two nearest neighbors. The corrected phase measurement is then obtained by

$$\Theta_{\text{A[L1]}}^{i*} = \Theta_{\text{A[L1]}}^i - \Delta\Theta_{\text{A[L1]}}^{i \text{ PCV}} \quad (2-80)$$

Θ^* : corrected phase measurement in meters

Θ : original phase measurement in meters ($\Theta = \phi \cdot \lambda$ with ϕ : phase in cycles, λ : wavelength)

$\Delta\Theta^{\text{PCV}}$: elevation-dependent PCV correction, linearly interpolated in PCV-file, in meters

Note that the elevation-dependent correction values are given in millimeters in the PCV-calibration files.

2.4 Handling Precise Orbits

Precise orbits are produced by the IGS analysis centers using parts of the global IGS tracking network at global scale. Three major products can be distinguished: *predicted orbits* are calculated 24 and 48 hours in advance, respectively, and have meanwhile reached an accuracy level of about 5 dm. They are designed for real-time purposes and can be used to replace the less accurate broadcast orbits. The IGS *rapid orbits* are produced with a latency of just 2 days and are accurate to 1-2 dm and the *final orbits* have a latency of 2 weeks and can be considered as the most precise product with a RMS of often better than 1 dm. The major difference between both types is that rapid analysis starts earlier and hence might suffer from data outages more severely than the final analysis.

¹⁸ See the IGS phase center variation file IGS_01.PCV for details which can be obtained via ftp://igscb.jpl.nasa.gov/igscb/station/general/igs_01.pcv. Moreover, the U. S. National Geodetic Survey (NGS) provides antenna calibration information for many more antennas, see <http://www.grdl.noaa.gov/GRD/GPS/Projects/ANTCAL>

IGS orbits are exchanged in the standard SP3-format, see REMONDI [1989]. In contrast to RINEX navigation files, no orbital elements are given, but the ECEF position vectors¹⁹ for each satellite in time intervals of 15 minutes. This kind of representation is sufficient to allow interpolation with an accuracy in the millimeter range.

2.4.1 Format Conversion of Broadcast Orbits

Broadcast orbits have an accuracy of 1 to 5 m. This is insufficient to filter tropospheric delays and, consequently, IGS orbits are used within the analysis system for most purposes with SP3-files being the only orbit format supported. However, the software can also be used for other purposes than tropospheric delay estimation and as a compatibility function, SP3 files can be created from RINEX navigation files. The formulas for computation of ECEF satellite coordinates from the standard GPS orbit representation are given below for the sake of completeness.

Following SEEGER [1993, pp. 220-224], the satellite clock error is

$$\delta t = a_0 + a_1 \cdot (t - t_{OC}) + a_2 \cdot (t - t_{OC})^2 \quad (2-81)$$

δt : satellite clock error

$a_{0,2}$: polynomial clock error coefficients for offset (a_0), drift (a_1) and aging (a_2)

t_{OC} : time of clock, reference epoch of clock error coefficients

t : time for which the satellite position is requested

where the time of clock t_{OC} is given in year, month, day, hour, minute and seconds of GPS time. The time t_k relative to the orbit reference epoch t_{OE} is

$$t_k = t - t_{OE} - \delta t \quad (2-82)$$

t_k : time elapsed since the reference epoch of the GPS satellite orbits

t_{OE} : time of ephemeris, reference epoch of the orbit elements

and here, the reference time t_{OE} is given in seconds of week starting with 0 seconds on Sunday, 0 h. From Kepler's 3rd law follows

$$n_0 = \sqrt{\frac{GM}{a^3}} \quad (2-83)$$

n_0 : computed, uncorrected mean motion

GM : geocentric gravitational constant (WGS84: $GM = 3.986005 \cdot 10^{14} \text{ m}^3/\text{s}^2$)

a : semi-major axis of satellite trajectory, \sqrt{a} is given in RINEX navigation file

which is corrected to

$$n = n_0 + \delta n \quad (2-84)$$

n : corrected mean motion

δn : correction value for mean motion supplied by RINEX navigation file

¹⁹ ECEF are earth-centered and earth-fixed positions, i. e. the coordinates are *not* referenced to the *inertial* reference frame.

and allows to compute the mean anomaly

$$M = M_0 + n \cdot t_k \quad (2-85)$$

M : mean anomaly at requested epoch t

M_0 : mean anomaly at reference epoch t_{0E}

The eccentric anomaly E must be solved in an iterative way using equation

$$E = M + e \cdot \sin E \quad (2-86)$$

E : eccentric anomaly

e : eccentricity of satellite trajectory, given in RINEX navigation file

with a suggested start value of $E = M$. Now, the true anomaly v can be determined non-ambiguously with help of the two formulas

$$\cos v = \frac{\cos E - e}{1 - e \cdot \cos E} \quad \wedge \quad \sin v = \frac{\sqrt{1 - e^2} \cdot \sin E}{1 - e \cdot \cos E} \quad \Rightarrow \quad v = \text{atan2}(\sin v; \cos v) \quad (2-87)$$

v : true anomaly

and the *atan2*-function which is implemented in the *C programming language* (and many other ones). The argument of latitude in the satellite system is

$$u_0 = v + w \quad (2-88)$$

u_0 : uncorrected argument of latitude in the satellite system

Now, the harmonic corrections can be determined with help of the values for CUC ... CIS given in the navigation message

$$\begin{aligned} \delta u &= CUC \cdot \cos u_0 + CUS \cdot \sin u_0 \\ \delta r &= CRC \cdot \cos u_0 + CRS \cdot \sin u_0 \\ \delta i &= CIC \cdot \cos u_0 + CIS \cdot \sin u_0 \end{aligned} \quad (2-89)$$

δu : correction term for latitude argument

δr : correction term for radius of trajectory

δi : correction term for inclination

and the corresponding corrected elements are found to be

$$\begin{aligned} u &= u_0 + \delta u \\ r &= a \cdot (1 - e \cdot \cos E) + \delta r \\ i &= i_0 + \frac{di}{dt} \cdot t_k + \delta i \end{aligned} \quad (2-90)$$

u : argument of latitude in the satellite system

r : radius of satellite trajectory

i : inclination of satellite trajectory

di/dt : change of inclination, first derivative of inclination, given in navigation file

The 2-D-coordinates referenced to the satellite's orbital plane

$$x = r \cdot \cos u \quad \wedge \quad y = r \cdot \sin u \quad (2-91)$$

x, y : coordinates of space vehicle, expressed in the orbital plane

can be transformed into global geocentric coordinates if the ascending node

$$\Omega = \Omega_0 + \left(\frac{d\Omega}{dt} - \omega_E \right) \cdot t_k - \omega_E \cdot t_{OE} \quad (2-92)$$

Ω : argument of ascending node

Ω_0 : ascending node at reference epoch t_{OE} , given in navigation file

$d\Omega/dt$: change in ascending node, given in navigation file

ω_E : angular velocity of the earth (WGS84: $\omega_E = 7.2921151467 \cdot 10^{-5}$ rad/s)

is determined:

$$\underline{X} = \begin{pmatrix} X \\ Y \\ Z \end{pmatrix} = \begin{pmatrix} x \cdot \cos \Omega - y \cdot \sin \Omega \cdot \cos i \\ x \cdot \sin \Omega + y \cdot \cos \Omega \cdot \cos i \\ y \cdot \sin i \end{pmatrix} \quad (2-93)$$

\underline{X} : ECEF position vector of satellite at requested epoch t

With this algorithm, the geocentric satellite positions can be computed and SP3-files can be easily created. It is pointed out that broadcast orbits refer to the antenna phase centers of the GPS transmitters, see ICD-GPS-200 [1997, p. 97]. Clearly, this is a different reference than that valid for the IGS orbit products which *always* refer to the mass center of the GPS satellite as stated by ROTHACHER [2000] and SCHENEWERK [2000].

2.4.2 Orbit Interpolation

REMONDY [1989] showed that it is possible to interpolate the satellite position vectors given each 15 minutes with sufficient accuracy using polynomials, despite of the disadvantages of polynomial interpolation (see Figure 2-5). He recommends polynomials of order 17 for high precision applications. A *Neville polynomial interpolator* is used within the tropospheric analysis system which is documented by PRESS et al. [1992, pp. 108-110]. The analyst may define how many points (nodes) shall be used²⁰ as well as the threshold for the interpolation error.

Experiments showed that symmetric interpolation (Figure 2-6) is needed to maintain a best-possible interpolation result. For 18-point-interpolators, this means that 9 satellite positions given in the SP3-file must lie directly before the epoch to interpolate and 9 nodes are to follow the interpolated point in time.

²⁰ At least 10 nodes are recommended, the default is 17 and the highest degree that should not be exceeded is around 22.

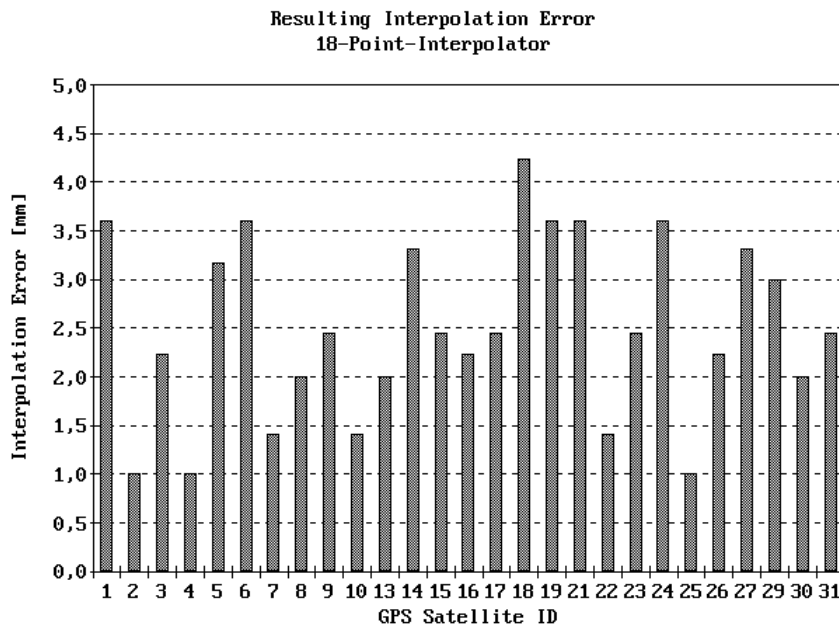


Figure 2-4 - Resulting interpolation error for 1998/11/20 at 12 h GPS time. The data record for this epoch has been cleaned in the original SP3-file and was interpolated with a 18-point-polynomial, i. e. a data gap of 30 minutes was bridged. In operational use, only 15 minutes need to be bridged. The average RMS error is about 2.5 mm; the RMS for a 17-point-interpolator is identical. The satellite ID corresponds to the PRN number given in RINEX measurement and SP3 orbit files.

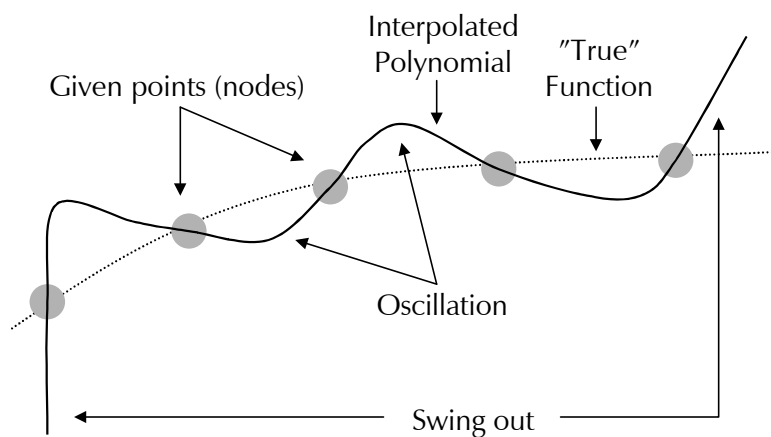


Figure 2-5 - Possible problems of the use of high-order polynomials for the approximation of functions. Especially high order polynomials tend to 'swing out' at the boundary regions defined by the given points. This is why extrapolation may turn out to be very critical. Moreover, 'oscillations' between given points may degrade the overall accuracy of polynomial approximations.

Figure 2-4 shows the resulting interpolation error for a selected day at 12 h GPS time. Using an interpolation polynomial which is built of 17 to 22 nodes, the resulting interpolation error is lower than 5 mm. Evidently, this interpolation uncertainty is much smaller than the orbit error itself (about 0.5 to 3.0 dm for precise IGS orbits).

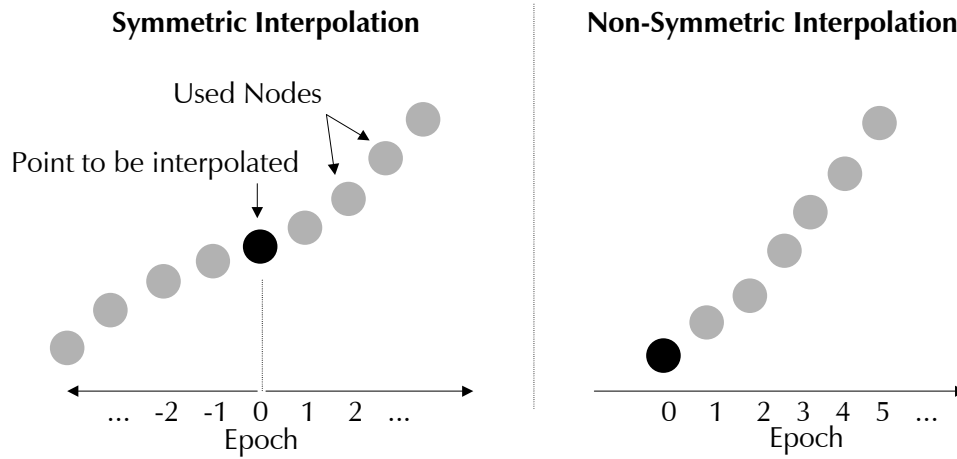


Figure 2-6 - Principle of symmetric and non-symmetric interpolation. Results showed that non-symmetric interpolation suffers from boundary problems related to swing-out effects and is therefore not recommended. Symmetric interpolation, however, requires that orbit data from both the previous and the following day are needed. (Example: The diurnal data batch starts at midnight, so that symmetric interpolation can only be carried out if orbit data starting at approximately 22 h GPS time of the previous day are available).

2.4.3 Epoch of Signal Transmission and Receiver Clock Check

2.4.3.1 Epoch of Signal Transmission

The position of a specific satellite is to be precisely determined for the epoch of signal transmission. This time index has to be computed in an iterative way since the receiver clock error is not well-known a priori. The analysis software makes use of the sufficiently known antenna positions and uses the code-ranges for clock error determination.

STEP 1: *Interpolation of approximate satellite position for t'_{OR}*
(time of receipt, given in RINEX file, recorded by GPS receiver)

Polynomial interpolation is used for orbit interpolation (\rightarrow 2.4.2).

STEP 2: *Computation of geometric elements*

$$S_A^i = |\underline{X}^i - \underline{X}_A| = \sqrt{\Delta X_A^{i^2} + \Delta Y_A^{i^2} + \Delta Z_A^{i^2}} \quad (2-94)$$

$\Delta X_A^i, \Delta Y_A^i, \Delta Z_A^i$: components of the distance vector between antenna A and satellite i
 S_A^i : distance between antenna A and satellite i

$$\cos Z_A^i = \frac{\cos \varphi_A \cdot \cos \lambda_A \cdot \Delta X_A^i + \cos \varphi_A \cdot \sin \lambda_A \cdot \Delta Y_A^i + \sin \varphi_A \cdot \Delta Z_A^i}{S_A^i} \quad (2-95)$$

z_A^i : zenith angle from receiver A to satellite i
 φ_A, λ_A : ellipsoidal latitude and longitude of receiver antenna A

The zenith angles z to the satellites in view are checked whether they exceed the cut-off mask and corresponding data records will be

deleted.

STEP 3: Atmospheric corrections and preliminary time of signal travel

$$\delta S_{A[ION,L1]}^i = f_{L2}^2 \cdot \frac{PR_{A[L2]}^i - PR_{A[L1]}^i}{f_{L1}^2 - f_{L2}^2} \quad (2-96)$$

$\delta S_{A[ION,L1]}^i$: ionospheric slant path correction for the L_1 carrier signal
 PR_A^i : measured pseudo-ranges between receiver A and satellite i
 $f_{L1/L2}$: carrier frequency of L_1 and L_2 , respectively
 $(f_1 = 154 \cdot f_0, f_2 = 120 \cdot f_0, f_0 = 10.23 \text{ MHz})$

The ionospheric correction is set to zero if only single-frequency data are available. This value is also checked for suitability, i. e. it must not exceed a pre-defined threshold. If it does, to corresponding data record will be deleted.

$$\delta S_{A[TROP]}^i \approx \frac{1}{\cos z_A^i} \cdot ZND \approx \frac{1}{\cos z_A^i} \cdot 2.4 \text{ [m]} \quad (2-97)$$

$\delta S_{A[TROP]}^i$: tropospheric slant path correction assuming a zenith neutral delay of 2.4 meters

$$\tau_{A[0]}^i = \frac{PR_{A[L1]}^i}{c} \quad (2-98)$$

$\tau_{A[0]}^i$: preliminary (approximated) time of signal travel
 c : speed of light ($c = 299\,792\,458 \text{ m/s}$)

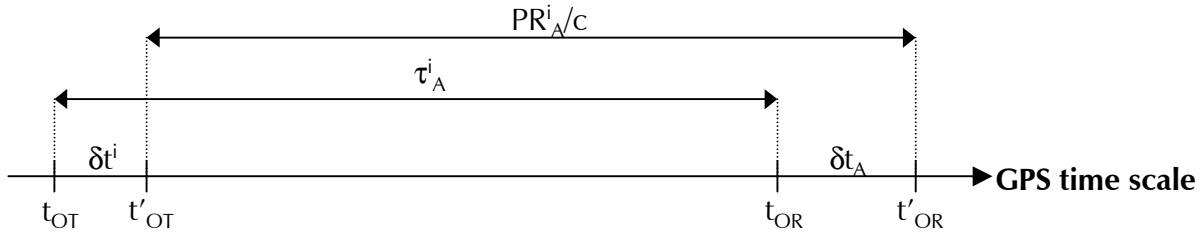


Figure 2-7 - Time indices for GPS signal transmission and receipt. The true GPS time of signal transmission is denoted as t_{OT} . This epoch is offset by the satellite clock error δt^i and yields t'_{OT} . The same is true for the receipt time: The true epoch of receipt t_{OR} is offset by the receiver clock error δt_A at station A and the error-corrupted epoch is denoted as t'_{OR} . This is the time recorded by the GPS receiver. As a consequence, the true time of signal transmission τ_A^i between satellite i and receiver A is not equal to the recorded signal transmission time PR_A^i/c .

STEP 4: Estimation of clock error, time of signal travel and time of signal transmission

a) Total clock error

Some orbit products, especially predicted orbits produced by some analysis centers and GFZ ultra-rapid orbits do not contain any information about the satellite clock error. In this case, the combined

clock error of satellite and receiver is computed. This can be easily done with help of the known receiver position. An approximate position of better than 200 m allows to compute the geometric distance between receiver and satellite with sufficient accuracy. The combined clock error can now be determined with help of the observation equation for pseudo-ranges (\rightarrow 2.2.1) solved for the combined clock error:

$$\delta t_{A[TOTAL]}^i = \frac{PR_{A[L1]}^i - S_A^i - \delta S_{A[ION,L1]}^i - \delta S_{A[TROP]}^i}{C} \quad (2-99)$$

$\delta t_{A[TOTAL]}^i$: combined satellite/receiver clock error

The corrected time of signal travel is

$$\tau_A^i = \tau_{A[0]}^i - \delta t_{A[TOTAL]}^i \quad (2-100)$$

b) Receiver clock error

If satellite clock errors are given, a separation is performed and for the receiver clock error

$$\delta t_A^i = \frac{PR_{A[L1]}^i - S_A^i - \delta S_{A[ION,L1]}^i - \delta S_{A[TROP]}^i}{C} + \delta t^i \quad (2-101)$$

δt_A^i : receiver clock error at station A determined via satellite i

δt^i : clock error of satellite i

the adjusted, mean receiver clock error is computed

$$\delta t_A = \frac{1}{n} \cdot \sum_{i=1}^n \delta t_A^i \quad (2-102)$$

δt_A : mean (adjusted) receiver clock error

n: number of satellites in view (or above the elevation mask)

and checked for blunders by having a look at the residuals²¹

$$v_i = \delta t_A - \delta t_A^i \quad (2-103)$$

Suspicious pseudo-ranges and their associated data records are deleted. Causes for blunder-corrupted ranges often have to do with S/A-effects.

The corrected time of signal travel is

$$\tau_A^i = \tau_{A[0]}^i - (\delta t_A - \delta t^i) \quad (2-104)$$

²¹ A blunder detector of *residual type* is used, see section \rightarrow 2.5.1.4 for details

and according to Figure 2-7, the epoch of signal transmission is

$$t_{OT}^i = t_{OR}' - \delta t_A - \tau_A^i = t_{OR} - \tau_A^i \quad (2-105)$$

t_{OT}^i : true GPS time of signal transmission by satellite i

t_{OR} : true GPS time of receipt

t_{OR}' : time of receipt as recorded by GPS receiver

STEP 5: *Interpolation of position of satellite i at t_{OT}*

... with polynomial of degree specified by analyst.

Note that both the L_1 and the L_2 signal are recorded by the receiver at the same receipt time. Due to the fact that the ionospheric effect is different on L_1 and L_2 , respectively, this essentially means that the L_1 signal has not been transmitted at the same time by the GPS satellite as the L_2 signal, i. e. both signals have a slightly different time of signal transmission. This also implies that the space vehicle position is not identical at the time of transmission of the two carrier wave signals. However, WÜBBENA [1991, p. 36] states that this difference will always remain at the sub-millimeter level and can be omitted. The TropAC system does only compute satellite positions for the L_1 carrier phase signal.

STEP 6: *Correction due to earth rotation during time of signal travel*

$$\Omega_A^i = \omega_E \cdot \tau_A^i \quad (2-106)$$

$$\begin{aligned} X^i &= X_*^i \cdot \cos \Omega_A^i + Y_*^i \cdot \sin \Omega_A^i \\ Y^i &= Y_*^i \cdot \cos \Omega_A^i - X_*^i \cdot \sin \Omega_A^i \\ Z^i &= Z_*^i \end{aligned} \quad (2-107)$$

ω_E : angular velocity of the earth (WGS84: $\omega_E = 7.2921151467 \cdot 10^{-5}$ rad/s)

Ω_A^i : rotation angle elapsed during time of signal travel

X_*^i, Y_*^i, Z_*^i : interpolated satellite position

X^i, Y^i, Z^i : satellite position, corrected for earth rotation effect

The algorithm is checked for proper convergence. The results are assumed to be of satisfactory numerical quality if the receiver clock or the combined clock error does not differ for more than 0.1 microseconds from the results of the previous iteration step. Otherwise, a next iteration is performed starting with step 2 again.

STEP 7: *Synchronization of measurements*

Double differencing will only fully eliminate the influence of the receiver clock error if all observations strictly refer to one and the same epoch and this time is called the nominal sampling epoch t_{NOM} here, whereas the observations actually refer to the time of receipt t_{OR} that is normally different from the nominal epoch due to the presence

of a receiver clock error unequal to zero. Synchronization of the observations means reduction to the nominal sampling epoch t_{NOM} that is common to all stations of the network per definition. We can compute the modified time of signal transmission,

$$t_{\text{OT}}^i = t_{\text{NOM}} - \tau_A^i \quad (2-108)$$

t_{OT}^i : modified time of signal transmission

t_{NOM} : nominal GPS sampling epoch, identical for all receivers in the network

compute the satellite position for this epoch and apply the earth rotation correction (step 6). Now, we can compute the distance vectors

$$\begin{aligned} S_A^i &= |X^i(t_{\text{OT}}^i) - X_A| \\ S_A^{i*} &= |X^i(t_{\text{OT}}^{i*}) - X_A| \end{aligned} \quad (2-109)$$

X^i : satellite position vector at the signal transmission epoch

X_A : receiver position vector

and the difference between both quantities

$$\delta S_{A[\text{SYNC}]}^i = S_A^i - S_A^{i*} \quad (2-110)$$

effectively corresponds to the synchronization correction (\rightarrow 2.2.2.2) that must be subtracted from the original carrier phase or pseudo-range measurements (\rightarrow 2.2.2). Note that this pure geometric correction cannot account for possible S/A clock dithering effects (\rightarrow 2.2.2.3) what is uncritical in most cases since the receiver clock errors are usually small enough to reduce the impact of dithering effects down to acceptable limits.

2.4.3.2 Check of Receiver Clock Error Behavior

A complete time series of receiver clock error estimates δt_A allows to check the receiver for poor clock behavior which may sometimes occur for certain receivers. The algorithm implemented in the analysis software is a moving average filter, i. e. the average value of a batch with length Δn is computed

$$\delta t_A^* = \sum_{j=i}^{i+\Delta n} \delta t_A(t_j) \quad (2-111)$$

δt_A^* : average receiver clock error estimate at station A

δt_A : receiver clock error estimate for receiver at station A at epoch t_j

Δn : filter length

i : start index of batch

and afterwards, the residuals belonging to the filter batch Δn

$$|\delta t_A^* - \delta t_A(t_j)| > \delta t_{MAX} \quad (2-112)$$

δt_{MAX} : maximum residual of receiver clock error allowed

are checked whether they exceed a pre-defined threshold δt_{MAX} . This threshold is chosen in the range of about 1 microsecond for data being sampled under S/A-conditions.

Note that this method cannot be applied for several older receiver types like Trimble 4000 SSE/SSI. These devices permit the receiver clock to drift freely up to an error threshold of 1 millisecond. After this threshold has been reached, the clock is abruptly reset to zero and the recorded sampling epoch will be increased (or decreased) by 1 millisecond. Here, a moving average filter will likely delete data which are not corrupted at all.

2.4.4 Antenna Phase Center Eccentricity Correction

The coordinates of the GPS space vehicles given in SP3 orbit files of the IGS are always referenced to the mass center of the satellites and not to the phase center of the transmitting L-band antenna array²².

According to FLIEGEL et al. [1992], the body-fixed coordinate system of a GPS spacecraft is defined as follows: (I) the positive z-axis is pointing along the antennas towards the earth, (II) the x-direction is positive towards the half plane containing the sun, and (III) the positive y-axis completes a right-handed system and points along one of the solar panel center beams.

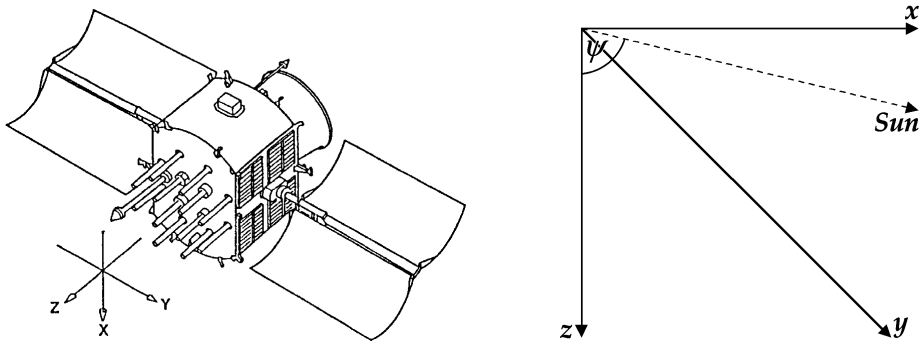


Figure 2-8 - GPS space vehicle body coordinate system after FLIEGEL et al. [1992]. The z-axis points towards the earth center. The z- and x-axis as well as the sun are within one and the same plane (the x-z-plane) and the y-axis points along one of the solar panels so that x-, y- and z-axis constitute a right-handed coordinate system having its origin in the satellite's mass center. The drawing shows a NAVSTAR Block I spacecraft. For all newer satellite types, the body-fixed coordinate system has been maintained as described, but the phase center offsets can be different.

With these definitions, the unit vectors relating the body-fixed coordinate system to the global geocentric ECEF system can be set up. The direction of the body z-axis is

²² see ROTHACHER [2000], Munich University of Technology and SCHERNEWERK [2000], NGS, personal communication.

$$\underline{e}_z = \frac{-\underline{X}_{SV}}{|\underline{X}_{SV}|} \quad (2-113)$$

\underline{e}_z : ECEF unit vector along the satellite-fixed z -axis

\underline{X}_{SV} : ECEF position vector of space vehicle

The distance vector between the sun and the space vehicle is

$$\Delta\underline{X}_{SV}^{SUN} = \underline{X}_S - \underline{X}_{SV} \quad (2-114)$$

\underline{X}_S : ECEF position vector of the sun

and can be used to find the direction of the positive y -axis

$$\underline{e}_y = \frac{\underline{e}_x \times \Delta\underline{X}_{SV}^{SUN}}{|\underline{e}_x \times \Delta\underline{X}_{SV}^{SUN}|} \quad (2-115)$$

\underline{e}_y : ECEF unit vector along the satellite-fixed y -axis

and, finally, the unit vector pointing along the body-fixed x -axis can be computed by

$$\underline{e}_x = \underline{e}_y \times \underline{e}_z \quad (2-116)$$

\underline{e}_x : ECEF unit vector along the satellite-fixed x -axis

Now, these unit vectors can be used to transform the satellite antenna phase center offset into the global geocentric system

$$\Delta\underline{X}_{PCV} = \Delta x \cdot \underline{e}_x + \Delta y \cdot \underline{e}_y + \Delta z \cdot \underline{e}_z \quad (2-117)$$

$\Delta\underline{X}_{PCV}$: ECEF satellite phase center correction vector

$\Delta x, y, z$: body-fixed satellite antenna phase center eccentricity components

and the corrected satellite position vector \underline{X}^* is

$$\underline{X}_{SV}^* = \underline{X}_{SV} + \Delta\underline{X}_{PCV} \quad (2-118)$$

The phase center offsets differ for the several types of GPS space vehicles and are given in Table 2-4 below.

GPS Space Vehicle Type	Dx [m]	Dy [m]	Dz [m]
Block I	0.211	0.000	0.854
Block II	0.279	0.000	0.952
Block IIA	0.279	0.000	0.952
Block IIR	0.000	0.000	0.000

Table 2-4 - Center of mass to antenna phase center offsets for GPS spacecraft in use after KING [2000]. The replenishment satellites Block IIR are designed differently from their predecessors Block II/IIA and have a negligibly small offset, although there is still some dispute about which values to use. For the TropAC analysis system, the values above have been adopted. The GAMIT software uses the following offsets: $\Delta x = -3.1$ mm, $\Delta y = -1.2$ mm, $\Delta z = 0.0$ m after KING [2000].

Table 2-5 can be used to determine the satellite type (Block) for a given PRN number that is given in RINEX observation files.

PRN	Block	Inauguration [yyyy mon dd hh min]	PRN	Block	Inauguration [yyyy mon dd hh min]
1	IIA	1995 09 21 05 24	17	II	1995 06 17 13 45
2	II	1995 11 17 00 00	18	II	1995 09 21 17 45
3	IIA	1996 03 28 00 00	19	II	1995 10 23 00 00
4	IIA	1995 06 13 22 07	20	IIR	2000 05 10 09 46
5	IIA	1995 11 17 00 00	21	II	1995 08 05 08 00
6	IIA	1995 04 02 19 44	22	II	1995 11 17 00 00
7	IIA	1995 03 31 04 00	23	IIA	1995 08 06 10 05
8	IIA	1997 11 06 00 20	24	IIA	1995 06 13 04 59
9	IIA	1995 10 23 00 00	25	IIA	1995 10 23 00 00
10	IIA	1996 07 16 00 00	26	IIA	1995 09 23 21 00
11	IIR	1999 10 07 00 00	27	IIA	1995 10 23 00 00
12	I	1984 10 03 00 00	28	IIR	2000 07 16 00 00
13	IIR	1997 07 23 00 00	29	IIA	1995 01 09 21 00
14	IIR	2000 11 10 00 00	30	IIA	1996 09 12 00 00
15	II	1995 06 15 19 16	31	IIA	1995 03 31 03 00
16	II	1995 08 07 08 16	32	IIA	1994 06 06 00 00

Table 2-5 - GPS satellite PRN numbers and corresponding satellite types (Block). The entries are valid from the date of inauguration and were updated in December 2000 by KING [2000].

2.4.5 Eclipsing Season

The computation of the eccentricity correction as depicted in the section before is complicated when the GPS spacecraft enters the earth's shadow. During this *eclipsing season* that can be divided into three phases (penumbra - umbra - penumbra), the satellite is not able to align the solar panels to the sun due to the invisibility of this body, but it constantly tries to trace it. This results into movements around the yaw-

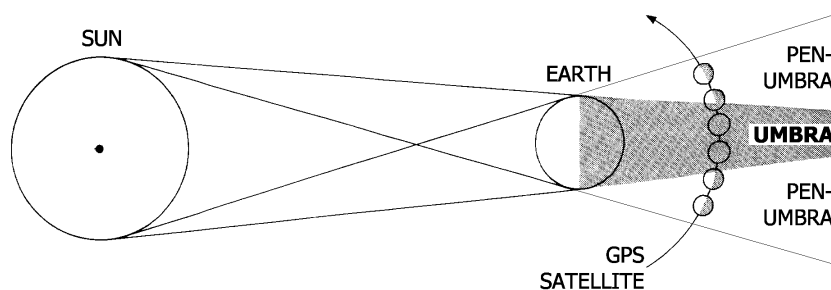


Figure 2-9 - Umbra and penumbra scenarios for GPS satellites following MITTON [1977]. The eclipsing season is difficult to model due to the fact that the satellite tries to adjust the solar panels towards the sun, but cannot find it and therefore begins to rotate around the yaw-axis.

axis and as no yaw-rate information is given in the orbit files, the analysis software cannot compensate this effect which results into a loss of orbit accuracy in the range of up to a 3 dm (worst case).

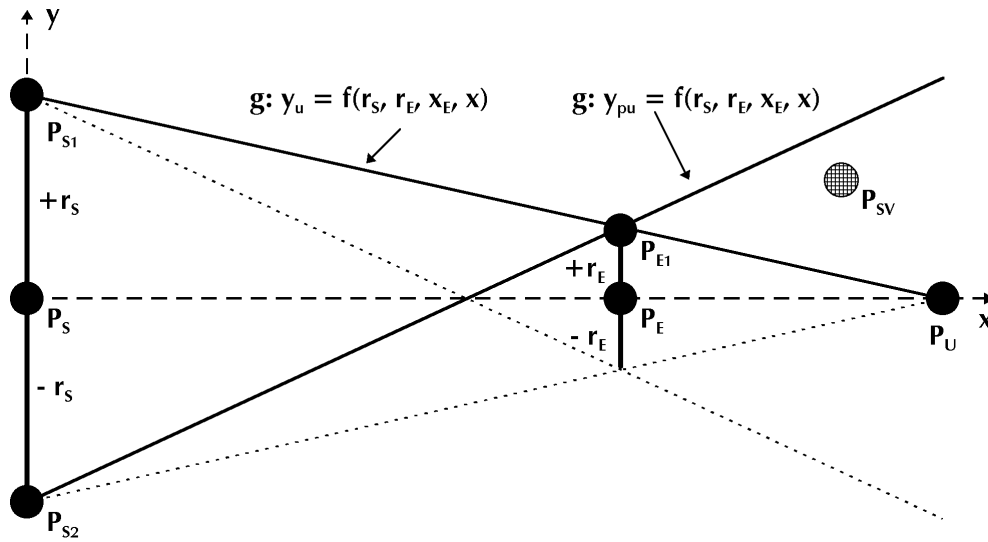


Figure 2-10 - Ray-tracing of umbra and penumbra events. Point P_s shows the center of the sun, P_{s1} an upper and P_{s2} a lower surface point of the solar body. P_E is the center of the earth and P_{E1} an upper surface point of it. P_{SV} shows the GPS space vehicle and P_U is the point of maximum umbra extend.

If highest precision is required and very long baselines of considerably more than 1000 km are part of the network, then the user may want to either exclude all satellites in eclipse or to weight down associated measurements. For this purpose, the eclipsing seasons need to be detected what can be performed in the following way:

A 2-D coordinate system is defined as shown in Figure 2-10 with the center of the sun P_s serving as origin. The x-axis is defined through the vector from the sun P_s to the earth P_E . The coordinates of all needed points can be defined in this ray-tracing coordinate system

$P_s = \{ x_s; y_s \} = \{ 0.0; 0.0 \}$	center of the sun
$P_{s1} = \{ 0.0; +r_s \}$	upward surface point of the sun
$P_{s2} = \{ 0.0; -r_s \}$	downward surface point of the sun
$P_E = \{ x_E; 0.0 \}$	center of the earth
$P_{E1} = \{ x_E; +r_E \}$	upward surface point of the earth

r_E : radius of the earth, $r_E \approx 6\,371$ km

r_s : radius of the sun, $r_s \approx 109 \cdot r_E \approx 696\,000$ km

where x_E directly follows from the distance vector between sun and earth:

$$x_E = |\underline{X}_E - \underline{X}_s| \quad (2-119)$$

The straight line $g: y_U$ represents a ray originating from the sun's surface in direction of the umbra-point P_U and is defined by points P_{s1} and P_{E1}

$$g: y_U = f(x) = \frac{r_E - r_s}{x_E} \cdot x + r_s \quad (2-120)$$

Setting $f(x) = 0$ yields the abscissa x_U of P_U

$$x_U = \frac{r_S \cdot x_E}{r_S - r_E} \quad (2-121)$$

and fully defines point P_U

$$P_U = \left\{ \frac{r_S \cdot x_E}{r_S - r_E}; 0 \right\} \quad \text{point of maximum umbra range}$$

which defines the umbra boundary. Any body with a larger x -coordinate den P_U is out of reach as far as the total eclipse is concerned. Finally, the straight line g : y_{PU} is the penumbra ray defined by points P_{S2} and P_{E1}

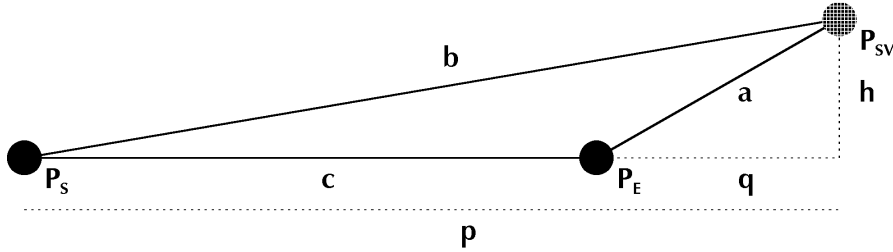


Figure 2-11 - Transformation of the space vehicle position into the ray-tracing coordinate system with help of triangle P_S - P_E - P_{SV} .

$$g: y_{PU} = f(x) = \frac{r_E + r_S}{x_E} \cdot x - r_S \quad (2-122)$$

The last step is to transform the space vehicle position into the 2-D ray-tracing coordinate system. This is done with help of Figure 2-11 where the three lines a , b , c of triangle P_S , P_E , P_{SV} are defined with help of the geocentric position vectors of the sun \underline{X}_S , the earth \underline{X}_E and the space vehicle \underline{X}_{SV} :

$$\begin{aligned} a &= |\underline{X}_{SV} - \underline{X}_E| \\ b &= |\underline{X}_{SV} - \underline{X}_S| \\ c &= |\underline{X}_E - \underline{X}_S| = x_E \end{aligned} \quad (2-123)$$

and the missing elements can be computed by

$$\begin{aligned} q &= \frac{a^2 + c^2 - b^2}{2 \cdot c} \\ p &= c - q \\ h &= \sqrt{b^2 - p^2} \end{aligned} \quad (2-124)$$

that define the transformed space vehicle position

$$P_{SV} = \{ x_E + q; h \} = \{ x_{SV}; y_{SV} \} \quad \text{position of space vehicle in 2-D ray-tracing system}$$

The GPS satellite is in eclipsing season, when the following conditions are true:

1. Umbra-Condition: The satellite is in total eclipse, when

$$a) \ x_{SV} \leq x_U$$

$$b) \ x_{SV} \geq x_E$$

$$c) \ y_{SV} \leq y_U = \frac{r_E - r_S}{x_E} \cdot x_{SV} + r_S$$

2. Penumbra-Condition: The satellite holds a position within a penumbra zone, when

a) condition (1b) is valid

b) condition (1c) is invalid

$$c) \ y_{SV} \leq y_{PU} = \frac{r_E + r_S}{x_E} \cdot x_{SV} - r_S$$

Note that condition (1a) $x_{SV} \leq x_U$ does not need to be checked as it is always fulfilled for GPS satellites which only have an orbit altitude of about 20 000 km.

A simplified approach to check for eclipsing season is to compute angle ψ which is shown in Figure 2-8 and can be determined by

$$\cos \psi = \frac{-\underline{X}_{SV} \cdot \underline{X}_S}{|\underline{X}_{SV} \cdot \underline{X}_S|} \quad (2-125)$$

FLIEGEL et al. [1992] found that the sun is eclipsed when $\psi < 14^\circ$.

2.5 Parameter Estimation Techniques

2.5.1 Least-Squares Adjustment

Although the GPS processing engine of the tropospheric analysis software is a Kalman filter, least-squares adjustment algorithms are widely used within the program package, e. g. for derivation of pressure reduction coefficients or in the combination module PAF_COMB. For this reason, the least-squares algorithm of the Gauss-Markov model is given here in brief form following PELZER [1985].

2.5.1.1 Observation Vector, Design Matrix and Stochastic Model

The parameter vector \underline{X} is to be solved for. Usually, an approximated set of unknowns has to be defined a priori²³ and is stored in vector \underline{X}_0 . The observation vector \underline{L} contains n measurements and the vector \underline{L}_0 consists of n approximated observations and is thereby linked to the functional model with help of the observation equations Ψ_i .

$$\underline{L} = \begin{bmatrix} L_1 \\ L_2 \\ \vdots \end{bmatrix} \quad \wedge \quad \underline{L}_0 = \begin{bmatrix} L_{01} \\ L_{02} \\ \vdots \end{bmatrix} = \begin{bmatrix} \Psi_1(\underline{X}_0) \\ \Psi_2(\underline{X}_0) \\ \vdots \end{bmatrix} \quad (2-126)$$

\underline{L} : vector of the observations (real measurements)

\underline{L}_0 : vector of the approximated observations

\underline{X}_0 : vector of the approximated unknowns

Ψ_i : observation equation i (here: function of the approximated unknowns \underline{X}_0) with $i = 1, 2, \dots, n$

The design or *functional matrix* \underline{A} contains the partial derivatives of the observation equations for the u unknowns:

$$\underline{A} = \begin{bmatrix} \left(\frac{\partial \Psi_1(\underline{X})}{\partial X_1} \right)_0 & \left(\frac{\partial \Psi_1(\underline{X})}{\partial X_2} \right)_0 & \cdots \\ \left(\frac{\partial \Psi_2(\underline{X})}{\partial X_1} \right)_0 & \left(\frac{\partial \Psi_2(\underline{X})}{\partial X_2} \right)_0 & \cdots \\ \vdots & \vdots & \ddots \end{bmatrix} \quad (2-127)$$

X_i : unknown parameter $i = 1, 2, \dots, u$

Since the unknowns are only known approximately at the beginning, the partial derivatives can only be defined with help of these approximations (indicated by subscript "0") and in case the partials are actually dependent on the unknowns (this is not the case for linear observation equations) iterations are usually necessary (\rightarrow 2.5.1.3). The covariance matrix of the observations is denoted as $\underline{\Sigma}_{LL}$ and constitutes the *stochastic model*.

$$\underline{\Sigma}_{LL} = \begin{bmatrix} \sigma_1^2 & \rho_{12} \cdot \sigma_1 \cdot \sigma_2 & \cdots \\ \rho_{12} \cdot \sigma_1 \cdot \sigma_2 & \sigma_2^2 & \cdots \\ \vdots & \vdots & \ddots \end{bmatrix} \quad \wedge \quad \underline{Q}_{LL} = \frac{1}{\sigma_0^2} \cdot \underline{\Sigma}_{LL} \quad \wedge \quad \underline{P} = \underline{Q}_{LL}^{-1} \quad (2-128)$$

$\underline{\Sigma}_{LL}$: covariance matrix of the observations

\underline{Q}_{LL} : cofactor matrix of the observations

\underline{P} : weight matrix of the observations

σ_i : theoretical standard deviation of observation $i = 1, 2, \dots, n$

σ_0 : standard deviation of the weight unit a priori (theoretical value)

²³ Approximated unknowns are always needed if non-linear observation equations need to be processed. Linear equations can be solved without any a priori knowledge.

The cofactor matrix \underline{Q}_{LL} can be obtained by division of the variance of the weight unit a priori σ_0^2 which can be chosen, in principle, as an arbitrary number. The mean variance

$$\sigma_0^2 = \frac{1}{n} \cdot \text{trace } \underline{\Sigma}_{LL} \quad (2-129)$$

n : number of observations

is a good choice that normally leads to a numerically more stable solution. If there are no concerns about numerical stability, the choice

$$\sigma_0^2 = 1 \Rightarrow \underline{Q}_{LL} \equiv \underline{\Sigma}_{LL} \Rightarrow \underline{P} = \underline{\Sigma}_{LL}^{-1} \quad (2-130)$$

is appropriate which leads to the identity of covariance and cofactor matrix.

The purpose of the stochastic model is to supply a weight matrix \underline{P} which carefully gives weight to precise and less weight to inaccurate measurements. In many cases, correlation terms (covariances) are omitted, be it due to poor knowledge of the actual correlations or due to the need to reduce the computation load. In such cases, the correlation coefficients are zero ($\rho_{ij} = 0$) and the covariance, cofactor and weight matrix will only contain diagonal elements. A special case occurs when all incoming observations obtain the same variance. In this case

$$\rho_{ij} = 0 \quad \wedge \quad \sigma_1^2 = \sigma_2^2 = \dots = \sigma_n^2 = \sigma_0^2 \Rightarrow \underline{Q}_{LL} = \underline{E} \Rightarrow \underline{P} = \underline{E}^{-1} = \underline{E} \quad (2-131)$$

ρ_{ij} : correlation coefficient between observation i and j

the weight matrix becomes an identity matrix \underline{E} . This simplifies the adjustment algorithm a bit.

2.5.1.2 Adjustment Algorithm

The normal equation matrix \underline{N} can be computed by

$$\underline{N} = \underline{A}^T \cdot \underline{P} \cdot \underline{A} \quad \wedge \quad \underline{Q}_{xx} = \underline{N}^{-1} \quad (2-132)$$

\underline{Q}_{xx} : cofactor matrix of the adjusted parameters

and the inverse of this symmetric matrix is the cofactor matrix \underline{Q}_{xx} of the adjusted parameter vector. With help of the vector \underline{l} of the reduced observations

$$\underline{l} = \underline{L} - \underline{L}_0 \quad (2-133)$$

which is often called vector of *pre-fit residuals*, it is possible to solve the system of normal equations

$$\underline{n} = \underline{A}^T \cdot \underline{P} \cdot \underline{l} \quad \wedge \quad \underline{x} = \underline{Q}_{xx} \cdot \underline{n} \quad \wedge \quad \underline{X} = \underline{X}_0 + \underline{x} \quad (2-134)$$

\underline{x} : reduced vector of adjusted parameters
 \underline{X} : vector of adjusted parameters
 \underline{X}_0 : vector of approximated unknowns

which first yields \underline{x} , the reduced vector of the adjusted unknowns, and finally \underline{X} , the vector of the adjusted parameters. Moreover, the vector of the post-fit residuals \underline{v} and the adjusted observations can be processed

$$\underline{v} = \underline{A} \cdot \underline{x} - \underline{l} \quad \wedge \quad \underline{l}' = \underline{l} + \underline{v} \quad (2-135)$$

\underline{v} : vector of post-fit residuals
 \underline{l}' : vector of adjusted observations

where the associated cofactor matrices are

$$\underline{Q}_{VV} = \underline{Q}_{LL} - \underline{Q}_{LL'} \quad \wedge \quad \underline{Q}_{LL'} = \underline{A} \cdot \underline{Q}_{XX} \cdot \underline{A}^T \quad (2-136)$$

\underline{Q}_{VV} : cofactor matrix of the residuals
 $\underline{Q}_{LL'}$: cofactor matrix of the adjusted observations in \underline{l}'

and offer another possibility to get the residual vector

$$\underline{v} = \underline{A} \cdot \underline{x} - \underline{l} = -\underline{Q}_{VV} \cdot \underline{Q}_{LL}^{-1} \cdot \underline{l} = -\underline{Q}_{VV} \cdot \underline{P} \cdot \underline{l} = -\underline{R} \cdot \underline{l} \quad (2-137)$$

\underline{R} : matrix of redundancies

The redundancy matrix \underline{R} is worth having a look at it:

$$\text{trace } \underline{R} = \sum_{i=1}^n r_i = f \quad \wedge \quad 0 \leq r_i \leq 1 \quad (2-138)$$

r_i : redundancy associated with measurement i
 f : number of statistical degrees of freedom

The redundancy r_i of observation i tells the user which ratio of the statistical degrees of freedom f has been soaked up by this particular measurement. The higher this proportion is, the better the measurement is internally controlled. The lower it is, the more difficult it will be to detect an outlier associated with this observation.

It is possible to transform the cofactor into the covariance matrix by simply multiplying it with either σ_0^2 a priori (theoretical value) or s_0^2 a posteriori (empirical value, see → 2.5.1.4.1), for example:

$$\underline{\Sigma}_{XX} = \sigma_0^2 \cdot \underline{Q}_{XX} \quad \vee \quad \underline{S}_{XX} = s_0^2 \cdot \underline{Q}_{XX} \quad (2-139)$$

$\underline{\Sigma}_{XX}$: theoretical covariance matrix of the adjusted parameters
 \underline{S}_{XX} : empirical covariance matrix of the adjusted parameters

Application of the empirical variance of the weight unit is an adequate choice if it can be considered as a reliable estimate for the theoretical σ_0^2 what mainly implies that

the number of statistical degrees of freedom f must be huge enough to be representative.

2.5.1.3 Iterating on a Previous Solution

If only linear observation equations are processed, then the final solution will be obtained after exactly one iteration, i. e. one run through the steps described above. If non-linear observation equations are present, then the algorithm corresponds to a Taylor series expansion of first order. In case of too inaccurate approximate parameters, it is usually necessary to iterate on the previous solution. This is done by substituting the approximate parameter vector (given a priori) by the adjusted one ($\underline{X}_0 \leftarrow \underline{X}$), re-initializing the vector \underline{L}_0 and the design matrix \underline{A} by using the new parameters and repeating all other steps of the adjustment algorithm again until the reduced parameter vector \underline{x} reaches zero (or a pre-defined threshold near zero).

2.5.1.4 Blunder Detection

Processing real measurements requires to be prepared for corrupted data. For this reason, outlier detection is useful and often essential to obtain results of acceptable quality. Several blunder detectors are routinely used in the program system which are depicted in the following section.

2.5.1.4.1 Global Test

A first global quality check can be done by computing the empirical variance of the weight unit a posteriori s_0^2

$$s_0^2 = \frac{\underline{v}^T \cdot \underline{P} \cdot \underline{v}}{n - u} \quad (2-140)$$

n : number of observations

u : number of unknowns

which can be compared with the theoretical variance of the weight unit a priori, σ_0^2 , and should not deviate from this value too much. The boundaries of the confidence interval

$$P \left\{ \sqrt{s_0^2 \cdot \frac{f}{\chi_{f, 1-\alpha/2}^2}} \leq \sigma_0^{\text{A POST}} \leq \sqrt{s_0^2 \cdot \frac{f}{\chi_{f, \alpha/2}^2}} \right\} = 1 - \alpha \quad (2-141)$$

$1-\alpha$: significance level, usually about 90 ... 98%

f : number of statistical degrees of freedom ($f = n - u$)

$\chi_{f,p}^2$: quantile of the χ^2 -distribution for f degrees of freedom and probability p

$\sigma_0^{\text{A POST}}$: theoretical value of the empirical standard deviation of the weight unit s_0

should include σ_0 a priori. If this is not the case, there might exist erroneous measurements, or either the functional or the stochastic model or both are not

appropriate. Otherwise, it can be assumed that $\sigma_0^{A\text{ POST}}$ is identical to σ_0 and the results of the least-squares adjustment can be expected to be not corrupted.

2.5.1.4.2 Blunder Detector of Residual-Type

Of course, it is possible to have a look at the vector of residuals \underline{v} ,

$$v_{\text{MAX}} = \max \{ |v_1|, |v_2|, \dots, |v_n| \} \quad (2-142)$$

to find the maximum absolute residual v_{MAX} and to test whether this value exceeds a certain threshold:

$$v_{\text{MAX}} > v_{\text{ALLOWED}} \Rightarrow p_{k,k} \rightarrow 0 \wedge p_{j,k} = p_{k,j} = 0 \quad k = i_{v_{\text{MAX}}}; j = 1, 2, \dots, n \quad (2-143)$$

v_{MAX} : maximum residual found in vector \underline{v}
 v_{ALLOWED} : maximum residual allowed (threshold)
 $p_{k,k}$: diagonal element at row k and column k of weight matrix \underline{P}
 $p_{j,k}$: element at row j and column k of weight matrix \underline{P}
 $i_{v_{\text{MAX}}}$: index of the observation associated with v_{MAX}

The threshold v_{ALLOWED} can be either defined by the analyst directly or derived from the empirical standard deviation of the weight unit s_0 , for example it could be set to $v_{\text{ALLOWED}} = 2 \cdot s_0$.

If v_{MAX} exceeds v_{ALLOWED} , the program may either eliminate the associated observation from vector \underline{L} and repeat the adjustment algorithm until no further outliers are detected or, alternatively, the corrupted observation may rest within \underline{L} , but its weight $p_{k,k}$ is set to a value near zero which practically means that this observation loses all its influence. Which way to use is dependent on the situation. The down-weighting-approach is often easier to implement, but can cause numerical problems in special situations.

The advantage of this kind of blunder detector is its simplicity. The disadvantage lies in the fact that it is not an optimal test for blunders as an outlier is not necessarily projected directly into the residuals. This depends on the concrete problem, i. e. on the design matrix. For fitting a number of points to a straight line (*linear regression*), this test is usually proper, for many other problems it is not.

2.5.1.4.3 Blunder Detector of Baarda- or Pope-Type

An outlier is computed by the formula²⁴

$$\Delta_i = \frac{-\underline{e}_i^T \cdot \underline{P} \cdot \underline{v}}{\underline{e}_i^T \cdot \underline{P} \cdot \underline{Q}_{VV} \cdot \underline{P} \cdot \underline{e}_i} \quad \underline{P} = \backslash \Rightarrow \Delta_i = \frac{-v_i}{p_{ii} \cdot q_{vii}} \quad (2-144)$$

Δ_i : outlier associated with observation i

²⁴ " $\underline{P} = \backslash$ " gives the simplified formula for the case of non-correlated observations, i. e. the weight matrix only consists of diagonal elements.

\underline{e}_i : unit vector (all cells are zero, but row i is 1)
 v_i : residual associated with observation i
 p_{ii} : weight associated with observation i
 q_{vii} : element of cofactor matrix \underline{Q}_W associated with observation i

and for the *Baarda blunder detector*, the corresponding standard deviation is

$$\sigma_{\Delta i} = \sqrt{\frac{\sigma_0^2}{\underline{e}_i^T \cdot \underline{P} \cdot \underline{Q}_W \cdot \underline{P} \cdot \underline{e}_i}} \quad \underline{P} = \backslash \Rightarrow \sigma_{\Delta i} = \sqrt{\frac{\sigma_0^2}{p_{ii} \cdot q_{vii}}} \quad (2-145)$$

$\sigma_{\Delta i}$: standard deviation of the outlier associated with observation i

Now, for all observations $i = 1, 2, \dots, n$ it is possible to determine the test quantities w and to find the maximum of the ensemble

$$w_i = \frac{|\Delta_i|}{\sigma_{\Delta i}} \Rightarrow w_{MAX} = \max \{ w_1, w_2, \dots, w_n \} \quad (2-146)$$

w_i : test quantity associated with the blunder in observation i

The maximum test quantity is assumed to follow the Gauss distribution, so either the condition $E\{w_{MAX}\} = 0$ is true, i. e. the expectation value of the maximum outlier is zero (and this essentially means that the value is not a significant outlier), or it is not. If it is not, then it should be either eliminated or down-weighted as outlined in the preceding section.

Care has to be taken to choose a proper detection threshold for this test because the values w_i are not stochastically independent. If the requested significance level is $1-\alpha/2$ (usually about 0.975), then the quantile of the Gauss distribution must use the level

$$1 - \frac{\alpha'}{2} = \sqrt[n]{1 - \frac{\alpha}{2}} \quad (2-147)$$

n : number of observations

Example: For $n = 20$ and $1-\alpha/2 = 0.975$, the quantile $Y_{0.9987} = 3.02$ (instead of $Y_{0.975} = 1.96$) must be taken from the Gauss distribution. Otherwise, the test will turn out to be too sensitive resulting in the detection of blunders which actually are not suspicious at all. The maximum outlier is suspicious if

$$w_{MAX} > Y_{1-\alpha/2} \Rightarrow p_{k,k} \rightarrow 0 \wedge p_{j,k} = p_{k,j} = 0 \quad k = i_{w_{MAX}}; j = 1, 2, \dots, n \quad (2-148)$$

w_{MAX} : maximum outlier

Y_p : quantile of normal (Gauss) distribution defining the threshold for outlier detection at a significance level of p (probability)

$p_{k,k}$: diagonal element of weight matrix \underline{P}

$i_{w_{MAX}}$: index of the observation associated with w_{MAX}

and can be defused by application of the same methods as mentioned in the preceding section.

The *Pope blunder detector* can be understood as a slight modification of the Baarda-type detector. The outliers are computed using exactly the same formula as given before, but the standard deviation of the outlier is based on individual, empirical variances of the weight unit for each outlier

$$s_{0i}^{2*} = \frac{1}{f-1} \cdot \left(f \cdot s_0^2 - \frac{\Delta_i^2}{q_{\Delta ii}} \right) \quad (2-149)$$

s_{0i}^{2*} : empirical variance of the weight unit, individual value for each observation (outlier)

s_0^2 : empirical variance of the weight unit a posteriori, global value

f : number of statistical degrees of freedom ($f = n - u$)

with the cofactor of outlier Δ_i being

$$q_{\Delta ii} = \frac{1}{\underline{e}_i^T \cdot \underline{P} \cdot \underline{Q}_{vv} \cdot \underline{P} \cdot \underline{e}_i} \quad \underline{P} = \backslash \Rightarrow q_{\Delta ii} = \frac{1}{\underline{p}_{ii}^2 \cdot \underline{q}_{vii}} \quad (2-150)$$

$q_{\Delta ii}$: cofactor associated with blunder i

\underline{e}_i : unit vector (all cells are zero, but row i is 1)

\underline{p}_{ii} : weight associated with observation i

q_{vii} : element of cofactor matrix \underline{Q}_{vv} associated with observation i

leading to the corresponding standard deviation of the outlier

$$s_{\Delta i} = \sqrt{s_{0i}^{2*} \cdot q_{\Delta ii}} \quad (2-151)$$

As this test is performed with empirical standard deviations (s_{Δ}) instead of theoretical ones (σ_{Δ}), the Gauss distribution cannot be used. Instead, the t-distribution delivers the needed quantile for the test of the maximum blunder. *Example:* For $n = 20$, $f = 16$ and $1-\alpha/2 = 0.975$, the quantile $t_{16;0.9987} = 3.56$ must be used.

2.5.2 Kalman Filtering

PELZER [1985] demonstrates how to apply Kalman filtering to kinematic networks. His description will be accommodated and modified for the case of GPS permanent arrays since the TropAC analysis system is primarily designed for static networks. The proposed Kalman filter is an entirely stochastic filter. This means that all parameters to be estimated are modeled as stochastic processes in the time domain, namely as random walk parameters. Chapter 3 will enhance the filter description for the estimation of tropospheric delays whereas this section primarily deals with coordinate estimation. Theory and practice of Kalman filtering are also discussed by BROWN and HWANG [1997] and GELB [1992].

2.5.2.1 Observations and Covariance Matrix

As already discussed, the incoming measurements are linked to the observation equation (\rightarrow 2.2.2)

$$\Theta_{A[L1]}^i = S_{A[L1]}^i + c \cdot (\delta t_A - \delta t^i) - \delta S_{A[ION,L1]}^i + \delta S_{A[TROP]}^i - N_{A[L1]}^i \cdot \lambda_{L1} + \varepsilon_\Phi \quad (2-152)$$

- Θ_A^i : carrier phase in [m] ($\Theta = \phi \cdot \lambda$ with ϕ : phase in cycles, λ : wavelength)
 S_A^i : geometric distance between receiver antenna A and satellite i
 c : speed of light (in vacuum, $c = 299\,792\,458$ m/s)
 δt_A : receiver clock error
 δt^i : satellite clock error
 $\delta S_{A[ION]}^i$: ionospheric propagation delay
 $\delta S_{A[TROP]}^i$: tropospheric propagation delay
 N_A^i : ambiguity term (phase bias) of measurement from antenna A to satellite i
 λ_{L1} : wavelength of carrier signal; *here*: L_1 ($\lambda_{L1} = 19.02$ cm)
 ε_Φ : noise term

These original measurements are differenced twice (\rightarrow 2.2.2.1)

$$\nabla \Delta \Theta_{AB[L1]}^{ij} = (\Theta_{B[L1]}^j - \Theta_{A[L1]}^j) - (\Theta_{B[L1]}^i - \Theta_{A[L1]}^i) \quad (2-153)$$

and linearly combined (\rightarrow 2.2.3) by the Kalman filter

$$\nabla \Delta \Phi_{AB[a1,a2]}^{ij} = a_1 \cdot \frac{\nabla \Delta \Theta_{AB[L1]}^{ij}}{\lambda_{L1}} - a_2 \cdot \frac{\nabla \Delta \Theta_{AB[L2]}^{ij}}{\lambda_{L2}} \quad (2-154)$$

- ϕ_A^i : carrier phase in cycles
 a_1, a_2 : linear combination coefficients

and introduced into the vector of observations \underline{L}

$$\underline{L} = \begin{bmatrix} \nabla \Delta \Phi_{AB[a1,a2]}^{ij} \\ \nabla \Delta \Phi_{AB[a1,a2]}^{ik} \\ \vdots \end{bmatrix} \quad (2-155)$$

which has n entries for n double difference phase measurements. Here, the double difference scheme ij, ik, il, \dots is chosen for baseline AB with reference satellite i having the highest elevation. Other schemes of forming double differences are, of course, possible as well (\rightarrow 2.2.2.1).

The *covariance matrix of the observations* $\underline{\Sigma}_L$ has to be derived. By theory, it cannot be approximated as diagonal matrix because the linear combinations are no original measurements, but derived observations which depend on each other²⁵, i. e. they are algebraically correlated. Thus, the law of error propagation is to be applied with the functional matrix \underline{F} containing the partial derivatives

²⁵ All measurements derived via the same baseline AB for a particular epoch are algebraically correlated if the double difference scheme ij, ik, il, \dots is used (i : reference satellite) and inter-correlation is also present for other baselines like AC or BD . For other schemes like ij, jk, kl, \dots , algebraic correlation does only affect direct neighbors, but may also be present for measurements to satellites that are also present in neighboring baselines.

$$\underline{F} = \begin{bmatrix} \frac{\partial \nabla \Delta \Phi_{AB[a1,a2]}^{ij}}{\partial \Theta_{A[L1]}^i} & \frac{\partial \nabla \Delta \Phi_{AB[a1,a2]}^{ij}}{\partial \Theta_{A[L2]}^i} & \frac{\partial \nabla \Delta \Phi_{AB[a1,a2]}^{ij}}{\partial \Theta_{A[L1]}^j} & \dots & \frac{\partial \nabla \Delta \Phi_{AB[a1,a2]}^{ij}}{\partial \Theta_{B[L1]}^i} & \dots \\ \frac{\partial \nabla \Delta \Phi_{AB[a1,a2]}^{ik}}{\partial \Theta_{A[L1]}^i} & \frac{\partial \nabla \Delta \Phi_{AB[a1,a2]}^{ik}}{\partial \Theta_{A[L2]}^i} & \frac{\partial \nabla \Delta \Phi_{AB[a1,a2]}^{ik}}{\partial \Theta_{A[L1]}^k} & \dots & \frac{\partial \nabla \Delta \Phi_{AB[a1,a2]}^{ik}}{\partial \Theta_{B[L1]}^i} & \dots \\ \vdots & \vdots & \vdots & & \vdots & \ddots \end{bmatrix} \quad (2-156)$$

\underline{F} : functional matrix

that turn out to be

$$\begin{aligned} \frac{\partial \nabla \Delta \Phi_{AB[a1,a2]}^{ij}}{\partial \Theta_{A[L1]}^i} &= -\frac{\partial \nabla \Delta \Phi_{AB[a1,a2]}^{ij}}{\partial \Theta_{A[L1]}^j} = \frac{a_1}{\lambda_1} \\ \frac{\partial \nabla \Delta \Phi_{AB[a1,a2]}^{ij}}{\partial \Theta_{A[L2]}^i} &= -\frac{\partial \nabla \Delta \Phi_{AB[a1,a2]}^{ij}}{\partial \Theta_{A[L2]}^j} = \frac{a_2}{\lambda_2} \\ \frac{\partial \nabla \Delta \Phi_{AB[a1,a2]}^{ij}}{\partial \Theta_{B[L1]}^i} &= -\frac{\partial \nabla \Delta \Phi_{AB[a1,a2]}^{ij}}{\partial \Theta_{B[L1]}^j} = -\frac{a_1}{\lambda_{L1}} \\ \frac{\partial \nabla \Delta \Phi_{AB[a1,a2]}^{ij}}{\partial \Theta_{B[L2]}^i} &= -\frac{\partial \nabla \Delta \Phi_{AB[a1,a2]}^{ij}}{\partial \Theta_{B[L2]}^j} = \frac{a_2}{\lambda_{L2}} \end{aligned} \quad (2-157)$$

and the a priori variances σ_{Θ^2} of the original phase measurements Θ in units of meters are stored in the diagonal matrix

$$\underline{\Sigma}_{\parallel} = \begin{bmatrix} \sigma_{\Theta_{A[L1]}^i}^2 & & & & \\ & \sigma_{\Theta_{A[L2]}^i}^2 & & & \\ & & \sigma_{\Theta_{A[L1]}^j}^2 & & \\ & & & \ddots & \\ & & & & \sigma_{\Theta_{B[L1]}^i}^2 & \\ & & & & & \ddots \end{bmatrix} \quad (2-158)$$

$\underline{\Sigma}_{\parallel}$: covariance matrix of the original observations, assumed to be a diagonal matrix

This assumes that no correlations between the original phase measurements are present. The derived double difference observation will be algebraically correlated. The associated covariance matrix is

$$\underline{\Sigma}_{LL} = \underline{F} \cdot \underline{\Sigma}_{\parallel} \cdot \underline{F}^T \quad (2-159)$$

$\underline{\Sigma}_{LL}$: covariance matrix of the derived, double-difference observations

Moreover, there are several simple methods to inject some additional variance which allows to model several problems stochastically. For example a direct amplifier

$$\sigma_x^2 = (\sigma_o \cdot q_x)^2 \quad (2-160)$$

σ_x : new standard deviation for phase measurement Θ (not differenced)

σ_O : original standard deviation of the phase measurement
 q_x : amplifier

or a baseline length-dependent increase in variance

$$\sigma_{AB}^2 = \sigma_O^2 + \left(\frac{d_{AB} \cdot q_{AB}}{\lambda_{a1,a2}} \right)^2 \quad (2-161)$$

σ_{AB} : new standard deviation for phase measurement Θ (not differenced)
 σ_O : original standard deviation of the phase measurement
 d_{AB} : length of baseline AB in the same units as σ_O
 q_{AB} : scaling factor
 $\lambda_{a1,a2}$: (virtual) wavelength of linear combination in the same units as σ_O

and an elevation-dependent increase

$$\sigma_i^2 = \sigma_O^2 + [\sigma_\theta \cdot \tan(q_z \cdot z_i)]^2 \quad (2-162)$$

σ_i : new standard deviation for phase measurement Θ (not differenced) to satellite i
 σ_O : original standard deviation of the phase measurement to satellite i
 σ_θ : scaling factor for elevation-dependent weighting
 q_z : zenith angle scaling factor
 z_i : zenith angle to satellite i

can be applied. The first method described is used to handle measurements at the threshold from good to bad signal-to-noise ratio²⁶ with a default value of $q_x = 2$ which means that measurements with poor C/N will have double variance. The second method can be used to model errors that are dependent on the baseline length. Following SEEGER [1993, p. 297], a typical example for this type are orbital errors that approximately follow the rule that the ratio of baseline error to the baseline length equals the ratio of orbit error (1...5 m for broadcast orbits) and orbit altitude. For precise IGS orbits, q_{AB} can be practically set to zero. Last, but not least, elevation-dependent weighting is rather important. On the one hand, C/N effects that are often a function of the elevation can be addressed and on the other hand, uncertainties of the ionospheric and tropospheric mapping functions can be handled. Chapter 3 will cover this issue more in detail.

2.5.2.2 State Vector, Transition and Prediction of State

The state vector may contain the following parameters:

- *Site coordinates*: Monitor station coordinates are estimated by default. For n network sites, $3 \times n$ coordinate components are to be estimated.
- *Orbit errors*: Orbit relaxation can be applied. This means that three orbit biases for the corresponding coordinate components for each satellite are estimated as additional parameters. These parameters are only necessary if low-quality orbits are used and has therefore not been applied very frequently yet as precise IGS

²⁶ To be more precise, this add-on will be applied if the RINEX C/N-flag for a particular observation is less than 5.

orbits are used by default. Application of orbit relaxation introduces about $24 \times 3 = 72$ additional parameters and significantly slows down network filtering.

- *Zenith wet delays:* One ZWD per site can be estimated; see chapter 3 for details.
- *Ambiguities:* The doubly differenced and linearly combined ambiguities are always treated as parameters whether they are held fixed or not. If they are fixed, the corresponding states will be tightly constrained by lowering their variance. For n sites and an average number of 5 double differences per site, there are $5 \times n$ parameters. For a network with 20 sites, this means 100 parameters to estimate. Handling ambiguities can therefore be considered as a rather CPU-consuming task.

A general description of the state vector is

$$\underline{X} = \begin{bmatrix} \underline{X}_{\text{COO}} \\ \underline{X}_{\text{ZWD}} \\ \underline{X}_{\text{SAT}} \\ \underline{X}_{\text{AMB}} \end{bmatrix} \quad (2-163)$$

$\underline{X}_{\text{COO}}$: sub-vector containing the ground station coordinates

$\underline{X}_{\text{ZWD}}$: sub-vector containing the tropospheric parameters

$\underline{X}_{\text{SAT}}$: sub-vector containing the satellite orbit biases

$\underline{X}_{\text{AMB}}$: sub-vector containing the ambiguities

with 4 sub-vectors for the ground station coordinates, the zenith wet delays, the satellite orbit biases and the ambiguities. In this chapter, only coordinates and ambiguities are treated:

$$\underline{X} = \begin{bmatrix} X_A & Y_A & Z_A & \cdots & \nabla \Delta N_{AB[a1,a2]}^{ij} & \nabla \Delta N_{AB[a1,a2]}^{ik} & \cdots \end{bmatrix}^T \quad (2-164)$$

X, Y, Z : global, geocentric coordinates of the ground stations (ECEF)

$\nabla \Delta N$: double-difference ambiguities

and the *covariance matrix of the state vector* is denoted as

$$\underline{\Sigma}_{\text{xx}} \text{ with } \sigma_0^2 = 1 \Rightarrow \underline{\Sigma}_{\text{xx}} \equiv \underline{Q}_{\text{xx}} \quad (2-165)$$

$\underline{\Sigma}_{\text{xx}}$: covariance matrix of the states

$\underline{Q}_{\text{xx}}$: cofactor matrix of the states

σ_0 : standard deviation of the weight unit

and equal to the cofactor matrix due to the special choice of the variance of the weight unit.

The *transition matrix* \underline{I} models the time-dependency of the states from epoch $k-1$ to k . Since this is a pure stochastic filter,

$$\underline{I}_k = \underline{E} \quad (2-166)$$

\underline{E} : identity matrix, only diagonal elements, all diagonal elements are 1

the transition matrix is simply an identity matrix \underline{E} and the *prediction of the state vector* simplifies to

$$\underline{X}_k = \underline{I}_k \cdot \underline{X}_{k-1}^* = \underline{E} \cdot \underline{X}_{k-1}^* = \underline{X}_{k-1}^* \quad (2-167)$$

k: current epoch

k-1: previous epoch

\underline{X} : predicted state vector

\underline{X}^* : updated state vector (previous epoch)

The *predicted covariance matrix of the states* is

$$\underline{\Sigma}_{XXk} = \underline{I} \cdot \underline{\Sigma}_{XXk-1}^* \cdot \underline{I}^T + \underline{\Sigma}_{SS} = \underline{\Sigma}_{XXk-1}^* + \underline{\Sigma}_{SS} \quad (2-168)$$

$\underline{\Sigma}_{XX}$: covariance matrix of the predicted states (previous epoch k)

$\underline{\Sigma}_{XX}^*$: covariance matrix of the updated states (previous epoch k-1)

$\underline{\Sigma}_{SS}$: process noise matrix, *here*: only diagonal elements

\underline{I} : transition matrix

where the process noise matrix $\underline{\Sigma}_{SS}$ injects some additional white noise, which is practically integrated over time. Such a stochastic process is called *random walk*. The particular process noise values are to defined cautiously as they govern the variability of the states, i. e. they give or do not give "freedom to evolve". For the ambiguities, one might assume that they should not be random walk processes for natural reasons and choose a process noise of zero. This is not done by default, because floating ambiguities might soak up certain systematic errors which can be time-varying and are therefore also treated as random walk processes with a noise of about 2 ... 5 cm/ \sqrt{h} . For the coordinates, a process noise of 1 ... 5 mm/ \sqrt{h} in case of static networks is assumed. The stochastic properties of zenith wet delays have been investigated in detail and are presented in the following chapter.

2.5.2.3 Design Matrix

The functional model follows from the observation equation

$$\underline{\Psi}(\underline{X}) = a_1 \cdot \frac{\underline{\Psi}_{L1}(\underline{X})}{\lambda_{L1}} - a_2 \cdot \frac{\underline{\Psi}_{L2}(\underline{X})}{\lambda_{L2}} \quad (2-169)$$

$\underline{\Psi}$: observation equation as function of vector \underline{X}

\underline{X} : vector of parameters

λ : carrier wavelength

a_1, a_2 : linear combination coefficients for the phase measurements on L_1 and L_2

which is the linearly combined double differences as function of the unknown parameters with

$$\underline{\Psi}_{L1}(\underline{X}) = \nabla \Delta S_{A[L1]}^i - \nabla \Delta N_{A[L1]}^i \cdot \lambda_{L1} - \nabla \Delta \delta S_{A[ION,L1]}^i + \nabla \Delta \delta S_{A[TROP]}^i \quad (2-170)$$

$\underline{\Psi}_{L1}$: observation equation of carrier wave L_1

- \underline{X} : parameter vector (state vector)
 S_A^i : geometric distance between receiver antenna A and satellite i
 $\delta S_{A[ION]}^i$: ionospheric propagation delay
 $\delta S_{A[TROP]}^i$: tropospheric propagation delay
 N_A^i : ambiguity term (phase bias) of measurement from antenna A to satellite i
 λ_{L1} : wavelength of carrier signal; *here*: L_1 ($\lambda_{L1} = 19.02$ cm)

The design matrix \underline{A} contains the partial derivatives of the observation equations in vector $\underline{\Psi}$ for the parameters in vector \underline{X}

$$\underline{A}_k = \frac{\partial \underline{\Psi}_k}{\partial \underline{X}_k} \approx \frac{\partial \underline{\Psi}_k}{\partial \underline{X}_{k-1}^*} \quad (2-171)$$

where the updated states \underline{X}^* of the previous epoch $k-1$ are treated as approximate unknowns denoted by subscript "0":

$$\underline{A}_k = \begin{bmatrix} \left(\frac{\partial \Psi_1}{\partial X_A} \right)_0 & \left(\frac{\partial \Psi_1}{\partial Y_A} \right)_0 & \cdots & \left(\frac{\partial \Psi_1}{\partial \nabla \Delta N_{AB[a1,a2]}^{ij}} \right)_0 & \cdots \\ \left(\frac{\partial \Psi_2}{\partial X_A} \right)_0 & \left(\frac{\partial \Psi_2}{\partial Y_A} \right)_0 & \cdots & \left(\frac{\partial \Psi_2}{\partial \nabla \Delta N_{AB[a1,a2]}^{ik}} \right)_0 & \cdots \\ \vdots & \vdots & & \vdots & \ddots \end{bmatrix} \quad (2-172)$$

The partials for the coordinates are derived by two-sided numerical differentiation

$$\frac{\partial f}{\partial x} \approx \frac{\Delta f}{\Delta x} = \frac{f(x + \Delta x) - f(x - \Delta x)}{2 \cdot \Delta x} \quad (2-173)$$

- f : function to differentiate
 x : parameter
 Δf : difference of the values of the function that is to be differenced
 Δx : differentiation spacing

where Δx is the spacing for differentiation and should be in the range of the expected accuracy of the estimate. For coordinates, a default value of $\Delta x = 5$ cm is applied. The partial derivatives of the ambiguities are simply -1.

A concluding remark should be devoted to the way of parameterization applied for coordinate estimation. The ground station coordinates are included in the equation expressing the distance between GPS receiver antenna and GPS satellite:

$$\begin{aligned}
 S_{A[L1]}^i &= \sqrt{(X_A + \Delta X_{CORR[L1]} - X^i)^2 + (Y_A + \Delta Y_{CORR[L1]} - Y^i)^2 + (Z_A + \Delta Z_{CORR[L1]} - Z^i)^2} \\
 S_{A[L2]}^i &= \sqrt{(X_A + \Delta X_{CORR[L2]} - X^i)^2 + (Y_A + \Delta Y_{CORR[L2]} - Y^i)^2 + (Z_A + \Delta Z_{CORR[L2]} - Z^i)^2}
 \end{aligned} \quad (2-174)$$

- \underline{X}_A : time-invariant ground-station coordinate vector
 $\underline{\Delta X}_{CORR}$: vector of time-varying coordinate corrections

What the filter actually estimates is not the current coordinate, but the mean vector \underline{X}_A which is not influenced by solid earth tides and other effects. This is achieved by strict separation of the mean point coordinates and all those corrections and reductions that are applied to model time-dependent behavior (earth tides, pole tide, ocean load), instrument biases (phase center corrections) and geometric corrections (antenna eccentricity correction). All these terms are accumulated in the correction vector $\Delta \underline{X}_{\text{CORR}}$ (\rightarrow 2.3) and due to the differences in antenna phase center, there are two correction vectors for L_1 and L_2 , respectively.

2.5.2.4 Filter Update

The first step is to find the covariance matrix of the innovations $\underline{\Sigma}_{dd}$ of the current epoch

$$\underline{\Sigma}_{ddk} = \underline{\Sigma}_{LLk} + \underline{A}_k \cdot \underline{\Sigma}_{XXk} \cdot \underline{A}_k^T \quad (2-175)$$

$\underline{\Sigma}_{dd}$: covariance matrix of the innovations \underline{d}
 $\underline{\Sigma}_{LL}$: covariance matrix of the observations
 $\underline{\Sigma}_{XX}$: covariance matrix of the predicted states
 \underline{A} : design matrix of current epoch k

which enables us to compute the gain matrix \underline{K}

$$\underline{K}_k = \underline{\Sigma}_{XXk} \cdot \underline{A}_k^T \cdot \underline{\Sigma}_{ddk}^{-1} \quad (2-176)$$

\underline{K} : gain matrix of current epoch k

The vector of innovations \underline{d} is equivalent to what is called vector of reduced observations or pre-fit residuals in least-squares adjustments:

$$\underline{d}_k = \underline{L}_k - \underline{\Psi}(\underline{X})_k = \underline{L}_k - \underline{A}_k \cdot \underline{X}_k \quad (2-177)$$

\underline{d} : vector of innovations
 \underline{L} : observation vector
 $\underline{\Psi}$: vector of observation equations as function of state vector \underline{X}
 \underline{X} : predicted state vector of current epoch k
 \underline{A} : design matrix

The state vector can now be updated

$$\underline{X}_k^* = \underline{X}_k + \underline{K}_k \cdot \underline{d}_k \quad (2-178)$$

\underline{X}^* : updated state vector of current epoch k
 \underline{X} : predicted state vector
 \underline{K} : gain matrix
 \underline{d} : vector of innovations

and the associated covariance matrix is

$$\underline{\Sigma}_{XXk}^* = \underline{\Sigma}_{XXk} - \underline{K}_k \cdot \underline{\Sigma}_{ddk} \cdot \underline{K}_k^T \quad (2-179)$$

$\underline{\Sigma}_{xx}^*$: updated covariance matrix of the states of current epoch k
 $\underline{\Sigma}_{xx}$: predicted covariance matrix of the states
 $\underline{\Sigma}_{dd}$: covariance matrix of the innovations
 \underline{K} : gain matrix

The stabilized filter only differs in terms of the method to compute the updated covariance matrix which can be alternatively expressed as

$$\underline{\Sigma}_{xxk}^* = (\underline{E} - \underline{K}_k \cdot \underline{A}_k) \cdot \underline{\Sigma}_{xxk} \cdot (\underline{E} - \underline{K}_k \cdot \underline{A}_k)^T + \underline{K}_k \cdot \underline{\Sigma}_{LLk} \cdot \underline{K}_k^T \quad (2-180)$$

\underline{E} : identity matrix

and is said to be more stable than the expression above, but also places a higher CPU-load on the computer. However, tests have not yet revealed any difference between the conventional and the stabilized version as numerical instabilities are no problem here. This is also the main reason why no *Square Root Information Filter* (SRIF) has been adopted for this task²⁷.

2.5.2.8 Tuning of Stochastic Model

The vector of residuals of the observations can be obtained by

$$\underline{v}_k = -\underline{\Sigma}_{LLk} \cdot \underline{\Sigma}_{ddk}^{-1} \cdot \underline{d}_k = \underline{A}_k \cdot \underline{X}_k^* - \underline{L}_k \quad (2-181)$$

\underline{v} : vector of residuals
 $\underline{\Sigma}_{LL}$: covariance matrix of the observations
 $\underline{\Sigma}_{dd}$: covariance matrix of the innovations
 \underline{d} : vector of innovations

but is not needed to compute the empirical variance of the weight unit

$$s_{0k}^2 = \frac{\underline{d}_k \cdot \underline{\Sigma}_{ddk}^{-1} \cdot \underline{d}_k^T}{n_k} \quad (2-182)$$

s_0 : empirical standard deviation of the weight unit
 \underline{d} : vector of innovations
 $\underline{\Sigma}_{dd}$: covariance matrix of the innovations
 n_k : number of observations of current epoch

As the theoretical variance of the weight unit σ_0^2 has been set to 1.0 before, the empirical value should be close to it. If this is not the case and we can assume that the deviations are not due to blunders because outlier detection has already been performed and the number of observations n_k is large enough to treat the empirical variance as a reliable precision estimate, then it can be used to tune the covariance matrix of the observations by

²⁷ Kalman filters of SRIF type are numerically highly stable. They were developed in the mid-seventies when the word length of the computers was not very large. The UDU^T factorization by THORNTON and BIERMANN [1978] is a well-known technique to improve the numerical stability with only minor increase in computation load in comparison to the conventional Kalman filter. Today, with computers having a word length of 64-bit and *long doubles* becoming more and more common, SRIF seems to become less important, albeit useful for special applications.

$$\underline{S}_{LLk} = s_{0k}^2 \cdot \underline{\Sigma}_{LLk} \quad (2-183)$$

\underline{S}_{LL} : empirically tuned stochastic model of the observations of current epoch k

$\underline{\Sigma}_{LL}$: non-tuned stochastic model of the observations

Observations which are treated in a pessimistic way at the beginning of the filter run - e. g. they are introduced with too high standard deviations - will only cause an inferior filter gain. On the other hand, standard deviations being too low will cause a superior gain which is not adequate as well. This method has been implemented in order to overcome such shortcomings. However, the a priori statistics for GPS phase measurements are quite well-known meanwhile and it is usually no longer necessary to apply this self-calibration algorithm.

2.5.2.7 Backward Filtering

One disadvantage of sequential filters is that the initial states are often only approximately known and are improved in subsequent filter steps. In order to obtain a precise history of results it is therefore necessary to filter the data in backward direction again which increases computation time as well as storage load because the results of the forward filter run must be archived.

2.5.2.7.1 Optimal Estimation

Following BROWN and HOFFMANN-WELLENHOF [1993, p. 209] and HWANG [1997, p. 314], a theoretically optimal way to smooth the data backward in time is to compute the gain matrix

$$\underline{K}_{k \leftarrow} = \underline{\Sigma}_{XXk \rightarrow}^* \cdot \underline{I}_k \cdot \underline{\Sigma}_{XXk+1 \rightarrow}^{-1} = \underline{\Sigma}_{XXk \rightarrow}^* \cdot \underline{E} \cdot \underline{\Sigma}_{XXk+1 \rightarrow}^{-1} = \underline{\Sigma}_{XXk \rightarrow}^* \cdot \underline{\Sigma}_{XXk+1 \rightarrow}^{-1} \quad (2-184)$$

$\underline{K}_{k \leftarrow}$: gain matrix for smoothing computations at epoch k (backward in time)

$\underline{\Sigma}_{XX \rightarrow}^*$: updated covariance matrix (forward run)

$\underline{\Sigma}_{XX \rightarrow}$: predicted covariance matrix (forward run)

\underline{I} : transition matrix ($\underline{I} = \underline{E}$ in this case)

\underline{E} : identity matrix

Note that the transition matrix \underline{I} is a unity matrix in our special case of a stochastic filter. The smoothed state vector is then

$$\underline{X}_{k \leftarrow} = \underline{X}_{k \rightarrow}^* + \underline{K}_{k \leftarrow} \cdot (\underline{X}_{k+1 \leftarrow} - \underline{X}_{k+1 \rightarrow}) \quad (2-185)$$

$\underline{X}_{k \leftarrow}$: combined/smoothed state vector matrix

$\underline{X}_{k \rightarrow}^*$: updated state vector matrix (forward run)

$\underline{X}_{k \rightarrow}$: predicted state vector matrix (forward run)

and the covariance matrix of the smoothed states is

$$\underline{\Sigma}_{XXk \leftarrow} = \underline{\Sigma}_{XX \rightarrow}^* + \underline{K}_{k \leftarrow} \cdot (\underline{\Sigma}_{XXk+1 \leftarrow} - \underline{\Sigma}_{XXk+1 \rightarrow}) \cdot \underline{K}_{k \leftarrow}^T \quad (2-186)$$

$\underline{\Sigma}_{XXk \leftarrow}$: smoothed/combined covariance matrix

2.5.2.7.2 Sub-Optimal Estimation

Another method which is sub-optimal in the theoretical sense is to filter the data set both in forward and backward direction using the same filter algorithm but simply applying it in both directions where the initial states for the backward run are equal to the updated states of the last epoch of the forward run. Then, the combined forward/backward result is obtained as the weighted mean of both runs. The design matrix \underline{A} consists of two identity matrices \underline{E}

$$\underline{A} = \begin{bmatrix} \underline{E} \\ \underline{E} \end{bmatrix} \quad \wedge \quad \underline{L} = \begin{bmatrix} \underline{X}_{\rightarrow}^* \\ \underline{X}_{\leftarrow}^* \end{bmatrix} \quad \wedge \quad \underline{P} = \begin{bmatrix} \underline{\Sigma}_{xx\rightarrow}^* & \\ & \underline{\Sigma}_{xx\leftarrow}^* \end{bmatrix}^{-1} \quad (2-187)$$

\underline{E} : identity matrix

\underline{L} : observation vector

\underline{P} : weight matrix

$\underline{X}_{\rightarrow}^*$: updated state vector (forward run)

$\underline{X}_{\leftarrow}^*$: updated state vector (backward run)

$\underline{\Sigma}_{xx\rightarrow}^*$: covariance matrix of updated state vector (forward run)

$\underline{\Sigma}_{xx\leftarrow}^*$: covariance matrix of updated state vector (backward run)

that have u rows and u columns for u states that are to be combined, i. e. the design matrix \underline{A} has $2u$ rows and u columns. Correspondingly, the observation vector is composed of the two updated state vectors of the forward and the backward run and the stochastic model is formed accordingly. The adjusted, combined state vector now becomes

$$\underline{\Sigma}_{xx\leftrightarrow} = (\underline{A}^T \cdot \underline{P} \cdot \underline{A})^{-1} \Rightarrow \underline{X}_{\leftrightarrow} = \underline{\Sigma}_{xx\leftrightarrow} \cdot (\underline{A}^T \cdot \underline{P} \cdot \underline{L}) \quad (2-188)$$

$\underline{X}_{\leftrightarrow}$: combined state vector

$\underline{\Sigma}_{xx\leftrightarrow}$: covariance matrix of combined state vector (variance of weight unit is 1.0)

and represents the final solution.

2.5.2.8 Blunder Detection

As for least-squares algorithms, blunder detection is also an essential part of Kalman filtering. None of the results presented in Chapter 6 would have been of acceptable quality if no outlier checks had been performed. Figure 2-12 shows the processing chain within the Kalman filter engine and also points out where blunder detection takes place.

Of course, a global test with help of the empirical variance of the weight unit similar to that performed by the least-squares algorithm (\rightarrow 2.5.1.4.1) would be possible here, too, but we can skip this step as it can only detect a problem without precisely stating where it occurred and, instead, we will have a closer look at each measurement (*level-D check*) and each state (*level-U check*).

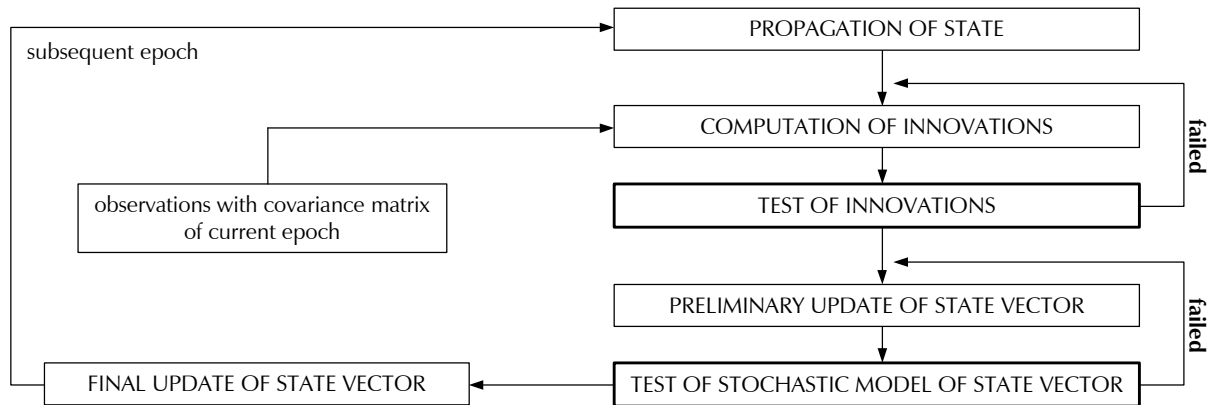


Figure 2-12 - Kalman filtering chain illustrating where blunder detection takes place. The level-D check is intended to reveal poor observations by testing the vector of innovations, whereas the level-U check is to reveal problems with the stochastic model of the parameter vector (not the measurements), e. g. due to the fact that the process noise of a particular state has been chosen much too small.

2.5.2.8.1 Level-D: Check of Innovations

The inputs for this test are the innovations \underline{d} and the associated covariance matrix $\underline{\Sigma}_{dd}$. This test practically checks that the measurements fit the predicted observations to a reasonable extend.

The null hypothesis assumes that the expectation value $E\{d_i\}$ of a particular element i in the vector of innovations is zero ($E\{d_i\} = 0$), i. e. that the measurement linked to this index is not corrupted by an outlier. The alternative hypothesis is $E\{d_i\} \neq 0$. All test quantities w_i are computed and the maximum w_{MAX} of the ensemble

$$w_i = \frac{|d_i|}{\sigma_{di}} \Rightarrow w_{MAX} = \max \{ w_1, w_2, \dots, w_n \} \quad (2-189)$$

d_i : innovation linked to measurement i

σ_{di} : (theoretical) standard deviation of this innovation

will be tested against the quantile

$$Y_{1-\alpha/2} = Y_{0.975} = 1.96 \quad (2-190)$$

Y_p : quantile of the Gauss distribution for a significance level of $p = 1-\alpha/2$

of the normal distribution²⁸ where a failure level of $\alpha = 5\%$ is usually accepted resulting in a quantile of about 2. The maximum test quantity indicates that a blunder is present if the condition

²⁸ The Gauss or normal distribution must be used due to the fact that the stochastic model is set up on a pure theoretical basis, error propagation is also performed for these theoretical values and - by default - no "empirical influences" on the filter are permitted. This situation changes if the self-calibration of the stochastic model of the observations is enabled by the analyst (\rightarrow 2.5.2.8).

$$w_{\text{MAX}} > Y_{1-\alpha/2} \quad (2-191)$$

w_{MAX} : maximum test quantity

Y_p : quantile of normal distribution defining the threshold for outlier detection at level $p = 1-\alpha/2$

is true. Typical reasons for detected outliers at this stage are multipath-corruption that has not been filtered out by the pre-processor, signals of poor quality (low signal-to-noise ratio) and also cycle slips that have not been flagged before.

The filter can now give very small weight to a blunder-corrupted observation. This would be a proper way if the reason had nothing to do with cycle slips. If the latter case, the problem is not related to the phase measurement, but to the corresponding ambiguity state. Consequently, it would be better to relax this ambiguity, i. e. to set the associated entry in the covariance matrix of the state vector to a huge number and to wipe out any correlation with this state for the moment. In a least-squares adjustment, this method corresponds to the insertion of a new ambiguity parameter. By default, the Kalman filter engine does both, it relaxes the measurement itself and the associated ambiguity state and repeats all necessary filter steps.

All blunders detected will be logged by the Kalman filter and with help of this log file, the quality of the network is analyzed afterwards. Baselines with suspiciously many outliers are marked and the bad sites are tried to be isolated. If there is one station which obviously performs rather poorly, this site can be excluded and the filtering can be repeated (\rightarrow 2.8.3).

2.5.2.8.2 Level-U: Check of Stochastic Model of the State Vector

Let us assume the following scenario: A network is to be filtered where the coordinates are well-known a priori, and therefore initialized in the state vector with an a priori standard deviation of 5 mm per component and a process noise²⁹ of 1 mm/ $\sqrt{\text{h}}$. At the middle of the diurnal filter batch, an earthquake occurs changing the position of a particular monitoring station abruptly for 1.5 m. Due to the low process noise and initial standard deviation, the filter will get rather confused - it would not be able to follow the abrupt coordinate change quickly enough and would possibly eliminate dozens of measurements by assuming that they are corrupted by multipath or due to other reasons.

For this reason, it can be advisable to enable the level-U check which tries to find inconsistencies in the stochastic model of the parameter vector. The first step is to do a preliminary update of the state vector \underline{X}^* and its covariance matrix

$$\begin{aligned} \underline{X}_k^* &= \underline{K}_k \cdot \underline{d}_k \\ \underline{\Sigma}_{\text{XX}k}^* &= \underline{K}_k \cdot \underline{\Sigma}_{\text{dd}k} \cdot \underline{K}_k^T \end{aligned} \quad (2-192)$$

²⁹ The analysis software allows to specify individual process noise values for each coordinate component and each zenith wet delay. A global process noise value is used for all ambiguities as well as for all orbit errors.

The test quantity is defined for each state separately,

$$w_i = \frac{X_i^2}{\sigma_{Xi}^2} \Rightarrow w_{MAX} = \max \{ w_1, w_1, \dots, w_n \} \quad (2-193)$$

X_i : entry i of the state vector (preliminary update)

σ_{Xi} : associated standard deviation

but it should be noted that this test is also suited for checking whole groups of parameters. One could also compute one test quantity for one point consisting of 3 coordinate components, i. e. 3 states. In this case the test quantity was

$$w_i = \underline{X}_i^T \cdot \underline{\Sigma}_{XXii}^{-1} \cdot \underline{X}_i \quad (2-194)$$

\underline{X}_i : sub-vector i containing all parameters of point i (3 coordinate components: X, Y, Z)

$\underline{\Sigma}_{XXii}$: associated sub-covariance matrix of dimension 3 x 3

and would allow to test whether a point in its entirety has moved or not. A sum of squared and normally distributed residuals follows the χ^2 -distribution. Therefore, the quantile $\chi^2_{n,1-\alpha}$ is needed with $n = 1$ (or 3 if coordinate triples are tested). The alternative hypothesis $E\{\underline{X}_i^*\} \neq 0$ is true if the condition

$$w_{MAX} > \chi^2_{1,1-\alpha} \quad (2-195)$$

w_{MAX} : maximum test quantity

$\chi^2_{1,p}$: quantile of χ^2 distribution defining the threshold for outlier detection at probability level $p = 1-\alpha$

holds. In this case, the associated state is relaxed, it is "re-incarnated", and all necessary steps of the filter algorithm must be repeated accordingly.

2.5.2.8.3 Analysis of Post-Fit Residuals

The analysis software offers an additional check called *post-fit residual analysis* that is also briefly mentioned here. The very idea of this data check is to let the Kalman filter perform a forward run and to log all residuals and the associated weights. After the filter has finished its run, the residuals are compared to their weights and a test quantity w is derived from this comparison (similar to \rightarrow 2.5.2.8.1). If this test quantity exceeds a pre-defined threshold, the related double difference measurement is flagged and will be wiped out from the network data file, but instead of cleaning this observation only for this particular epoch, it is faded out for a total time Δt , i. e. for a time span of $-1/2\Delta t$ before the epoch of detection and $+1/2\Delta t$ following the epoch of detection. The fading time Δt can be defined by the analyst and is usually in the range of about 120 seconds. The primary purpose of the residual analysis is to find multipath-affected measurements and to clean them from the data set.

2.5.2.9 Summarizing Coordinates

Diurnal network solutions are produced by the filter engine with the mean coordinates being the primary outcome. Of course, the state vector of the last epoch (for a forward run only) or of the first epoch (for a forward and backward run) should

represent the final network solution if the Kalman filter was optimally tuned. In practice, this goal is not always reached: Let us assume that strong multipath affection occurs right at the end of the diurnal batch. This will certainly have an impact on the coordinates and so, the solution vector of the last epoch will be much more corrupted than the state vector before multipath occurred. For this reason, the analysis software offers some additional methods to obtain average coordinate estimates.

2.5.2.9.1 Arithmetic Weighted Mean

For each component the weighted mean over all estimates is computed

$$X' = \sum_{i=1}^n \frac{X_i}{\sigma_{X_i}^2} / \sum_{i=1}^n \frac{1}{\sigma_{X_i}^2} \quad (2-196)$$

X' : final coordinate estimate, *here*: weighted mean coordinate component

X_i : filtered coordinate component at epoch i

σ_{X_i} : associated standard deviation

n : number of epochs

where the weights are defined by the reciprocal variance of the corresponding state.

2.5.2.9.2 Median

If the analyst does not trust the Kalman filter's abilities to propagate the variances and covariances properly nor to detect outliers, the median can be computed alternatively by first sorting the coordinate estimates by value

$$X' = X_{\text{MEDIAN}} = X_{n/2} \quad \wedge \quad X_1 \leq X_2 \leq \dots \leq X_n \quad (2-197)$$

and taking the value at position $n/2$ - i. e. at the middle of the sorted data batch - as final solution. The median is also called a *robust estimator* because it is relatively insensitive against blunders.

2.5.2.9.3 Jump Detection

In special cases there might be irregularly large movements of points, e. g. in case of earthquakes. For these special occurrences, the program can try to detect movements by comparison of previous/subsequent coordinate estimates

$$|X_{i-1} - X_i| > \Delta X_{\text{MAX}} \quad (2-198)$$

ΔX_{MAX} : point jump detection threshold

and mark jumps. The final coordinate solution is then obtained by building the weighted mean beginning with the time of the occurrence of the last jump up to the last epoch.

2.6 Ambiguities

For many static applications using permanent GPS arrays, treating ambiguities as floating numbers instead of integers has proven to be an acceptable method if the observation time is long enough. This is certainly the case for permanent arrays tracking the whole day, i. e. observing two full revolutions of the GPS satellites per day.

Nevertheless, the analysis software provides some methods to fix ambiguities. Two algorithms can be distinguished: (a) All linear combinations of integer nature like L_{54} can be directly fixed using statistical tests at two stages to confirm that a correct decision has been made. (b) This method cannot be applied for L_C because this signal has no integer ambiguity nature. Here, wide- and narrow-laning is performed to find a nominal solution for the ionosphere-free ambiguity.

2.6.1 Direct Fixing

In the first place, linear combinations with integer ambiguities like L_{43} , L_{54} or L_{97} are treated in exactly the same manner as the ionosphere-free signal L_C : The ambiguity combinations are estimated as float numbers by the Kalman filter. After a certain time, the variance of these states is low enough to allow a closer look on whether they are fixable or not.

STEP 1: Is the filter allowed to fix ambiguity combination $\nabla \Delta N_{AB[a1,a2]}^i$?

Only those ambiguities related to baselines of a length smaller than a pre-defined threshold

$$d_{AB} < d_{MAX} \quad (2-199)$$

d_{AB} : length of baseline AB

d_{MAX} : user-defined threshold for maximum baseline length accepted, usually less than 1000 km

and only down to a certain minimum elevation angle

$$\epsilon_A^i, \epsilon_A^j, \epsilon_B^i, \epsilon_B^j > \epsilon_{MIN} \quad (2-200)$$

ϵ_A^i : elevation angle from ground station A to satellite i

ϵ_{MIN} : user-defined threshold for minimum elevation accepted, usually about 30°

are fixed. The background for these additional checks is related to the fact that ionospheric as well as tropospheric errors decorrelate with increasing baseline length and uncertainties in atmospheric modeling, signal-strength problems, etc. affect low-elevation signals more than those at high elevation.

STEP 2: Is the standard deviation of the floating ambiguity small enough?

This decision is made with knowledge of the virtual wavelength $\lambda_{a1,a2}$ which is compared to the standard deviation of the ambiguity. This standard deviation is given in cycles, so the value to compare it with is 1 cycle. If the test ratio

$$\frac{1[\text{cycle}]}{\sigma_{\nabla\Delta N_{AB[a1,a2]}^{ij}}} > Y_{\text{MIN}} \quad (2-201)$$

Y_{MIN} : quantile of the Gauss distribution defining the threshold that must be exceeded for fixing

$\nabla\Delta N$: double difference ambiguity

$\sigma_{\nabla\Delta N}$: standard deviation of ambiguity

is greater than the quantile Y_{MIN} of the Gauss distribution, it is considered to be fixable. By default, a threshold of $Y_{\text{MIN}} = 4$ is set that corresponds to a significance level of 99.997%. Practically, this threshold means that the standard deviation of the ambiguity must be less than one quarter of the corresponding wavelength³⁰.

STEP 3: Fixing the floating ambiguity to its nearest integer neighbor

The nearest integer neighbor is computed by

$$\nabla\Delta N_{AB[a1,a2]}^{ij*} = \text{int} \left(\nabla\Delta N_{AB[a1,a2]}^{ij} + \frac{1}{2} \cdot \text{sgn} \nabla\Delta N_{AB[a1,a2]}^{ij} \right) \quad (2-202)$$

$\nabla\Delta N^*$: double-difference ambiguity with integer nature

$\nabla\Delta N$: double-difference ambiguity with float nature (Kalman filter estimate)

and has to be tested in the following step. Note that the formula above takes the sign of the ambiguity into account in order to find the correctly rounded integer neighbor.

STEP 4: Is the difference between integer and float solution within reasonable limits?

The difference v between the integer and the float solution is

$$v = \left| \nabla\Delta N_{AB[a1,a2]}^{ij*} - \nabla\Delta N_{AB[a1,a2]}^{ij} \right| \quad (2-203)$$

and is tested against the quantile Y_{MAX}

$$\frac{v}{\sigma_{\nabla\Delta N_{AB[a1,a2]}^{ij}}} \leq Y_{\text{MAX}} \quad (2-204)$$

Y_{MAX} : quantile of the Gauss distribution defining the maximum threshold for fixing

that must not be exceeded. Note that the user can define different significance levels for the quantiles Y_{MIN} (\rightarrow step 2) and Y_{MAX} ³¹. In case of success, the integer value will be inserted into the state vector, the associated variance is substituted by a small variance that tightly constraints this state and all states related to this ambiguity are decorrelated in the covariance matrix, i. e. all affected covariances are set to zero. Nevertheless, the ambiguity combination will be checked by this algorithm at any

³⁰ The higher the threshold is selected, the more rigorous this statistical test will be. Suitable thresholds should not lie below 3.5 as a matter of caution against wrong fixing that may occur otherwise.

³¹ For this step, the smaller the threshold Y_{MAX} is selected, the more rigorous the statistical test will be. The default value for the quantile is about 1.2.

future epoch and in case a future test shows that the ambiguity combination is not fixable any longer, the constraints will vanish.

Note that all near-ionosphere-free combinations supported by the analysis system have the disadvantage of a relatively small wavelength. Whereas it is possible to fix the L_{43} and L_{54} signals, it is much more difficult for L_{97} .

2.6.2 Indirect Fixing of the Ionosphere-Free Signal

The linear combination L_C has floating ambiguities. Nevertheless, it is possible to compute a nominal solution. At a first guess, one could try to fix the original carrier signals L_1 and L_2 , but this is not done here, because the wide lane has much larger wavelength and therefore allows more easily to be fixed. This part is done by the pre-processor, not by the Kalman filter. In a second step, the filter tries to find a suitable integer solution for the narrow lane with help of the previously fixed wide lane and the floating filter estimate for the ionosphere-free signal. In case of a successful fixing of the narrow lane, the nominal value of the L_C ambiguity can be computed.

2.6.2.1 Wide Lane Fixing

Two methods can be used to fix the wide lane signal. The first method is to apply a special code-carrier combination, sometimes referred to as L_6 and the other method is to compute the wide lane directly from phase measurements.

2.6.2.1.1 Code-Carrier-Combination

Following ROTHACHER and MERVART [1996], the wide lane ambiguity can be computed by combining code and carrier phase measurements

$$N_{[W]} = - \frac{\frac{f_{L1} \cdot \Theta_{L1} - f_{L2} \cdot \Theta_{L2}}{f_{L1} - f_{L2}} - \frac{f_{L1} \cdot PR_{L1} + f_{L2} \cdot PR_{L2}}{f_{L1} + f_{L2}}}{\lambda_W} \quad (2-205)$$

λ_W : virtual wavelength of the wide lane linear combination, about 86 cm

Θ_{L1} : carrier phase measurement on L_1 in units of the wavelength λ_W

PR_{L1} : pseudo-range measurement on L_1

f_{L1} : frequency of carrier signal L_1

This estimate is not corrupted by the troposphere, ionosphere, geometric uncertainties (coordinates) nor clock errors. The analysis software makes use of the formula in its doubly differenced form

$$\nabla \Delta N_{AB[W]}^{ij} = (N_{B[W]}^j - N_{A[W]}^j) - (N_{B[W]}^i - N_{A[W]}^i) \quad (2-206)$$

and is applied for all ambiguity combinations baseline per baseline by the GPS pre-processor. Unfortunately, code ranges have a considerably higher noise level in

comparison to carrier phase measurements³². Therefore, instantaneous fixing of the wide lane is hardly possible to achieve. Instead, the mean of all samples

$$\nabla\Delta N_{AB[W]}^{ij*} = \frac{1}{n} \cdot \sum_{k=1}^n \nabla\Delta N_{AB[W],k}^{ij} \quad (2-207)$$

$\nabla\Delta N^*$: mean wide lane ambiguity
 n : number of samples

is computed and its empirical standard deviation is found with help of the residuals

$$v_k = \nabla\Delta N_{AB[W]}^{ij*} - \nabla\Delta N_{AB[W],k}^{ij} \quad \wedge \quad s_{[W]} = \sqrt{\frac{\sum_{k=1}^n v_k^2}{n \cdot (n-1)}} \quad (2-208)$$

v_k : residual with respect to the mean wide lane ambiguity
 $s_{[W]}$: empirical standard deviation of the mean wide lane ambiguity

Now, it is tried to fix the mean wide lane ambiguity to the nearest integer in the same way as it has been depicted before (\rightarrow 2.6.1) without checking the baseline-length nor the elevation angle because this method is designed for very long baselines and the elevation varies due to the fact that samples over a time span as long as possible are to be collected in order to obtain a mean value with sufficiently low standard deviation.

Care must be taken to avoid any corruption of remaining cycle slips. For this reason, the current ambiguity estimates are compared with the previous ones

$$\left| \nabla\Delta N_{AB[W],k-1}^{ij} - \nabla\Delta N_{AB[W],k}^{ij} \right| > \delta\nabla\Delta N_{MAX} \quad (2-209)$$

$\delta\nabla\Delta N_{MAX}$: maximum difference between two ambiguity estimates allowed,
threshold for cycle slip detection

and if the difference exceeds the user-defined threshold $\delta\nabla\Delta N_{MAX}$, e. g. 6 meters, all following estimates are considered to belong to a new wide lane ambiguity and both time intervals are treated separately.

Moreover, a minimum time window can be defined by the analyst with a default value of 1800 seconds. If a certain ambiguity combination is not present for at least this period, no wide lane fixing is tried. It is pointed out that 1800 seconds should be a minimum value recommended for this option. Usually, at least 2700 seconds are used in the analysis of GPS data.

³² It is not advisable to use smoothed code-ranges because these observations have about the same noise level as the phase measurements. As a consequence, the empirical standard deviation $s_{[W]}$ will become very small, although there might be systematic errors in the smoothed ranges that are no longer reflected. So, the application of smoothed ranges may likely lead to wrong decisions as far as the wide lane fixing is concerned.

2.6.2.1.2 IONEX-Supported Carrier Solution

An alternative way is to compute the wide lane ambiguities directly from the pre-processed ambiguities for L_1 and L_2 (\rightarrow 2.2.5):

$$\nabla \Delta N_{AB[W]}^{ij} = \nabla \Delta N_{AB[L1]}^{ij} - \nabla \Delta N_{AB[L2]}^{ij} \quad (2-210)$$

The advantage of this method is that no noisy pseudo-range measurements are used, but on the other hand, several disadvantages are to be mentioned: Geometric effects remain (ground station coordinates must be known a priori to at least 3 dm or better) as well as tropospheric (are normally modeled with sufficient accuracy by the pre-processor) and ionospheric effects (critical, IONEX files must be used, \rightarrow 2.2.4.3). Especially due to ionospheric propagation delays, this method is only recommended for baselines up to a few hundred kilometers if IONEX files are available.

2.6.2.2 Narrow Lane Fixing

The wide lane

$$\nabla \Delta N_{AB[W]}^{ij} = \nabla \Delta N_{AB[L1]}^{ij} - \nabla \Delta N_{AB[L2]}^{ij} \quad (2-211)$$

is fixed by the pre-processor, and the floating ionosphere-free ambiguity for L_C

$$\nabla \Delta N_{AB[LC]}^{ij} = \nabla \Delta N_{AB[L1]}^{ij} - \frac{f_{L2}}{f_{L1}} \cdot \nabla \Delta N_{AB[L2]}^{ij} \quad (2-212)$$

is estimated by the Kalman filter. The narrow lane

$$\nabla \Delta N_{AB[N]}^{ij} = \nabla \Delta N_{AB[L1]}^{ij} + \nabla \Delta N_{AB[L2]}^{ij} \quad (2-213)$$

can now be determined with help of the wide lane and the L_C ambiguity

$$\nabla \Delta N_{AB[N]}^{ij} = \frac{f_{L1} \cdot (2 \cdot \nabla \Delta N_{AB[LC]}^{ij} - \nabla \Delta N_{AB[W]}^{ij}) - f_{L2} \cdot \nabla \Delta N_{AB[W]}^{ij}}{f_{L1} - f_{L2}} \quad (2-214)$$

with restored integer nature. The standard deviation of this estimate is

$$\sigma_{\nabla \Delta N_{AB[N]}^{ij}} = \frac{2 \cdot f_{L1}}{f_{L1} - f_{L2}} \cdot \sigma_{\nabla \Delta N_{AB[LC]}^{ij}} \quad (2-215)$$

Due to the *even-odd-condition*, the narrow lane ambiguity must be even if the wide lane ambiguity is even and vice versa. This effectively doubles the wavelength of the narrow lane and significantly supports the process of ambiguity fixing. Therefore, the first test of section 2.6.1 becomes

$$\frac{2 [\text{cycles}]}{\sigma_{\nabla \Delta N_{[N]}}} > Y_{\text{MIN}} \quad (2-216)$$

Y_{MIN} : quantile of the Gauss distribution defining the threshold that must be exceeded for fixing

here. The second test is carried out

$$v = \left| \nabla \Delta N_{AB[N]}^{ij*} - \nabla \Delta N_{AB[N]}^{ij} \right| \quad (2-217)$$

using the difference between the fixed and the floating narrow lane in exactly the same way as described before.

2.6.2.3 Nominal L_C -Ambiguity

The fixed narrow lane is used together with the pre-processed wide lane to compute the nominal L_C ambiguity

$$\nabla \Delta N_{AB[LC]}^{ij*} = \frac{f_{L1} \cdot (\nabla \Delta N_{AB[N]}^{ij} - \nabla \Delta N_{AB[W]}^{ij}) + f_{L2} \cdot (\nabla \Delta N_{AB[W]}^{ij} - \nabla \Delta N_{AB[N]}^{ij})}{2 \cdot f_{L1}} \quad (2-218)$$

that will replace the state vector entry accordingly.

2.6.3 Ambiguity Back-Tracing

Special situations occur when the reference satellite changes from one epoch to the next. By default, the filter will implement totally new states for the new ambiguity combinations as a consequence of the change in reference satellite. However, it is often possible to compute the new ambiguity combinations from the old states and this method is called *ambiguity back-tracing* in this acquisition.

For the ij , ik , il scheme (\rightarrow 2.2.2.1), the following two double difference ambiguity combinations

$$\begin{aligned} \nabla \Delta N_{AB}^{ij} &= (\nabla \Delta N_B^j - \nabla \Delta N_A^j) - (\nabla \Delta N_B^i - \nabla \Delta N_A^i) \\ \nabla \Delta N_{AB}^{ik} &= (\nabla \Delta N_B^k - \nabla \Delta N_A^k) - (\nabla \Delta N_B^i - \nabla \Delta N_A^i) \end{aligned} \quad (2-219)$$

are considered. Given a change in reference satellite from i to j in the following epoch, it is possible to compute the new ambiguity combination

$$\nabla \Delta N_{AB}^{jk} = (\nabla \Delta N_B^k - \nabla \Delta N_A^k) - (\nabla \Delta N_B^j - \nabla \Delta N_A^j) \quad (2-220)$$

from the old ambiguity states as follows

$$\begin{aligned} \nabla \Delta N_{AB}^{jk} &= \nabla \Delta N_{AB}^{ik} - \nabla \Delta N_{AB}^{ij} \\ &= (\nabla \Delta N_B^k - \nabla \Delta N_A^k) - (\nabla \Delta N_B^i - \nabla \Delta N_A^i) - (\nabla \Delta N_B^j - \nabla \Delta N_A^j) + (\nabla \Delta N_B^i - \nabla \Delta N_A^i) \\ &= (\nabla \Delta N_B^k - \nabla \Delta N_A^k) - (\nabla \Delta N_B^j - \nabla \Delta N_A^j) \end{aligned} \quad (2-221)$$

and ambiguity

$$\nabla\Delta N_{AB}^{ij} = (\nabla\Delta N_B^i - \nabla\Delta N_A^i) - (\nabla\Delta N_B^j - \nabla\Delta N_A^j) \quad (2-222)$$

is simply obtained by

$$\nabla\Delta N_{AB}^{ji} = -\nabla\Delta N_{AB}^{ij} \quad (2-223)$$

In a similar way, ambiguity combinations can be traced back for the *ij, jk, kl scheme*³³: Given the two ambiguities

$$\begin{aligned} \nabla\Delta N_{AB}^{ij} &= (\nabla\Delta N_B^j - \nabla\Delta N_A^j) - (\nabla\Delta N_B^i - \nabla\Delta N_A^i) \\ \nabla\Delta N_{AB}^{jk} &= (\nabla\Delta N_B^k - \nabla\Delta N_A^k) - (\nabla\Delta N_B^j - \nabla\Delta N_A^j) \end{aligned} \quad (2-224)$$

and the same change in reference as depicted before, the new ambiguity combination

$$\nabla\Delta N_{AB}^{ik} = (\nabla\Delta N_B^k - \nabla\Delta N_A^k) - (\nabla\Delta N_B^i - \nabla\Delta N_A^i) \quad (2-225)$$

can be traced back to

$$\begin{aligned} \nabla\Delta N_{AB}^{ik} &= \nabla\Delta N_{AB}^{jk} + \nabla\Delta N_{AB}^{ij} \\ &= (\nabla\Delta N_B^k - \nabla\Delta N_A^k) - (\nabla\Delta N_B^j - \nabla\Delta N_A^j) + (\nabla\Delta N_B^j - \nabla\Delta N_A^j) - (\nabla\Delta N_B^i - \nabla\Delta N_A^i) \\ &= (\nabla\Delta N_B^k - \nabla\Delta N_A^k) - (\nabla\Delta N_B^i - \nabla\Delta N_A^i) \end{aligned} \quad (2-226)$$

However, the back-traced ambiguities should be checked for consistency. For static networks, the TropAC analysis system does so by comparing the computed ambiguities with the pre-processed ones (\rightarrow 2.2.5). The difference between the back-traced and the pre-processed ambiguities should not exceed a user-defined threshold, e. g. 1 or 2 cycles. The choice of the threshold depends on the a priori accuracy of the coordinates as well as on that of the predicted atmospheric errors.

2.7 Geodetic Datum

The geodetic datum of the network is defined at the time of filter initialization: The a priori coordinates are assigned to the state vector and the datum is defined stochastically by giving proper weight to the corresponding coordinate components. The common way is to assign tight constraints (low variances) to all those points which shall be treated as datum points.

If a free network solution is the target, then the network must not be set under tension, i. e. only d coordinate components can be tightly constrained with d being the number of datum defects. If the number of actual constraints is higher than d , no

³³ For this double difference scheme, no back-tracing algorithm has been implemented in the analysis software yet as it is less often used in comparison to the *ij, ik, il* scheme.

similarity system (S-system) will be created and similarity transformations cannot be performed afterwards. For 3-D GPS networks, there are at least 3 and up to 7 datum defects. Table 2-6 gives an overview of datum defects and the order in which they are handled by the analysis software. For extended information about datum definition and Kalman filtering see also STELZER and PAPO [1994].

Parameter Index	Datum Element	Notation
1	translation in direction of X-axis (datum shift)	ΔX
2	translation in direction of Y-axis	ΔY
3	translation in direction of Z-axis	ΔZ
4	rotation around X-axis	ε_x
5	rotation around Y-axis	ε_y
6	rotation around Z-axis	ε_z
7	scaling factor of network	$q = (1 + m)$

Table 2-6 - Datum defects of 3-D space-geodetic networks. The parameter index defines the order in which the datum parameters are handled by the analysis software. Example: If - for any reason - only 4 datum defects are to be compensated, then module PAF_TRAN will choose the 3 datum shift constants (translations) and a rotation around the X-axis.

2.7.1 Datum Transformation

A transformation of coordinate vector \underline{X} (network datum I) to \underline{X}^* (network datum II) is possible if the datum parameters describing the transition from system I to II are given. The corresponding transformation equation³⁴ is

$$\underline{X}^* = \begin{pmatrix} X^* \\ Y^* \\ Z^* \end{pmatrix} = \Delta \underline{X} + \underline{R} \cdot \underline{X} = \begin{pmatrix} \Delta X \\ \Delta Y \\ \Delta Z \end{pmatrix} + \begin{pmatrix} q & -\varepsilon_z & +\varepsilon_y \\ +\varepsilon_z & q & -\varepsilon_x \\ -\varepsilon_y & +\varepsilon_x & q \end{pmatrix} \cdot \begin{pmatrix} X \\ Y \\ Z \end{pmatrix} \quad (2-227)$$

X, Y, Z : coordinates referring to network datum I, to be transformed

X^*, Y^*, Z^* : transformed coordinates referring to network datum II

\underline{R} : rotation and scaling matrix

and can be rewritten in component form as:

$$\begin{aligned} X^* &= \Delta X + q \cdot X - \varepsilon_z \cdot Y + \varepsilon_y \cdot Z \\ Y^* &= \Delta Y + \varepsilon_z \cdot X + q \cdot Y - \varepsilon_x \cdot Z \\ Z^* &= \Delta Z - \varepsilon_y \cdot X + \varepsilon_x \cdot Y + q \cdot Z \end{aligned} \quad (2-228)$$

To determine the datum parameters, a set of identical points in system I and system II is needed and the transformation formulas are treated as observation equations with X^*, Y^*, Z^* as observations, X, Y, Z as fixed constants and the datum parameters as unknowns which are estimated by a least-squares algorithm.

³⁴ This kind of transformation corresponds to the so-called 7-parameter Helmert-transformation.

It should be pointed out that the approach discussed here is only valid for small rotation angles. This is almost always the case when regional or global networks are transformed.

2.7.2 Similarity Transformation

A free network solution is obtained by a similarity transformation as described by HÖPCKE [1980, pp. 119-123]. This practically corresponds to a Helmert transformation. First of all, the center of the network is computed

$$X^* = \frac{1}{n} \cdot \sum_{i=1}^n X_i \quad \wedge \quad Y^* = \frac{1}{n} \cdot \sum_{i=1}^n Y_i \quad \wedge \quad Z^* = \frac{1}{n} \cdot \sum_{i=1}^n Z_i \quad (2-229)$$

X, Y, Z : global, geocentric coordinates (ECEF)

X^*, Y^*, Z^* : center point of the network, mean coordinate components

n : number of network points

Now, the coordinates are referred to this center point

$$x_i = X_i - X^* \quad \wedge \quad y_i = Y_i - Y^* \quad \wedge \quad z_i = Z_i - Z^* \quad (2-230)$$

x, y, z : centered coordinates

and the scaling factor c as well as value τ are used to normalize the columns

$$c = \frac{1}{\sqrt{\sum_{i=1}^n (x_i^2 + y_i^2 + z_i^2)}} \quad \wedge \quad \tau = \frac{1}{\sqrt{n}} \quad (2-231)$$

within similarity matrix \underline{S} that is composed in the same order as defined by Table 2-6

$$\underline{S} = \begin{bmatrix} \tau & 0 & 0 & 0 & -c \cdot z_1 & +c \cdot y_1 & +c \cdot x_1 \\ 0 & \tau & 0 & +c \cdot z_1 & 0 & -c \cdot x_1 & +c \cdot y_1 \\ 0 & 0 & \tau & -c \cdot y_1 & +c \cdot x_1 & 0 & +c \cdot z_1 \\ \vdots & \vdots & \vdots & \vdots & \vdots & \vdots & \vdots \end{bmatrix} \quad (2-232)$$

\underline{S} : similarity matrix

and deals with the x -component in line 1, the y -component in line 2 and the z -component of the first point in line 3. The transformation matrix \underline{J} can now be determined

$$\underline{J} = \underline{E} - \underline{S} \cdot \underline{S}^T \quad (2-233)$$

\underline{J} : transformation matrix

\underline{E} : identity matrix

\underline{S} : similarity matrix

and the similarity-transformed coordinate vector is

$$\underline{X}_S = \underline{X}_0 + \underline{J} \cdot (\underline{X} - \underline{X}_0) \quad (2-234)$$

\underline{X}_0 : a priori network coordinates

\underline{X} : original coordinate solution (a posteriori coordinates)

\underline{X}_S : coordinate vector of S-transformed network solution

with its associated covariance matrix

$$\underline{\Sigma}_{XXS} = \underline{J} \cdot \underline{\Sigma}_{XX} \cdot \underline{J} \quad (2-235)$$

$\underline{\Sigma}_{XX}$: covariance matrix of original network solution (a posteriori, *not* a priori)

$\underline{\Sigma}_{XXS}$: covariance matrix of S-transformed network solution

This free network solution depicted here minimizes the full trace of the covariance matrix. For special applications, e. g. in deformation monitoring, it is advisable not to minimize the full, but only the partial trace. This means that certain points are excluded from the definition of the datum because they are suspect to movements. In this case, the center of the network is only defined by the datum points and not by all available network points.

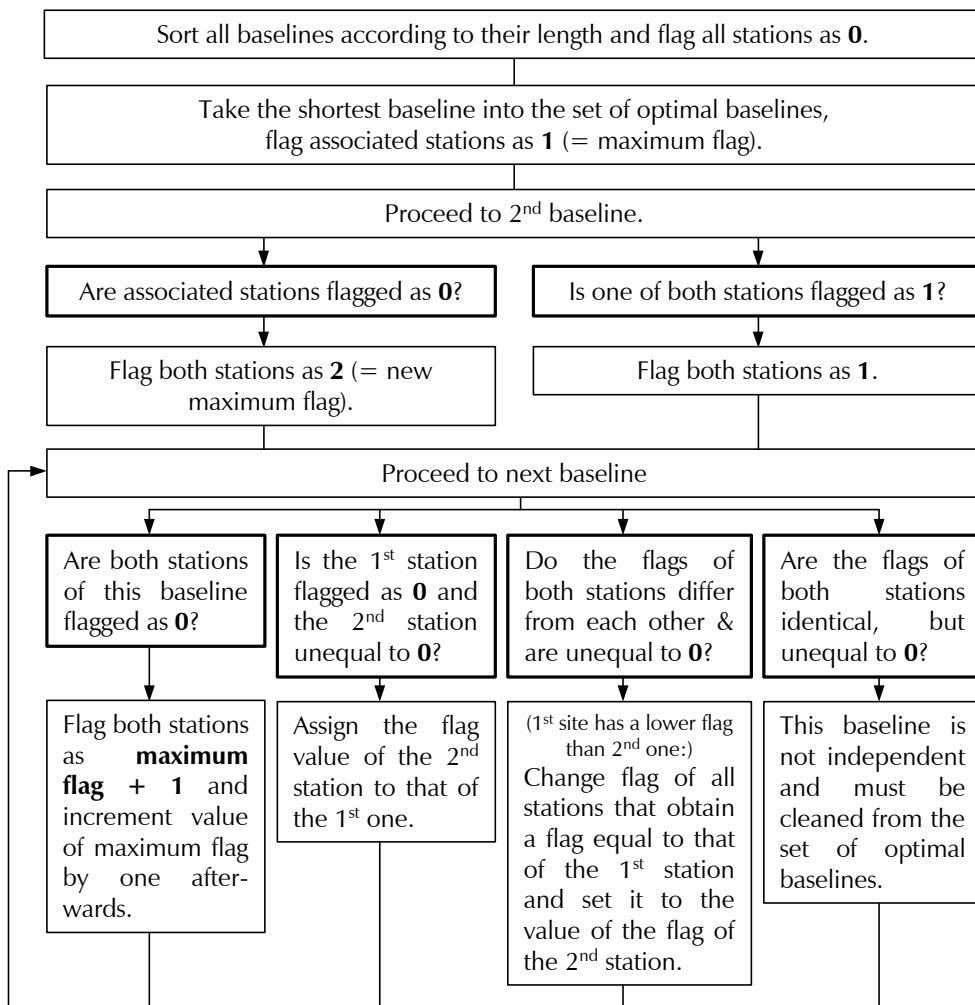


Figure 2-13 - Algorithm to find the optimal and independent set of shortest baselines after MERVART et al. [1994]. The criterion chosen here is the baseline length which is minimized. It is also possible to select the number of measurements as criterion to compose the network.

2.8 Network Composition

2.8.1 Centered Networks

Centered networks are easy to compose and may serve a good job if the user is mainly interested in parameters related to the particular station on which the baselines are centered. Figure 2-14 shows an example for a centered network, but it is stressed here that less stations than shown in the plot are usually fully sufficient to obtain reasonably good results for the centered site.

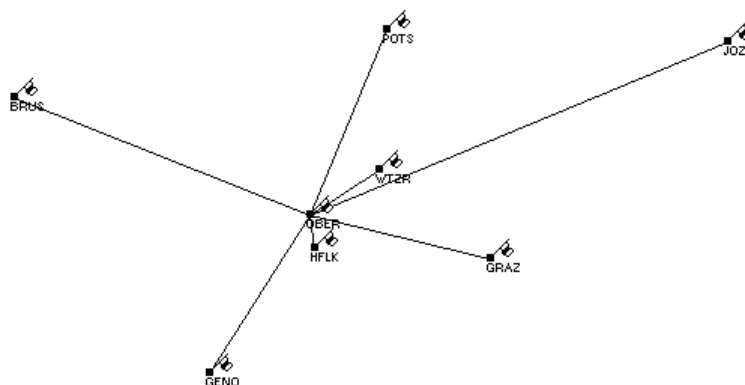


Figure 2-14 - Centered network. In this example, monitoring station Oberpfaffenhofen (OBER) is of primary interest and therefore, all other network points are centered on this station.

Data gaps occurring at a particular (non-centered) station are most likely compensated by another one which is part of the network.

2.8.2 Shortest Baseline Networks

In most cases, the set of shortest and independent baselines is a good choice for filtering a whole network without concentrating on a particular site. For a network with n stations, there are $n-1$ independent baselines. The task is to find exactly those from $n \cdot (n-1)$ possible baselines which are absolutely independent from each other and are as short as somehow possible. This is especially interesting for ambiguity fixing since there are usually some remaining baseline length-dependent effects which can hereby be minimized. Figure 2-15 shows the network from the preceding section, but now connected by shortest baselines.

An algorithm to find such a set of shortest baselines could be to create a list of all possible baselines, to choose those $n-1$ baselines which have shortest length, to connect the network points accordingly and to compose the design matrix for this network. The normal equation matrix can now be tested for singularity: If it is not, the optimal set of baselines is apparently defined. If it is, successive replacement by other baselines and repeated testing has to be carried out in order to search for the optimal solution. A similar algorithm like this one outlined here was developed by GOAD and MUELLER [1988], but suffers from high CPU-load. MERVART et al. [1994] precisely describe an efficient solution for this problem that is based on logical decisions and illustrated in Figure 2-13. This algorithm was implemented in the analysis software and is almost always applied for automatic network filtering.

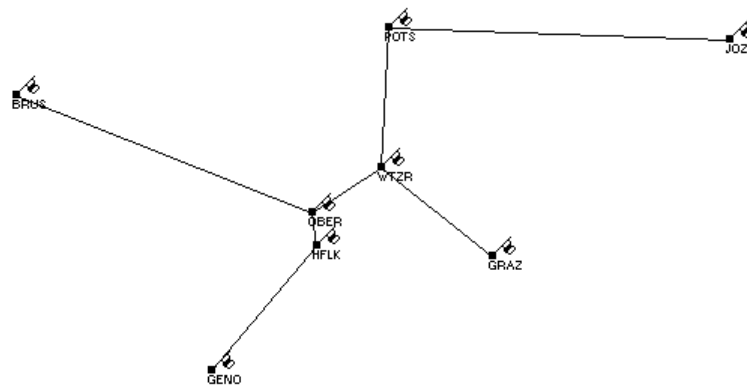


Figure 2-15 - Network composed of a set of shortest independent baselines. For n sites, all those $n-1$ independent baselines are used that have shortest baseline length. This may reduce remaining uncertainties that are proportional to the distance between two stations.

2.8.3 Site Isolation Logic

As already pointed out, a network connected by shortest baselines is one important criterion for the minimization of remaining baseline length-dependent effects, but automatic data processing usually requires further considerations as shown in Figure 2-16: All baselines connected to site Wettzell (*WTZR*) have a suspiciously low number of double difference observations. The average number for diurnal data batches with 30 second data sampling is about 10000 to 15000 observations.

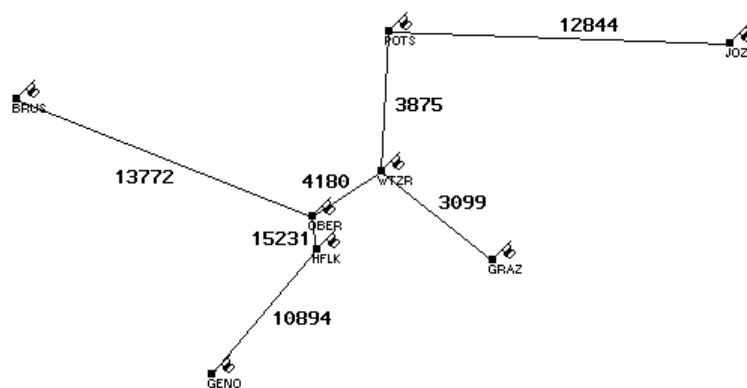


Figure 2-16 - Identification of poorly performing network stations. The values connected to each baseline are the numbers of double difference observations (linearly combined phase measurements) that could be built for the particular baseline. Clearly, site Wettzell (*WTZR*) can be isolated as mal-functioning.

Apparently, the pre-processor has deleted many observations related to *WTZR* due to bad signal-to-noise ratio, multipath affection or poorly behaving receiver clocks or there have been data gaps or other receiver failures. In any case, simply using the algorithm to compose the network by shortest baselines would be a very bad method here because this would lead to a destabilization of huge parts of the network since *WTZR* plays a central role in it.

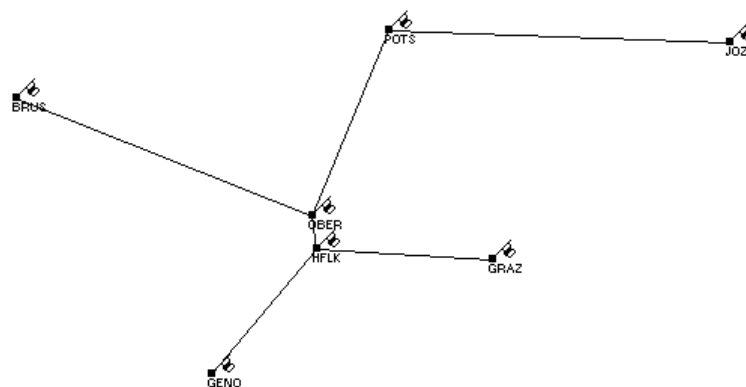


Figure 2-17 - Exclusion of bad tracking site. Monitor station Wettzell (WTZR) has been excluded from the network and the remaining network is composed of a new set of shortest independent baselines.

The baseline quality check algorithm of the GPS pre-processor therefore compares the number of double difference observations for each baseline with the maximum number reached in this network. If the ratio is less than 60%, for instance, the associated baseline is marked as suspicious. By nature, two stations are connected to a suspicious baseline and the quality checker looks whether at least one of these two sites also occurs in another baseline that is marked as weak. If this is not the case, then the bad baseline is obviously linked to a poorly behaving site which is isolated, i. e. it is located in the exterior part of the network and cannot harm other sites. If it is the case, the low number of observations is assumed to be caused by the malfunctioning receiver at the ground station found, this tracking site is deleted from the network and a new, reduced set of shortest baselines is composed as shown in Figure 2-17.

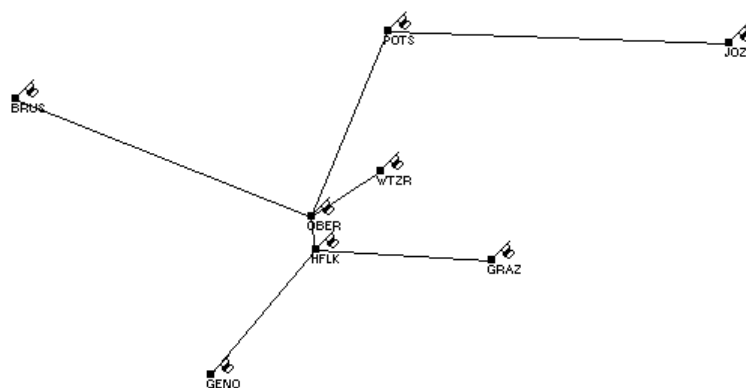


Figure 2-18 - Re-connection of bad tracking site. Station Wettzell (WTZR) is relinked to the network, but in contrast to the original network setup it is connected as an isolated site that cannot destabilize the network any longer.

Finally, if the user does not want to omit the few measurements provided by the poorly behaving receiver, this station may optionally be reconnected to the new network as an isolated site. Figure 2-18 depicts this last step that relinks the poorly behaving receiver in order to exploit any information available without giving it the opportunity to degrade the overall quality of the network.

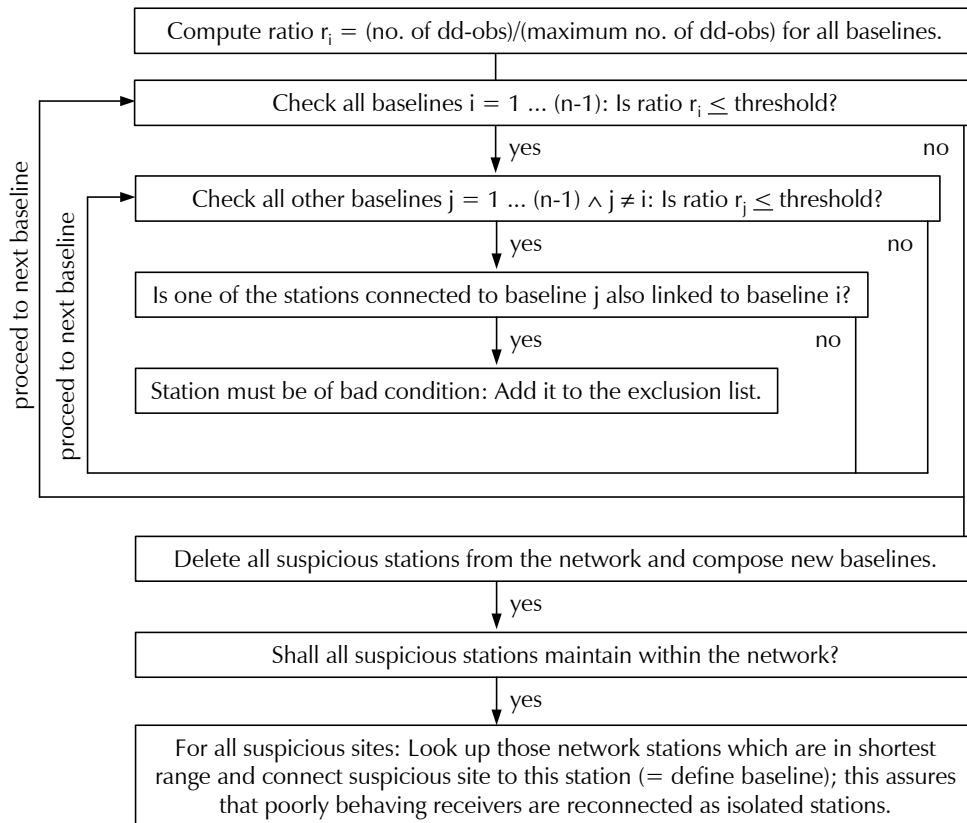


Figure 2-19 - Outline of algorithm for detection and isolation of bad receivers. The criterion for the test is the number of double difference (dd) observations in comparison to the maximum number of dd-observations reached in the network (about 12000 to 15000 linearly combined double differences for diurnal data batches with 30 second data sampling). The total number of stations is denoted with symbol 'n', so there are exactly 'n-1' baselines to check. The detection threshold usually lies in the range of 0.6 (60%).

Figure 2-19 provides an overview of this algorithm which is applied by the GPS pre-processor PAF_PREP. The filter engine PAF_FILTER uses a similar algorithm to check for suspicious network stations after finishing the filter runs: Here, the criterion is the number of outliers that has been detected by the Kalman filter. This number is compared to the number of double difference observations of the particular baseline and the ratio should not exceed a threshold of typically 1% to 2%.

2.9 Network Partitioning

The CPU-load increases roughly to the 3rd power of the number of network stations to filter what is mainly caused by the ambiguity states to determine. For this reason, it is desirable to filter only smaller network parts and to combine all partitions to one network solution afterwards. Although the optimal solution might be to filter the network in its entirety, network partitioning can tremendously decrease the total time for network filtering, esp. if multi-processor machines are used³⁵.

³⁵ Processing has been mostly performed on the Compute Server Origin 2000 (Silicon Graphics) which uses the operation system IRIX (64-bit) and is optimized for parallel computing with 32 MIPS processors.

The module PAF_TRAN provides a possibility to combine several network solutions. The first network with its solution vector \underline{X}^* and the covariance matrix $\underline{\Sigma}_{xx}^*$ is treated as master network and the second network denoted as \underline{X} and $\underline{\Sigma}_{xx}$ is the child network. Combination is performed using a least-squares algorithm with observation vector \underline{L} and the associated covariance matrix $\underline{\Sigma}_{LL}$:

$$\underline{L} = \begin{bmatrix} \underline{X}^* \\ \underline{X} \end{bmatrix} \quad \wedge \quad \underline{\Sigma}_{LL} = \begin{bmatrix} \underline{\Sigma}_{xx}^* & \\ & \underline{\Sigma}_{xx} \end{bmatrix} \quad (2-236)$$

\underline{L} : observation vector

\underline{X}^* : vector of primary network solution

\underline{X} : vector of secondary network solution

$\underline{\Sigma}_{LL}$: covariance matrix

$\underline{\Sigma}_{xx}^*$: covariance matrix of primary network solution

$\underline{\Sigma}_{xx}$: covariance matrix of secondary network solution

Note that the covariance matrices of the network solution can be singular what has to be addressed by the program accordingly. It is allowed to override existing datum defects of the child network, i. e. up to 7 datum parameters describing the transition of the child network to the datum of the master network can be estimated if there are enough identical points in both networks. Consequently, the design matrix has the structure

$$\underline{A} = \begin{bmatrix} \underline{A}_x^* & \underline{0} \\ \underline{A}_x & \underline{I} \end{bmatrix} \quad (2-237)$$

\underline{A}_x^* : design sub-matrix of the master network

\underline{A}_x : design sub-matrix of the child network

\underline{I} : partial derivatives of the datum parameters

where \underline{A}_x^* is the design sub-matrix of the master network and \underline{A}_x refers to the child network. If the master network contained exactly the same points as the child network, the design sub-matrices were an identity matrix: $\underline{A}_x^* = \underline{A}_x = \underline{E}$. The partial derivatives of the datum parameters are contained in matrix \underline{I} and can be set up using the equations provided in section → 2.7.1. The parameter vector of the adjusted, combined solution will consequently consist of the sub-vectors

$$\underline{X}_{ALL} = \begin{bmatrix} \underline{X}^* \\ \underline{t} \end{bmatrix} \quad (2-238)$$

\underline{X}_{ALL} : adjusted vector of unknowns

\underline{X} : combined network solution vector

\underline{t} : adjusted datum parameters

containing the combined coordinate solution vector (\underline{X}^i) as well as the adjusted datum parameters (\underline{t}).

3. Modeling and Estimating Tropospheric Propagation Delays

The primary purpose of the TropAC analysis system is to estimate wet tropospheric delays that can be converted into integrated water vapor and thereby serve as a valuable input into numerical weather and climate models. For this reason, an entire chapter is devoted to tropospheric delay modeling and estimation.

3.1 Brief Overview of the Lower Atmosphere

The atmosphere is a mixture of dry gases that primarily contribute to the hydrostatic delay (\rightarrow Table 3-1) and water vapor which is responsible for the wet delay. SPILKER [1996] states that the dry atmosphere is uniform and uncomplicated in modeling whereas the wet part is unevenly distributed. The vertical profiles of the most important meteorological quantities are plotted in Figure 3-2 for an arbitrarily chosen day at IGS monitor station Oberpfaffenhofen (OBER, Germany).

The following layers are to be distinguished: The *troposphere* ranges from sea level (≈ 0 m) to a height of about 12 km and is characterized by a relatively linear temperature decrease. The *tropopause* is a small boundary layer between 12 and 16 km where the temperature remains approximately constant at a level of -60 to -80 °C and in the *stratosphere* (16 to 50 km), a slow temperature increase occurs. As far as the wet component is concerned, the lower troposphere is of major interest whereas the hydrostatic component is influenced up to the stratopause. SPILKER [1996] mentions that about one quarter of the total delay is caused by gases above the tropopause. Most of the *water vapor* contents, however, is concentrated at a height right below 4 km and above 12 km, almost no more water vapor is present.

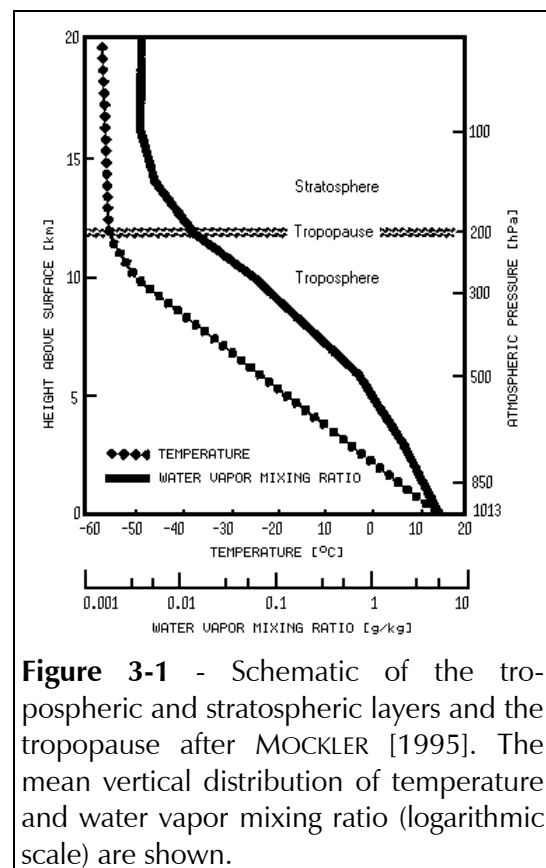


Figure 3-1 - Schematic of the tropospheric and stratospheric layers and the tropopause after MOCKLER [1995]. The mean vertical distribution of temperature and water vapor mixing ratio (logarithmic scale) are shown.

3.1.1 Pressure

The sea level pressure is about 1013 hPa in average, a value that is used in most standard atmosphere models. Figure 3-2 shows that the pressure decreases exponentially with increasing altitude. The tropopause height is reached at a pressure between 300 hPa at the poles and 70 hPa at the equator and a value of approximately 1 hPa can be stated at the stratopause height.

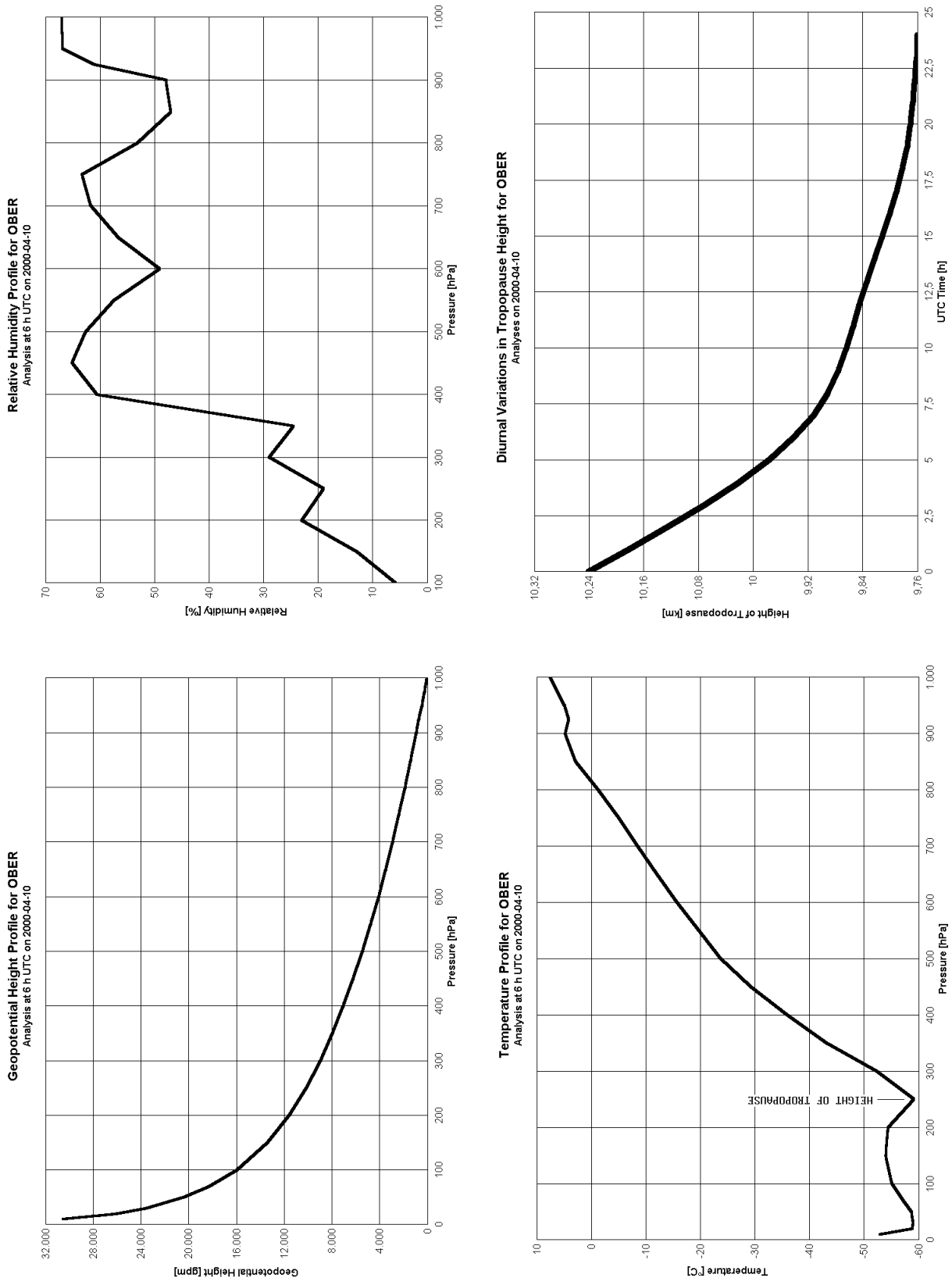


Figure 3-2 - Typical vertical profiles for IGS tracking station Oberpfaffenhofen (OBER) near Munich, Germany on 10 April 2000. The data were extracted from the NOAA/NCEP GDAS numerical weather model (\rightarrow chapter 4). Note that the height axis is expressed by pressure because all vertically distributed data stored in weather models are referenced to pre-defined pressure levels and not to height. Geopotential height corresponds to what is known in geodesy by the term "dynamic height".

Constituent	Molar Weight [kg/mol]	Fractional Volume [/]
N ₂	28.0134	0.78084
O ₂	31.9988	0.209476
Ar	39.948	0.0934
CO ₂	44.00995	0.000314
Ne	20.183	0.00001818
He	4.0026	0.00000524
Kr	83.30	0.00000114
Xe	131.30	0.000000087

Table 3-1 - Primary constituents of dry air after DAVIS et al. [1985]. It should be pointed out that none of these primary constituents possesses a permanent dipole moment; this characteristic property is almost solely devoted to the nature of water molecules.

3.1.2 Temperature

The temperature shows a linear decrease up to the tropopause (→ Figure 3-1 and Figure 3-2), but note that this linear trend can be considerably disturbed in the first few hundred meters above the surface due to inversion layers. The so-called *temperature lapse rate* is in the range of -5 to -7 K/km below the tropopause height. At the tropopause itself, the temperature remains approximately constant and slowly increases in the stratosphere.

3.1.3 Water Vapor

The relative humidity diagram in Figure 3-2 indicates that not only the horizontal distribution, but also the vertical distribution of water vapor in the troposphere cannot be expected to be homogenous. The reason for this is linked to the rapid turnover of water in the air as well as to the variation of temperature with height and location¹, see MOCKLER [1995].

Although there are considerable variations, Figure 3-1 also implies that there are certain trends: water vapor decreases rapidly with height as the atmosphere gets colder. Nearly half the total water in the air is located between sea level and about 1.5 km above sea level. Less than 5-6% of the water is present above 5 km, and less than 1% is found in the stratosphere. Relative humidity shown in Figure 3-2 also tends to decrease with height, from an average value of about 60-80% at the surface to 20-40% at 300 hPa (9 km).

3.2 Modeling of Tropospheric Delays

The following sections briefly outline the principles on which tropospheric delay modeling is based. Meteorological inputs that are necessary for the delay models, their vertical distribution and the relations between them are treated in chapter 4 as well. It should be emphasized that the term *tropospheric* propagation delay is used here despite the fact that the hydrostatic component is also influenced by gases above the troposphere.

¹ Note that the amount of vapor that saturates the air is dependent on the temperature.

3.2.1 Generalized Functional Description

The geometrical distance differs from the actual ray path by the difference

$$\delta S_{A[NEU]}^i = \int_{ATM} n(s) \cdot ds - \int_{VAC} ds \quad (3-1)$$

$\delta S_{A[NEU]}^i$: total/neutral slant path delay from receiver antenna A to satellite i
 n : index of atmospheric refraction
 ds : differential increment in distance with respect to the line of sight
 ATM : ray path passing from antenna in direction to satellite through the atmosphere
 VAC : virtual path of a ray passing from antenna in direction to satellite through vacuum

which is called total or *neutral slant path delay*. The neutral delay can be separated into

$$\delta S_{A[NEU]}^i = \delta S_{A[HYD]}^i + \delta S_{A[WET]}^i \quad (3-2)$$

$\delta S_{A[HYD]}^i$: hydrostatic slant path delay
 $\delta S_{A[WET]}^i$: non-hydrostatic or wet slant path delay

a hydrostatic and a non-hydrostatic component. The latter is often called *wet* component which is not too wrong as it is mainly caused by the vertical distribution of water vapor in the tropopause and the first component is also called *dry* delay which is partly misleading². A relatively new aspect in tropospheric delay modeling is to further distinguish between the azimuthally symmetric delay and asymmetric parts

$$\delta S_{A[NEU]}^i = \delta S_{A[HYD,SYMM]}^i + \delta S_{A[HYD,ASYMM]}^i + \delta S_{A[WET,SYMM]}^i + \delta S_{A[WET,ASYMM]}^i \quad (3-3)$$

$\delta S_{[...SYMM]}^i$: tropospheric delay term under the assumption of symmetry in azimuth
 $\delta S_{[...ASYMM]}^i$: tropospheric correction term taking asymmetric effects into account

where the asymmetric components are usually determined by application of a horizontal tropospheric gradient model. Consequently, the full notation for the neutral delay is

$$\begin{aligned} \delta S_{A[NEU]}^i = & m(\epsilon_A^i)_{[HYD]} \cdot ZHD_A + m(\epsilon_A^i)_{[AZI,HYD]} \cdot [G_{A[N,HYD]} \cdot \cos \alpha_A^i + G_{A[E,HYD]} \cdot \sin \alpha_A^i] \\ & + m(\epsilon_A^i)_{[WET]} \cdot ZWD_A + m(\epsilon_A^i)_{[AZI,WET]} \cdot [G_{A[N,WET]} \cdot \cos \alpha_A^i + G_{A[E,WET]} \cdot \sin \alpha_A^i] \end{aligned} \quad (3-4)$$

$m(\epsilon)$: mapping function
 ZHD : zenith hydrostatic delay
 ZWD : zenith wet delay
 $G_{[N]}$: gradient in northward direction
 $G_{[E]}$: gradient in eastward direction

² According to BEVIS et al. [1992], the hydrostatic delay is often referred to as *dry* component. This omits the fact that water vapor actually actively influences both the wet *and* the hydrostatic delay components. Nevertheless, the largest contribution to the hydrostatic delay can be traced back to the dry air.

where the tropospheric delay is modeled into zenith direction (\rightarrow 3.2.1) at first instance and then projected into the direction of the satellite using a mapping function m (\rightarrow 3.2.2) that is not only a function of the elevation angle as the simplified notation implies, but can also be dependent on several atmospheric parameters. Note that the mapping function for the horizontal gradients differs significantly in comparison to the hydrostatic and wet functions (\rightarrow 3.2.2.3).

For practical reasons, the asymmetric hydrostatic and wet components can be combined without any severe loss of accuracy

$$\begin{aligned} m(\epsilon_A^i)_{[AZI]} &\approx m(\epsilon_A^i)_{[AZI, HYD]} \approx m(\epsilon_A^i)_{[AZI, WET]} \quad \wedge \\ G_{A[N]} &= G_{A[N, HYD]} + G_{A[N, WET]} \quad \wedge \quad G_{A[E]} = G_{A[E, HYD]} + G_{A[E, WET]} \end{aligned} \quad (3-5)$$

$$\begin{aligned} \Rightarrow \delta S_{A[NEU]}^i &= m(\epsilon_A^i)_{[HYD]} \cdot ZHD_A + m(\epsilon_A^i)_{[WET]} \cdot ZWD_A \\ &\quad + m(\epsilon_A^i)_{[AZI]} \cdot [G_{A[N]} \cdot \cos \alpha_A^i + G_{A[E]} \cdot \sin \alpha_A^i] \end{aligned}$$

what simplifies the model a bit. This functional component description represents the general type of tropospheric delay model that is most commonly used today without specifying the components directly. It is the purpose of the next two sections to find expressions for the zenith delay as well as for the mapping functions which allow to use this equation in practice.

3.2.1 Modeling Zenith Delays

Following THAYER [1974], the neutral zenith path delay can be derived from the radio refractive index of the air

$$N = k_1 \cdot \frac{p_d}{T} \cdot Z_d^{-1} + k_2 \cdot \frac{e}{T} \cdot Z_w^{-1} + k_3 \cdot \frac{e}{T^2} \cdot Z_w^{-1} \quad \wedge \quad N(s) = [n(s) - 1] \cdot 10^6 \quad (3-6)$$

- $n(s)$: index of refraction as function of the distance 's'
- N : reduced index of tropospheric refraction
- $k_{1..3}$: refraction constants
- $Z_{d/w}^{-1}$: inverse compressibility factors for dry and wet air
- p_d : dry pressure; $p_d = p - e$ with p being the total pressure (measured quantity)
- e : partial water vapor pressure

DAVIS et al. [1985] give the following interpretation of this formula: The very first term characterizes the effect of the induced dipole moment of the dry constituents, the second term is due to the dipole moment of water vapor and the third term represents the dipole orientation effects of the permanent dipole moment of water molecules.

The refraction constants are discussed by BEVIS et al. [1994]. In summary, the following mean values can be applied:

$$\begin{aligned} k_1 &= 77.60 \pm 0.09 \quad [\text{K/hPa}] \\ k_2 &= 69.4 \pm 2.2 \quad [\text{K/hPa}] \\ k_3 &= 370100 \pm 1200 \quad [\text{K}^2/\text{hPa}] \end{aligned}$$

The dimensionless inverse compressibility factors account for non-ideal gas behavior and were derived by OWENS [1967]:

$$Z_d^{-1} = 1 + p_d \cdot \left[57.97 \cdot 10^{-8} \cdot \left(1 + \frac{0.52}{T} \right) - 9.4611 \cdot 10^{-4} \cdot \frac{t}{T^2} \right] \quad (3-7)$$

$$Z_w^{-1} = 1 + 1650 \cdot \frac{e}{T^3} \cdot (1 - 0.01317 \cdot t + 1.75 \cdot 10^{-4} \cdot t^2 + 1.44 \cdot 10^{-6} \cdot t^3)$$

t: temperature in units of [°C]

T: temperature in units of [K]

The equation of state for ideal gases is

$$\frac{p_i \cdot V}{m \cdot T} = R_i \Leftrightarrow p_i = \rho_i \cdot R_i \cdot T = \frac{\rho_i \cdot R_0 \cdot T}{M_i} \wedge R_i = \frac{R_0}{M_i}; \rho_i = \frac{m}{V} \quad (3-8)$$

p_i : pressure of ideal gas i

T: temperature

V: volume

m: mass

M_i : molar mass of gas i

R_i : specific gas constant

R_0 : universal gas constant; $R_0 = 8.31434 \text{ [J mol}^{-1} \text{ K}^{-1}]$

ρ_i : density of gas i

and, following SPILKER [1996, p. 528], this equation can also be applied for non-ideal gases by inserting the compressibility

$$p_i = \rho_i \cdot R_i \cdot T \cdot Z_i \quad (3-9)$$

Z_i : compressibility factor of gas i

It should be mentioned that the approximation

$$Z_d^{-1} \approx Z_w^{-1} \approx 1 \quad (3-10)$$

is sufficient in terms of accuracy in most cases, i. e. wet and dry air can actually be treated as ideal gases although the theoretically more precise formulation is maintained here.

Let us now consider the very first term of the refractivity formula

$$k_1 \cdot \frac{p_d}{T} \cdot Z_d^{-1} = k_1 \cdot \frac{\rho_d \cdot R_d \cdot T \cdot Z_d}{T} \cdot Z_d^{-1} = k_1 \cdot \rho_d \cdot R_d = k_1 \cdot \frac{\rho_d \cdot R_0}{M_d} \quad (3-11)$$

M_d : molar weight of dry air ($M_d = 28.9644 \text{ kg/kmol}$)

where the ratio

$$\frac{\rho_d \cdot R_0}{M_d} \quad (3-12)$$

can be rewritten as

$$\begin{aligned} \frac{\rho_d \cdot R_0}{M_d} &= \frac{\rho_d \cdot R_0}{M_d} + \frac{\rho_w \cdot R_0}{M_d} - \frac{\rho_w \cdot R_0}{M_d} \\ &= \frac{\rho_d \cdot R_0 + \rho_w \cdot R_0}{M_d} - \frac{\rho_w \cdot R_0}{M_d} \\ &= \frac{R_0 \cdot (\rho_d + \rho_w)}{M_d} - \frac{\rho_w \cdot R_0}{M_d} \cdot \frac{M_w}{M_w} \cdot \frac{T}{T} \cdot \frac{Z_w}{Z_w} \\ &= \frac{R_0 \cdot (\rho_d + \rho_w)}{M_d} - \left(\rho_w \cdot \frac{R_0}{M_w} \cdot T \cdot Z_w \right) \cdot \frac{1}{T} \cdot Z_w^{-1} \cdot \frac{M_w}{M_d} \\ &= \frac{R_0 \cdot \rho}{M_d} - \frac{e}{T} \cdot Z_w^{-1} \cdot \frac{M_w}{M_d} \end{aligned} \quad (3-13)$$

M_d : molar weight of dry air ($M_d = 28.9644$ kg/kmol)

M_w : molar weight of wet air ($M_w = 18.0152$ kg/kmol)

Substitution of this expression into the refractivity formula yields

$$\begin{aligned} N &= k_1 \cdot \left(\frac{R_0 \cdot \rho}{M_d} - \frac{e}{T} \cdot Z_w^{-1} \cdot \frac{M_w}{M_d} \right) + k_2 \cdot \frac{e}{T} \cdot Z_w^{-1} + k_3 \cdot \frac{e}{T^2} \cdot Z_w^{-1} \\ &= k_1 \cdot \frac{R_0 \cdot \rho}{M_d} - k_1 \cdot \frac{e}{T} \cdot Z_w^{-1} \cdot \frac{M_w}{M_d} + k_2 \cdot \frac{e}{T} \cdot Z_w^{-1} + k_3 \cdot \frac{e}{T^2} \cdot Z_w^{-1} \\ &= k_1 \cdot \frac{R_0 \cdot \rho}{M_d} + \left(k_2 - k_1 \cdot \frac{M_w}{M_d} \right) \cdot \frac{e}{T} \cdot Z_w^{-1} + k_3 \cdot \frac{e}{T^2} \cdot Z_w^{-1} \\ &= k_1 \cdot \frac{R_0 \cdot \rho}{M_d} + k'_2 \cdot \frac{e}{T} \cdot Z_w^{-1} + k_3 \cdot \frac{e}{T^2} \cdot Z_w^{-1} \end{aligned} \quad (3-14)$$

This notation is advantageous because it allows a strict separation between the hydrostatic

$$N_{[\text{HYD}]} = k_1 \cdot \frac{R_0 \cdot \rho}{M_d} = k_1 \cdot R_d \cdot \rho \quad (3-15)$$

and the wet term

$$N_{[\text{WET}]} = \left(k'_2 \cdot \frac{e}{T} + k_3 \cdot \frac{e}{T^2} \right) \cdot Z_w^{-1} \quad (3-16)$$

BEVIS et al. [1994] found the following weighted mean value for the derived constant k'_2 :

$$k'_2 = k_2 - k_1 \cdot \frac{M_w}{M_d} = 22.1 \pm 2.2 \left[\frac{\text{K}}{\text{hPa}} \right] \quad (3-17)$$

The zenith delay components can now be obtained by integration of the vertical refractivity profile as it is provided by radiosonde launches and numerical weather fields, for instance:

$$\begin{aligned} \text{ZND} &= 10^{-6} \cdot \int_{h_s}^{\infty} N(h) \cdot dh \\ \text{ZHD} &= 10^{-6} \cdot \int_{h_s}^{\infty} N_{[\text{HYD}]}(h) \cdot dh \\ \text{ZWD} &= 10^{-6} \cdot \int_{h_s}^{\infty} N_{[\text{WET}]}(h) \cdot dh \end{aligned} \quad (3-18)$$

ZND: zenith neutral/total delay in units of [m] for p_d and e in units of [hPa] and T in [K]

ZHD: zenith hydrostatic delay

ZWD: zenith wet delay

h_s : surface height

dh : differential increment in height

Note that it is not sufficient to finish integration for the hydrostatic (and neutral) delay when the height of the tropopause is reached because the hydrostatic component is also significantly influenced by gases up to the stratosphere; see SPILKER [1996, p. 517ff]. In the following two paragraphs, it is tried to find expressions for the hydrostatic and the wet delays that allow their determination without knowledge of the complete refractivity profile. As already stated, this approach is likely to fail for the wet component, but not for the hydrostatic delay.

3.2.1.1 Zenith Hydrostatic Delay

Three hydrostatic delay models will be presented in this section. The Hopfield and the Saastamoinen model are discussed in detail and compared with each other. Furthermore, the MOPS model that does not need any meteorological measurements as input is described.

3.2.1.1.1 Hopfield Hydrostatic Delay Model

The equation for hydrostatic equilibrium follows from the ideal gas laws of Boyle-Mariotte and Gay-Lussac and can be expressed in differential form as

$$dp = -g \cdot \rho \cdot dH \quad g(\varphi, \lambda, h) \approx \text{constant} = g \quad \wedge \quad \rho(\varphi, \lambda, h) \approx \text{constant} = \rho \quad (3-19)$$

dp : differential change in pressure

g : gravity, assumed to be constant, esp. with height

ρ : density of dry air, assumed to be constant

dH : differential change in height

and the density can also be expressed by

$$p = \rho \cdot R_d \cdot T \Leftrightarrow \rho = \frac{p}{R_d \cdot T} \quad (3-20)$$

and leads to the differential equation

$$dp = -g \cdot \frac{p}{R_d \cdot T} \cdot dH \Leftrightarrow \frac{dp}{p} = -\frac{g}{R_d \cdot T} \cdot dH \quad (3-21)$$

p : pressure

T : temperature

R_d : specific gas constant of dry air

As already discussed, the vertical evolution of the temperature in the troposphere can be approximated by a linear trend using the temperature lapse rate

$$T = f(h) = T_0 + \beta \cdot H \quad (3-22)$$

T : temperature as function of altitude ' $f(h)$ '

T_0 : temperature at surface (or antenna) height $h_0 = 0$ m

β : temperature lapse rate

H : height above sea level

and is used as model for the entire atmosphere. The differential equation becomes

$$\frac{dp}{p} = -\frac{g}{R_d \cdot (T_0 + \beta \cdot H)} \cdot dH \quad (3-23)$$

and is solved by integration from $H_0 = 0$ m to H and p_0 to p_d

$$\begin{aligned} \int_{p_0}^p \frac{1}{p} \cdot dp &= -\frac{g}{R_d} \cdot \int_{H_0}^H \frac{1}{T_0 + \beta \cdot H} \cdot dH \\ \Rightarrow \ln\left(\frac{p}{p_0}\right) &= \ln\left[\left(\frac{T_0 + \beta \cdot H}{T_0}\right)^{-\frac{g}{R_d \cdot \beta}}\right] \\ \Rightarrow p &= p_0 \cdot \left(\frac{T_0 + \beta \cdot H}{T_0}\right)^{-\frac{g}{R_d \cdot \beta}} \end{aligned} \quad (3-24)$$

Now, let us recall the hydrostatic refractivity formula:

$$N_{[\text{HYD}]} = k_1 \cdot \frac{R_0 \cdot \rho}{M_d} = k_1 \cdot R_d \cdot \rho \quad (3-25)$$

k_1 : hydrostatic refractivity constant ($k_1 = 77.6$ h/hPa)

R_0 : universal gas constant ($R_0 = 8.31434$ J mol⁻¹ K⁻¹)

ρ : total density

M_d : molar weight of dry air ($M_d = 28.9644$ kg/kmol)

The total density is

$$\rho = \rho_d + \rho_w = \frac{p_d \cdot M_d}{R \cdot T} + \frac{e \cdot M_w}{R \cdot T} \quad (3-26)$$

and under the consideration that

$$p_d \gg e \quad \wedge \quad p_d \cdot M_d \gg e \cdot M_w \quad (3-27)$$

it is acceptable to approximate

$$M_w \approx M_d \quad (3-28)$$

This simplification allows to obtain the total pressure

$$\rho = \rho_d + \rho_w = \frac{p_d \cdot M_d + e \cdot M_w}{R \cdot T} \approx \frac{p_d \cdot M_d + e \cdot M_d}{R \cdot T} = \frac{p \cdot M_d}{R \cdot T} = \frac{p}{R_d \cdot T} \quad (3-29)$$

and alters the hydrostatic refractivity formula in the following way:

$$N_{[HYD]} = k_1 \cdot R_d \cdot \rho \approx k_1 \cdot R_d \cdot \frac{p}{R_d \cdot T} = k_1 \cdot \frac{p}{T} \quad (3-30)$$

The relation between pressure and temperature is inserted into this formula and yields the expression

$$N_{[HYD]} = k_1 \cdot \frac{p}{T} = k_1 \cdot \frac{p_0 \cdot \left(\frac{T_0 + \beta \cdot H}{T_0} \right)^{-\frac{g}{R_d \cdot \beta}}}{T} = k_1 \cdot \frac{1}{T_0 + \beta \cdot H} \cdot p_0 \cdot \left(\frac{T_0 + \beta \cdot H}{T_0} \right)^{-\frac{g}{R_d \cdot \beta}} \quad (3-31)$$

and can be further simplified to

$$\begin{aligned} N_{[HYD]} &= k_1 \cdot \frac{p}{T} = k_1 \cdot \frac{p_0}{T_0} \cdot \left(\frac{T_0}{T_0 + \beta \cdot H} \right)^1 \cdot \left(\frac{T_0 + \beta \cdot H}{T_0} \right)^{-\frac{g}{R_d \cdot \beta}} \quad \wedge \quad R_d = \frac{R_0}{M_d} \\ &= N_{[HYD]_0} \cdot \left(\frac{T_0 + \beta \cdot H}{T_0} \right)^{-\left(1 + \frac{g \cdot M_d}{\beta \cdot R_0}\right)} = N_{[HYD]_0} \cdot \left(\frac{T_0 + \beta \cdot H}{T_0} \right)^{\eta} = N_{[HYD]_0} \cdot \left(1 + \frac{\beta \cdot H}{T_0} \right)^{\eta} \end{aligned} \quad (3-32)$$

k_1 : hydrostatic refractivity constant ($k_1 = 77.6$ h/hPa)

T : Temperature in [K], T_0 denotes the surface temperature

p : pressure in [hPa], p_0 denotes the surface pressure

β : temperature lapse rate in [K/m]

H : geopotential height in [m]

g : gravity acceleration in [m/s²]

M_d : molar weight of dry air ($M_d = 28.9644$ kg/kmol)

R_0 : universal gas constant ($R_0 = 8.31434$ J mol⁻¹ K⁻¹)

For a default temperature lapse rate of $\beta = -6.81$ K/km, a molar weight of dry air of $M_d = 28.9644$ kg/kmol, a universal gas constant of $R_0 = 8.31434$ [J·mol⁻¹·K⁻¹] and a mean gravity acceleration of $g = 9.806$ m/s² the exponent becomes $\eta = 4.02 \approx 4$ that is adopted for the Hopfield two-quartic model. Another modification is made by substitution of

$$\frac{\beta}{T_0} = \frac{1}{\frac{1}{\beta} \cdot t_0 - H_{d0}} = - \frac{1}{H_{d0} - \frac{1}{\beta} \cdot t_0} = - \frac{1}{H_d} \quad (3-33)$$

β : temperature lapse rate in [K/km]

T_0 : surface/antenna temperature in [K]

t_0 : surface/antenna temperature in [°C]

H_d : effective height of the dry atmosphere above the surface in [km]

H_{d0} : effective height of the dry atmosphere for a temperature of 0 °C in [km]

with the inverse negative height H_d which is the effective height for the hydrostatic component and was obtained by a fit of global radiosonde data to

$$H_d = 40136 \text{ [m]} + 148.72 \left[\frac{\text{m}}{^\circ\text{C}} \right] \cdot t_0 \quad (3-34)$$

after SEEGER [1989, p. 53]. A look at the scale factor reveals that its reciprocal value is $1/0.14872$ km = 6.72 K/km and matches the (unsigned) temperature lapse rate. Actually, the temperature can be interpreted as an input to account for the height dependence and H_d is defined as effective height of the dry atmosphere above the surface. For this reason, the surface height H_0 is always set to zero and thereby transforms the height system what will simplify the expression found for the hydrostatic delay.

With this substitute, the expression for the hydrostatic refractivity finally becomes

$$N_{[\text{HYD}]} = N_{[\text{HYD}]_0} \cdot \left(1 - \frac{H}{H_d} \right)^4 \quad (3-35)$$

and can be formally integrated between $H_0 = 0$ and H_d

$$\text{ZHD} = 10^{-6} \cdot N_{[\text{HYD}]_0} \cdot \int_{h_0}^{h_d} \left(1 - \frac{H}{H_d} \right)^4 \cdot dH = 10^{-6} \cdot N_{[\text{HYD}]_0} \cdot \frac{H_d}{5} = 2 \cdot 10^{-7} \cdot N_{[\text{HYD}]_0} \cdot H_d \quad (3-36)$$

with the surface refractivity already defined as

$$N_{[\text{HYD}]_0} = k_1 \cdot \frac{p_0}{T_0} \quad (3-37)$$

The zenith hydrostatic delay of the Hopfield model can now be written in closed form as

$$\begin{aligned} \text{ZHD} &= 1.552 \cdot 10^{-5} \left[\frac{\text{K}}{\text{hPa}} \right] \cdot \frac{p_0}{T_0} \cdot \left(40136 [\text{m}] + 148.72 \left[\frac{\text{m}}{\text{K}} \right] \cdot T_0 \right) \\ &= \left(0.62291 \left[\frac{\text{m} \cdot \text{K}}{\text{hPa}} \right] \cdot \frac{1}{T_0} + 0.0023081 \left[\frac{\text{m}}{\text{hPa}} \right] \right) \cdot p_0 \end{aligned} \quad (3-38)$$

and can be computed with knowledge of surface temperature and pressure³. As has become clear, a number of approximations lead to this simple formula. Apart from the fact that the air is treated as an ideal gas which is not too critical, the assumption of a constant temperature lapse rate is one important approximation that should be stressed as well as the fact that the gravity is not modeled with dependence on the height⁴. The next model presented will overcome this shortcoming.

3.2.1.1.2 Saastamoinen Hydrostatic Delay Model

The starting point for the development of this model is identical to the approach accomplished to derive the Hopfield model. Again, the assumption is that the dry atmosphere is in hydrostatic equilibrium and the equation of state

$$dp = -g(h) \cdot \rho(H) \cdot dH \quad (3-39)$$

is true. But this time, the gravity acceleration is treated as a function of height. At first instance, it is possible to treat the gravity as constant again

$$\rho = -\frac{1}{g_m} \cdot \frac{dp}{dH} \quad (3-40)$$

g_m : weighted mean gravity acceleration

ρ : density of the air

and denoting it as mean gravity acceleration g_m . A proper value must be found for it afterwards. First of all, the hydrostatic refractivity equation is substituted by the formula above which yields

$$N_{[\text{HYD}]} = k_1 \cdot R_d \cdot \rho = -k_1 \cdot R_d \cdot \frac{1}{g_m} \cdot \frac{dp}{dH} \quad (3-41)$$

k_1 : hydrostatic refractivity constant ($k_1 = 77.6 \text{ h/hPa}$)

p : pressure in [hPa]

H : geopotential height in [m]

R_d : gas constant of dry air in [$\text{J mol}^{-1} \text{ K}^{-1}$]

³ Or, to be more precise, with knowledge of these meteorological quantities at the *antenna* site.

⁴ Actually, the gravity will decrease with increasing altitude by approximately $-3.086 \mu\text{m/s}^2$ per meter.

and leads to⁵

$$\begin{aligned} \text{ZHD} &= 10^{-6} \cdot \int_{H_0}^{\infty} N_{[\text{HYD}]} \cdot dH = -10^{-6} \cdot k_1 \cdot R_d \cdot \frac{1}{g_m} \cdot \int_{p_0}^{\infty} dp = -10^{-6} \cdot k_1 \cdot R_d \cdot \frac{1}{g_m} \cdot (p_{\infty} - p_0) \\ &= -10^{-6} \cdot k_1 \cdot R_d \cdot \frac{1}{g_m} \cdot (0 - p_0) = \frac{10^{-6} \cdot k_1 \cdot R_0}{M_d} \cdot \frac{p_0}{g_m} = 0.022275 \left[\frac{\text{m}^2}{\text{s}^2 \cdot \text{hPa}} \right] \cdot \frac{p_0}{g_m} \end{aligned} \quad (3-42)$$

The weighted mean gravity acceleration is defined as

$$g_m = \frac{\int_{h_0}^{\infty} \rho(h) \cdot g(h) \cdot dh}{\int_{h_0}^{\infty} \rho(h) \cdot dh} \quad (3-43)$$

and can be interpreted as the gravity at the centroid of the atmospheric column according to SAASTAMOINEN [1972]. The local gravity acceleration must be reduced to the corresponding height using the equations for the normal gravity field following DAVIS et al. [1985]:

$$g_m = 9.8062 \left[\frac{\text{m}}{\text{s}^2} \right] \cdot \left(1 - 0.00265 \cdot \cos 2\varphi - 0.00031 \left[\frac{1}{\text{km}} \right] \cdot h_c \right) \quad (3-44)$$

φ : ellipsoidal latitude

h_c : height of the center of the atmospheric column above the ellipsoid in [km]

Saastamoinen found an approximation for the height of the center by the linear relation

$$h_c = 7.3 [\text{km}] + 0.9 \cdot h \quad (3-45)$$

h : height of the antenna site above the ellipsoid in [km]

and, by substitution, the final formula for the mean gravity is found to be

$$g_m = 9.784 \left[\frac{\text{m}}{\text{s}^2} \right] \cdot \left(1 - 0.00266 \cdot \cos 2\varphi - 0.00028 \left[\frac{1}{\text{km}} \right] \cdot h \right) \quad (3-46)$$

Now, we are able to express the zenith hydrostatic delay in closed form:

⁵ Please note that p_0 is not necessarily the total pressure at zero altitude, but at the antenna height h_0 . In the preceding section about the Hopfield model, H_0 was set to zero just to simplify calculations. This is not a pre-requisite here.

$$\begin{aligned}
\text{ZHD} &= \frac{0.022275 \left[\frac{\text{m}^2}{\text{s}^2 \cdot \text{hPa}} \right] \cdot p_0}{9.784 \left[\frac{\text{m}}{\text{s}^2} \right] \cdot \left(1 - 0.00266 \cdot \cos 2\varphi - 0.00028 \left[\frac{1}{\text{km}} \right] \cdot h \right)} \\
&= \frac{0.0022767 \left[\frac{\text{m}}{\text{hPa}} \right] \cdot p_0}{1 - 0.00266 \cdot \cos 2\varphi - 0.00028 \left[\frac{1}{\text{km}} \right] \cdot h}
\end{aligned} \tag{3-47}$$

φ : ellipsoidal latitude

h : surface/antenna height above the ellipsoid in [km]

p_0 : surface/antenna pressure in [hPa]

This model has become very popular due to its high accuracy. ELGERED et al. [1991] give the following RMS error budget: The error in the refractivity constant contributes to about 2.4 mm, the uncertainty of the gravity reduction has a marginal influence of 0.2 mm as well as the uncertainty of the universal gas constant (0.1 mm) and the variability of the dry mean molar mass (0.1 mm). Furthermore, it should be noted that no temperature measurements are needed in contrast to the Hopfield model, but instead, the height of the station and its latitude are used for the computation of the gravity correction.

3.2.1.1.3 MOPS Hydrostatic Delay Model

If no meteorological data are available, the MOPS [1998] tropospheric algorithm can be applied. This approach uses standard meteorological data dependent on latitude and takes seasonal variations into account.

First, the latitude-dependent mean meteorological elements are taken from Table 3-2 and subsequently denoted as ξ_0 . Starting with 1 January, the day of year DoY has to be computed in order to account for seasonal changes and the corresponding values are to be taken from Table 3-3 and denoted as $\Delta\xi$.

Latitude [°]	p_0 [hPa]	T_0 [K]	e_0 [hPa]	b_0 [K/m]	l_0 [1]
15°	1013.25	299.65	26.31	0.00630	2.77
30°	1017.25	294.15	21.79	0.00605	3.15
45°	1015.75	283.15	11.66	0.00558	2.57
60°	1011.75	272.15	6.78	0.00539	1.81
75°	1013.00	263.65	4.11	0.00453	1.55

Table 3-2 - Average values for the meteorological parameters used for tropospheric delay prediction. The formulas given in the following paragraph for interpolation are identical for all values. For this reason, the corresponding symbols will be substituted by ξ_0 . Note that the sign of the temperature lapse rate is naturally negative what is accounted for directly in the formulas of this model. λ describes the dimensionless lapse rate of water vapor and is needed for computation of the wet component only.

Latitude [°]	Dp [hPa]	DT [K]	De [hPa]	Db [K/m]	DI [1]
£ 15°	0.00	0.00	0.00	0.0000	0.00
30°	-3.75	7.00	8.85	0.0025	0.33
45°	-2.25	11.00	7.24	0.0032	0.46
60°	-1.75	15.00	5.36	0.0081	0.74
³ 75°	-0.50	14.50	3.39	0.0062	0.30

Table 3-3 - Seasonal variations of the meteorological parameters used for tropospheric delay estimation. The formulas given in the following paragraph for interpolation are identical for all values. For this reason, the corresponding symbols will be substituted by $\Delta\xi$.

Now, each meteorological parameter can be computed for the current day using the formula

$$\xi(\varphi, \text{DoY}) = \xi_0(\varphi) - \Delta\xi(\varphi) \cdot \cos\left[\frac{2\pi \cdot (\text{DoY} - \text{DoY}_0)}{365.25 [\text{d}]}\right] \quad (3-48)$$

φ : latitude of station

ξ_0 : average meteorological value

$\Delta\xi$: seasonal variation of meteorological value

DoY: day of year (January, 1st = 1)

DoY₀: day of "maximum winter", 28 for northern and 211 for southern hemisphere

where DoY₀ is equal to 28 days for northern and 211 for southern latitudes. The meteorological values themselves are obtained by linear interpolation:

$$\xi_0(\varphi) = \xi_0(\varphi_i) + [\xi_0(\varphi_{i+1}) - \xi_0(\varphi_i)] \cdot \frac{\varphi - \varphi_i}{\varphi_{i+1} - \varphi_i} \quad (3-49)$$

The latitudes φ_i and φ_{i+1} are those closest to the site latitude φ to interpolate data for. Exactly the same is done for the seasonal variations:

$$\Delta\xi(\varphi) = \Delta\xi(\varphi_i) + [\Delta\xi(\varphi_{i+1}) - \Delta\xi(\varphi_i)] \cdot \frac{\varphi - \varphi_i}{\varphi_{i+1} - \varphi_i} \quad (3-50)$$

The next step of the algorithm is to determine the zenith hydrostatic delay at zero altitude

$$\text{ZHD}_0 = 10^{-6} \cdot k_1 \cdot \frac{R_d \cdot p}{g_m} \quad (3-51)$$

with the following constants⁶: $k_1 = 77.604 \text{ K hPa}^{-1}$

$R_d = 287.054 \text{ J kg}^{-1} \text{ K}^{-1}$

$g_m = 9.784 \text{ m/s}^2$ (effective gravity)

⁶ Note that most of these constants have already been introduced and may numerically slightly differ, but are re-defined here for the sake of authentic recapitulation.

Finally, the tropospheric delays are reduced to the observation height H above the sea level in meters

$$\text{ZHD} = \text{ZHD}_0 \cdot \left(1 - \frac{\beta \cdot H}{T}\right)^{\frac{g}{R_d \cdot \beta}} \quad (3-52)$$

g : surface gravity of the normal gravity field at 45° latitude, $g = 9.80665 \text{ m/s}^2$

The advantage of this approach is that meteorological measurements are not necessary and modeled with help of default data sets. This advantage is also the major disadvantage of this model as no one can expect a superior accuracy of this approach: mismodeled pressure values, for example, will quickly degrade the accuracy of the hydrostatic delay. An error of 10 hPa contributes to approximately 2.2 cm which may likely occur in some regions. The following section is therefore devoted to a quality assessment of the hydrostatic models presented so far in order to get some independent knowledge about the accuracy that can be expected.

3.2.1.1.4 Comparison of Hydrostatic Models

For more than 100 sites of the IGS tracking network, zenith neutral delays are made available by the IGS analysis centers which were used to assess the accuracy of selected tropospheric models. The hydrostatic components were processed with help of meteorological measurements provided either by the IGS stations or from numerical weather fields. Comparisons between the three models presented so far are summarized below. The Saastamoinen model was selected as reference due to its superior accuracy. The time span for this comparison ranges from June 1999 up to March 2000.

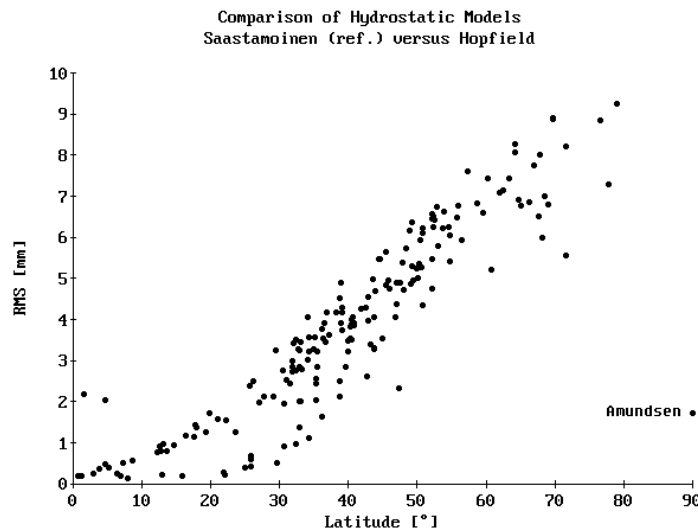


Figure 3-3 - Comparison of Hopfield and Saastamoinen hydrostatic models in zenith direction. The Saastamoinen model is assumed to be the most accurate hydrostatic model and is therefore treated as reference. Each dot marks the RMS precision of the Hopfield model with respect to the chosen reference for a particular site of the IGS tracking network. Data were collected and processed from June 1999 up to March 2000.

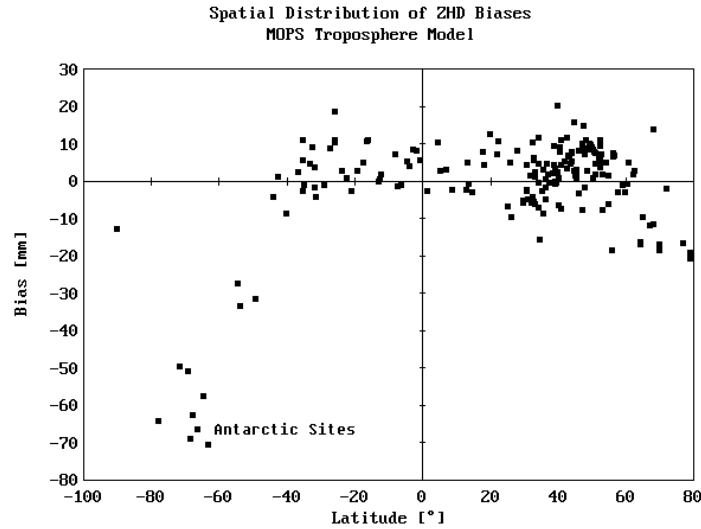


Figure 3-4 - Accuracy assessment of the MOPS hydrostatic model in zenith direction with the Saastamoinen model as reference.

The Hopfield model only shows a very small standard deviation⁷ of 0.2 mm with respect to the Saastamoinen reference model, but as can be seen in Figure 3-3, the RMS values show a systematic trend with increasing latitude. Smallest deviations occur near the equator, largest (more than 9 mm) in polar regions. This effect is mainly due to the missing gravity reduction in the Hopfield approach which treats the gravity as a constant value. In global average, the systematic error is about -4 mm.

As expected, the MOPS model performs much worse than the Hopfield model in comparison to Saastamoinen's approach. Since systematic effects are the dominant contributors to the error budget of this model, Figure 3-4 shows a plot of these biases. Pressure prediction is especially poor for some sites in the polar regions of the southern hemisphere. In global average, the RMS is about 16 mm. This is more than 4 times larger than the RMS of the Hopfield model.

3.2.1.2 Zenith Wet Delay

Zenith wet delays are affected by the distribution of water vapor. It is very difficult to derive highly accurate models using only surface measurements for this component, but it is possible to estimate zenith wet delays

$$\text{ZWD} = 10^{-6} \cdot \int_{H_0}^{\infty} \left[k'_2 \cdot \frac{e}{T} + k_3 \cdot \frac{e}{T^2} \right] \cdot dH \quad (3-53)$$

as additional parameters during network filtering. This issue will be covered by section 3.4. Nevertheless, some approaches for the approximation of zenith wet delays are given here that may serve to predict wet delays in order to initialize the Kalman filter.

⁷ The standard deviation is computed from the residuals and is therefore bias-free whereas the RMS is computed from the differences and may include systematic effects.

3.2.1.2.1 Hopfield Wet Delay Model

The wet component can be derived in a similar form as it has been demonstrated for the hydrostatic component, but the inherent approximations are more problematic here. Hopfield models the wet refractivity analogously to the hydrostatic formula as

$$N_{[WET]} = N_{[WET]_0} \cdot \left(1 - \frac{H}{H_w}\right)^4 \quad \wedge \quad H_w = H_T \quad (3-54)$$

H_w : effective height for the wet component

H_T : height of the tropopause

and the wet delay becomes

$$ZWD = 10^{-6} \cdot N_{[WET]_0} \cdot \frac{H_w}{5} = 2 \cdot 10^{-7} \cdot N_{[WET]_0} \cdot H_w \quad (3-55)$$

The tropopause height H_T is usually set to a default value of 11000 m. Alternatively, MENDES and LANGLEY [1998a] found a relation between the surface temperature and H_T of

$$H_T = 7508 [m] + 0.002421 [m] \cdot \exp\left(\frac{t_0}{22.90 [^{\circ}C]}\right) \quad (3-56)$$

t_0 : surface temperature in $[^{\circ}C]$

that is preferred to the default value. The surface wet refractivity was found to be

$$N_{[WET]_0} = \left(k'_2 \cdot \frac{e_0}{T_0} + k_3 \cdot \frac{e_0}{T_0^2}\right) \cdot Z_w^{-1} \approx k_3 \cdot \frac{e_0}{T_0^2} = 370100 \left[\frac{K^2}{hPa}\right] \cdot \frac{e_0}{T_0^2} \quad (3-57)$$

where the second term is by far the most dominant term. The zenith wet delay of the Hopfield model can now be written in closed form as

$$\begin{aligned} ZWD &= 0.07402 \left[\frac{K^2}{hPa}\right] \cdot \frac{e_0}{T_0^2} \cdot H_T \\ &= 0.07402 \left[\frac{K^2}{hPa}\right] \cdot \frac{e_0}{T_0^2} \cdot \left[7508 [m] + 0.002421 [m] \cdot \exp\left(\frac{t_0}{22.90 [^{\circ}C]}\right)\right] \\ &= \left(555.7 \left[\frac{m \cdot K^2}{hPa}\right] + 1.792 \cdot 10^{-4} \left[\frac{m \cdot K^2}{hPa}\right] \cdot \exp\left(\frac{t_0}{22.90 [^{\circ}C]}\right)\right) \cdot \frac{e_0}{T_0^2} \end{aligned} \quad (3-58)$$

e_0 : partial water vapor pressure at surface/antenna in [hPa]

t_0 : temperature at surface/antenna in $[^{\circ}C]$

T_0 : temperature at surface/antenna in [K]

and can be computed with knowledge of surface (antenna) temperature and relative humidity⁸.

3.2.1.2.2 Ifadis Wet Delay Model

IFADIS [1986, p. 76] proposes to model the zenith wet delay

$$\begin{aligned} \text{ZWD} = & 0.554 \cdot 10^{-2} [\text{m}] - 0.880 \cdot 10^{-4} \left[\frac{\text{m}}{\text{hPa}} \right] \cdot (p - 1000) \\ & + 0.272 \cdot 10^{-4} \left[\frac{\text{m}}{\text{hPa}} \right] \cdot e + 2.771 \left[\frac{\text{m} \cdot ^\circ\text{C}}{\text{hPa}} \right] \cdot \frac{e}{T} \end{aligned} \quad (3-59)$$

as a function of the surface pressure, partial water vapor pressure and temperature.

3.2.1.2.3 Mendes Wet Delay Model

MENDES and LANGLEY [1998b] derived a linear relation

$$\text{ZWD} = 0.122 [\text{m}] + 0.00943 \left[\frac{\text{m}}{\text{hPa}} \right] \cdot e \quad (3-60)$$

between zenith wet delay and partial water vapor pressure.

3.2.1.2.4 MOPS Wet Delay Model

All needed input data are given in the preceding section (\rightarrow 3.2.1.1.3). The zenith wet delay at zero altitude is

$$\text{ZWD} = \frac{10^{-6} \cdot k_3 \cdot R_d}{g_m \cdot (\lambda + 1) - \beta \cdot R_d} \cdot \frac{e}{T} \quad (3-61)$$

with the following constants: $k_1 = 77.604 \text{ K hPa}^{-1}$
 $k_3 = 382000 \text{ K}^2 \text{ hPa}^{-1}$ (adopted from MOPS [1998])
 $R_d = 287.054 \text{ J kg}^{-1} \text{ K}^{-1}$
 $g_m = 9.784 \text{ m s}^{-2}$

Finally, the wet delay is reduced to the observation height H above the sea level in meters

$$\text{ZWD} = \text{ZWD}_0 \cdot \left(1 - \frac{\beta \cdot H}{T} \right)^{\frac{(\lambda-1) \cdot g}{R_d \cdot \beta} - 1} \quad (3-62)$$

with a mean gravity of $g = 9.80665 \text{ m/s}^2$.

⁸ Chapter 4 discusses formulas to derive the partial water vapor pressure e from relative humidity RH and temperature T .

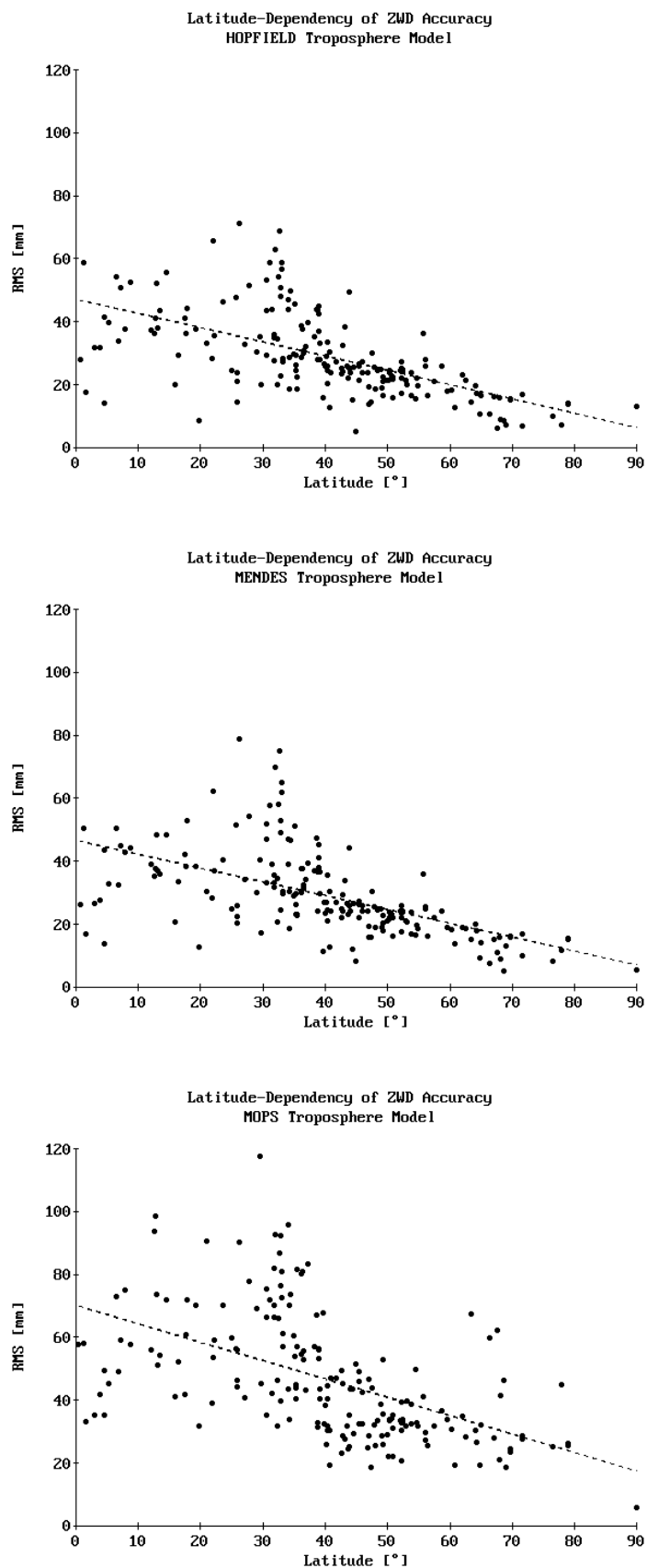


Figure 3-5 - RMS diagrams for accuracy assessments of the Hopfield, Mendes and MOPS zenith wet delay models. A linear latitude-dependent trend function is indicated by dashed lines. Each dot represents the average RMS for a particular station of the IGS tracking network.

3.2.1.2.5 Comparison of Wet Delay Models

The accuracy assessment for the wet models presented in Figure 3-5 is once again based on the analysis of the neutral delays from the IGS network. The wet delays in zenith direction were derived by subtracting the modeled hydrostatic delay from the total value by using the Saastamoinen hydrostatic delay model.

The Hopfield and Mendes model both have the same global, average RMS of about 3 cm, but there is a minor difference between both models: Mendes' approach has a slightly higher bias of -6 mm (Hopfield: -1 mm) and a smaller standard deviation of 12 mm (Hopfield: 12.4 mm). The MOPS model performs significantly worse with a global RMS of almost 5 cm.

3.2.2 Projecting Zenith Delays into Slant Direction

The tropospheric delay is shortest in zenith direction and will become larger with increasing zenith angle. Projection of zenith path delays into slant direction is performed by application of a *mapping function* or *obliquity factor* that is defined as

$$m(z, p, T, \dots) = \frac{\delta S_{[NEU]}}{\delta S_{[NEU]}^{Z=0}} = \frac{\delta S_{[NEU]}}{ZND} \quad (3-63)$$

$\delta S_{[NEU]}$: neutral/total delay in slant direction

ZND: zenith neutral delay

m: mapping function

z: zenith angle from ground station to GPS satellite

for the neutral component⁹, for instance, and is easily found to be

$$\frac{ZND}{SND} = \cos z = \frac{1}{m(z)} \Rightarrow m(z) = \csc z = \frac{1}{\cos z} \quad (3-64)$$

SND: slant neutral delay, identical with $\delta S_{[NEU]}$

at first instance. Unfortunately, this cosecant model is only an approximation assuming a planar surface without taking the curvature of the earth into account. Moreover, the refractivity profile, esp. the temperature and water vapor distribution may cause deviations from this simple formula. Therefore, it can only be used for small zenith distances. The limit for application of this function for precise applications is about 60° (→ 3.3.4.6).

The definition of the slant tropospheric propagation delay is

$$SND = \delta S_{[NEU]} = \int_{ATM} n(s) \cdot ds - \int_{VAC} ds \quad (3-65)$$

⁹ At first instance, the mapping function problem is discussed for the neutral delay for the sake of generality, although it will be shown that the hydrostatic and the wet mapping functions may differ significantly.

and implies that there are two different ray paths, the actual path through the atmosphere and the straight geometric path in the vacuum. Figure 3-6 illustrates the ray bending if the atmosphere is assumed to consist of spherical shells. It becomes clear that according to Snell's law¹⁰

$$n \cdot r \cdot \sin z = n_1 \cdot r_1 \cdot \sin z_1 = \text{constant} \quad (3-66)$$

the zenith angle z is not constant for the refractivity profile, but varies with height. According to SPILKER [1996, p. 526] the bending impact is not too problematic as it reaches only about 3 mm for elevations higher than 20°. Thus SAASTAMOINEN [1972] approximates

$$\int_{\text{VAC}} ds \approx \int_{\text{ATM}} ds \quad (3-67)$$

but also presents the correction formula

$$\Delta z = 16 \left[\frac{''}{\text{K} \cdot \text{hPa}} \right] \cdot \frac{\tan z}{T} \cdot \left(p + \frac{4800 [\text{K}]}{T} \cdot e \right) - 0.07'' \cdot (\tan^3 z + \tan z) \cdot \frac{p}{1000 [\text{hPa}]} \quad (3-68)$$

Δz : difference between geometric and apparent ("actual") zenith angle at the surface (antenna)
 z : geometric zenith angle at the antenna site
 T : surface (antenna) temperature in [K]
 p : surface (antenna) pressure [hPa]
 e : surface (antenna) partial pressure of water vapor [hPa]

in order to account for the curvature of the ray path that is given here in the full notation found in SPILKER [1996]. The corrected zenith distance is

$$z^* = z - \Delta z \quad (3-69)$$

z^* : apparent ("actual") zenith angle at the surface (antenna)
 z : geometric zenith angle

and is used within the Saastamoinen total delay model. To sum the discussion up, the integrals defining the slant path delay can be rewritten as

$$\begin{aligned} \text{SND} &= \int_{\text{ATM}} n(s) \cdot ds - \int_{\text{VAC}} ds = \int_{\text{ATM}} [n(s) - 1] \cdot ds + \left[\int_{\text{ATM}} ds - \int_{\text{VAC}} ds \right] \\ &= \int_{p_0}^{\infty} [n(s) - 1] \cdot ds + \Delta b = \int_{h_0}^{\infty} \frac{1}{\cos z} \cdot [n(h) - 1] \cdot dh + \Delta b \end{aligned} \quad (3-70)$$

Δb : bending correction

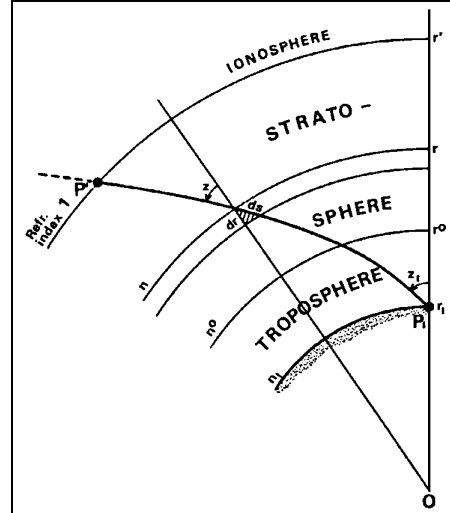


Figure 3-6 - Curved path of microwave rays in an atmosphere being composed of spherical shells, from SAASTAMOINEN [1972].

¹⁰ This version is valid for the spherical case; in the planar case it is $r = r_1 = r_2$.

and it must be stated that an analytic expression for the obliquity factor m cannot be easily derived. This is the reason why many - more or less similar - approximations for mapping functions are in use. However, the fractional expansion of MARINI [1972] and MARINI and MURRAY [1973] was found to be superior. It meets the following two boundary conditions: The tropospheric mapping function is asymptotic in $\cos z$ for $z \rightarrow 0$ and asymptotic in $1/\cos z$ for $z \rightarrow 90^\circ$. The continued fraction that is also presented by HERRING [1992]

$$m(z) = \frac{1 + \frac{a}{1 + \frac{b}{1 + \frac{c}{\dots}}}}{\cos z + \frac{a}{\cos z + \frac{b}{\cos z + \frac{c}{\dots}}}} = \frac{1 + \frac{a}{1 + \frac{b}{1 + \frac{c}{\dots}}}}{\sin \epsilon + \frac{a}{\sin \epsilon + \frac{b}{\sin \epsilon + \frac{c}{\dots}}}} \quad (3-71)$$

z : zenith angle

ϵ : elevation angle

a, b, c : mapping function coefficients, to be determined

satisfies both conditions and can be truncated according to the accuracy requirements¹¹. In older versions of this mapping function, the numerator was frequently set to 1 without any fractional expansion which lead to the problem that the mapping function became unequal to 1 in zenith direction. To compensate for this contradiction to theory, the second (and the following) sine-terms can be replaced by the tangent:

$$m(\epsilon) = \frac{1}{\sin \epsilon + \frac{a}{\tan \epsilon + \frac{b}{\sin \epsilon + \frac{c}{\dots}}}} \quad \vee \quad m(\epsilon) = \frac{1}{\sin \epsilon + \frac{a}{\tan \epsilon + \frac{b}{\tan \epsilon + \frac{c}{\dots}}}} \quad (3-72)$$

Nevertheless, one major task still remains: the definition of the mapping function coefficients. In general, these coefficients are functions of several atmospheric properties and various approximations will be presented in the following paragraphs. Moreover, some older - but also usable - types of mapping functions will be depicted.

3.2.2.1 Hydrostatic Mapping Functions

Most of the obliquity functions discussed here will follow the continued fraction approach. Additionally, the mapping functions derived via the Black hydrostatic and the Saastamoinen total delay model are presented. It is emphasized that the choice of a suitable hydrostatic mapping function is much more important than the choice of the wet one because the hydrostatic component is about 10 to 20 times larger than

¹¹ For low precision, the coefficients can be set to $a = b = c = 0$ which yields the cosecant model introduced at the beginning of this section.

the wet component. Consequently, errors in the mapping function will scale into the slant path delay at much higher magnitude than for the wet delay. Although the hydrostatic component can be modeled precisely in zenith direction, care must be taken not to lose this advantage by inappropriate obliquity factors.

3.2.2.1.1 Saastamoinen Mapping Function

SAASTAMOINEN [1972] developed a total delay model for the troposphere from which a "neutral" mapping function can be derived. It is given here because it can be applied for the hydrostatic delay as well as for the wet delay and has been popular among broad parts of the GPS user community in the past. Several stages of refinement exist for Saastamoinen's approach. Here, the description of SPILKER [1996, p. 534] is recapitulated

$$\delta S_{[\text{NEU}]} = \frac{0.002277 \left[\frac{\text{m}}{\text{hPa}} \right] \cdot (1+D)}{\cos z^*} \cdot \left(p_0 + \left(\frac{1255 [\text{K}]}{T_0} + 0.005 \right) \cdot e_0 - B \cdot \tan^2 z^* \right) + \delta_R \quad (3-73)$$

z^* : apparent ("actual") zenith angle at the surface (antenna)

D: gravity correction

T_0 : surface (antenna) temperature in [K]

p_0 : surface (antenna) pressure [hPa]

e_0 : surface (antenna) partial pressure of water vapor [hPa]

B: height-dependent correction

δ_R : elevation/height-dependent correction

$H_0 \rightarrow$	z^*_{\downarrow}	0.0 km	0.5 km	1.0 km	1.5 km	2.0 km	3.0 km	4.0 km	5.0 km
d_R [m]	60°00'	0.003	0.003	0.002	0.002	0.002	0.002	0.001	0.001
	66°00'	0.006	0.006	0.005	0.005	0.004	0.003	0.003	0.002
	70°00'	0.012	0.011	0.010	0.009	0.008	0.006	0.005	0.004
	73°00'	0.020	0.018	0.017	0.015	0.013	0.011	0.009	0.007
	75°00'	0.031	0.028	0.025	0.023	0.021	0.017	0.014	0.011
	76°00'	0.039	0.035	0.032	0.029	0.026	0.021	0.017	0.014
	77°00'	0.050	0.045	0.041	0.037	0.033	0.027	0.022	0.018
	78°00'	0.065	0.059	0.054	0.049	0.044	0.036	0.030	0.024
	78°30'	0.075	0.068	0.062	0.056	0.051	0.042	0.034	0.028
	79°00'	0.087	0.079	0.072	0.065	0.059	0.049	0.040	0.033
	79°30'	0.102	0.093	0.085	0.077	0.070	0.058	0.047	0.039
	79°45'	0.111	0.101	0.092	0.083	0.076	0.063	0.052	0.043
	80°00'	0.121	0.110	0.100	0.091	0.083	0.068	0.056	0.047
B [hPa] \rightarrow		1.156	1.079	1.006	0.938	0.874	0.757	0.654	0.563

Table 3-4 - Correction terms for the Saastamoinen neutral delay model from SPILKER [1996]. A slightly different table for the B-values can be found in SAASTAMOINEN [1972]. H_0 is the station height above the mean sea level.

with D accounting for the gravity acceleration

$$D = 0.0026 \cdot \cos 2\varphi + 0.00028 \left[\frac{1}{\text{km}} \right] \cdot h_0 \quad (3-74)$$

φ : site latitude

h_0 : ellipsoidal height of site in [km]

Table 3-4 gives the values of B and δ_R . Note that the zenith angle has to be corrected as discussed in the introductory paragraph (\rightarrow 3.2.2).

$$m(\epsilon)_{[\text{NEU}]} = \frac{\delta S_{[\text{NEU}]}}{\delta S_{[\text{NEU}]}^{Z=0}} = \frac{\delta S_{[\text{NEU}]}}{\text{ZND}} = \frac{\text{SND}}{\text{ZND}} \quad (3-75)$$

SND: slant neutral delay

The mapping function derived via this model is the ratio between the slant and the zenith delay and can be applied for both the hydrostatic and the wet delay.

3.2.2.1.2 Chao Hydrostatic Mapping Function

Chao developed mapping functions for both the hydrostatic and the wet component. The version given by IFADIS [1986, p. 36] and originally published by CHAO [1972] was implemented in the tropospheric analysis software:

$$m(\epsilon)_{[\text{HYD}]} = \frac{1}{\sin \epsilon + \frac{0.00143}{\tan \epsilon + 0.00035}} \quad (3-76)$$

The mapping function coefficients are defined as global constants and the fractional expansion is discontinued after the second coefficient. Despite of its simplicity, this function proved to be unexpectedly precise and has been widely used for many data sets that are presented in chapter 6.

3.2.2.1.3 Black Hydrostatic Mapping Function

BLACK [1978] developed a tropospheric model based on Hopfield's work. SEEGER [1989, p. 52] gives the formulas for the hydrostatic component

$$\delta S_{[\text{HYD}]} = \frac{1.552 \cdot 10^{-5} \left[\frac{\text{K}}{\text{hPa}} \right] \cdot \frac{p_0}{T_0} \cdot H_d - \frac{1.92 \left[\frac{\text{m}}{\circ} \right]}{\epsilon^2 + 0.6^\circ}}{\sqrt{1 - \left(\frac{\cos \epsilon}{1 + l_c \cdot \frac{H_d}{r}} \right)^2}} \quad (3-77)$$

p_0 : pressure at site in [hPa]

T_0 : temperature at site in [K]

H_d : upper boundary height for the hydrostatic delay

r : radial distance from earth center to GPS antenna

ϵ : elevation angle in [degrees]

where the second term describes the bending correction. Height H_d has been already discussed (\rightarrow 3.2.1.1.1) and the scale factor l_c is

$$l_c = 0.167 - (0.076 + 0.00015 \cdot t_0) \cdot \exp\left(-0.3 \left[\frac{1}{\circ}\right] \cdot \epsilon\right) \quad (3-78)$$

t_0 : temperature at site in $^{\circ}\text{C}$

and the mapping function value is

$$m(\epsilon)_{[\text{HYD}]} = \frac{\delta S_{[\text{HYD}]}}{\delta S_{[\text{HYD}]}^{Z=0}} = \frac{\delta S_{[\text{HYD}]}}{\text{ZHD}} = \frac{\text{SHD}}{\text{ZHD}} \quad (3-79)$$

SHD: slant hydrostatic delay

The structure of this mapping function deviates from that of the Marini/Murray-approach (\rightarrow 3.2.2). Nevertheless, this algorithm proved to be suitable in GPS processing for elevation masks being no lower than 15° .

3.2.2.1.4 Davis Hydrostatic Mapping Function

The function developed by Davis is for the hydrostatic component only and also known under the name *CfA 2.2 mapping function*. It is said to be accurate to about 2.5 cm for the hydrostatic slant delay at an elevation of 5° if all the atmospheric properties including the temperature lapse rate and the height of the tropopause are well-known. In the literature, several versions with either $\tan \epsilon$ or $\sin \epsilon$ (2nd coefficient) can be found. Here, the version presented by DAVIS et al. [1985]

$$m(\epsilon)_{[\text{HYD}]} = \frac{1}{\sin \epsilon + \frac{a}{\tan \epsilon + \frac{b}{\sin \epsilon + c}}} \quad (3-80)$$

is employed. The mapping function coefficients are defined with help of surface meteorological data as well as other atmospheric properties like the temperature lapse rate and the height of the tropopause:

$$\begin{aligned} a = & 0.001185 \cdot \left(1 + 6.071 \cdot 10^{-5} \left[\frac{1}{\text{hPa}} \right] \cdot (p_0 - 1000 [\text{hPa}]) - 1.471 \cdot 10^{-4} \left[\frac{1}{\text{hPa}} \right] \cdot e_0 \right. \\ & + 3.072 \cdot 10^{-3} \left[\frac{1}{^{\circ}\text{C}} \right] \cdot (t_0 - 20 [^{\circ}\text{C}]) + 1.965 \cdot 10^{-2} \left[\frac{\text{km}}{^{\circ}\text{C}} \right] \cdot \left(\beta + 6.5 \left[\frac{^{\circ}\text{C}}{\text{km}} \right] \right) \\ & \left. - 5.645 \cdot 10^{-3} \left[\frac{1}{\text{km}} \right] \cdot (H_T - 11.231 [\text{km}]) \right) \end{aligned} \quad (3-81)$$

$$\begin{aligned}
b = & 0.001144 \cdot 1 + \left(1.164 \cdot 10^{-5} \left[\frac{1}{\text{hPa}} \right] \cdot (p_0 - 1000 [\text{hPa}]) - 2.795 \cdot 10^{-5} \left[\frac{1}{\text{hPa}} \right] \cdot e_0 \right. \\
& + 3.109 \cdot 10^{-3} \left[\frac{1}{^\circ\text{C}} \right] \cdot (t_0 - 20 [^\circ\text{C}]) + 3.038 \cdot 10^{-2} \left[\frac{\text{km}}{^\circ\text{C}} \right] \cdot \left(\beta + 6.5 \left[\frac{^\circ\text{C}}{\text{km}} \right] \right) \\
& \left. - 1.217 \cdot 10^{-3} \left[\frac{1}{\text{km}} \right] \cdot (H_T - 11.231 [\text{km}]) \right)
\end{aligned} \quad (3-82)$$

$$c = -0.0090 \quad (3-83)$$

p_0 : surface (antenna) pressure in [hPa]
 t_0 : surface (antenna) temperature in [$^\circ\text{C}$]
 e_0 : surface (antenna) partial water vapor pressure in [hPa]
 β : temperature lapse rate in [$^\circ\text{C}/\text{km}$] = [K/km]
 H_T : tropopause height [km]

If the temperature lapse rate or the tropopause height are not available from radiosonde launches or numerical weather models, the approximations of MENDES and LANGLEY [1998a] can be used. The model for the tropopause height

$$H_T = 7.508 [\text{km}] + 2.421 [\text{km}] \cdot \exp\left(\frac{t_0}{22.90 [^\circ\text{C}]}\right) \quad (3-84)$$

has already been introduced, and for the temperature lapse rate, Mendes found the linear relation

$$\beta = -5.930 \left[\frac{^\circ\text{C}}{\text{km}} \right] - 0.0359 \left[\frac{1}{\text{km}} \right] \cdot t_0 \quad (3-85)$$

t_0 : surface temperature in [$^\circ\text{C}$]

If no surface temperature readings are available, the default values of

$$\begin{aligned}
H_T &= 11.3 [\text{km}] \\
\beta &= -6.5 \left[\frac{^\circ\text{C}}{\text{km}} \right]
\end{aligned} \quad (3-86)$$

can be applied (or local mean values if known).

3.2.2.1.5 Ifadis Hydrostatic Mapping Function

IFADIS [1986] published his studies to derive accurate mapping functions one year after Davis. He applies the mapping function formula

$$m(\epsilon)_{[\text{HYD}]} = \frac{1}{\sin \epsilon + \frac{a}{\sin \epsilon + \frac{b}{\sin \epsilon + c}}} \quad (3-87)$$

and defines the coefficients for the global hydrostatic mapping function as follows:

$$\begin{aligned}
 a &= 0.1237 \cdot 10^{-2} + 0.1316 \cdot 10^{-6} \left[\frac{1}{\text{hPa}} \right] \cdot (p_0 - 1000 [\text{hPa}]) \\
 &\quad + 0.1378 \cdot 10^{-5} \left[\frac{1}{^\circ\text{C}} \right] \cdot (t_0 - 15 [^\circ\text{C}]) + 0.8057 \cdot 10^{-5} \left[\frac{1}{\sqrt{\text{hPa}}} \right] \cdot \sqrt{e_0} \\
 b &= 0.3333 \cdot 10^{-2} + 0.1946 \cdot 10^{-6} \left[\frac{1}{\text{hPa}} \right] \cdot (p_0 - 1000 [\text{hPa}]) \\
 &\quad + 0.1040 \cdot 10^{-6} \left[\frac{1}{^\circ\text{C}} \right] \cdot (t_0 - 15 [^\circ\text{C}]) + 0.1747 \cdot 10^{-6} \left[\frac{1}{\sqrt{\text{hPa}}} \right] \cdot \sqrt{e_0} \\
 c &= 0.078
 \end{aligned} \tag{3-88}$$

p_0 : pressure at site in [hPa]
 e_0 : partial water vapor pressure at site in [hPa]
 t_0 : temperature at site in [$^\circ\text{C}$]

The author gives coefficients tuned to particular climate regions, too. The function presented here is applicable at global scale. The accuracy is reported to be a RMS of 2.2 cm for an elevation angle of 5° .

3.2.2.1.6 Herring Hydrostatic Mapping Function

HERRING [1992] derived coefficients for the mapping function of Marini-type

$$m(z) = \frac{1 + \frac{a}{1 + \frac{b}{1 + c}}}{\sin \epsilon + \frac{a}{\sin \epsilon + \frac{b}{\sin \epsilon + c}}} \tag{3-89}$$

by ray tracing of rawinsonde data for 10 sites in Northern America. The surface temperature, site latitude and height above sea level are introduced to obtain the 3 coefficients

$$\begin{aligned}
 a &= \left(1.2320 + 0.0139 \cdot \cos \varphi - 0.0209 \left[\frac{1}{\text{km}} \right] \cdot H_0 + 0.00215 \left[\frac{1}{^\circ\text{C}} \right] \cdot (t_0 - 10 [^\circ\text{C}]) \right) \cdot 10^{-3} \\
 b &= \left(3.1612 - 0.1600 \cdot \cos \varphi - 0.0331 \left[\frac{1}{\text{km}} \right] \cdot H_0 + 0.00206 \left[\frac{1}{^\circ\text{C}} \right] \cdot (t_0 - 10 [^\circ\text{C}]) \right) \cdot 10^{-3} \\
 c &= \left(171.244 - 4.293 \cdot \cos \varphi - 0.149 \left[\frac{1}{\text{km}} \right] \cdot H_0 - 0.0021 \left[\frac{1}{^\circ\text{C}} \right] \cdot (t_0 - 10 [^\circ\text{C}]) \right) \cdot 10^{-3}
 \end{aligned} \tag{3-90}$$

t_0 : temperature at site in [$^\circ\text{C}$]
 φ : latitude of site
 H_0 : height of site above sea level in [km]

composing the mapping function.

3.2.2.1.7 Niell Hydrostatic Mapping Function

NIELL [1996] also uses the continued fraction

$$m(z) = \frac{1 + \frac{a}{1 + \frac{b}{1 + \frac{c}{\sin \epsilon}}}}{\sin \epsilon + \frac{a}{\sin \epsilon + \frac{b}{\sin \epsilon + c}}} \quad (3-91)$$

to project the zenith delays into slant direction. The coefficients are modeled in a similar way as it is done for the MOPS troposphere delay model (\rightarrow 3.2.1.1.3). The mean and the seasonally varying values are melted together in the following manner:

$$a(\varphi, \text{DoY}) = a(\varphi)_{\text{average}} - a(\varphi)_{\text{amplitude}} \cdot \cos \left(2\pi \cdot \frac{\text{DoY} - \text{DoY}_0}{365.25 [\text{d}]} \right) \quad (3-92)$$

a: mapping function coefficient, separated into average value and amplitude

φ : site latitude

DoY: day of year

DoY₀: day of year for "maximum winter"

with DoY₀ being set to 28 days for the northern and 211 for the southern hemisphere. Again, the latitude dependent coefficients are interpolated linearly, but the seasonal variations are *subtracted* from the average values. The values for selected latitudes are given in Table 3-5 and Table 3-6 below.

Coefficient	$\varphi = 15^\circ$	$\varphi = 30^\circ$	$\varphi = 45^\circ$	$\varphi = 60^\circ$	$\varphi = 75^\circ$
a	$1.2769934 \cdot 10^{-3}$	$1.2683230 \cdot 10^{-3}$	$1.2465397 \cdot 10^{-3}$	$1.2196049 \cdot 10^{-3}$	$1.2045996 \cdot 10^{-3}$
b	$2.9153695 \cdot 10^{-3}$	$2.9152299 \cdot 10^{-3}$	$2.9288445 \cdot 10^{-3}$	$2.9022565 \cdot 10^{-3}$	$2.9024912 \cdot 10^{-3}$
c	$62.610505 \cdot 10^{-3}$	$62.837393 \cdot 10^{-3}$	$63.721774 \cdot 10^{-3}$	$63.824265 \cdot 10^{-3}$	$62.258455 \cdot 10^{-3}$

Table 3-5 - Coefficients of the Niell hydrostatic mapping function (**average** values).

Coefficient	$\varphi = 15^\circ$	$\varphi = 30^\circ$	$\varphi = 45^\circ$	$\varphi = 60^\circ$	$\varphi = 75^\circ$
a	0.0	$1.2709626 \cdot 10^{-5}$	$2.6523662 \cdot 10^{-5}$	$3.4000452 \cdot 10^{-5}$	$4.1202191 \cdot 10^{-5}$
b	0.0	$2.1414979 \cdot 10^{-5}$	$3.0160779 \cdot 10^{-5}$	$7.2562722 \cdot 10^{-5}$	$11.723375 \cdot 10^{-5}$
c	0.0	$9.0128400 \cdot 10^{-5}$	$4.3497037 \cdot 10^{-5}$	$84.795348 \cdot 10^{-5}$	$170.37206 \cdot 10^{-5}$

Table 3-6 - Seasonal variations/**amplitudes** of the Niell hydrostatic mapping function.

Coefficient	Height Correction
a_{ht}	$2.53 \cdot 10^{-5}$
b_{ht}	$5.49 \cdot 10^{-3}$
c_{ht}	$1.14 \cdot 10^{-3}$

Table 3-7 - Coefficients of the Niell hydrostatic mapping function (**height correction**).

Furthermore, the mapping function height correction is estimated:

$$\frac{dm(\epsilon)}{dh} = \frac{1}{\sin \epsilon} - f(\epsilon, a_{ht}, b_{ht}, c_{ht}) \quad (3-93)$$

The coefficients $a \dots c_{ht}$ are interpolated with help of Table 3-7 and the function f is the Marini mapping function shown at the beginning of this section (formula 3-71). The absolute height correction is then

$$\Delta m(\epsilon) = \frac{dm(\epsilon)}{dh} \cdot H_0 \quad (3-94)$$

H_0 : height of site above sea level in [km]

This correction is added to the Marini mapping function value $m\{\epsilon, a \dots c(\phi, DoY)\}$.

3.2.2.2 Wet Mapping Functions

Wet delay mapping functions usually differ from their hydrostatic counterparts and are given below. The Saastamoinen function will not be repeated as it is implemented as neutral delay mapping function. The Davis mapping function has no wet equivalent.

3.2.2.2.1 Chao Wet Mapping Function

The wet mapping function developed by CHAO [1972] is given by IFADIS [1986, p. 36]

$$m(\epsilon)_{[WET]} = \frac{1}{\sin \epsilon + \frac{0.00035}{\tan \epsilon + 0.0017}} \quad (3-95)$$

and has been frequently applied in VLBI processing, esp. in conjunction with the Davis hydrostatic mapping function (\rightarrow 3.2.2.1.4).

3.2.2.2.2 Black Wet Mapping Function

The wet mapping function derived by BLACK [1978] is described by SEEBER [1989, p. 52]. The slant wet delay is

$$\delta S_{[WET]} = \frac{0.07465 \left[\frac{K^2}{hPa} \right] \cdot \frac{e_0}{T_0^2} \cdot H_T}{\sqrt{1 - \left(\frac{\cos \epsilon}{1 + I_C \cdot \frac{H_T}{r}} \right)^2}} - \frac{1.92 \left[\frac{m}{^\circ} \right]}{\epsilon^2 + 0.6^\circ} \quad (3-96)$$

e_0 : partial water vapor pressure at site in [hPa]

T_0 : temperature at site in [K]

H_T : upper boundary height for the wet delay/height of the tropopause

r : radial distance from earth center to site

ϵ : elevation angle in [degrees]

and the mapping function is

$$m(\epsilon)_{[WET]} = \frac{\delta S_{[WET]}}{\delta S_{Z=0}^{[WET]}} = \frac{\delta S_{[WET]}}{ZWD} = \frac{SWD}{ZWD} \quad (3-97)$$

The tropopause height H_T can be approximated with help of surface temperature (\rightarrow 3.2.2.1.4) and l_c has already been defined (\rightarrow 3.2.2.1.3).

3.2.2.2.3 Ifadis Wet Mapping Function

The global wet mapping function of IFADIS [1986] adopts the mapping function type

$$m(\epsilon)_{[HYD]} = \frac{1}{\sin \epsilon + \frac{a}{\sin \epsilon + \frac{b}{\sin \epsilon + c}}} \quad (3-98)$$

The wet mapping function coefficients are

$$\begin{aligned} a &= 0.5236 \cdot 10^{-2} + 0.2471 \cdot 10^{-6} \left[\frac{1}{\text{hPa}} \right] \cdot (p_0 - 1000 [\text{hPa}]) \\ &\quad - 0.1724 \cdot 10^{-6} \left[\frac{1}{^\circ\text{C}} \right] \cdot (t_0 - 15 [^\circ\text{C}]) + 0.1328 \cdot 10^{-4} \left[\frac{1}{\sqrt{\text{hPa}}} \right] \cdot \sqrt{e_0} \\ b &= 0.1705 \cdot 10^{-2} + 0.7384 \cdot 10^{-6} \left[\frac{1}{\text{hPa}} \right] \cdot (p_0 - 1000 [\text{hPa}]) \\ &\quad + 0.3767 \cdot 10^{-6} \left[\frac{1}{^\circ\text{C}} \right] \cdot (t_0 - 15 [^\circ\text{C}]) + 0.2147 \cdot 10^{-4} \left[\frac{1}{\sqrt{\text{hPa}}} \right] \cdot \sqrt{e_0} \\ c &= 0.05917 \end{aligned} \quad (3-99)$$

p_0 : pressure at site in [hPa]

e_0 : partial water vapor pressure at site in [hPa]

t_0 : temperature at site in [$^\circ\text{C}$]

Ifadis reports that these coefficients allow the slant wet delay to be modeled with an accuracy of 8.5 mm at an elevation of 5° .

3.2.2.2.4 Herring Wet Mapping Function

The Marini mapping function coefficients derived by HERRING [1992] are

$$\begin{aligned} a &= \left(0.583 - 0.011 \cdot \cos \varphi - 0.052 \left[\frac{1}{\text{km}} \right] \cdot H_0 + 0.0014 \left[\frac{1}{^\circ\text{C}} \right] \cdot (t_0 - 10 [^\circ\text{C}]) \right) \cdot 10^{-3} \\ b &= \left(1.402 - 0.102 \cdot \cos \varphi - 0.101 \left[\frac{1}{\text{km}} \right] \cdot H_0 + 0.0020 \left[\frac{1}{^\circ\text{C}} \right] \cdot (t_0 - 10 [^\circ\text{C}]) \right) \cdot 10^{-3} \end{aligned} \quad (3-100)$$

$$c = \left(45.85 - 1.91 \cdot \cos \varphi - 1.29 \left[\frac{1}{\text{km}} \right] \cdot H_0 + 0.015 \left[\frac{1}{^\circ\text{C}} \right] \cdot (t_0 - 10 [^\circ\text{C}]) \right) \cdot 10^{-3}$$

t_0 : temperature at site in $[^\circ\text{C}]$

φ : latitude of site

H_0 : height of site above sea level in $[\text{km}]$

and are to be inserted into

$$m(z) = \frac{1 + \frac{a}{1 + \frac{b}{1 + c}}}{\sin \varepsilon + \frac{a}{\sin \varepsilon + \frac{b}{\sin \varepsilon + c}}} \quad (3-101)$$

to obtain the mapping function value.

3.2.2.2.5 Niell Wet Mapping Function

The wet mapping function derived by NIELL [1996] only uses the average coefficients given in Table 3-8. Seasonal variations are not taken into account nor a height correction.

Coefficient	$\varphi = 15^\circ$	$\varphi = 30^\circ$	$\varphi = 45^\circ$	$\varphi = 60^\circ$	$\varphi = 75^\circ$
a	$5.8021897 \cdot 10^{-4}$	$5.6794847 \cdot 10^{-4}$	$5.8118019 \cdot 10^{-4}$	$5.9727542 \cdot 10^{-4}$	$6.1641693 \cdot 10^{-4}$
b	$1.4275268 \cdot 10^{-3}$	$1.5138625 \cdot 10^{-3}$	$1.4572752 \cdot 10^{-3}$	$1.5007428 \cdot 10^{-3}$	$1.7599082 \cdot 10^{-3}$
c	$4.3472961 \cdot 10^{-2}$	$4.6729510 \cdot 10^{-2}$	$4.3908931 \cdot 10^{-2}$	$4.4626982 \cdot 10^{-2}$	$5.4736038 \cdot 10^{-2}$

Table 3-8 - Coefficients of the Niell wet mapping function. This table contains average values in dependency of latitude. Seasonal variations are not modeled for the wet component.

The linearly interpolated coefficients are inserted into the Marini mapping function (\rightarrow 3.2.2.2.4).

3.2.2.3 Gradient Mapping Functions

The mapping function for horizontal gradients is different from the zenith delay mapping functions. BAR-SEVER et al. [1998] practically apply the obliquity factor

$$m(\varepsilon)_{[AZI]} = m(\varepsilon)_{[HYD/WET]} \cdot \frac{1}{\tan \varepsilon} \quad (3-102)$$

and either use the hydrostatic or wet mapping function in conjunction with the reciprocal value of $\tan \varepsilon$. HERRING [1992, p. 163] and CHEN and HERRING [1997, p. 20491] give a similar mapping function

$$m(\varepsilon)_{[AZI]} = \frac{1}{\sin \varepsilon \cdot \tan \varepsilon + C} = \frac{1}{\sin \varepsilon \cdot \tan \varepsilon + 0.0032} \quad (3-103)$$

which was implemented in the analysis software. More details on the gradient model are also supplied by DAVIS et al. [1993, pp. 1006ff].

3.3 Estimation of Tropospheric Parameters

The undifferenced neutral tropospheric delay in slant direction (\rightarrow 3.2.1) was found to be

$$\delta S_{A[NEU]}^i = m(\epsilon_A^i)_{[HYD]} \cdot ZHD_A + m(\epsilon_A^i)_{[WET]} \cdot ZWD_A + m(\epsilon_A^i)_{[AZI]} \cdot [G_{A[N]} \cdot \cos \alpha_A^i + G_{A[E]} \cdot \sin \alpha_A^i] \quad (3-104)$$

and is introduced in doubly differenced (\rightarrow 2.2.2.1)

$$\nabla \Delta \delta S_{AB[NEU]}^{ij} = (\delta S_{B[NEU]}^j - \delta S_{A[NEU]}^j) - (\delta S_{B[NEU]}^i - \delta S_{A[NEU]}^i) \quad (3-105)$$

and linearly combined (\rightarrow 2.2.3)

$$\nabla \Delta \delta S_{AB[a1,a2]}^{ij} = a_1 \cdot \frac{\nabla \Delta \delta S_{AB}^{ij}}{\lambda_{L1}} - a_2 \cdot \frac{\nabla \Delta \delta S_{AB}^{ij}}{\lambda_{L2}} \quad (3-106)$$

form to the filter engine. The hydrostatic delay can be accurately modeled and is not estimated. The parameter of primary interest is the relatively variable zenith wet delay. Moreover, several IGS analysis centers also estimate horizontal gradients. Note that both parameter sets remain as linear terms within the observation equations. This means that the only non-linear terms are associated with the ground-station coordinates. Since reasonably precise a priori values for these unknowns almost always exist and static networks are filtered, non-linearity should not place a burden on the filter.

3.3.1 Zenith Wet Delays

Zenith wet delays are those components of the neutral delay which both geodesists as well as meteorologists are most interested in. The average value of this quantity is between 1 and 3 dm with a variability of 40%. In space geodesy it is necessary or at least useful to filter this parameter that cannot be modeled adequately with simple means like it is possible for the hydrostatic component. Meteorologists are interested in the wet delay because it is possible to transform this quantity into precipitable water or integrated water vapor. This is important for precipitation forecasts and for modeling the energy balance in the atmosphere. The partial derivatives are given below

$$\begin{aligned} \frac{\partial \nabla \Delta \Phi_{AB[a1,a2]}^{ij}}{\partial ZWD_A} &= \left(\frac{a_1}{\lambda_{L1}} - \frac{a_2}{\lambda_{L2}} \right) \cdot [m(\epsilon_A^i)_{[WET]} - m(\epsilon_A^j)_{[WET]}] \\ \frac{\partial \nabla \Delta \Phi_{AB[a1,a2]}^{ij}}{\partial ZWD_B} &= \left(\frac{a_2}{\lambda_{L2}} - \frac{a_1}{\lambda_{L1}} \right) \cdot [m(\epsilon_B^i)_{[WET]} - m(\epsilon_B^j)_{[WET]}] \end{aligned} \quad (3-107)$$

ZWD_A : zenith wet delay at site A

ZWD_B : zenith wet delay at site B

and are independent of the unknowns due to their linear nature within the observation equation. It should be pointed out that double differences are *relative* observations whereas *absolute* zenith wet delays will be estimated. It will be shown that double differences are suitable to do so despite their relative nature (\rightarrow 3.3.4.3), but certain pre-requisites as far as the network design is concerned are necessary.

It is pointed out again that the tropospheric analysis system filters zenith *wet* delays and not zenith *neutral* delays. This means that the hydrostatic component must be derived with help of a hydrostatic model (e. g. Saastamoinen model, \rightarrow 3.2.1.1.2 or Hopfield model, \rightarrow 3.2.1.1.1) or by integration of the hydrostatic refractivity profile in numerical weather fields or radiosonde profiles in order to carry out proper separation. If the required meteorological data are unavailable, the program will use the MOPS model (\rightarrow 3.2.1.1.3) to predict the hydrostatic delay, but note that this may result in considerable biases. The outputs of the tropospheric analysis are (I) daily files with hydrostatic and wet delays at highest temporal resolution, (II) smoothed, hourly zenith neutral and wet delays from linear trend analysis and (III) hourly values for integrated water vapor that are derived by conversion of the wet delays with help of the mean atmospheric temperature (\rightarrow 3.5).

3.3.2 Horizontal Gradients

Horizontal gradients $G_{[N]}$ and $G_{[E]}$ per site can be estimated as additional parameters and are usually treated as random walk stochastic processes. The same is done for the zenith wet delays. The partial derivatives are given below.

$$\begin{aligned} \frac{\partial \nabla \Delta \Phi_{AB[a1,a2]}^{ij}}{\partial G_{A[N]}} &= \left[\frac{a_2 \cdot m(\epsilon_A^j)_{[AZI]}}{\lambda_{L2}} - \frac{a_1 \cdot m(\epsilon_A^j)_{[AZI]}}{\lambda_{L1}} \right] \cdot \cos \alpha_A^j \\ &+ \left[\frac{a_1 \cdot m(\epsilon_A^i)_{[AZI]}}{\lambda_{L1}} - \frac{a_2 \cdot m(\epsilon_A^i)_{[AZI]}}{\lambda_{L2}} \right] \cdot \cos \alpha_A^i \end{aligned} \quad (3-108)$$

$$\begin{aligned} \frac{\partial \nabla \Delta \Phi_{AB[a1,a2]}^{ij}}{\partial G_{A[E]}} &= \left[\frac{a_2 \cdot m(\epsilon_A^j)_{[AZI]}}{\lambda_{L2}} - \frac{a_1 \cdot m(\epsilon_A^j)_{[AZI]}}{\lambda_{L1}} \right] \cdot \sin \alpha_A^j \\ &+ \left[\frac{a_1 \cdot m(\epsilon_A^i)_{[AZI]}}{\lambda_{L1}} - \frac{a_2 \cdot m(\epsilon_A^i)_{[AZI]}}{\lambda_{L2}} \right] \cdot \sin \alpha_A^i \end{aligned} \quad (3-109)$$

$$\begin{aligned} \frac{\partial \nabla \Delta \Phi_{AB[a1,a2]}^{ij}}{\partial G_{B[N]}} &= \left[\frac{a_1 \cdot m(\epsilon_B^j)_{[AZI]}}{\lambda_{L1}} - \frac{a_2 \cdot m(\epsilon_B^j)_{[AZI]}}{\lambda_{L2}} \right] \cdot \cos \alpha_B^j \\ &+ \left[\frac{a_2 \cdot m(\epsilon_B^i)_{[AZI]}}{\lambda_{L2}} - \frac{a_1 \cdot m(\epsilon_B^i)_{[AZI]}}{\lambda_{L1}} \right] \cdot \cos \alpha_B^i \end{aligned} \quad (3-110)$$

$$\frac{\partial \nabla \Delta \Phi_{AB[a1,a2]}^j}{\partial G_{B[E]}} = \left[\frac{a_1 \cdot m(\epsilon_B^j)_{[AZI]}}{\lambda_{L1}} - \frac{a_2 \cdot m(\epsilon_B^j)_{[AZI]}}{\lambda_{L2}} \right] \cdot \sin \alpha_B^j + \left[\frac{a_2 \cdot m(\epsilon_B^i)_{[AZI]}}{\lambda_{L2}} - \frac{a_1 \cdot m(\epsilon_B^i)_{[AZI]}}{\lambda_{L1}} \right] \cdot \sin \alpha_B^i \quad (3-111)$$

$G_{A[N]}$: horizontal gradient at site A in northward direction

$G_{A[E]}$: horizontal gradient at site A in eastward direction

$G_{B[N]}$: horizontal gradient at site B in northward direction

$G_{B[E]}$: horizontal gradient at site B in eastward direction

Results obtained with additionally estimated gradients were presented by BAR-SEVER et al. [1998], but to give a general judgement, were only partly promising. EMARDSON [1998, paper E, p. 2] mentions that the "*improvements in the vertical coordinate and the wet delay estimations have, however, been marginal*". Nevertheless, horizontal gradient estimation was implemented in the experimental version of TropAC, but also showed that it is difficult to obtain better results with additional gradient parameters. Especially the stochastic properties have to be adjusted much more properly than it is usually necessary for zenith wet delay estimation. This is the reason why gradient estimation has been excluded from the operational version TropAC TRIDENT. Instead, external sources can be used to inject gradients into the model, namely numerical weather models (\rightarrow 4.).

3.3.3 Mapping Function Coefficients

Another trial to improve the accuracy of coordinate and wet delay estimates is to additionally introduce mapping function coefficients as unknowns and thereby to tune the obliquity factor empirically. This method was also implemented in the experimental version only. The Chao hydrostatic mapping function is

$$m(\epsilon)_{[HYD]} = \frac{1}{\sin \epsilon + \frac{a}{\tan \epsilon + b}} = \frac{1}{\sin \epsilon + \frac{0.00143}{\tan \epsilon + 0.00035}} \quad (3-112)$$

applied with holding mapping function coefficient b fixed as given and introducing coefficient a as parameter into the state vector. Note that only the hydrostatic and not the wet mapping function becomes an active part of the estimation process. The wet delay is much smaller than the hydrostatic one and therefore much more insensitive against small deviations from the true mapping function value. The partial derivative for coefficient a is determined by numerical differentiation (\rightarrow 2.5.2.3).

As for the horizontal gradients, results of the experiments with mapping function tuning were sobering, although a small increase in accuracy could be found. Despite of this fact, this approach was not taken over into the operational software as well.

3.3.4 Error Budget and Stochastic Modeling

The achievable accuracy of zenith wet delay estimation will be exposed by several empirical experiments (\rightarrow 6.) and summarized in the résumé (\rightarrow 8.). Nevertheless, a brief discussion of the error budget and possible strategies to model uncertainties stochastically will be discussed in the following paragraphs.

Error propagation is performed for a simulated scenario using ionosphere-free linear phase measurements with a minimum satellite constellation. Such a constellation consists of exactly two double differences from which the zenith wet delays at both stations of the baseline can be computed with 3 satellites being involved in the computations. The day chosen for the simulation was 1999/08/25 at 0 h GPS time. The baseline used was *OBER* (Oberpfaffenhofen) - *POTS* (Potsdam). Both tracking stations are separated by about 500 km, a length that can be considered to belong to the category of medium long baselines compared to typical networks in use for troposphere parameter estimation. Further discussion of the GPS error budget can be found by BEUTLER et al. [1989] and ROCKEN et al. [1997], for instance.

Note that the accuracy achieved by filtering of typical GPS data batches should be significantly better than the simulation results presented here since there are considerably more observations available than just those forming the minimum constellation treated here and, moreover, the results will be smoothed.

3.3.4.1 Position Error

In case of fixed ground station coordinates, BEUTLER et al. [1989] mention that an error in zenith troposphere delay of 1 m will cause a relative baseline error of 0.3 ppm. For the length of baseline *OBER* - *POTS* (500 km) and a realistic baseline uncertainty of 1 cm (0.02 ppm), this rule yields a zenith delay error of 6.7 cm.

dX, dY, dZ	Satellites	dZWD _A	dZWD _B	S _{ZWD[A]}	S _{ZWD[B]}	r _{ZWD[A,B]}
1.0 cm	6 (61°) 8 (42°) 25 (33°)	-4.8 cm	+1.7 cm	6.6 cm	1.8 cm	-0.91
0.3 cm	6 (61°) 8 (42°) 25 (33°)	-1.4 cm	+0.5 cm	2.0 cm	0.5 cm	-0.91
1.0 cm	6 (61°) 8 (42°) 1 (16°)	-2.5 cm	+0.7 cm	4.3 cm	0.6 cm	-0.72
0.3 cm	6 (61°) 8 (42°) 1 (16°)	-0.7 cm	+0.2 cm	1.3 cm	0.2 cm	-0.72

Table 3-9 - Impact of 1.0/0.3 cm position error for each coordinate component at site A on the zenith wet delay estimates. δ -values denote the actual error whereas σ -values represent the standard deviations; ρ is the correlation coefficient between ZWD on site A and B.

The simulation results given in table Table 3-9 generally confirm this statement, albeit not in such a dramatic way like suggested by the rule of thumb: *An error in positions maps as its multiple value into the zenith wet delays*. For the high/low constellation 6-8-1 the influence is smaller by a factor of 2 in comparison to the high/medium constellation 6-8-25. Note that the δ -values come from the formula $\underline{F} \cdot \delta \underline{x}$ where \underline{F} is the functional matrix containing the partial derivatives of ZWD_{A/B} with respect to the point coordinates and $\delta \underline{x}$ is the vector containing the coordinate errors. The standard deviations are obtained by regular error propagation $\underline{F} \cdot \underline{\Sigma}_{LL} \cdot \underline{F}^T$ with $\underline{\Sigma}_{LL}$ being the covariance matrix of the point coordinates.

3.3.4.2 Orbit Error

Following SEEGER [1993, p. 297], orbital errors approximately follow the rule

$$\frac{db}{b} \approx \frac{dr}{r} \quad (3-113)$$

db: error in baseline length

b: baseline length

dr: orbit error

r: orbit altitude ($r = 20000$ km)

where $dr = 1 \dots 5$ m for broadcast orbits and about 0.1 m (or better) for precise orbits. The resulting baseline error for baseline *OBER - POTS* would be 0.25 cm for precise orbits and 2.5 cm for broadcast orbits with an orbit error of 1 m. Applying the factors inherent in Table 3-9, one should expect a ZWD error of about 5 mm for precise and 5 cm for broadcast orbits.

Table 3-10 shows that the influence is weaker, but in this simulation, only PRN 6 got an orbit error of 0.1/1.0 m per component. The other two satellites remained untouched. Generally speaking, it becomes clear that the accuracy of broadcast orbits is clearly inferior to that of precise IGS orbits and can be troublesome in zenith wet delay estimation.

dX, dY, dZ	Satellites	dZWD _A	dZWD _B	S _{ZWD[A]}	S _{ZWD[B]}	r _{ZWD[A,B]}
0.1 m	6 (61°) 8 (42°) 25 (33°)	-0.1 cm	-0.2 cm	0.2 cm	0.4 cm	1.00
1.0 m	6 (61°) 8 (42°) 25 (33°)	-1.3 cm	-2.0 cm	2.4 cm	3.8 cm	1.00
0.1 m	6 (61°) 8 (42°) 1 (16°)	-0.4 cm	-0.1 cm	0.8 cm	0.1 cm	1.00
1.0 m	6 (61°) 8 (42°) 1 (16°)	-4.3 cm	-0.6 cm	8.1 cm	1.1 cm	1.00

Table 3-10 - Impact of 0.1/1.0 m satellite position error for each coordinate component of PRN 6 on the zenith wet delay estimates. δ -values denote the error whereas σ -values represent the standard deviations; ρ is the correlation coefficient between ZWD on site A and B.

3.3.4.3 Convergence Error

Single as well as double differencing of the observations reveals a problem that is inherent to *relative* measurements: The difference in ZWD (wet delay) does not permit the estimation of absolute values if the baseline is short, i. e. the satellites are observed under similar elevation angles ($\epsilon_A^i \approx \epsilon_B^i \approx \epsilon^i$) yielding

$$\begin{aligned} \Delta\delta S_{[WET]} &= m(\epsilon_B^i) \cdot ZWD_B - m(\epsilon_A^i) \cdot ZWD_A \approx m(\epsilon^i) \cdot ZWD_B - m(\epsilon^i) \cdot ZWD_A \\ &= m(\epsilon^i) \cdot (ZWD_B - ZWD_A) = m(\epsilon^i) \cdot \Delta ZWD_{AB} \end{aligned} \quad (3-114)$$

and shows that it is impossible to sense absolute wet delays, but the delay difference between site A and B can be precisely determined. If parameterization is done with respect to *absolute* delays, the results for short baselines will be highly correlated and

have a high standard deviation whereas their difference is accurate. During Kalman filtering, a tardy convergence towards the true value can be observed.

To illustrate this phenomenon, filtering has been performed for baseline *OBER* - *WTZR* (about 150 km) and for baseline *OBER* - *POTS* (about 500 km) independently. The results for the redundant station *OBER* are shown in Figure 3-7. This simulation was carried out applying a process noise of 10 mm/ \sqrt{h} to the wet delays. Algebraic correlation between the observations (ionosphere-free signals) was modeled and an elevation-dependent down-weighting of the phase measurements was performed. The "true" wet delay was exactly 110 mm, but the initial state of the Kalman filter was intentionally set to zero and the corresponding standard deviation to 300 mm. The cutoff elevation was chosen to be 15°.

Generally speaking, both solutions first rapidly converge towards the true value, but after approaching to it for about 90%, convergence considerably slows down. This change is much more evident for the short baseline than for the longer one (*OBER* - *POTS*) that effectively needs 88 epochs (about 45 minutes) to reach 99% of the true value whereas the same process lasts 1624 epochs (about 13.5 h) for baseline *OBER* - *WTZR*.

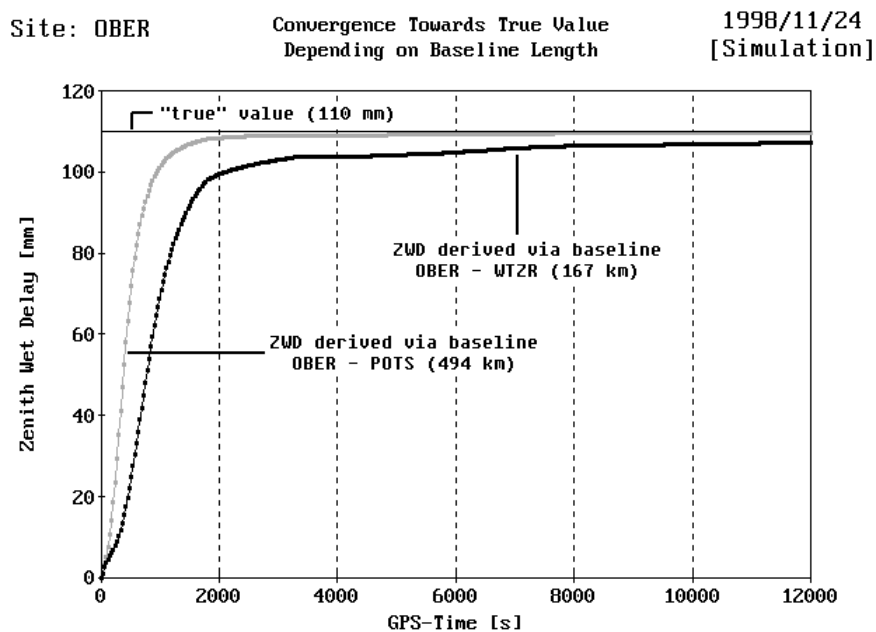


Figure 3-7 - Results of simulated filter run demonstrating the convergence problem. Apparently, absolute zenith wet delay parameters show a faster convergence if they are derived via long baselines.

3.3.4.3.1 Network Considerations for Absolute Delay Estimation

In order to measure absolute delays and changes (variations with time) the network should either have a huge diameter or at least one baseline that is longer than 700 km (better: 1000-2000 km). DUAN et al. [1996] recommend to use remote stations which are at least 500 km distant from the core network. Very long baselines (e. g. *OBER* - *BAHR*: 4110 km) have the disadvantage that the visibility conditions for one and the

same satellite can be rather different at both sites and, consequently, the minimum elevation angle (usually 15°) has to be lowered to allow the formation of a sufficiently large number of double-differences.

Figure 3-8 illustrates the recommended network structure that can be divided into two major belts, namely the core network and the belt of remote stations. It is pointed out that in practice, less remote sites than shown in the network plots are fully sufficient. The core network can be further divided into the region of interest (ROI) and a belt of peripheral stations that are located in the vicinity of the ROI. Such peripherals are only needed if the final goal of the network analysis is a 2-D data set of interpolated zenith wet delays, because they reduce the need to extrapolate data. The network of peripheral stations shown in this example is a bit thin and should be more dense in operational analysis.

3.3.4.3.2 Relative Tropospheric Delay Estimation

Relative tropospheric delay estimation is possible in any network. Remote sites are not necessary, but if the overall aim is to derive absolute values from these relative estimates afterwards, there must be at least one reference station that is able to deliver absolute wet delays and thereby allows to transform all other relative delays into absolute zenith wet delays:

$$\begin{aligned} ZWD_B &= ZWD_A + \Delta ZWD_{AB} \quad \wedge \quad \Delta ZWD_{AB} = ZWD_B - ZWD_A \\ ZWD_C &= ZWD_A + \Delta ZWD_{AB} + \Delta ZWD_{BC} \end{aligned} \quad (3-115)$$

ZWD_A : absolute zenith wet delay at station A, reference point

ΔZWD_{AB} : estimated relative zenith wet delay between station A and B

ΔZWD_{BC} : estimated relative zenith wet delay between station B and C

The same method is applied to leveling networks where height differences are measured and absolute heights are obtained with help of absolute reference points.

Absolute zenith wet delays can be derived either with help of an absolute reference GPS network composed under the conditions outlined before (\rightarrow 3.3.4.3.1), from radiosonde data, water vapor radiometers or similar sensors.

Note that it is possible to parameterize the observation equation with respect to the zenith wet delay difference ΔZWD_{AB} . However, it is not necessary nor recommended to do so. Instead, parameterization can be carried out with respect to the absolute delays (\rightarrow 3.3.1), i. e. it is not necessary to alter the algorithm. Instead, we accept the estimated absolute delays themselves to be more inaccurate (for short baselines) due to the convergence error. After parameter estimation is finished, the relative delays

$$\Delta ZWD_{AB} = ZWD_B - ZWD_A \quad (3-116)$$

are derived from the filter results and their associated standard deviation

$$\sigma_{\Delta ZWD_{AB}} = \sqrt{\sigma_{ZWD_A}^2 + \sigma_{ZWD_B}^2 - 2 \cdot \rho_{ZWD_A, ZWD_B} \cdot \sigma_{ZWD_A} \cdot \sigma_{ZWD_B}} \quad (3-117)$$

σ_{ZWD_A} : standard deviation of estimated absolute zenith wet delay at site A

ρ_{ZWD_A, ZWD_B} : correlation coefficient between ZWD at site A and that at site B

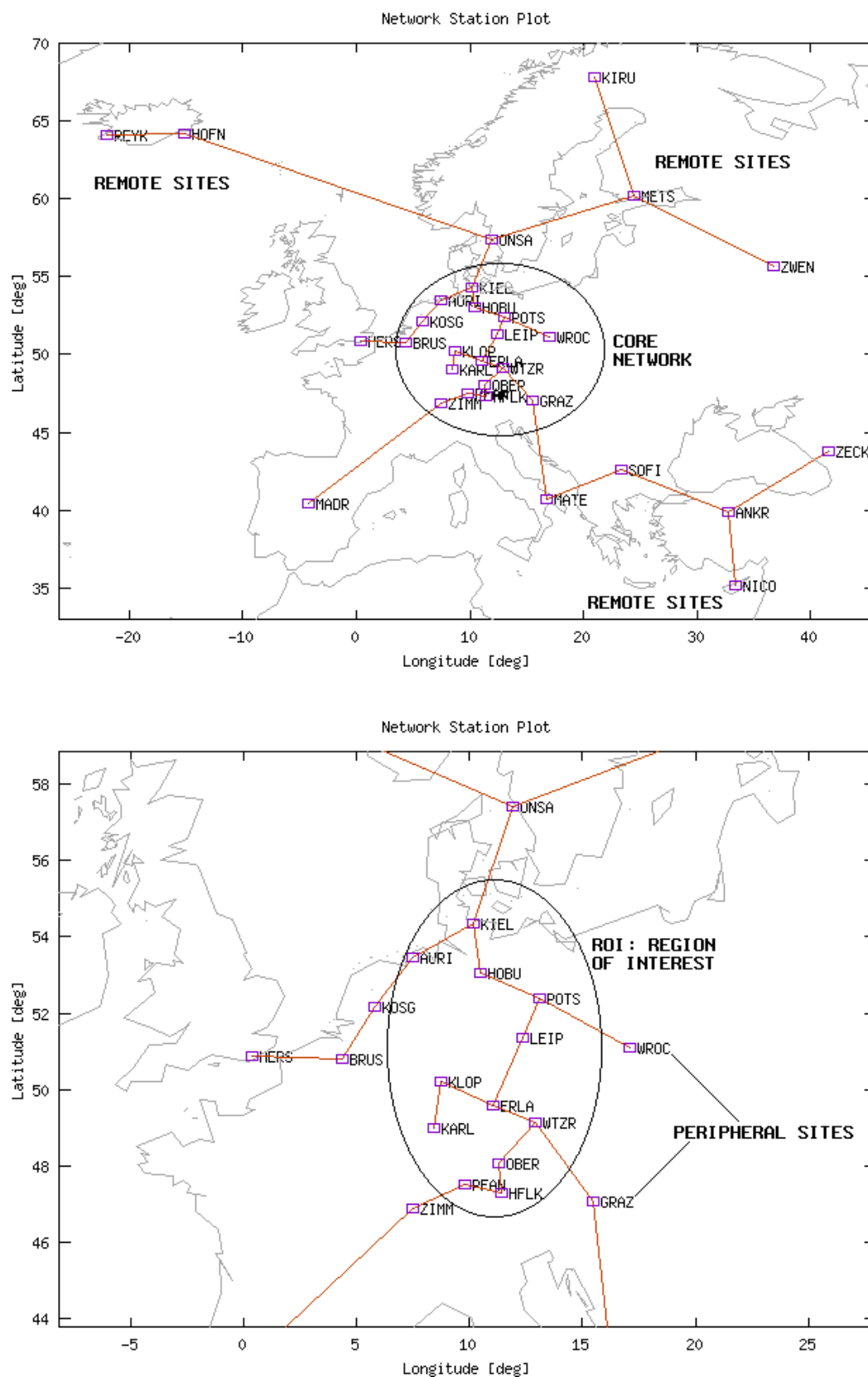


Figure 3-8 - Typical network structure for absolute zenith wet delay estimation. This example illustrates the two basic belts, the belt of remote stations and the core network. The latter can be further divided into the region of interest (ROI) and a belt of peripheral stations that will be necessary if 2-D interpolation of the results shall be performed.

will be free of the convergence error.

Due to the fact that absolute delay estimation is the primary focus of GPS meteorology and the network pre-requisites discussed before can be easily met with help of the IGS tracking network, relative delay estimation is of very limited concern. Actually, all results of this study presented in chapter 6 were obtained with help of the absolute method. Nevertheless, it should be mentioned that relative delay estimation can be very advantageous in terms of CPU speed: Absolute delay estimation requires either a long baseline or a network with a huge diameter. Consequently, absolute delays are almost always obtained by filtering complete networks. In contrast to this approach, relative delay estimation can be carried out without any particular regard on the baseline length nor the network composition and it can be performed in a baseline per baseline manner. This essentially means that each baseline can be filtered independently from the other parts of the network effectively turning the "network filter task" into a "baseline filter task". Single baseline estimation is much faster than processing whole networks since there are less ambiguities to cope with and, moreover, it is much easier to apply the principles of parallel computing to this approach. Under these considerations, relative delay estimation might be attractive for processing huge networks. The absolute delays for leveraging the relative results could be easily derived using a small sub-network with some remote sites.

3.3.4.4 Multipath

Multipath can be considered as an important contributor to the overall error budget. However, the impact of this effect depends on several factors, e. g. on the antenna site itself and the surrounding topography and monuments, on the GPS receiver and its abilities to mitigate multipath, on the GPS antenna and its abilities to reject multipath (choke ring) and on the analysis software and its capabilities to compensate these error sources. Using choke ring antennas in a typical environment, multipath contributions should be smaller than 1 cm in average and about 2 to 5 mm should be anticipated.

3.3.4.5 Hydrostatic Delay

Errors in hydrostatic delay introduce biases in the estimated wet delay. Fortunately, the hydrostatic component can be modeled with superior accuracy. Applying the Saastamoinen model in a simplified form

$$\text{ZHD} \approx 0.0023 \left[\frac{\text{m}}{\text{hPa}} \right] \cdot p_0 \quad (3-118)$$

p_0 : surface (antenna) pressure in [hPa]

yields an accuracy function of approximately

$$\sigma_{\text{ZHD}} \approx 0.003 \left[\frac{\text{m}}{\text{hPa}} \right] \cdot \sigma_{p_0} \quad (3-119)$$

where the enlarged factor tries to account not only for the pressure accuracy, but also for model errors.

3.3.4.6 Mapping Function

Applying the law of error propagation to

$$\text{SND} = m(\epsilon) \cdot \text{ZND} \quad (3-120)$$

SND: slant neutral delay

m: mapping function

ZND: zenith neutral delay

yields

$$\sigma_{\text{SND}}^2 = m(\epsilon)^2 \cdot \sigma_{\text{ZND}}^2 + \text{ZND}^2 \cdot \sigma_{m(\epsilon)}^2 \quad (3-121)$$

Omission of the influence of the zenith neutral delay error σ_{ZND} simplifies this formula to

$$\sigma_{\text{SND}} = \text{ZND} \cdot \sigma_{m(\epsilon)} \quad (3-122)$$

and shows that uncertainties in the obliquity factor directly scale into the slant path delay.

Figure 3-9 shows the discrepancies between selected mapping functions for the hydrostatic delay and the Niell model that serves as reference. Such uncertainties can be modeled stochastically by application of an elevation-dependent increase in standard deviation (or variance):

$$\sigma_z = \sigma_\emptyset \cdot \tan(q_z \cdot z_i) \quad (3-123)$$

σ_\emptyset : scaling for elevation-dependent weighting

q_z : zenith angle scaling factor

z_i : zenith angle to satellite i

By doing so, measurements at low elevations will receive less weight during the filter update and may not harm the solution as much as it would be the case if no down-weighting was applied.

The mean discrepancies of the Herring, Black and Davis models were fitted to this function and the adjusted results are given below and are valid for stochastic modeling of the total tropospheric delay¹²

$$\sigma_\emptyset = 0.79 \pm 0.05 \text{ [mm]}; \quad q_z = 1.1044 \pm 0.0016 \quad (3-124)$$

¹² Note that the differences of the mapping functions were scaled by 2.3 m in order to account for the average total zenith delay whereas the differences in the preceding figure were only scaled by 2.2 m in order to demonstrate the effect for the mean hydrostatic delay.

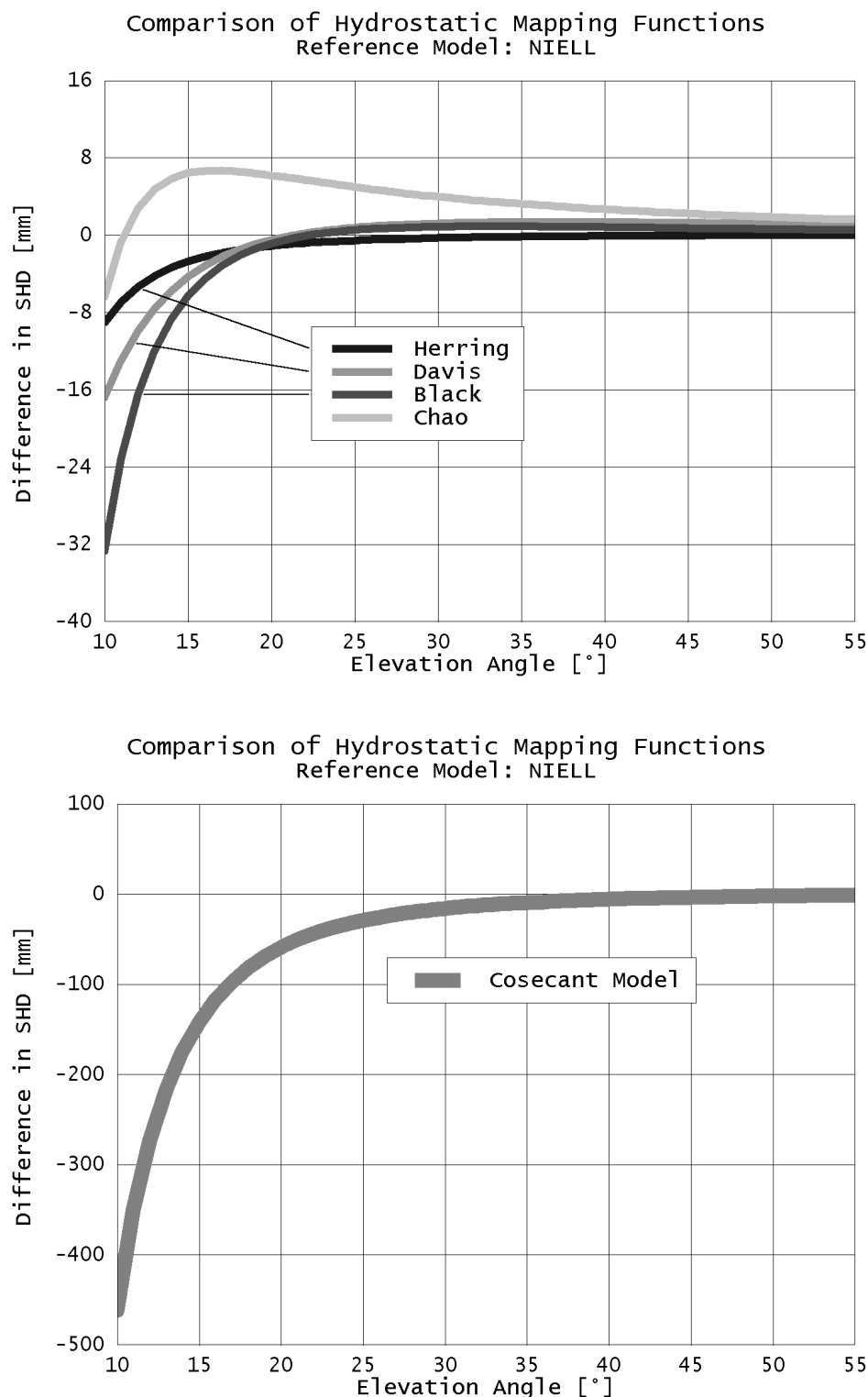


Figure 3-9 - Comparison of selected hydrostatic mapping functions with the Niell model serving as reference. The left diagram shows mapping functions of high precision and the figure on the right deals with the most simple approach, the cosecant model which is insufficiently weak for lower elevations. The models are computed for a virtual point at 48° latitude, a geopotential height of 550 m and a radial distance of 6855 km with a surface pressure of 985 hPa, a temperature of 15 °C, a relative humidity of 60%, a temperature lapse rate of -6.81 K/km and a tropopause height of 11 km. The differences in mapping function value were scaled by 2200 mm of zenith hydrostatic delay in order to obtain quantities in units of slant path delay.

For the cosecant model, the values

$$\sigma_{\vartheta} = 17.0 \pm 0.8 \text{ [mm]}; \quad q_z = 1.1014 \pm 0.0015 \quad (3-125)$$

were obtained. From these coefficients, it is also possible to give a recommendation for a suitable elevation cut-off. If the slant path delay error due to mapping function inaccuracies shall not exceed 10 mm, then the corresponding elevation cut-off for precise mapping functions like those of Niell, Saastamoinen, Black, Herring, Davis and Chao should not lie below

$$z_{\text{MAX}} \approx \arctan\left(\frac{10 \text{ mm}}{0.79 \text{ mm}}\right) \cdot \frac{1}{1.1044} = 77^\circ \Rightarrow \varepsilon_{\text{MIN}} = 13^\circ \quad (3-126)$$

and under the consideration of worse signal-to-noise ratio at lower elevation angles, a good compromise should be to use a cut-off mask of 15°. For the cosecant model, this threshold

$$z_{\text{MAX}} \approx \arctan\left(\frac{10 \text{ mm}}{17 \text{ mm}}\right) \cdot \frac{1}{1.1014} = 28^\circ \Rightarrow \varepsilon_{\text{MIN}} = 62^\circ \quad (3-127)$$

is as much as 50° higher. It becomes clear that this simple model is absolutely inappropriate for the needs of high-precision GPS delay estimation.

3.3.4.7 Measurement Noise

Combining the two pairs of double differences of the simulation run (\rightarrow 3.3.4.1) with the satellite constellation 6-8-25 and 6-8-1 and assuming a standard deviation of 1.0 cm for the carrier phase measurement allows to estimate the zenith wet delay with a standard deviation of about 5.8 cm. For a phase noise of 3 mm, the resulting ZWD standard deviation is 1.7 cm. In routine processing, about 4 to 6 double differences per baseline can be expected what further improves the error budget. Consequently, tropospheric delay estimation at the level of better than 2 cm should be feasible and filtering/smoothing may improve the accuracy further. Practical results will be presented in chapter 7 and the overall summary of the error budget updated by practical experiences will be discussed in chapter 8.

3.4 Stochastic Properties of Zenith Wet Delays

Kalman filtering is certainly a suitable and efficient technique for the estimation of troposphere parameters like zenith wet delays. This quantity possesses a high variability of several centimeters per day (and sometimes even more). A suitable way to model this parameter in time is to treat it as a stochastic process. However, one major problem is the proper definition of the underlying stochastic behavior of the wet delays that are treated as random walk stochastic processes in the TropAC analysis system. Several methods were developed to find appropriate process noise values.

One method to find average process noise parameters is to analyze GPS-derived tropospheric delay time series. A number of globally distributed IGS tracking stations is available for this purpose. The results suggest values of about 2 to 9 mm/ \sqrt{h} depending on the location of the station. Nevertheless, time series analysis provides only mean values for the process noise. Wet delay variations occurring within a particular time window can be rather different. For this reason, the concept of dynamic process noise definition has also been implemented in order to account for such deviations from the mean behavior: Instead of defining an average process noise value for the whole diurnal data batch, hourly process noise values are derived from the wet delays either by applying models or by a priori knowledge of the delays. The latter gives best results but normally requires an extra iteration as the variability analysis has to be carried out by using results from the initial filter run.

3.4.1 Stochastic Filtering

The Kalman filter methodology is briefly repeated here (see also \rightarrow 2.5.2, \rightarrow 2.5.2.2) under special consideration of the process noise problem. Kalman filtering normally consists of two steps, the state vector prediction and its update with help of real measurements. The prediction of the state vector is given by

$$\underline{X}_k = \underline{I}_k \cdot \underline{X}_{k-1}^* \quad (3-128)$$

\underline{X}_k : predicted state vector of current epoch k

\underline{I}_k : transition matrix of current epoch

\underline{X}_{k-1}^* : updated state vector of previous epoch k-1

with k being the current and k-1 being the previous epoch. \underline{X} denotes the predicted and \underline{X}^* the updated state vector. \underline{I} is the so-called transition matrix. Its purpose is to model the transition in time of the states from the previous to the current epoch.

Treating zenith wet delays as stochastic parameters implies that the predicted delay states are equal to the updated ones of the previous epoch. Thus, the transition matrix \underline{I} simply becomes

$$\underline{I}_k = \underline{E} \quad (3-129)$$

\underline{E} : identity matrix

an identity matrix \underline{E} . Since the first (and higher) derivatives of the zenith wet delays are not part of the state vector, i. e. the "velocity" (and "acceleration") of the delays is not estimated, we must find another way to permit the states to change their value with time. This is done by injection of some process noise into the predicted covariance matrix of the states:

$$\underline{\Sigma}_k = \underline{I} \cdot \underline{\Sigma}_{k-1}^* \cdot \underline{I}^T + \underline{\Sigma}_{SS} = \underline{\Sigma}_{k-1}^* + \underline{\Sigma}_{SS} \quad (3-130)$$

$\underline{\Sigma}_k$: predicted covariance matrix of the states of current epoch k

$\underline{\Sigma}_{k-1}^*$: updated covariance matrix of the states of previous epoch k-1

$\underline{\Sigma}_{SS}$: process/system noise matrix

$\underline{\Sigma}$ is the covariance matrix of the predicted states, $\underline{\Sigma}^*$ is that of the updated states (previous epoch) and $\underline{\Sigma}_{ss}$ is the *process or system noise matrix*.

Practically speaking, this method means that the variances and covariances are propagated to the current epoch k , but additionally, the variance level is raised a bit by the process noise variances (and covariance components) added to this matrix. During the update process of the Kalman filter, predicted states and observations are combined. A higher variance level of the predicted states will cause the filter to give more weight to the observations and thereby magnify the gain matrix. Albeit the predicted states themselves do not differ in comparison to the updated states of the previous epoch, the filter thereby gets "freedom to innovate" because the smoothing mechanism is weakened slightly. This method corresponds to modeling zenith wet delays as *random walk* stochastic processes, i. e. integrated white noise with the white noise components being present in the process noise matrix $\underline{\Sigma}_{ss}$.

The very problem is to define the process noise parameters properly. If the process noise is chosen too small, the Kalman filter will work similar to a low-pass filter. Fine structures in the wet delay variations will not be visible in the results. Otherwise, if the process noise is chosen too high, the observations will get too much weight during the update process which may result in a rather scattered time series that will reveal the measurement noise at an unwanted high level as well as other disturbing effects like multipath. In this case, the Kalman filter does not act any longer as a *filter* because of the relatively high noise level hiding the wet delay signal actually wanted by the user.

3.4.2 Stochastic Processes

Two important stochastic processes should be briefly discussed before concrete results for process noise parameters are presented. Following common theory¹³, a stochastic process of a time series, here zenith wet delays (ZWD),

$$ZWD(t_1), ZWD(t_2), ZWD(t_3), \dots, ZWD(t_n) \quad (3-131)$$

with an expectation value of

$$\mu(t) = E\{ZWD(t)\} = \lim_{n \rightarrow \infty} \frac{1}{n} \cdot \sum_{i=1}^n ZWD(t) \quad (3-132)$$

μ : mean (true) value of ensemble

$E\{..\}$: expectation value

t : epoch (time)

n : number of realizations

and a variance of

$$\sigma^2(t) = E\{(ZWD(t) - \mu(t))^2\} = \lim_{n \rightarrow \infty} \left(\frac{1}{n} \cdot \sum_{i=1}^n [ZWD(t) - \mu(t)]^2 \right) \quad (3-133)$$

¹³ see EISSFELLER [1998], PELZER [1996] and HERRING et al. [1990]

is characterized by its associated auto-covariance function

$$C(t, \tau) = E\{ [ZWD(t) - \mu(t)] \cdot [ZWD(t + \tau) - \mu(t + \tau)] \} \quad \wedge \quad C(t, 0) = \sigma^2(t) \quad (3-134)$$

τ : increment in time

3.4.2.1 First Order Gauss-Markov Process

Many stochastic processes occurring in nature can be suitably approximated as Gauss-Markov processes that can be defined by their derivative in time

$$\frac{dZWD}{dt} = -\beta \cdot ZWD + w = -\frac{ZWD}{T} + w \quad (3-135)$$

T : period of process

t : time

β : reciprocal period $1/T$

w : white noise

with β being the reciprocal period $1/T$ of this process and w is white Gaussian noise. The so-called *Matrix-Ricatti equation* of this process is

$$\frac{d(\sigma^2)}{dt} = -2 \cdot \beta \cdot \sigma^2 + q \quad (3-136)$$

q : process noise parameter, often called *q-factor*

and this differential equation can be solved:

$$\sigma^2(t) = \sigma_0^2 \cdot \exp\left(-\frac{2}{T} \cdot t\right) + \frac{q}{2} \cdot T \cdot \left[1 - \exp\left(-\frac{2}{T} \cdot t\right)\right] \quad (3-137)$$

Obviously, the variance varies with time t , but converges to a limit of

$$\lim_{t \rightarrow \infty} \sigma^2(t) = \frac{q}{2} \cdot T \quad (3-138)$$

For this reason, Gauss-Markov processes are also called *stationary processes*. The mean of the time series of such processes, their expectation value, is not time-dependent

$$\mu(t_1) = \mu(t_2) = \dots = \mu(t_n) = \mu \quad (3-139)$$

and the same yields for the auto-covariance function

$$C(t_1, \tau) = C(t_2, \tau) = \dots = C(t_n, \tau) = C(\tau) \quad \wedge \quad C(\tau) = C(-\tau) \quad (3-140)$$

Empirically, the auto-covariance function of a discrete, stationary time series can be computed by

$$C(k) = \frac{1}{n-k-1} \cdot \sum_{i=1}^{n-k} [(ZWD_i - ZWD_0) \cdot (ZWD_{i+k} - ZWD_0)] \quad \wedge \quad \tau = k \cdot \Delta t \quad (3-141)$$

τ : increment in time

n : number of samples of the time series

m : number of entries of the auto-covariance function (recommendation: $m = n/10$)

k : index of the auto-covariance function

where k has a range from $k = 0, 1, 2, \dots, m$ and, according to PELZER [1996], m is recommended to be chosen no higher than $m = n/10$ due to accuracy considerations. ZWD_0 is the arithmetic mean of the time series

$$ZWD_0 = \frac{1}{n} \cdot \sum_{i=1}^n ZWD_i \quad (3-142)$$

and is treated to be the true value μ or expectation value $E\{ZWD\}$.

3.4.2.2 Random Walk

Random walk is defined as integrated white noise and can be considered as a variation of Gauss-Markov processes for the very special case of

$$T \rightarrow \infty \Rightarrow \beta \rightarrow 0 \quad (3-143)$$

Thus the derivative in time of this process becomes

$$\frac{dZWD}{dt} = w \quad (3-144)$$

and the Matrix-Ricatti equation simply is

$$\frac{d(\sigma^2)}{dt} = q \quad (3-145)$$

or

$$\sigma^2(t) = \sigma_0^2 + q \cdot t \quad (3-146)$$

Apparently, the variance of this process does not converge to a constant value for t approaching infinity as it is the case for Gauss-Markov processes. Therefore, random walk time series are not stationary. However, as far as zenith wet delay estimation is concerned, they are an appropriate approximation of reality as long as the time difference between two subsequent epochs $\Delta t = t_k - t_{k-1}$ is not too large. In matrix form we can write the preceding equation as

$$\underline{\Sigma} = \underline{\Sigma}_0 + \Delta t \cdot \underline{Q} = \underline{\Sigma}_0 + \underline{\Sigma}_{ss} \quad (3-147)$$

$\underline{\Sigma}$: covariance matrix of current epoch
 $\underline{\Sigma}_0$: covariance matrix of previous epoch
 $\underline{\Sigma}_{ss}$: process/system noise matrix
 \underline{Q} : process noise parameter matrix

which exactly corresponds to our definition of the predicted covariance matrix of the states (\rightarrow 3.4.1).

GPS data taken from the IGS network have a sampling interval of just 30 seconds, so the assumption of modeling zenith wet delays as random walk stochastic processes is certainly valid, but as we will see, the empirical auto-covariance functions will significantly differ from the typical structure of random walks *in the long run*.

3.4.3 Mean Process Noise Parameters from Time Series Analysis

Following BROWN and HWANG [1997], the auto-covariance function completely describes the properties of a stochastic process. The empirical auto-covariance functions for zenith wet delay time series can be computed (\rightarrow 3.4.2.1) and from these functions, the process noise parameters denoted as q-values can be obtained. For the special case of random walk stochastic processes, the process noise parameter q turns out to be

$$q = -\frac{C(t_2) - C(t_1)}{t_2 - t_1} = -\frac{C(t) - \sigma^2}{t} \quad (3-148)$$

q: q-factor defining the process noise
 C: value of the auto-covariance function
 σ : standard deviation of the stochastic process
 t: epoch

where $C(t_2)$ is the value of the empirical auto-covariance function at epoch t_2 and t is any epoch unequal to zero. See SCHUELER [1998c] for further details on the analysis of empirical delay time series as well as for a discussion of the derivation of q-factors with special focus on the case of random walk stochastic processes. Practically speaking, the auto-covariance function is used to determine the decorrelation between the initial epoch 0 and the current epoch t . If we predict the states and treat the states themselves as stochastic parameters, the decorrelation between epoch k and $k-1$ gives us a measure for the increase in variance $q \cdot t$ of the particular states and can be implemented in the Kalman filter with help of the system noise matrix $\underline{\Sigma}_{ss}$.

3.4.3.1 Results for the IGS Tracking Network

The IGS troposphere products were used to derive zenith wet delay time series and to compute the empirical auto-covariance functions in order to gain a realistic insight into the stochastic properties. More than 100 sites of the global IGS tracking network for which a combined troposphere product is available were analyzed with the temporal resolution of 1 hour.

Figure 3-10 and Figure 3-11 show examples for empirical auto-covariance functions for two monitor stations of this network, Potsdam (POTS/Berlin) in Germany and

Bahrain (*BAHR*). Compared to the fact that the data are currently processed in diurnal batches with a time interval of 30 seconds between two subsequent epochs, the auto-covariance functions are given for a rather large time span. In the long run, the curves look like a mixture of Gauss-Markov processes and several other noise components. Negative correlation can be seen (this is not possible for Gauss-Markov processes) as well as a certain amount of colored noise at different frequencies. A closer look at the functions (part II of Figure 3-11) reveals oscillations with a period of one day - apart from other harmonics with higher amplitude and periods of considerably more than one day (seasonal variations, for instance).

However, for the first day or the first few days (part I of Figure 3-11 and Figure 3-10), there is a clear linear decorrelation without any disturbances due to colored noise or similar effects. This characteristic property allows to apply the methods described before (\rightarrow 3.4.3) for the derivation of the q-factors.

3.4.3.2 Process Noise Values

Process noise parameters were derived from time series analysis for a number of IGS stations. Appendix I gives the full table of random walk process noise parameters that were derived by a linear fit to the auto-covariance function for the first 24 hours.

Figure 3-12 shows the spatial distribution of the \sqrt{q} -factors and reveals a light decrease in q-value for higher latitudes. Most sites have values near 5 mm/ \sqrt{h} . The highest process noise is to be expected in very humid regions (*PIMO*: Philippines, *WUHN*: Wuhan, China, humid climate, more than 9 mm/ \sqrt{h}) and lowest values of even less than 1 mm/ \sqrt{h} in three cases can be stated esp. for the polar regions, e. g. *AMUN* (Amundsen, South Pole) and *MAW1* (also Antarctica).

For sites not listed in Appendix I, the following approximation function can be used:

$$\begin{aligned} \sqrt{q} \approx a + b \cdot \varphi + c \cdot \varphi^2 + d \cdot \lambda + e \cdot H = & 5.7 \left[\frac{\text{mm}}{\sqrt{h}} \right] + 0.014 \left[\frac{\text{mm}}{\sqrt{h} \cdot \text{deg}} \right] \cdot \varphi \\ & - 0.0005 \left[\frac{\text{mm}}{\sqrt{h} \cdot \text{deg}^2} \right] \cdot \varphi^2 + 0.003 \left[\frac{\text{mm}}{\sqrt{h} \cdot \text{deg}} \right] \cdot \lambda - 0.001 \left[\frac{\text{mm}}{\sqrt{h} \cdot \text{m}} \right] \cdot H \end{aligned} \quad (3-149)$$

φ : latitude of station in degrees

λ : longitude of station in degrees

H: orthometric height of station in [m]

that was derived by a least-squares fit of the given process noise values to the approximate model as a function of the site location. The residuals of this fit are shown in Figure 3-13; the standard error of the estimate is about 1.2 mm/ \sqrt{h} .

However, to be realistic, it must be stated that this fit can only inappropriately model the given data. Instead, the following rule of thumb may also be applied: For sites near the tropics, a random walk parameter of about $\sqrt{q} = 10$ mm/ \sqrt{h} , for mid-latitudes 5 mm/ \sqrt{h} and for polar regions about 4 mm/ \sqrt{h} seem to be proper.

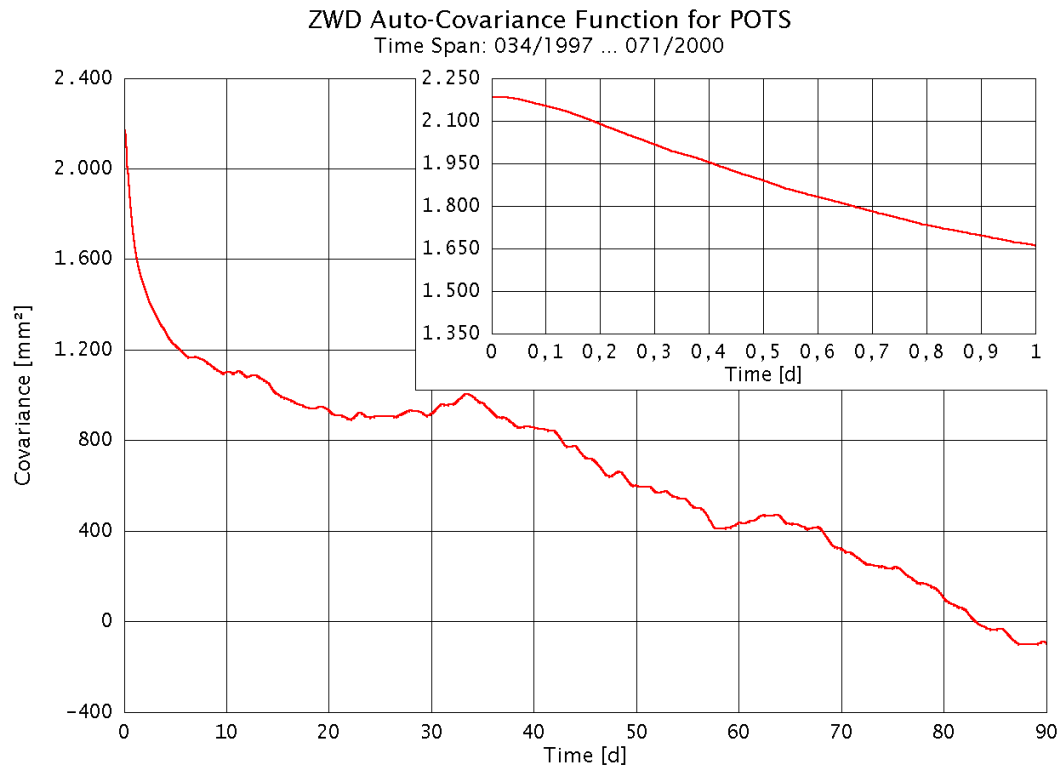


Figure 3-10 - Empirical auto-covariance function for IGS tracking station Potsdam (POTS, Germany). The function is given for the first day in a zoom-window on the upper right of the diagram.

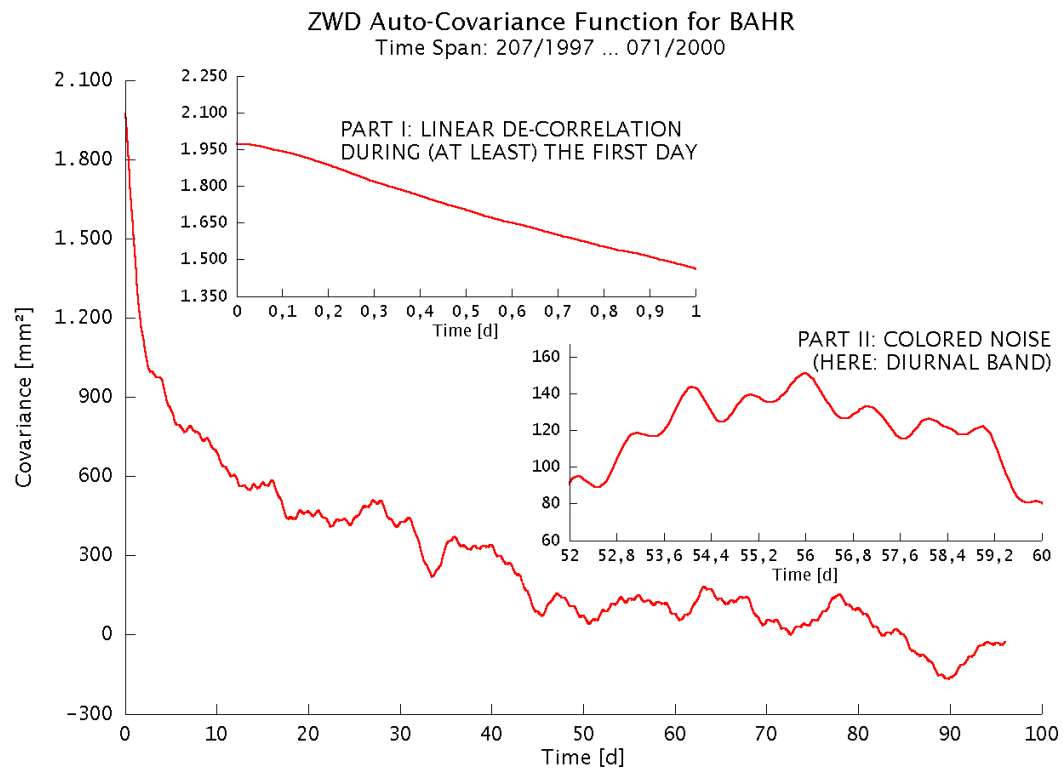


Figure 3-11 - Auto-covariance function for IGS tracking station Bahrain (BAHR). The upper zoom-window shows the function during the first 24 hours. Moreover, colored noise components are shown in the zoom-window on the middle, right part of the diagram.

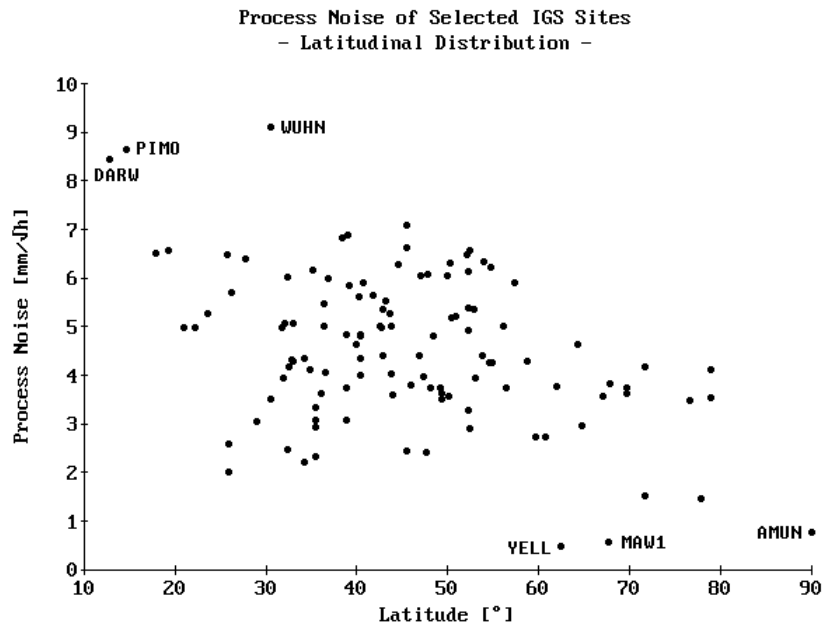


Figure 3-12 - Spatial distribution of the process noise parameters for selected tracking stations of the IGS network. A slight latitudinal dependency can be stated where highest process noise lies in the tropics and smallest values can be found pole-wards. This corresponds to the amplitude of zenith wet delays which are highest near the equator and smallest at the poles as well. See Appendix I for a complete table of the process noise values determined with help of the TropAC database.

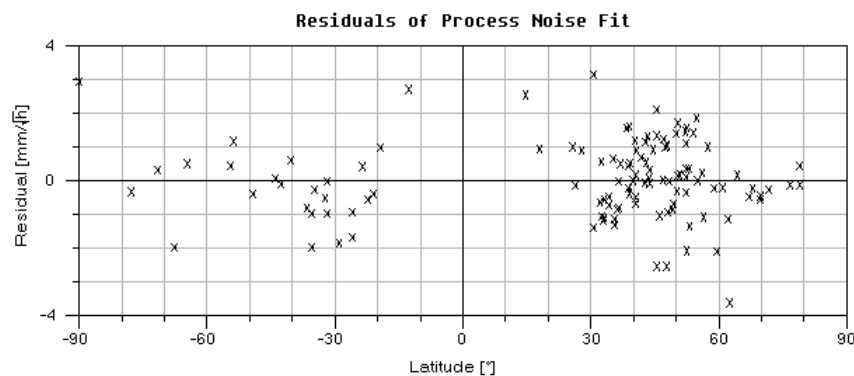


Figure 3-13 - Residuals of the least-squares fit of the process noise values to the approximation function.

3.4.4 Dynamic Tuning and Maximum Tuning

It should be noted that the results presented so far are average \sqrt{q} -factors, i. e. they can be useful to express the mean variability of zenith wet delays, but without any doubt, certain situations may occur where much higher delay variations will be present. Based on the analysis of wet delays from numerical weather fields it can be shown that about 90% of all hourly differences in zenith wet delay are less than 6 mm

(→ Figure 3-14). This proves that the mean process noise parameter of about 5 mm/ \sqrt{h} given in Appendix I is realistic.

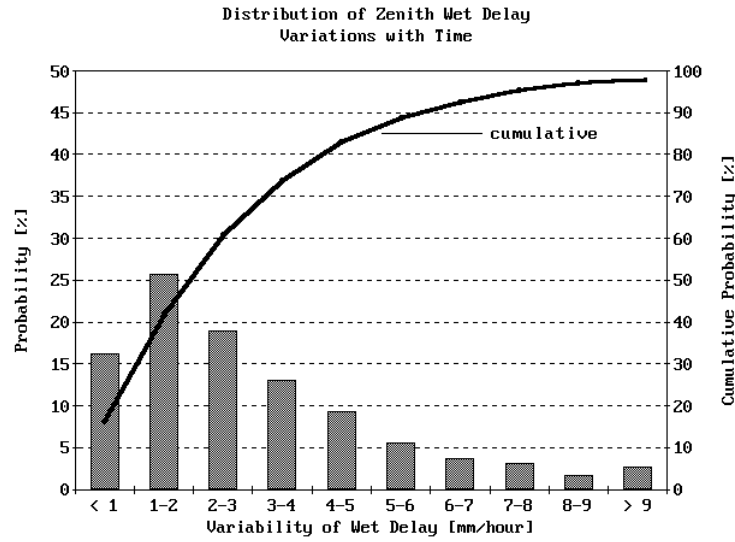


Figure 3-14 - Zenith wet delay variability from analysis with help of numerical weather fields. The left y-axis shows the group-variability, e. g. hourly differences of 1 up to 2 mm occur in about 25% of the cases. The right y-axis gives the integrated, cumulative probability, e. g. in 60% of the cases, the variability is equal to or less than 3 mm. The diagram presents the mean ZWD distribution for the sites Oberpfaffenhofen (OBER, Germany), Zimmerwald (ZIMM, Switzerland) and Seychelles (SEY1).

Nevertheless, during the remaining 10% of the time, the stochastic noise defined by application of the random walk parameters is too small and, on the contrary, in more than 70% the variability is less than 4 mm and the chosen process noise is too high. It would be desirable to find a way that defines the process noise under consideration of the actual variability and thereby to obtain optimally tuned wet delay filter estimates.

The concept of *dynamic tuning* is applied to provide a method of defining the process noise with greater respect to the actual variations in ZWD. The final products of the TropAC analysis software are hourly zenith wet and neutral delays. For each hourly data batch, an individual process noise

$$q \approx \frac{\Delta \text{ZWD}^2}{\Delta t} = \frac{[\text{ZWD}(t_i + 1[h]) - \text{ZWD}(t_i)]^2}{1[h]} \quad (3-150)$$

can be defined. Alternatively, instead of defining individual noise coefficients hour per hour, the maximum q-factor of the day

$$q \approx \max\{q(0\text{ h}), q(1\text{ h}), \dots, q(23\text{ h})\} \quad (3-151)$$

can also be used as new default value throughout this particular day. This method is called *maximum tuning*.

3.4.4.1 Methods of Dynamic and Maximum Process Noise Definition

The following possibilities are most commonly available to determine dynamic process noise coefficients:

1. *Standard zenith wet delay models.* A number of troposphere models exists (→ 3.2.1.2). In most cases, it is tried to predict the zenith wet delay with help of surface temperature and relative humidity. Unfortunately, surface data are not suited to predict wet delays with sufficient accuracy, so this method may likely fail.
2. *Numerical weather fields.* 3-D numerical weather models can be used to integrate the refractivity profile (→ 4.). In most cases, this yields more realistic estimates in comparison to method 1.
3. *GPS delay estimates.* The GPS filter estimates themselves can be used to define the process noise. However, this implies that *at least* one iteration has to be performed on the previous solution. The first run uses the default process noise as obtained via time series analysis. From these results, tuned noise coefficients are determined and used in the subsequent iteration. The disadvantage of this method is a considerably higher processing load.

3.4.4.2 Validation Study

Figure 3-15 and Figure 3-16 shall help to evaluate the suitability of the three proposed approaches. An arbitrary day for monitoring station *BAHR* is plotted. GPS estimates and numerical weather model results agree rather well except for the last 3.5 hours of the day. Agreement is worse with respect to the Hopfield troposphere model (→ 3.2.1.2.1) that computes wet delays with help of surface meteorological measurements.

For the determination of process noise coefficients, it is most important that the trends agree well. This can be checked with help of Figure 3-16 where the curves of Figure 3-15 have been differentiated. Not unexpectedly, the Hopfield model is partly highly mistaken in comparison to the GPS ZWD partials. Apparently, it cannot be used to define the process noise. Application of these results would lead to severe weighting problems during the Kalman filter process.

Process noise definition with help of numerical weather fields obviously works better but may also show discrepancies of several millimeters per hour in comparison to the GPS results.

Therefore, method 3 seems to be the most favorable way: Dynamic tuning with help of GPS ZWD estimates is most challenging in terms of processing speed due to the needed iteration(s), but is most likely to provide the most realistic q-factors. Usage of GPS ZWD results is also the major reason why *hourly* process noise values are computed because the smoothed hourly results are at least partly free of multipath and similar effects that might be otherwise harmful. A disadvantage of hourly values lies in the fact that the temporal resolution can be inadequate in some cases. Fine structures in delay variability cannot always be resolved. Moreover, if the dynamic process noise coefficients are derived via an initial GPS Kalman filter run with a

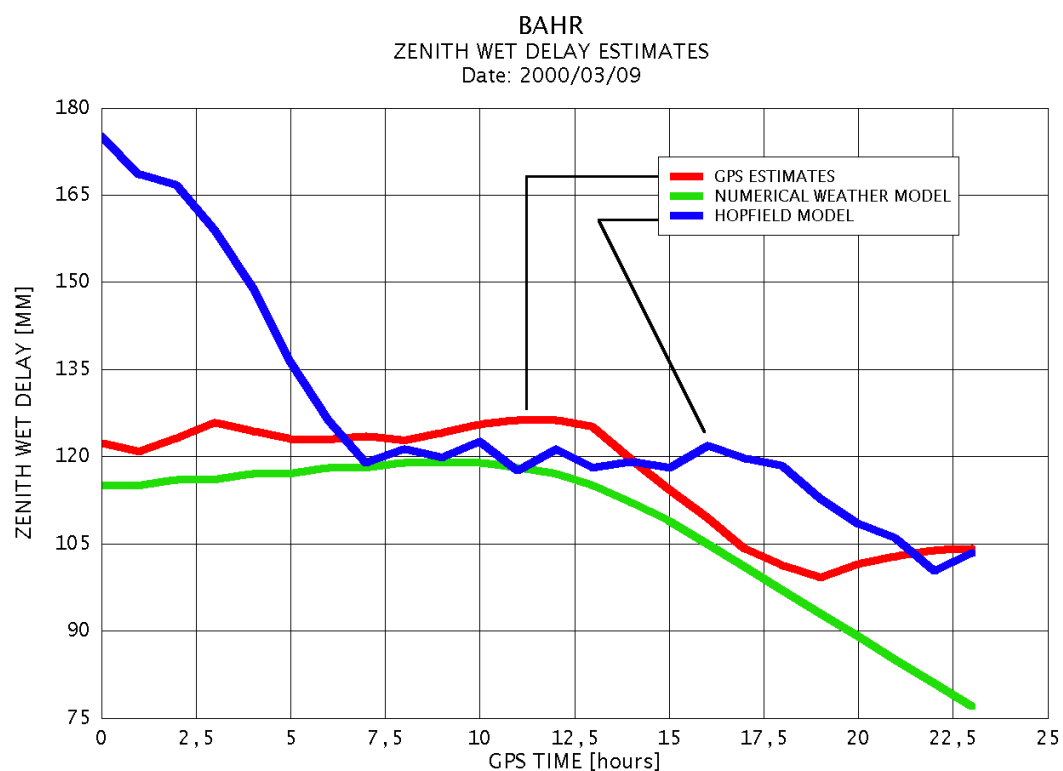


Figure 3-15 - Comparison of zenith wet delays filtered from GPS phase measurements, vertically integrated delays from global numerical weather fields of medium resolution (NOAA/NCEP GDAS $1^\circ \times 1^\circ$) and predictions using the well-known Hopfield troposphere model.

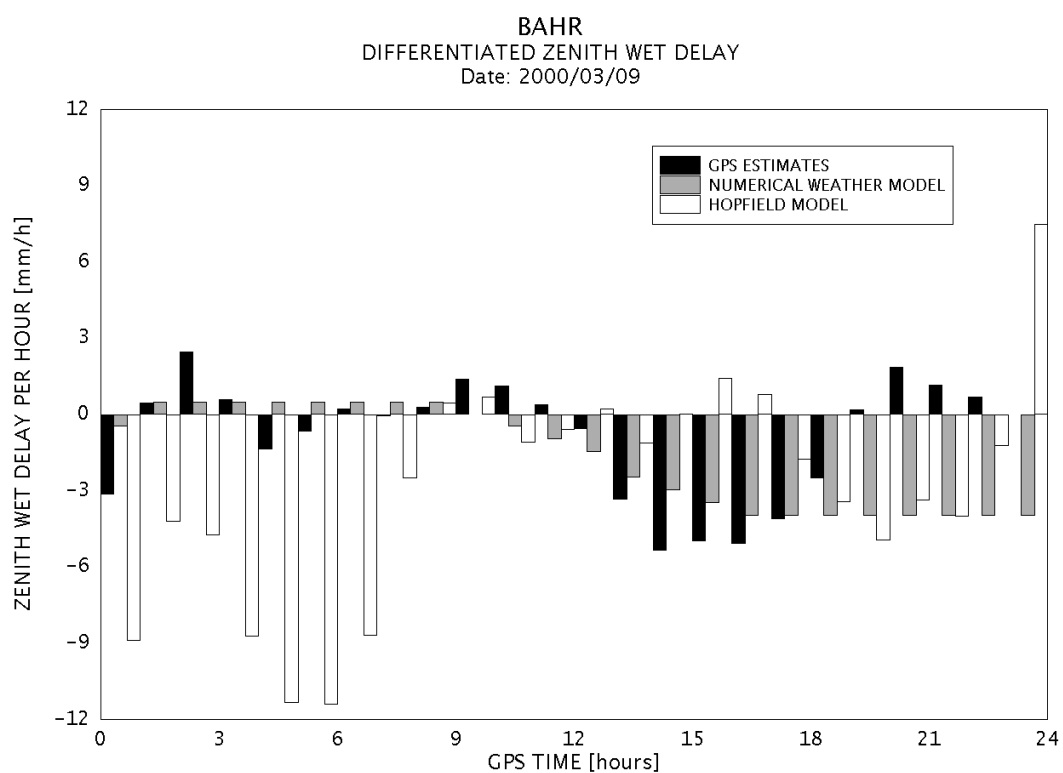


Figure 3-16 - Differentiated ZWD time series of the different estimates shown before. The values numerically correspond to the (signed) \sqrt{q} -factors.

default process noise being too small for the particular day, then the trends of this initial ZWD time series will also be too small resulting in q-factors which are under-dimensioned as well. For this reason, an additional amplification has proven to be useful in practice

$$q \approx \frac{\Delta ZWD^2}{\Delta t} \cdot q_{AMP} \quad (3-152)$$

with q_{AMP} being the amplifier that normally ranges between 1 and 2. The alternative is to perform more than one single iteration. This further increases the processing load or to use the maximum q-factor of the day as default value for this day. The *maximum tuning method* also proved to be useful in everyday use and normally provides sufficiently tuned results after one single iteration.

3.5 Conversion of Wet Delays into Precipitable Water

The zenith wet delay was found to be

$$ZWD = 10^{-6} \cdot \int_{H_0}^{\infty} \left(k'_2 \cdot \frac{e}{T} + k_3 \cdot \frac{e}{T^2} \right) \cdot Z_w^{-1} \cdot dH \quad (3-153)$$

H_0 : surface (antenna) height

k'_2, k_3 : refractivity constants ($k'_2 = 22.1 \text{ K/hPa}$, $k_3 = 370100 \text{ K}^2/\text{hPa}$)

e : partial water vapor pressure in [hPa]

T : temperature in [K]

Z_w^{-1} : inverse compressibility of wet air

and the weighted mean temperature of the atmosphere is defined by MENDES et al. [2000]

$$T_M = \frac{\int_{H_0}^{\infty} \frac{e}{T} \cdot Z_w^{-1} \cdot dH}{\int_{H_0}^{\infty} \frac{e}{T^2} \cdot Z_w^{-1} \cdot dH} \quad (3-154)$$

T_M : weighted mean temperature of the troposphere

3.5.1 Relation between Integrated Water Vapor and Zenith Wet Delay

Under consideration of the preceding definition, the integral for zenith wet delay computation can be rewritten as

$$ZWD = 10^{-6} \cdot \left(k'_2 \cdot \int_{H_0}^{\infty} \frac{e}{T} \cdot Z_w^{-1} \cdot dH + k_3 \cdot \int_{H_0}^{\infty} \frac{e}{T^2} \cdot Z_w^{-1} \cdot dH \right)$$

$$\begin{aligned}
&= 10^{-6} \cdot \left(k'_2 \cdot \int_{H_0}^{\infty} \frac{e}{T} \cdot Z_w^{-1} \cdot dH + k_3 \cdot \int_{H_0}^{\infty} \frac{e}{T^2} \cdot Z_w^{-1} \cdot dH \cdot \frac{\int_{H_0}^{\infty} \frac{e}{T} \cdot Z_w^{-1} \cdot dH}{\int_{H_0}^{\infty} \frac{e}{T} \cdot Z_w^{-1} \cdot dH} \right) \\
&= 10^{-6} \cdot \left(k'_2 \cdot \int_{H_0}^{\infty} \frac{e}{T} \cdot Z_w^{-1} \cdot dH + k_3 \cdot \frac{1}{T_M} \cdot \int_{H_0}^{\infty} \frac{e}{T} \cdot Z_w^{-1} \cdot dH \right) \\
&= 10^{-6} \cdot \left(k'_2 + \frac{k_3}{T_M} \right) \cdot \int_{H_0}^{\infty} \frac{e}{T} \cdot Z_w^{-1} \cdot dH
\end{aligned} \tag{3-155}$$

and with

$$\frac{e \cdot V}{m \cdot T} = R_w \cdot Z_w \Leftrightarrow \frac{e}{T} \cdot Z_w^{-1} = R_w \cdot \frac{m}{V} = R_w \cdot \rho_w \tag{3-156}$$

V: volume

m: mass

M_w : molar mass of water vapor

R_w : specific gas constant for water vapor

ρ_w : density of water vapor

we obtain

$$\begin{aligned}
ZWD &= 10^{-6} \cdot \left(k'_2 + \frac{k_3}{T_M} \right) \cdot \int_{H_0}^{\infty} \rho_w \cdot R_w \cdot dH \\
&= 10^{-6} \cdot \left(k'_2 + \frac{k_3}{T_M} \right) \cdot R_w \cdot \int_{H_0}^{\infty} \rho_w \cdot dH \\
&= 10^{-6} \cdot \left(k'_2 + \frac{k_3}{T_M} \right) \cdot R_w \cdot IWV
\end{aligned} \tag{3-157}$$

a relation between the integrated water vapor IWV and the zenith wet delay ZWD. This conversion factor is furthermore denoted as

$$\varpi = \frac{ZWD}{IWV} = 10^{-6} \cdot R_w \cdot \left(k'_2 + \frac{k_3}{T_M} \right) \tag{3-158}$$

3.5.2 Relation between Precipitable Water and Zenith Wet Delay

Integrated water vapor and precipitable water are related by

$$PW = \frac{IWV}{\rho_{LW}} = \frac{1}{\rho_{LW}} \cdot \int_{H_0}^{\infty} \rho_w \cdot dH \tag{3-159}$$

ρ_{LW} : density of liquid water

and the ratio of wet delay and precipitable water is

$$Q = \frac{ZWD}{PV} = \frac{ZWD}{IWW / \rho_{LW}} = 10^{-6} \cdot R_w \cdot \rho_{LW} \cdot \left(k'_2 + \frac{k_3}{T_M} \right) = 10^{-6} \cdot \rho_{LW} \cdot \frac{R_0}{M_w} \cdot \left(k'_2 + \frac{k_3}{T_M} \right) \quad (3-160)$$

PW: precipitable water

IWW: integrated water vapor

ZWD: zenith wet delay

where the unit of this conversion factor is, of course,

$$[Q] = 1 \frac{\frac{J}{\frac{kg}{mol} \cdot K} \cdot \frac{kg}{m^3}}{\frac{kg}{mol}} \cdot \left(1 \frac{K}{Pa} + 1 \frac{K^2/Pa}{K} \right) = 1 \frac{J}{K \cdot kg} \cdot \frac{kg}{m^3} \cdot \frac{K}{Pa} = 1 \frac{J}{m^3 \cdot Pa} \quad (3-161)$$

$$1 J = 1 N \cdot m \quad 1 Pa = 1 \frac{N}{m^2} \Rightarrow [Q] = 1 \frac{N \cdot m}{m^3 \cdot \frac{N}{m^2}} = 1 \frac{N \cdot m}{N \cdot m}$$

dimensionless. The constants needed for conversion of zenith wet delays into precipitable water or integrated water vapor are known with sufficient accuracy.

3.5.3 Mean Temperature and Conversion Factor Q

It remains to determine the mean temperature of the atmosphere. If the mean temperature is known, conversion is supplied by

$$Q = 0.10200 + \frac{1708.08 [K]}{T_M} \quad (3-162)$$

T_M : weighted mean temperature of the troposphere in [K]

The most accurate way to obtain the mean temperature is the evaluation of the integral expression

$$T_M = \frac{\int_{H_0}^{\infty} \frac{e}{T} \cdot Z_w^{-1} \cdot dH}{\int_{H_0}^{\infty} \frac{e}{T^2} \cdot Z_w^{-1} \cdot dH} \quad (3-163)$$

with help of numerical weather models or radiosonde profiles (\rightarrow 4.). However, it is also possible to determine this quantity with help of surface temperature as demonstrated by numerous authors, e. g. BEVIS et al. [1992 and 1994], EMARDSON [1998, paper F] and MENDES et al. [2000].

3.5.3.1 Global Functions

BEVIS et al. [1992 and 1994] empirically derived the linear function

$$T_M = 70.2 \text{ [K]} + 0.72 \cdot T_0 \quad (3-164)$$

T_0 : surface temperature in [K]

T_M : mean temperature of the atmosphere in [K]

to predict the mean temperature for the region between Alaska and Florida. Further results showed that this function can be applied globally. The RMS shatter of the linear fit with data of 13 radiosonde stations covering two years was about 4.7 K. MENDES et al. [2000] presented slightly different coefficients

$$T_M = 50.4 \text{ [K]} + 0.789 \cdot T_0 \quad (3-165)$$

derived via 50 radiosonde stations and a period of one year. He also points out that for high latitudes, a cubic term

$$T_M = 196.05 \text{ [K]} + 3.402 \cdot 10^{-6} \left[\frac{1}{\text{K}^2} \right] \cdot T_0^3 \quad (3-166)$$

may better approximate the mean temperature. Finally, SOLBRIG [2000] analyzed data sets derived from numerical weather fields for the region of Germany and found

$$T_M = 54.7 \text{ [K]} + 0.77 \cdot T_0 \quad (3-167)$$

what corresponds to the results of Mendes and is therefore also adopted as global function here despite the fact that it has been actually derived for model grid points covering only Germany.

3.5.3.2 Regional Functions

EMARDSON [1998, paper F] analyzed radiosonde data for the European region and developed several empirical models to obtain the conversion coefficient Q . If no surface temperatures are available, Q is modeled as function of latitude ϕ and day of year (DoY)

$$Q = b_0 + b_1 \cdot \phi + b_2 \cdot \sin\left(2\pi \cdot \frac{\text{DoY}}{365}\right) + b_3 \cdot \cos\left(2\pi \cdot \frac{\text{DoY}}{365}\right) \quad (3-168)$$

The coefficients for this model are $b_0 = 5.882$, $b_1 = 0.01113$, $b_2 = 0.064$, $b_3 = 0.127$ and are valid for most parts of the European continent. In case the surface temperature is known, EMARDSON uses several approaches to derive the conversion factor. Only the polynomial expansion of the form

$$Q = a_0 + a_1 \cdot \Delta T + a_2 \cdot \Delta T^2 \quad (3-169)$$

ΔT : difference between surface and average surface temperature, $\Delta T = T_0 - T_{\text{average}}$

Region	a_0	a_1 [1/K]	a_2 [1/K ²]	T_{average} [K]
Baltic	6.550	$-1.56 \cdot 10^{-2}$	$-8.0 \cdot 10^{-5}$	279.19
Central	6.448	$-1.59 \cdot 10^{-2}$	$-1.2 \cdot 10^{-5}$	283.71
Atlantic	6.558	$-2.08 \cdot 10^{-2}$	$-3.7 \cdot 10^{-5}$	279.10
Mediterranean	6.324	$-1.77 \cdot 10^{-2}$	$-7.5 \cdot 10^{-5}$	289.76

Table 3-11 - Mean regional values for the coefficients of the polynomial Q-model taking surface temperature into account; from EMARDSON [1998, paper F].

is presented here. The coefficients a_0 , a_1 , a_2 , and T_{average} are known for a number of European radiosonde sites. Mean regional coefficients are given in Table 3-11; for a full record of site-coefficients the reader may refer to the original publication.

3.5.3.3 Individual Functions

Appendix II gives a table for a large number of tracking stations within the IGS network supplying individual linear conversion coefficients that have been retrieved by ray-tracing in numerical weather models (\rightarrow 4.). Note that the coefficients given there require the surface temperature to be input in degrees centigrade [°C] and the results for the mean temperature will have the same unit.

Region (Latitude)	Regression Coefficient	a [°C]	b [/]
0° ... 20°	0.43	2.9	0.356
20° ... 40°	0.85	-7.3	0.767
40° ... 60°	0.95	-9.4	0.817
> 60°	0.96	-11.4	0.877

Table 3-12 - Regression coefficients and mean regional conversion coefficients sorted by major climatic regions. The tropics are assumed to range from 0° to 20° latitude and the temperate zone from 40° to 60°.

A brief study of the results is interesting because some typical properties are owned by stations lying in the climatic regions listed in Table 3-12: In the tropics, linear trends are rather weak and, consequently, coefficient b approaches zero. Higher latitudes show regression coefficients of clearly more than 0.8, i. e. linear relationships are obviously present.

Figure 3-17 and Figure 3-18 show 4 examples for selected IGS tracking stations of the 4 climate zones. Mauna Kea (*MKEA*, Hawaii) is an extreme example for the tropical belt - but in contrast to many other sites it owns a high altitude - where no linear dependencies can be found. Another example for this group is Cocos Islands (*COCO*) which is not given here. All other stations show clear linear trends.

3.5.3.4 Height Dependency

The mean temperature refers to the atmospheric column between the antenna and the tropopause height. As a consequence, the mean temperature will decrease if the antenna moves upwards, e. g. during a flight experiment. The decrease in temperature

can be easily modeled with help of the vertical temperature gradients, i. e. the temperature lapse rates β for the dry and β_M for the mean temperature. Assuming a linear relation between surface temperature T_0 and mean temperature T_{M0} at height H_0 , the temperature at height H above the surface H_0

$$\begin{aligned} T_{M0} + \beta_M \cdot \Delta H &= a + b \cdot [T_0 + \beta \cdot \Delta H] \quad \wedge \quad \Delta H = H - H_0 \\ \beta_M \cdot \Delta H &= b \cdot \beta \cdot \Delta H + \{a + b \cdot T_0\} - T_{M0} \\ \beta_M \cdot \Delta H &= b \cdot \beta \cdot \Delta H \end{aligned} \quad (3-170)$$

yields the condition

$$\beta_M \stackrel{!}{=} \beta \cdot b \quad (3-171)$$

This means: The linear surface-mean-temperature model could be applied for any height above the surface if the lapse rate of the mean temperature β_M equaled $\beta \cdot b$. Since coefficient b is in the range of 0.75 to 0.9, the lapse rate of the mean temperature must be smaller than that of dry air which usually is about -6.5 K/km. Actually, results from numerical weather fields suggest that the lapse rate of the mean temperature is smaller, around -6 K/km in mid-latitude regions, so that the condition defined above is approximately fulfilled:

$$\beta_M \approx b \cdot \beta \quad (3-172)$$

The linear model for the mean temperature can therefore also be applied for heights above the surface, but a loss of accuracy will likely occur when the height difference ΔH increases.

3.5.4 Conversion Uncertainty

Given the fact that the constants needed for computation of the conversion factor Q are known with sufficient accuracy as stated by BEVIS et al. [1994], the major error contributor is the mean temperature T_M

$$\sigma_Q = \frac{1708.08 \text{ [K]}}{T_M^2} \cdot \sigma_{T_M} \approx \frac{Q}{T_M} \cdot \sigma_{T_M} \quad \Leftrightarrow \quad \frac{\sigma_Q}{Q} = \frac{\sigma_{T_M}}{T_M} \quad (3-173)$$

σ_Q : standard deviation of conversion factor Q

σ_{T_M} : standard deviation of mean temperature T_M

and the relative uncertainties of conversion factor and mean temperature equal each other. Q is typically around 6.2 and the mean temperature is 278 K for a surface temperature of 15 °C. For a standard deviation of the mean temperature of 2 K, the conversion factor is accurate to $\sigma_Q = 0.044$. This uncertainty maps into precipitable water by $\sigma_{PW} = 0.18 \text{ mm}$ (0.18 kg/m² of IWV) for a mean zenith wet delay of 15 cm. This accuracy should be achievable if the mean temperature is extracted from numerical weather models. Using the linear surface-to-mean-temperature relation, one may expect a higher RMS of about 4 K for certain cases what deteriorates the

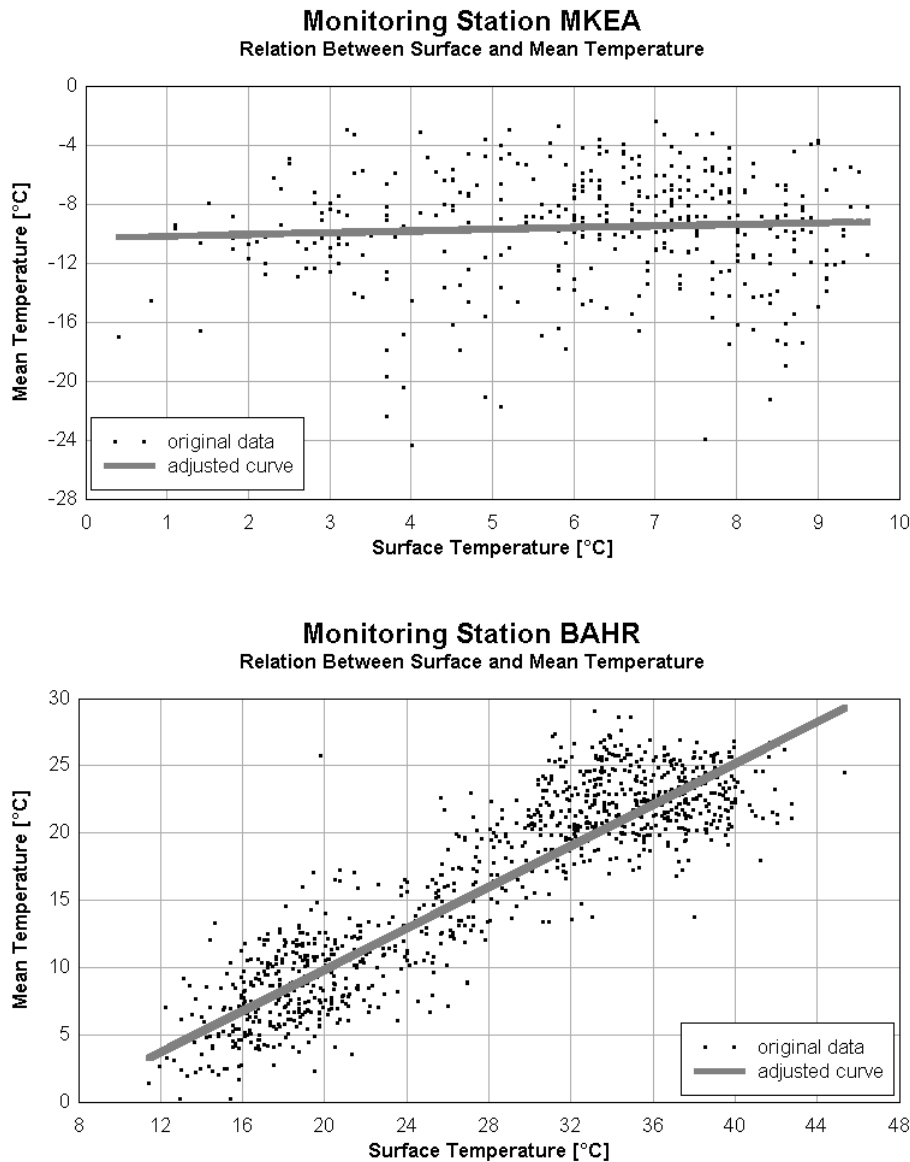


Figure 3-17 - Linear regression analysis results for two tracking stations representing the tropics and sub-tropics. Mauna Kea (MKEA, Hawaii) lies in the tropical belt and does not show any linear trends. Bahrain (BAHR) as an example for the sub-tropics obtains clear linear trend properties, but has a higher shatter than sites in the temperate zone. [scales may differ]

conversion accuracy by a factor of 2 and leads to $\sigma_{pw} = 0.35$ mm. Obviously, the conversion factor is a significant, albeit not the most dominant factor of the total error budget, compared to the other effects discussed in section 3.3.5. For highest precision it is therefore recommended to make use of numerical weather fields or radiosonde data if available. All in all, the outcome of this chapter indicates that the integrated water vapor content can be estimated with an overall accuracy of about 1 to 2 kg/m².

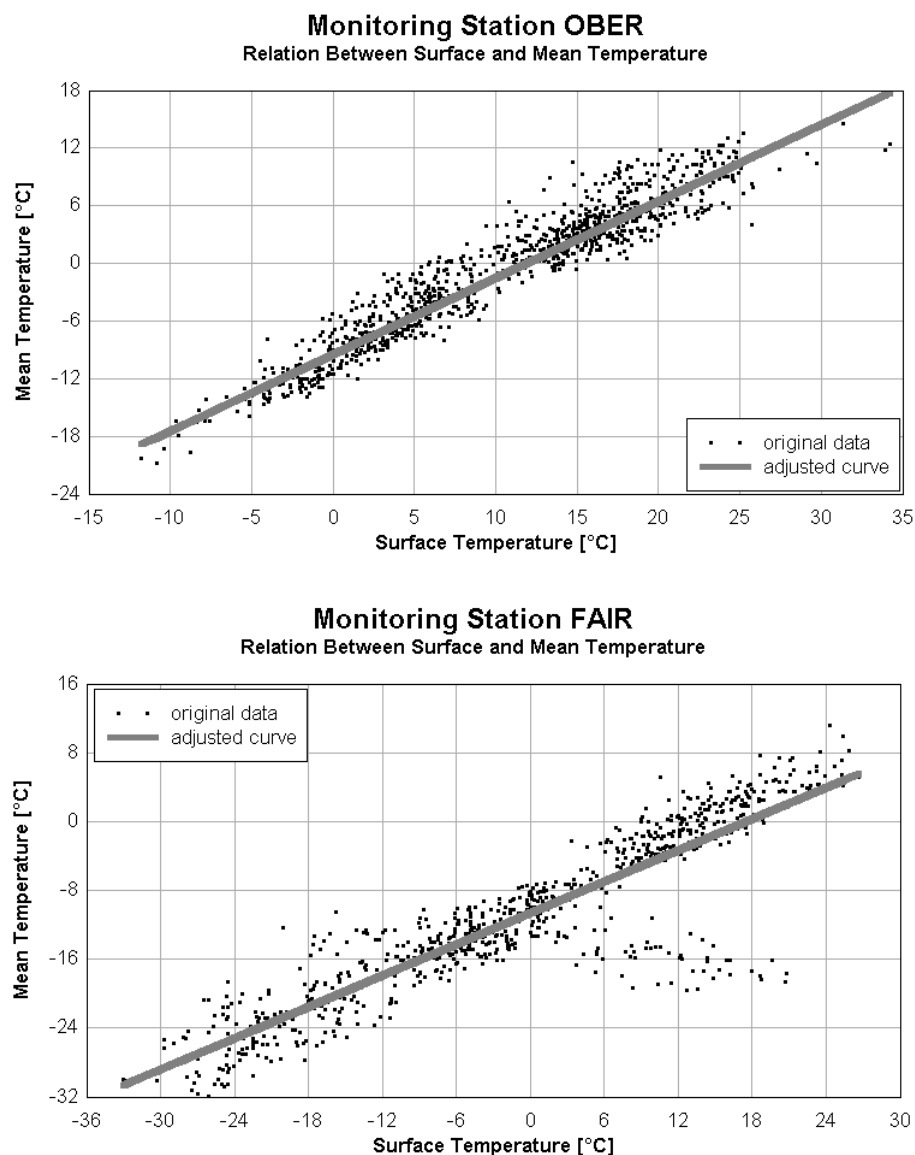


Figure 3-18 - Linear regression analysis results for two tracking stations representing the temperate and the polar zone. Oberpfaffenhofen (OBER, temperate zone) and Fairbanks (FAIR, Alaska/polar region) show clear linear relations. Fairbanks reveals an outlying cluster in the range of 4 to 20 °C of surface temperature. This site is meteorologically problematic as it often suffers from inversion scenarios in the very lower troposphere, see HERRING [1992]. [scales may differ]

4. Application of Numerical Weather Models

The preceding chapter has underlined that the application of GPS to climate research and meteorology is only possible in conjunction with meteorological information. Most important quantities are surface pressure for the separation of hydrostatic and wet delays as well as the mean atmospheric temperature or, alternatively, surface temperature. Unfortunately, most stations of permanent tracking networks used for this study proved to be incapable of providing the needed meteorological data. This fact was the primary motivation for investigating the potential of numerical weather models as source for the needed surface and atmospheric data. At first instance, surface meteorological data are of interest (\rightarrow 4.2), but 3-D weather fields also allow to perform ray-tracing for the derivation of regional mapping function coefficients as well as horizontal gradients (\rightarrow 4.3). Moreover, weather fields can be used for vertical profile integration yielding wet delays that can be used for Kalman filter initialization and may even provide stand-alone gridded tropospheric corrections files (\rightarrow 4.4) that also serve as basis for the combination of numerical weather model and GPS delays (\rightarrow 4.5) providing an improved solution.

4.1 Contents of Numerical Weather Fields

All weather fields that have been used for this study are operationally produced by the National Center for Environmental Prediction (NCEP) of the U. S. National Oceanic and Atmospheric Administration (NOAA). A summary of the output field characteristics is given in Table 4-1 below. All output fields are supplied in standard GRIB format, a binary, compressed format for gridded data documented by DEY [1998]. For details on how numerical weather models work refer to PARRISH and DERBER [1992], KANAMITSU et al. [1991] and BLACK [1994] for instance¹.

Acronym	Dimension of Field	Resolution of Field	Projection and Coverage	Remarks
GDAS	360 x 181 = 65 160 points/layer	1° x 1° (111 km at equator)	equi-rectangular (matrix layout), entire globe	GRIB ID 3, global model final analysis (FNL) takes place each 6 hours
EDAS	129 x 185 = 23 865 points/layer	40.6 km	Lambert conformal, USA only	GRIB ID 212, regional (USA) Mesoscale Eta model analysis each 3 hours
ETA	110 x 147 = 16 170 points/layer	90.8 km at 60° N latitude	polar stereographic, Alaska, Canada, Northern USA	GRIB ID 104, North America NGM Super C grid Eta Analysis (each 6 hours)

Table 4-1 - Characteristics of the numerical weather fields available from the U. S. National Center for Environmental Prediction (NCEP, NOAA). The abbreviations given are only used to provide a simple identification within the text and do not necessarily represent official names. The GRID IDs specifying the contents are given in the very right column.

¹ Latest modifications to the weather models operated by the National Center for Environmental Prediction (NCEP) and further materials can also be found online in the "EMC Model Documentation" via <http://www.emc.ncep.noaa.gov/modelinfo/index.html>

4.1.1 Contents and Resolution of GDAS-Fields

The *Global Data Assimilation System* (GDAS) is by far the most extensively used weather field for this work² and the output field representation is shown in Figure 4-1. The output grid has a horizontal resolution of about 111 km at the equator and a temporal resolution of 6 hours with 3 h forecast cycles. This means that a final analysis takes place at 00, 06, 12 and 18 h UTC and serves as basis for predictions in 3 h intervals. A full diurnal data set will therefore contain 4 analysis and 4 prediction fields as well as the very first analysis fields of the following day in order to suppress any extrapolation of data.

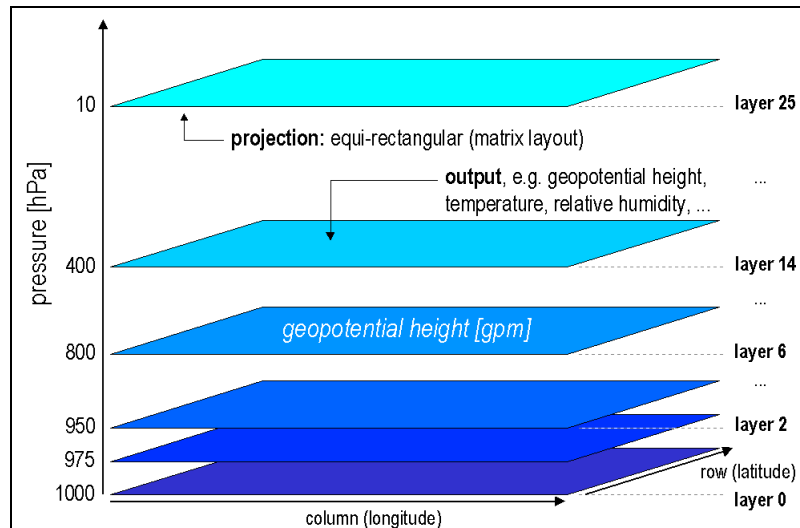


Figure 4-1 - Data representation in global numerical weather fields of type GRIB 3 (NOAA NCEP GDAS $1^\circ \times 1^\circ$). The data in the output fields are organized in 26 vertical layers containing geopotential heights for the corresponding pressure levels as well as temperature. Relative humidity is given for 21 layers. In horizontal direction, the data are stored in matrix layout (i. e. an equi-rectangular projection is used) with 181 rows and 360 columns corresponding to a resolution of $1^\circ \times 1^\circ$.

The vertical coordinate is normally given in form of pressure layers. Geopotential height values as well as temperature and relative humidity are associated with levels of constant pressure. GDAS weather fields contain 26 vertical pressure layers up to 10 hPa (corresponds to a height of approx. 26 km). Relative humidity is given for the lowest 21 vertical levels up to 100 hPa (about 15 km). Surface layers for geopotential height (digital elevation model), pressure, temperature and relative humidity complete the data set needed for computation of refractivity profiles. Moreover, special information like the tropopause height and the precipitable water layer for the total atmospheric column are used in routine analysis.

4.1.2 Height Systems

Following HEISKANEN and MORITZ [1993, p. 162], dynamic heights that are hereafter synonymously called *geopotential heights*³ describe a height system that is linked to potential layers and defined by the difference in geopotential of

² For this reason, all algorithms described here refer to GDAS $1^\circ \times 1^\circ$ weather fields, but can be applied to the other weather fields in a similar manner.

³ The dynamic height system is most commonly used in meteorology and climatology. However, meteorologists prefer the term *geopotential height* instead of *dynamic height* since this height is directly derived from a difference in *geopotential*. For the sake of compatibility, the term *geopotential height* is applied throughout this thesis.

$$W_0 - W_P = \int_0^P g \cdot dn \quad (4-1)$$

W_0 : geopotential at mean sea level (zero altitude)

W_P : geopotential at point P

g : gravity acceleration

dn : leveled height difference

where W_0 denotes the geopotential at mean sea level, i. e. it represents the geoid, and W_P denotes the geopotential at point P . This difference in geopotential is scaled by the normal gravity at a latitude of $\varphi = 45^\circ$

$$H = \frac{\int_0^P g \cdot dn}{\gamma_0^{45}} \quad (4-2)$$

H : geopotential height at point P

γ_0^{45} : normal gravity at $\varphi = 45^\circ$ (WGS84: $\gamma_0^{45} = 9.806200 \text{ m/s}^2$)

and yields the geopotential height at point P . A usually sufficient approximation for geopotential heights for our purposes are orthometric heights

$$H_{OM} = h - N = \frac{\int_0^P g \cdot dn}{g^*} \quad \wedge \quad g^* = \frac{1}{H_{OM}} \cdot \int_0^P g \cdot dH_{OM} \approx g + 4.24 \cdot 10^{-7} \left[\frac{1}{s^2} \right] \cdot H_{OM} \quad (4-3)$$

H_{OM} : orthometric height

h : ellipsoidal height

N : geoid height

g^* : gravity acceleration at $\frac{1}{2} \cdot H_{OM}$

g : gravity acceleration at H_{OM}

that can be easily determined by knowledge of ellipsoidal heights derived via GPS and the geoid undulation. The latter is determined using the global geopotential model EGM96 [NASA/NIMA, 1998] and has an accuracy of 1-2 m, in non-mountainous regions even better. A height uncertainty of 2 meters will map into a pressure bias of roughly 0.25 hPa and is about to be tolerable. The difference between geopotential and orthometric heights is in the range of a few decimeters in most cases, but with increased uncertainty for high altitudes. Therefore, the following approximation based on the WGS84 normal gravity potential is suggested where the zero level normal gravity is

$$\gamma_0 = 9.780327 \left[\frac{m}{s^2} \right] \cdot (1 + 0.0053024 \cdot \sin^2 \varphi - 5.8 \cdot 10^{-6} \cdot \sin^2 2\varphi) \quad (4-4)$$

γ_0 : normal gravity at $h = 0 \text{ m}$

and is height-referenced by

$$\gamma = \gamma_0 \cdot \left(1 + \frac{2 \cdot h}{a} \cdot (1 + f + m - 2 \cdot f \cdot \sin^2 \varphi) + \left(\frac{9 \cdot h}{a} \right)^2 \right) \quad (4-5)$$

γ : normal gravity at ellipsoidal height h

a : semi-major axis of WGS84 ellipsoid ($a = 6378137.0$ m)

f : flattening of WGS84 ellipsoid ($f = 0.00335281068$)

m : WGS84-constant accounting for centrifugal potential ($m = 3.449786 \cdot 10^{-3}$)

Now, the value g^* is computed

$$g^* = g + 4.24 \cdot 10^{-7} \left[\frac{1}{s^2} \right] \cdot H_{OM} \approx \gamma + 4.24 \cdot 10^{-7} \left[\frac{1}{s^2} \right] \cdot H_{OM} \quad (4-6)$$

by substitution of the actual gravity g at point P by the normal gravity γ . Consequently, the geopotential can be derived by

$$W_0 - W_P = H_{OM} \cdot g^* \quad (4-7)$$

and the geopotential height is then computed by

$$H = \frac{W_0 - W_P}{\gamma_0^{45}} \quad (4-8)$$

Alternatively, the reduction term can be determined having a look at the difference between orthometric and geopotential heights

$$H - H_{OM} = \frac{g^* - \gamma_0^{45}}{\gamma_0^{45}} \cdot H_{OM} - \frac{g_0^* - \gamma_0^{45}}{\gamma_0^{45}} \cdot H_{OM0} = \frac{g^* - \gamma_0^{45}}{\gamma_0^{45}} \cdot H_{OM} \quad (4-9)$$

H_{OM} : orthometric height

H_{OM0} : orthometric height at mean sea level (zero by definition)

Again, g^* will be usually evaluated with help of the normal gravity potential what is sufficient as far as the accuracy is concerned.

4.1.3 Horizontal Coordinates

The horizontal coordinates are originally given in form of row and column where the row corresponds to the latitude and the column to the longitude. As for the case of IONEX files (\rightarrow 2.2.4.3.1), the ellipsoidal latitude φ is not used, but the geocentric latitude φ^*

$$\tan \varphi^* = (1 - f)^2 \cdot \tan \varphi \quad (4-10)$$

φ^* : geocentric latitude (WGS84)

φ : ellipsoidal latitude (WGS84)

f : flattening of WGS84 ellipsoid ($f = 1/298.257224$)

The latitude/longitude coordinate pair ϕ^*, λ is called *geographic coordinates* in this chapter in order to distinguish it from the ellipsoidal (*geodetic*) coordinates. The detailed transformation equations to convert rows/columns into latitude/longitude will be presented in → 4.2.1.3.

4.2 Surface Data Extraction

Surface meteorological data⁴ comprise total pressure, temperature and relative humidity (or partial water vapor pressure) and are exchanged in standardized RINEX format, see GURTNER [1998]. Many troposphere models need surface data as input (→ 3.2.1), especially surface pressure is of high importance for the determination of hydrostatic delays in zenith direction (→ 3.2.1.1.2). The accuracy requirement for pressure is in the range of 0.5 hPa to a maximum of 1 hPa corresponding to roughly 1.5 to 3 mm error in ZHD. Surface temperature is less important, but can be necessary to model the mean atmospheric temperature for conversion of ZWD into precipitable water PW (→ 3.5). Surface humidity together with temperature is frequently input into wet delay models (→ 3.2.1.2.1, → 3.2.1.2.3). Such models can be used to predict tropospheric delays and may serve for Kalman filter initialization. However, it should be noted that numerical weather models also allow to integrate the wet refractivity profiles directly (→ 4.3, → 4.4) yielding wet delays of higher accuracy.

4.2.1 Surface Pressure

Surface pressure is by far the most important quantity discussed here because of its importance for hydrostatic delay estimation. The main steps for data extraction are outlined for this quantity in detail and can be applied analogously to the other types of surface data. Major algorithmic differences occur in terms of vertical interpolation that is handled differently for pressure (exponential interpolation) in comparison to surface temperature (linear interpolation), for instance.

4.2.1.1 Interpolation Sequences

Two approaches for horizontal-vertical-interpolation sequences are displayed in Figure 4-2 and both methods are based on the 4 nearest neighboring horizontal grid points of the weather field.

The first method is called *1-pillar-method* in this context. For each layer, all grid points are linked to the same pressure value p , of course, and the dependent variable is the geopotential height. p^{i-1} denotes the pressure associated with vertical layer number $i-1$ and the geopotential heights H_1^{i-1} , H_2^{i-1} , H_3^{i-1} and H_4^{i-1} are certainly different for the four nearest horizontal neighbors surrounding the target point that is to be interpolated. For each - or at least the two nearest - pressure layers, the corresponding geopotential height is horizontally interpolated for the geographical coordinates ϕ^*, λ of the antenna site giving a set of height/pressure pairs, i. e. the vertical pressure-profile above the antenna is extracted. Afterwards, vertical interpolation is performed

⁴ The term *surface data* is used synonymously for *antenna height data* for matters of convenience, albeit it is clear that meteorological data at the antenna site are to be extracted that might differ from the surface height.

between the two nearest geopotential height/pressure pairs H^{i-1}, p^{i-1} and H^{i+1}, p^{i+1} . In this way, the requested pressure p^i at the antenna height H^i is determined.

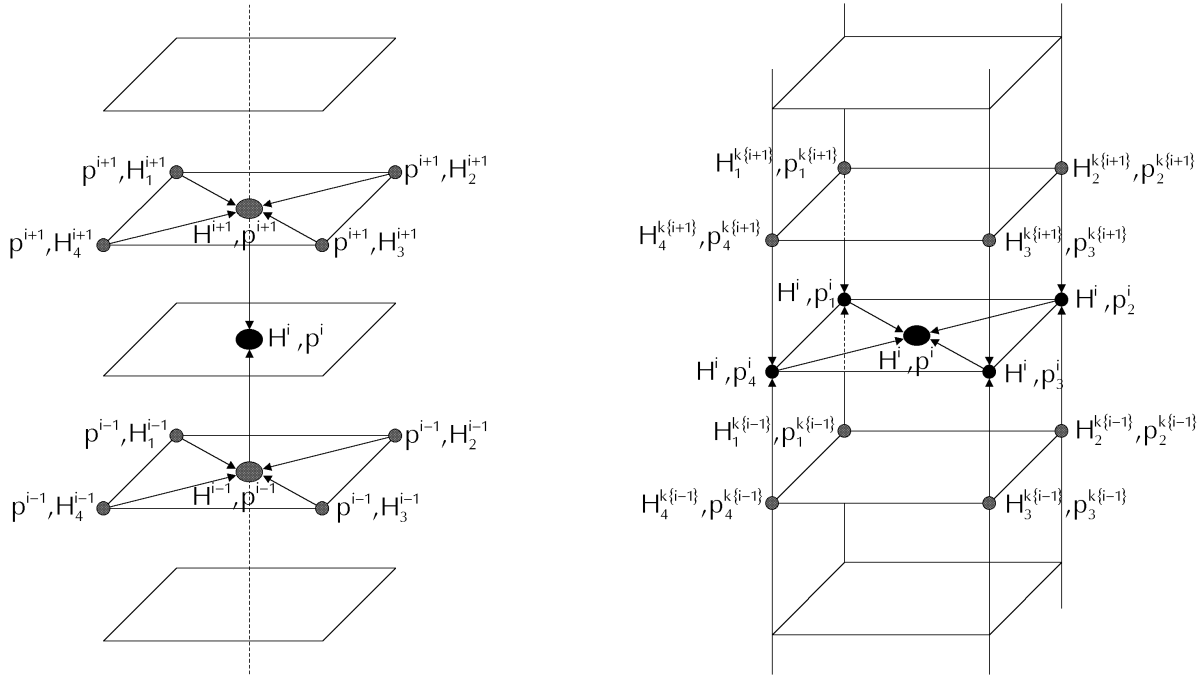


Figure 4-2 - Vertical and horizontal interpolation sequences illustrated for surface pressure determination. The 1-pillar-method performs horizontal interpolation for the pressure layers first and thereby interpolates the geopotential height for the horizontal position of the target point at the corresponding pressure level. Afterwards, vertical interpolation is performed using the two nearest vertical neighbors. The 4-pillar-method follows a different strategy: First, vertical interpolation is performed for all 4 neighboring pillars. This yields pressure values which are already referenced to the height of the target point. After this, horizontal interpolation takes place.

The *4-pillar-method* makes use of the 4 neighboring pressure profiles and performs vertical interpolation first of all. This means that the two nearest geopotential heights, e. g. $H_1^{k\{i-1\}}$ and $H_1^{k\{i+1\}}$ are looked up⁵ as well as their pressure values $p_1^{k\{i-1\}}$ and $p_1^{k\{i+1\}}$. The latter are interpolated at the antenna height H^i and afterwards, all 4 pressure values $p_1^i, p_2^i, p_3^i, p_4^i$ referenced to the antenna height are horizontally interpolated for the geographical coordinates φ^*, λ of the tracking station.

Both methods have been used with good results. A slight preference is set for the 4-pillar-method, because vertical interpolation is based a bit more on physical models than horizontal interpolation: The vertical pressure profile can be modeled with exponential functions (\rightarrow 4.2.1.2) that meet reality rather well whereas horizontal interpolation is mainly based on nearest neighbor algorithms and stochastic

⁵ It is emphasized that the layer indices $k\{i-1\}$ and $k\{i+1\}$ are individually specified for each of the 4 columnar profiles by the nearest neighbor criterion. k is the layer index and is a function of H_j , i. e. of the vertical profile of pillar $j = 1, 2, 3, 4$ with respect to the nearest downward $\{i-1\}$ or the nearest upward $\{i+1\}$ height value. Consequently, $k\{i-1\}$ for H_1 might be different from $k\{i-1\}$ for H_2 . Albeit Figure 4-2 (right) displays the data in layered order, the vertically nearest quantities may in principle belong to different pressure layers. In contrast to the 1-pillar-method, geopotential height H is the primary variable here and p is the dependent one.

interpolation. In contrast to the 1-pillar-method, the weight of the 4-pillar-method lies more on vertical interpolation that is performed for all 4 neighboring columns and horizontal interpolation is only performed once. This fact should be especially valuable in cases where extrapolation⁶ is necessary.

4.2.1.2 Vertical Interpolation

Recalling the state equation for ideal gases

$$dp = -g \cdot \rho \cdot dH \quad (4-11)$$

dp : differential change in pressure

g : gravity, assumed to be constant with height

ρ : density of dry air, assumed to be constant

dH : differential change in height

and inserting

$$\frac{\rho}{\rho_0} = \frac{p}{p_0} \Leftrightarrow \rho = \rho_0 \cdot \frac{p}{p_0} \quad (4-12)$$

ρ : mass density at height H

ρ_0 : mass density at surface height H_0

p : pressure at height H

p_0 : surface pressure

into the state equation yields

$$dp = -g \cdot \rho_0 \cdot \frac{p}{p_0} \cdot dH \Leftrightarrow \frac{dp}{p} = -\frac{g \cdot \rho_0}{p_0} \cdot dH \quad (4-13)$$

Evaluation of the integral equation

$$\int_{p_0}^p \frac{1}{p} \cdot dp = -\frac{g \cdot \rho_0}{p_0} \cdot \int_{H_0}^H dH \quad (4-14)$$

leads to the model

$$\ln p - \ln p_0 = \ln \frac{p}{p_0} = -\frac{g \cdot \rho_0}{p_0} \cdot (H - H_0) \Leftrightarrow p = p_0 \cdot \exp\left(-\frac{g \cdot \rho_0}{p_0} \cdot (H - H_0)\right) \quad (4-15)$$

describing the vertical decrease of pressure⁷. The term $g \cdot \rho_0 \cdot p_0^{-1}$ can be interpreted as the inverse scale height q_p

⁶ Extrapolation is one of the major problems of surface data extraction in numerical weather fields. For this reason, the algorithms do not only make use of the vertical layers, but also take the surface layers for pressure, geopotential height, temperature and humidity into account.

⁷ In many cases, but not here, this formula is applied for the case of H_0 and p_0 being the sea level values of height (zero) and pressure (about 1013 hPa).

$$p = p_0 \cdot \exp\left(-\frac{H-H_0}{q_p}\right) \quad \wedge \quad q_p = \frac{p_0}{g \cdot \rho_0} \quad (4-16)$$

and this pressure scale height becomes $q_p = 8$ km with $p_0 = 1013.25$ hPa, $g = 9.806$ m/s² and $\rho_0 = 1.293$ kg/m³. We will see later that this scale height is about 4 to 6 times larger than the water vapor scale height. WITTE and SCHMIDT [1991, p. 345] give a modified formula that can be rewritten in the form

$$p = p_0 \cdot \exp\left(-\frac{H-H_0}{q_p \cdot q_t \cdot q_e \cdot q_\phi \cdot q_H}\right) \quad (4-17)$$

q_t : temperature correction

q_e : water vapor (humidity) correction

q_ϕ : latitudinal gravity correction

q_H : height gravity correction

and applies corrections for temperature and humidity as well as for the gravity impact. The corrections are

$$\begin{aligned} q_t &= 1 + \alpha \cdot t \\ q_e &= 1 + \delta \cdot \frac{e_m}{H_m} \\ q_\phi &= 1 + \beta \cdot \cos 2\phi \\ q_H &= 1 + \frac{2 \cdot H_m}{r} \end{aligned} \quad (4-18)$$

α : temperature expansion coefficient for air ($\alpha = 0.003665$ [1/°C])

t : temperature in [°C]

δ : ratio of water vapor density to density of dry air ($\delta = 0.377$)

H_m : mean height, $H_m = \frac{1}{2} \cdot (H + H_0)$

e_m : water vapor at H_m

β : flattening coefficient describing the gravity field ($\beta = 0.00264$)

ϕ : latitude of station

r : earth radius ($r = 6371$ km)

BEAVAN et al. [1997] use the following standard formula for pressure reduction

$$p = p_0 \cdot \left[1 + \left(\frac{8.419 \cdot 10^{-5} \cdot (H_0 - H)}{p_0^{0.190284}} \right) \right]^{5.255303} \quad (4-19)$$

that is optimized for New Zealand, but also proved to be applicable globally.

Generally speaking, it is possible to predict the pressure p at height H directly with knowledge of one single pressure-height-pair p_0, H_0 . However, the formulas presented so far will show an increasing error with increasing height difference $H-H_0$. Therefore,

it is recommended to apply the formula to both the nearest upper and lower pressure layer

$$\begin{aligned} p_{\uparrow}^i &= f(p^{i-1}, H^{i-1}, H^i) \quad \wedge \quad w_{\uparrow}^i = \frac{1}{(H^{i-1} - H^i)^2} \\ p_{\downarrow}^i &= f(p^{i+1}, H^{i+1}, H^i) \quad \wedge \quad w_{\downarrow}^i = \frac{1}{(H^{i+1} - H^i)^2} \end{aligned} \quad (4-20)$$

p_{\uparrow}^i : pressure at height H^i , computed via the nearest lower point at H^{i-1}

w_{\uparrow}^i : weight of pressure p_{\uparrow}^i

where for $f(p, \dots)$ either formula 4-16, 4-17 or 4-19 can be adopted. The weights are denoted as w and defined by the reciprocal squared height difference. The weighted mean pressure

$$p^i = \frac{w_{\uparrow}^i}{w_{\uparrow}^i + w_{\downarrow}^i} \cdot p_{\uparrow}^i + \frac{w_{\downarrow}^i}{w_{\uparrow}^i + w_{\downarrow}^i} \cdot p_{\downarrow}^i \quad (4-21)$$

is treated as the final, vertically interpolated value. Alternatively, formula 4-16 can be used to derive the scale height q_p empirically

$$q_p = - \frac{H^{i+1} - H^{i-1}}{\ln p^{i+1} - \ln p^{i-1}} \quad (4-22)$$

with the height/pressure-pairs H^{i-1} , p^{i-1} and H^{i+1} , p^{i+1} of the two nearest vertical neighbors being used. Now, the pressure p at target height H can be exponentially interpolated with formula 4-16 where for H_0 and p_0 either the values for the downward ($i-1$) or the upward ($i+1$) vertical neighbors can be inserted.

4.2.1.3 Horizontal Interpolation

First, a relation between the geographical coordinates and the computer-internal matrix of rows (z) and columns (s) must be established. Since GDAS weather fields are projected in an equi-rectangular matrix layout, transformation is accomplished with the linear functions

$$\begin{aligned} z &= \Delta z + f_z \cdot \phi^* \\ s &= \Delta s + f_s \cdot \lambda \end{aligned} \quad (4-23)$$

Δz : offset (rows)

Δs : offset (columns)

f_z : scaling factor (rows)

f_s : scaling factor (columns)

ϕ^*, λ : geographic coordinates (latitude and longitude)

with

$$\begin{aligned}
f_z &= \frac{z_N - z_S}{\phi_N^* - \phi_S^*} = \frac{0 - 180}{+90^\circ - (-90^\circ)} = -1 [\text{rows}/^\circ] \quad \wedge \quad \Delta z = z_N - f_z \cdot \phi_N^* = -90 [\text{rows}] \\
f_s &= \frac{s_E - s_W}{\lambda_E - \lambda_W} = \frac{359 - 0}{359^\circ - 0^\circ} = +1 [\text{cols}/^\circ] \quad \wedge \quad \Delta s = s_W - f_s \cdot \lambda_W = 0 [\text{cols}]
\end{aligned}
\tag{4-24}$$

For a given coordinate ϕ^*, λ , the (floating) grid coordinates z, s can be determined. With help of the integer-to-float differences

$$\Delta z_{1,1} = \text{int}(z) - z \quad \wedge \quad \Delta s_{1,1} = \text{int}(s) - s \tag{4-25}$$

$\Delta z_{1,1}$: difference of integer row and floating row, offset to nearest neighbor with index 1,1

$\Delta s_{1,1}$: difference of integer and floating column, offset to nearest neighbor with index 1,1

and

$$\Delta z_{2,2} = 1 + \Delta z_{1,1} \quad \wedge \quad \Delta s_{2,2} = 1 + \Delta s_{1,1} \tag{4-26}$$

$\Delta z_{2,2}$: difference of integer row and floating row, offset to nearest neighbor with index 2,2

$\Delta s_{2,2}$: difference of integer and floating column, offset to nearest neighbor with index 2,2

it is possible to derive the matrix coordinates of the 4 nearest neighbors:

$$\begin{aligned}
z_{1,1} &= \text{int}(z + \Delta z_{1,1}) \quad \wedge \quad s_{1,1} = \text{int}(s + \Delta s_{1,1}) \\
z_{2,2} &= \text{int}(z + \Delta z_{2,2}) \quad \wedge \quad s_{2,2} = \text{int}(s + \Delta s_{2,2}) \\
z_{1,2} &= z_{1,1} \quad \wedge \quad s_{1,2} = s_{2,2} \\
z_{2,1} &= z_{2,2} \quad \wedge \quad s_{2,1} = s_{1,1}
\end{aligned}
\tag{4-27}$$

The locations of these points are illustrated in Figure 4-3. Note that 9 nearest neighbors instead of 4 are used for the EDAS and ETA weather fields.

Horizontal interpolation is performed by weighted averaging. The weights are determined with help of the spherical distance between the grid and the antenna points. For this purpose, the row/column coordinates are transformed into geographical coordinates

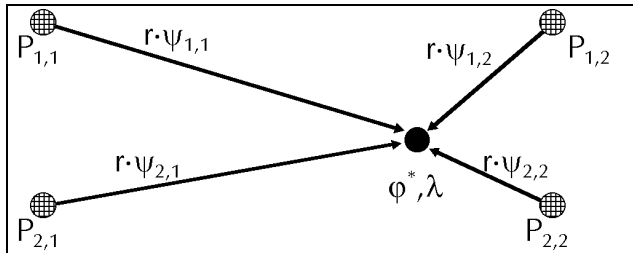


Figure 4-3 - Nearest horizontal neighbors for point ϕ^*, λ . The spherical distances between the grid points P_{ij} and the target point are indicated by $r \cdot \psi_{ij}$ with r being the earth radius.

$$\phi_{i,j}^* = \frac{\Delta z_{i,j} - \Delta z}{f_z} \quad \wedge \quad \lambda_{i,j} = \frac{\Delta s_{i,j} - \Delta s}{f_s} \tag{4-28}$$

and the spherical distance is calculated with help of

$$\cos \psi_{i,j} = \sin \phi_{i,j}^* \cdot \sin \phi^* + \cos \phi_{i,j}^* \cdot \cos \phi_{i,j}^* \cdot \cos(\lambda_{i,j} - \lambda) \tag{4-29}$$

ψ_{ij} : spherical distance between point P_{ij} and ϕ^*, λ in [rad]

yielding normalized weights w

$$w_{ij}^* = \psi_{ij}^{-c} \Rightarrow w_{ij} = \frac{w_{ij}^*}{w_{1,1}^* + w_{1,2}^* + w_{2,1}^* + w_{2,2}^*} \quad (4-30)$$

w_{ij}^* : weighting coefficient associated with point P_{ij} , not normalized

w_{ij} : normalized weighting coefficient associated with point P_{ij}

where c is the weighting-power⁸. Now, the horizontally interpolated pressure

$$p = w_{1,1} \cdot p_{1,1} + w_{1,2} \cdot p_{1,2} + w_{2,1} \cdot p_{2,1} + w_{2,2} \cdot p_{2,2} \quad (4-31)$$

can be calculated. Note that the sum of all weights equals 1 as they have been normalized before.

4.2.1.4 Temporal Interpolation

Interpolation in time domain is performed using either linear trend functions or cubic splines. For further information on their theory and implementation refer to PRESS et al. [1992, pp. 113-116]. Generally speaking, splines are preferred if only the final analysis fields are processed that are given each 6 hours. If the intermediate predictions at 3 hour intervals are also computed, linear interpolation is appropriate as well.

4.2.2 Surface Temperature

Horizontal and temporal interpolation is performed in the same way as for surface pressure. The vertical interpolation of temperature, however, does not follow an exponential function. Instead, a linear decrease up to the tropopause height can be assumed. Therefore, linear interpolation

$$T^i = T^{i-1} + \frac{H^i - H^{i-1}}{H^{i+1} - H^{i-1}} \cdot (T^{i+1} - T^{i-1}) \quad (4-32)$$

T : temperature, i denotes the interpolated surface temperature, $i-1$ is the temperature of the nearest downward pressure layer and $i+1$ is that of the nearest upward layer

H : geopotential height

between the two nearest vertical neighbors is proper here. Actually, inversion layers may occur in the first few hundred meters above the surface that can cause deviations from a homogenous, linear temperature decrease. Although the vertical resolution of the weather fields is higher in the lower troposphere and hence mitigates inversion problems, the accuracy of the interpolated surface temperature can be deteriorated in presence of inversion situations.

⁸ The weighting power is normally chosen to be between 1 and 2. For pressure, a value between 1 and 1.5 is suitable.

4.2.3 Surface Humidity

Surface humidity is a rather difficult data type to extract due to its more or less irregular distribution that can be seen in Figure 3-2. Temporal and horizontal interpolation methods equal those applied for surface pressure extraction again. As far as vertical interpolation is concerned, relative humidity quantities can be interpolated linearly as it is done for temperature data

$$RH^i = RH^{i-1} + \frac{H^i - H^{i-1}}{H^{i+1} - H^{i-1}} \cdot (RH^{i+1} - RH^{i-1}) \quad (4-33)$$

RH: relative humidity, i denotes the interpolated surface humidity, $i-1$ is the humidity of the next lower pressure layer and $i+1$ is that of the next higher layer

H: geopotential height

or, alternatively, a transformation into partial water vapor pressure can be performed. Relative humidity is defined as

$$RH = \frac{e}{e_s} \cdot 100 \Leftrightarrow e = e_s \cdot \frac{RH}{100} \quad (4-34)$$

e : partial water vapor pressure

e_s : saturation water vapor pressure

where, after HANSEN [1998, p. 15], the saturation water vapor pressure can be computed with the Clausius-Clapeyron equation

$$e_s = e_0 \cdot \exp\left(\frac{L}{R_e} \cdot \left(\frac{1}{T_0} - \frac{1}{T}\right)\right) \quad (4-35)$$

T_0 : freezing-point temperature in [K], $T_0 = 273.15$ K

e_0 : partial water vapor pressure corresponding to T_0 , $e_0 = 6.11$ hPa

L : latent heat of vaporization over a flat water surface, $L = 2.83 \cdot 10^6$ J/kg

R_e : specific gas constant for water vapor, $R_e = 461$ J·K⁻¹·kg⁻¹

that is a function of temperature and other atmospheric constants. The *Honeywell Moisture Tutorial*, HONEYWELL [1999], gives results of non-linear regression fits for precise computation of the saturation pressure over ice for a temperature range of -100 °C to 0 °C

$$\ln e_s = \frac{C_1}{T} + C_2 + C_3 \cdot T + C_4 \cdot T^2 + C_5 \cdot T^3 + C_6 \cdot T^4 + C_7 \cdot \ln T \quad (4-36)$$

e_s : water vapor saturation pressure in [psia], 1 psia = 68.94745 hPa

T : absolute temperature in [°R] where $T_{[°R]} = T_{[°F]} + 459.67$ [°R] = $T_{[°C]} \cdot 1.8$ [°R/°C] + 491.67 [°R]

$C_1 = -1.0214165 \cdot 10^4$

$C_5 = 3.5575832 \cdot 10^{-10}$

$C_2 = -4.8932428$

$C_6 = -9.0344688 \cdot 10^{-14}$

$C_3 = -5.3765794 \cdot 10^{-3}$

$C_7 = 4.1635019$

$C_4 = 1.9202377 \cdot 10^{-7}$

and over liquid water for a temperature range of 0 °C to 200 °C

$$\ln e_s = \frac{C_8}{T} + C_9 + C_{10} \cdot T + C_{11} \cdot T^2 + C_{12} \cdot T^3 + C_{13} \cdot \ln T \quad (4-37)$$

$$\begin{aligned} C_8 &= -1.0440397 \cdot 10^4 & C_{11} &= 1.2890360 \cdot 10^{-5} \\ C_9 &= -1.1294650 \cdot 10^1 & C_{12} &= -2.4780681 \cdot 10^{-9} \\ C_{10} &= -2.7022355 \cdot 10^{-2} & C_{13} &= 6.5459673 \end{aligned}$$

With the water vapor pressure values e^{i-1} , e^{i+1} at the two nearest vertical layers it is possible to perform exponential interpolation, as already exercised for surface total pressure, with

$$q_e = -\frac{H^{i+1} - H^{i-1}}{\ln e^{i+1} - \ln e^{i-1}} \quad (4-38)$$

e : partial water vapor pressure, i denotes the interpolated surface water vapor pressure,
 $i-1$ is the vapor pressure of the next lower layer and $i+1$ is that of the next higher layer
 H : geopotential height

and the interpolated partial water vapor pressure

$$e^i = e^{i-1} \cdot \exp\left(-\frac{H^i - H^{i-1}}{q_e}\right) \quad (4-39)$$

can be back-transformed into relative humidity by using the Clausius-Clapeyron equation.

4.3 Mapping Function Coefficients and Horizontal Gradients

3-D numerical weather fields allow to integrate slant path refractivity profiles. The results of such ray-tracing operations are the slant hydrostatic and wet delays that can be fitted to a tropospheric model resulting in regionally tuned mapping function coefficients as well as horizontal gradients. The following sections describe the ray-tracing algorithm and analysis procedure implemented in module PAF_MEO.

4.3.1 Ray-Tracing Algorithm

4.3.1.1 Ray-Tracing

The position of a virtual GPS satellite is computed in the local level system for an antenna site with the coordinates φ_0^* , λ_0 , h_0 as well as H_0 and X_0 , Y_0 , Z_0

$$\underline{x}_s = \begin{pmatrix} x_s \\ y_s \\ z_s \end{pmatrix} = 22\,000\,000 \text{ [m]} \cdot \begin{pmatrix} \cos \alpha \cdot \sin z \\ \sin \alpha \cdot \sin z \\ \cos z \end{pmatrix} \quad (4-40)$$

x_s, y_s, z_s : local level coordinates of virtual satellite
 α, z : azimuth and zenith angle to satellite

and given azimuth and zenith angle. The local level coordinates can be transformed into global geocentric coordinates X_s, Y_s, Z_s (\rightarrow 2.3). This virtual position is only needed to define the slant path traced by the program. It is, of course, not necessary to integrate the entire path of 22000 km.

The starting point of the path is the antenna site. All necessary meteorological quantities are extracted for this initial as well as all following points of the slant profile, namely total pressure p , temperature T and partial water vapor pressure e (or relative humidity RH). The hydrostatic refractivity (\rightarrow 3.2.1) is

$$N_{[HYD]} = k_1 \cdot \frac{R_0}{M_d} \cdot p = k_1 \cdot \frac{R_0}{M_d} \cdot \left(\frac{(p - e) \cdot M_d}{T \cdot R_0} \cdot Z_d^{-1} + \frac{e \cdot M_w}{T \cdot R_0} \cdot Z_w^{-1} \right) \quad (4-41)$$

and the wet refractivity is

$$N_{[WET]} = \left(k'_2 \cdot \frac{e}{T} + k_3 \cdot \frac{e}{T^2} \right) \cdot Z_w^{-1} \quad (4-42)$$

Note that the geometric zenith angle can be optionally corrected for bending impact

$$\Delta z = 16 \left[\frac{''}{K \cdot hPa} \right] \cdot \frac{\tan z}{T} \cdot \left(p + \frac{4800 [K]}{T} \cdot e \right) - 0.07'' \cdot (\tan^3 z + \tan z) \cdot \frac{p}{1000 [hPa]} \quad (4-43)$$

Δz : difference between geometric and actual zenith angle at the antenna

z : geometric zenith angle at the antenna site

in order to account for the curvature of the ray path (\rightarrow 3.2.2). In this case, the corrected zenith distance

$$z^* = z - \Delta z \quad (4-44)$$

z^* : actual zenith angle at the antenna

replaces the geometric zenith distance of

$$\cos Z = \frac{Z_s - Z_n}{|X_s - X_n|} \quad (4-45)$$

X_s : virtual satellite position in local level system

X_n : current slant path point in local level system

Subsequent points of the slant path profile are computed in the local horizon system

$$X_n = X_{n-1} + \Delta s \cdot \begin{pmatrix} \cos \alpha \cdot \sin z \\ \sin \alpha \cdot \sin z \\ \cos z \end{pmatrix} \quad (4-46)$$

X_n : current slant path point in local level system

X_{n-1} : preceding slant path point

Δs : increment in path length

with help of the path length increment Δs and can be converted into global geocentric coordinates X_n, Y_n, Z_n and ϕ_n^*, λ_n, h_n and H_n afterwards. The incremental tropospheric slant path delay for a distance Δs can be computed

$$\Delta \delta S_{[HYD]}^{n-1,n} = \Delta s \cdot \frac{N_{[HYD]}^{n-1} + N_{[HYD]}^n}{2} \cdot 10^{-6} \quad \wedge \quad \Delta \delta S_{[WET]}^{n-1,n} = \Delta s \cdot \frac{N_{[WET]}^{n-1} + N_{[WET]}^n}{2} \cdot 10^{-6} \quad (4-47)$$

$\Delta \delta S^{n-1,n}$: tropospheric slant path delay increment between ray points $n-1$ and n in [m]

for all points and the sum of all increments

$$\delta S_{[HYD]} = \int_{P_0}^{\infty} N_{[HYD]} \cdot ds \approx \sum_{i=1}^{\infty} \Delta \delta S_{[HYD]}^{i-1,i} \quad \wedge \quad \delta S_{[WET]} = \int_{P_0}^{\infty} N_{[WET]} \cdot ds \approx \sum_{i=1}^{\infty} \Delta \delta S_{[WET]}^{i-1,i} \quad (4-48)$$

is the slant path delay. As far as the wet delay is concerned, the vertical coverage of the numerical weather fields up to 100 hPa is fully sufficient to evaluate the integral completely. For the hydrostatic delay, this is not the case because the GDAS weather fields have a final pressure layer of 10 hPa. The remaining hydrostatic delay increment is about more than 2 cm and cannot be omitted. Therefore, the Saastamoinen model (\rightarrow 3.2.1.1.2)

$$\Delta \delta S_{[HYD]}^{n,\infty} = \frac{ZHD_{[SAAS]}(p, \phi, h)}{\cos Z} \quad (4-49)$$

$ZHD_{[SAAS]}$: zenith hydrostatic delay from Saastamoinen model ($p \approx 10$ hPa for GDAS FNL $1^\circ \times 1^\circ$)

is applied to evaluate the remaining increment.

4.3.1.2 Alternative Ray-Tracing Algorithm

A slightly different algorithm is presented by IFADIS [1986]. This method has also been implemented and differs from the preceding algorithm in terms of the direct application of Snell's law.

The angle f_i is computed by

$$f_i = \arctan \left(\frac{\sqrt{x_i^2 + y_i^2}}{z_i + r_E + h} \right) \quad (4-50)$$

f_i : difference angle between tangent to atmospheric shell and parallel line to surface

z_i : radial coordinate of upper slant profile point i of current slant path increment

r_E : radius of the earth

h : ellipsoidal height of topocenter (origin of local level system, antenna position)

and the increment in elevation due to refraction is

$$\delta\tau_i = -\frac{n_i - n_{i-1}}{n_i \cdot \tan \theta_i} \quad \wedge \quad n_i = 1 + (N_{[\text{HYD}]}_i + N_{[\text{WET}]}_i) \cdot 10^{-6} \quad (4-51)$$

$\delta\tau_i$: increment in elevation, correction due to refraction from Snell's law

n_i : index of refraction of upper slant profile point i of current slant path increment

N_i : reduced index of refraction

θ_i : angle between ray and tangent to the spherical shell passing through slant profile point i

applied to compute the apparent elevation angle valid for the next following path increment of the profile

$$\varepsilon_{i+1} = \varepsilon_i + \delta\tau_i \quad (4-52)$$

ε_{i+1} : apparent elevation to be applied for the following increment in slant profile path

ε_i : apparent elevation used for the current slant path increment

and angle θ is updated as follows:

$$\theta_{i+1} = \varepsilon_{i+1} + f_i \quad (4-53)$$

4.3.1.3 Horizontal Resolution

The path length increment Δs defines the horizontal as well as the vertical resolution. If the pressure is higher than 400 hPa (default value), the path length resolution is doubled to $\Delta s/2$, so that the resolution in the lower troposphere is higher than in the upper part. Another parameter is the horizontal angular resolution of the ray-tracing algorithm that is defined by the azimuth increment $\Delta\alpha$. Normally, $\Delta\alpha = 45^\circ$ is chosen with an initial azimuth of $\alpha_0 = 0^\circ$.

4.3.1.4 Vertical Resolution

The vertical angular resolution is defined by the zenith angle increment Δz starting with an initial angle of $z_0 = 0^\circ$ and tracing downward to a maximum zenith angle z_{MAX} that is usually around 80° (10° elevation angle). Additionally, a double density option allows double resolution for zenith distances higher than z_{DD} and has a default value of 60° . This means that the zenith angle increment becomes half its initial value for lower elevations. The reason to do so lies in the fact that all ray-traces near the zenith are less important than those near the horizon because the zenith direction is rather uncritical⁹. Consequently, the rays are densified for lower elevations.

4.3.2 Ray-Tracing Analysis

The set of slant delays is fitted separately to the standard tropospheric model (\rightarrow 3.2.1) for both the hydrostatic

$$\delta S_{[\text{HYD}]} = m(z)_{[\text{HYD}]} \cdot \text{ZHD} + m(z)_{[\text{AZI}]} \cdot [G_{[\text{N},\text{HYD}]} \cdot \cos \alpha + G_{[\text{E},\text{HYD}]} \cdot \sin \alpha] \quad (4-54)$$

⁹ One may even use the simple cosecant-model for small zenith angles, so there is no need for more sophisticated mapping functions in this region whereas small elevations are rather critical.

and the wet delay. The zenith hydrostatic and wet delays (ZHD and ZWD) are determined by ray-tracing in zenith direction and introduced as fixed values in the equation. Remaining unknowns are the horizontal gradients and mapping function coefficients. The preferred type of mapping function is the fractional expansion (→ 3.2.2)

$$m(z) = \frac{1 + \frac{a}{1+b}}{\cos z + \frac{a}{\cos z + b}} \quad (4-55)$$

of Marini and Murray that is discontinued after the second mapping function coefficient b , so two coefficients have to be determined for either the hydrostatic and the wet delay. Parameter estimation is performed by least-squares adjustment (→ 2.5.1) and the hydrostatic and wet gradients are melted together afterwards.

A second approach was implemented based on the Chao mapping function $m_{[\text{CHAO}]}$ (→ 3.2.2.1.2 and → 3.2.2.2.1) that is used as the default model

$$m(\epsilon) = m_{[\text{CHAO}]}(\epsilon) + \cos(\epsilon) \cdot \left(a_1 + \frac{a_2}{\sqrt{\epsilon}} + \frac{a_3}{\epsilon} + \frac{a_4}{\epsilon^2} \right) \quad (4-56)$$

ϵ : elevation angle from antenna to satellite

$a_{1..4}$: mapping function correction coefficients

and the correction coefficients $a_{1..4}$ try to model the deviations of the Chao mapping functions from the actually measured slant path delays of the ray-tracing analysis.

The fit of the slant delays to one of these models does not only allow to obtain regionally tuned mapping function coefficients, but also gives an opportunity to import horizontal gradients into the filter software and is an alternative to the additional estimation of gradients within the GPS filter engine.

4.4 Gridded Tropospheric Correction Files (TROPEX)

Numerical weather models can be used to compute tropospheric delays as it has been demonstrated in the preceding paragraph. A file format called *TROPEX*¹⁰ has been developed to carry all those gridded¹¹ information that are necessary for delay computation in zenith direction. Figure 4-4 emphasizes the central function of these tropospheric files because they do not only serve as carrier for tropospheric information, but also as basis for the combination of GPS tropospheric delays and those derived from numerical weather models (→ 4.5).

¹⁰ *TROPEX* = tropospheric exchange format

¹¹ Additionally, *TROPEX* files may also contain irregularly gridded data, for example if only results from GPS tracking networks are assimilated, but this is not the default mode.

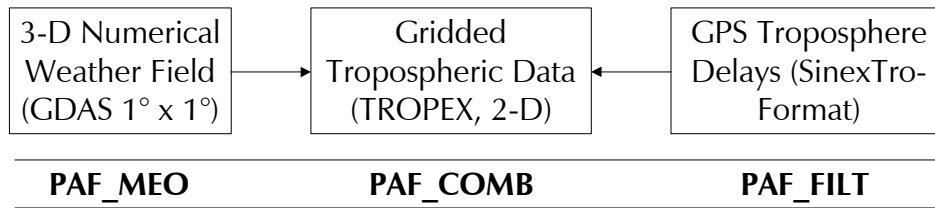


Figure 4-4 - TROPEX troposphere correction files contain all gridded information necessary to compute tropospheric delays in zenith direction. These files are created from 3-D numerical weather fields, but in contrast to the NWM-data, TROPEX uses a 2-D data representation and models vertical dependencies with help of reduction coefficients. Moreover, tropospheric delays from numerical weather models and those derived from GPS measurements can be combined.

TROPEX files store data in ASCII-compressed form and are therefore absolutely platform-independent. Whereas numerical weather fields are 3-D files, the TROPEX approach decreases the memory load by only using a 2-D representation of the data and models the vertical direction with help of reduction coefficients. The major purpose of these troposphere correction files is to offer a precise way to determine tropospheric delays for all those GPS applications that suffer from an inability to estimate tropospheric delays as additional parameters, e. g. kinematic applications, and to provide a gridded data set of water vapor measurements.

Category	Layer	Contents
geo-reference	N	geoid height from EGM96 geopotential model, $1^\circ \times 1^\circ$ grid
	H	geopotential height of grid point (surface value)
	φ^*	geocentric latitude, only for irregularly distributed data
	λ	geocentric longitude, only for irregularly distributed data
zenith hydrostatic delay	p	surface total pressure
	σ_p	standard deviation of vertical pressure profile fit
	a_p	linear trend coefficient for vertical pressure reduction
	b_p	parabolic trend coefficient for vertical pressure reduction
	c_p	exponential trend coefficient, reciprocal scale height $1/q_p$
zenith wet delay	ZWD	zenith wet delay, total atmospheric column
	σ_{ZWD}	standard deviation of vertical zenith wet delay profile fit
	q_{ZWD}	water vapor scale height, exp. trend for vertical reduction
other atmospheric properties (optional)	e	partial water vapor pressure at surface
	t	surface temperature
	β	temperature lapse rate, up to tropopause height
	t_M	mean temperature of atmosphere, total atmospheric column
	β_M	temperature lapse rate of mean atmospheric temperature
	H_T	tropopause height

Table 4-2 - Contents of TROPEX troposphere correction files (typical data layers from the analysis of GDAS numerical weather fields). Note that the geo-reference layers are only given once as they are no time-varying data and latitude/longitude are only given for the special case of irregular data (i. e. GPS only). Data belonging to the category "other atmospheric properties" are optional data that may be included, but are not necessary in order to compute zenith neutral delays.

4.4.1 Contents and Structure of TROPEX Files

The contents of TROPEX files is given in Table 4-2. Generally speaking, the hydrostatic and the wet component are strictly separated. The first component is represented indirectly by total pressure and the wet delay is given directly.

All data are referenced to the model surface or the total atmospheric column, respectively, and can be vertically reduced with help of reduction coefficients. Three reduction coefficients are usually needed (\rightarrow 4.4.2.2) for pressure, and one coefficient is sufficient for zenith wet delay reduction (\rightarrow 4.4.3.2).

The gridded data sets are always stored in equi-rectangular projection, but not necessarily in plain plate projection. The data are ASCII differentially compressed (1st order compression), binary compression with standard packing programs can be applied afterwards. The reader may refer to Appendix V for a more detailed description of the file format.

4.4.2 Zenith Hydrostatic Delay

There are several possibilities to evaluate the hydrostatic delay with help of numerical weather fields. The method practiced for ray-tracing (\rightarrow 4.3) is to integrate the hydrostatic refractivity profile, but this is not a necessity if the delay is to be modeled in zenith direction only. Due to the highly precise hydrostatic model of Saastamoinen (\rightarrow 3.2.1.1.2)

$$\text{ZHD} = \frac{0.0022767 \left[\frac{\text{m}}{\text{hPa}} \right] \cdot p}{1 - 0.00266 \cdot \cos 2\varphi - 0.00028 \left[\frac{1}{\text{km}} \right] \cdot h} \quad (3-57)$$

φ : ellipsoidal latitude

h : surface height above the ellipsoid in [km]

p : surface pressure in [hPa]

the alternative is to simply use surface pressure to compute the zenith hydrostatic delay with high accuracy.

4.4.2.1 Surface Pressure

Surface pressure and the associated geopotential heights are directly contained as separate layers in the GDAS 1° x 1° numerical weather fields. It is therefore not necessary to perform any operations on the weather model data. However, the question of modeling pressure in vertical direction remains. This is an important point as in every-day use, pressure data will be requested for heights which are unequal to the model grid surface. Accurate hydrostatic delay determination consequently requires precise height reduction. Figure 4-5 shows a pressure-plot for Germany, visualized and reduced via TROPEX files.

4.4.2.2 Vertical Profile Modeling

The vertical pressure profile is given in the numerical weather fields and is used to estimate reduction coefficients that describe the pressure decrease with increasing height. At first instance, the exponential model presented (\rightarrow 4.2.1.2) can be used

$$p_i = p_0 \cdot \exp\left(-\frac{H_i - H_0}{q_p}\right) = p_0 \cdot \exp(c_p \cdot (H_0 - H_i)) = p_0 \cdot \exp(c_p \cdot \Delta H_i) \quad (4-58)$$

H : geopotential height; subscript i denotes the height of the current profile point,
 0 stands for the initial value, i. e. that of the surface point

p : total pressure

q_p : pressure scale height

c_p : reciprocal scale height; $c_p = 1/q_p$

and the exponential trend coefficient c_p is to be determined by least-squares adjustment. Experiments showed that this approach is not proper to reach the requested precision level of better than 1 hPa. For this reason, a linear and a parabolic trend coefficient were added

$$p_i = a_p \cdot \Delta H_i + b_p \cdot \Delta H_i^2 + p_0 \cdot \exp(c_p \cdot \Delta H_i) \quad \wedge \quad \Delta H_i = H_0 - H_i \quad (4-59)$$

a_p : linear vertical trend coefficient

b_p : parabolic vertical trend coefficient

what guarantees a high (internal) accuracy of pressure up to highest altitudes of 12 km or more. The precision of the vertical profile fit to this model is better than 1 hPa for the majority of the mid-latitude grid points and often around 0.5 hPa. Note that in special cases, the least-squares algorithm may turn into convergence problems if the exponential coefficient is not a significant parameter. In routine analysis, this sometimes happens for points at very high altitudes in the Himalayan region (more than 5000 m), for instance, where the exponential trend can be omitted because the parabolic trend function is appropriate for height reduction in these cases.

4.4.3 Zenith Wet Delay

In contrast to the hydrostatic component, it is necessary to integrate the wet vertical refractivity profile in order to obtain accurate zenith wet delays. Vertical reduction can be performed with one single parameter, the water vapor scale height, without any significant loss of accuracy.

4.4.3.1 Integral Evaluation

Zenith wet delays are vertically integrated in the same manner as depicted for ray-tracing in (\rightarrow 4.3) by numerical methods using the wet refractivity values of all available vertical layers (max. 21 for GDAS) of the weather field.

$$ZWD = 10^{-6} \cdot \int_{H_0}^{\infty} N_{[WET]}(H) \cdot dH \approx 10^{-6} \cdot \sum_{i=1}^n \frac{N_{[WET]}^{i-1} + N_{[WET]}^i}{2} \cdot \Delta H_{i-1,i} \quad (4-60)$$

$N_{[WET]}$: wet refractivity; superscript $i-1$ denotes the nearest downward profile point,
 i is the current profile point

$\Delta H_{i-1,i}$: geopotential height difference between the nearest downward and the current profile point i

The profile is densified by a factor of 4 to 10 in order to minimize errors of the numerical integrator. Figure 4-7 illustrates the wet delay distribution over Germany on 11 March 2000.

4.4.3.2 Vertical Profile Modeling

Since partial water vapor pressure is the main contributor to the wet delay and decreases exponentially with height as total pressure does, it can be assumed that the wet delay also follows a vertical model like

$$ZWD_i = ZWD_0 \cdot \exp\left(-\frac{H_i - H_0}{q_{ZWD}}\right) \quad (4-61)$$

H : geopotential height; subscript i denotes the height of the current profile point,
 0 stands for the initial value, i. e. that of the surface point

ZWD : zenith wet delay

q_{ZWD} : zenith wet delay or water vapor scale height

that is recommended by EMARDSON [1998, paper G]. Least-squares profile fits up to more than 10 km revealed a precision of some millimeters in mid-latitude regions. Figure 4-8 illustrates the water vapor scale height variability over Germany on 11 March 2000.

4.4.4 Other Atmospheric Properties

Other atmospheric properties contained in TROPEX files comprise the tropopause height and the temperature lapse rate as well as the mean temperature of the troposphere. The latter is needed to convert zenith wet delays into precipitable water (\rightarrow 3.5) and the first two quantities serve as inputs for several mapping functions (\rightarrow 3.2.2.1.4, \rightarrow 3.2.2.2.2) and can be considered as valuable by-products of the weather field analysis.

4.4.4.1 Mean Temperature of Troposphere

The integral formula for the mean atmospheric temperature

$$T_M = \frac{\int_{H_0}^{\infty} \frac{e}{T} \cdot Z_w^{-1} \cdot dH}{\int_{H_0}^{\infty} \frac{e}{T^2} \cdot Z_w^{-1} \cdot dH} \approx \frac{\sum_{i=1}^n \left[\frac{1}{2} \cdot \left(\frac{e_{i-1}}{T_{i-1}} + \frac{e_i}{T_i} \right) \cdot Z_w^{-1} \cdot \Delta H_{i-1,i} \right]}{\sum_{i=1}^n \left[\frac{1}{2} \cdot \left(\frac{e_{i-1}}{T_{i-1}^2} + \frac{e_i}{T_i^2} \right) \cdot Z_w^{-1} \cdot \Delta H_{i-1,i} \right]} \quad (4-62)$$

H : geopotential height; subscript i denotes the height of the current profile point,
 0 stands for the initial value, i. e. that of the surface point

$\Delta H_{i-1,i}$: geopotential height difference between the nearest downward and the current profile point i

T_M : weighted mean temperature of the troposphere

is numerically evaluated. Figure 4-9 shows the distribution of the mean temperature over Germany on 11 March 2000.

Furthermore, the lapse rate of the mean temperature β_M is computed by fitting the vertical temperature profile to the model

$$T_M = T_{M0} + \beta_M \cdot H \quad (4-63)$$

T_M : mean temperature between height H and tropopause height

T_{M0} : mean temperature between sea level (0 m) and tropopause height

β_M : temperature lapse rate of mean temperature

H : geopotential height

This additional parameter is estimated because the lapse rate of the dry temperature (see following section) does not exactly equal the lapse rate of the mean temperature. Actually, the latter is usually smaller, roughly about 0.5 K/km less than the dry temperature gradient.

4.4.4.2 Temperature Lapse Rate

The temperature profile is modeled in vertical direction by the equation

$$T = T_0 + \beta \cdot H \quad (4-64)$$

T : temperature

T_0 : sea-level temperature (0 m)

β : temperature lapse rate

H : geopotential height

where β is the temperature lapse rate characterizing the mean linear decrease in temperature with height. The temperature profile of the numerical weather field is fitted to this model using least-squares methods (\rightarrow 2.5.1). Usually, all temperature-height-pairs up to the tropopause height are used for this analysis that is complicated in presence of low-altitude inversion layers. A blunder detector of residual type (\rightarrow 2.5.1.4) tries to identify and to eliminate such disturbing occurrences leaving only those profile data into the analysis chain that show a considerably good agreement with the linear model.

4.4.4.3 Height of the Tropopause

The tropopause height can be identified by analyzing the vertical temperature profile for trend changes at typical heights between 9 and 16 km. A significant change of the temperature lapse rate from -6.5 K/km towards zero indicates this layer (\rightarrow section 3.1). However, it is not necessary to carry out any weather field data analysis since all models in use for this study output the tropopause height directly. See Figure 4-11 for a plot of tropopause heights over Germany illustrating the variability of this quantity.

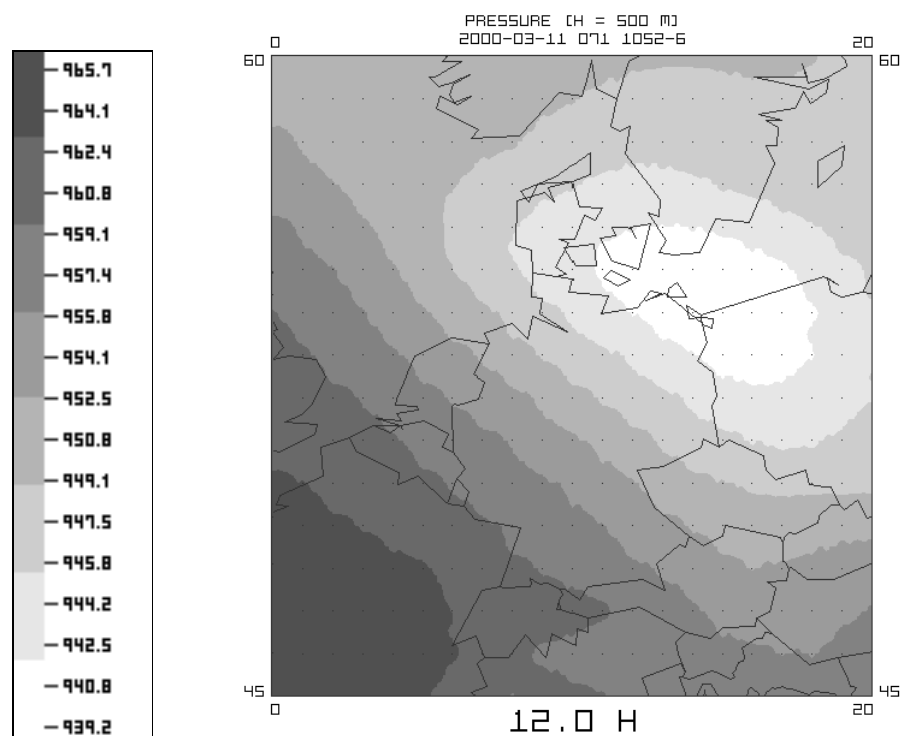


Figure 4-5 - Total pressure over Germany on 11 March 2000 at 12 h UTC. All pressure data are given in units of [hPa] and referenced to a common geopotential height of 500 m in order to reduce topographic effects. The model output grid with a resolution of $1^\circ \times 1^\circ$ has been projected into the image and is indicated by dots.

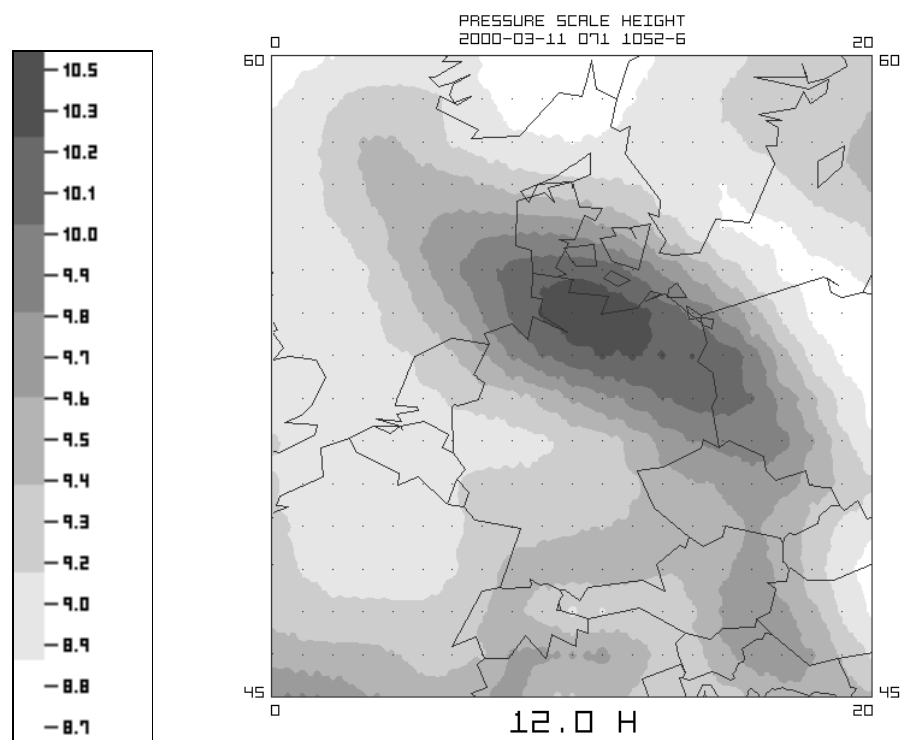


Figure 4-6 - Pressure scale heights q_p over Germany on 11 March 2000 at 12 h UTC in units of [km]. The theoretical value of 8 km derived in section 4.2.1.2 marks the very lowest range of those scale heights actually occurring that also show a considerable variability of 2 km and particularly high horizontal gradients over northern Germany.

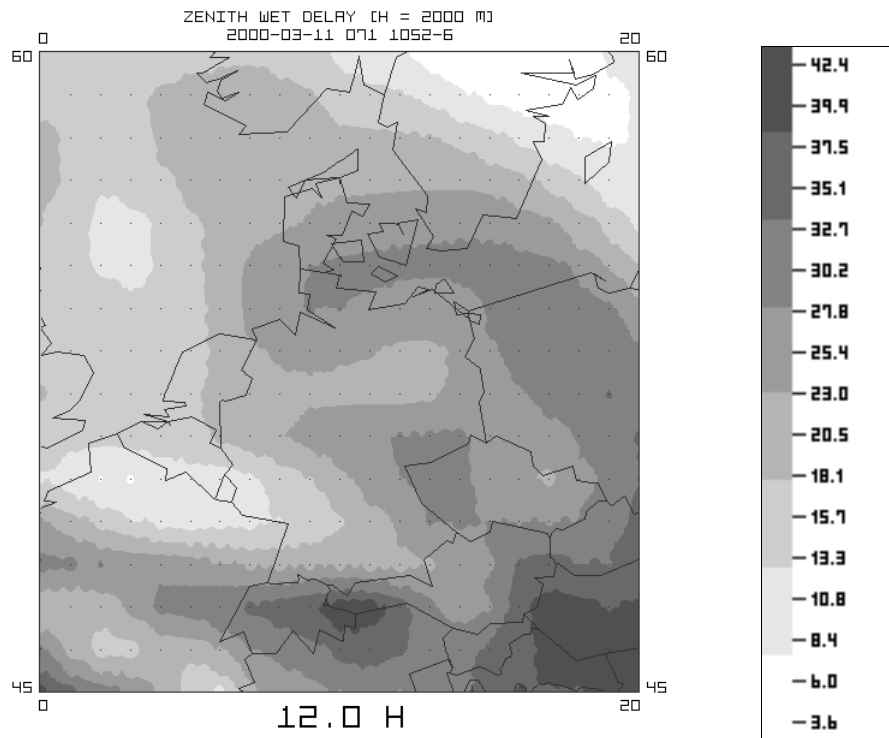


Figure 4-7 - Zenith wet delays over Germany on 11 March 2000 at 12 h UTC. All delay data are given in units of [mm] and referenced to a common geopotential height of 2000 m in order to reduce topographic effects. For this reason, the zenith delay values are rather small in comparison to those at usual heights of 100 to 500 m.

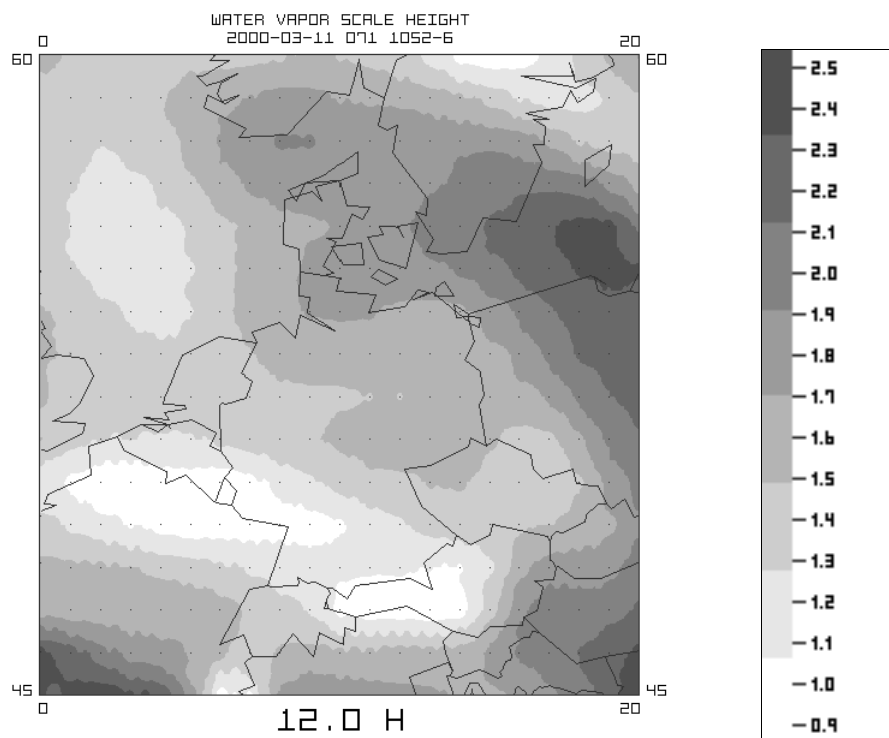


Figure 4-8 - Water vapor/zenith wet delay scale heights over Germany on 11 March 2000 at 12 h UTC in units of [km]. The plot shows that actual scale heights may reasonably deviate from the average value of about 2.0 km.

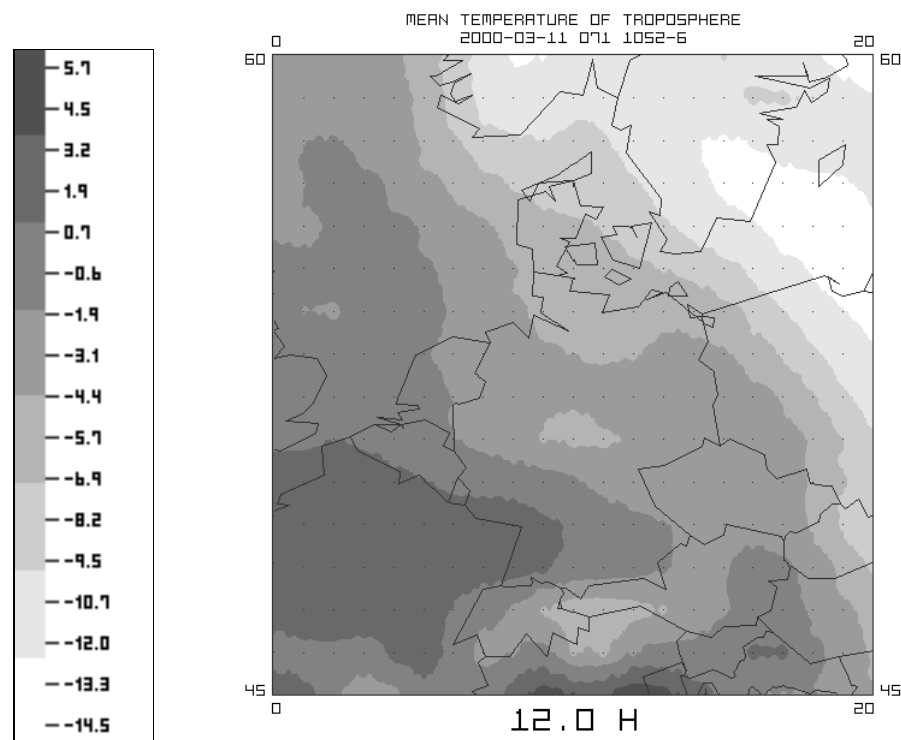


Figure 4-9 - Mean atmospheric temperature between the surface and the tropopause height over Germany on 11 March 2000 at 12 h UTC in units of [°C].

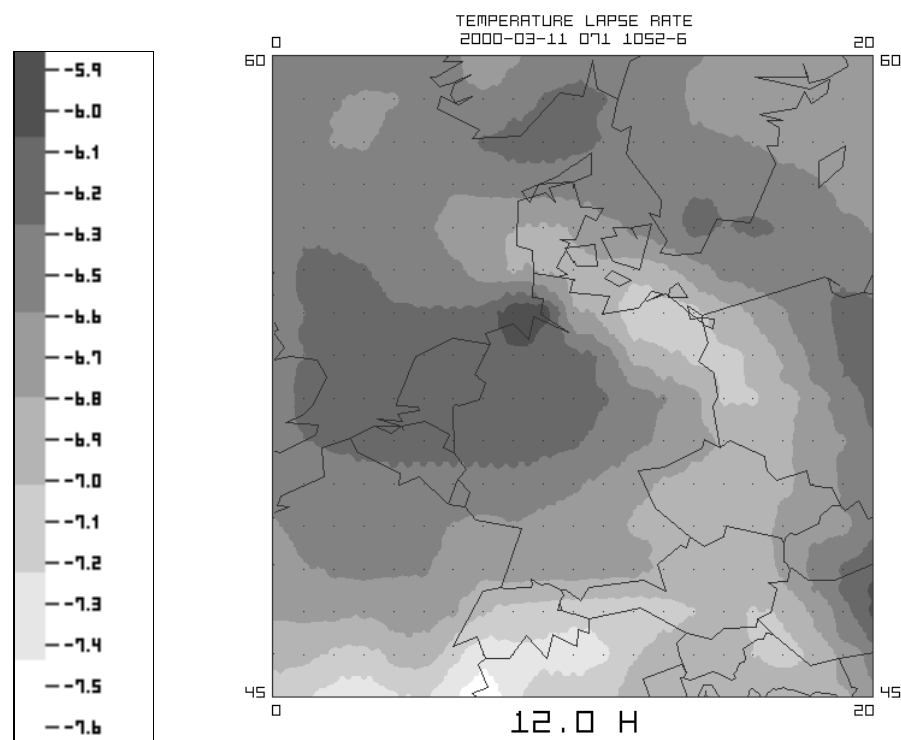


Figure 4-10 - Temperature lapse rates over Germany on 11 March 2000 at 12 h UTC in units of [K/km]. Smallest lapse rates of about -6 K/km occur at the German North Sea coast, steeper temperature gradients can be seen at Germany's north-eastern part.

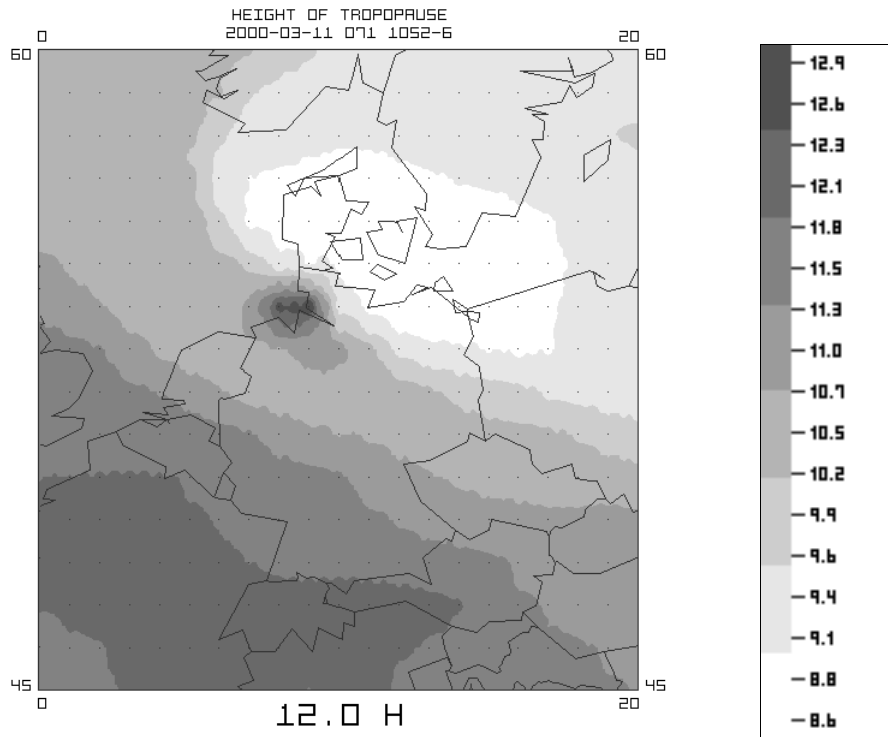


Figure 4-11 - Tropopause heights over Germany on 11 March 2000 at 12 h UTC in units of [km]. It becomes evident that variations of more than 4 km may occur over distances as small as the north-south extension of Germany and - what is even more important - anomalies of regional extent are apparently possible as shown over the eastern part of the German North Sea coast.

4.4.5 Horizontal Interpolation in TROPEX Files

Generally speaking, horizontal interpolation in TROPEX files is accomplished by nearest neighbor algorithms. For instance, the interpolated zenith wet delay at a location ϕ^*, λ is obtained by

$$ZWD_{\phi^*, \lambda, H} = \sum_{i=1}^n [w_i \cdot (ZWD_i + \Delta ZWD_i)] \quad \wedge \quad \sum_{i=1}^n w_i = 1 \quad (4-65)$$

$ZWD_{\phi^*, \lambda, H}$: interpolated zenith wet delay at position ϕ^*, λ (latitude, longitude) and height H

w : normalized weighting coefficient; sum of all normalized weights equals 1

ZWD_i : zenith wet delay at grid point i being a nearest neighbor to ϕ^*, λ

ΔZWD_i : height reduction term in order to reduce ZWD_i from H_i to H of the interpolation point

where w denotes the normalized weights, i. e. their sum always equals 1. The height reduction is processed via formula 4-61 for zenith wet delays and formula 4-59 for pressure data.

In contrast to the surface meteorological data extraction algorithm that only uses simple distance-dependent weighting, some more weighting methods are in use for TROPEX data.

4.4.5.1 Distance Weighting

The weighting function for the distance method has already been presented:

$$w_i^* = \psi_{i,k}^{-c} \Rightarrow w_i = \frac{w_i^*}{\sum_{i=1}^n w_i^*} \quad (4-66)$$

w_i^* : weighting coefficient associated with nearest neighbor i , not normalized

w_i : normalized weighting coefficient associated with nearest neighbor i

$\psi_{i,k}$: spherical distance between neighbor i and interpolation point k at ϕ, λ in [rad], [m], ...

c : weighting power ($c \approx 1$ to 2)

The weighting power c is to be defined and lies between 1 and 2 in most cases. This method is the most simple way to define the weights. It models spatial decorrelation, but does not take the accuracy of the individual neighbors into account. However, it is not difficult to introduce the variance

$$w_i^* = \sigma_i^{-2} \cdot \psi_{i,k}^{-c} \quad (4-67)$$

σ_i : standard deviation of the quantity at neighboring point i used for interpolation

to the weighting function. The remaining difficulty is to find proper values for the standard deviations. Of course, it is possible to adopt the standard deviations of the weight unit of the vertical profile fit for pressure and zenith wet delay as quantities describing the accuracy of the delays themselves, but experience underpins that these values are often too optimistic because they mainly reflect the internal accuracy of the vertical reduction model whereas the actual accuracy of these quantities can be significantly higher and systematically biased. An alternative way to find standard deviations for zenith wet delays from GDAS numerical weather fields as function of the site latitude

$$\sigma_{\text{ZWD}}(\phi) = 22 [\text{mm}] - 0.2 \left[\frac{\text{mm}}{\text{deg}} \right] \cdot |\phi| \quad (4-68)$$

is proposed that was derived from a comparison of GPS and GDAS wet delays.

4.4.5.2 Gauss-Markov Weighting

Another functional approach to define distance-dependent weights is to assume that spatial correlation follows the behavior of Gauss-Markov processes

$$w_i^* = \sigma_i^{-2} \cdot \exp(-\gamma \cdot |\psi_{i,k}|) \quad (4-69)$$

γ : decorrelation factor

SOLBRIG [2000] investigated empirical auto-covariance functions of zenith wet delays and found out that it is possible to approximate these functions by Gauss-Markov processes, but chose a preference for the squared spherical distance

$$w_i^* = \sigma_i^{-2} \cdot \exp(-\Gamma \cdot \psi_{i,k}^2) \quad (4-70)$$

Γ : decorrelation factor

which was able to better approximate the curvature of the empirically derived auto-covariance functions. The average value of Γ was specified by 0.35 [1/Mm²] with the spherical distance given in megameters.

4.4.5.3 Best Linear Unbiased Estimator (BLUE)

Following EMARDSON [1998, paper G], the vector of optimal and normalized weights can be computed using the formula

$$\underline{w} = \underline{\Sigma}_{n,n}^{-1} \cdot \underline{\Sigma}_{n,k} + \frac{(1 - \underline{\Sigma}_{n,k}^T \cdot \underline{\Sigma}_{n,n}^{-1} \cdot \underline{e}) \cdot \underline{\Sigma}_{n,n}^{-1} \cdot \underline{e}}{\underline{e}^T \cdot \underline{\Sigma}_{n,n}^{-1} \cdot \underline{e}} \quad (4-71)$$

\underline{w} : vector of normalized weights

$\underline{\Sigma}_{n,n}$: covariance matrix of the n nearest neighbors

$\underline{\Sigma}_{n,k}$: covariance vector between the n nearest neighbors and point k to interpolate

\underline{e} : unit vector (filled with ones)

with

$$\underline{\Sigma}_{n,n} = \begin{bmatrix} \sigma_1^2 & \rho_{1,2} \cdot \sigma_1 \cdot \sigma_2 & \dots \\ \rho_{1,2} \cdot \sigma_1 \cdot \sigma_2 & \sigma_2^2 & \dots \\ \vdots & \vdots & \ddots \end{bmatrix} = \begin{bmatrix} \sigma_1^2 & \sigma_{1,2} & \dots \\ \sigma_{1,2} & \sigma_2^2 & \dots \\ \vdots & \vdots & \ddots \end{bmatrix} \quad (4-72)$$

σ_1 : standard deviation of the first nearest neighbor

$\rho_{1,2}$: correlation coefficient between neighbor 1 and 2

$\sigma_{1,2}$: covariance between neighboring points 1 and 2

and

$$\underline{\Sigma}_{n,k} = \begin{bmatrix} \sigma_{1,k} \\ \sigma_{2,k} \\ \vdots \end{bmatrix} = \begin{bmatrix} \rho_{1,k} \cdot \sigma_1 \cdot \sigma_k \\ \rho_{2,k} \cdot \sigma_2 \cdot \sigma_k \\ \vdots \end{bmatrix} \quad (4-73)$$

$\rho_{1,k}$: correlation coefficient between nearest neighbor 1 and interpolation point k

$\sigma_{1,k}$: covariance between neighboring point 1 and interpolation point k

The covariances of the requested matrices $\underline{\Sigma}_{n,n}$ and $\underline{\Sigma}_{n,k}$ can be determined with Gauss-Markov functions like

$$\rho_{i,k} = \exp(-\gamma \cdot |\psi_{i,k}|) \quad (4-74)$$

i: neighboring point with index i
 k: point to be interpolated with index k

or the modified version

$$\rho_{i,k} = \exp(-\Gamma \cdot \psi_{i,k}^2) \quad (4-75)$$

as described before.

4.5 Combination of NWM Data and GPS Estimates

Several approaches are possible in order to combine GPS-derived tropospheric delays and numerical weather models. From the meteorologist's and climatologist's point of view, GPS results are to be assimilated into the weather or climate models. Here, two major possibilities can be distinguished: The first method assimilates zenith total delays that are the primary output of GPS network analyses and can be estimated without any additional meteorological information. Separation into the hydrostatic and wet component as well as the conversion into precipitable water is modeled inside the weather models themselves as they provide all necessary information to do so. The other method is to assimilate the wet delays or, even better, the integrated water vapor estimates as independent quantities into the models. Independent estimates can be only obtained if meteorological in-situ measurements are available at the antenna site. Although it is desirable to assimilate data that are as independent from other data as somehow possible because this strengthens the reliability of the model and reduces inter-correlation, only limited efforts have been made inside the IGS network so far to do so. For further information on assimilation studies refer to KUO et al. [1993].

A different approach is presented here that does not focus on assimilation into a fully featured numerical weather model, but tries to combine both the troposphere delay data integrated in 3-D numerical weather fields and the GPS-derived wet delays. The result is a combined and improved solution for the gridded data sets. Note that, apart from the experiments presented in the following chapters, tropospheric delays are determined by several IGS analysis centers¹² for about 150 stations world-wide and the GDAS 1° x 1° model provides a very promising basis for the combination of these data sets in terms of horizontal resolution. This fact was the primary motivation to implement a combination procedure in module PAF_COMB that is optimized with respect to CPU and memory load and uses *TROPEX* files as data basis. The basic procedure used to combine both data sets is a least-squares algorithm (→ 2.5.1). In contrast to the standard algorithm itself, certain enhancements like variance component estimation were implemented and have proven to be useful in order to obtain adequate results since uncertainties of the stochastic model are one dominant problem of this combined adjustment.

¹² The primary - and in almost all cases the only - IGS product are zenith total delays. Combination is performed for zenith wet delays. This means that the separation into hydrostatic and wet components must be conducted before. For this task either pressure measurements or the pressure data contained in the numerical weather fields are used.

4.5.1 Observations, Parameters and Stochastic Model

The following two data sets are to be melted together: The gridded zenith wet delays of the numerical weather field and the irregularly distributed GPS-derived delays. Consequently, the observation vector consists of two sub-vectors

$$\underline{L} = \begin{bmatrix} \underline{L}_{NWM} \\ \underline{L}_{GPS} \end{bmatrix} \quad (4-76)$$

\underline{L} : observation vector containing all data sets to be processed
 \underline{L}_{NWM} : observation vector of the numerical weather model zenith wet delays
 \underline{L}_{GPS} : observation vector of the GPS wet delays

The set of unknown parameters to estimate is limited to those zenith wet delays contained in the GDAS-derived TROPEX file that are affected by the stations where GPS-delays are available. The observations in vector \underline{L}_{NWM} are directly linked to these unknowns, i. e. their partial derivatives in the design matrix \underline{A} are equal to 1. The stochastic model is given by the covariance matrix

$$\underline{\Sigma}_{LL} = \begin{bmatrix} \underline{\Sigma}_{NWM} & \underline{\Sigma}_{NWM,GPS} \\ \underline{\Sigma}_{GPS,NWM} & \underline{\Sigma}_{GPS} \end{bmatrix} \quad (4-77)$$

$\underline{\Sigma}_{LL}$: covariance matrix of all observations
 $\underline{\Sigma}_{NWM}$: covariance sub-matrix of the numerical weather model delays
 $\underline{\Sigma}_{GPS}$: covariance sub-matrix of the GPS-derived delays
 $\underline{\Sigma}_{NWM,GPS}$: covariance matrix between numerical weather model and GPS-derived delays

and can be simplified to

$$\underline{\Sigma}_{LL} = \begin{bmatrix} \underline{\Sigma}_{NWM} & \\ & \underline{\Sigma}_{GPS} \end{bmatrix} \quad (4-78)$$

if NWM and GPS observations can be assumed to be independent from each other. No information on correlations is provided by the IGS troposphere product in SinexTro format¹³, so the covariance matrix

$$\underline{\Sigma}_{GPS} = \begin{bmatrix} \sigma_{1,GPS}^2 & & \\ & \sigma_{2,GPS}^2 & \\ & & \ddots \end{bmatrix} \quad (4-79)$$

will be approximated as diagonal matrix as well in most cases¹⁴. The situation for the numerical weather model data is quite the same. Information about the accuracy as

¹³ Zenith path delays are exchanged in the standardized SinexTro (solution independent exchange format for combination of tropospheric estimates) that has been defined by GENDT [1997] and is used by the IGS analysis centers. These files contain the tropospheric estimates and their precision. Covariances are not contained in the combined IGS solution files.

well as the correlations is rather limited, so the first choice would be to set the correlation coefficients to zero as well. However, assumptions about the correlations between these delays can be derived from the models discussed in section 4.4.7 and, in principle, a full covariance matrix

$$\underline{\Sigma}_{\text{NWM}} = \begin{bmatrix} \sigma_{1,\text{NWM}}^2 & \rho_{1,2,\text{NWM}} \cdot \sigma_{1,\text{NWM}} \cdot \sigma_{2,\text{NWM}} & \cdots \\ \rho_{2,1,\text{NWM}} \cdot \sigma_{2,\text{NWM}} \cdot \sigma_{1,\text{NWM}} & \sigma_{2,\text{NWM}}^2 & \cdots \\ \vdots & \vdots & \ddots \end{bmatrix} \quad (4-80)$$

can be established. However, it is stressed that the correlation coefficients ρ derived by the Gauss-Markov functions can cause numerical instabilities during the inversion of the covariance matrix, esp. in the case of high correlation between nearby points. This fact is even amplified by the choice of $-\Gamma \cdot \psi^2$ rather than $-\gamma \cdot |\psi|$ for the exponent¹⁵. Moreover, correlation functions like this can only be applied for points of equal height. If the height difference between the grid points becomes larger, decorrelation effects have to be taken into account. For an initial zenith wet delay of 0.2 m at sea level, a linear decorrelation of -0.0004 per meter can be found that is valid up to a height (difference) of 800 m. This means that the correlation coefficient between the ZWD at sea level and the ZWD above the same point at an altitude of 500 m is 0.8 instead of 1.0.

4.5.2 Functional Model

The observation equations for the numerical weather model delays are easily derived because the parameters are the zenith wet delays at the model grid points. As a consequence, the observations equal the parameters themselves and the approximated observation sub-vector becomes

$$\overset{\circ}{\underline{L}}_{\text{NWM}} = \underline{\Psi} \left(\overset{\circ}{\underline{X}} \right) \equiv \overset{\circ}{\underline{X}} \quad (4-81)$$

\underline{X} : parameter vector, superscript "0" denotes that the vector contains approximated values

$\underline{\Psi}(\underline{X})$: vector of functions of the unknowns defining the observation equation

and the adjusted NWM observation and parameter vector are identical. The partial derivatives for this observation type is 1 and the sub-design matrix is an identity matrix.

The basic problem is to find a relation between the irregularly distributed tracking stations and their GPS-delays on the one side and the regular TROPEX grid with the numerical weather field ZWD data on the other side. Figure 4-12 illustrates the method used which is closely related to the interpolation methodology (\rightarrow 4.2.1.3). Again, only the 4 nearest neighbors of the particular GPS-station are taken into

¹⁴ Note that it is not easy to make a guess about correlation coefficients in GPS-derived zenith wet delays since these values are not only dependent on the baseline-length, but also on the network configuration, their extend and other criteria which are normally not known to the user.

¹⁵ Even for points having a distance of 150 km there is a correlation coefficient of $\rho = 0.992$ with $\Gamma = 0.35$ [1/Mm²].

account and only these points are affected by the combination procedure. For a horizontal resolution of $1^\circ \times 1^\circ$ this appears to be suitable since the diagonal distance between two grid points is about 140 km and relating GPS-stations to more than just the 4 nearest neighbors would be certainly of limited use. On the other hand, certain grid points will remain totally unaffected because no GPS-tracking stations are within their region. This is true for large regions of the oceans. Here, the combination procedure will not change the values of the grid points and accordingly, these points are not introduced into the combination module what saves computation time.

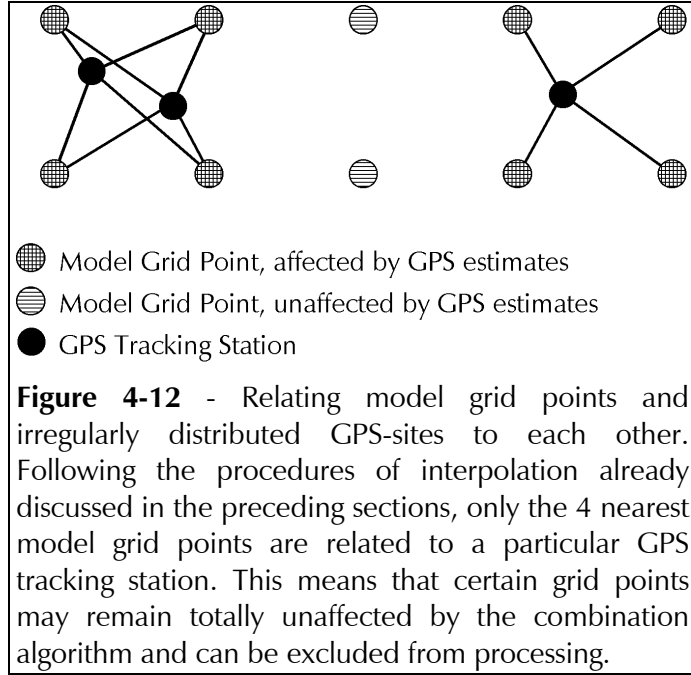


Figure 4-12 - Relating model grid points and irregularly distributed GPS-sites to each other. Following the procedures of interpolation already discussed in the preceding sections, only the 4 nearest model grid points are related to a particular GPS tracking station. This means that certain grid points may remain totally unaffected by the combination algorithm and can be excluded from processing.

The observation equation for GPS wet delays (compare with → 4.4.5) becomes

$$L_{i,\text{GPS}} = w_{z,s,i} \cdot (X_{z,s,i} + \Delta\text{ZWD}_{z,s,i}) + w_{z,s+1,i} \cdot (X_{z,s+1,i} + \Delta\text{ZWD}_{z,s+1,i}) + w_{z+1,s,i} \cdot (X_{z+1,s,i} + \Delta\text{ZWD}_{z+1,s,i}) + w_{z+1,s+1,i} \cdot (X_{z+1,s+1,i} + \Delta\text{ZWD}_{z+1,s+1,i}) \quad (4-82)$$

$L_{i,\text{GPS}}$: GPS-derived wet delay number i

$w_{z,s,i}$: normalized weight for grid point at row z and column s , nearest neighbor of GPS site i

$X_{z,s,i}$: unknown zenith wet delay (ZWD) for grid point z, s

ΔZWD : height reduction term to reduce the model grid ZWD to the actual height of GPS site i

where the normalized weighting coefficients w are determined via one of the methods discussed in section 4.4.5, but without taking the standard deviations of the 4 neighbors into account because stochastic and functional description are separated here. The observation equation with explicit notation of the exponential height reduction is

$$L_{i,\text{GPS}} = w_{z,s,i} \cdot X_{z,s,i} \cdot \exp\left(-\frac{H_{i,\text{GPS}} - H_{z,s,i}}{q_{\text{ZWD}_{z,s,i}}}\right) + w_{z,s+1,i} \cdot X_{z,s+1,i} \cdot \exp\left(-\frac{H_{i,\text{GPS}} - H_{z,s+1,i}}{q_{\text{ZWD}_{z,s+1,i}}}\right) + w_{z+1,s,i} \cdot X_{z+1,s,i} \cdot \exp\left(-\frac{H_{i,\text{GPS}} - H_{z+1,s,i}}{q_{\text{ZWD}_{z+1,s,i}}}\right) + w_{z+1,s+1,i} \cdot X_{z+1,s+1,i} \cdot \exp\left(-\frac{H_{i,\text{GPS}} - H_{z+1,s+1,i}}{q_{\text{ZWD}_{z+1,s+1,i}}}\right) \quad (4-83)$$

$H_{i,\text{GPS}}$: height of antenna at GPS tracking station i

$H_{z,s,i}$: height of grid point at row z and column s , nearest neighbor of GPS site i

$X_{z,s,i}$: unknown zenith wet delay (ZWD) for grid point z, s

$q_{\text{ZWD}_{z,s,i}}$: water vapor scale height at grid point z, s

and thus, the partial derivatives are the normalized weights $w_{z,s,i}$ multiplied by the height reduction term, i. e.

$$\frac{\partial L_{i,\text{GPS}}}{\partial X_{z,s,i}} = w_{z,s,i} \cdot \exp\left(-\frac{H_{i,\text{GPS}} - H_{z,s,i}}{q_{\text{ZWD}_{z,s,i}}}\right) \quad (4-84)$$

and the complete design matrix becomes

$$\underline{A} = \begin{bmatrix} \underline{A}_{\text{NWM}} \\ \underline{A}_{\text{GPS}} \end{bmatrix} = \begin{bmatrix} \underline{E} \\ \underline{A}_{\text{GPS}} \end{bmatrix} \quad (4-85)$$

$\underline{A}_{\text{NWM}}$: design sub-matrix of NWM ZWD observations, identity matrix \underline{E}

$\underline{A}_{\text{GPS}}$: design sub-matrix of GPS ZWD observations, partial derivatives are the weighting coefficients

with the two sub-matrices $\underline{A}_{\text{NWM}}$ for the numerical weather model partials and $\underline{A}_{\text{GPS}}$ for the GPS-related zenith wet delays.

4.5.4 Stochastic Optimization

Problems with the stochastic model of the observations may likely occur during the combination of two different data sets. This is particularly true in this context because most GPS software packages deliver highly optimistic error estimates. If such data are assimilated, they will get an unjustifiably high weight. On the other hand, the accuracy of tropospheric delays derived from the numerical weather model is not easy to assess as well. Several methods have been implemented to overcome these problems. Suspicious observations can be detected with a Pope type blunder detector (\rightarrow 4.5.4.1) and the estimation of variance components may lead to an optimized stochastic model (\rightarrow 4.5.4.2). Alternatively, a pre-weighting approach can be useful under special conditions (\rightarrow 4.5.4.3).

4.5.4.1 Sensing Inconsistencies (Outlier Detection)

In order to improve the reliability of the combined solution, a blunder detector of Pope type (\rightarrow 2.5.1.4.3) can be applied to either the NWM or the GPS delays, or to both observation sets. However, the NWM nor the GPS inputs are frequently outlier-corrupted - this only happens in very few cases. The more likely reason for detected blunders lies in inconsistencies of the associated variances. In this way, the blunder detector can be understood as a method to improve the stochastic model for certain, critical data: If a computed outlier Δ_i is considered to be significant by the combination module, the outlier will be used to replace the old standard deviation of the measurement by a new value of $\sigma_i = \Delta_i \cdot q_{\text{AMP}}$ where q_{AMP} is an additional, user-defined amplifier.

4.5.4.2 Variance Component Estimation

Weighting problems can be overcome by the estimation of variance components that can lead to an optimized stochastic model. This procedure works iteratively and is described by PELZER [1985].

Two variance components are estimated for the two groups of observations, NWM and GPS delays. Following section 4.5.1, the stochastic model of the observations can be rewritten as

$$\underline{\Sigma}_{LL} = \begin{bmatrix} \underline{\Sigma}_{NWM} & \\ & \underline{\Sigma}_{GPS} \end{bmatrix} = \begin{bmatrix} \sigma_{NWM}^2 \cdot \underline{Q}_{NWM} & \\ & \sigma_{GPS}^2 \cdot \underline{Q}_{GPS} \end{bmatrix} \quad (4-86)$$

σ_{NWM}^2 : variance component of the numerical weather model delays

σ_{GPS}^2 : variance component of the GPS-derived delays

\underline{Q} : cofactor matrix of the NWM and GPS observations

and the target of this operation is to find suitable values for the variance components. This goal is reached by separation of the cofactor matrices of the residuals¹⁶

$$\begin{aligned} \underline{Q}_{NWM}^* &= \underline{Q}_{NWM} - \underline{A}_{NWM} \cdot \underline{Q}_{XX} \cdot \underline{A}_{NWM}^T \\ \underline{Q}_{GPS}^* &= \underline{Q}_{GPS} - \underline{A}_{GPS} \cdot \underline{Q}_{XX} \cdot \underline{A}_{GPS}^T \\ \underline{Q}_{NWM,GPS}^* &= -\underline{A}_{NWM} \cdot \underline{Q}_{XX} \cdot \underline{A}_{GPS}^T \end{aligned} \quad (4-87)$$

\underline{Q}^* : separated cofactor matrix of the residuals for NWM, GPS and between NWM and GPS

\underline{Q}_{XX} : cofactor matrix of the adjusted parameters

and the equation for the vector of residuals is

$$- \begin{bmatrix} \underline{Q}_{NWM}^* & \underline{Q}_{NWM,GPS}^* \\ \underline{Q}_{GPS,NWM}^* & \underline{Q}_{GPS}^* \end{bmatrix} \cdot \begin{bmatrix} \underline{P}_{NWM} \\ \underline{P}_{GPS} \end{bmatrix} \cdot \begin{bmatrix} \underline{l}_1 \\ \underline{l}_1 \end{bmatrix} = \begin{bmatrix} \underline{v}_{NWM} \\ \underline{v}_{GPS} \end{bmatrix} \quad (4-88)$$

\underline{P} : weight matrix of the NWM and GPS observations

\underline{l} : vector of pre-fit residuals (reduced observations) of the NWM and GPS observations

\underline{v} : vectors of post-fit residuals of the NWM and GPS observations

Now, the variance components can be estimated

$$\sigma_{NWM}^2 = \frac{\underline{v}_{NWM}^T \cdot \underline{P}_{NWM} \cdot \underline{v}_{NWM}}{\text{trace}(\underline{P}_{NWM} \cdot \underline{Q}_{NWM}^*)} \quad \wedge \quad \sigma_{GPS}^2 = \frac{\underline{v}_{GPS}^T \cdot \underline{P}_{GPS} \cdot \underline{v}_{GPS}}{\text{trace}(\underline{P}_{GPS} \cdot \underline{Q}_{GPS}^*)} \quad (4-89)$$

and the ratio between the a posteriori estimate of the variance component and the a priori choice for the standard deviation of the weight unit

$$\frac{\sigma_{NWM}^2}{\sigma_0^2} \approx \frac{\sigma_{GPS}^2}{\sigma_0^2} \approx 1.0 \quad (4-90)$$

σ_0 : standard deviation of the weight unit a posteriori

should be near 1. If the deviation from this nominal value is too large - deviations of up to approximately 10% are tolerable - the variance components should be used to optimize the a priori stochastic model of the observations and the adjustment

¹⁶ Refer to section 2.5.1.1 and 2.5.1.2 for details on the standard least-squares adjustment algorithm.

algorithm is to be repeated until a suitable level of convergence is reached. Normally, only one iteration is necessary to reach a level of agreement of better than 10%.

4.5.4.3 Pre-Weighting Approach

The pre-weighting approach uses the pre-fit residuals to optimize the stochastic model. All pre-fit residuals of the NWM-delays are zero because the vector of unknowns is initialized with these observations (\rightarrow 4.5.2), but the GPS pre-fit residuals, i. e. the differences between the GPS wet delays and those interpolated in the weather fields, will not be zero. These discrepancies can be used to tune the stochastic model of the NWM data. The pre-fit residual l_i

$$l_{\text{GPS}}^2 \equiv \sigma_{\text{TOT}}^2 = \sigma_{\text{GPS}}^2 + \sigma_{\text{NWM}}^2 \quad (4-91)$$

l_i : pre-fit residual for GPS observation

σ_{TOT} : combined NWM/GPS standard deviation, identical with pre-fit residual

σ_{GPS} : standard deviation of GPS delay

σ_{NWM} : standard deviation of delay at GPS site that is interpolated in NWM data set

is formally treated as the standard deviation σ_{TOT} , and the standard deviation of the interpolated ("approximated") delay at the GPS site is related to the 4 nearest grid points of the NWM data by

$$\sigma_{\text{NWM}}^2 = \sigma_{\text{TOT}}^2 - \sigma_{\text{GPS}}^2 = \sum_{i=1}^4 (p_i \cdot \sigma_i)^2 \quad \wedge \quad \sum_{i=1}^4 p_i \approx 1 \quad (4-92)$$

p_i : partial derivative as defined by formula 4-84

σ_i : standard deviation of the NWM delay at grid point i

The error budget of the interpolated point must now be transformed into standard deviations of the grid points. This task can be performed if we consider 3 cases that cover most situations. In the first case, it is assumed that all differentials p_i approximately equal each other

$$p_1 \approx p_2 \approx \dots \approx p_i \quad \Rightarrow \quad \sigma_i = \frac{\sigma_{\text{NWM}}}{2 \cdot p_i} \approx 2 \cdot \sigma_{\text{NWM}} \quad (4-93)$$

and the new standard deviation of all 4 neighboring grid points is given by σ_i . In the second case, we assume that the NWM delay at grid point $i=1$ has a dominant impact on the interpolated value. As a consequence, the other 3 grid points will (almost) remain untouched and a new standard deviation of

$$p_1 \approx 1, \quad p_2 \approx p_3 \approx p_4 \approx 0 \quad \Rightarrow \quad \sigma_1 = \frac{\sqrt{\sigma_{\text{NWM}}^2 - \sum_{i=2}^4 (p_i \cdot \sigma_i)^2}}{p_1} \approx \frac{\sigma_{\text{NWM}}}{p_1} \approx \sigma_{\text{NWM}} \quad (4-94)$$

will only be assigned to the dominant one. The last case considered here assumes that the partials for the first 2 points equal each other, i. e. these 2 points are the dominant grid points. Then, the standard deviation

$$p_1 \approx p_2 \approx 0.5, \quad p_3 \approx p_4 \approx 0 \quad \Rightarrow \quad \sigma_{1/2} = \sqrt{\frac{\sigma_{NWM}^2 - \sum_{i=3}^4 (p_i \cdot \sigma_i)^2}{p_1^2 + p_2^2}} \approx \frac{\sigma_{NWM}}{\sqrt{2} \cdot p_1} \approx 1.41 \cdot \sigma_{NWM} \quad (4.95)$$

can be used to substitute the old values for these points. In this way, a certain tuning of the stochastic model can be accomplished.

However, it is stressed that this method has some incisive disadvantages. The most critical assumption is that the standard deviation σ_{GPS} of the GPS delays are assumed to be trustworthy and that the GPS delays themselves are never outlier-corrupted. The pre-weighting method effectively renders the blunder detection ineffective, and this means a loss of integrity.

5. Validation of Numerical Weather Model Data

Selected validation results of some quantities routinely extracted from the GDAS 1° x 1° numerical weather fields are discussed in this chapter. Comparisons include surface meteorological data (→ 5.1), the temperature lapse rate (→ 5.2) and the mean atmospheric temperature (→ 5.3). Moreover, mapping functions coefficients derived from the numerical weather model via ray-tracing are presented (→ 5.4). Furthermore, the reader may also refer to SOLBRIG [2000] who also discusses results from comparisons with other weather fields like ETA and EDAS (→ 4.1).

It should be noted that Chapter 7 partly deals with validation studies of numerical weather models as well, e. g. pressure and water vapor scale heights, and the combination of NWM-derived and GPS-derived wet delays.

5.1 Surface Meteorological Data

Surface meteorological data, i. e. total pressure, dry temperature and relative humidity, can be validated with help of those IGS tracking stations that own precise meteorological sensors and distribute these data. Unfortunately, this is only the case

SITE	NUMBER SAMPLES	BIAS PRESSURE	SIGMA [hPa]	BIAS TEMPERATURE	SIGMA [K]	BIAS HUMIDITY [%]	SIGMA
AUCK	696	-0.1	0.6	-1.8	1.2	9	7
BAHR	648	-0.8	0.4	-1.2	2.5	15	12
BRUS	648	-0.2	0.3	1.2	1.8	-7	7
CHAT	696	-0.1	0.9	-2.6	« 1.3	9	6
CRFP	648	-0.5	0.4	-0.2	2.4	11	9
GODE	456	-1.5	« 0.7	2.3	2.6	-79	« 10
GRAZ	528	-2.3	« 0.5	0.4	2.0	-1	9
HERS	648	-0.2	0.3	0.4	1.6	-4	5
MDO1	672	-0.6	0.5	-0.4	2.7	-2	23
MONP	672	-0.0	0.4	-0.4	3.3	9	8
OBER	648	0.5	0.4	-0.6	2.1	-1	9
POTS	576	0.4	0.4	-0.3	1.3	-4	8
SIO3	696	0.5	0.4	0.8	1.6	16	4
SOL1	720	-0.5	0.5	1.8	1.4	-12	7
USNO	576	-1.2	0.6	1.3	1.5	-34	6
VNDP	576	-0.1	0.4	-1.2	1.6	9	6
ZIMM	648	-0.3	0.4	-0.5	1.2	14	10
AOML	696	-0.2	0.6	0.6	0.8	-7	4
KOKB	432	0.4	0.5	2.7	« 1.3	-84	« 4
FAIR	432	-0.9	0.5	-1.9	2.7	2	16
METS	120	-0.7	0.4	1.1	2.5	-5	10
WES2	240	1.0	0.5	0.6	2.1	1	10
MEAN		-0.33	0.47	-0.02	1.83	-4.3	8.5

Table 5-1 - Result table of surface meteorological data comparison for July 1999. The first column gives the name of the IGS tracking station (refer to Appendix III for the location of these stations), the second contains the number of samples used for the comparison followed by the biases and standard deviations ("sigma") of the particular quantities. The results printed here belong to configuration I (→ 5.1.1.1).

for a very small subset of the global network. Daily meteorological files are only available for 10 to 30 stations. All data available for July 1999 were used for this comparison with a temporal resolution of 1 hour. The 4-pillar-method (\rightarrow 4.2.1.1) was used for interpolation with a weighting power of 1.5 for the horizontal interpolation (\rightarrow 4.2.1.3).

5.1.1 Surface Pressure

The comparison with surface pressure measurements from meteorological sensors at the IGS monitor stations is very satisfactory. The average standard deviation¹ is in the range of 0.5 hPa and meets the accuracy requirements for precise zenith hydrostatic delay prediction. The systematic errors are also moderate for most stations (about 0.5 hPa or less).

However, certain problematic sites can be identified, e. g. *GODE* and *USNO* with biases of more than 1 hPa. A bias of more than 2 hPa was calculated for *GRAZ*. In most cases, such high deviations from the reference data are *not* entirely related to systematic errors of the models. Actually, a wrong height reference is the reason for the discrepancies in the case of *GRAZ*: The biases are very small at the beginning of July 1999, but they suddenly reach values of about 5 hPa because the operator obviously and erroneously changed the height entry in the RINEX MET files from ellipsoidal height (as it should be done and was done for the previous days) to geopotential (or orthometric) height. The geoid height is about 47 m for *GRAZ* and a height error of 50 m causes a pressure bias in the range of 5.5 hPa.

Nevertheless, biases may occur and cannot always be traced back to operating a device errors. A good example is the detailed comparison of Potsdam (*POTS*) and Oberpfaffenhofen (*OBEP*) plotted in Figure 5-1 and Figure 5-2, respectively. Whereas the mean results summarized in Table 5-1 suggest almost the same, excellent accuracy situation for both sites with biases and standard deviations not higher than 0.5 hPa, the diagrams show a considerably different situation: The biases at Potsdam are always below 1 hPa and often smaller than 0.5 hPa. Moreover, they follow a one-sided distribution as they are always positive except for two minor cases. The diagram for Oberpfaffenhofen shows reasonably higher biases that may reach a level of 1.5 hPa. In most cases, they are positive, too, but some strong negative offsets can be seen at the beginning of July that compensate some of the strong positive biases. As a consequence, the mean bias turns out to be rather small as well.

Several reasons might be responsible for the occurrence of intermittent, strong biases at Oberpfaffenhofen. In contrast to Potsdam, this station is located in the vicinity of the Alps, northward of the boundaries of these mountains. It is well-known that special climatic conditions are linked to this topography that are possibly difficult to assess for a global numerical weather model like GDAS with a resolution of just

¹ The accuracy is expressed with help of the following quantities: Given the difference $d_i = \text{val}_{\text{REF}} - \text{val}_{\text{SAM}}$ between the sampled (val_{SAM}) and the reference value (val_{REF}). The bias is the arithmetic mean of all these differences: $\text{BIAS} = 1/n \cdot \sum d_i$ with n being the number of samples compared and the RMS is defined as $\text{RMS} = [1/n \cdot \sum d_i^2]^{1/2}$. Finally, the standard deviation, also denoted as SIG or SIGMA here, is the bias-reduced accuracy: $\text{SIGMA} = [1/(n-1) \cdot \sum (d_i - \text{BIAS})^2]^{1/2}$.

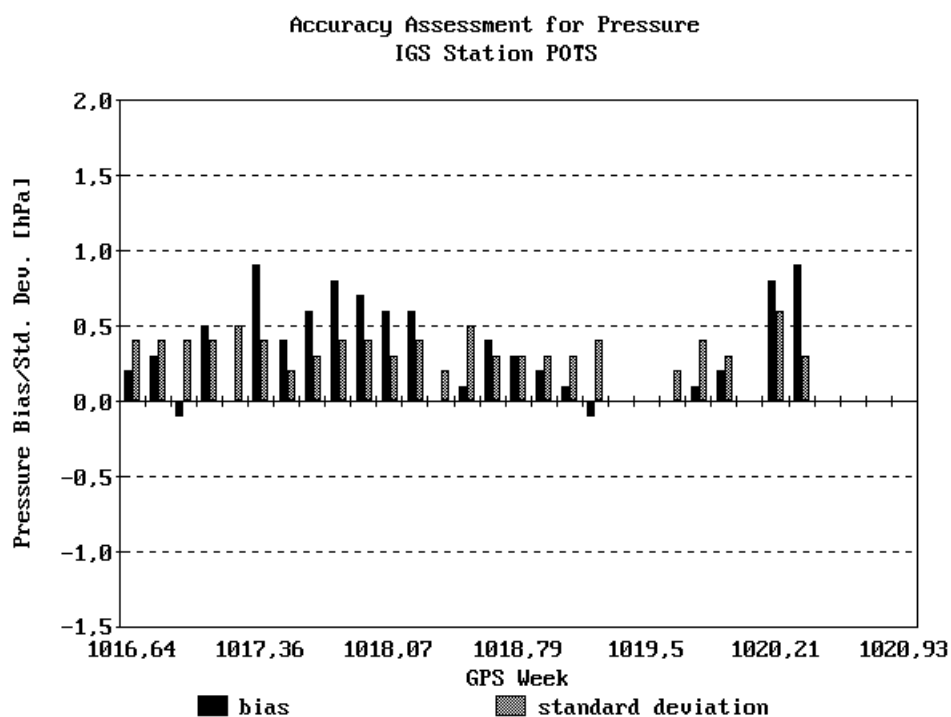


Figure 5-1 - Diagram of diurnal pressure biases and standard deviations (sigma) for IGS monitor station Potsdam (POTS, Germany) in July 1999.

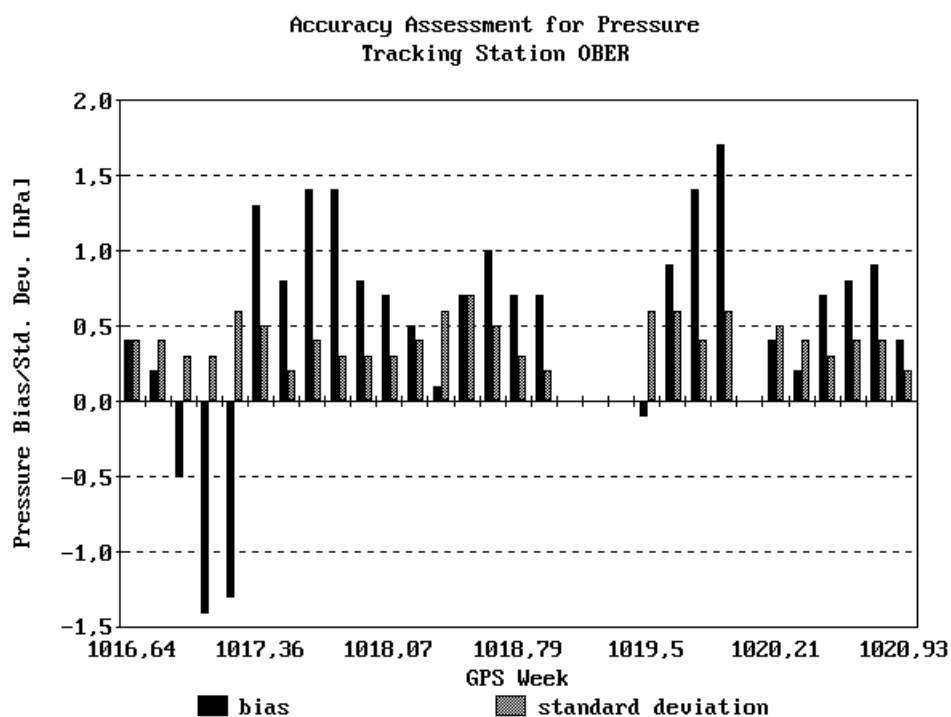


Figure 5-2 - Diagram of diurnal pressure biases and standard deviations (sigma) for IGS monitor station Oberpfaffenhofen (OBER, Germany) in July 1999.

about 1° . Moreover, another important problem can be seen in the fact that vertical extrapolation is necessary when surface data for Oberpfaffenhofen are to be extracted since the lowest geopotential height/pressure pair of some of the 4 nearest neighboring grid points is notably higher than the height of the target station ($\rightarrow 7.3$) what may deteriorate the accuracy of the interpolation algorithm, because *extrapolation* is actually necessary.

5.1.1.1 Impact of Vertical Interpolation

Three different configurations were tested concerning the vertical pressure profile interpolation. Configuration I applies the *adjustment-method*: All available points of the profile are fitted to the mixed polynomial/exponential-model ($\rightarrow 4.4.2.2$) given with formula 4-54. The unknown vertical reduction coefficients a_p , b_p and c_p are determined via least-squares adjustment. Afterwards, the model is used to interpolate (or - as sometimes necessary - to extrapolate) the pressure at the antenna height. Configuration II uses *exponential interpolation* between the two nearest vertical neighbors ($\rightarrow 4.2.1.2$, formula 4-22 and 4-16) and configuration III applies the *upward/downward-method* ($\rightarrow 4.2.1.2$, formulas 4-19 to 4-21).

The accuracy only varies marginally as far as these different vertical interpolation methods are concerned:

Configuration	Bias [hPa]	Standard Deviation [hPa]
I	-0.33	0.47
II	-0.30	0.48
III	-0.34	0.48

Table 5-2 - Mean biases and standard deviations (sigma) for the three different configurations applied to the vertical pressure interpolation.

As a consequence, one may conclude that the method of vertical pressure interpolation is only of minor importance as all models discussed in Chapter 4 are obviously suited for this task.

5.1.1.2 Long-Term Comparison

A long-term comparison for the same numerical weather model was performed by SCHUELER et al. [2000a] from June 1999 to March 2000. In contrast to the results presented here, the *1-pillar-method* ($\rightarrow 4.2.1.1$) was used for the long-term comparison. The final results are very similar to those for July 1999 with a mean standard deviation of 0.55 hPa (*here*: 0.47 hPa). This indicates that the 1-pillar-method is not (or only marginally) inferior to the 4-pillar-method.

5.1.2 Surface Temperature

Surface temperature is of minor importance for ground-based GPS water vapor estimation. If the mean temperature of the atmosphere is not available, the surface temperature can be used to compute the mean temperature ($\rightarrow 3.5.3.1$). A surface temperature accuracy of about 2 K is desirable for this task. However, the modeling

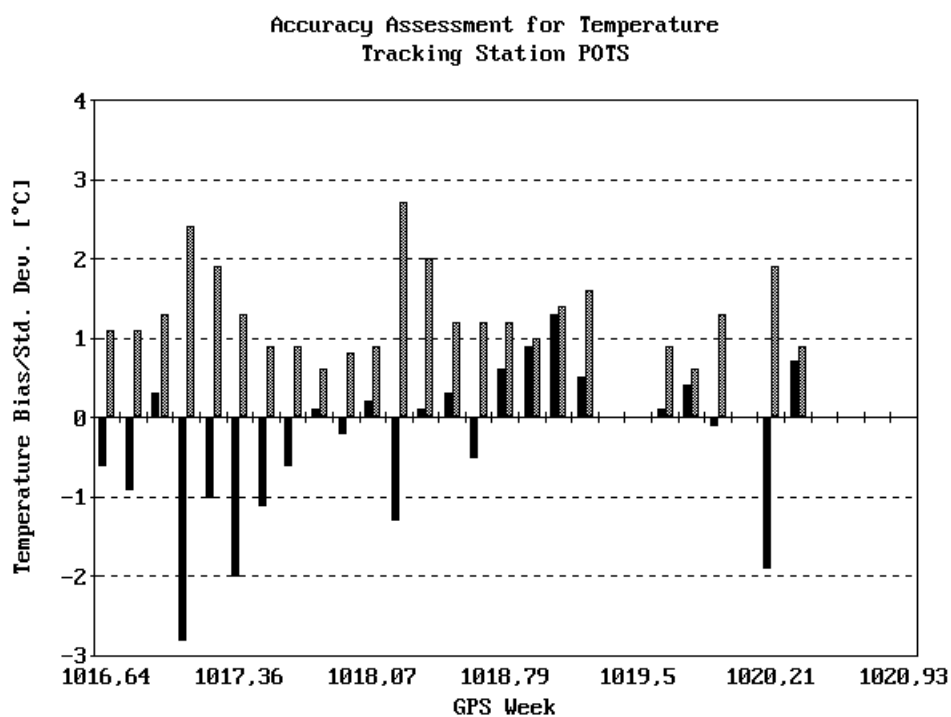


Figure 5-3 - Diagram of diurnal temperature biases and standard deviations (sigma) for IGS monitor station Potsdam (POTS, Germany) in July 1999.

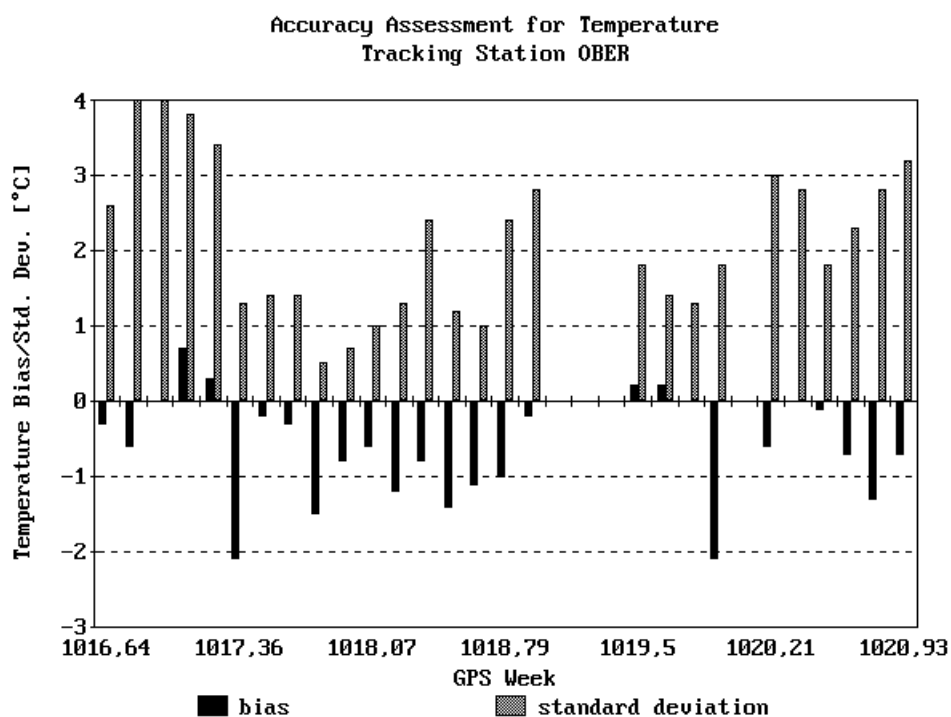


Figure 5-4 - Diagram of diurnal temperature biases and standard deviations (sigma) for IGS monitor station Oberpfaffenhofen (OBER, Germany) in July 1999.

error will also contribute to the total error budget if this method is applied. Consequently, the error budget can be reduced if the mean temperature is integrated in the numerical weather field (\rightarrow 5.3). Nevertheless, surface temperature is useful for other purposes, e. g. the prediction of zenith wet and hydrostatic delays (\rightarrow 3.2.1.2, \rightarrow 3.2.1.1.1) and the determination of precise obliquity factors (\rightarrow 3.2.2).

Table 5-1 shows that the standard deviation of the surface temperature data is better than 2 K and only one single site (*MONP*) shows a shatter of more than 3 K. Several sites are apparently prone to systematic offsets, although 50% of the stations have biases of less than 1 K. Especially *CHAT* and *KOKB* are critical stations, but it is pointed out that *KOKB* is one of those stations where there are serious concerns about the integrity of the RINEX meteorological data. This is esp. true as far as the relative humidity samples (\rightarrow 5.1.3) of this station are concerned.

Diagrams for IGS monitor station Potsdam (*POTS*, Figure 5-3) and Oberpfaffenhofen (*OBER*, Figure 5-4) are given on the preceding page. Oberpfaffenhofen shows higher standard deviations than Potsdam, but the bias-behavior is more homogeneous since the systematic errors are mostly negative whereas those for Potsdam are more variable.

The results from long-term comparisons presented by SCHUELER et. al. [2000a] who found a mean standard deviation of 1.8 K correspond to those discussed here.

5.1.3 Relative Humidity

Surface relative humidity is only of minor importance for the tropospheric analysis software. Like surface temperature, it can be used to predict zenith wet delays (\rightarrow 3.2.1.2) and may also serve as input for several mapping functions (\rightarrow 3.2.2).

Well-calibrated humidity sensors should be able to measure relative humidity at an accuracy level² of 5%. Table 5-1 illustrates that this level could not be reached for comparison of NWM-extracted data and in situ measurements is concerned. A mean standard deviation of 9% can be stated. Station *MDO1* (located in the middle part of the USA) has the highest standard deviation of more than 20% that might be caused by a temporarily mal-functioning humidity device at this site.

Quite a number of stations show heavy biases. In a few cases, these biases can be definitely traced back to erroneous measurements of the IGS meteorological sensors. This is undoubtedly true for *KOKB*: for many days, the sensor reads a relative humidity of 0.5% which is almost constant over the whole day. This value cannot be considered to be reliable.

Apart from extrapolation problems (\rightarrow 5.1.1), the humidity sensors can be highly influenced by micro climate what is not at all representative for the vertical atmos-

² The accuracy depends on the kind of sensor used. A number of different sensors technologies exists and the sensitivity of some types is dependent on the amount of humidity itself, e. g. ENGLAND [1992] mentions that certain sensors are not able to provide humidity below 20% very precisely, others show temperature-dependent errors in the range of 2% to 8%.

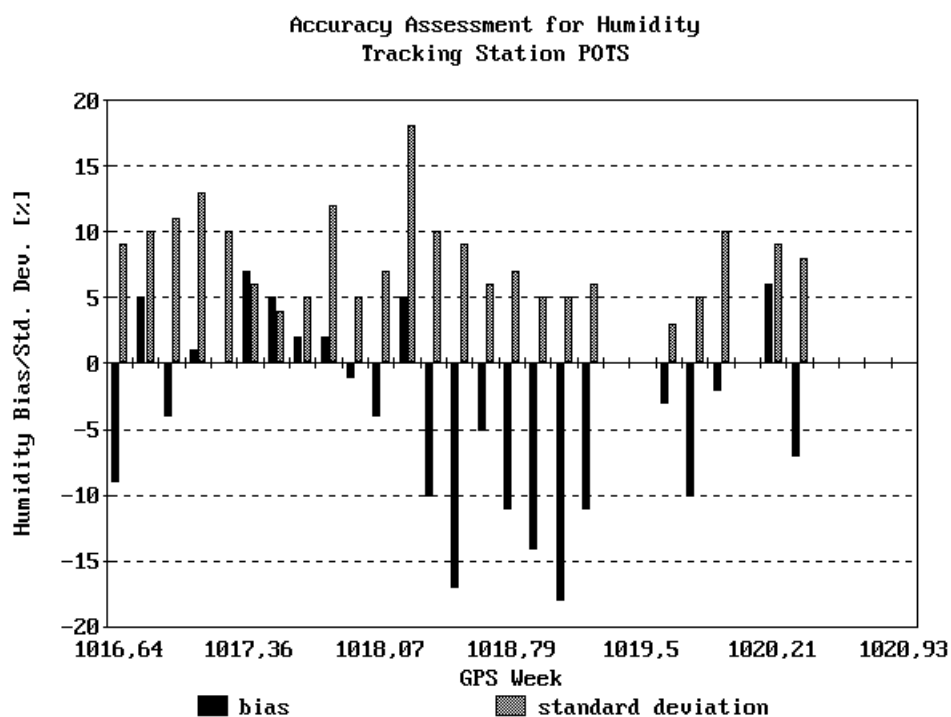


Figure 5-5 - Diagram of diurnal relative humidity biases and standard deviations (sigma) for IGS monitor station Potsdam (POTS, Germany) in July 1999.

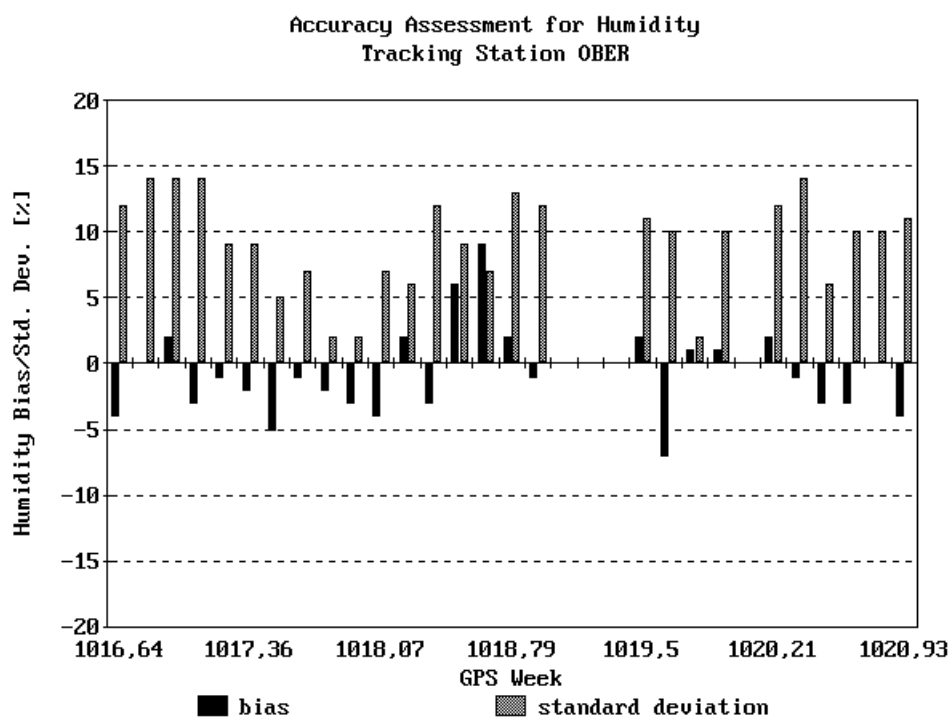


Figure 5-6 - Diagram of diurnal relative humidity biases and standard deviations (sigma) for IGS monitor station Oberpfaffenhofen (OBER, Germany) in July 1999.

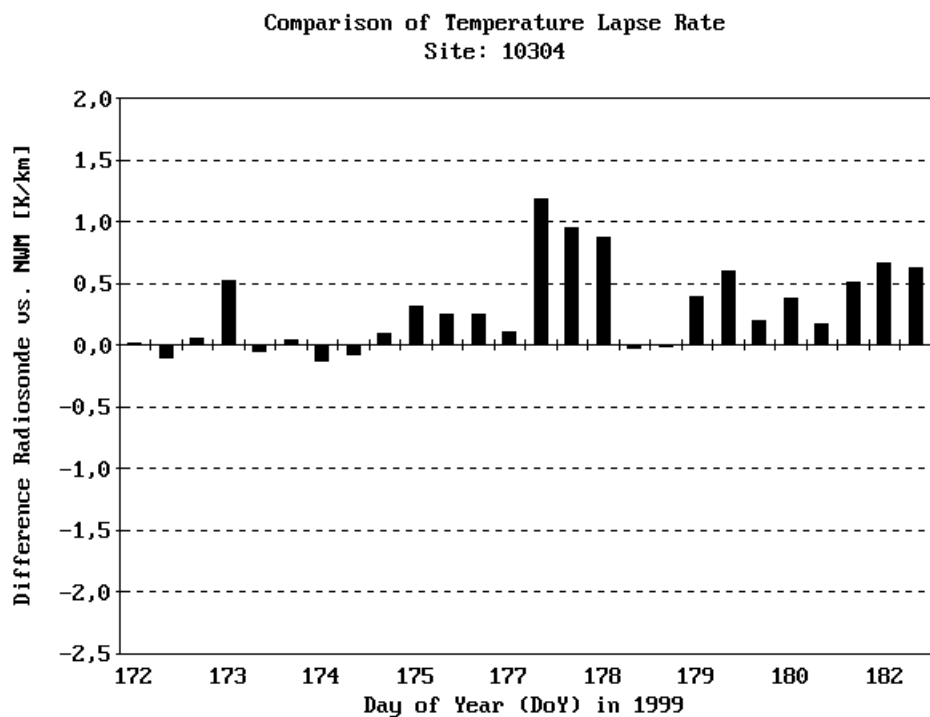


Figure 5-7 - Differences between the temperature lapse rates from radiosonde launches at site 10304 and those derived from the vertical temperature profiles of the GDAS weather fields.

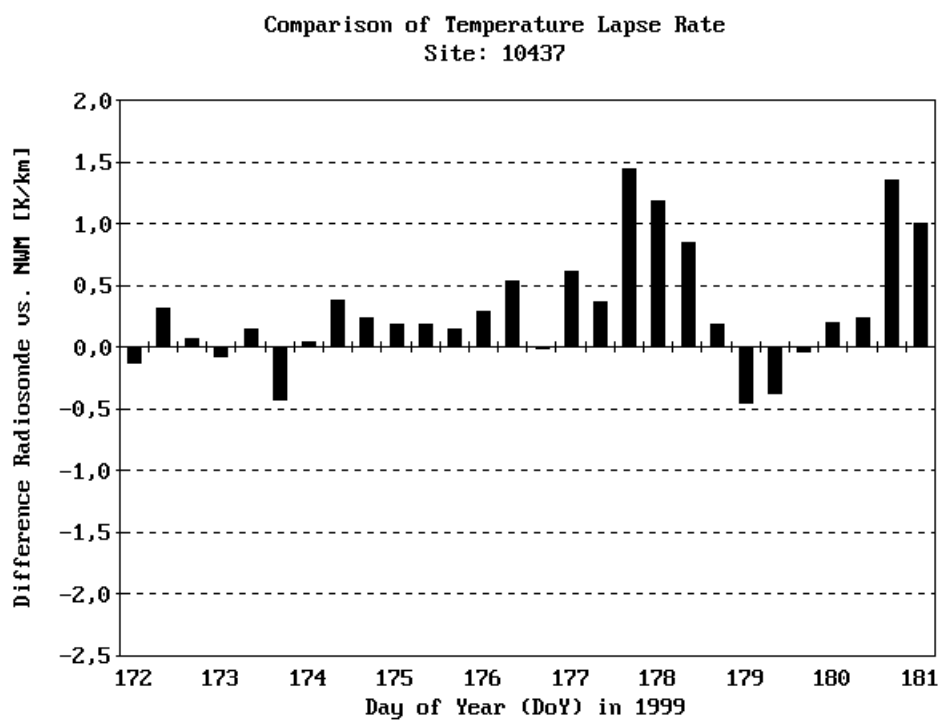


Figure 5-8 - Differences between the temperature lapse rates from radiosonde launches at site 10437 and those derived from the vertical temperature profiles of the GDAS weather fields.

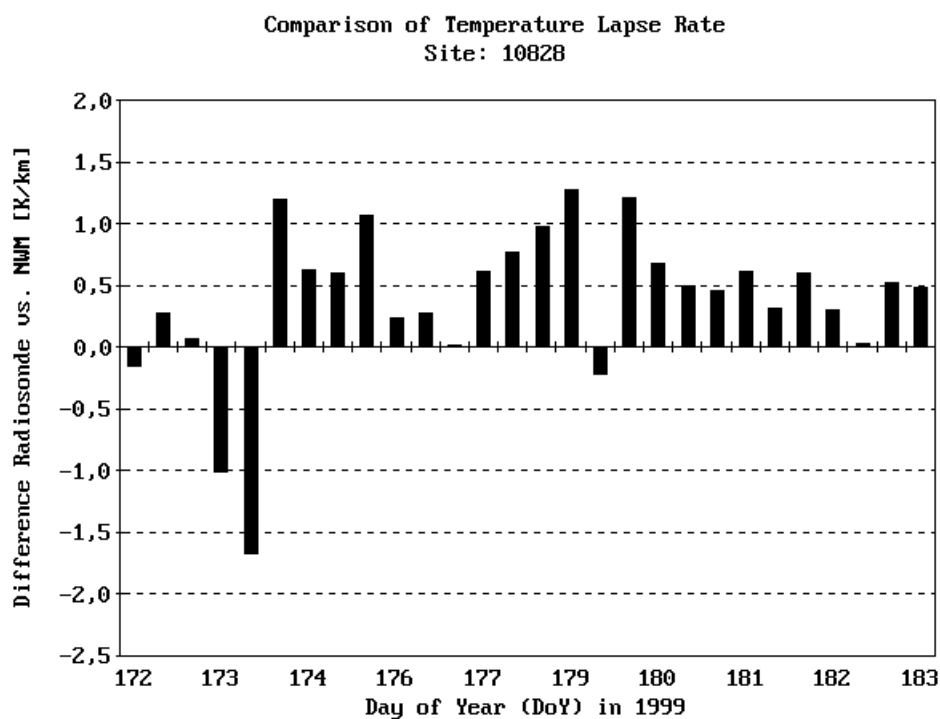


Figure 5-9 - Differences between the temperature lapse rates from radiosonde launches at site 10828 and those derived from the vertical temperature profiles of the GDAS weather fields.

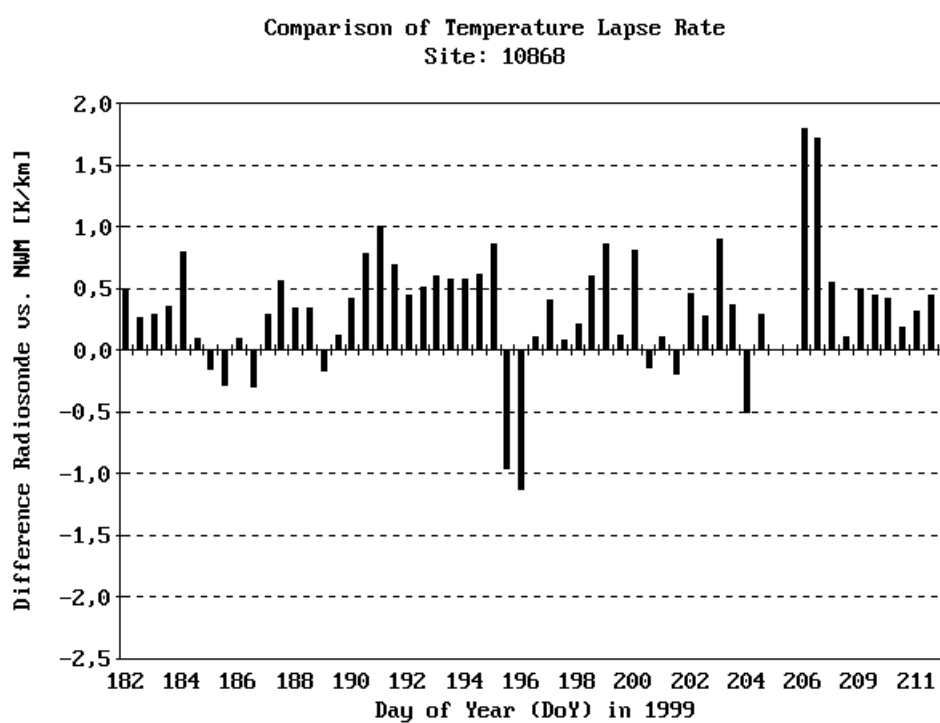


Figure 5-10 - Differences between the temperature lapse rates from radiosonde launches at site 10868 and those derived from the vertical temperature profiles of the GDAS weather fields.

pheric profile, although this is exactly what is necessary to determine the wet delay with help of conventional models. If such local conditions are present, the data extracted from the numerical weather fields can certainly have offsets in comparison to the in situ measurements though they should be expected to be better suited for application in wet delay models.

Figure 5-5 and Figure 5-6 show the accuracy situation for Potsdam (*POTS*) and Oberpfaffenhofen (*OBEP*). Potsdam seems to suffer more from systematic errors - the biases sometimes reach values of more than 15% - than Oberpfaffenhofen does. The mean standard deviation is similar for both sites and has a level of 8% to 9%.

5.1.4 Results for High-Resolution Weather Fields

Surface meteorological data from high-resolution weather fields were available for a validation experiment covering the period from 1 October to 31 October 1997. The weather model used for the region inside Germany had a horizontal resolution of 14 km, and outside Germany a 55 km model was used. Table 5-3 gives the summarized accuracy quantities.

SITE	NUMBER SAMPLES	BIAS PRESSURE	SIGMA [hPa]	BIAS TEMPERATURE	SIGMA [K]	BIAS HUMIDITY	SIGMA [%]
HERS	624	-0.0	0.5	-0.2	1.0	-5.7	6.2
METS	456	0.5	0.4	-1.0	1.4	4.3	7.1
POTS	672	0.8	0.6	-0.1	1.4	6.1	7.5
REYK	648	0.7	0.7	-3.1	1.1	-8.5	5.5
WTZR	672	0.9	0.5	-0.5	1.3	-1.1	8.5
ZIMM	600	0.6	0.5	-0.8	1.4	7.0	8.6
MEAN		0.6	0.5	-0.9	1.3	0.3	7.2

Table 5-3 - Result table of surface meteorological data comparison with high-resolution numerical weather fields for October 1997. The first column gives the name of the IGS tracking station (refer to Appendix III for the location of these stations), the second contains the number of samples used for the comparison followed by the biases and standard deviations ("sigma") of the particular quantities. The stations inside Germany (POTS, WTZR) are covered by the Germany-model (14 km horizontal resolution) of the German Weather Service (DWD), and the Europe-model (55 km horizontal resolution) was applied for the stations outside Germany.

Taking the higher resolution in contrast to the GDAS weather fields (Table 5-1) into consideration, the accuracy increase is apparently rather small. This statement is especially true for the surface pressure. Bias and standard deviation are even higher for Potsdam (*POTS*) in comparison to the GDAS model. Figure 5-11 and Figure 5-12 show diagrams of the diurnal biases and standard deviations for the 2 sites located within Germany.

The fact of pressure showing no difference in accuracy is not too surprising since the horizontal distribution of pressure is not governed by high-frequency terms. Instead, surface pressure layers or, to be more precise, geopotential height fields are relatively homogenous and therefore easy to interpolate even for the case of medium-resolution weather fields like GDAS ($1^\circ \times 1^\circ$).

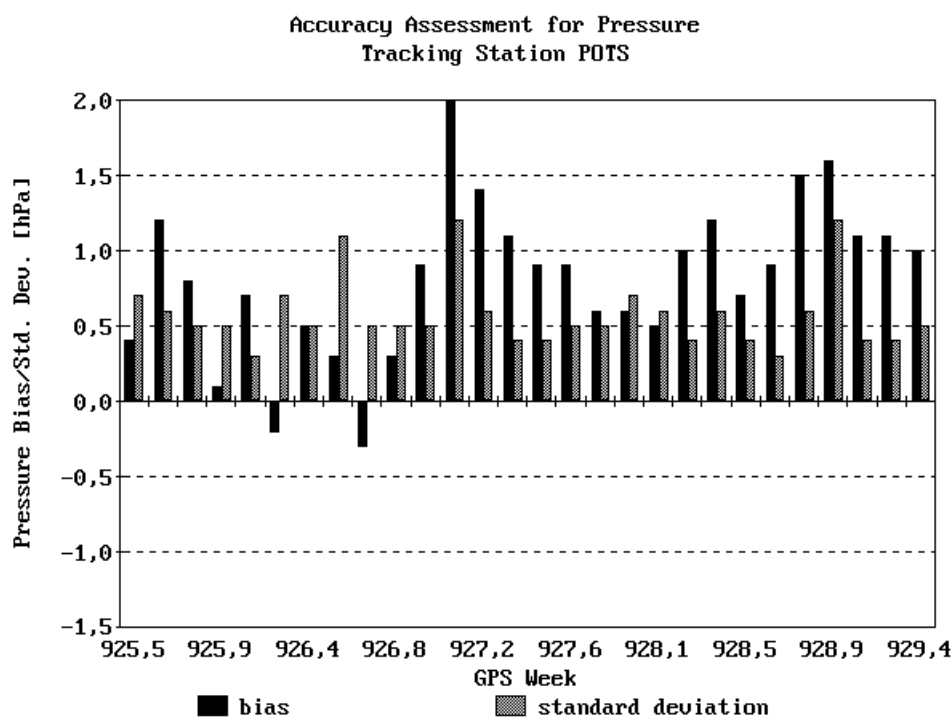


Figure 5-11 - Comparison of pressure data from the DWD weather model with in situ measurements. Diurnal pressure biases and standard deviations (sigma) for IGS monitor station Potsdam (POTS, Germany) in July 1999 are shown.

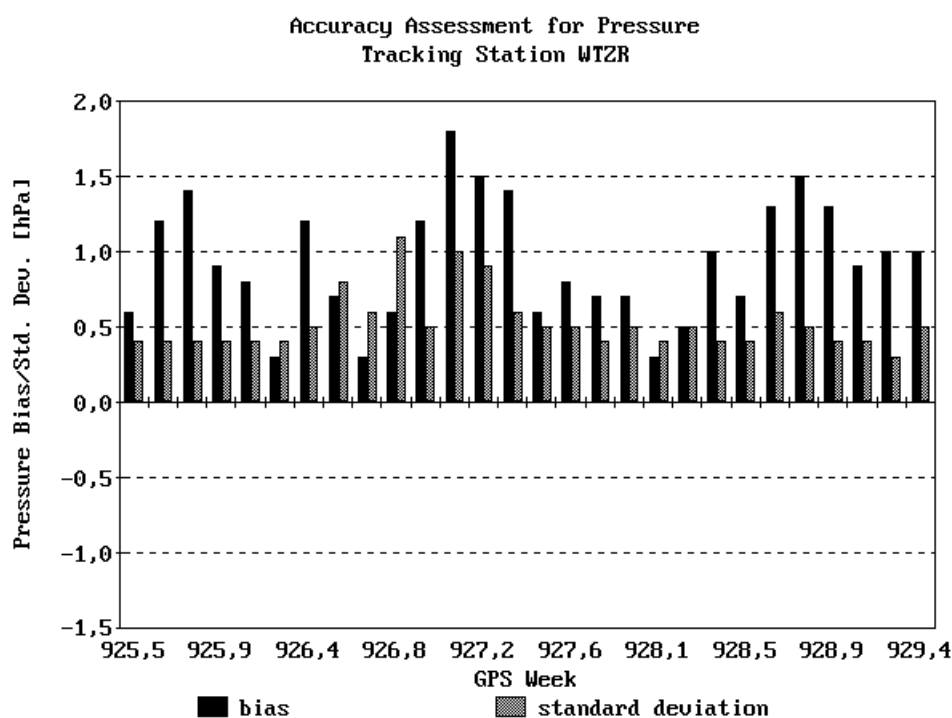


Figure 5-12 - Comparison of pressure data from the DWD weather model with in situ measurements. Diurnal pressure biases and standard deviations (sigma) for IGS monitor station Wettzell (WTZR, Germany) in July 1999 are shown.

5.2 Temperature Lapse Rate

The temperature lapse rate (\rightarrow 4.4.4.2) is routinely computed by vertical temperature profile fit and a constituent of TROPEX files (\rightarrow 4.4). There is mainly one reason for this: The hydrostatic mapping function of Davis (\rightarrow 3.2.2.1.4) uses this parameter to determine precise tropospheric obliquity factors. Radiosonde data were used to validate this quantity. The locations of the launch sites and the time spans used for the comparison are given in Table 5-4. The outcome of the synopsis between the radiosonde and the numerical weather model data is summarized in Table 5-5. Figure 5-7 to Figure 5-10 give detailed plots of the differences.

Launch Site Identifier	Latitude [deg]	Longitude [deg]	Height H [gpm]	Interval (DoY of 1999) Launch Epochs (UTC)
10304 Meppen	52°43' N	7°19' E	19	172 ... 181 4 h, 7 h, 10 h
10437 Fritzlar	51°08' N	9°17' E	222	172 ... 181 1 h, 7 h, 13 h
10828 Sigmaringen	48°06' N	9°15' E	645	172 ... 181 1 h, 7 h, 13 h
10868 Oberschleißheim	48°15' N	11°33' E	484	182 ... 212 0 h, 12 h

Table 5-4 - Location of those radiosonde launch sites used for the comparison of temperature lapse rates and mean atmospheric temperatures.

Radiosonde Site	Bias [K/km]	Standard Deviation [K/km]	RMS [K/km]
10304	0.30	0.35	0.46
10437	0.30	0.49	0.57
10828	0.38	0.68	0.73
10868	0.34	0.49	0.60

Table 5-5 - Mean accuracy quantities for the temperature lapse rate. The radiosonde launch site identifier is given in the first column followed by the bias (systematic offset), the standard deviation (bias-reduced precision) and the RMS (bias inclusive).

The systematic errors are in the range of 0.3 to 0.4 K/km and all have a positive sign. The RMS-values - that can be thought of as standard deviations including possible systematic errors - are in the range of 0.6 K/km in most cases and 0.1 K/km higher than the standard deviations.

An error in the vertical temperature gradient of 0.6 K/km causes a mapping function error of approximately 0.002 under average atmospheric conditions and an elevation angle of 10 degrees. Scaling this mapping function uncertainty by a zenith total delay of 2.3 m yields a total slant path delay error of 5 mm. This error contribution appears to be tolerable.

However, the temperature lapse rate typically varies for ± 0.5 K/m per day. The uncertainty of this parameter is in the same range, so these changes are hardly to be

significantly traced by the numerical weather model. As a consequence, it might be advisable to compute the mean temperature lapse rate for the whole diurnal data batch and to use this mean lapse rate throughout the whole day instead of applying individual lapse rates.

5.3 Mean Temperature of the Troposphere

The weighted mean temperature of the atmosphere (\rightarrow 3.5, \rightarrow 4.4.4.1) is important for the conversion of the Kalman-filtered zenith wet delays into integrated water vapor. The desired accuracy level is approximately 2 K and causes an uncertainty in integrated water vapor in the range of 0.2 kg/m². The same radiosonde data sets already used for the temperature lapse rate comparison (\rightarrow 5.2) were also applied to validate the mean temperature. The results of this study are printed in Table 5-6 and plotted in Figure 5-13 to Figure 5-16. Note that the diagrams do not only show the differences, but also the residuals. Residuals can be thought of as bias-reduced differences, i. e. their sum over the total time interval used for the comparison equals zero.

Radiosonde Site	Bias [K]	Standard Deviation [K]	RMS [K]
10304	0.3	1.8	1.8
10437	0.9	2.0	2.2
10828	0.8	1.9	2.1
10868	2.9	1.0	3.1

Table 5-6 - Mean accuracy quantities for the mean temperature of the troposphere. The radiosonde launch site identifier is given in the first column followed by the bias (systematic offset), the standard deviation (bias-reduced precision) and the RMS (bias inclusive).

All in all, it can be stated that the requested accuracy level can be reached. The RMS is near 2 K for all points except for radiosonde site 10868 (Oberschleißheim near Munich, Germany) where an exceptional bias of 3 K occurred. This systematic deviation is likely related to the unfortunate topography: The surface of all surrounding grid points is higher than that of the interpolation site. The height correction of the mean temperature with help of the temperature lapse rate β_M (\rightarrow 3.5.3.4, \rightarrow 4.4.4.1) was not performed here and can be made responsible for most of the bias that occurred.

5.4 NWM-derived Mapping Functions

A ray-tracing algorithm was discussed in section \rightarrow 4.3 that allows to compute slant hydrostatic and wet delays in 3-D numerical weather models. Mapping function coefficients and horizontal gradients can be estimated from such data sets (\rightarrow 4.3.2). This section compares the mapping functions derived for July 1999 for IGS tracking station Oberpfaffenhofen (*OBER*). The most important ray-tracing configuration settings were (see also \rightarrow Appendix VI): Bending correction (\rightarrow 4.3.1.1, formula 4-43) was applied, the saturation water vapor pressure was calculated with help of the regression formula (\rightarrow 4.2.3, formula 4-37) and the real-gas corrections (\rightarrow 3.2.1,

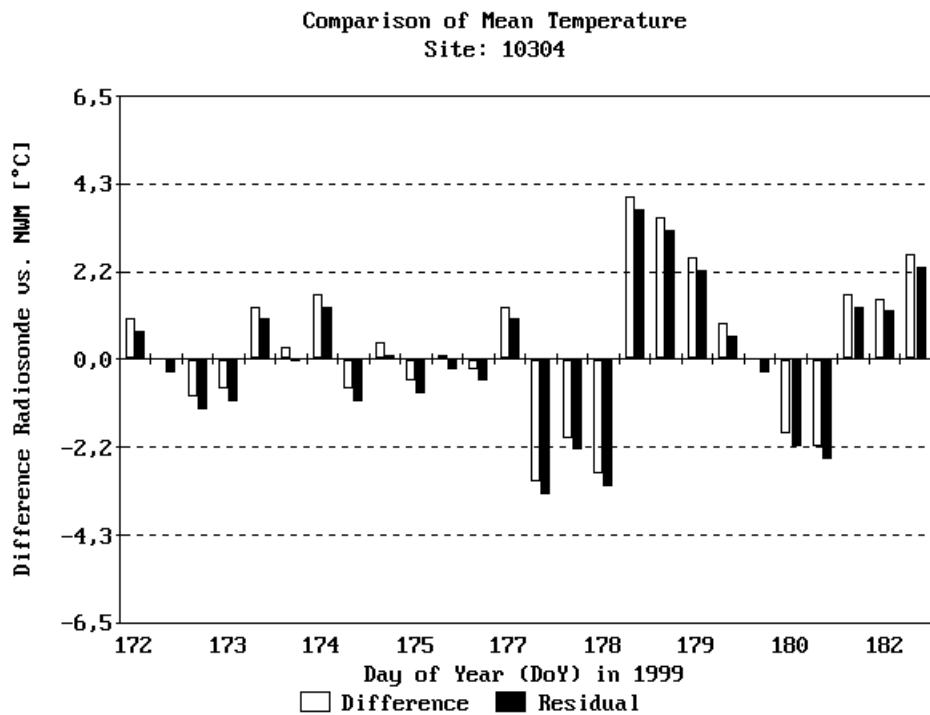


Figure 5-13 - Differences between the mean temperatures from radiosonde launches at site 10304 and those derived from the wet refractivity profiles of the GDAS weather fields.

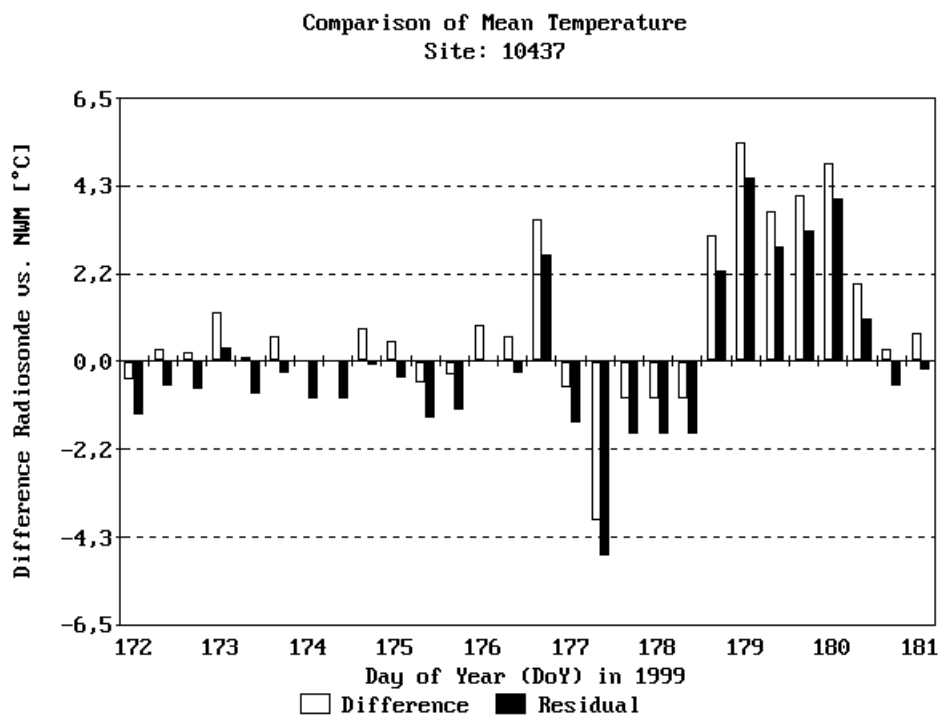


Figure 5-14 - Differences between the mean temperatures from radiosonde launches at site 10437 and those derived from the wet refractivity profiles of the GDAS weather fields.

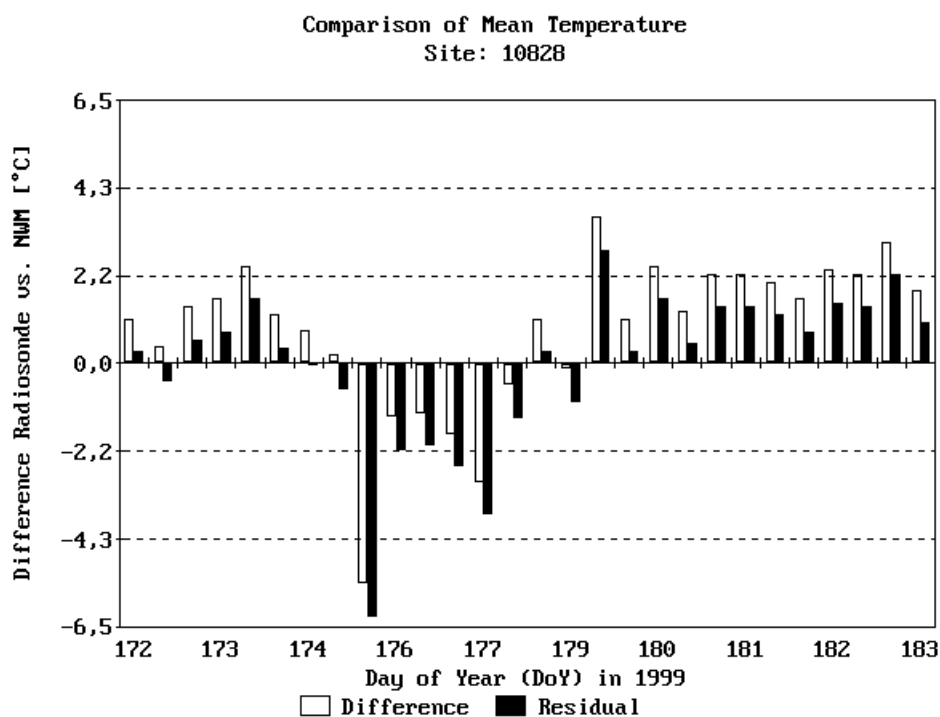


Figure 5-15 - Differences between the mean temperatures from radiosonde launches at site 10828 and those derived from the wet refractivity profiles of the GDAS weather fields.

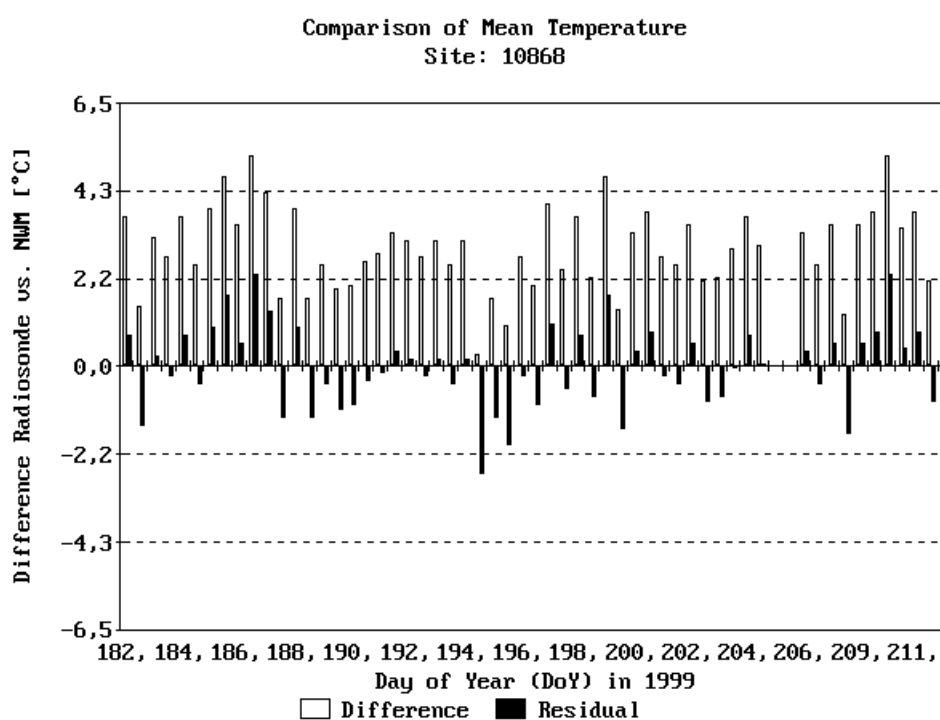


Figure 5-16 - Differences between the mean temperatures from radiosonde launches at site 10868 and those derived from the wet refractivity profiles of the GDAS weather fields.

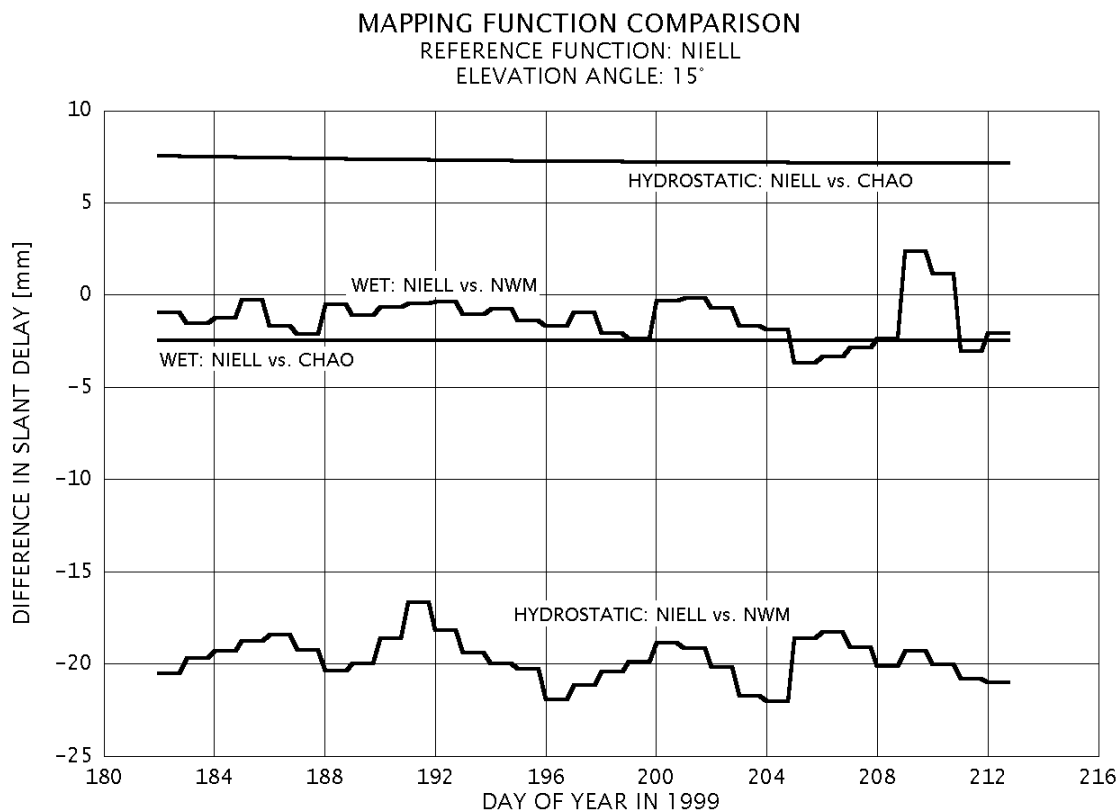


Figure 5-17 - Comparison of the Chao mapping function and obliquity factors derived from the GDAS numerical weather fields interpolated for IGS tracking station Oberpfaffenhofen. The reference model is the mapping function of Niell. The differences in hydrostatic delay were scaled by 2.2 m and the wet delay differences by 2 dm, so that the resulting difference can be compared to the error in slant hydrostatic/wet delay at an elevation angle of 15°.

formula 3-7) were used. Ray-tracing was performed down to an elevation angle of 10° with the double density option (→ 4.3.1.3) being applied for all zenith angles larger than 50°. The default increment in zenith angle was $\Delta z = 5^\circ$, the increment in slant path $\Delta s = 100$ m (→ 4.3.1.2) and the increment in azimuth was $\Delta \alpha = 45^\circ$. The weighted mean was determined from all mapping function coefficients of one day and used for the comparison.

Table 5-7 and Figure 5-16 portray the resulting errors for the hydrostatic and the wet slant delay at an elevation of 15°. The Niell mapping function (→ 3.2.2.1.7, → 3.2.2.2.5) was used as reference model and, additionally, the Chao mapping function (→ 3.2.2.1.2, → 3.2.2.2.1) was included in the comparison as well.

Mapping Function	Bias [mm]	RMS [mm]
Chao, hydrostatic	7.3	7.3
GDAS/NWM, hydrostatic	-20.7	20.8
Chao, wet	-2.5	2.5
GDAS/NWM, wet	-1.3	1.8

Table 5-7 - Mean accuracy quantities for the hydrostatic and wet delay mapping functions plotted in Figure 5-17.

The results are partly promising and partly insufficient. They are discouraging as far as the hydrostatic component is concerned: An offset of the GDAS-derived mapping function of as much as 2 cm from the reference model is not satisfactory. The Chao mapping function agrees to the Niell function at a RMS-level of just 7 mm what is acceptable. However, problems with the accuracy of GDAS hydrostatic obliquity factors are not too unexpected. The major error contribution is the uncertainty of the pressure. Systematic errors in the pressure will cause biases in the mapping function. This situation is rather problematic since the zenith hydrostatic delay is about 2.2 m, so to reach a high precision for the slant hydrostatic delay at 15° elevation, reasonably accurate knowledge of the hydrostatic refractivity profile is needed. It might really be possible that the medium-resolution GDAS weather fields are not capable to supply this level of precision.

This situation is much more uncritical for the wet delay that only reaches values of about 2 dm in zenith direction. Moreover, it is independent of dry pressure, but needs relative humidity (partial water vapor pressure) and temperature. Figure 5-17 proves that the GDAS-derived mapping function corresponds better to the reference model (RMS: < 2 mm) than the Chao wet mapping function does (RMS: 2.5 mm). These results are quite promising.

6. GPS Validation Experiments

Several selected GPS validation experiments are discussed in this chapter. All tropospheric parameters were estimated with the analysis system TropAC TRIDENT (\rightarrow 2., 3., 4.) that was developed as part of this study. As far as the tropospheric delays are concerned, three levels of comparison are possible.

The first level is the comparison of *zenith neutral delays* (\rightarrow 6.1, \rightarrow 6.3, \rightarrow 6.5). Note that total delays are not estimated by the TropAC analysis software, but the zenith wet delays. However, the hydrostatic delay is modeled with help of surface pressure (\rightarrow 3.2.1.1.2) and therefore, it is not difficult to derive the neutral delay

$$ZND = ZWD + ZHD \quad (6-1)$$

ZND: zenith neutral (total) delay

ZHD: zenith hydrostatic delay (modeled/predicted by pre-processor)

ZWD: zenith wet delay (estimated by Kalman filter)

but mind the error budget: The variance for the neutral delay must be *smaller* than the variance of the wet delay

$$\sigma_{ZND}^2 = \sigma_{ZWD}^2 - \sigma_{ZHD}^2 \quad (6-2)$$

because GPS alone is *not* able to sense wet delays. Instead, the hydrostatic component must be derived from external information including additional measurement and modeling uncertainties. Valuable reference data for this validation level come from the IGS analysis centers that provide a combined tropospheric product. These combined data sets are total delays in zenith direction that are derived as the weighted mean of the individual solutions of the particular analysis centers.

The second level is the comparison of *zenith wet delays* which are an output of the TropAC software (\rightarrow 6.2, \rightarrow 6.3). Reference data can be taken from radiosonde launches, for instance: The wet, vertical refractivity profile is integrated and yields zenith wet delays.

Finally, the third level of comparison (\rightarrow 6.6) is the most interesting one for meteorology and climate research, because it focuses on *integrated water vapor (IWV)* or *precipitable water*:

$$PW = \frac{ZWD}{Q} \Rightarrow \sigma_{PW}^2 = \frac{1}{Q^2} \cdot \sigma_{ZWD}^2 + \frac{ZWD^2}{Q^4} \cdot \sigma_Q^2 = \left(\frac{\sigma_{ZWD}}{Q} \right)^2 + \left(PW \cdot \frac{\sigma_Q}{Q} \right)^2 \quad (6-3)$$

PW: precipitable water

Q: conversion factor to transform zenith wet delays into precipitable water and vice versa

The uncertainty of the conversion factor Q is an additional contributor to the total error budget of precipitable water, but in most cases of minor concern. Water vapor radiometers can supply reference data for water vapor comparisons.

6.1 Long-term Experiment

The long-term experiment was conducted for a period of approximately half a year. The basic characteristics and objectives are given in Table 6-1 and a network plot with the nominal baseline configuration is given in Figure 6-1. The primary objective of this experiment was to validate the tropospheric zenith delays that are filtered in routine, automatic processing mode. For this reason, the standard configuration settings were applied (→ Appendix VI). Apart from accuracy considerations (→ 6.1.3, → 6.1.4), the availability of the observation data (→ 6.1.1) and the reliability of the measurements (→ 6.1.2) are addressed in the following sections.

Nominal network setup:	shortest baselines
Time span:	17 October 1998 ... 30 April 1999
Number of stations:	10
Validation period:	<i>BAHR, BRUS, GRAZ, HERS, METS, OBER, POTS, REYK, WTZR, ZWEN</i>
Objectives:	<ul style="list-style-type: none"> • validation of long-term performance • long-baseline performance analysis
Reference data:	combined IGS zenith total delays

Table 6-1 - Characteristics and objectives of the long-term experiment. The standard configuration was used for this analysis. Ambiguity fixing was disabled, the Chao hydrostatic and wet mapping functions were used and the elevation mask was set to 15°. See → Appendix VI for the full configuration file.

6.1.1 Availability Statistics

The value of GPS receivers as atmospheric sounders must not solely be defined in terms of accuracy. Other criteria like the data availability are also of concern as these sensors are expected to provide tropospheric estimates in routine, continuous operation.

Table 6-2 shows the number of days that a particular station was present during processing. Oberpfaffenhofen (*OBER*) has the highest value with 186, Wettzell (*WTZR*) was only present for 170 days. Note that there can be several reasons why a tracking station is marked as "missing" by the processing system. Of course, the most common reason is that the data simply could not be downloaded from the IGS data center. Moreover, the station might have been excluded by the pre-processor or by the Kalman filter engine due to poor performance and this would also lead to a "missing" entry in the statistics, although the data were available. In any case, there are usually incisive reasons to exclude a station completely from processing. 16 missing days for Wettzell in comparison to Oberpfaffenhofen mean more than 8% loss during the long-term experiment - an unsatisfactory situation.

Table 6-3 shows the number of "internal" data gaps: At all those days for which a station was present during processing, there should be data available for exactly 2779 epochs since the data sampling is done every 30 seconds and one data batch covers

one day beginning with 0 h GPS time and finishing with 23 h 30 min 30 s. In most cases, some more or less long data gaps occur. Wettzell (WTZR) and Reykjavik

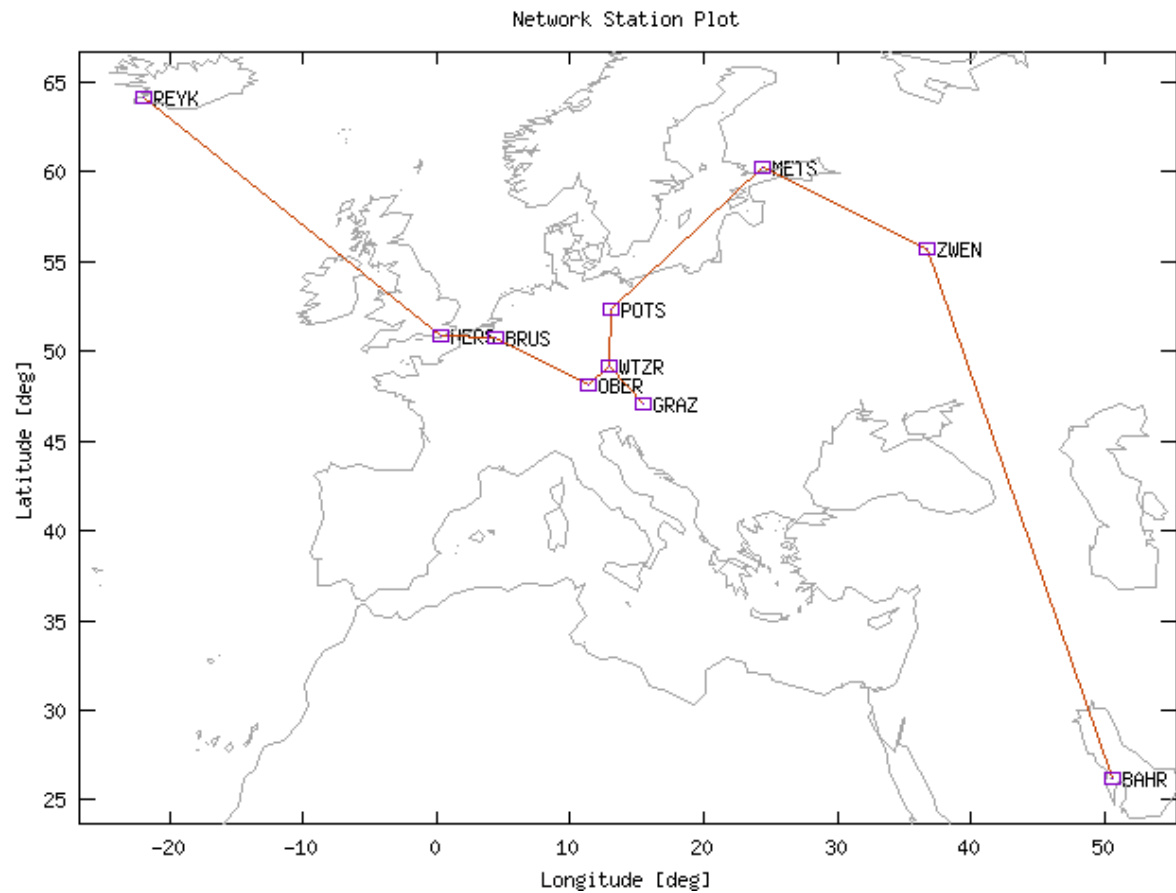


Figure 6-1 - Network stations and baseline setup for the long-term experiment from October 1998 to April 1999. Long baselines are those from ZWEN to BAHR (3460 km) and from HERS to REYK (1970 km).

STATION ID.	AVAILABILITY [DAYS]	PERCENTAGE [%]
ZWEN	131	70.4
BRUS	173	93.0
POTS	180	96.8
METS	181	97.3
OBER	186	100.0
WTZR	170	91.4
GRAZ	58	31.2
HERS	185	99.5
REYK	119	64.0
BAHR	183	98.4

Table 6-2 - Overview of the availability of the network stations. Oberpfaffenhofen (OBER, Germany) is the station with maximum availability. REYK and ZWEN were intentionally not continually present and the observation data for GRAZ became available at the beginning of 1999.

STATION ID.	MISSING EPOCHS	RATIO [EPOCHS/D]
ZWEN	773	6
BRUS	869	5
POTS	336	2
METS	59	0
OBER	627	3
WTZR	3028	18
GRAZ	36	1
HERS	1025	6
REYK	2004	17
BAHR	1824	10

Table 6-3 - Overview of the diurnal data availability for the network stations. Each diurnal data batch comprises dual-frequency carrier phase measurements and pseudo-ranges with a sampling interval of 30 seconds, i. e. 2779 epochs. This table lists the total number of epochs that were missing inside these diurnal data batches - it does **not** account for total receiver failures (see preceding table for this statistic). Example: WTZR had 3028 missing epochs and was available for 170 days, so 17.8 epochs (= "ratio") were missing per day in average. This corresponds to a data gap of about 9 minutes per day.

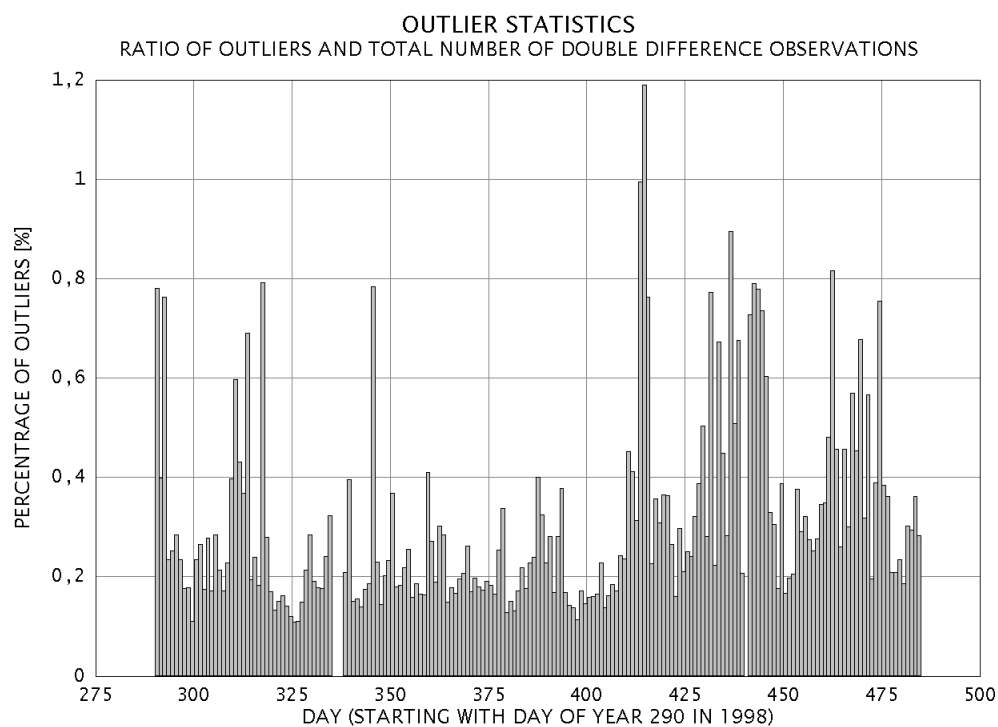


Figure 6-2 - Diagram of the ratio of rejected observations for each day of the long-term experiment. This percentage is defined by dividing the number of outliers per baseline by the total number of double difference observations. The average ratio is around 0.3% what corresponds to about 30 detected blunders per baseline and day.

(REYK) are two examples for poorly performing receivers: In average, 17 to 18 epochs are missing in the observation files or are not accepted by the pre-processor, e. g. due to missing data on L_2 . This corresponds to data gaps as long as almost 9 minutes. Most other receivers perform better. However, data gaps of 9 minutes are not problematic

because the final troposphere products are mean *hourly* values. Missing data for just some minutes are not very harmful.

6.1.2 Outlier Statistics

The reliability of the observations is summarized in Figure 6-2. The diagram shows the mean ratio of detected outliers and total double difference observations per baseline and day. In average, the filter engine treated 0.3% of the observation as blunder-corrupted. This corresponds to a total number of about 30 outliers per baseline and day (24 hours). Days with large outlier-to-observation ratios can sometimes be linked to problematic ionospheric conditions, e. g. ionospheric scintillation causing frequent loss-of-lock. Other reasons can be poor signal-to-noise ratios, tropospheric modeling errors at low elevations, unmarked cycle slips and inaccurate satellite orbits.

The threshold for the maximum ratio allowed was set to 2% during the long-term experiment. This means that the filter engine flagged all baselines with higher ratios as suspicious and tried to exclude the poorly performing sites (\rightarrow 2.8.3) connected to these baselines.

NO.	SITE	SAMPLES	BIAS	SIGMA	RMS
1	BAHR	180	-7.5	6.3	10.2
2	BRUS	173	-0.2	6.0	6.8
3	HERS	179	1.9	6.8	7.8
4	METS	161	1.0	4.5	5.4
5	OBER	186	-1.6	4.7	5.7
6	POTS	181	-1.5	5.1	6.1
7	WTZR	171	-1.2	5.1	5.9
8	ZWEN	121	3.6	4.4	6.1
9	REYK	118	4.1	5.6	7.7
10	GRAZ	58	-1.3	4.3	5.4
MEAN			-0.3	5.3	6.7

Table 6-4 - Mean biases, standard deviations ("sigma") and RMS values for the network stations of the long-term experiment. The column labeled "samples" is identical to the number of days compared. Each day comprises 24 hourly zenith neutral and wet delays.

6.1.3 Comparison with IGS Neutral Delays

The hourly zenith neutral delays estimated by the tropospheric analysis software TropAC were compared with the combined IGS troposphere product. In most cases, the network stations are routinely analyzed by several IGS analysis centers. The combined results of these data sets are treated as reference data here. Table 6-4 shows the mean biases¹, standard deviations ("sigma", bias-reduced) and RMS values.

¹ The accuracy is expressed with help of the following quantities: Given the difference $d_i = \text{val}_{\text{REF}} - \text{val}_{\text{SAM}}$ between the sampled (val_{SAM}) and the reference value (val_{REF}). The bias is the arithmetic mean of all these differences: $\text{BIAS} = 1/n \cdot \sum d_i$ with n being the number of samples compared and the RMS is defined as $\text{RMS} = [1/n \cdot \sum d_i^2]^{1/2}$. Finally, the standard deviation, also denoted as SIG or SIGMA here, is the bias-reduced accuracy: $\text{SIGMA} = [1/(n-1) \cdot \sum (d_i - \text{BIAS})^2]^{1/2}$.

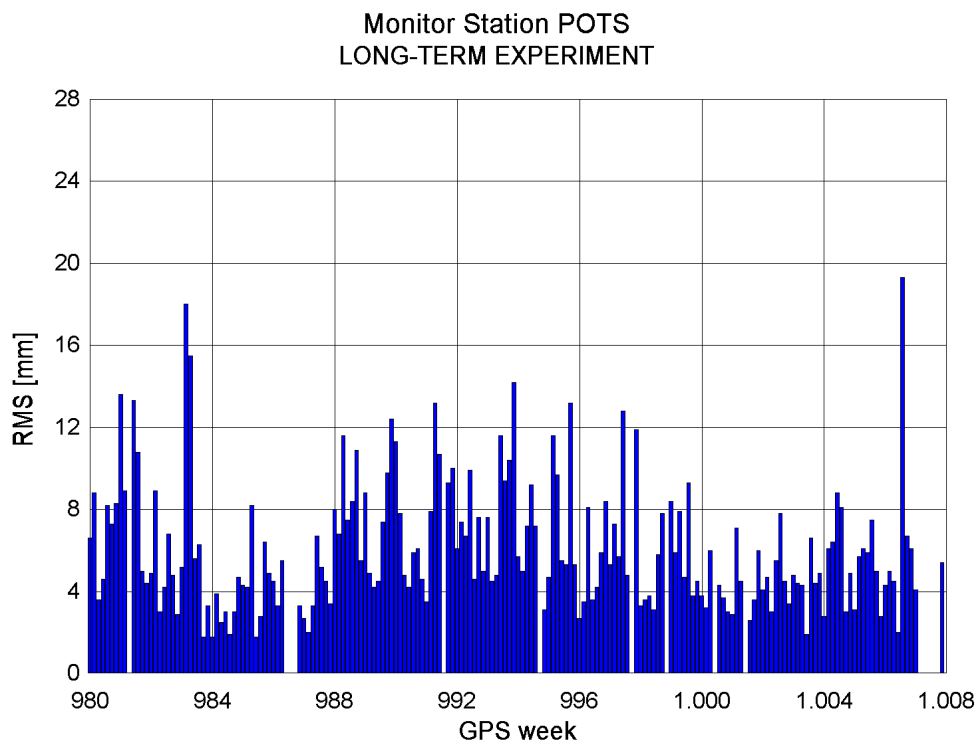


Figure 6-3 - Diagram of diurnal RMS values during the long-term experiment for tracking station Potsdam (POTS, Germany).

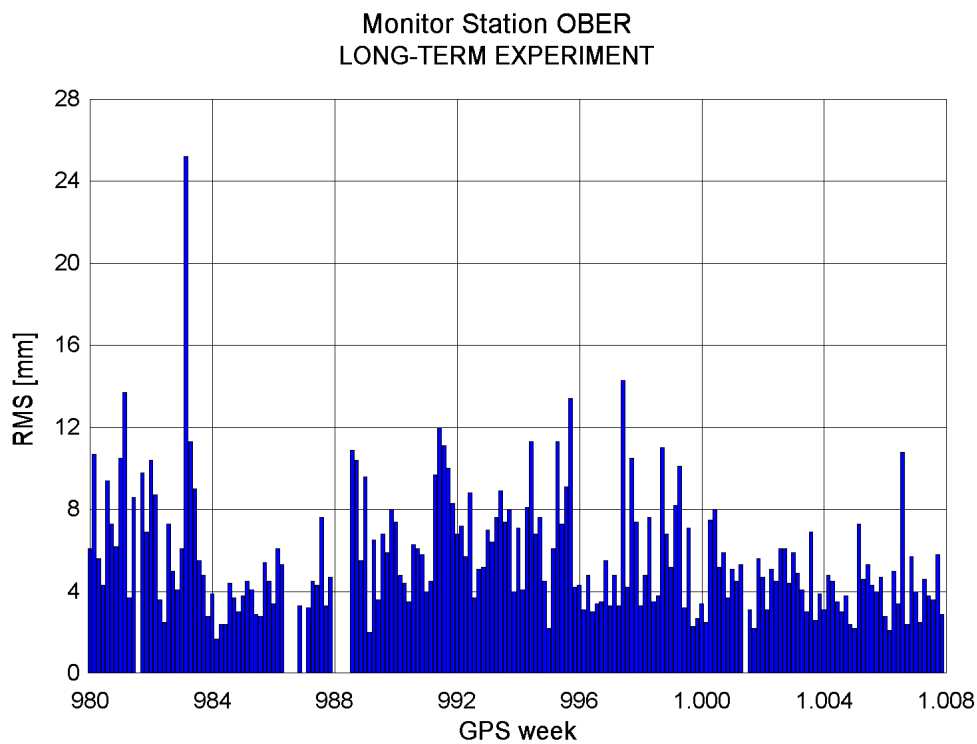


Figure 6-4 - Diagram of diurnal RMS values during the long-term experiment for tracking station Oberpfaffenhofen (OBER, Germany).

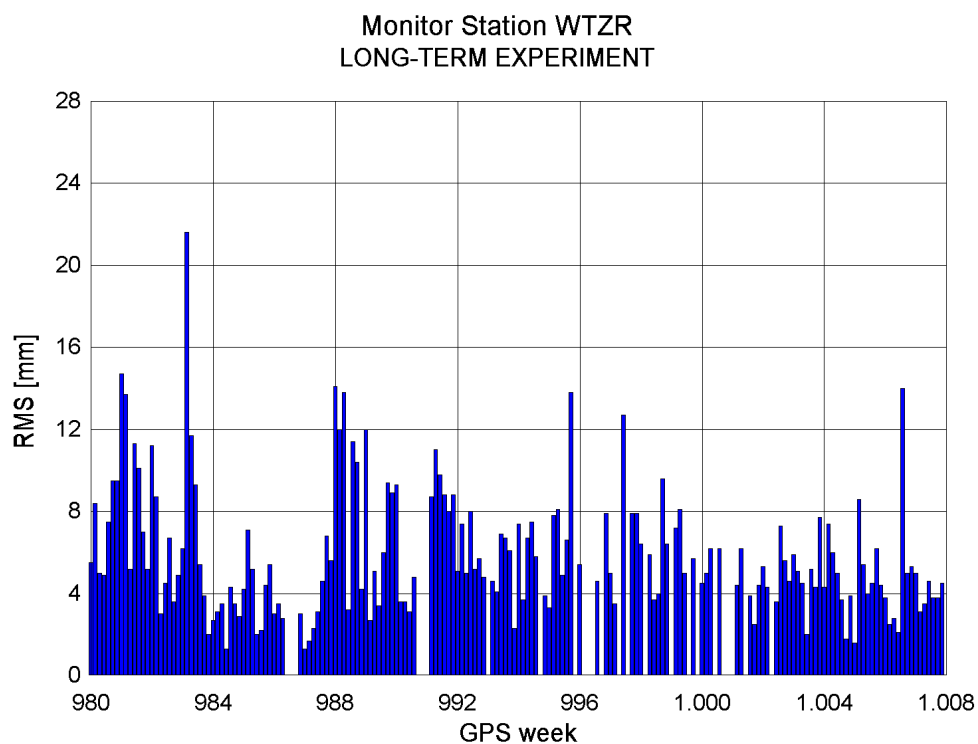


Figure 6-5 - Diagram of diurnal RMS values during the long-term experiment for tracking station Wettzell (WTZR, Germany).

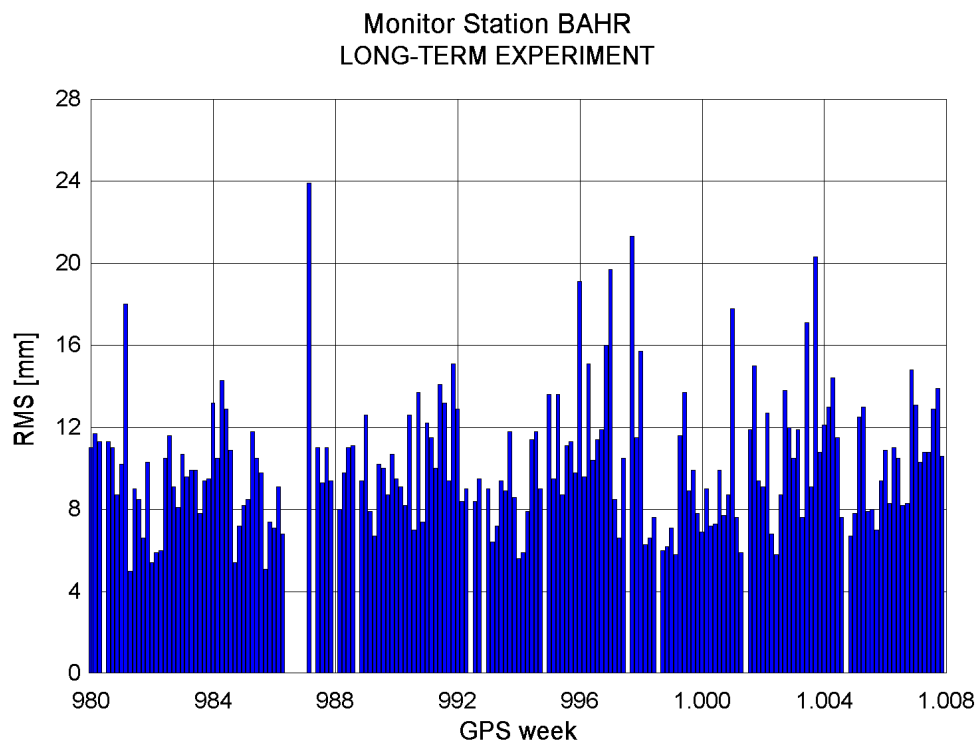


Figure 6-6 - Diagram of diurnal RMS values during the long-term experiment for tracking station Bahrain (BAHR).

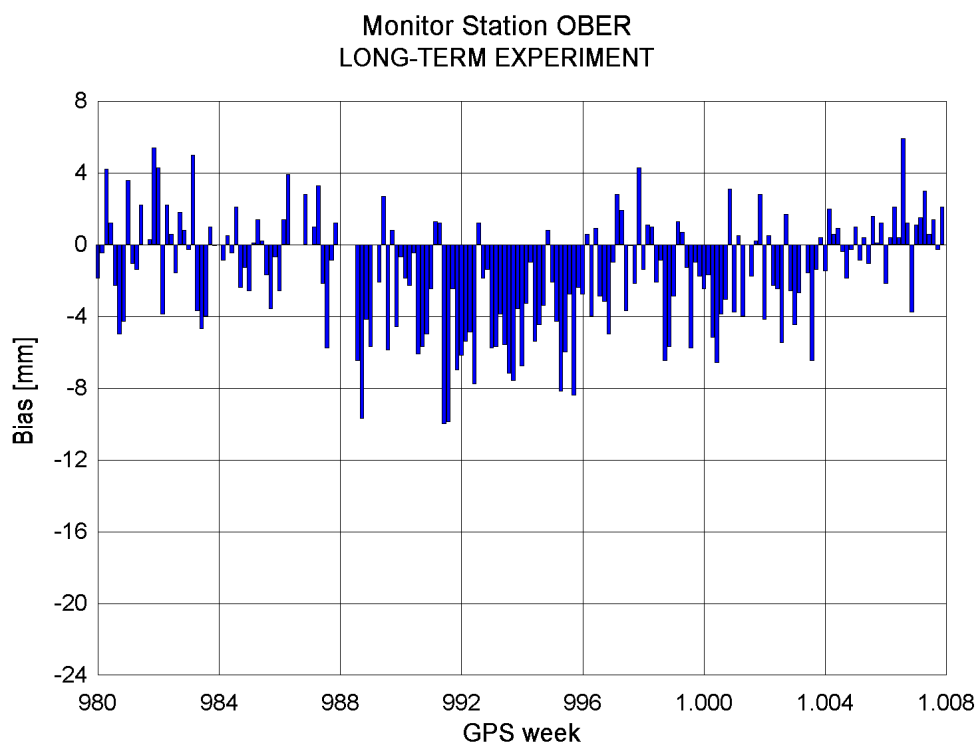


Figure 6-7 - Diagram of diurnal biases during the long-term experiment for tracking station Oberpfaffenhofen (OBER, Germany).

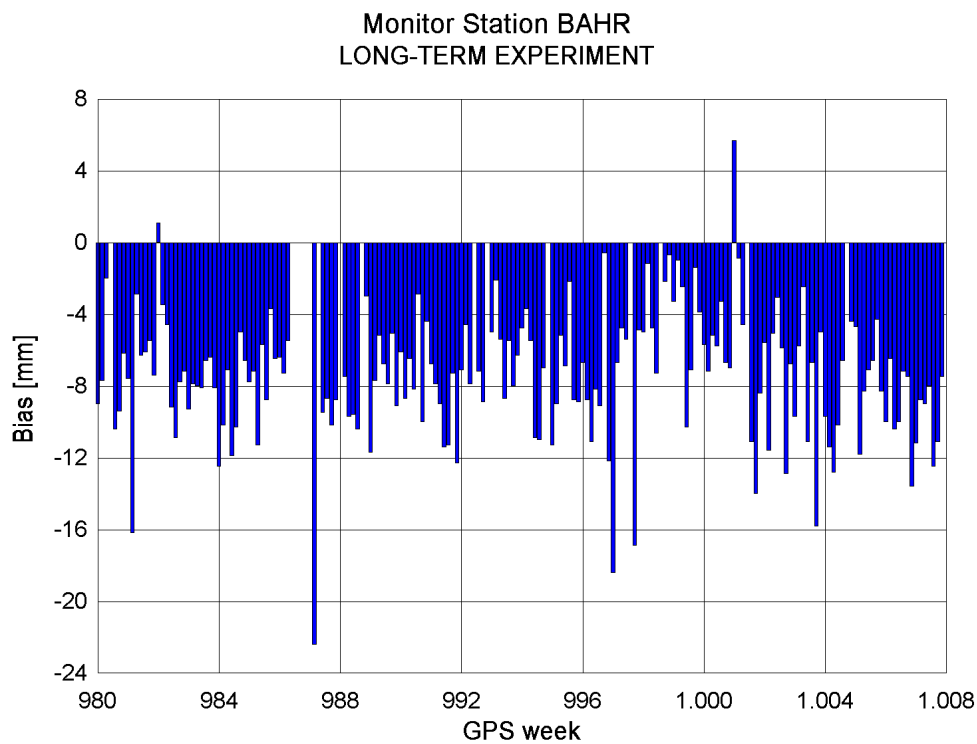


Figure 6-8 - Diagram of diurnal biases during the long-term experiment for tracking station Bahrain (BAHR).

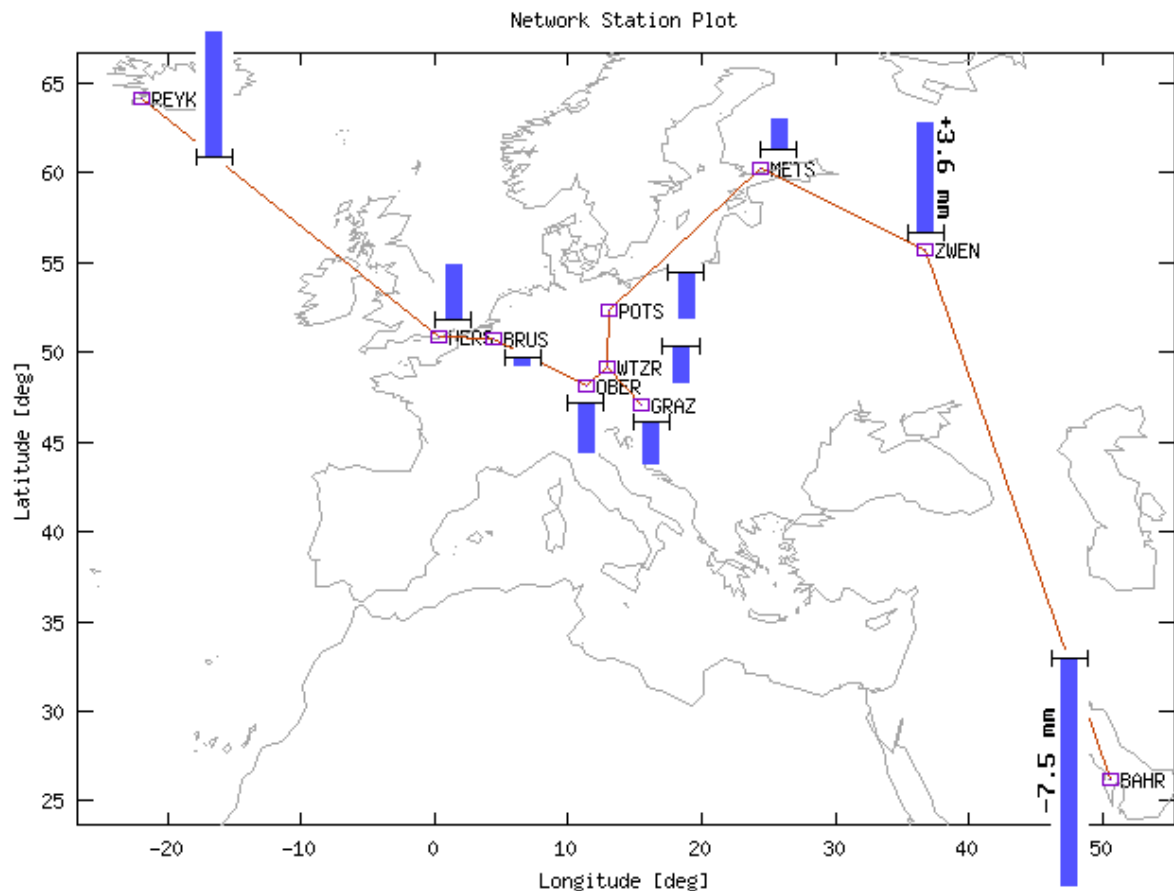


Figure 6-9 - Network plot illustrating the mean systematic errors during the long-term experiment for all network stations. Largest biases can be seen at the network periphery, i. e. at stations connected to the network via long baselines.

Figure 6-3 to Figure 6-6 give RMS diagrams for the 3 network stations inside Germany (*POTS*, *OBER*, *WTZR*) plus the remote station Bahrain (*BAHR*).

The average RMS from this comparison is about 7 mm. Expecting no further decrease in accuracy from separation (hydrostatic and wet delay) and conversion, the accuracy of the integrated water vapor should be slightly above 1 kg/m² - a satisfactory result. The standard deviation, that is free from systematic effects, is about 5 mm corresponding to 0.8 kg/m² of integrated water vapor. Highest standard deviations can be found for *HERS* (G. B.). The receiver located at this station seems to be rather weak on carrier frequency L_2 what can be seen from the relatively small C/N flags in the RINEX measurement files.

In average, the standard deviation is about 1.5 mm smaller than the RMS and in several cases even several millimeters. This means that systematic deviations must be important error contributors in some cases.

6.1.4 Systematic Effects

The mean biases of Table 6-4 are graphically illustrated in Figure 6-9. The diurnal biases for Oberpfaffenhofen (*OBER*) and Bahrain (*BAHR*) are plotted in Figure 6-7 and Figure 6-8.

Clearly, systematic errors increase at the periphery of the network. An especially high bias is present at Bahrain that is connected to the network via a long baseline of more than 3500 km. The diurnal biases plotted in Figure 6-8 are negative in almost all cases, but they also vary for several millimeter from day to day. The systematic effects are very moderate in the core network. The offsets at *OBER* shown in Figure 6-7 are more randomly distributed, albeit they also show a small negative trend in average.

Several reasons can be responsible for these offsets. First, errors in tropospheric modeling should be mentioned, particularly in terms of the tropospheric mapping functions. The Chao wet and hydrostatic mapping functions were used for the long-term experiment. An additional run with the Niell mapping function lead to the conclusion that mapping function errors only cause relatively small differences in the biases of up to 2 mm, but mostly less than 1.5 mm. As a consequence, tropospheric modeling errors are not considered to be the primary error contributor. Largest offsets occur at those stations connected to the longest baselines. This indicates that remaining baseline length-dependent modeling errors are responsible for the systematic effects, e. g. uncertainties of the site displacements. Additionally, the network datum definition is considered as a dominant contributor to the systematic errors here. The datum was defined as "weak datum" here, but it might be possible that the constraints applied to some coordinates were too tight.

6.2 Experiment OBER-I

Experiment *OBER-I* was conducted (see Table 6-5 and Figure 6-10 for the characteristics) for several reasons: A radiosonde launch site is located at Oberschleißheim, less than 30 km away from Oberpfaffenhofen (*OBER*). Zenith wet delays can be derived from the wet refractivity profiles measured by the radiosonde and compared to the output of the tropospheric GPS analysis software (→ 6.2.7). Moreover, a lot of more investigations were carried out concerning the accuracy of the tropospheric mapping functions (→ 6.2.3), the impact of horizontal gradients (→ 6.2.4) and the ionosphere (→ 6.2.5), and the dependence of the estimates on the elevation mask (→ 6.2.6).

6.2.1 Availability and Reliability

Data for 7 of 9 stations were used for at least 90% of the month in the analysis (Table 6-6). For those files available, only *ONSA* and *BRUS* showed data gaps amounting to a mean value of more than 20 epochs per day (Table 6-7). The number of rejected observations per baseline is plotted in Figure 6-11. The mean ratio is around 0.2%, but a clear peak can be seen on 30 July 1999 that is linked to monitoring station Potsdam (*POTS*) as Table 6-9 proves.

Nominal network setup:	centered on <i>OBER</i>
Validation period:	1 July 1999 ... 31 July 1999
Number of stations:	9
Test network:	<i>OBER, WTZR, METS, WSRT, BRUS, POTS, GRAZ, ZWEN, ONSA</i>
Objectives:	<ul style="list-style-type: none"> • evaluation of tropospheric mapping functions • evaluation of influence of horizontal gradients • evaluation of ionospheric impact • evaluation of optimal elevation mask • validation of zenith wet and neutral delays
Reference data:	<ul style="list-style-type: none"> • combined IGS zenith total delays • zenith wet delays from radiosonde launches

Table 6-5 - Characteristics and objectives of experiment OBER-I. See → Appendix VI for the full configuration file.

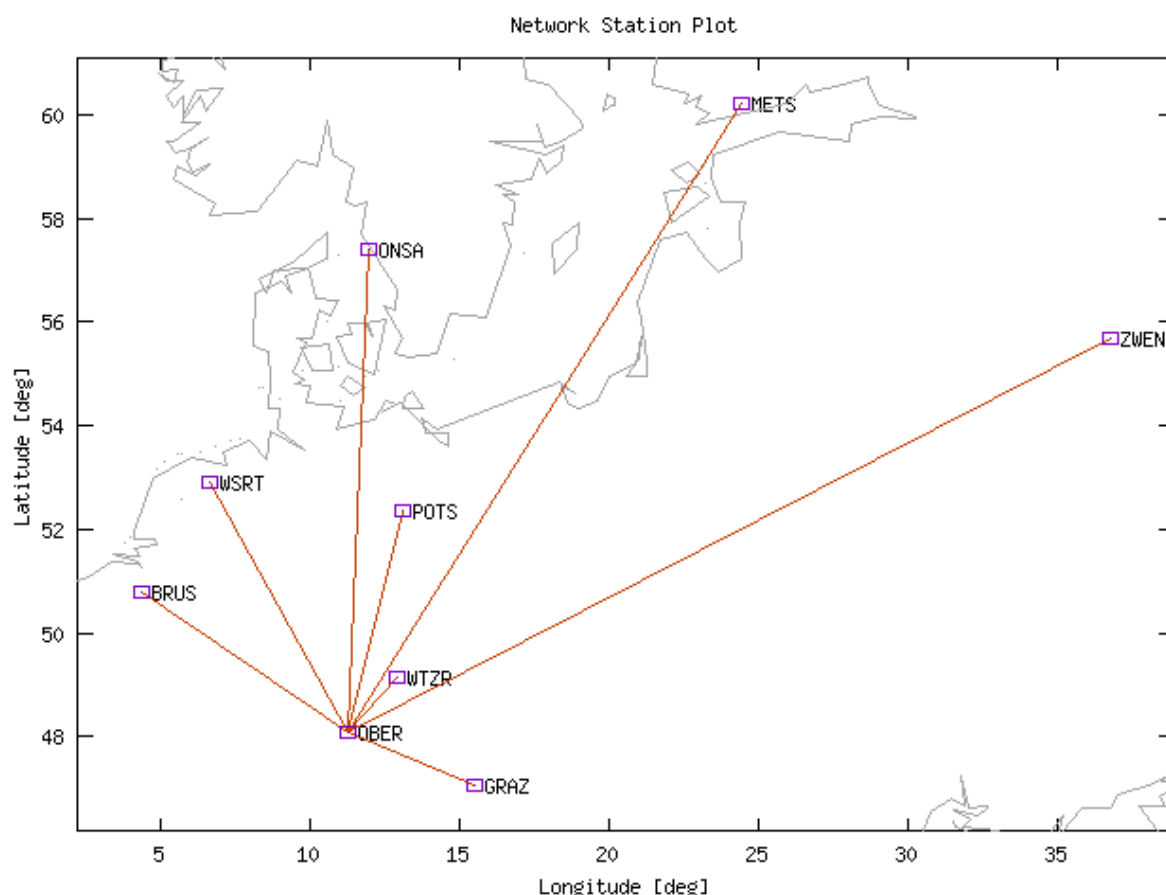


Figure 6-10 - Network stations and baseline setup for the experiments OBER-I and OBER-II. The network is centered on Oberpfaffenhofen (OBER, Germany).

6.2.2 Comparison with IGS Zenith Neutral Delays

Table 6-8 lists the average accuracy values for the zenith neutral delays estimated with help of the default configuration. Most important settings were a minimum elevation angle of 15° and the application of the Chao hydrostatic and wet mapping

STATION ID.	AVAILABILITY [DAYS]	PERCENTAGE [%]
OBER	31	100
GRAZ	31	100
ONSA	31	100
ZWEN	31	100
BRUS	30	96
WSRT	30	96
WTZR	28	90
METS	24	77
POTS	14	45

Table 6-6 - Overview of the availability of the network stations. OBER, GRAZ, ONSA and ZWEN were continually present, data from POTS were only used for half of the month.

STATION ID.	MISSING EPOCHS	RATIO [EPOCHS/D]
OBER	3	0
GRAZ	82	3
ONSA	722	23
ZWEN	5	0
BRUS	1078	36
WSRT	65	2
WTZR	22	1
METS	1	0
POTS	83	6

Table 6-7 - Overview of the diurnal data availability of the network stations. This table lists the total number of epochs that were missing inside these diurnal data batches and the number of missing epoch per day ("ratio") - it does **not** account for total receiver failures (see preceding table for this statistic).

NO.	SITE	SAMPLES	BIAS	SIGMA	RMS
1	BRUS	30	1.1	4.6	5.4
2	GRAZ	31	-1.6	4.4	5.4
3	METS	23	5.7	3.8	7.1
4	OBER	31	-2.3	4.6	5.9
5	ONSA	31	2.9	3.6	5.0
6	WSRT	28	2.7	4.2	5.6
7	WTZR	28	-2.4	3.8	5.1
8	ZWEN	31	2.8	4.3	5.8
9	POTS	13	0.3	4.1	4.7
MEAN			1.0	4.2	5.5

Table 6-8 - Mean biases, standard deviations ("sigma") and RMS values for the network stations of the OBER-I experiment in comparison to the IGS combined tropospheric product (= reference data). The column labeled "samples" is identical to the number of days compared. Each day comprises 24 hourly zenith neutral and wet delays.

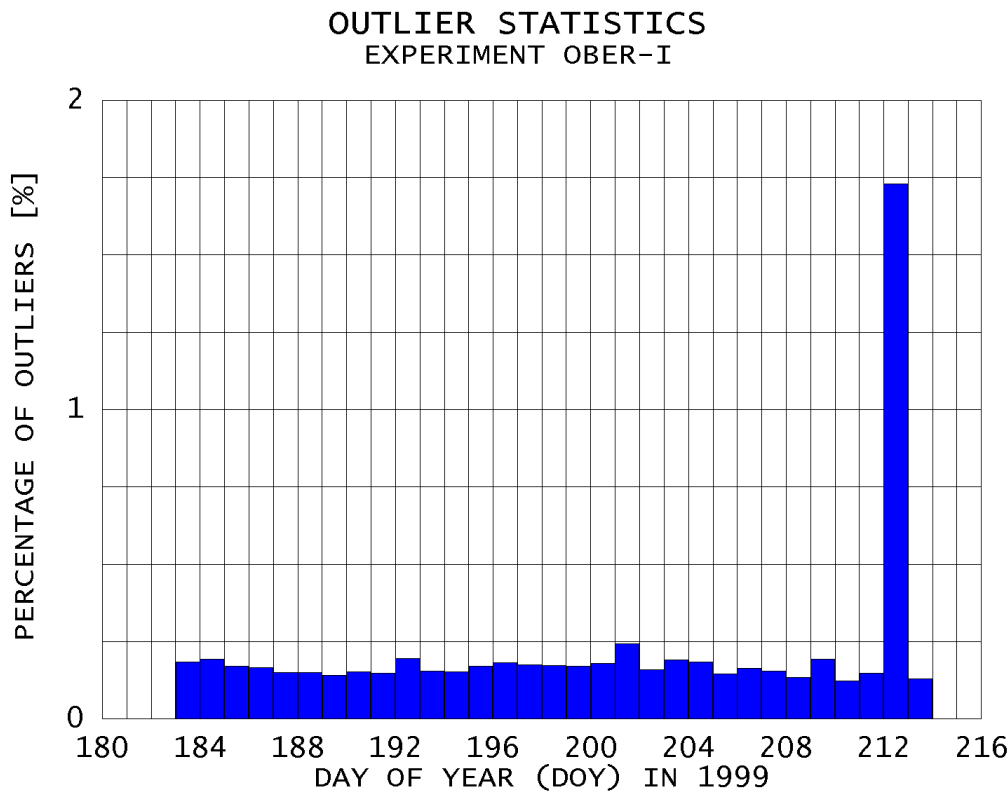


Figure 6-11 - Diagram of the ratio of rejected observations for each day of the OBER-I experiment. This percentage is defined by dividing the mean number of outliers per baseline by the total number of double difference observations. The average ratio is around 0.2% what corresponds to less than 25 detected blunders per baseline and day.

OUTLIER STATISTICS: 1380 measurements rejected = 197 per baseline

TIME DOMAIN				BASELINE DOMAIN			
Time	# outliers	% outliers		from	to	# outliers	% outliers
0 h	267	19		OBER	POTS	1269	92
1 h	278	20		OBER	GRAZ	16	1
2 h	249	18		OBER	WSRT	22	2
3 h	278	20		OBER	BRUS	32	2
4 h	172	12		OBER	ONSA	15	1
5 h	41	3		OBER	WTZR	16	1
6 h	1	0		OBER	ZWEN	9	1
7 h	0	0					
8 h	1	0					
9 h	1	0					
10 h	12	1					
11 h	5	0					
12 h	38	3					
13 h	1	0					
14 h	3	0					
15 h	4	0					
16 h	0	0					
17 h	0	0					
18 h	0	0					
19 h	0	0					
20 h	10	1					
21 h	14	1					
22 h	3	0					
23 h	0	0					

Table 6-9 - Extract from the information file of the TropAC TRIDENT software for 30 July 1999 (experiment OBER-I). All baselines are well-performing expect for baseline OBER-POTS. Obviously, the measurement data for Potsdam (POTS, Germany) were corrupted from 0 h to 4 h GPS time.

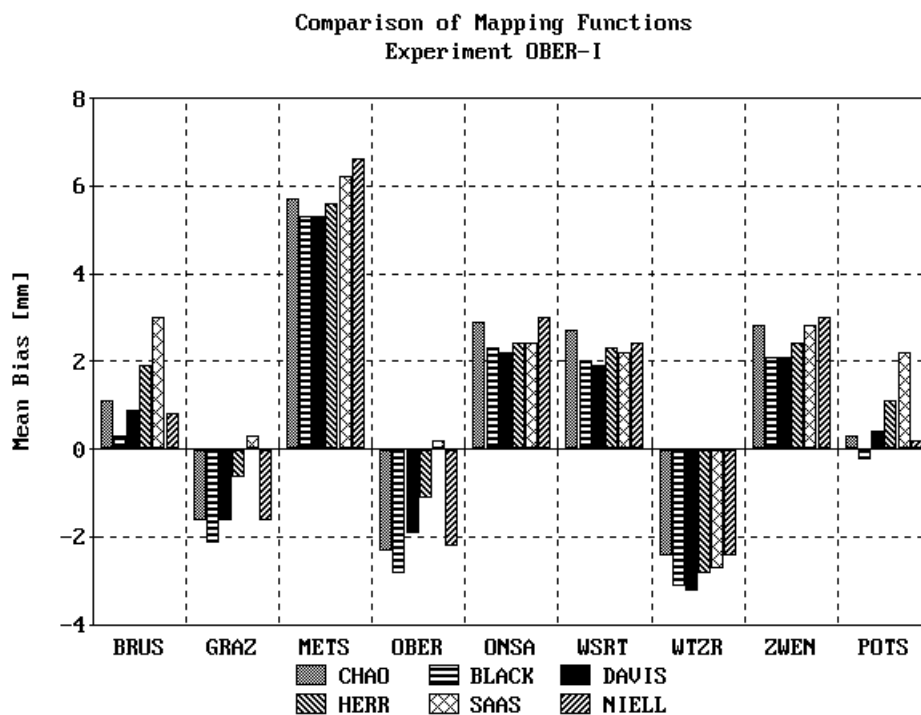


Figure 6-12 - Comparison of mean biases for different tropospheric mapping functions. (HERR: Herring mapping function, → 3.2.2.1.6 and → 3.2.2.2.4; SAAS: Saastamoinen mapping function, → 3.2.2.1.1)

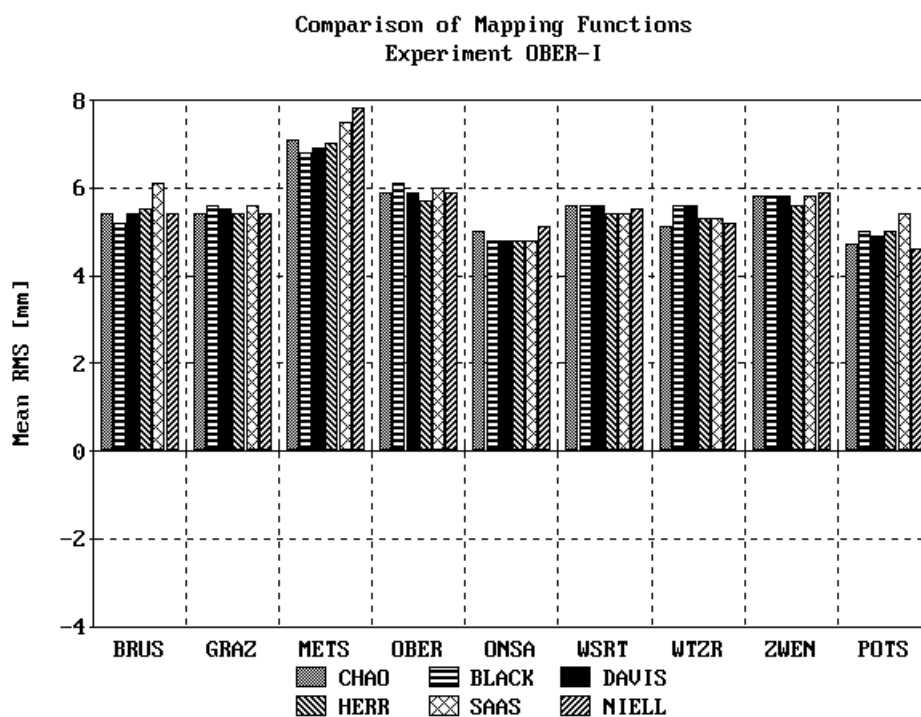


Figure 6-13 - Comparison of mean RMS values for different tropospheric mapping functions. (HERR: Herring mapping function, SAAS: Saastamoinen mapping function)

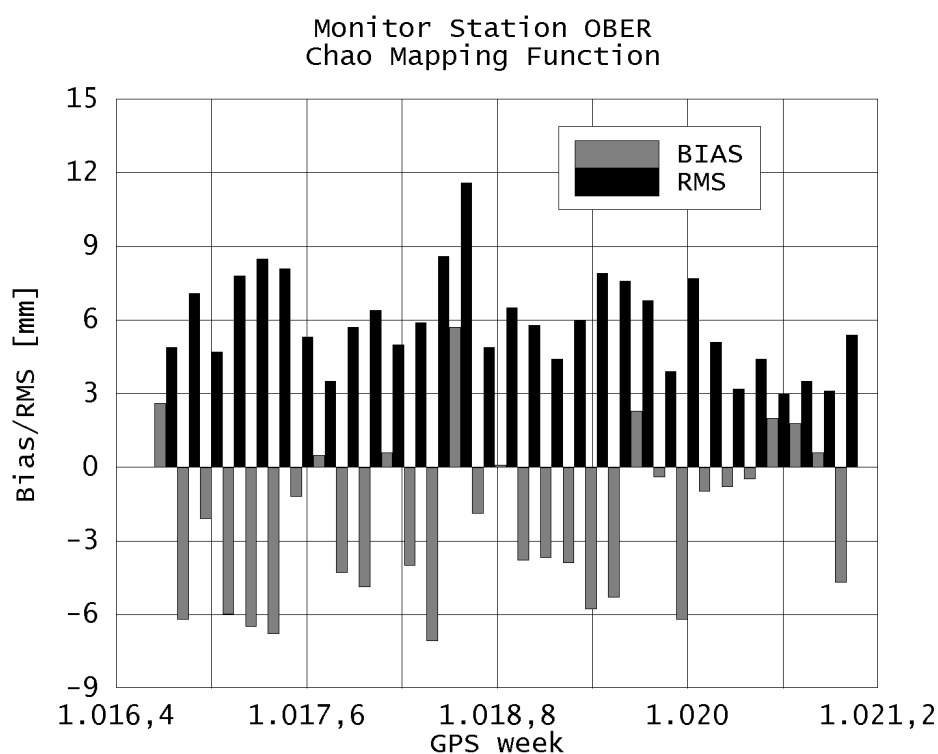


Figure 6-14 - Diurnal biases and RMS values that occurred during the OBER-I experiment with the Chao tropospheric mapping functions in use.

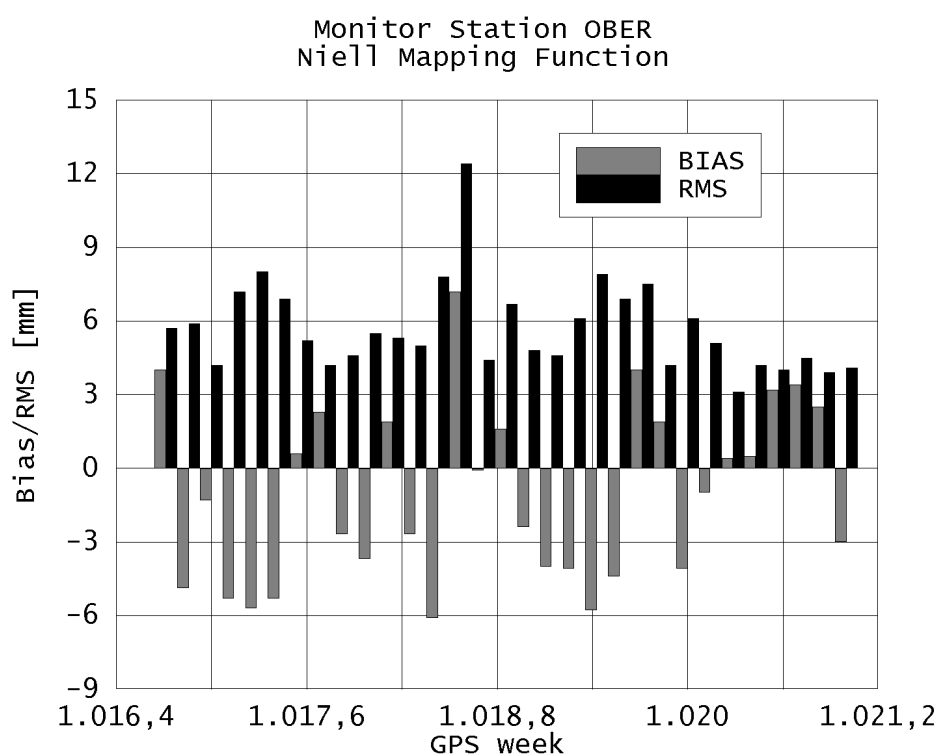


Figure 6-15 - Diurnal biases and RMS values that occurred during the OBER-I experiment with the Niell tropospheric mapping functions in use.

functions. The reference data for this comparison were again taken from the combined IGS troposphere product. Treating these data as absolutely true, one can assume a mean accuracy of integrated water vapor of even better than 1 kg/m²: The average RMS for all network stations is as small as 5.5 mm. The mean biases are less than 3 mm in all cases except for *METS* that has almost 6 mm.

6.2.3 Evaluation of Tropospheric Mapping Functions

The Kalman filter does not estimate tropospheric slant delays. Instead, the slant delays are projected into zenith direction and the zenith wet or neutral delays are estimated. Undoubtedly, this method makes sense, but it relies on the accuracy of the mapping functions (→ 3.2.2). For this reason, a number of mapping functions were tested during the OBER-I experiment. The results are given in Figure 6-12 (biases) and Figure 6-13 (RMS). They represent the deviations from the zenith neutral delays of the IGS troposphere product. The results obtained with the Chao mapping function are those presented in the preceding section (see Table 6-8). The minimum elevation was 15° and is the recommended elevation cutoff (→ 6.2.6).

As far as the mean systematic deviations are concerned, the different mapping functions only show discrepancies in the range of less than 3 mm. The mean RMS values even deviate less from each other, often only for some tens of a millimeter. As a consequence, we may conclude that the choice of the mapping function is of minor relevance as far as the accuracy of the results is concerned. Of course, one should never use the simple cosecant model, but all mapping functions that are commonly considered as "precise" ones - and this is esp. true for those developed for VLBI applications - can be used.

The most interesting outcome of this investigation is the fact that even mapping functions that do not need any meteorological measurement inputs like that of Niell and Chao prove to be in no way inferior to the other ones tested during this experiment. The diurnal biases and RMS values for the runs with these two mapping functions are given in Figure 6-14 and Figure 6-15. Evidently, both results do not differ very much, so the old and very easily implemented approach of Chao (→ 3.2.2.1.2, → 3.2.2.2.1) is evidently a good choice for standard GPS applications.

6.2.4 Horizontal Gradients

The tropospheric analysis software allows to introduce horizontal gradients from external data sources. Such gradients can be retrieved from the ray-tracing analysis in numerical weather fields (→ 4.3.2). Table 6-10 shows both the results of the default run (compare with Table 6-8) and the run with horizontal gradients introduced into the analysis. Apparently, gradients have a very limited influence on the estimated zenith neutral delays, esp. for an elevation cutoff of 15° - this statement is, at least, true for July 1999. Only the mean biases decrease for about 0.3 mm, but the standard deviation slightly increases.

WITHOUT HORIZONTAL GRADIENTS					WITH HORIZONTAL GRADIENTS				
NO.	SITE	BIAS	SIGMA	RMS	NO.	SITE	BIAS	SIGMA	RMS
1	BRUS	1.1	4.6	5.4	1	BRUS	0.9	4.6	5.2
2	GRAZ	-1.6	4.4	5.4	2	GRAZ	-1.9	4.4	5.5
3	METS	5.7	3.8	7.1	3	METS	5.5	3.9	7.0
4	OBER	-2.3	4.6	5.9	4	OBER	-2.5	4.5	5.9
5	ONSA	2.9	3.6	5.0	5	ONSA	2.6	3.8	5.0
6	WSRT	2.7	4.2	5.6	6	WSRT	2.3	4.6	5.7
7	WTZR	-2.4	3.8	5.1	7	WTZR	-2.8	4.1	5.4
8	ZWEN	2.8	4.3	5.8	8	ZWEN	2.4	4.6	5.9
9	POTS	0.3	4.1	4.7	9	POTS	0.1	4.2	4.8
MEAN		1.0	4.2	5.5	MEAN		0.7	4.3	5.6

Table 6-10 - Result tables for the default run without horizontal gradients (left) and the run with horizontal gradients from GDAS numerical weather fields (right). Reference data: IGS zenith neutral delays.

NO 2 ND ORDER IONOSPHERIC CORRECTION					WITH 2 ND ORDER IONOSPHERIC CORRECTION				
NO.	SITE	BIAS	SIGMA	RMS	NO.	SITE	BIAS	SIGMA	RMS
1	BRUS	1.1	4.6	5.4	1	BRUS	1.1	4.6	5.4
2	GRAZ	-1.6	4.4	5.4	2	GRAZ	-1.6	4.4	5.4
3	METS	5.7	3.8	7.1	3	METS	5.7	3.8	7.1
4	OBER	-2.3	4.6	5.9	4	OBER	-2.3	4.6	5.9
5	ONSA	2.9	3.6	5.0	5	ONSA	2.9	3.6	5.0
6	WSRT	2.7	4.2	5.6	6	WSRT	2.7	4.2	5.6
7	WTZR	-2.4	3.8	5.1	7	WTZR	-2.4	3.9	5.1
8	ZWEN	2.8	4.3	5.8	8	ZWEN	2.8	4.4	5.8
9	POTS	0.3	4.1	4.7	9	POTS	0.3	4.1	4.6
MEAN		1.0	4.2	5.5	MEAN		1.0	4.2	5.5

Table 6-11 - Result tables for the run without (left) and with (right) 2nd order ionospheric corrections applied. Reference data: IGS zenith neutral delays.

6.2.5 Ionospheric Impact

Normally, the ionosphere-free linear combination is used to filter zenith wet delays. This virtual signal can eliminate the 1st order ionospheric effect. The TropAC analysis system additionally allows to model the 2nd order effect (\rightarrow 2.2.4.2). Results for the default run and an additional run with 2nd order correction enabled are shown in Table 6-11 - almost no differences can be seen. Generally speaking, a 2nd order correction is not necessary since the processes of double differencing reduces this remaining effect to such an extend that it is no harmful error contributor any longer.

Several linear combinations reduce the ionospheric influence, e. g. L_{43} and L_{54} (\rightarrow 2.2.3). Figure 6-16 and Figure 6-17 show the mean biases and RMS values for several test runs with such signals. The linear combination L_{54} reduces the ionospheric influence down to 5.5%. However, for precise applications, the remaining ionospheric error is still too big. IONEX files can be used to determine the ionospheric delay and can considerably reduce the mean biases (see " $L_{54}+IONEX$ "), but they are still in the range of 1 to 2 cm. Apart from the remaining errors of the IONEX VTEC data, the temporal resolution of 2 hours limits the accuracy of this correction approach.

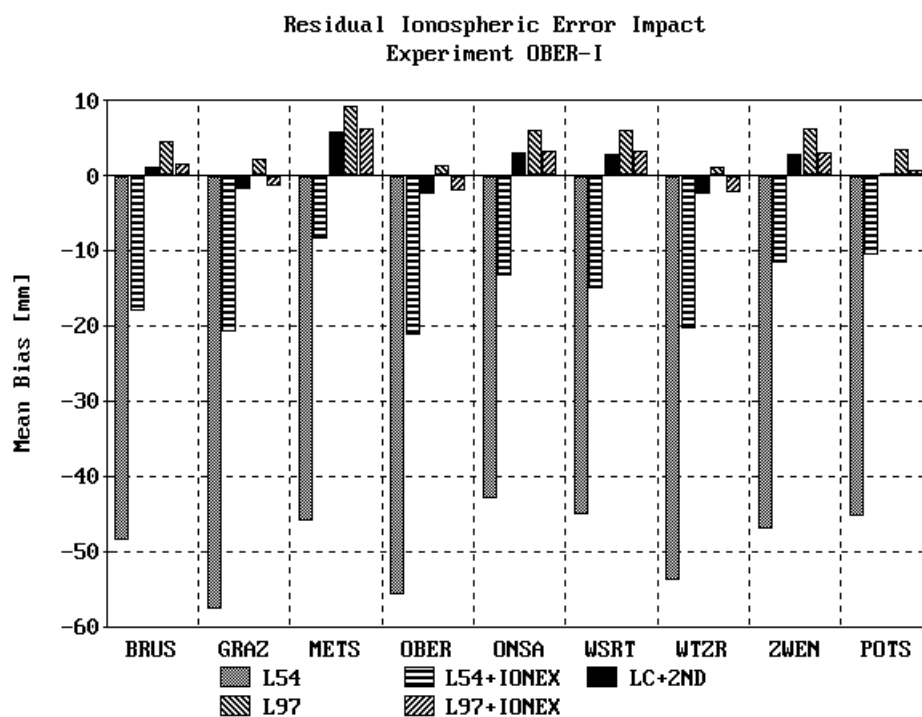


Figure 6-16 - Comparison of mean biases introduced through residual ionospheric errors in the linear combinations of the GPS measurements. IGS zenith neutral delays were used as reference data.

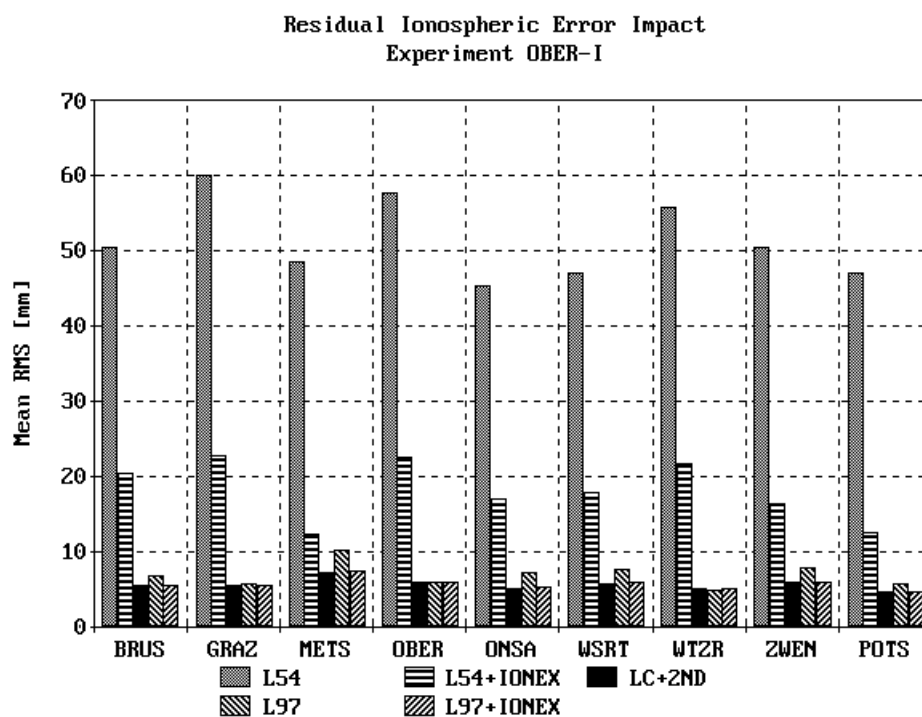


Figure 6-17 - Comparison of the mean RMS values for the different linear combinations of the GPS measurements without and with ionospheric propagation delay modeling using IONEX files.

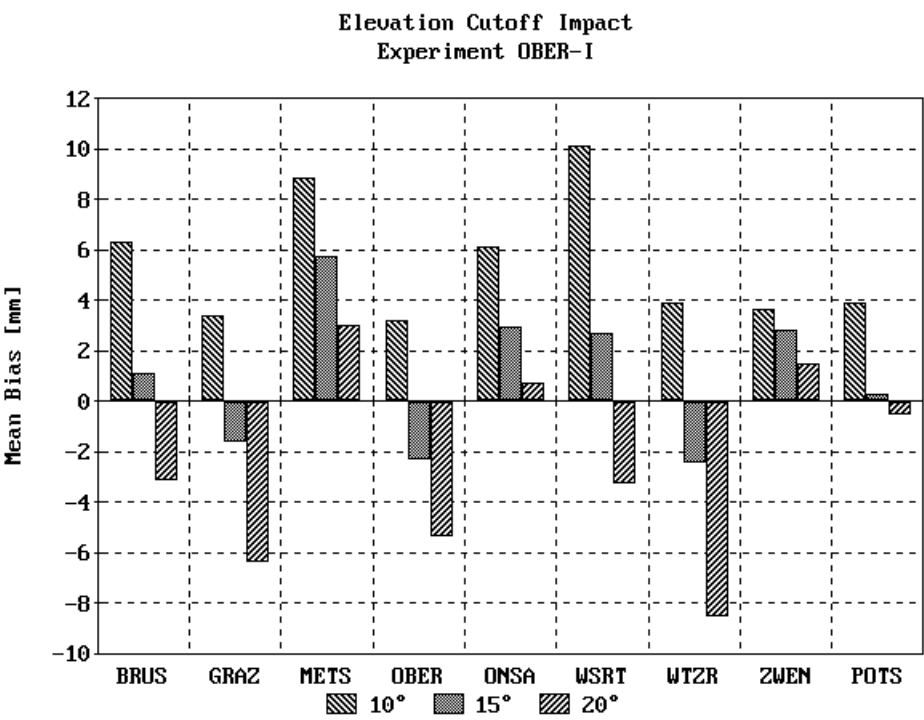


Figure 6-18 - Comparison of mean biases depending of the elevation cutoff. IGS zenith neutral delays were used as reference data.

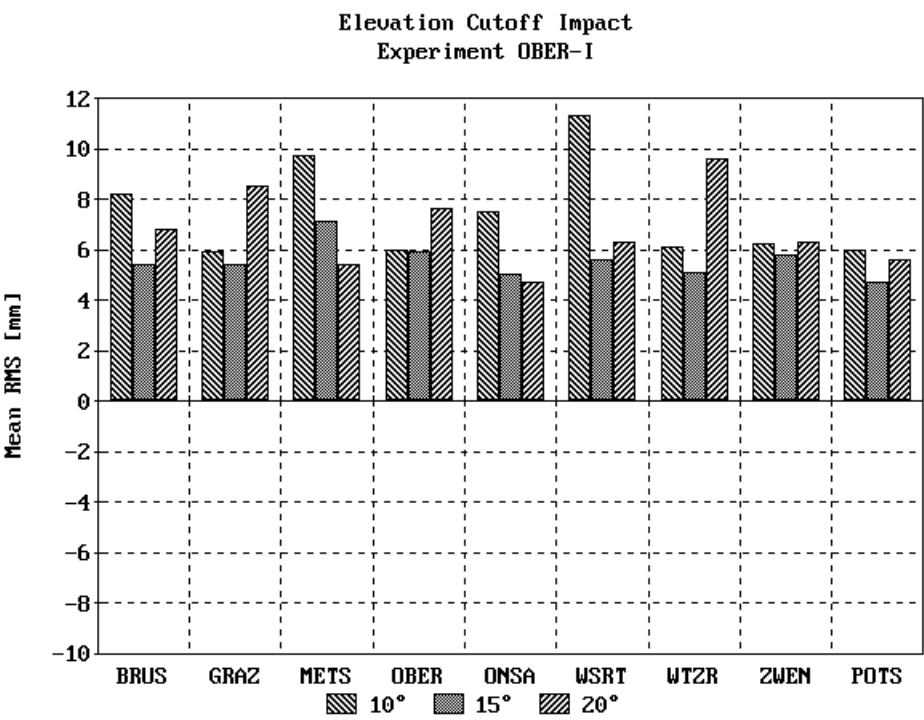


Figure 6-19 - Comparison of the mean RMS values depending of the elevation cutoff. IGS zenith neutral delays were used as reference data.

Linear combination L_{97} is only prone to ionospheric propagation delays at the level of 0.4%, and actually, the biases and RMS reach a limit similar to the best configuration using the ionosphere-free signal and applying the 2nd order ionospheric correction (see "LC+2ND"). Again, the use of IONEX files improves the situation (see "L97+IONEX") and leads to an accuracy level that is practically identical to the "LC+2ND" configuration. Unfortunately, L_{97} has a very short wavelength of less than 6 cm - it possesses an integer ambiguity nature, but can hardly be used for ambiguity fixing.

6.2.6 Elevation Masking

All preceding test runs were conducted with a minimum elevation angle of 15°. Additional runs with an elevation mask of 10° and 20°, respectively, were conducted. The mean biases and RMS values are plotted in Figure 6-18 and Figure 6-19. Again, the IGS troposphere product serves as reference data. In comparison to these data, i. e. treating them as true values, an elevation angle of 15° can be recommended as optimum elevation mask for data analysis with TropAC TRIDENT, because the best RMS is reached with a mean value of 5.5 mm in comparison to 7.4 mm for 10° and 6.8 mm for 20°. The reason for the increased uncertainty for an elevation mask of 10° can be seen in poorer signal-to-noise ratios, higher uncertainties in the tropospheric mapping functions and, perhaps, the higher influence of horizontal gradients for low-elevation measurements. The RMS for 20° is slightly better, but worse than the RMS for 15°. This is likely due to the reduced number of observations. An optimal elevation mask must consider both criteria: Higher scatter and higher modeling errors for low-elevations observations on the one hand and a decrease in the number of double difference observations for high elevation masks, especially for long baselines. A good compromise seems to be a cutoff near 15°.

6.2.7 Comparison with Radiosonde Data

Radiosonde data were available for Oberschleißheim. This launch site is located near IGS tracking station Oberpfaffenhofen (*OBER*). A comparison between the zenith tropospheric delays from GPS and radiosonde is given in Table 6-12.

Quantity	Analysis	Bias [mm]	Std. Dev. [mm]	RMS [mm]
ZND	IGS	-10.6	17.1	20.0
ZND	TropAC	-13.2	16.5	21.1
ZWD	TropAC	-11.2	17.9	21.0

Table 6-12 - Comparison of GPS-derived zenith neutral and wet delays with integrated quantities from radiosonde profiles for Oberschleißheim near Oberpfaffenhofen (*OBER*, Germany). The entry "IGS" means that the comparison is based on the IGS combined zenith total delay product whereas "TropAC" stands for the results from the TropAC analysis software.

The agreement between the radiosonde data and the GPS-derived zenith delays is in the range of 2 cm and the mean biases are around -1 cm. This is about 1 cm better than the zenith neutral delays derived from GDAS weather fields/TROPEX files (→ 7.2) for this particular situation. Nevertheless, the accuracy of radiosonde data is apparently not high enough to be suitable for the validation of GPS-derived

tropospheric delays because a RMS of much better than 15 mm can be expected for the GPS results. For this purpose, water vapor radiometers can be more valuable (→ 6.6).

6.3 Experiment OBER-II

Experiment *OBER-II* is an extension to *OBER-I* and was primarily conducted in order to evaluate the influence of orbit accuracy on the estimated zenith tropospheric delays (→ 6.3.1). Once more, radiosonde data for Oberschleißheim near Oberpfaffenhofen (*OBER*) were available and used for a comparison (→ 6.3.2). See Table 6-13 for the characteristics of this experiment and have a look at Figure 6-10 for the network plot.

Nominal network setup:	centered on <i>OBER</i>
Validation period:	1 October 1999 ... 30 November 1999
Number of stations:	9
Test network:	<i>OBER</i> , <i>WTZR</i> , <i>METS</i> , <i>WSRT</i> , <i>BRUS</i> , <i>POTS</i> , <i>GRAZ</i> , <i>ZWEN</i> , <i>ONSA</i>
Objectives:	<ul style="list-style-type: none"> • GPS satellite orbits and their impact on tropospheric delay estimation
Reference data:	<ul style="list-style-type: none"> • combined IGS zenith total delays • zenith wet delays from radiosonde launches

Table 6-13 - Characteristics and objectives of experiment *OBER-II*. See Appendix VI for the full configuration file.

6.3.1 Impact of Orbit Accuracy

Four orbit products of the IGS analysis centers were tested within this experiment. The predicted orbits (*IGP*) are available for real-time applications. The prediction interval is 24 h and 48 h, respectively. These orbits have a higher accuracy than the GPS broadcast ephemeris and are also suited for ground-based GPS tropospheric delay estimation in most cases. The ultra-rapid orbits (*ULT*) are currently in the pilot phase and available for real-time applications, too. The orbits produced by the GeoForschungsZentrum Potsdam (GFZ) were used during this experiment. The standard IGS rapid orbits (*IGR*) are - like the predicted *IGP*-orbits - a combined solution from all analysis centers participating into the orbit determination program. They are usually available with a delay of 2 days whereas the final orbit products (*IGS*) are most precise, but available with a latency of about 2 weeks.

Orbit Product	Bias [mm]	Std. Dev. [mm]	RMS [mm]
IGP	-0.9	7.8	9.5
ULT	0.8	5.7	6.5
IGR	-1.4	3.3	4.6
IGS	-1.2	3.1	4.3

Table 6-14 - Results of the *OBER-II* experiment. The IGS combined troposphere product was used as reference data set. The results of the tropospheric analysis software TropAC were derived using 4 different orbit products from the IGS, namely predicted (*IGP*), ultra-rapid (*ULT*), rapid (*IGR*) and final orbits (*IGS*). The accuracy quantities given here are the mean values over the full analysis period of 2 months.

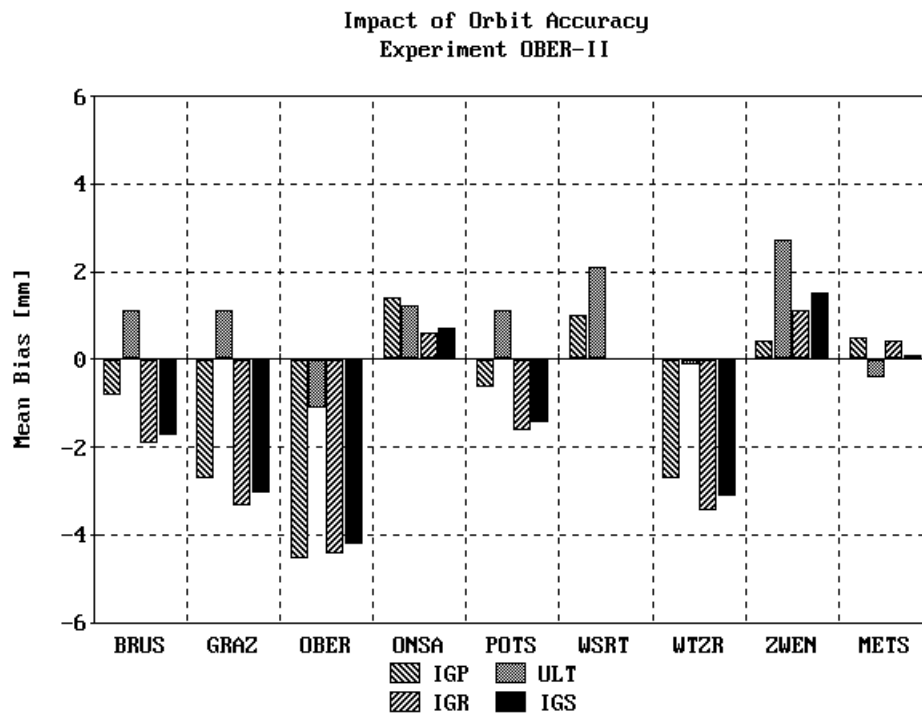


Figure 6-20 - Comparison of mean biases using different GPS orbit products. IGS zenith neutral delays were used as reference data.

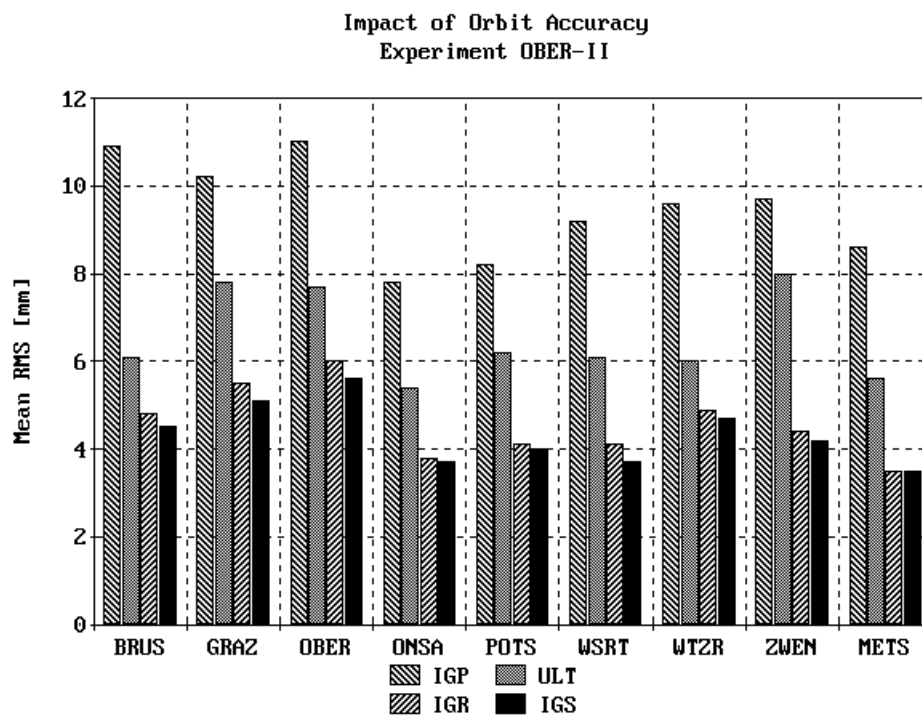


Figure 6-21 - Comparison of mean RMS values using different GPS orbit products. IGS zenith neutral delays were used as reference data.

Table 6-14 shows the mean accuracy estimates, Figure 6-20 and Figure 6-21 show the site-specific biases and RMS values. The conclusions that can be drawn from these results are not too unexpected: Highest accuracy is achieved with help of final IGS orbits. This is the best GPS orbit product available world-wide, but a latency of about 2 weeks must be accepted. However, rapid orbits are available much faster and allow to estimate zenith tropospheric delays at almost exactly the same accuracy level. The predicted orbits (*IGP*) are attractive for real-time applications, but have a RMS that is 5 mm higher than that for the final and rapid orbits. For this reason, it is recommended to use ultra-rapid orbits (*ULT*) for real-time analysis. These orbits have a RMS that is 3 mm better than that of the predicted orbits.

6.3.2 Comparison with Radiosonde Data

Like for the *OBER-I* experiment, a comparison with radiosonde data for Oberschleißheim shall conclude this section. Table 6-15 lists the accuracy quantities. Note that zenith wet delays were not computed by the TropAC analysis system because the distribution of surface meteorological data for *OBER* has been abruptly discontinued by the IGS after mid-1999.

Quantity	Analysis	Bias [mm]	Std. Dev. [mm]	RMS [mm]
ZND	IGS	-0.0	18.0	18.0
ZND	TropAC	-3.6	18.4	18.7

Table 6-15 - Comparison of GPS-derived zenith neutral delays with integrated quantities from radiosonde profiles for Oberschleißheim near Oberpfaffenhofen (OBER, Germany). The entry "IGS" means that the comparison is based on the IGS combined zenith total delays product whereas "TropAC" stands for the results from the tropospheric analysis software.

The results have a good agreement in comparison to those presented for experiment *OBER-I*. Apparently, the accuracy of the radiosonde package used at Oberschleißheim can be determined in the range of about 2 cm for zenith neutral and wet delays. This corresponds to an accuracy in the range of 3 kg/m² for integrated water vapor.

6.4 EUREF/GREF Experiment

The EUREF/GREF experiment presented here focuses on integrated water vapor as target value. After comparing the TropAC results with those of the IGS analysis centers at the zenith neutral delay level (→ 6.4.1), the accuracy of the conversion of zenith wet delays into precipitable water vapor is discussed (→ 6.4.2), results from different analysis centers for integrated water vapor are shown (→ 6.4.3) and a comparison with high-resolution numerical weather model data is outlined. Refer to Table 6-16 and Figure 6-22 for more information about this experiment.

6.4.1 Comparison with IGS Delays

Table 6-17 lists the mean biases, standard deviations and RMS values with the IGS combined tropospheric product used as reference data as it has been done in all preceding sections. The level of agreement achieved in comparison to the IGS data is satisfactory. Only the results for REYK show a clearly higher noise level.

Nominal network setup:	shortest baselines
Validation period:	1 October 1997 ... 31 October 1997
Number of stations:	12
Test network:	<i>ANKR, GRAZ, KOSG, MATE, ONSA, POTS, WTZR, ZIMM, ZWEN, KIRU, REYK, ZECK</i>
Objectives:	<ul style="list-style-type: none"> • assessment of uncertainty of conversion of zenith wet delays into precipitable water/integrated water vapor • comparison with integrated water vapor from CODE results • comparison with integrated water vapor from high-resolution weather fields
Reference data:	<ul style="list-style-type: none"> • combined IGS zenith total delays • integrated water vapor from IGS and CODE results • integrated water vapor from high-resolution numerical weather models

Table 6-16 - Characteristics and objectives of the EUREF/GREF experiment. See Appendix VI for the full configuration file.

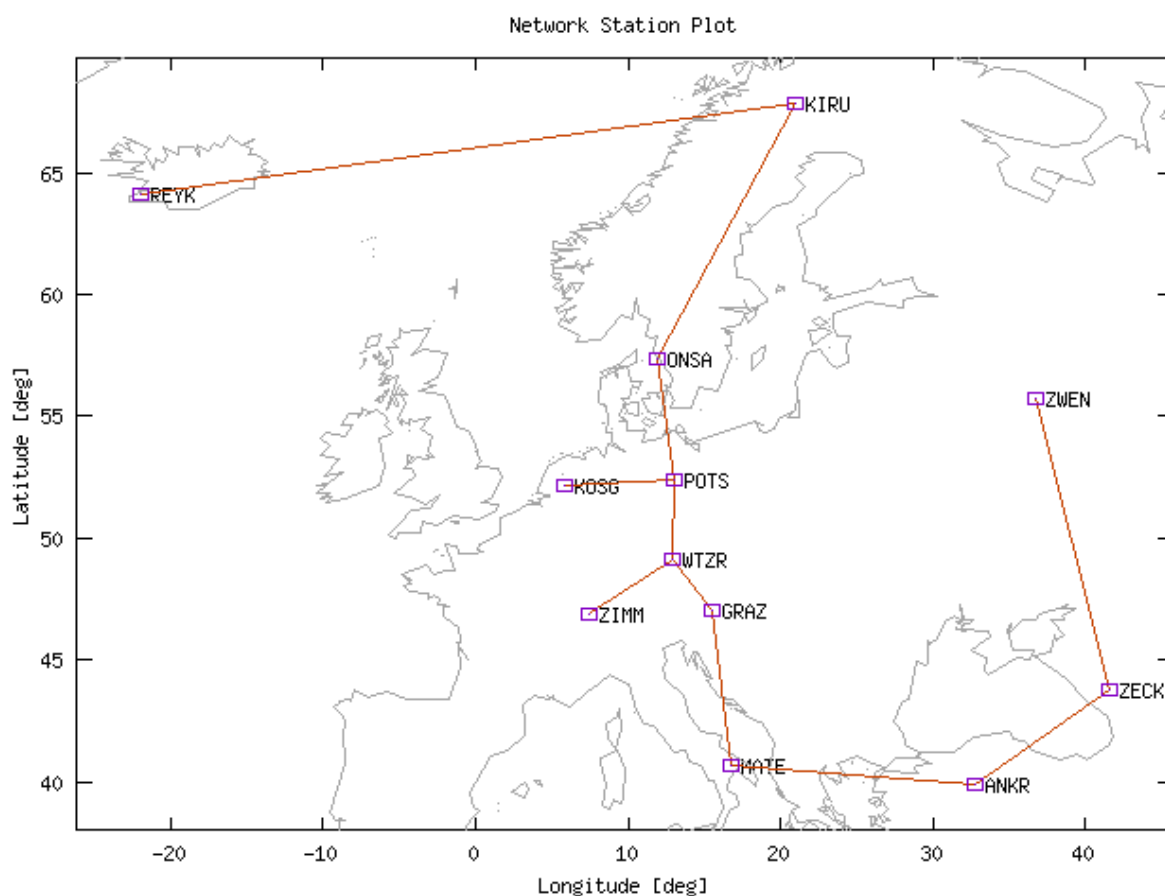


Figure 6-22 - Network stations and baseline setup for the EUREF/GREF experiment (October 1997). The experiment discussed here only makes use of the sub-network shown in this plot. The full GREF network is not shown.

NO.	SITE	SAMPLES	BIAS	SIGMA	RMS
1	ANKR	22	-2.8	4.7	6.1
2	GRAZ	31	1.9	3.7	4.8
3	KOSG	31	1.7	3.7	4.3
4	MATE	31	-2.5	4.2	5.4
5	ONSA	31	3.5	3.9	5.3
6	POTS	31	1.6	3.9	4.5
7	WTZR	27	1.1	3.1	3.6
8	ZIMM	31	2.4	4.1	5.2
9	ZWEN	19	-0.6	4.8	5.6
10	KIRU	29	2.0	4.2	5.1
11	REYK	28	5.7	9.0	10.8
12	ZECK	10	1.5	3.9	4.7
MEAN			1.3	4.4	5.4

Table 6-17 - Mean biases, standard deviations ("sigma") and RMS values for the network stations of the EUREF/GREF experiment in comparison to the IGS combined tropospheric product (= reference data). The column labeled "samples" is identical to the number of days compared. Each day comprises 24 hourly zenith neutral and wet delays.

6.4.2 Conversion into Integrated Water Vapor

The zenith wet delays estimated by the Kalman filter engine must be converted into precipitable water or integrated water vapor (\rightarrow 3.5). This conversion imposes an additional uncertainty on the accuracy of the final data product. The goal of this experiment was to evaluate existing models to determine the conversion factor with help of surface temperature. The following models were used:

Model	Reference	Description
Bevis	\rightarrow 3.5.3.1	linear relation between surface and mean temperature of the troposphere, derived for region between Alaska and Florida
Emardson	\rightarrow 3.5.3.2	parabolic or sinusoidal model for many radiosonde sites of Europe
TropAC	\rightarrow 3.5.3.3	individual linear functions for many IGS tracking stations, derived from GDAS numerical weather models by routine database analysis of the tropospheric analysis system TropAC
Solbrig	\rightarrow 3.5.3.1	linear relation for region of Germany, derived from GDAS numerical weather models

Table 6-18 - Different approaches to derive the mean temperature of the atmospheric and/or the conversion factor to transform zenith wet delays into precipitable water.

These results were compared to the IWV values obtained by conversion with help of the mean temperature of the troposphere derived from high-resolution numerical weather models. Either the DWD-NWM for Germany (*DM4*, 14 km horizontal resolution, 30 vertical layers), or the Europe-model (*EM3*, 55 km horizontal resolution, 20 vertical layers) were used to derive the conversion factor Q . The full result table is given in \rightarrow Appendix III. The differences between the IWV results are

plotted in Figure 6-23 for the first 3 methods (Bevis, Emaradson and TropAC). The mean RMS for the Bevis model is 0.15 kg/m^2 , for the Emaradson model 0.16 kg/m^2 , for the individual TropAC functions 0.19 kg/m^2 and for the Solbrig model 0.20 kg/m^2 . One may conclude that the conversion methods do not differ much from each other. The TropAC approach has a slightly higher RMS than the Bevis and Emaradson models, but it should be noted that these individual functions were based on the database analysis covering only about 0.5 year and these functions will be certainly improved in the future. Nevertheless, the residual plots clearly show that deviations of up to more than 0.5 kg/m^2 may occur. As a conclusion, it can be stated that the conversion uncertainty is a significant contributor to the overall error budget, albeit not the dominant one. Highest accuracy can be expected when the vertically integrated mean temperature from numerical weather fields is preferred and the surface temperature models presented here are only used when no NWM data are available.

6.4.3 Comparison of Integrated Water Vapor Results

GPS-derived integrated water vapor results from 2 analysis centers, namely IGS (combined product) and CODE, were compared with the TropAC IWV-values. The results are plotted for station POTS (Figure 6-24 and Figure 6-26) as well as WTZR (Figure 6-25 and Figure 6-27). The mean accuracy quantities are given in Table 6-19.

It becomes evident that the agreement of the TropAC results with respect to the IGS troposphere products is better than the agreement with CODE results in all cases except REYK where CODE and TropAC data are clearly more unbiased than it is the case for the IGS data. On the other hand, very heavy biases can be found in the CODE/TropAC comparison for station KIRU which are not present in the IGS/TropAC comparison. Consequently, the CODE results must contain systematic errors. All in all, a RMS level of clearly better than 1 kg/m^2 could be reached by the IGS/TropAC data pairs and a level of better than 2 kg/m^2 for most of the CODE/TropAC results.

Station	Bias IGS	Bias CODE	Std. Dev. IGS	Std. Dev. CODE	RMS IGS	RMS CODE
ANKR	0.43	0.58	0.92	1.65	1.02	1.75
GRAZ	-0.28	0.36	0.76	1.76	0.81	1.79
KOSG	-0.29	0.53	0.69	1.08	0.75	1.20
MATE	0.38	0.91	0.82	1.01	0.91	1.36
ONSA	-0.54	-0.40	0.72	2.04	0.90	2.08
POTS	-0.27	0.60	0.76	0.92	0.80	1.10
WTZR	-0.18	0.27	0.56	0.74	0.59	0.78
ZIMM	-0.41	0.22	0.75	1.00	0.86	1.03
ZWEN	0.08	0.66	0.89	2.25	0.89	2.35
KIRU	-0.33	4.77	0.71	1.12	0.79	4.90
REYK	-0.90	0.29	1.52	1.56	1.77	1.59

Table 6-19 - Table of mean biases, standard deviations and RMS values for the IWV comparison in units of $[\text{kg/m}^2]$. The columns labeled "IGS" show the results from the comparison of the TropAC and the IGS data whereas the columns labeled "CODE" refer to the data of the CODE analysis center. Station ZECK is not included due to obvious inconsistencies of the CODE results.

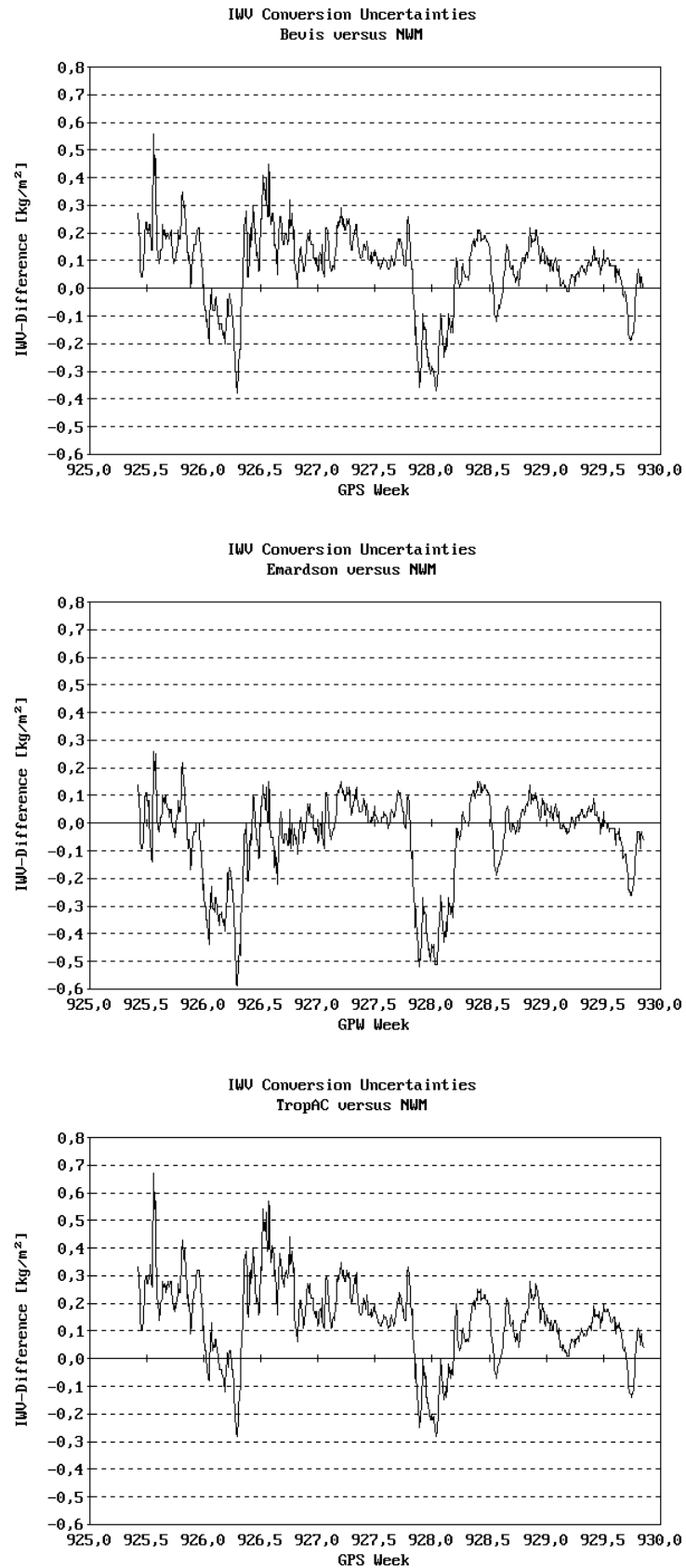


Figure 6-23 - Uncertainty of the IUV conversion for POTS. The reference data were computed with help of NWM-derived Q-factors and compared with the following models: Emardson (top, see → 3.5.3.2), Bevis (middle, see → 3.5.3.1) and TropAC/GDAS (bottom, see → 3.5.3.3).

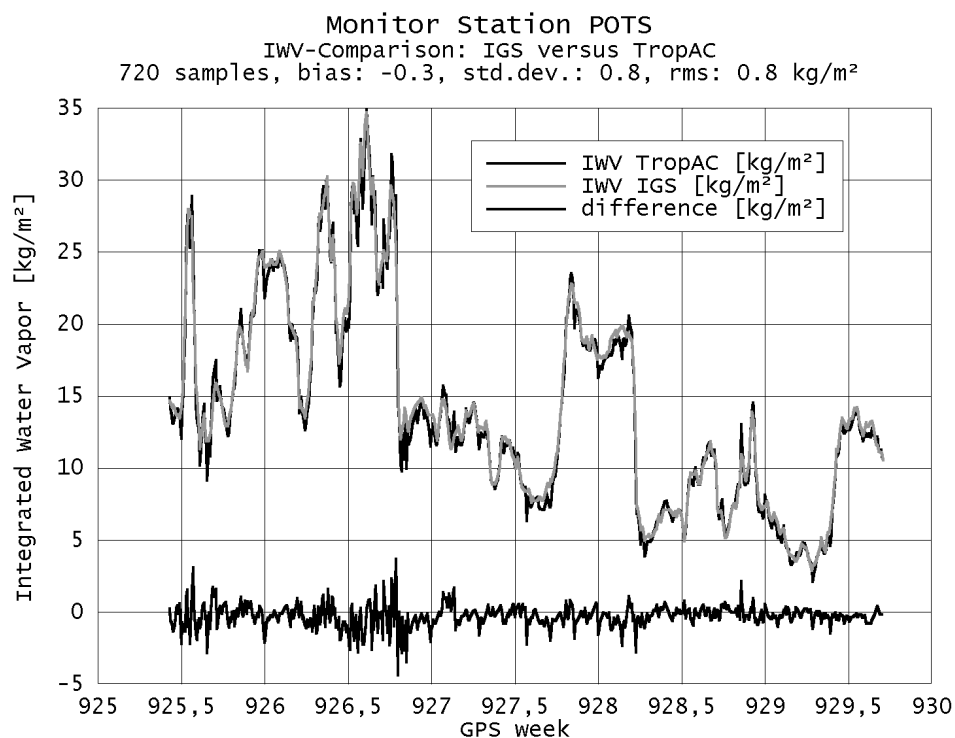


Figure 6-24 - Integrated water vapor time series for Potsdam (POTS, Germany) analyzed by TropAC (black) and IGS (grey). The differences between both water vapor curves are plotted as well.

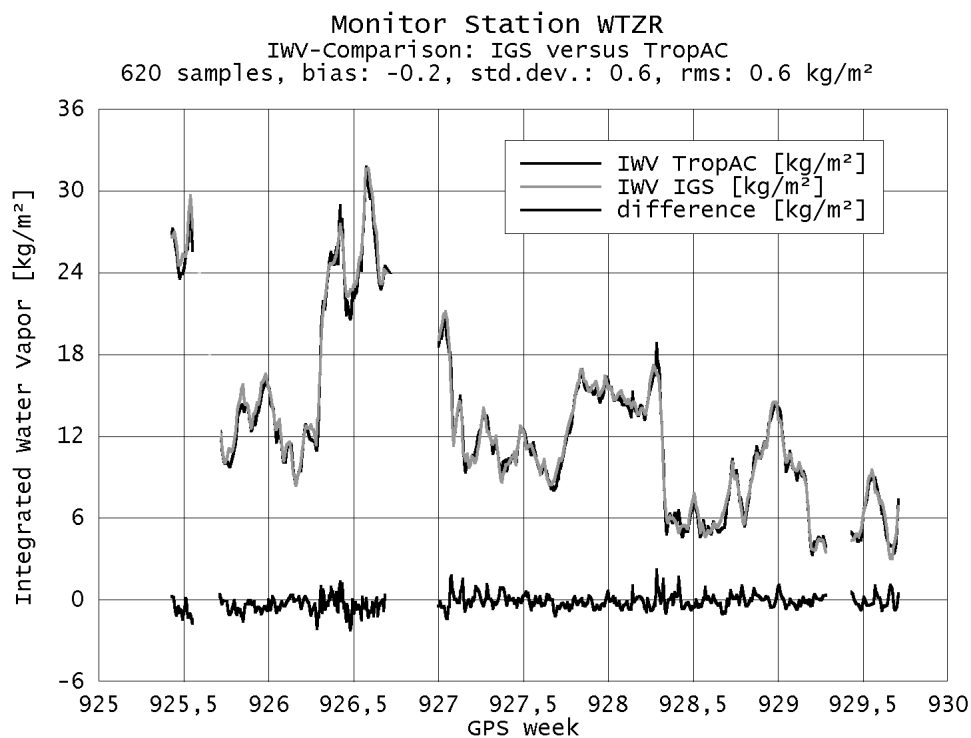


Figure 6-25 - Integrated water vapor time series for Wettzell (WTZR, Germany) analyzed by TropAC (black) and IGS (grey). The differences between both water vapor curves are plotted as well.

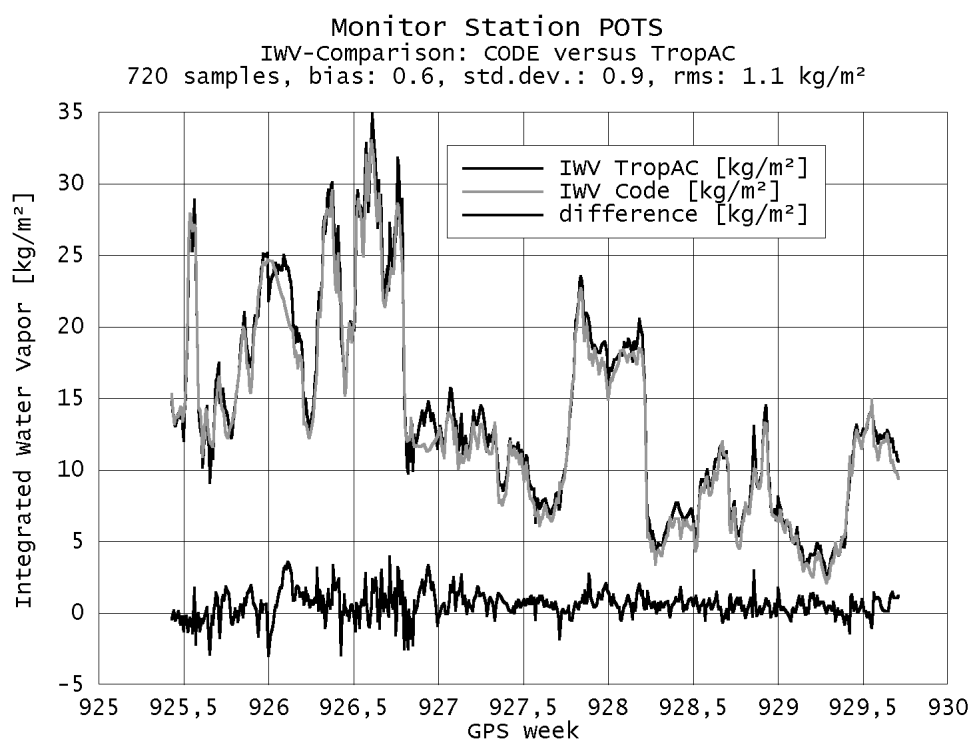


Figure 6-26 - Integrated water vapor time series for Potsdam (POTS, Germany) analyzed by TropAC (black) and CODE (grey). The differences between both water vapor curves are plotted as well.

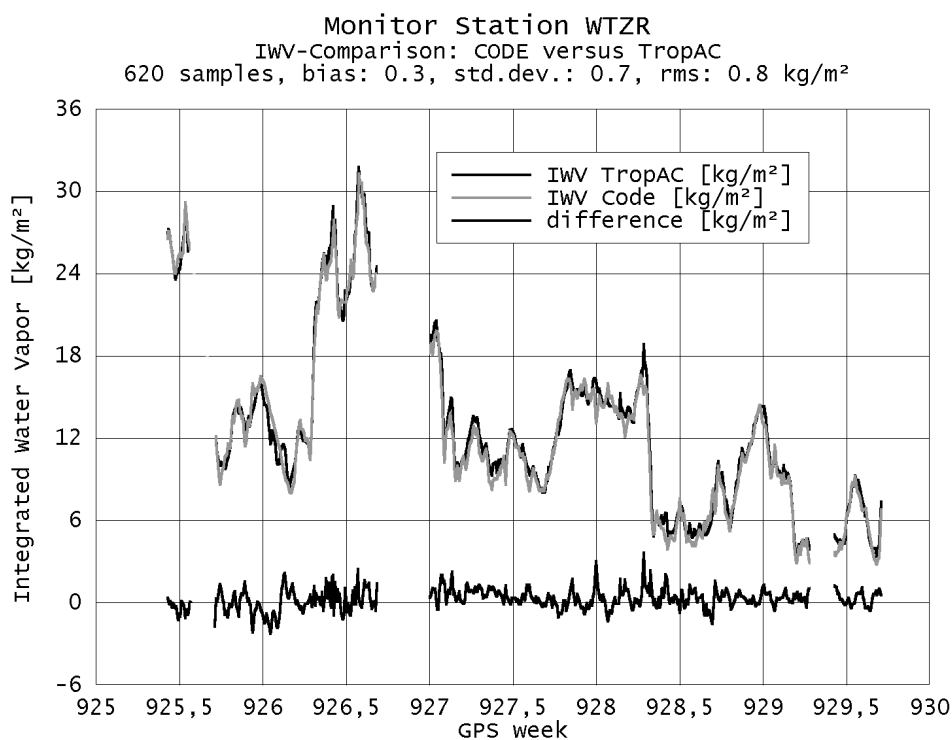


Figure 6-27 - Integrated water vapor time series for Wettzell (WTZR, Germany) analyzed by TropAC (black) and CODE (grey). The differences between both water vapor curves are plotted as well.

6.4.4 Comparison with Integrated Water Vapor from Numerical Weather Fields

The IWV results of the CODE analysis center, the combined IGS solution and the TropAC data were also compared with the high-resolution weather models mentioned before (\rightarrow 6.4.2). Figure 6-28 shows the biases of this comparison for all 3 analysis centers and Figure 6-29 illustrates the RMS values.

The mean biases over the whole period and all sites are 1.94 kg/m² for CODE, 1.09 kg/m² for TropAC and 0.87 kg/m² for the IGS troposphere product. The diagrams clearly show that all biases have a positive sign except for ANKR where the biases are negligibly small. The positive sign suggests that significant systematic errors are present in the numerical weather models. Nevertheless, distinct differences of up to 1 kg/m² can also be seen between the results of the 3 different analysis centers².

The mean RMS values are 3.18 kg/m² for CODE, 2.36 kg/m² for TropAC and 2.13 kg/m². The scatter of the CODE data is higher than that of the TropAC and the combined IGS results. The TropAC and the IGS IWV data have already been compared with each other (see Table 6-19) and the agreement was at a level below 1 kg/m². Now, both the TropAC as well as the IGS data show a RMS level of more than 2 kg/m² in comparison to the numerical weather fields. This suggests that the accuracy of the existing weather models is inferior to that of the GPS IWV estimates. Consequently, an assimilation of GPS-derived data into numerical weather models makes sense as it is likely to improve the accuracy of the model.

6.5 Multipath Experiment/Receiver Comparison

Two GPS receivers are available for Wettzell that are associated with the site IDs WTZR (receiver: *ROGUE SNR-8000*, antenna: *DORNE MARGOLIN T*) and WTZT (receiver: *Trimble 4000SSi*, antenna: *TR GEOD L1/L2 GP*). This receiver pair is located only 4 meters apart, so the zenith hydrostatic and wet delays are the same. Multipath effects and receiver-internal errors should be considered as the major effects causing deviations. Table 6-20 summarizes the characteristics of this experiment and Figure 6-30 gives the corresponding network plot.

The outcome of this experiment can be summarized as follows: The mean RMS for all days analyzed (one month) was about 5 mm. Indeed, this is a typical value that we can trace back to average multipath effects. Generally speaking, it can be concluded that WTZT should suffer more from multipath than WTZR since a choke ring antenna is used in the latter case whereas the Trimble receiver at WTZT is connected to a ground-plane antenna that is more prone to multipath effects. Apart from multipath, uncertainty in the phase center correction can be an error contributor. The Dorne Margolin antenna is used as reference antenna³, so it practically has no elevation-

² KIRU is not taken into consideration here as it seems that there was a problem with the CODE analysis for this site that does not occur for the TropAC results or the IGS combined product.

³ The current antenna phase center calibration strategy applied among the IGS analysis centers is a relative method. This means that the elevation-dependent PCV correction terms of the reference antenna are arbitrarily set to zero and the second antenna is calibrated with respect to this reference antenna.

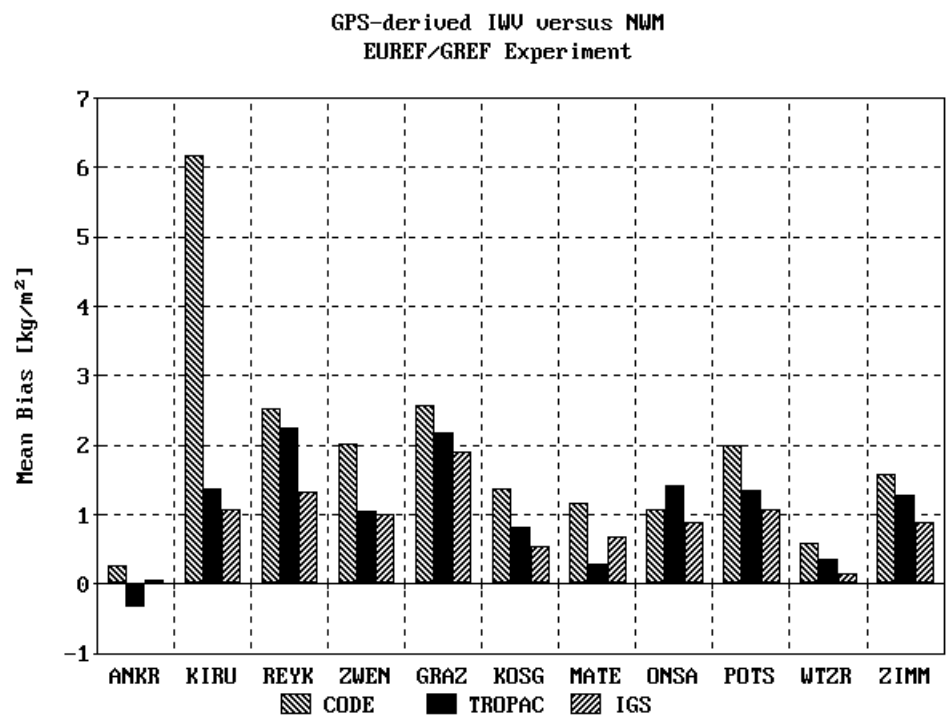


Figure 6-28 - Site-specific mean biases from the comparison of GPS-derived IWV (3 different analysis centers) and IWV from high-resolution numerical weather models.

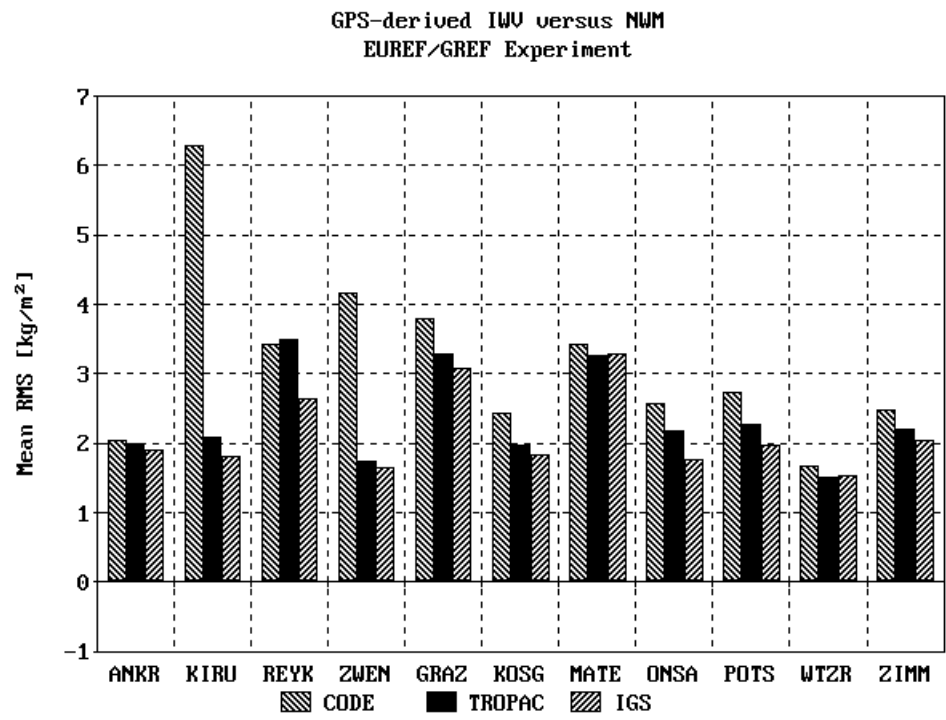


Figure 6-29 - Site-specific mean RMS values from the comparison of GPS-derived IWV (3 different analysis centers) and IWV from high-resolution numerical weather models.

dependent PCV corrections whereas the Trimble antenna can have corrections in the range of up to 1.5 cm. Uncertainties in the calibration table may cause systematic errors. Indeed, Figure 6-31 and Figure 6-32 show certain systematic signatures. However, these offsets can also be due to multipath as diurnal data batches are compared with each other and multipath is dependent on the satellite constellation that is repeated each sidereal day (corresponds to about 24 hours). Consequently, approximately the same multipath effects can be expected in both diagrams leading to biases between both curves. Actually, a mean bias of 4.3 mm over all days causes a RMS of 5.5 m. The average standard deviation is only about 3.3 mm, so systematic effects are clearly the dominant kind of error here what supports the assumption of multipath corruption.

Nominal network setup:	centered on <i>WTZR</i> and <i>WTZT</i> , respectively
Validation period:	1 October 1997 ... 31 October 1997
Number of stations:	7
Test network:	<i>WTZT/WTZR</i> , <i>BRUS</i> , <i>POTS</i> , <i>METS</i> , <i>OBER</i> , <i>ONSA</i> , <i>ZWEN</i>
Objectives:	<ul style="list-style-type: none"> • evaluation of multipath effects • comparison of receiver performance
Reference data:	comparison between <i>WTZR</i> and <i>WTZT</i> results

Table 6-20 - Characteristics and objectives of the multipath experiment. See Appendix VI for the full configuration file.

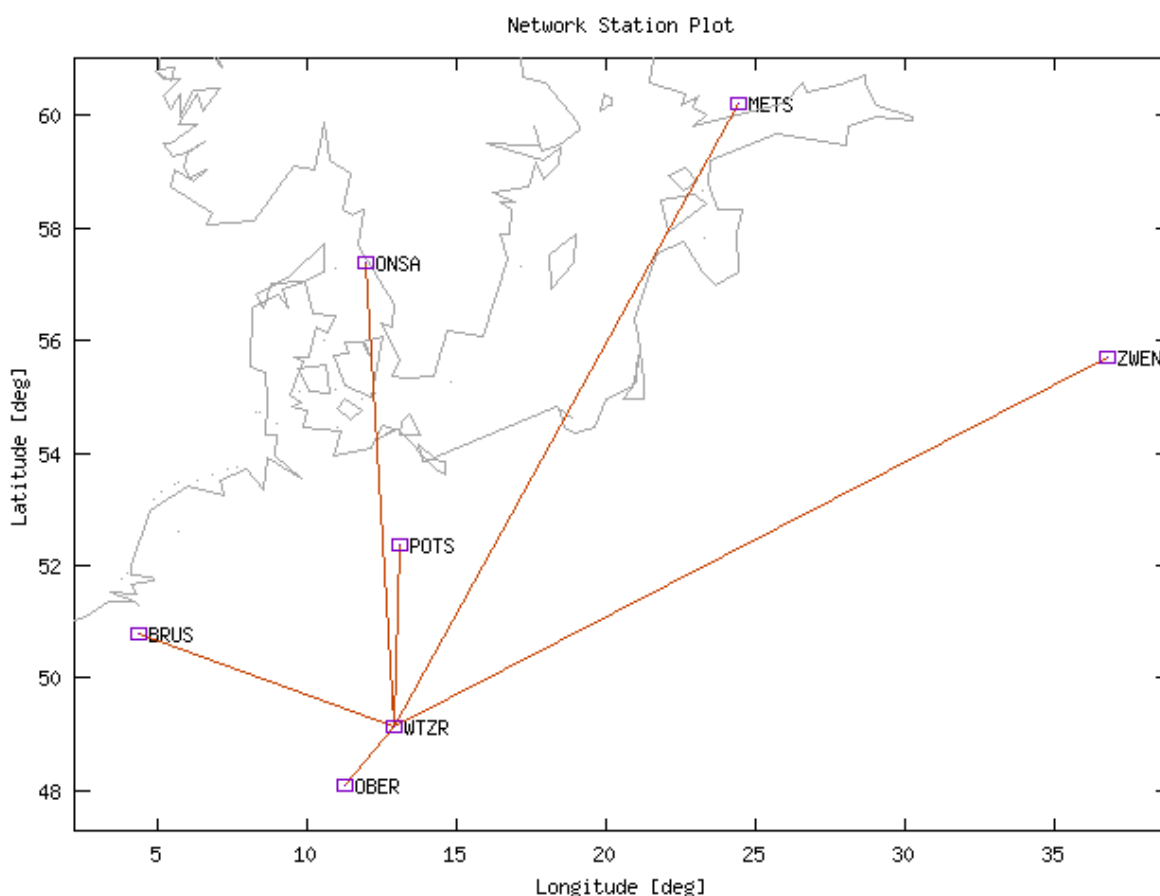


Figure 6-30 - Network stations and baseline setup for the multipath experiment during October 1997. The network was centered either on *WTZR* (shown here) or *WTZT*.

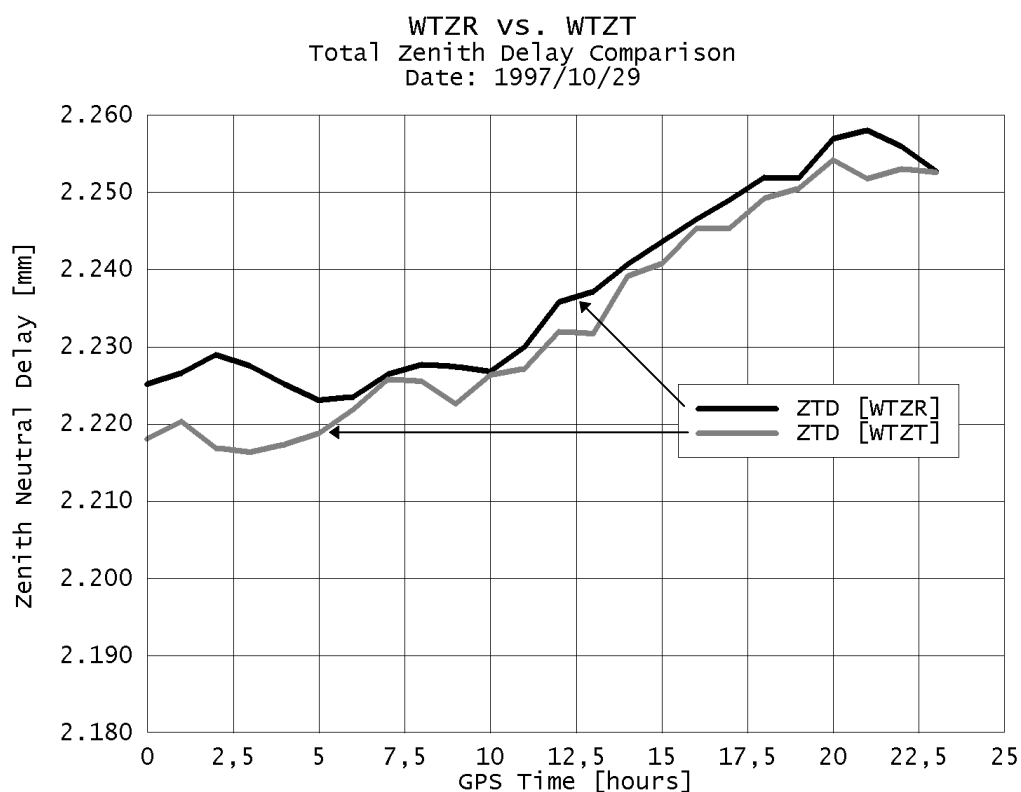


Figure 6-31 - Comparison of hourly zenith neutral delays estimated at tracking station WTZR and at WTZT on 29 October 1997.

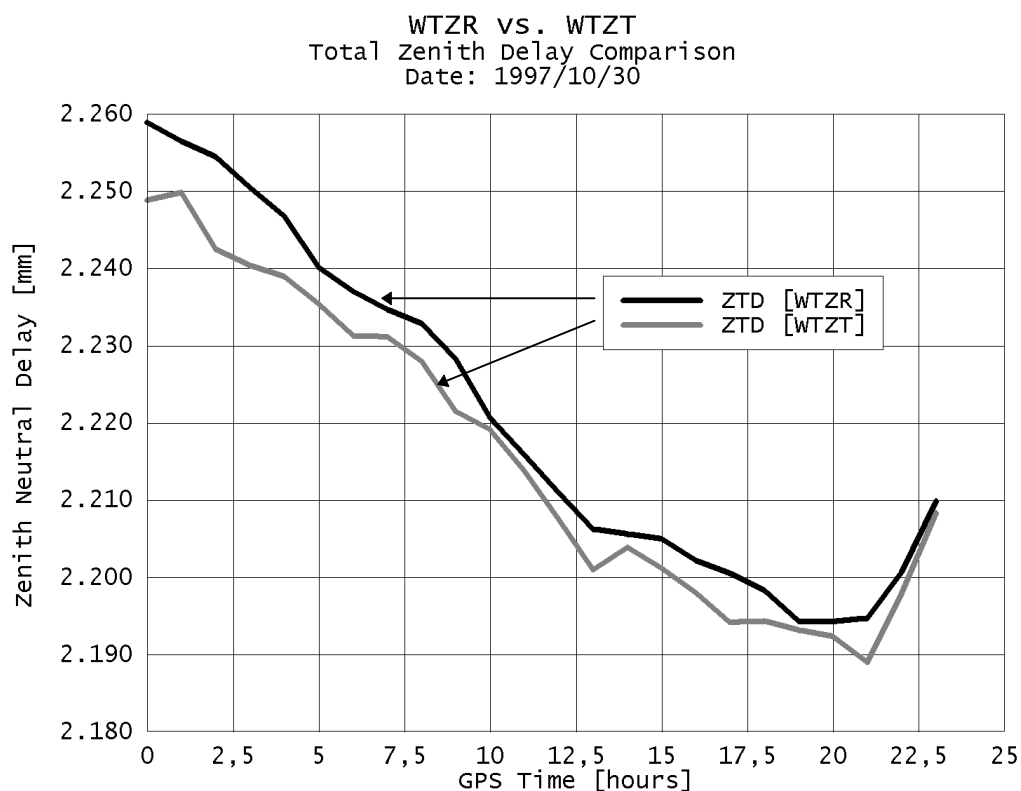


Figure 6-32 - Comparison of hourly zenith neutral delays estimated at tracking station WTZR and at WTZT on 30 October 1997.

6.6 WVR Validation Experiment

As far as ground-based water vapor estimation is concerned, there are only few sensors that can compete with GPS, namely ground-based water vapor radiometers and LIDAR. The radiosonde data discussed in → 6.2.7 and → 6.3.2 proved to be less precise in comparison to the projected accuracy of GPS-derived wet delays and integrated water vapor.

To validate the GPS performance as independently as possible, data for IGS tracking station Potsdam (POTS) were analyzed from January until the beginning of March

Nominal network setup:	centered on <i>POTS</i>
Time span:	1 January 1999 ... 15 March 1999
Number of stations:	6
Test network:	<i>POTS, REYK, METS, ZWEN, OBER, BRUS</i>
Objectives:	<ul style="list-style-type: none"> • validation of GPS results with help of WVR measurements • estimation of mapping functions coefficients • estimation of horizontal gradients
Reference data:	<ul style="list-style-type: none"> • WVR measurements • IGS combined troposphere product

Table 6-21 - Characteristics and objectives of the water vapor radiometer validation experiment.

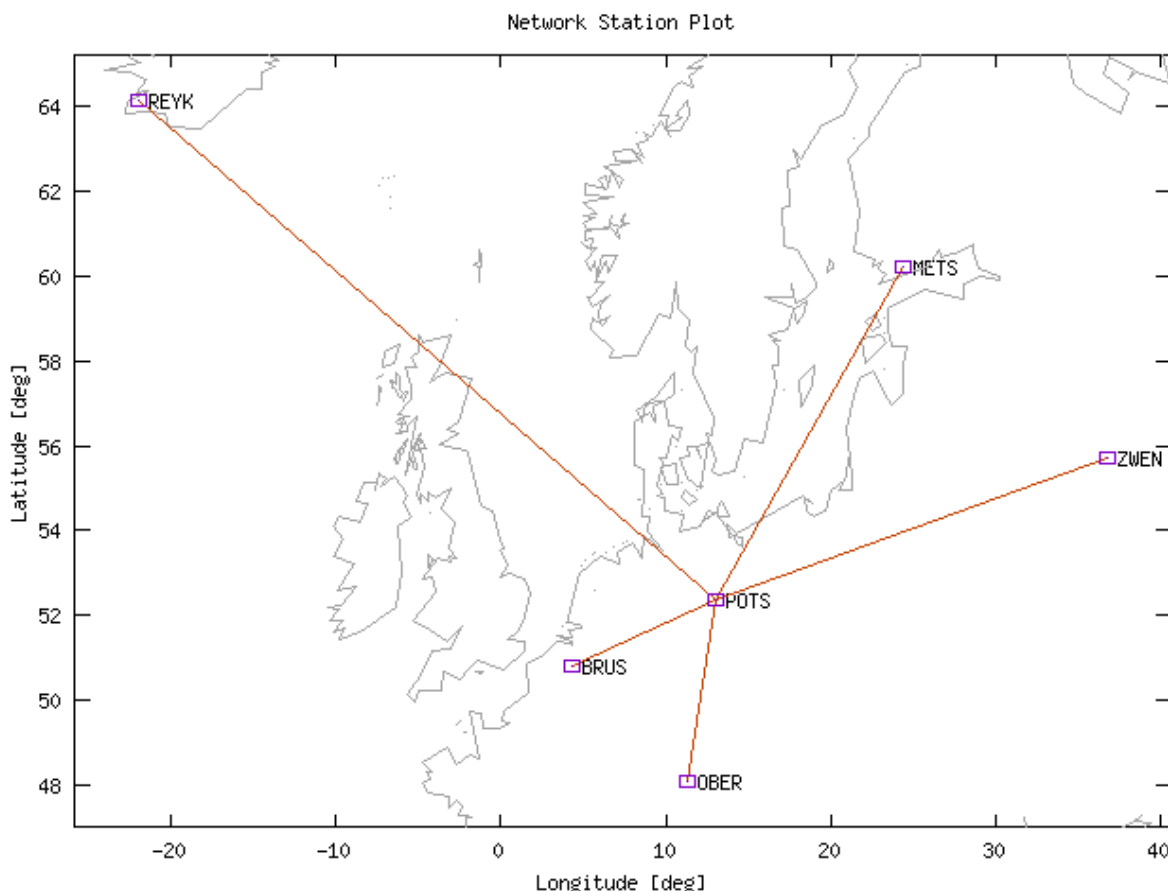


Figure 6-33 - Network stations and baseline setup for the water vapor radiometer validation experiment. The network was centered IGS tracking station Potsdam (POTS, Germany).

1999. The filtered wet delays were converted into precipitable water with the Emardson model (→ 3.5.3.2) and compared to the measurements of a water vapor radiometer collocated in the vicinity of the GPS receiver (→ 6.6.1). Moreover, analysis results with additional estimation of hydrostatic mapping function coefficients (→ 6.6.2) and horizontal gradients (→ 6.6.3) are presented.

6.6.1 Integrated Water Vapor

The most important parameter is integrated water vapor or precipitable water. Special emphasis is paid on the results of the standard configuration (→ 6.6.1.1) and on the differences between several GPS processing settings (→ 6.6.1.2) with respect to the WVR samples that serve as reference data.

6.6.1.1 Comparison of Results

The standard configuration uses the Chao mapping functions (→ 3.2.2.1.2, → 3.2.2.2.1) and an elevation mask of 15° . The process noise (→ 3.4) is defined dynamically with an amplifier of $q_{AMP} = 1.0$ (→ 3.4.4.2).

Table 6-22 lists the distribution of the differences between the WVR and the GPS filter estimates for Potsdam. The vast majority of the samples shows a discrepancy of less than 1.5 kg/m^2 . Only very few measurements exceed 2.5 kg/m^2 and in many cases, a closer look at the data reveals that the problems leading to these high deviations were likely related to reliability problems of the WVR (see also → 6.6.4). Table 6-23 gives the daily accuracy quantities of the WVR/GPS comparison. Those day missing in the table were excluded from the comparison due to rainfall as the WVR is incapable of measuring during such periods.

Figure 6-34 and Figure 6-35 show two short-term time series of this experiment covering 4 days each. The WVR and the GPS measurements as well as their differences are plotted. The GPS data were plotted with highest resolution (30 seconds) and the WVR that were interpolated accordingly. Generally speaking, the agreement between both curves is quite acceptable, but some low-pass filter effects seem to be present, e. g. at 10 h (Figure 6-34) where the GPS samples do not follow the WVR curve to sufficient extend. It is likely that these shortcomings are related to an unsuitable process noise. The process noise was defined dynamically, but the amplification factor was set to 1.0. Extra investigations carried out after the occurrence of discrepancies was recognized as a problem of the Kalman filter are presented in section → 6.6.4 and suggest that a factor of at least 1.5 should be applied or the maximum tuning method (→ 3.4.4). The latter method was applied for many experiments discussed so far, e. g. *OBER-I*, *OBER-II* and *EUREF/GREF*, but not here.

6.6.1.2 Comparison of Different Configuration Settings

Results for several runs with different configuration settings are given in Table 6-24. Most configurations are able to deliver results that agree to the WVR measurements at a RMS level of better than or equal to 0.85 kg/m^2 . These accuracy level is very promising. Most runs were conducted using an elevation mask of 15° (Table 6-24,

DISTRIBUTION OF DIFFERENCES				
0.0 - 0.5	kg/m ² :	205		28.7%
0.5 - 1.0	kg/m ² :	282		39.5%
1.0 - 1.5	kg/m ² :	124		17.4%
1.5 - 2.0	kg/m ² :	70		9.8%
2.0 - 2.5	kg/m ² :	23		3.2%
> 2.5	kg/m ² :	5		0.7%

Table 6-22 - Distribution of the difference between the reference data (IWW measured by WVR) and the GPS filter estimated. The column in the middle gives the number of samples belonging to the designated class and the very right column expresses this amount as relative percentage. Less than 4% of the discrepancies exceed a level of 2 kg/m² and more than 68% of all samples agreed at a level of better than 1 kg/m².

DOY	BIAS	SIGMA	RMS	MIN	MAX
3	-0.3	0.9	0.9	0.1	1.6
4	1.0	1.0	1.4	0.1	3.0
5	-0.3	1.3	1.3	0.0	2.9
10	-0.5	0.4	0.6	0.0	1.0
15	0.1	0.8	0.8	0.1	2.0
16	0.1	0.9	0.9	0.0	2.0
17	-0.8	0.6	1.0	0.0	1.9
18	-0.5	0.6	0.8	0.0	1.7
19	-0.4	0.9	1.0	0.0	2.0
20	0.2	0.5	0.6	0.0	1.1
21	-0.2	0.6	0.6	0.0	1.2
22	-0.4	0.5	0.6	0.1	1.1
23	0.0	0.5	0.5	0.0	1.1
24	-0.6	0.8	1.0	0.0	1.9
25	-0.2	1.0	1.0	0.0	2.1
26	-0.5	0.6	0.8	0.0	1.8
29	0.1	0.5	0.5	0.1	1.2
34	0.3	0.8	0.8	0.0	1.6
39	-0.8	0.7	1.0	0.1	1.7
40	0.0	1.5	1.4	0.0	5.3
41	-0.3	0.3	0.4	0.0	0.7
42	-0.2	0.2	0.3	0.0	0.6
43	-0.1	0.3	0.3	0.0	0.6
44	-0.0	0.4	0.4	0.0	1.1
45	0.0	0.5	0.5	0.0	1.0
46	-0.2	0.7	0.7	0.0	1.6
49	0.7	1.2	1.4	0.1	2.8
51	0.4	0.6	0.7	0.0	1.6
54	0.5	1.0	1.0	0.1	2.7
56	-0.5	1.1	1.2	0.1	2.1
63	0.4	0.4	0.6	0.0	1.0
65	-0.5	0.6	0.8	0.0	1.5

Table 6-23 - Diurnal biases, standard deviations ("sigma", bias-reduced) and RMS values (not bias-reduced) as well as minimum and maximum of the absolute difference between the GPS and the WVR integrated water vapor measurements in units of [kg/m²].

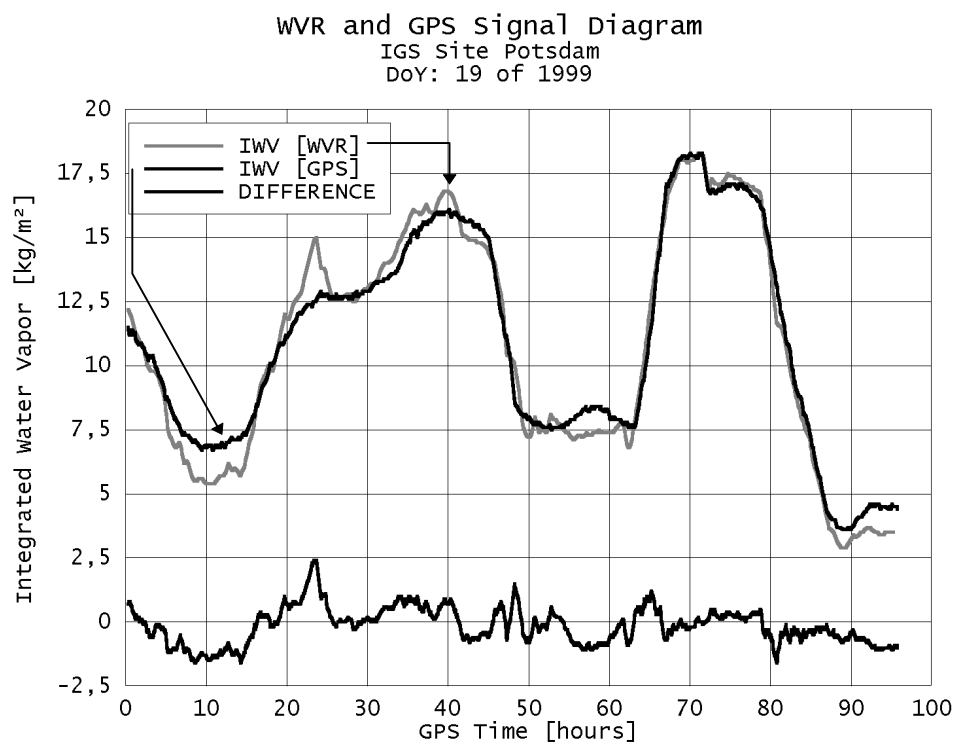


Figure 6-34 - Water vapor time series from WVR (gray) and GPS (black) at tracking station Potsdam (POTS, Germany) starting on 3 January 1999. The difference between both curves is plotted at the bottom of the diagram.

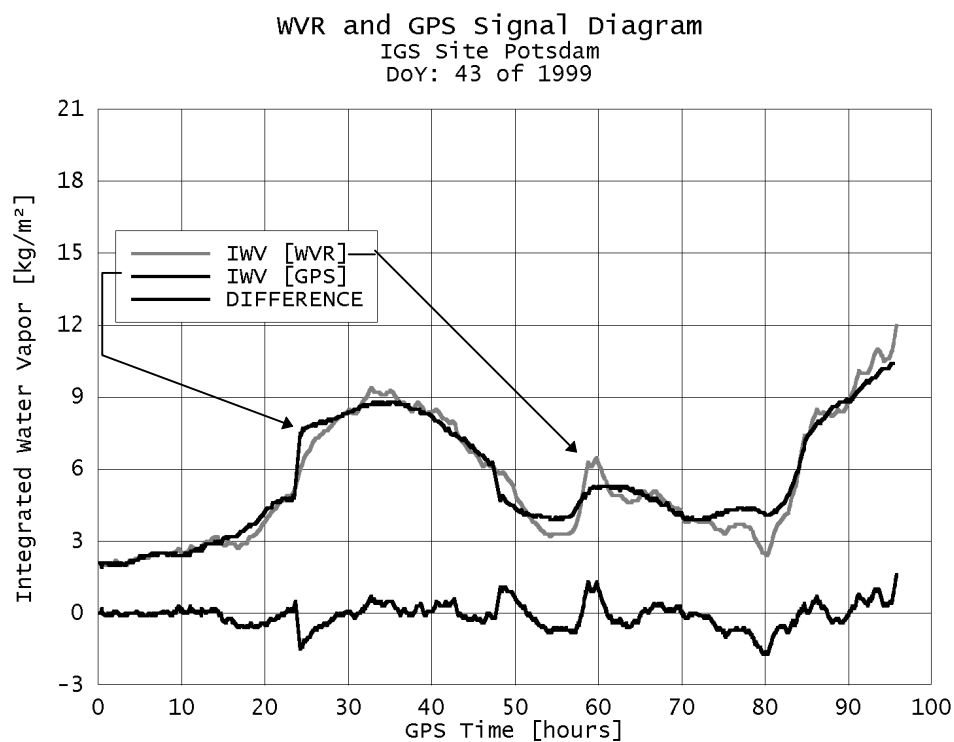


Figure 6-35 - Water vapor time series from WVR (gray) and GPS (black) at tracking station Potsdam (POTS, Germany) starting on 12 February 1999. The difference between both curves is plotted at the bottom of the diagram.

No.	Main Settings	Bias	Std. Dev.	RMS
1	elevation cutoff: 15°, medium weighting, coordinates estimated	-0.15 kg/m ²	0.69 kg/m ²	0.82 kg/m ²
2	elevation cutoff: 15°, medium weighting, coordinates estimated, mapping function coefficients estimated (→ 6.6.2)	0.11	0.69	0.80
3	elevation cutoff: 10°, weak weighting, coordinates estimated	0.12	0.67	0.85
4	elevation cutoff: 15°, weak weighting, coordinates estimated, Niell mapping function used instead of Chao	-0.13	0.81	1.03
5	elevation cutoff: 15°, weak weighting, coordinates estimated	-0.07	0.73	0.84
6	elevation cutoff: 15°, weak weighting, coordinates not estimated	0.04	0.71	0.82
7	elevation cutoff: 15°, weak weighting, coordinates not estimated, no dynamic process noise definition (10 mm/√h used instead)	0.07	0.63	0.75

Table 6-24 - Agreement between GPS and WVR results using different processing settings. Some of the configuration options are explained in the text more detailed.

e. g. #5), although a minimum elevation of 10° (Table 6-24, #3) did not show significantly worse results. Elevation dependent weighting (→ 3.3.4.6) was supplied during all analysis runs. The term "weak weighting" refers to a stochastic scaling of $\sigma_\theta = 3.0$ mm and a zenith angle scaling factor of $q_z = 1.05$, whereas "medium weighting" refers to coefficients of $\sigma_\theta = 3.7$ mm and $q_z = 1.12$. Note that these factors were results of a previous analysis and, actually, the results presented in section → 3.3.4.6 suggest that esp. the σ_θ coefficient was defined too pessimistically for precise mapping functions, even for the "weak weighting" configuration. All experiments discussed in the preceding sections were driven by the weighting coefficients given with formula 3-124. However, the elevation-dependent weighting discrepancies do not cause severe problems, there is only a RMS difference of 0.02 kg/m² between both runs (#5 and #1).

In contrast to experiment *OBER-I*, the WVR experiments showed that the Chao mapping functions (#5) performed better than the Niell mapping functions (#4): There is a difference in mean standard deviation of 0.14 kg/m² what corresponds to 0.9 mm of zenith wet delay. Additional estimation of the a-coefficient of the Chao mapping function (→ 3.2.2, formula 3-72) slightly improved the solution from a RMS level of 0.82 (#1) to 0.80 kg/m² (#2) and is discussed in section → 6.6.2.

The best agreement between WVR and GPS estimates of 0.75 kg/m² was achieved by fixing the coordinates (#7) of all stations and applying a \sqrt{q} -factor of 10 mm/√h to define the process noise of the stochastic process. Dynamic process noise definition delivered slightly worse results of 0.82 kg/m² (#6). However, this does not necessarily mean that the concept of dynamic tuning is inferior, but as already mentioned, the amplification factor was chosen too small. For this reason, the problem of process noise definition will be covered by section → 6.6.4 in detail.

6.6.2 Mapping Function Coefficients

Tropospheric parameter estimation may include filtering of mapping function coefficients (\rightarrow 3.3.3). Such a trial was conducted during the WVR experiment: The a -coefficient of the hydrostatic Chao mapping function was estimated as additional parameter with the intention to tune the mapping function to the local conditions of IGS tracking station Potsdam (*POTS*). Like all other parameters, a random walk stochastic process was assumed for the mapping function coefficient. The initial standard deviation was set to 0.00005 and the value itself initialized by the default mapping function coefficient of $a = 0.00143$ as determined by Chao. The process noise was circumspectly defined by a q -factor of $\sqrt{q} = 0.00001 \text{ 1}/\sqrt{\text{h}}$.

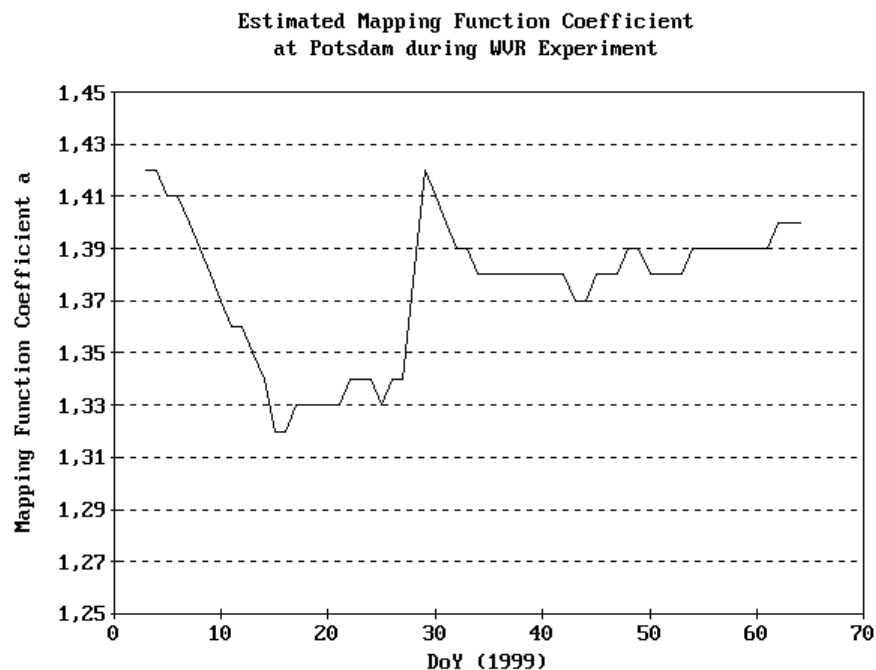


Figure 6-36 - Estimated mapping function coefficients at tracking station Potsdam (*POTS*, Germany) during the WVR experiment. The values of the y-axis need to be divided by a factor of 1000 in order to yield the mapping function coefficient.

Table 6-24 (#2) gives the mean accuracy quantities in comparison to other configurations and shows that the RMS improved in comparison to the default configuration (#1), but only marginally. Figure 6-36 shows the filtered coefficients for monitor station Potsdam. Apparently, the estimated parameters suggest that the default value of $a = 0.00143$ is a bit too large for the conditions present at Potsdam from January to March 1999. Variations of up to 0.00010 occur during the validation experiment period. Steep decreases can be seen during the first half of January and a rapid increase at the end of January.

6.6.3 Horizontal Gradients

Other quantities that can be estimated are horizontal gradients (\rightarrow 3.3.2). For this test run, the elevation mask was lowered to 10° , the initial of the gradient pair was set to 5 mm with a process noise of $\sqrt{q} = 0.3 \text{ mm}/\sqrt{\text{h}}$. Figure 6-37 and 6-38 show the north-

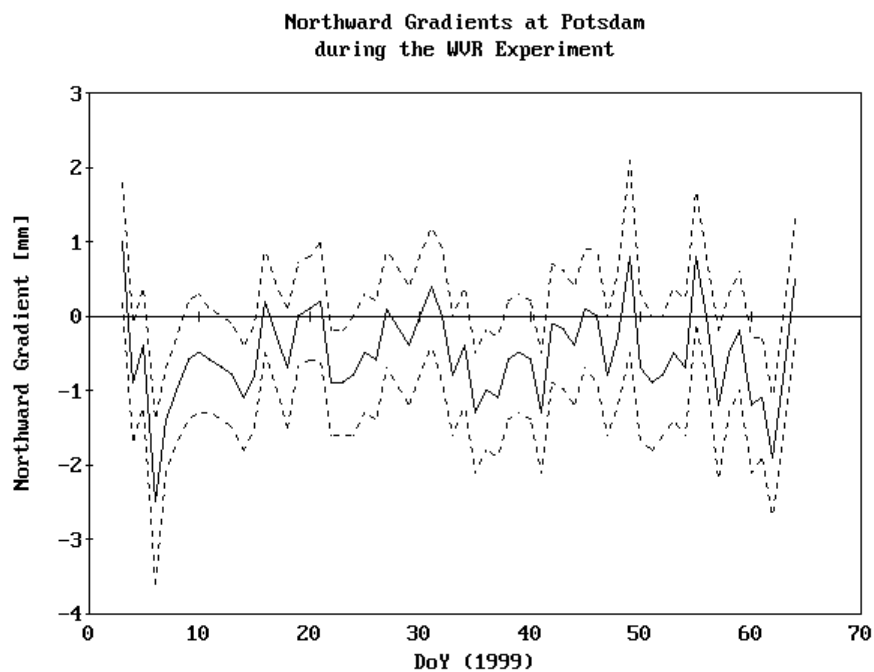


Figure 6-37 - Estimated northward horizontal gradients at tracking station Potsdam (POTS, Germany) during the WVR experiment. The band of standard deviations is plotted as well in order to allow an assessment of the significance of the gradients.

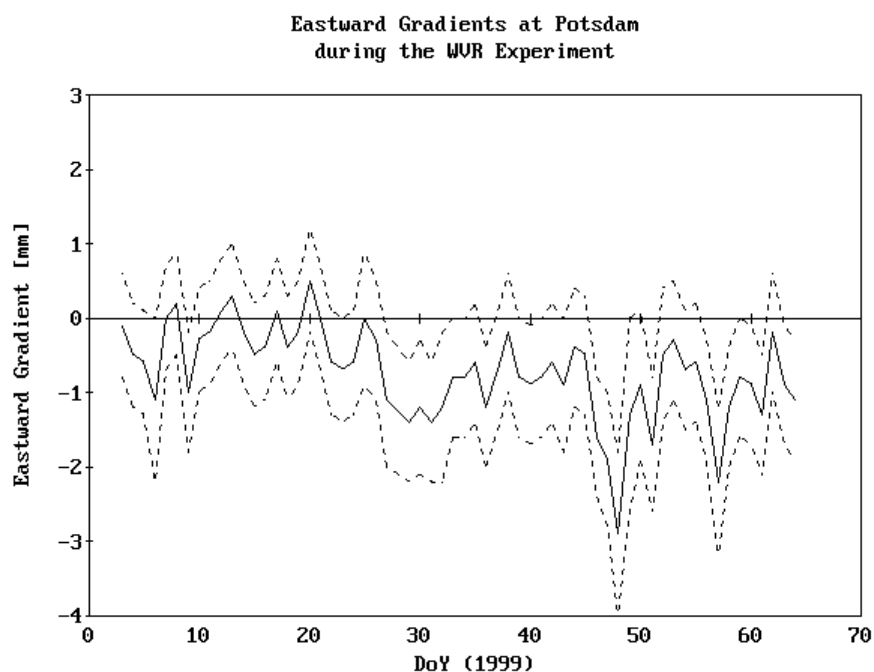


Figure 6-38 - Estimated eastward horizontal gradients at tracking station Potsdam (POTS, Germany) during the WVR experiment. The band of standard deviations is plotted as well in order to allow an assessment of the significance of the gradients.

as well as the eastward gradients and their standard deviations. It becomes evident that these parameters are almost never significant, i. e. the filter is not able to estimate the gradients at an accuracy level that makes them distinguishable from zero. Generally speaking, gradient estimation is not recommended and only useful under very special weather conditions that do not occur very often. The mean RMS of the gradient trial was about 1.1 kg/m^2 . This is worse than the results of all other runs. Possible reasons for this fact are the insignificance of the parameters leading to over-parameterized equations and the high level of initial standard deviation of 5 mm. The results suggest that 1 mm would have been sufficient. One may conclude that gradient estimation does not necessarily improve the filter solution and, if the user decides to estimate them, it seems necessary to rigorously test the gradients for significance and eliminate them from the analysis in case of insignificance.

6.6.4 Process Noise Definition

A strong variation of as much as 9 cm in zenith wet delay was monitored at IGS station Potsdam on 4 January 1999. This day is therefore highly suited to demonstrate the effects of process noise definition on ZWD filtering with GPS phase measurements.

Again, the water vapor radiometer (WVR) measurements serve as reference for the GPS results. Again, it is pointed out that a WVR may have a high accuracy comparable to that of GPS (or even a bit better), but is an extremely unreliable (albeit expensive) device as it cannot provide useful measurements during periods of rainfall. Although it is possible to detect rainfall and to flag corrupted WVR measurements, the beginning of such periods is often not detected correctly and additional filtering of the data is usually necessary. The day chosen here is almost free of problems related to the WVR, but one may see a spike in Figure 6-39 at a little later than 15 h that is obviously not related to ZWD variations, but to corrupted WVR measurements. The GPS filter estimates are given with maximum temporal resolution of 30 seconds, the standard sampling interval for the IGS network that is much higher than the output frequency of the WVR used here.

A very small q -factor of $1 \text{ mm}^2/\text{h}$ was intentionally chosen for the run shown in Figure 6-39 in order to demonstrate the low-pass filter effect that occurs in such cases: The filter is not able to follow the high variations. Instead, only the mean tendency is reflected. Figure 6-40 shows much better results. Here, the q -factor obtained from the auto-covariance function ($\rightarrow 3.4.3$), the default value, is used. Nevertheless, $\sqrt{q} = 2.9 \text{ mm}/\sqrt{\text{h}}$ is not a very good choice for this particular day either. It is also too small resulting in errors of several centimeters for the time window from 10 h to 20 h.

Dynamic tuning ($\rightarrow 3.4.4$, formula 3-150) improves the situation significantly, but also reveals one shortcoming: If we only perform one iteration on the default solution (with an initial $\sqrt{q} = 2.9 \text{ mm}/\sqrt{\text{h}}$), then the dynamic process noise coefficients will be too small because the initial solution is not able to provide a realistic image of the ZWD dynamics, it is also a low-pass filtered image. One way to compensate this shortcoming is a double amplification ($\rightarrow 3.4.4.2$) of the hourly q -factors ($q_{\text{AMP}} = 2.0$). The results for this run are plotted in Figure 6-41. Without applying this amplifier, one has to perform *at least* a second iteration.

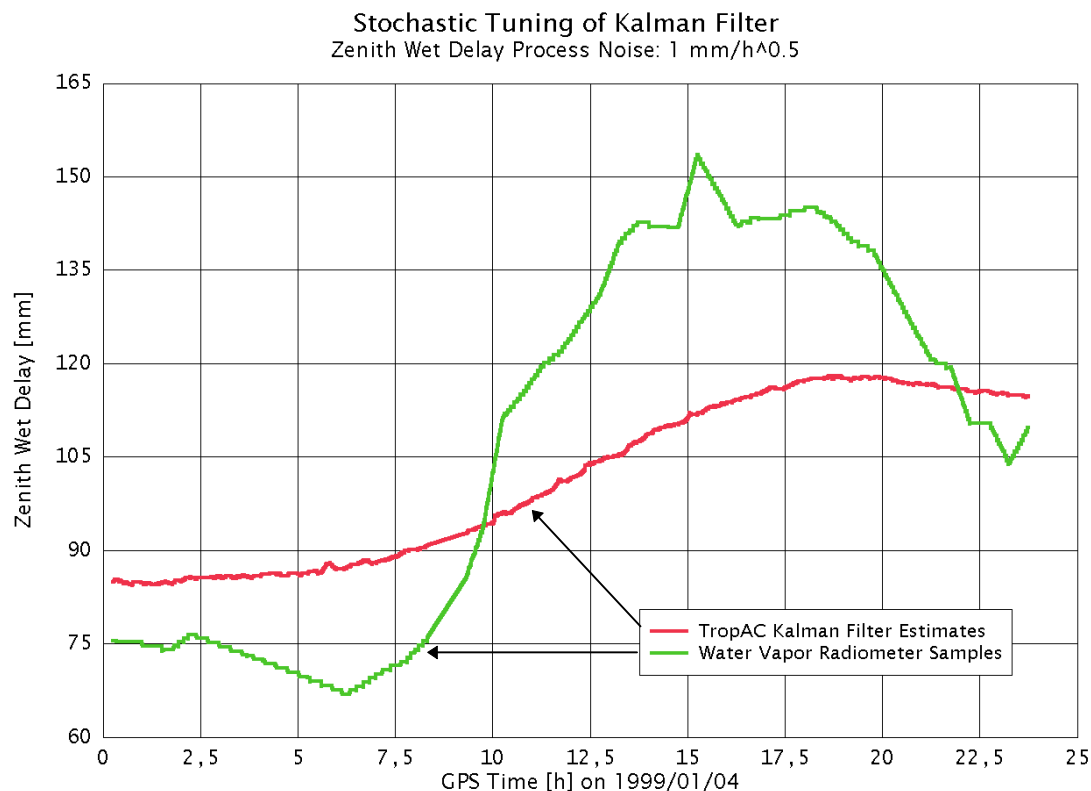


Figure 6-39 - Zenith wet delays from water vapor radiometer in comparison to GPS Kalman filter estimates with a process noise of $q = 1 \text{ mm}^2/\text{h}$.

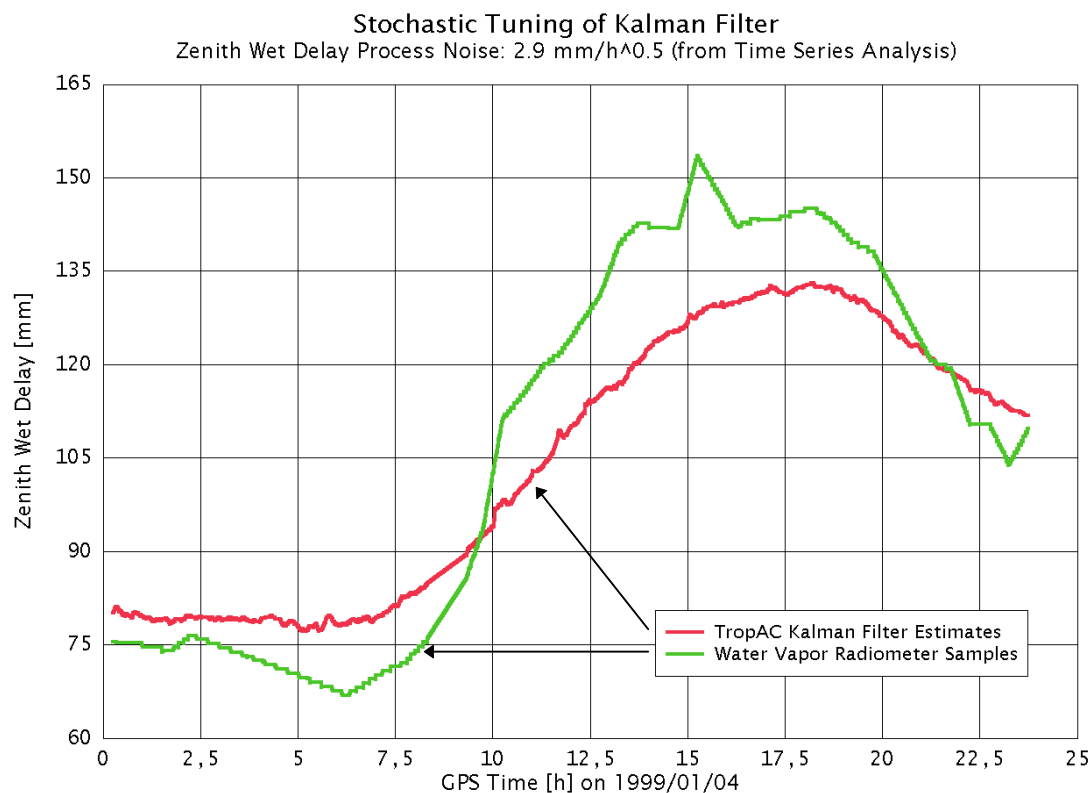


Figure 6-40 - Zenith wet delays from water vapor radiometer in comparison to GPS Kalman filter estimates with a process noise of $q = 8.4 \text{ mm}^2/\text{h}$.

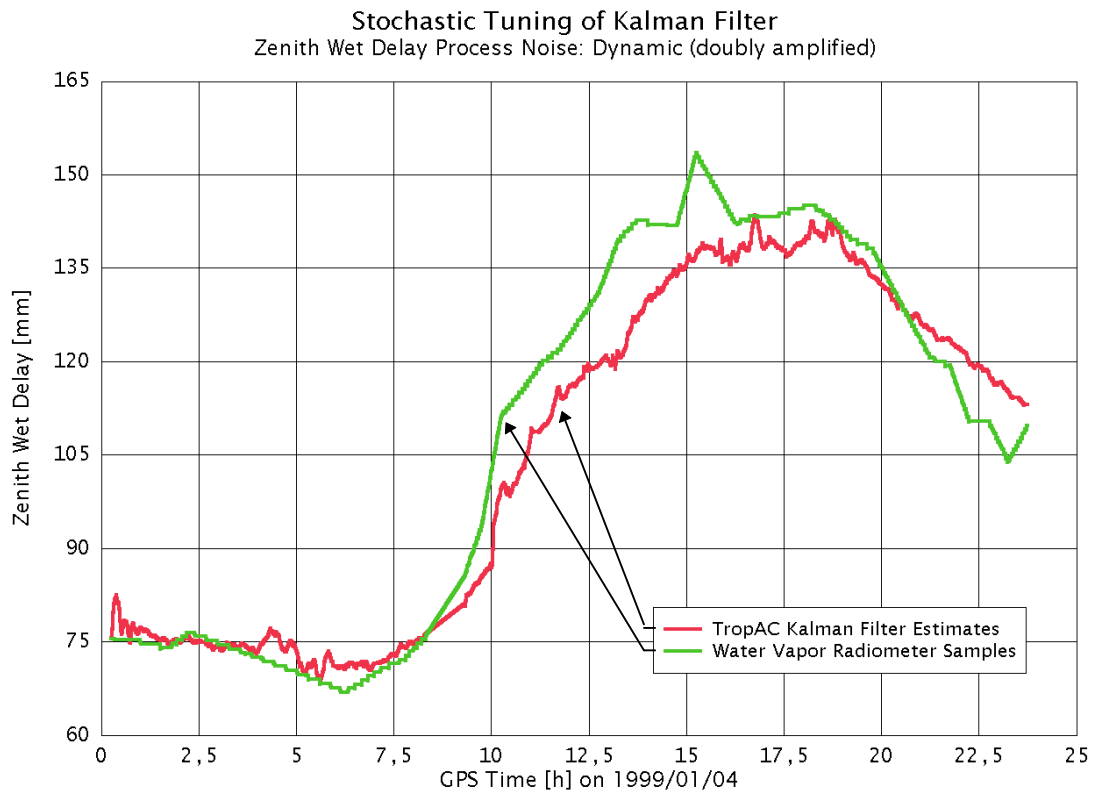


Figure 6-41 - Zenith wet delays from water vapor radiometer in comparison to GPS Kalman filter estimates; q was defined dynamically and doubly amplified ($q_{AMP} = 2.0$).

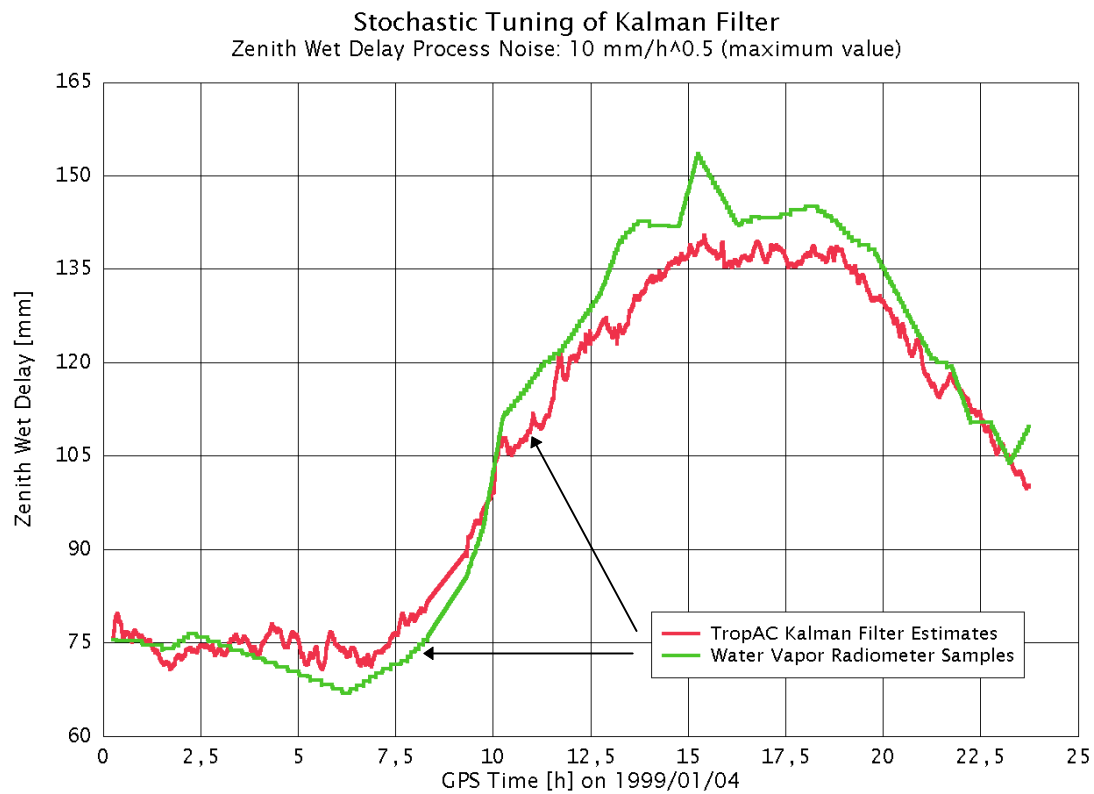


Figure 6-42 - Zenith wet delays from water vapor radiometer in comparison to GPS Kalman filter estimates; q was chosen to be the maximum of all dynamically determined q -factors for the entire data batch resulting in $q = 100 \text{ mm}^2/\text{h}$.

Last but not least, Figure 6-42 depicts the results for the tuning process following the *maximum tuning* method (\rightarrow 3.4.4, formula 3-151): The maximum q-factor of all hourly values is used as new default value for the entire day. The results are approximately the same as for dynamic tuning with hourly process noise coefficients applied. We can even state a slightly better overall fit to the reference curve from WVR data.

In both solutions making use of dynamic or maximum tuning, a considerable loss of low-pass filter efficiency can be seen leading to the advent of high-frequency variations that cannot necessarily be traced back to tropospheric delays. Typical reasons for such deviations are multipath effects.

7. Quality Assessment of TROPEX Data

The gridded tropospheric correction files, *TROPEX* (→ 4.4), may either contain tropospheric parameters derived from GDAS numerical weather fields (→ 7.1, → 7.2) or combined GPS/NWM data (→ 7.3). The purpose of this chapter is to validate the zenith path delays derived from TROPEX files either in NWM mode or in combined GPS/NWM mode. The contents of these files allows to compute the hydrostatic and the wet component separately. Both components must not only be interpolated in horizontal direction, but also reduced to the height of the target point. This height reduction problem is addressed in this chapter (→ 7.1) before zenith total delays from GPS tracking stations and the GDAS-derived delays from TROPEX files are compared (→ 7.2). Finally, the combined NWM/GPS solutions are discussed (→ 7.3).

7.1 Vertical Reduction

Both, the hydrostatic and the wet component are modeled in vertical direction with independent models. The most important reduction coefficients from TROPEX files, the pressure and the water vapor scale height, are validated with data derived from radiosonde launches within Germany.

7.1.1 Pressure Scale Height

The hydrostatic delay is computed with help of surface pressure and the vertical reduction of pressure is mainly performed using an exponential law¹, the barometric height formula (→ 4.2.1.2), where the major reduction coefficient is the pressure scale height q_p . The theoretical, non-corrected global value for this reduction parameter is about 8 km. Table 7-1 proves that the pressure scale height is typically about 9.6 to 9.7 km in mid-latitude regions like Germany and thus notably higher than the theoretical value. Figure 7-1 to Figure 7-4 show plots of the differences between the pressure scale heights from TROPEX (GDAS) and radiosonde launches. The residuals, i. e. bias-reduced differences, are illustrated as well.

For the first 3 locations, the biases are not significant and the RMS is around 0.3 to 0.5 km. This corresponds to a relative error of 3% to 5% of the pressure scale height. Oberschleißheim (10868) shows a huge bias of as much as -0.7 km. This systematic offset is the most import error contributor leading to a RMS of 0.8 km or 8% of the scale height. As already stated, this particular radiosonde site also proved to be problematic with respect to other quantities (→ 5.3), but horizontal interpolation errors of the TROPEX data might also be an error contributor in this special case due to the unfortunate topographical situation.

7.1.1.1 Impact of Scale Height on Hydrostatic Delay

The standard deviation of the reduced pressure follows from formula 4-16 or 4-53 if we omit the impact of the two polynomial reduction coefficients used in formula 4-54

¹ Actually, the mixed polynomial/exponential reduction model with 3 coefficients (→ 4.4.2.2) is used within TROPEX, but only the scale, i. e. the exponential coefficient, is validated here.

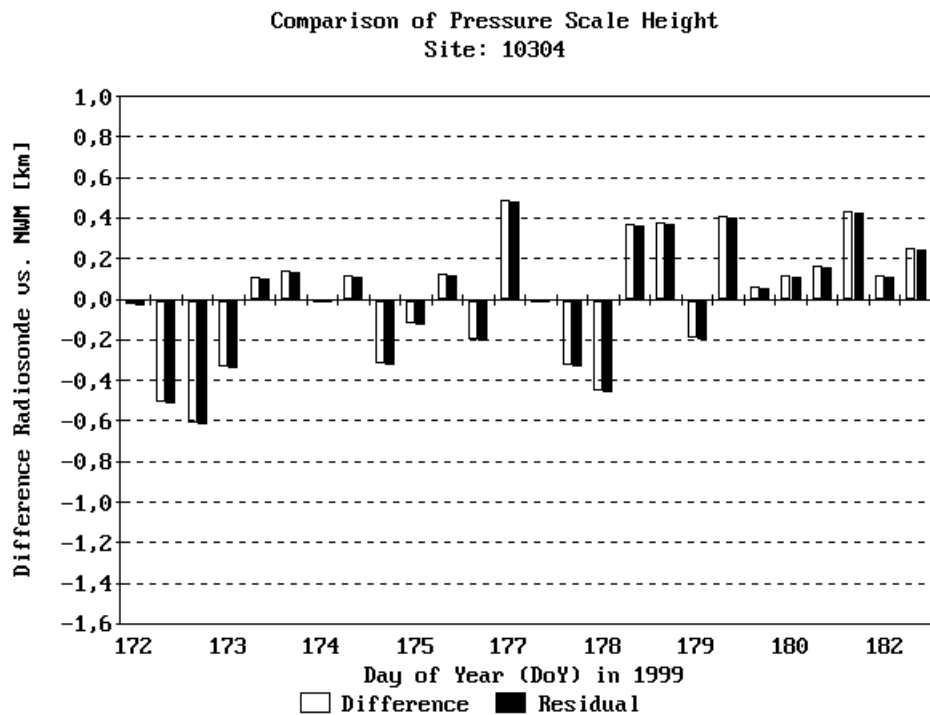


Figure 7-1 - Differences between the pressure scale heights from radiosonde launches at site 10304 and those derived from the vertical pressure profiles of the GDAS weather fields.

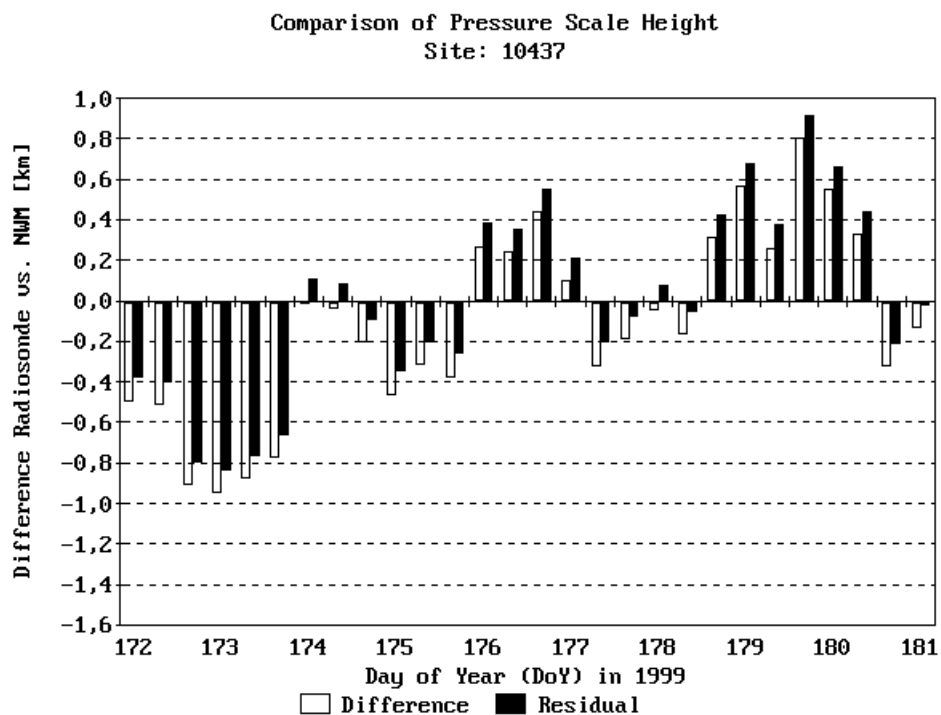


Figure 7-2 - Differences between the pressure scale heights from radiosonde launches at site 10437 and those derived from the vertical pressure profiles of the GDAS weather fields.

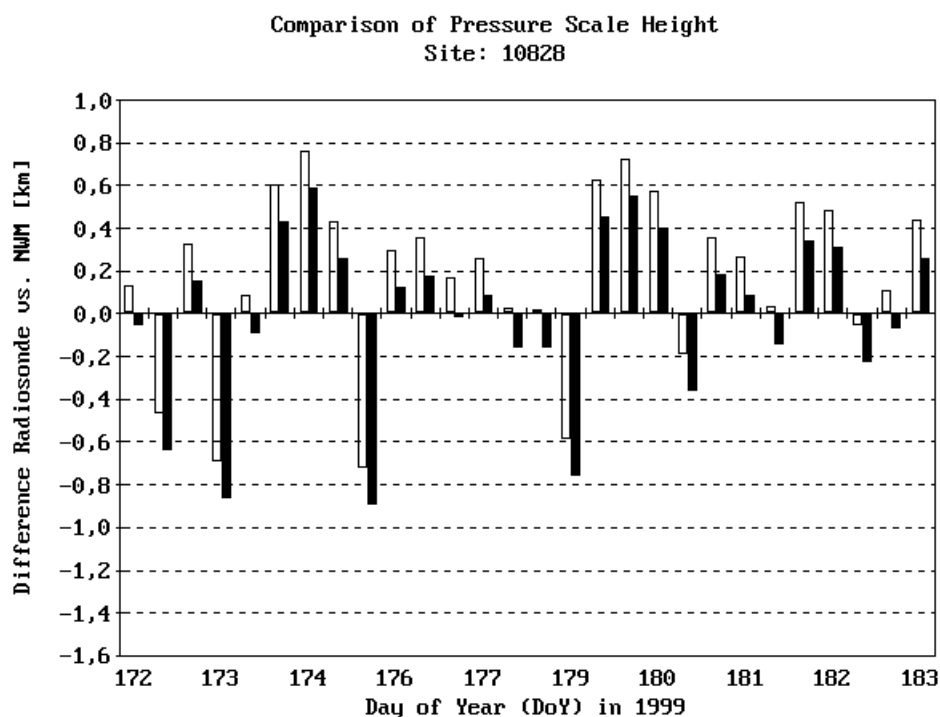


Figure 7-3 - Differences between the pressure scale heights from radiosonde launches at site 10828 and those derived from the vertical pressure profiles of the GDAS weather fields.

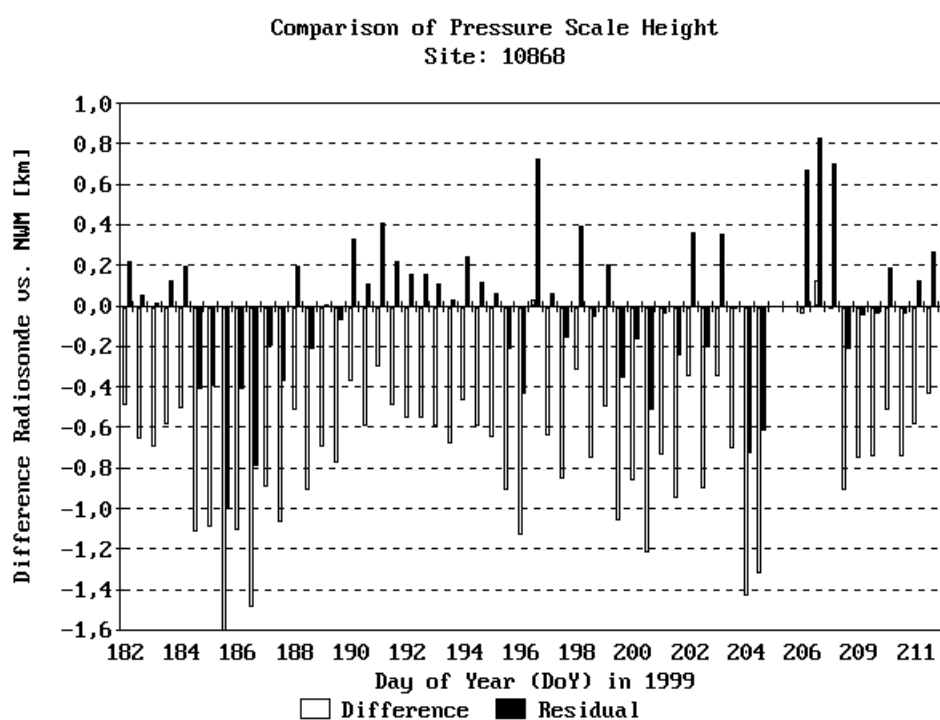


Figure 7-4 - Differences between the pressure scale heights from radiosonde launches at site 10868 and those derived from the vertical pressure profiles of the GDAS weather fields.

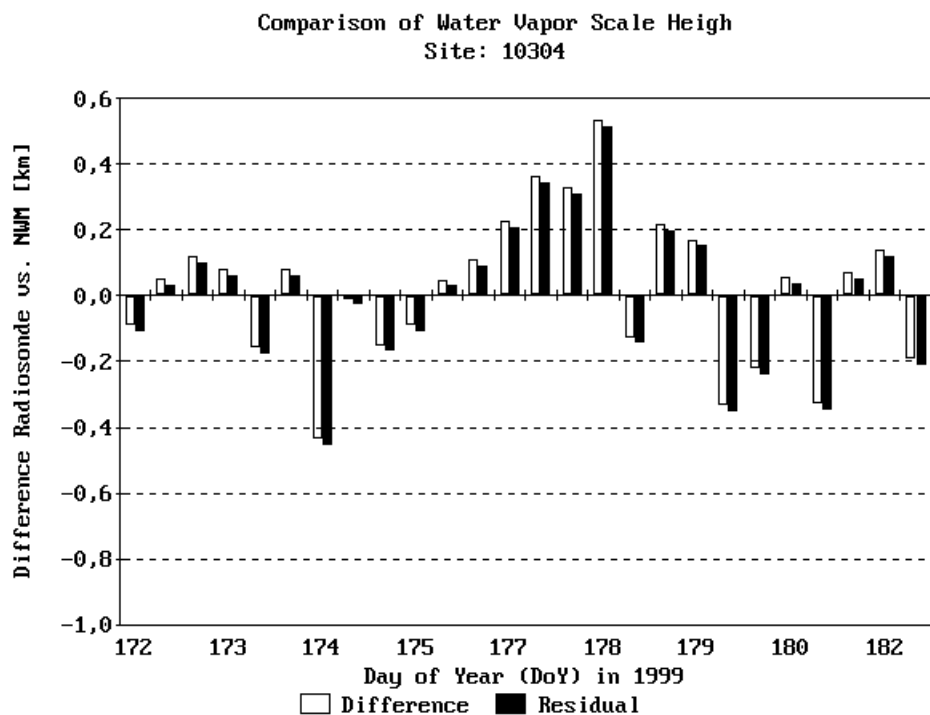


Figure 7-5 - Differences between the water vapor scale heights from radiosonde launches at site 10304 and those derived from the vertical ZWD profiles of the GDAS weather fields.

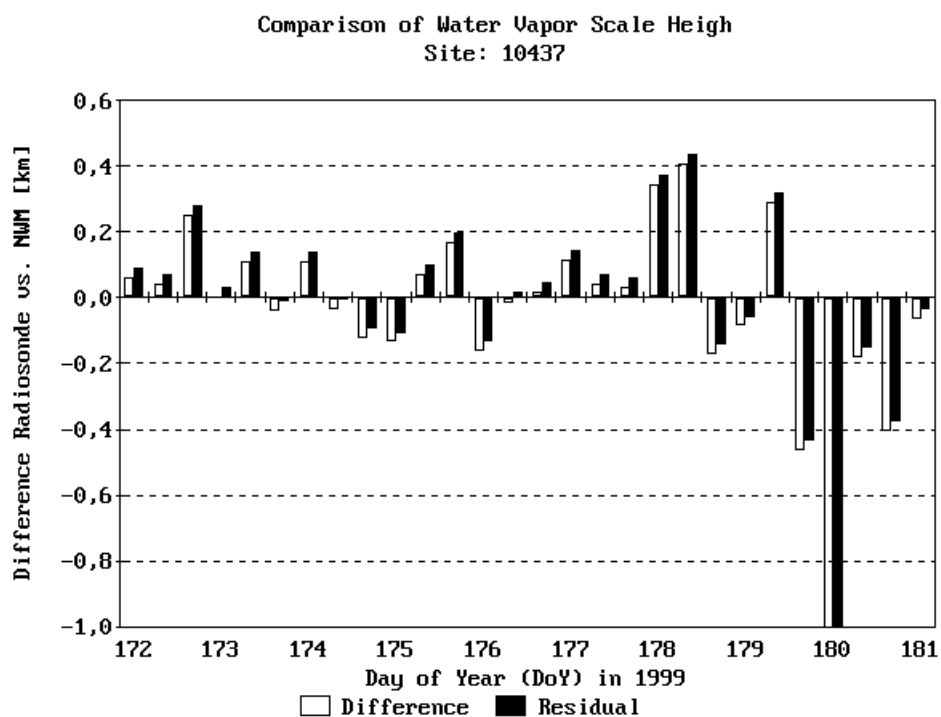


Figure 7-6 - Differences between the water vapor scale heights from radiosonde launches at site 10437 and those derived from the vertical ZWD profiles of the GDAS weather fields.

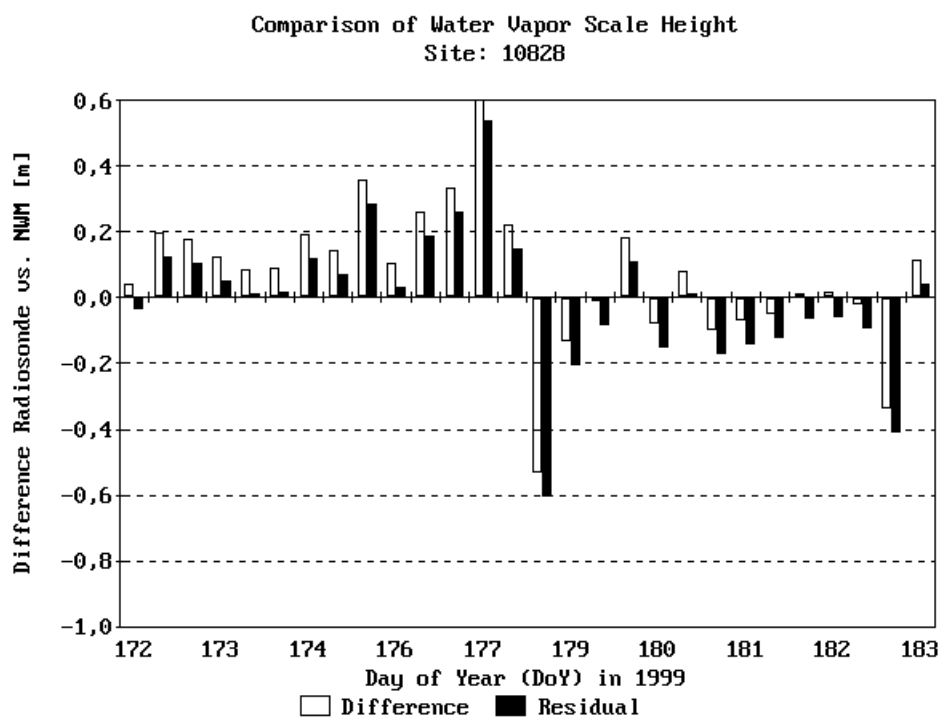


Figure 7-7 - Differences between the water vapor scale heights from radiosonde launches at site 10828 and those derived from the vertical ZWD profiles of the GDAS weather fields.

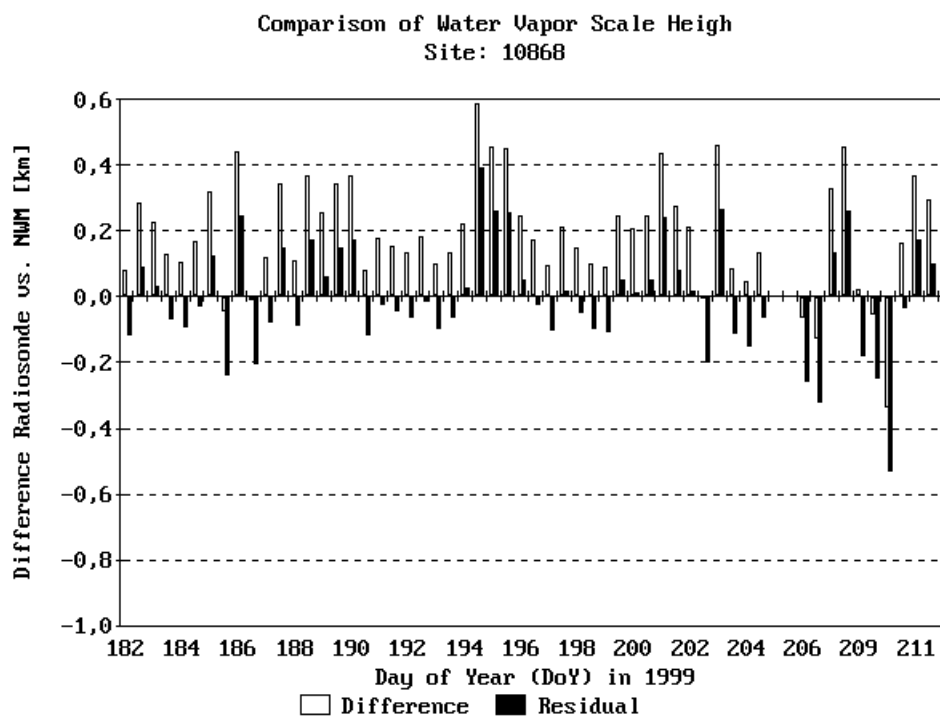


Figure 7-8 - Differences between the water vapor scale heights from radiosonde launches at site 10868 and those derived from the vertical ZWD profiles of the GDAS weather fields.

Site	Bias [km]	Std. Dev. [km]	RMS [km]	RMS [%]	q_p [km]
10304	0.01	0.30	0.29	3%	9.69
10437	-0.11	0.47	0.47	5%	9.75
10828	0.18	0.40	0.43	4%	9.72
10868	-0.70	0.36	0.79	8%	9.57

Table 7-1 - Comparison of the TROPEX pressure scale heights (derived from GDAS weather fields) and those derived from radiosonde launches (\rightarrow 5.2) for July 1999. See footnote below².

$$\sigma_p = \frac{p_0}{q_p^2} \cdot |H - H_0| \cdot \exp\left(\frac{H_0 - H}{q_p}\right) \cdot \sigma_{q_p} \quad (7-1)$$

σ_p : standard deviation of reduced pressure p at height H

σ_{q_p} : standard deviation of pressure scale height q_p

q_p : pressure scale height

H : geopotential height of target point

H_0 : height of reference point

p_0 : pressure at reference height H_0

and allows to estimate the influence of the scale height uncertainty on the height-reduced pressure. For a reference point at $H_0 = 0$ m and $p_0 = 1000$ hPa, a scale height of $q_p = 9.65$ km with a standard deviation of $\sigma_{q_p} = 0.5$ km and a reduction height of $H = 500$ m, a standard deviation of 2.8 hPa is to be expected for the pressure. This uncertainty maps into 7 mm of zenith hydrostatic delay. For an accuracy of the scale height of 0.3 km, the pressure uncertainty is only about 1.7 hPa causing a delay error of 4 mm.

7.1.1.2 Internal Consistency of Numerical Weather Model

Generally speaking, the internal accuracy of the pressure profile fits to the vertical reduction model are better in comparison to the validation with the external radiosonde data. Figure 7-9 shows the distribution of the pressure profile fits over Germany, i. e. the standard deviations of the weight unit. The height/pressure pairs all have equal weights during the least-squares adjustment. As a consequence, the empirical standard deviation of the weight unit can be considered as the mean error of the pressure measurements as long as the vertical reduction model corresponds to reality. The highest standard deviation is about 0.6 hPa for the profile up to a maximum height of as much as 12 km. However, it should be noted that the weather fields do not really contain pressure *measurements*. Instead, the pressure *values* are based on the numerical weather model and the low standard deviations of the weight

² The accuracy is expressed with help of the following quantities: Given the difference $d_i = \text{val}_{\text{REF}} - \text{val}_{\text{SAM}}$ between the sampled (val_{SAM}) and the reference value (val_{REF}). The bias is the arithmetic mean of all these differences: $\text{BIAS} = 1/n \cdot \sum d_i$ with n being the number of samples compared and the RMS is defined as $\text{RMS} = [1/n \cdot \sum d_i^2]^{1/2}$. Finally, the standard deviation, also denoted as SIG or SIGMA here, is the bias-reduced accuracy: $\text{SIGMA} = [1/(n-1) \cdot \sum (d_i - \text{BIAS})^2]^{1/2}$. Note that the standard deviation ("sigma", bias-reduced) can be larger than the RMS in special cases, because the sum of the squared residuals must be divided by $n-1$ whereas, for the RMS, the sum of the squared differences is divided by n .

unit mainly suggest that the TROPEX vertical reduction model is apparently well-suited to the numerical weather model.

The validation with external radiosonde data shows uncertainties in the scale heights that would lead to higher pressure inaccuracies than those from the internal profile fits. As long as interpolation uncertainties can be considered as minor error contributors and the radiosonde data can be treated as sensor packages of superior accuracy, this discrepancy means that there must be systematic errors in the vertical profiles of the numerical weather model.

7.1.2 Water Vapor Scale Height

The water vapor scale height was validated with the same set of radiosonde data. A typical value for this reduction coefficient is in the range of 2 km. Table 7-2 gives mean values of 1.8 to 2.0 km over Germany for the time period of June and July 1999. The differences and residuals are plotted in Figure 7-5 to Figure 7-8.

Site	Bias [km]	Sigma [km]	RMS [km]	RMS [%]	q_{ZWD} [km]
10304	0.02	0.23	0.22	11%	1.995
10437	-0.03	0.28	0.27	14%	1.942
10828	0.07	0.21	0.22	12%	1.823
10868	0.20	0.17	0.26	14%	1.849

Table 7-2 - Comparison of the TROPEX zenith wet delay/water vapor scale heights (derived from GDAS weather fields) and those derived from radiosonde launches (→ 5.2) for July 1999.

Except for launch site 10868, the scale height biases are negligible and the RMS is around 0.2 to 0.3 km. The relative errors are between 10% and 15%³.

Given a zenith wet delay or water vapor scale height of $q_{\text{ZWD}} = 1.9$ km, a reference height of $H_0 = 0$ m with a wet delay of $\text{ZWD}_0 = 0.15$ m and a height of the target point of $H = 500$ m. For an error in scale height of 0.2 km, the resulting error in zenith wet delay at target height H would be 3.2 mm and for an error in scale height of 0.3 km, the ZWD uncertainties would increase up to a level of 4.8 mm.

As for the pressure scale heights, the internal accuracy of the zenith wet delay profile fits (Figure 7-10) is much better, too. The standard deviations of the weight unit suggest that for the whole profile up to the tropopause, the zenith wet delay can be reduced with a precision of 7 mm in the worst case. Again, internal and external data show considerable discrepancies.

7.1.3 Summary

The primary goal of the vertical reduction methods validated here (formula 4-54 for pressure and 4-56 for zenith wet delays) is to perform the transition from a 3-D numerical weather field to the 2-D representation in TROPEX files. Whereas the

³ The relative uncertainties of the pressure scale heights are usually smaller since the pressure scale height is about 5 times larger than the water vapor scale height.

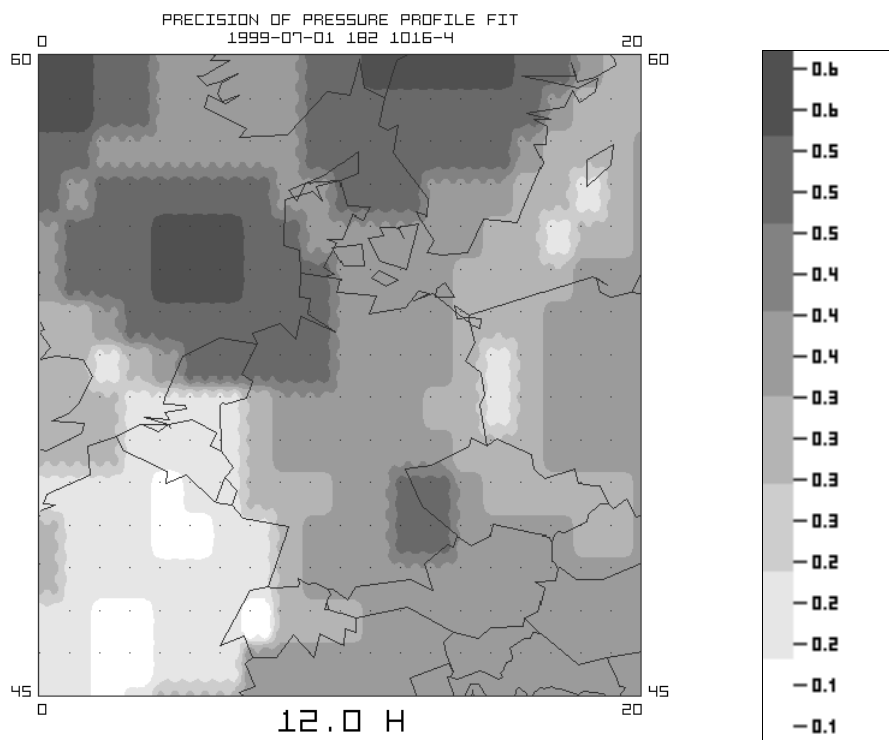


Figure 7-9 - Precision of the pressure profile fits over Germany on 1 July 1999 at 12 h UTC in units of [hPa]. The standard deviations plotted in the map are the standard deviations of the weight unit resulting from the fit of the vertical pressure profiles to the TROPEX pressure reduction model (\rightarrow 4.4.2.2, formula 4-54).

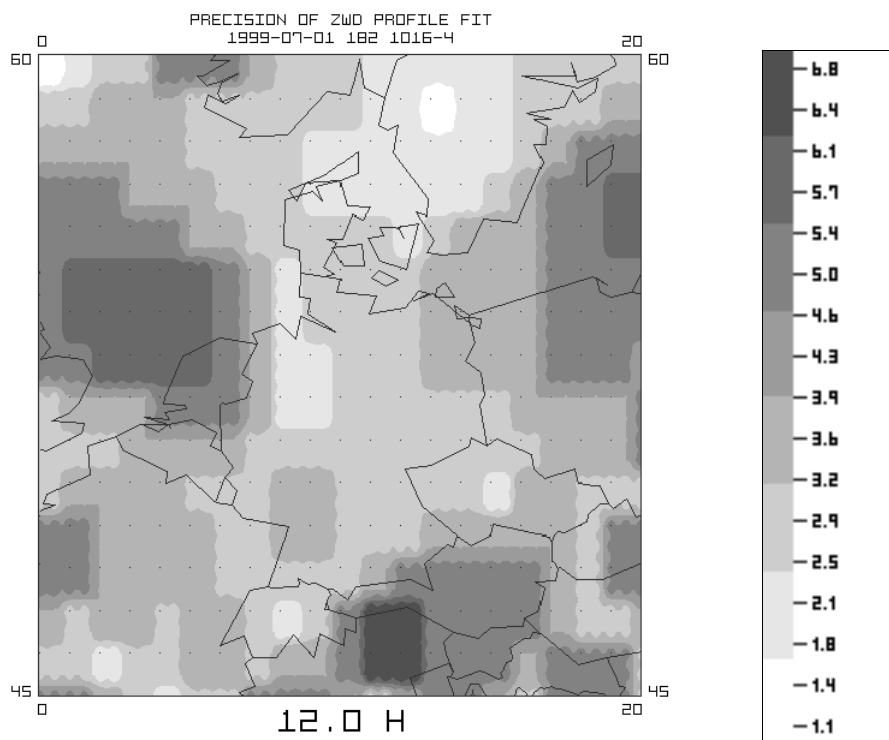


Figure 7-10 - Precision of the zenith wet delay profile fits over Germany on 1 July 1999 at 12 h UTC in units of [mm]. The standard deviations plotted in the map are the standard deviations of the weight unit resulting from the fit of the vertical zenith wet delay profiles to the TROPEX ZWD reduction model (\rightarrow 4.4.3.2, formula 4-56).

weather fields use 3 dimensions, the TROPEX data can save a reasonable amount of memory by only using 2 dimensions. Figure 7-9 and Figure 7-10 prove that the vertical modeling of TROPEX data is possible with a high degree of internal precision in comparison to the 3-D weather model. The TROPEX representation allows to reduce surface zenith wet delays to heights of 10 km that is covered by the original 3-D numerical weather field data at a level of 7 mm or better in comparison to the profile data of the numerical weather fields. The same is true for the pressure where the maximum standard deviation is about 0.6 hPa causing a ZHD uncertainty of less than 2 mm.

The validation of the scale heights with external data, however, suggests that there are discrepancies between the numerical weather fields and the radiosonde profiles. These differences can partly be traced back to interpolation errors in the TROPEX fields, but such uncertainties are not considered as major error contributors. The validation results suggest that errors in both the hydrostatic and the wet delay of about 5 mm may occur for a height reduction from 0 m to 500 m. The following section validates the tropospheric delay data and is intended to lead to a realistic understanding of the total error budget.

7.2 Zenith Neutral Delays from GDAS Weather Fields

The GDAS-derived zenith neutral delays (ZND) from TROPEX files were validated with help of GPS tropospheric delays for almost 140 IGS tracking stations. The total delay was chosen for the validation because it is the primary GPS product of the IGS analysis centers and, on the other hand, it is the quantity of the TROPEX data sets containing the full error budget. The major contributors to the zenith neutral delay uncertainty from TROPEX data are

$$\sigma_{\text{ZND}}^2 = \sigma_{\text{ZHD}}^2 + \sigma_{\Delta\text{ZHD(H)}}^2 + \sigma_{\text{ZWD}}^2 + \sigma_{\Delta\text{ZWD(H)}}^2 + \sigma_{\text{HOR}}^2 \quad (7-2)$$

σ_{ZND} : standard deviation of the TROPEX zenith neutral delay

σ_{ZHD} : standard deviation of the surface zenith hydrostatic delay (i. e. surface pressure)

$\sigma_{\Delta\text{ZND}}$: standard deviation of the height reduction of the ZHD (i. e. pressure reduction)

σ_{ZWD} : standard deviation of the surface zenith wet delay

$\sigma_{\Delta\text{ZWD}}$: standard deviation of the height reduction of the ZWD

σ_{HOR} : horizontal interpolation error (combined standard deviation for hydrostatic and wet component)

the horizontal interpolation error σ_{HOR} , the vertical modeling errors for the hydrostatic ($\sigma_{\Delta\text{ZHD(H)}}$) and wet component ($\sigma_{\Delta\text{ZWD(H)}}$) and the uncertainties in surface wet delay (σ_{ZWD}) and hydrostatic delay (σ_{ZHD}).

Several configuration settings were tried - with marginal differences in the mean results of about 0.3 mm (see → Appendix VI for a configuration file template). The results presented here were obtained with a weighting power of 1.5 (horizontal interpolation, → 4.4.5.1).

A look at Table 7-3 suggests a mean RMS of 1.7 cm for the zenith neutral delay. SCHUELER et al. [2000a] also investigated the accuracy of zenith wet delays that were directly derived from GDAS weather fields, i. e. not from TROPEX data fields. This

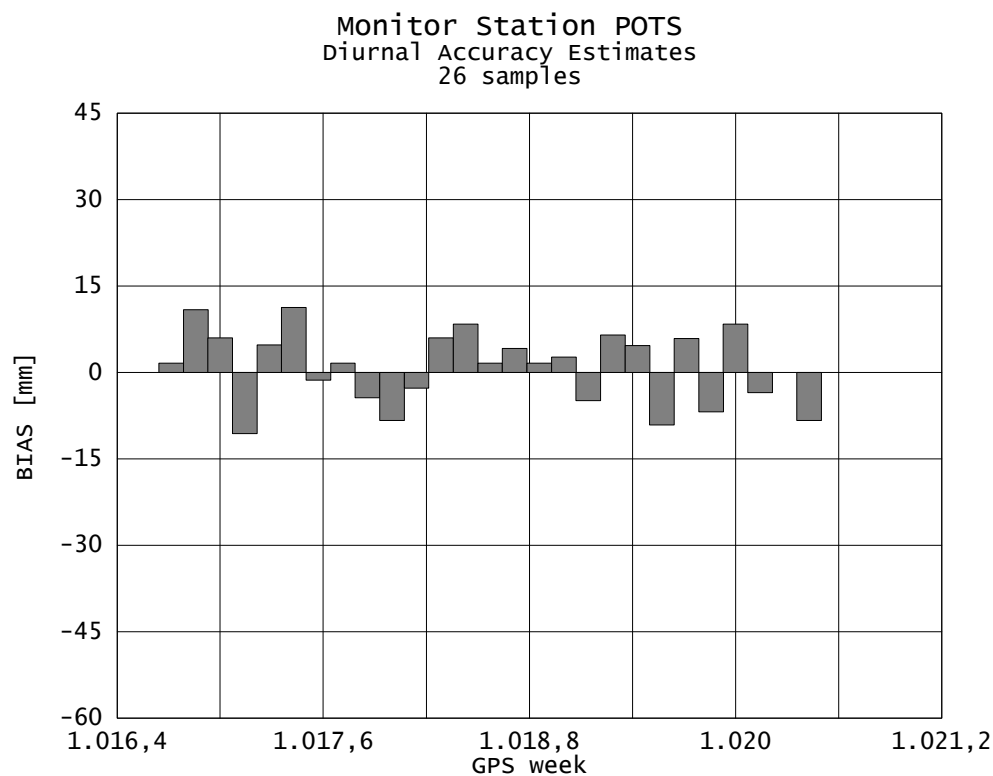


Figure 7-11 - Diurnal biases between zenith total delays from TROPEX files (GDAS-derived) and GPS total delays for IGS tracking station Potsdam (POTS, Germany).

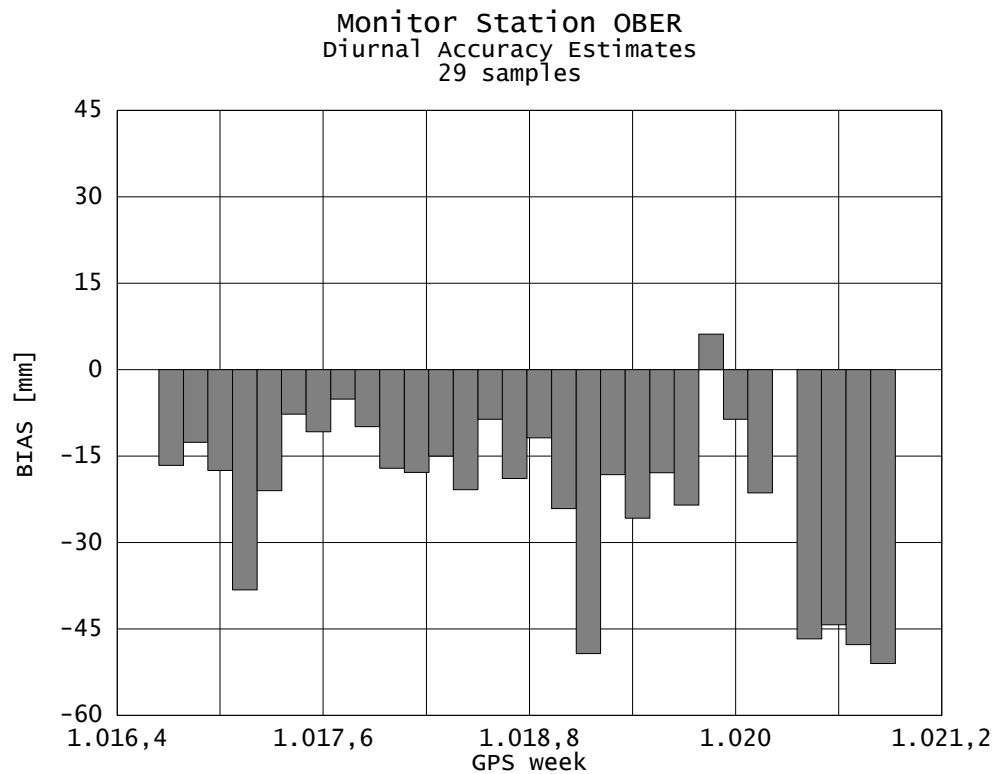


Figure 7-12 - Diurnal biases between zenith total delays from TROPEX files (GDAS-derived) and GPS total delays for IGS tracking station Oberpfaffenhofen (OBER, Germany).

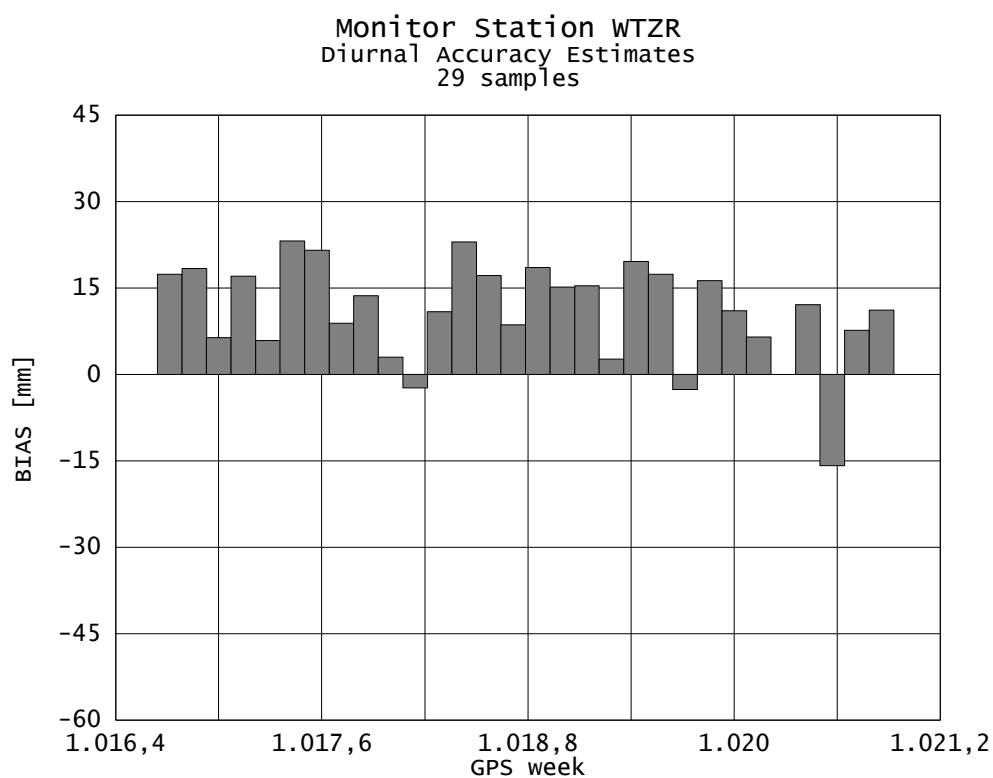


Figure 7-13 - Diurnal biases between zenith total delays from TROPEX files (GDAS-derived) and GPS total delays for IGS tracking station Wettzell (WTZR, Germany).

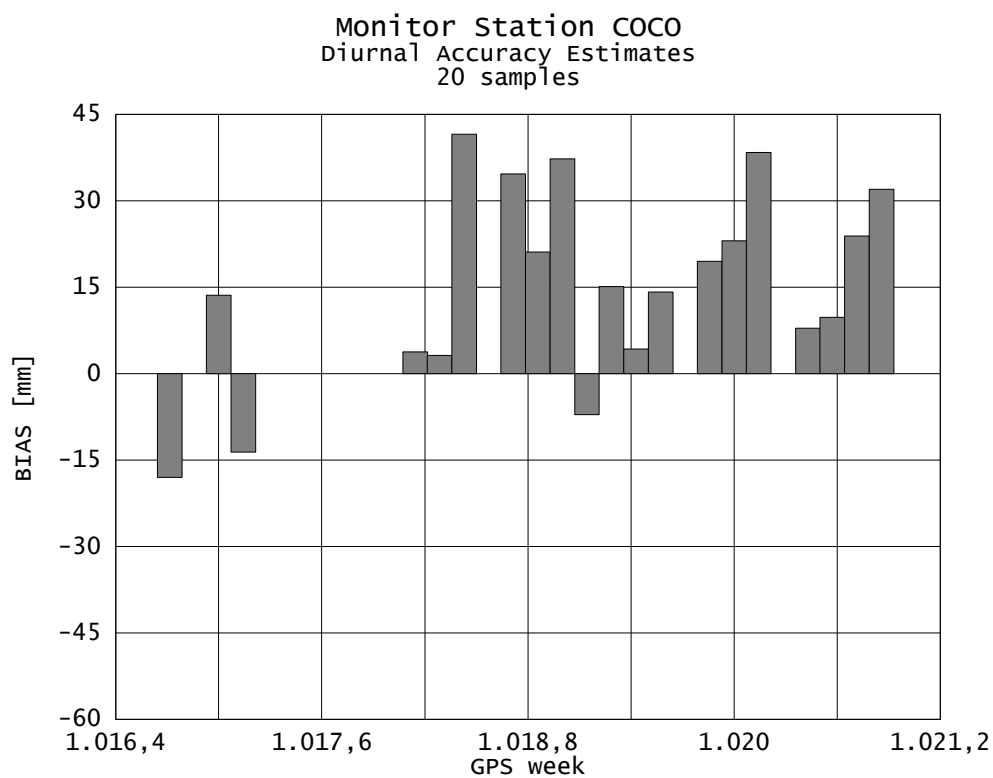


Figure 7-14 - Diurnal biases between zenith total delays from TROPEX files (GDAS-derived) and GPS total delays for IGS tracking station Cocos Island (COCO).

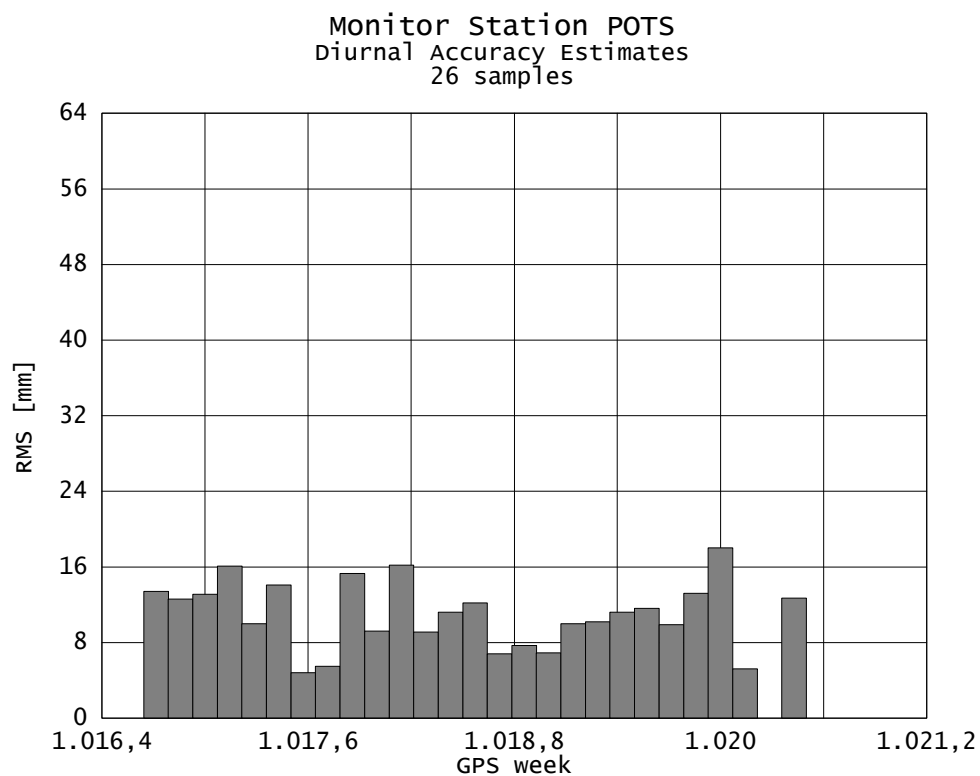


Figure 7-15 - Diurnal RMS values between zenith total delays from TROPEX files (GDAS-derived) and GPS total delays for IGS tracking station Potsdam (POTS, Germany).

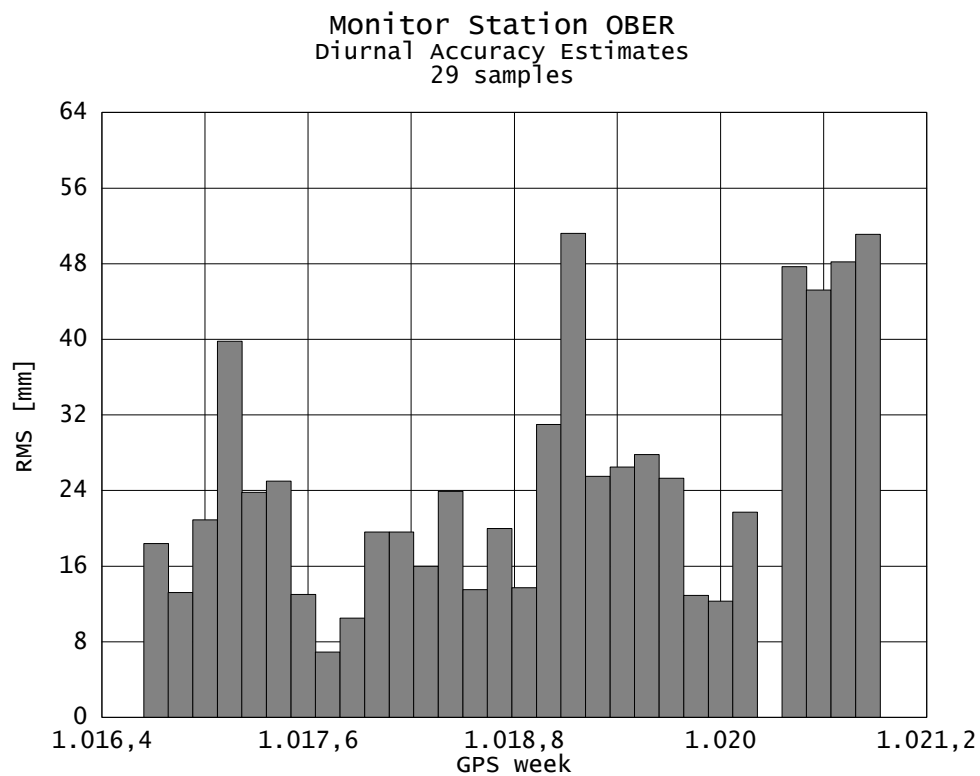


Figure 7-16 - Diurnal RMS values between zenith total delays from TROPEX files (GDAS-derived) and GPS total delays for IGS tracking station Oberpfaffenhofen (OBER, Germany).

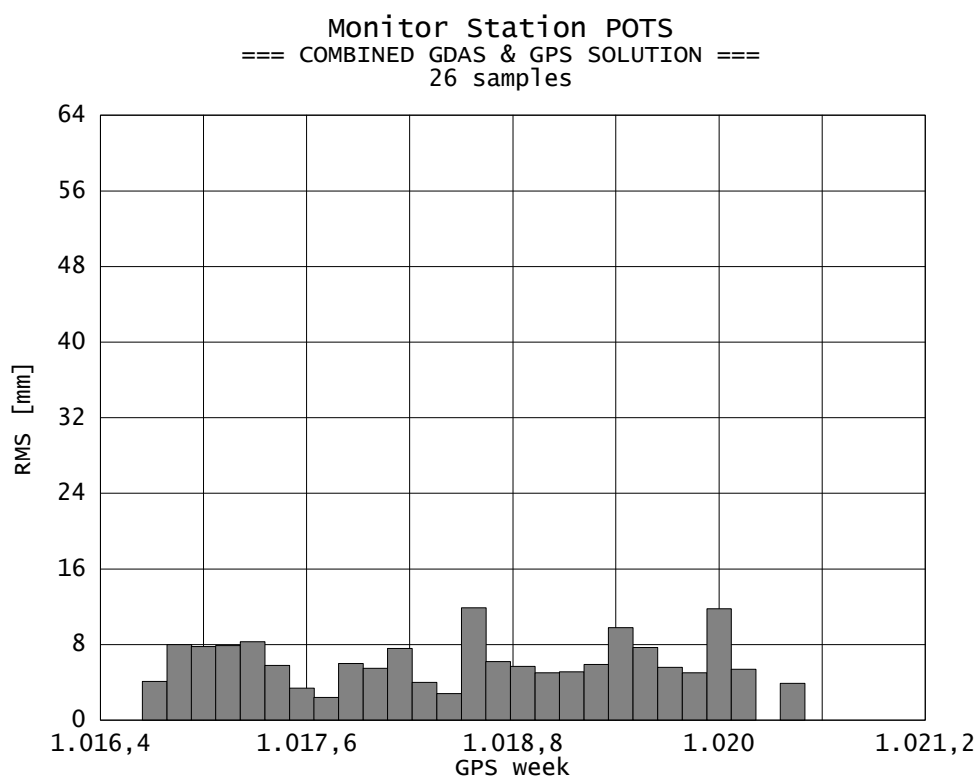


Figure 7-17 - Diurnal RMS values between zenith total delays from combined TROPEX solution fields and GPS total delays for IGS tracking station Potsdam (POTS, Germany).

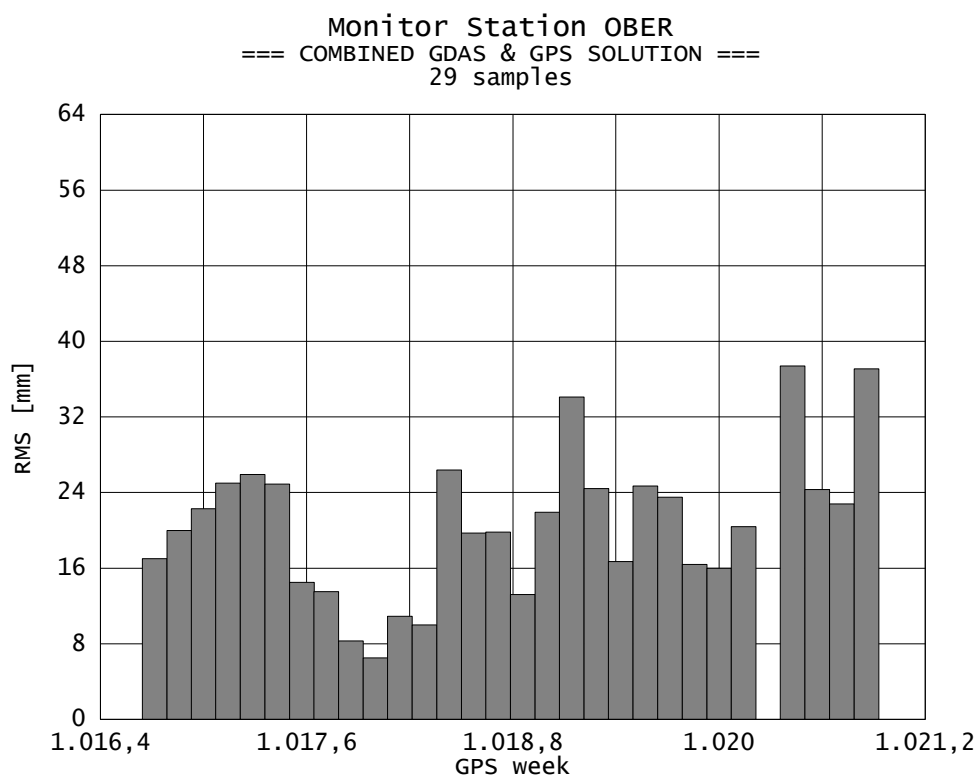


Figure 7-18 - Diurnal RMS values between zenith total delays from combined TROPEX solution fields and GPS total delays for IGS tracking station Oberpfaffenhofen (OBER, Germany).

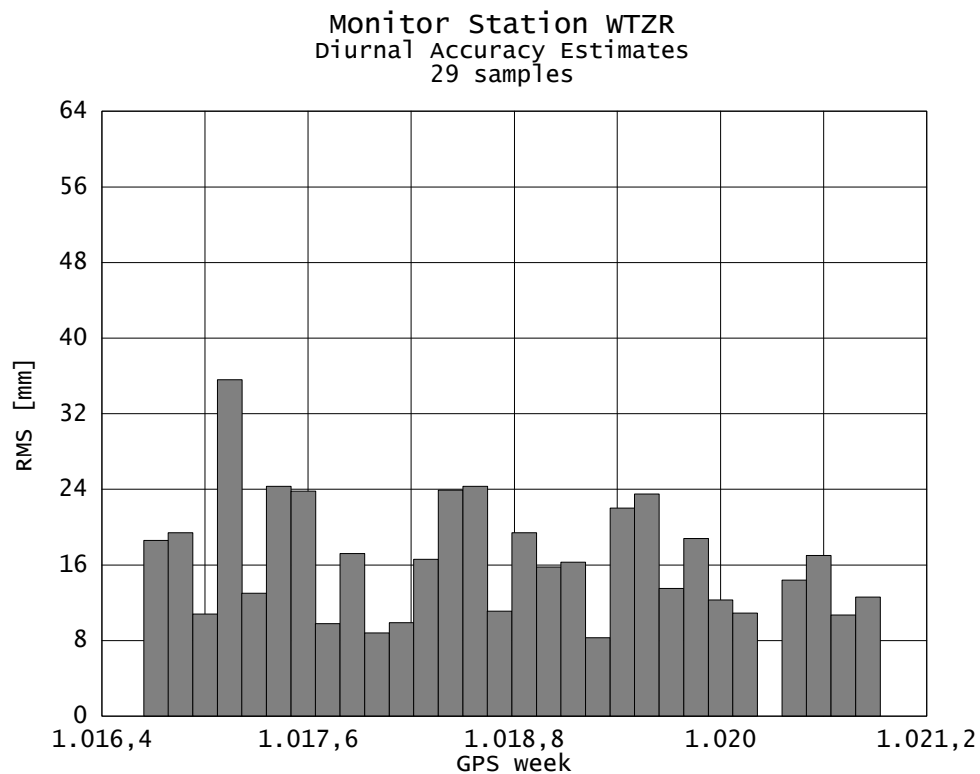


Figure 7-19 - Diurnal RMS values between zenith total delays from TROPEX files (GDAS-derived) and GPS total delays for IGS tracking station Wettzell (WTZR, Germany).

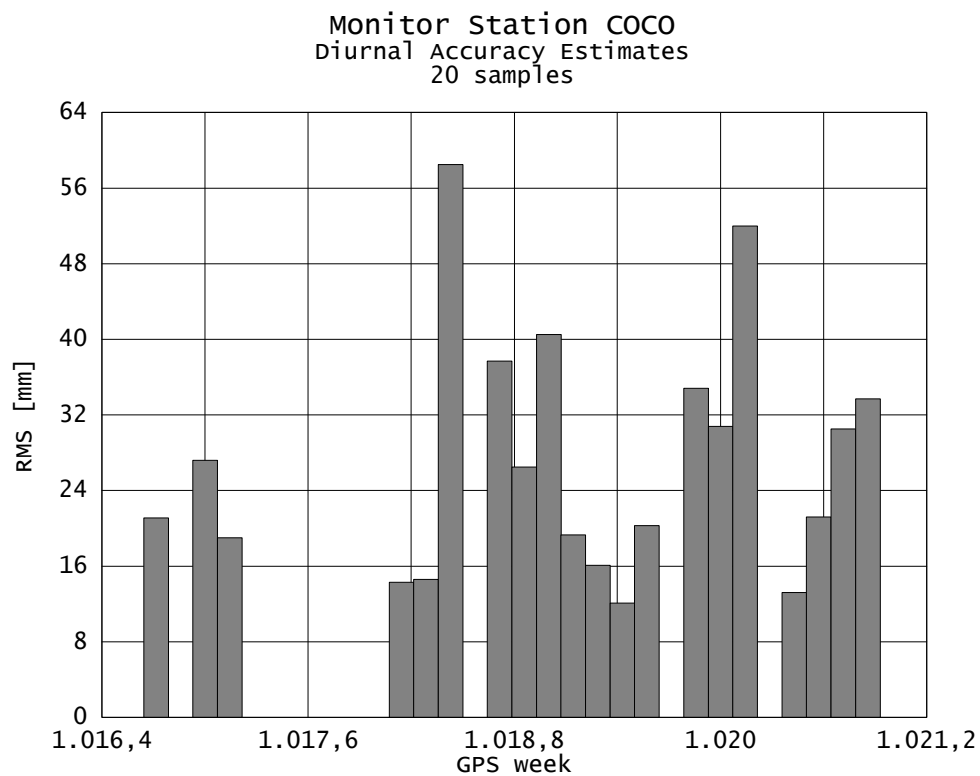


Figure 7-20 - Diurnal RMS values between zenith total delays from TROPEX files (GDAS-derived) and GPS total delays for IGS tracking station Cocos Island (COCO).

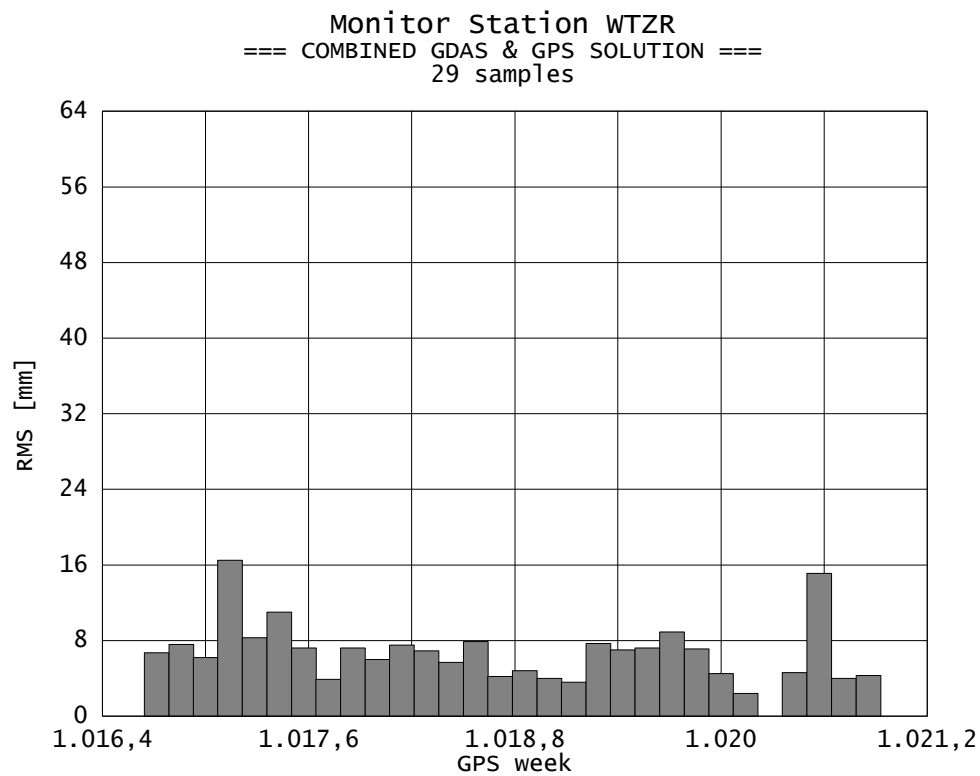


Figure 7-21 - Diurnal RMS values between zenith total delays from combined TROPEX solution fields and GPS total delays for IGS tracking station Wettzell (WTZR, Germany).

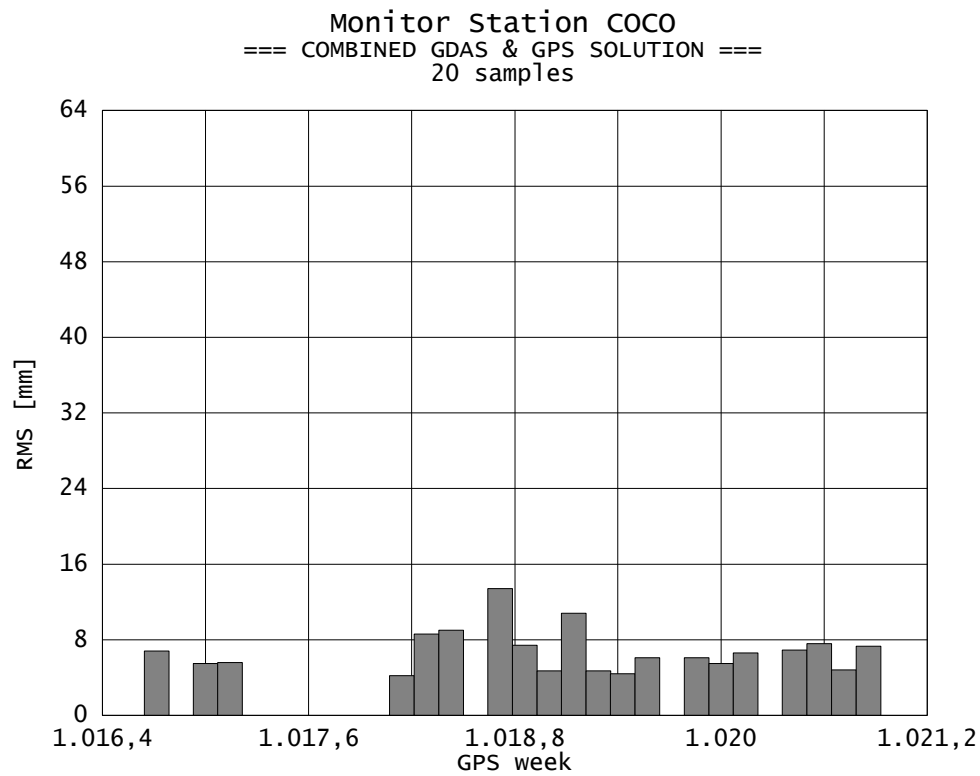


Figure 7-22 - Diurnal RMS values between zenith total delays from combined TROPEX solution fields and GPS total delays for IGS tracking station Cocos Island (COCO).

SITE	BIAS	SIGMA	RMS	SITE	BIAS	SIGMA	RMS
ALBH	-2.0	9.1	12.7	MADR	-6.6	11.6	17.0
ALGO	10.7	14.2	20.6	MAGO	3.9	12.4	16.9
ALIC	13.3	6.9	15.7	MALI	8.3	12.7	18.1
AMCT	18.1	20.2	27.0	MATE	8.8	12.9	17.7
ANKR	-13.1	12.5	20.1	MAW1	-4.1	3.9	6.2
AOML	-1.7	12.6	16.4	MDO1	10.5	10.4	20.4
AREQ	-25.8	8.5	30.2	MDVO	1.7	11.5	17.9
ASC1	5.2	11.5	18.2	MEDI	-13.9	13.1	20.8
AUCK	5.6	9.2	12.1	METS	0.2	8.3	10.8
BAHR	-6.3	12.7	17.9	MKEA	3.6	5.2	6.9
BARB	14.1	10.7	18.5	MONP	13.6	10.0	21.0
BISH	-32.3	14.9	39.0	NLIB	18.3	17.4	28.5
BOGO	6.7	11.4	14.8	NOTO	13.5	13.6	21.3
BOGT	10.8	11.0	18.4	NOUM	1.5	12.3	17.4
BOR1	0.4	10.3	13.0	NRC1	-1.3	13.0	16.6
BRAZ	-8.6	3.2	9.2	NSSP	-20.1	11.5	28.0
BRMU	8.9	15.9	22.1	NTUS	7.4	11.0	18.0
BRUS	0.7	8.6	12.7	NYA1	-5.1	7.8	12.6
CAGL	12.7	13.1	20.6	NYAL	-5.2	9.1	13.2
CAS1	7.1	4.8	9.6	OBER	-21.4	10.0	25.0
CASC	-2.2	12.9	13.9	ONSA	-3.7	9.7	12.0
CHAT	3.4	9.1	12.5	PENC	-7.5	10.7	16.2
CHUR	7.1	10.7	15.9	PERT	-3.1	9.0	12.3
COCO	15.2	18.2	27.2	PIE1	2.9	8.7	12.8
CRO1	1.3	11.2	14.4	POL2	-16.8	12.1	28.6
DARW	2.6	5.7	7.4	POTS	1.0	9.2	11.0
DAV1	7.7	4.0	8.8	PRDS	12.6	11.7	18.8
DGAR	0.6	15.8	23.2	RAMO	-4.7	9.9	13.6
DRAO	-20.6	10.8	23.9	REYK	-5.9	9.4	13.5
DUBO	5.2	12.2	19.9	RIOG	3.2	8.4	10.6
EISL	0.7	10.5	14.1	SANT	-20.0	16.5	28.3
ELAT	-21.9	14.3	27.2	SCH2	-0.6	10.6	14.8
FAIR	7.1	9.5	17.7	SELE	-3.0	13.2	20.8
FLIN	1.9	11.9	13.7	SEY1	1.2	9.4	12.7
FORT	17.6	14.2	26.9	SFER	7.9	8.0	12.8
GALA	1.2	6.9	9.8	SHAO	-1.5	12.8	14.6
GLSV	-3.0	11.1	20.9	SJDV	-4.8	9.8	12.1
GODE	-5.2	16.6	23.1	SOL1	-4.6	18.8	27.9
GOLD	-31.2	11.8	33.4	STJO	0.4	14.6	18.3
GOPE	6.9	7.9	12.3	SUTH	2.4	6.6	8.7
GRAS	14.0	11.5	21.9	SUWN	9.6	13.6	18.6
GRAZ	2.5	9.8	13.6	TELA	-6.8	10.3	14.9
GUAM	5.2	13.3	18.9	THU1	9.1	6.0	11.9
HARK	2.8	6.1	8.8	TIDB	-2.5	6.7	7.8
HART	-2.6	5.7	6.2	TOUL	-12.6	13.1	23.8
HERS	-2.7	10.1	12.8	TRO1	-4.3	8.8	12.8
HFLK	3.2	7.6	11.2	TROM	-6.6	8.2	12.1
HOB2	-3.8	8.3	10.9	TSKB	0.7	15.5	21.1
HOFN	-3.8	10.5	15.2	UCLU	-5.9	11.4	14.2
HOLB	-5.7	10.1	12.8	UPAD	12.9	12.5	19.9
HRAO	4.9	6.0	9.5	URUM	20.2	13.8	33.1
IISC	24.2	11.0	27.1	USNA	-4.5	16.2	22.6
IRKT	-0.2	17.2	28.4	USNO	-5.2	16.2	22.6
JOZE	-3.0	10.7	14.1	USUD	-2.1	11.5	14.6
JPLM	4.9	10.8	16.3	VILL	5.8	10.5	16.1
KARR	4.1	7.5	14.1	WES2	15.1	17.0	26.6
KATZ	-9.7	13.9	19.5	WHIT	4.6	6.8	10.0
KELY	-0.7	6.8	11.0	WILL	-4.9	6.9	9.9
KERG	-12.9	9.8	16.4	WSRT	8.0	9.4	13.1
KIRU	-9.4	10.8	15.2	WTZR	11.3	9.5	16.6
KIT3	-5.9	13.3	22.7	WUHN	-5.9	16.8	25.2
KOKB	9.2	11.3	16.8	XIAN	-9.2	14.6	22.1
KOSG	1.9	9.1	11.2	YAKZ	5.1	13.3	25.1
KOUR	9.4	13.4	18.8	YAR1	11.6	9.4	15.8
KWJ1	0.9	15.8	21.6	YELL	18.8	10.9	23.4
LAMA	-4.4	11.0	14.0	ZECK	-19.5	9.2	21.6
LHAS	-30.0	11.7	32.5	ZIMM	-1.1	9.7	14.1
LPGS	0.3	10.4	13.4	ZWEN	-10.4	11.9	19.4
MAC1	-4.3	7.0	9.3	MEAN	0.1	11.0	17.4

Table 7-3 - Mean biases, standard deviations ("sigma") and RMS values in [mm] for the stations involved in the TROPEX/GDAS validation experiment. IGS ZPD estimates served as reference data. Please refer to → Appendix IV for information about the location of the particular sites.

work indicates that the mean RMS of the wet delays is near 1.4 to 1.6 cm. Obviously, the error contribution of the zenith hydrostatic delay, i. e. surface pressure, has a minor impact in the range of 1 to 4 mm, whereas the uncertainties involved in the vertical wet refractivity profile seem to be the more dominant error source.

Despite of these promising results, the reader may also find several stations in Table 7-3 that are obviously biased. Figure 7-11 to Figure 7-14 illustrate the systematic error behavior of 4 selected sites and Figure 7-15, Figure 7-16, Figure 7-19 and Figure 7-20 show the corresponding diurnal RMS values (systematic effects inclusive).

It becomes evident that the biases either govern the total error budget or are significant contributors to it, whereas the mean standard deviation is only in the range of 1.1 cm. In July 1999, Oberpfaffenhofen (*OBER*) was apparently one of those stations with very poor performance as far as the numerical weather model is concerned. Diurnal offsets of about -2.1 cm with peaks of up to -5.0 cm can be seen. For all other sites, these values are smaller. Cocos Islands reaches considerable biases of up to 4 cm. However, this station lies in the tropics where larger errors must be expected anyway⁴.

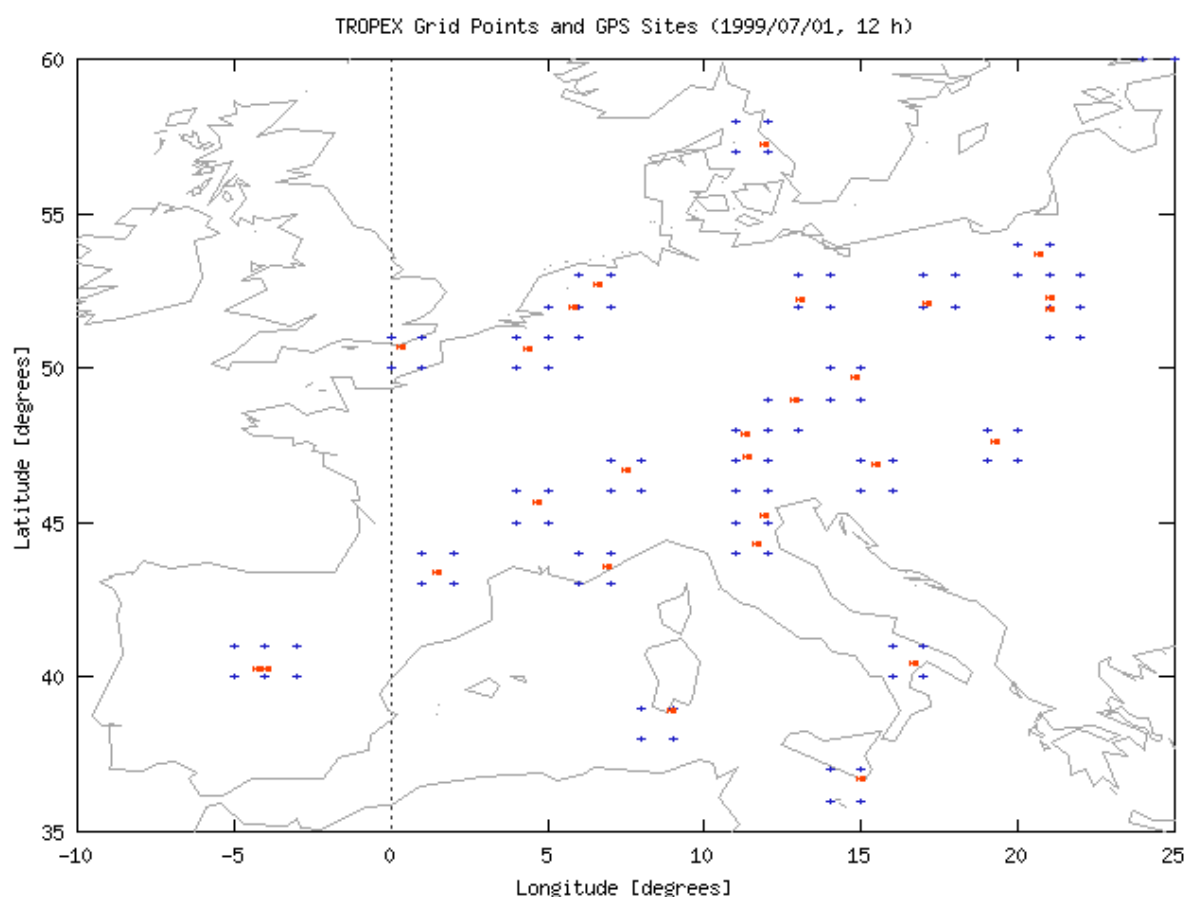


Figure 7-23 - Assimilated GPS stations of the IGS tracking network (European part) and affected grid points of the GDAS/TROPEX file (symbol "+").

⁴ See SCHUELER et al. [2000a]: a RMS of more than 2 cm for tropical sites is to be expected that decreases with increasing latitude.

SITE	BIAS	SIGMA	RMS	SITE	BIAS	SIGMA	RMS
ALBH	-0.7	4.5	4.9	MADR	0.5	5.6	6.4
ALGO	4.1	9.6	11.7	MAGO	3.1	5.6	7.0
ALIC	1.7	2.8	3.3	MALI	1.4	6.6	7.4
AMCT	-0.8	7.8	8.0	MATE	0.9	5.7	6.4
ANKR	-2.5	7.9	9.0	MAW1	-1.4	2.7	3.2
AOML	0.4	6.4	7.2	MDO1	2.2	6.1	7.7
AREQ	0.6	2.8	3.4	MDVO	1.7	6.1	8.2
ASCL	1.5	6.8	8.5	MEDI	-0.4	5.3	6.1
AUCK	-0.7	5.1	5.5	METS	-0.8	4.4	5.3
BAHR	-0.9	5.6	7.0	MKEA	3.3	5.7	7.2
BARB	0.9	6.9	8.0	MONP	2.7	5.0	6.7
BISH	-16.1	6.9	17.9	NLIB	4.6	11.8	13.6
BOGO	4.1	6.2	8.5	NOTO	5.4	6.8	9.5
BOGT	2.0	5.6	6.9	NOUM	0.4	4.5	4.8
BOR1	0.0	4.1	4.7	NRC1	-0.4	8.2	8.4
BRAZ	-1.8	2.3	2.9	NSSP	-3.5	5.2	8.4
BRMU	-0.4	7.5	7.8	NTUS	0.5	8.6	10.1
BRUS	-1.7	5.5	6.5	NYA1	0.0	3.1	3.7
CAGL	4.4	7.2	9.4	NYAL	-0.1	4.3	4.6
CAS1	1.2	2.6	3.1	OBER	-19.1	7.2	20.5
CASC	0.3	4.4	4.5	ONSA	-2.1	5.6	6.4
CHAT	0.9	4.8	5.5	PENC	-0.8	4.8	5.6
CHUR	0.7	5.6	6.5	PERT	-0.6	4.7	5.5
COCO	0.8	6.8	7.3	PIE1	0.4	4.1	4.5
CRO1	0.4	5.8	6.3	POL2	-7.5	5.9	10.4
DARW	-0.2	3.4	3.5	POTS	0.5	5.3	6.0
DAV1	2.0	2.9	3.7	PRDS	1.2	7.0	7.3
DGAR	0.0	7.7	9.2	RAMO	-0.7	3.8	4.6
DRAO	2.7	4.5	6.0	REYK	-3.2	5.6	7.0
DUBO	0.6	6.7	7.6	RIOG	1.0	4.6	5.1
EISL	1.5	6.5	7.6	SANT	-2.4	3.3	4.7
ELAT	5.8	8.2	11.6	SCH2	-1.0	5.8	6.8
FAIR	-0.5	4.9	5.9	SELE	-15.7	7.6	17.7
FLIN	0.4	5.9	6.8	SEY1	0.8	6.3	7.2
FORT	3.5	6.3	8.0	SFER	-0.6	4.8	5.0
GALA	0.1	3.6	3.7	SHAO	-2.4	7.0	7.7
GLSV	-0.6	4.7	5.4	SJDV	-3.8	5.0	7.2
GODE	-3.3	10.7	12.5	SOL1	-7.3	10.7	16.3
GOLD	0.5	3.6	4.0	STJO	-1.7	9.0	10.1
GOPE	2.2	4.8	6.2	SUTH	-0.5	3.2	3.4
GRAS	6.6	6.0	9.8	SUWN	0.5	5.9	6.7
GRAZ	1.1	4.4	5.2	TELA	-1.6	4.4	5.5
GUAM	2.7	8.1	9.7	THU1	1.9	2.3	3.1
HARK	-0.4	2.6	3.9	TIDB	-0.8	3.8	3.8
HART	-2.4	3.2	4.0	TOUL	-1.6	5.3	5.9
HERS	-1.8	6.5	7.7	TRO1	0.1	4.2	4.8
HFLK	-2.4	3.5	5.2	TROM	-3.0	4.2	5.3
HOB2	-2.0	4.3	5.3	TSKB	2.3	8.7	11.1
HOFN	0.0	4.9	5.1	UCLU	-1.2	4.9	5.4
HOLB	-0.7	5.7	6.0	UPAD	8.5	6.8	11.5
HRAO	1.9	2.7	4.1	URUM	-3.1	3.9	6.7
IISC	5.9	6.9	9.6	USNA	-4.3	9.2	11.2
IRKT	-2.9	7.6	10.4	USNO	-4.5	9.8	12.4
JOZE	-3.1	5.8	7.3	USUD	0.2	6.3	7.0
JPLM	2.7	3.7	5.8	VILL	4.0	6.0	8.2
KARR	0.2	3.6	4.6	WES2	3.2	9.6	11.6
KATZ	0.1	5.2	5.9	WHIT	1.1	4.5	5.2
KELY	-1.2	3.6	4.8	WILL	-1.9	3.6	4.4
KERG	-4.3	5.4	7.0	WSRT	0.8	5.4	5.8
KIRU	-2.3	5.7	6.6	WTZR	1.1	5.1	6.5
KIT3	5.8	5.6	8.6	WUHN	-2.9	7.6	8.8
KOKB	6.8	10.5	13.3	XIAN	-0.5	5.3	5.8
KOSG	-0.3	5.8	6.2	YAKZ	-0.3	5.9	8.2
KOUR	1.5	8.4	8.8	YAR1	3.4	5.2	6.6
KWJ1	1.3	8.6	10.1	YELL	2.2	4.6	5.2
LAMA	-2.2	5.2	6.6	ZECK	-3.1	5.5	7.0
LHAS	-6.3	6.6	9.6	ZIMM	-2.1	4.1	5.7
LPGS	-0.6	5.0	5.9	ZWEN	-2.1	6.1	7.7
MAC1	-0.7	4.7	5.3	MEAN	-0.3	5.7	7.1

Table 7-4 - Mean biases, standard deviations ("sigma") and RMS values in [mm] after the combination of NWM and GPS delays using blunder detection and variance component estimation.

SITE	BIAS	SIGMA	RMS	SITE	BIAS	SIGMA	RMS
ALBH	-0.5	4.5	4.9	MADR	0.5	6.0	6.8
ALGO	4.5	9.6	11.9	MAGO	3.0	4.7	5.9
ALIC	1.5	2.9	3.3	MALI	0.9	6.3	6.9
AMCT	0.7	7.3	7.2	MATE	-0.9	5.2	5.5
ANKR	-4.0	8.8	10.5	MAW1	-1.5	2.8	3.3
AOML	0.6	6.0	6.7	MD01	-0.2	4.6	5.0
AREQ	-0.5	3.3	4.5	MDVO	1.8	6.0	8.2
ASC1	0.9	5.5	6.5	MEDI	0.3	5.6	6.5
AUCK	-1.2	5.1	5.6	METS	-0.8	4.4	5.3
BAHR	-0.5	5.3	6.4	MKEA	2.3	5.2	5.9
BARB	0.0	7.0	8.1	MONP	1.2	4.6	5.3
BISH	-17.5	7.6	19.5	NLIB	2.5	9.4	10.6
BOGO	4.1	6.1	8.5	NOTO	6.3	7.3	10.4
BOGT	1.7	4.9	5.6	NOUM	0.3	4.5	4.8
BOR1	0.0	4.2	4.7	NRC1	-0.2	8.1	8.3
BRAZ	-1.7	2.4	2.9	NSSP	-2.4	5.1	7.9
BRMU	-1.6	7.2	7.8	NTUS	-0.6	7.9	8.6
BRUS	-2.1	5.6	6.8	NYA1	-0.1	3.2	3.9
CAGL	4.3	7.2	9.4	NYAL	-0.2	4.4	4.8
CAS1	0.8	2.7	3.0	OBER	-19.2	7.3	20.6
CASC	0.4	4.3	4.4	ONSA	-2.0	5.9	6.9
CHAT	1.0	4.9	5.7	PENC	-0.5	4.7	5.3
CHUR	0.0	5.4	6.1	PERT	-0.9	5.2	6.1
COCO	-0.5	6.6	6.8	PIE1	0.4	4.1	4.5
CRO1	0.6	5.1	5.4	POL2	-9.7	7.6	13.3
DARW	-0.2	3.4	3.6	POTS	0.6	5.5	6.3
DAV1	1.7	2.8	3.5	PRDS	1.4	6.8	7.2
DGAR	0.2	6.1	6.7	RAMO	-0.4	4.2	4.9
DRAO	3.9	4.5	6.6	REYK	-3.2	5.6	6.9
DUBO	0.4	6.7	7.5	RIOG	0.9	4.5	5.0
EISL	1.5	6.0	6.8	SANT	-3.0	3.8	5.4
ELAT	6.3	9.0	12.6	SCH2	-0.8	5.7	6.6
FAIR	-0.9	4.6	5.3	SELE	-15.8	7.6	17.8
FLIN	0.4	5.8	6.6	SEY1	0.8	6.0	6.5
FORT	1.5	5.3	5.7	SFER	-1.4	4.9	5.6
GALA	0.1	3.6	3.9	SHAO	-2.2	6.7	7.4
GLSV	-0.4	4.5	5.4	SJDV	-3.8	5.0	7.1
GODE	-3.9	10.5	12.2	SOL1	-8.7	12.0	18.0
GOLD	5.7	4.6	7.6	STJO	-1.4	8.5	9.1
GOPE	2.5	5.0	6.6	SUTH	-0.8	3.2	3.5
GRAS	5.4	5.3	8.3	SUWN	0.5	6.0	6.6
GRAZ	1.1	4.3	5.1	TELA	-1.7	4.5	5.7
GUAM	0.9	6.6	7.2	THU1	0.8	2.1	2.5
HARK	-0.2	2.7	4.0	TIDB	-0.8	3.6	3.7
HART	-2.4	3.2	4.0	TOUL	-0.2	5.5	6.4
HERS	-1.8	6.3	7.5	TRO1	0.3	4.2	4.7
HFLK	-2.4	3.6	5.2	TROM	-2.9	4.3	5.3
HOB2	-2.1	4.4	5.4	TSKB	2.3	8.4	10.7
HOFN	0.6	5.0	5.3	UCLU	-1.4	5.2	5.8
HOLB	0.0	5.9	6.5	UPAD	7.3	7.3	11.1
HRAO	2.1	2.8	4.2	URUM	-1.1	4.4	7.7
IISC	2.3	5.3	6.0	USNA	-4.4	9.1	11.1
IRKT	-3.1	7.2	9.8	USNO	-5.0	9.9	12.4
JOZE	-2.9	5.9	7.3	USUD	0.5	6.2	6.8
JPLM	2.8	3.7	5.8	VILL	3.7	6.8	9.2
KARR	0.3	3.6	4.7	WES2	1.1	8.8	10.0
KATZ	0.5	5.3	6.1	WHIT	1.3	4.7	5.5
KELY	-1.2	3.7	5.0	WILL	-2.0	3.6	4.5
KERG	-2.9	5.2	6.1	WSRT	1.1	5.6	6.1
KIRU	-2.5	5.7	6.6	WTZR	1.4	5.3	6.8
KIT3	5.8	5.8	8.8	WUHN	-3.1	8.6	10.0
KOKB	4.1	8.7	9.9	XIAN	-0.7	5.3	5.8
KOSG	-0.4	5.8	6.2	YAKZ	0.0	6.5	9.1
KOUR	1.2	8.5	8.7	YAR1	4.2	5.7	7.5
KWJ1	1.1	6.7	7.5	YELL	3.8	5.5	6.9
LAMA	-2.4	5.3	6.7	ZECK	-3.2	5.5	7.0
LHAS	-5.9	6.3	9.2	ZIMM	-2.0	4.2	6.0
LPGS	-0.5	5.3	6.3	ZWEN	-3.1	6.7	9.0
MAC1	-0.3	5.2	6.0				
				MEAN	-0.4	5.7	7.0

Table 7-5 - Mean biases, standard deviations ("sigma") and RMS values in [mm] after the combination of NWM and GPS delays using pre-weighting and variance component estimation.

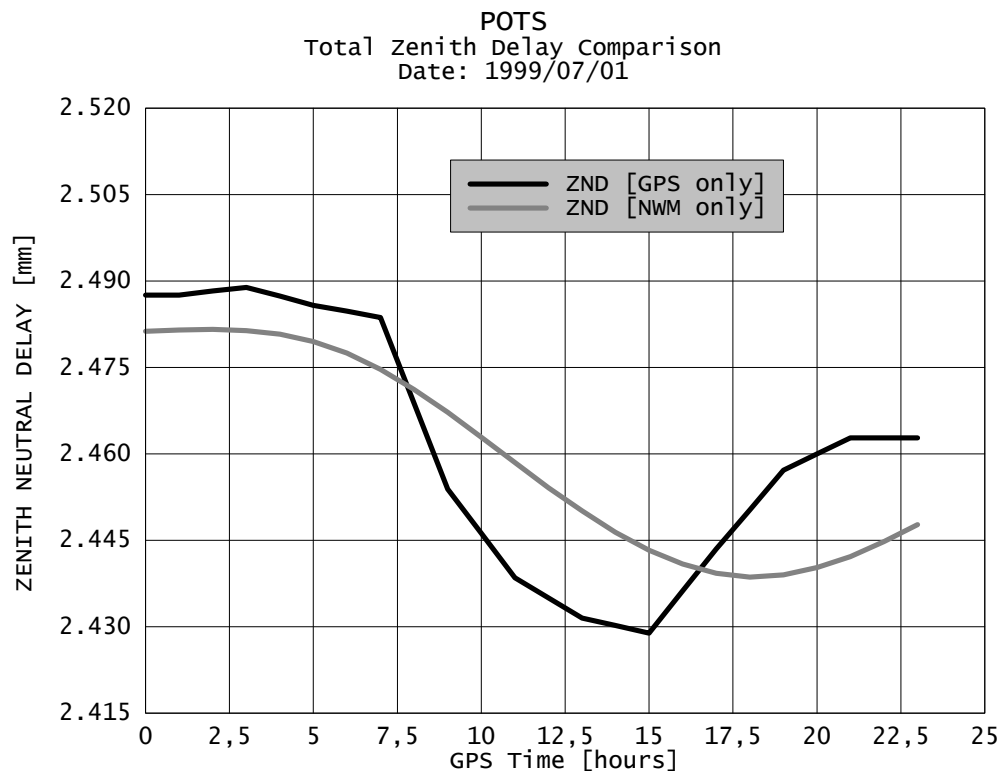


Figure 7-24 - Comparison of ZND from GPS and GDAS/TROPEX files for tracking station Potsdam (POTS, Germany).

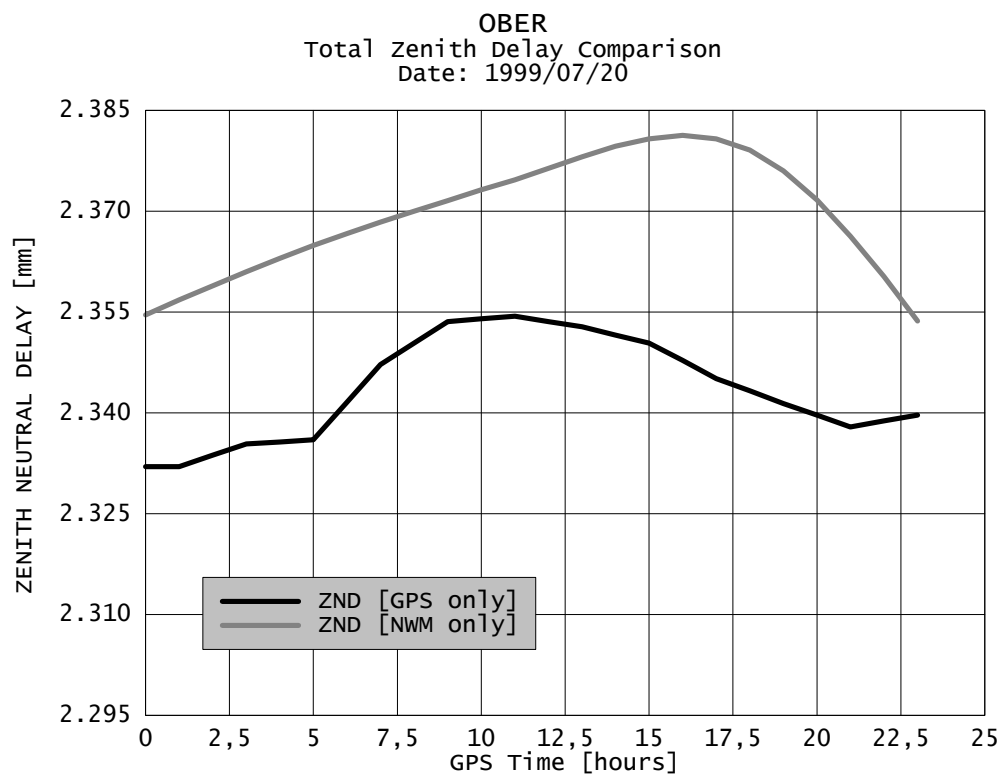


Figure 7-25 - Comparison of ZND from GPS and GDAS/TROPEX files for tracking station Oberpfaffenhofen (OBER, Germany).

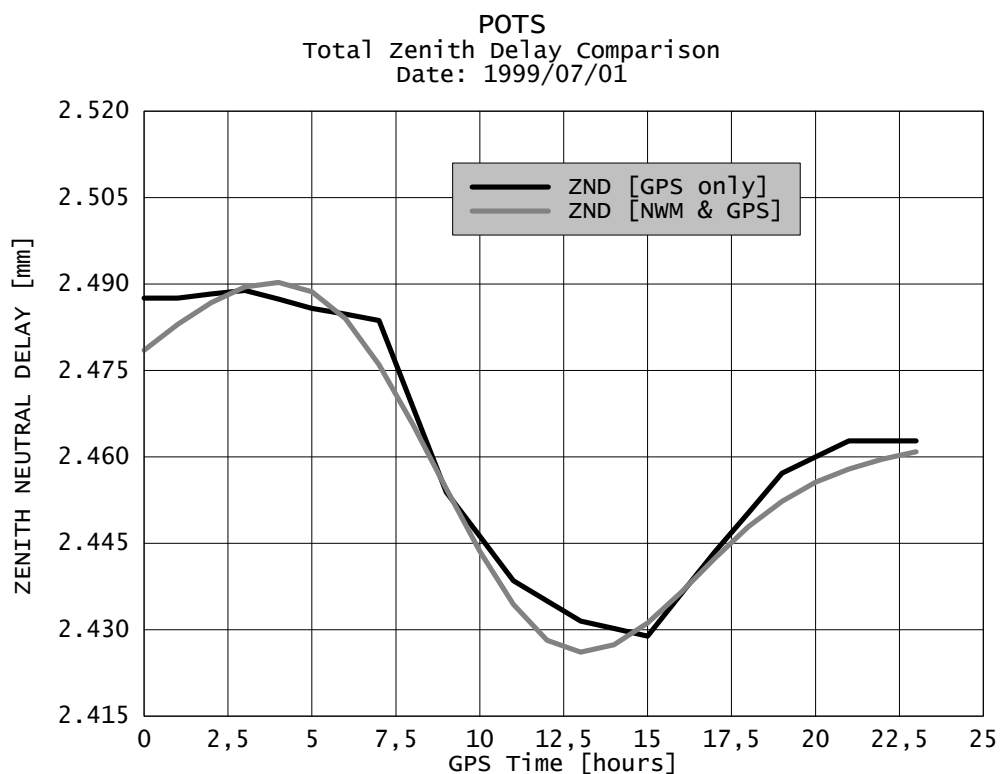


Figure 7-26 - Comparison of ZND from GPS and combined GDAS & GPS TROPEX files for tracking station Potsdam (POTS, Germany).

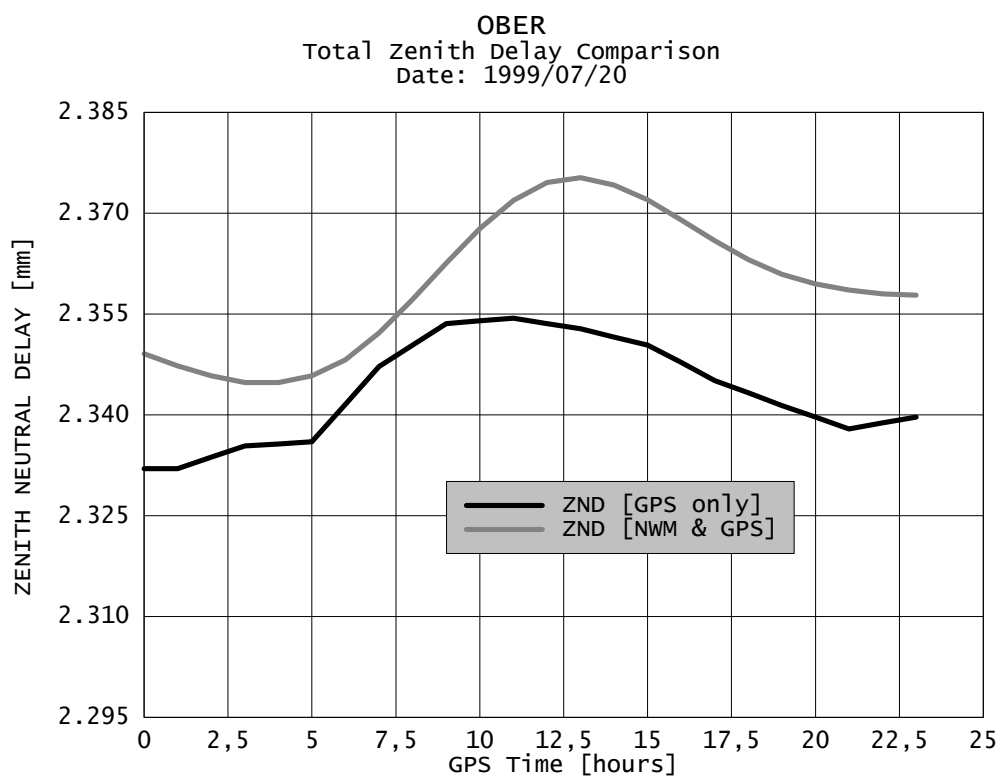


Figure 7-27 - Comparison of ZND from GPS and combined GDAS & GPS TROPEX files for tracking station Oberpfaffenhofen (OBER, Germany).

As a conclusion of this comparison, one can state that it makes sense to combine the numerical weather model delays and the GPS-derived data. This might reduce systematic effects and will be dealt with in the following section.

7.3 Combined GDAS/GPS Solution Fields

Results obtained with the combination method discussed in section → 4.5 are presented here using two different configuration settings: Blunder detection (→ 4.5.4.1) was used in run (I) whereas the pre-weighting approach (→ 4.5.4.3) was used in run (II). Variance components (→ 4.5.4.2) were estimated during both runs.

Figure 7-23 displays most European IGS tracking stations that were used for the combination on 1 July 1999 as well as the GDAS/TROPEX grid points that were affected by these sites (symbolized by crosses "+"). Apparently, the IGS network has a considerable density in Europe and the combined adjustment might really improve the wet delays over certain parts of Europe. However, it also becomes evident that it would be desirable to assimilate many more stations in order to increase the area that participates into the combination process. This goal can be reached if not only the IGS tracking network is used, but also continental (EUREF) and regional densifications (e. g. GREF).

Again, the zenith neutral delays are compared with those from GPS and given in Table 7-4 for combination run (I) and in Table 7-5 for combination run (II). It is stressed that this comparison is based on exactly the same GPS troposphere data that have been previously assimilated into the TROPEX combination procedure⁵. For this reason, the comparison described here is not a true validation with external, independent data, but a look at the mean, site-specific post-fit residual with the following add-ons: The combination, of course, does only take part for those epochs present in the TROPEX files, i. e. every 6 hours during July 1999, whereas the comparison is always based on hourly values. As a consequence, the results given here do not only reflect the post-fit residuals, but also temporal interpolation problem if present. Temporal interpolation was performed using cubic splines. Generally speaking, both configurations have almost the same average accuracy level. The mean RMS decreases down to 7 mm (previous to combined adjustment: 17 mm) and the standard deviation is almost the same with 6 mm. This essentially means that the systematic deviations between GPS and NWM wet delays could be successfully removed. Remaining errors are due to temporal interpolation, for instance, but the spline interpolation method seems to be able to bridge even gaps of 6 hours with sufficient accuracy⁶.

Figure 7-17, Figure 7-18, Figure 7-21 and Figure 7-22 are plots of the diurnal RMS values for 4 selected stations that can be directly with the outcome of the GDAS/TROPEX comparison without combined adjustment (left page). All stations

⁵ But note that *wet* delays are combined, not neutral delays. If only GPS-derived ZND data are available, the wet component will be separated from the total component with help of surface pressure contained in the TROPEX files.

⁶ The temporal resolution of the GDAS/TROPEX files was doubled in 2000, so the interval could be reduced to 3 hours what further reduces temporal interpolation errors.

show a clearly smaller RMS after the combined adjustment, but Oberpfaffenhofen (*OBER*) cannot fully convince, because the increase in accuracy is rather moderate and not as clear as for the other stations. Figure 7-24 to Figure 7-27 show the ZND curves over one selected day (hourly values) in original (NWM only, left page) and combined mode. After the combined adjustment, the ZND curve for Potsdam (*POTS*) very closely resembles the GPS-derived ZND data. The same is not true for Oberpfaffenhofen (*OBER*) where a systematic offset still remains, although an improvement is visible. There are also some other stations that do not perform very well and only improve little during the combined adjustment, e. g. *SELE*.

The possible reason for the poor performance must be related to the height-reduction problem as well as to the necessity to extrapolate the NWM-data in these cases. The 4 nearest TROPEX grid points for Oberpfaffenhofen have geopotential heights of 925 m, 1007 m (northward neighbors) and 1807 m, 1870 m (southward neighbors), but IGS tracking station *OBER* has a height of 595 m, so an extrapolation in height of 300 up to 950 m is necessary to relate the grid point to the height level of the GPS site⁷. For *SELE*, the situation is even more problematic: The grid points have heights of 1689 m, 1955 m, 3255 m and 3480 m whereas the GPS station is located at only 1382 m, so an extrapolation in height of 300 m to 2100 m is necessary. The height reduction coefficients are, of course, derived for all heights above (not below) the grid points. Such an extrapolation will certainly cause height reduction errors. This reveals the major disadvantage of the medium resolution GDAS weather fields in mountainous regions. A higher horizontal resolution, e. g. 0.5° instead of 1° , would certainly improve the situation. However, a horizontal resolution of $1^\circ \times 1^\circ$ is appropriate for average situations given the fact that only about 140 IGS stations world-wide are available.

⁷ This height reduction term is, of course, taken into account during the combined adjustment and considered the design matrix (see → 4.5.2, formulas 4-76 to 4-78).

8. Résumé

The theory and practice of ground-based GPS tropospheric delay estimation was discussed in the preceding chapters and proved that the analysis of precise carrier phase observations from permanent GPS networks provides estimates of zenith wet delays and integrated water vapor at an accuracy level that effectively turns GPS receivers into high-precision water vapor sensors which are economically attractive in comparison to other ground-based techniques like water vapor radiometers or LIDAR.

8.1 GPS Tropospheric Delay Estimation

In this study, the technique of *Kalman filtering* was applied to estimate tropospheric delays. Major benefits of this data processing technique are a moderate memory load due to the fact that only a limited set of observations needs to be present in memory, a very efficient handling of the ambiguity unknowns (\rightarrow 2.5.2.8.1) as well as a highest possible temporal resolution of the filtered delays (\rightarrow 6.6.1). An important disadvantage can be seen in the necessity to define the process noise of the parameters properly (\rightarrow 3.4). This problem was successfully solved with help of the *dynamic* or *maximum tuning* method (\rightarrow 3.4.4, \rightarrow 6.6.4).

The results obtained with the tropospheric analysis software TropAC TRIDENT agree with the combined IGS troposphere products at a RMS level of 5 to 7 mm (\rightarrow 6.1.3, \rightarrow 6.2.2, \rightarrow 6.4.1) and the (bias-reduced) standard deviation is around 4.5 to 5.5 mm. Comparisons with ground-based water vapor radiometer results at Potsdam showed a mean RMS of better than 0.9 kg/m² (\rightarrow 6.6.1). These results can be considered as satisfactory and confirm the appropriate implementation of the algorithms to filter tropospheric zenith delays from dual-band GPS phase measurements.

8.1.1 Error Budget

Several GPS validation experiments were carried out to evaluate the error budget of zenith wet delay estimation that is summarized in Table 8-1.

Station coordinates (\rightarrow 3.3.4.1) were estimated during almost all experiments as additional unknowns. As far as the IGS network and sub-networks like EUREF are concerned, it is feasible to fix them (\rightarrow 6.6.1) because the site coordinates are known with such superior accuracy that coordinate uncertainties are not harmful to zenith wet delay estimation. However, it is repeated here that zenith wet delays are very prone to antenna coordinate errors.

The uncertainty caused by the *orbit error* (\rightarrow 3.3.4.2) is, of course, dependent on the orbit product and its accuracy. It was shown (\rightarrow 6.3.1) that most accurate results can be obtained with final, combined IGS orbits (*IGS*) that have a latency of about 2 weeks. Rapid IGS orbits (*IGR*) produce only marginally less accurate delays and can be used instead of the final orbits. Predicted orbits (*IGP*) significantly deteriorate the zenith wet delay accuracy. In comparison to final and rapid orbits, the mean RMS is about 5 mm worse, but a wet delay estimation with an accuracy of approximately 10

Error Source	S_{ZWD} [mm]	S_{IWV} [kg/m ²]	Comments
antenna position	2 ... 7	0.3 ... 1.1	antenna coordinate offsets should be estimated as additional unknowns, fixed coordinates are only recommended if antenna position is known with superior accuracy; given numbers refer to an approximate coordinate uncertainty of 3 mm for each coordinate component
satellite position	2 ... 10	0.3 ... 1.6	depends on baseline length and orbit product, most precise solutions with final IGS orbits (post-processing only), worst accuracy for predicts IGS orbits (real-time applications)
convergence error	-	-	negligible if network has a diameter of more than 500 km (1000 km recommended)
antenna PCV	1 ... 3	0.1 ... 0.5	unmodeled phase center variations of GPS antenna, e.g. azimuth-dependent terms
multipath effects	2 ... 4	0.3 ... 0.6	depend on local environment, antenna type, receiver firmware (multipath mitigation software)
hydrostatic delay	1 ... 3	0.1 ... 0.5	depends on accuracy of surface pressure (0.3 hPa to 1.0 hPa)
mapping function	-	-	negligible if precise mapping functions are used and elevation mask is not lower than 15°
conversion error	-	0.1 ... 0.3	use of numerical weather fields is recommended; models using surface temperature are suitable in most cases, too
total budget	5 ... 14	0.5 ... 2.2	

Table 8-1 - Error budget for ground-based GPS zenith wet delay and integrated water vapor estimation. The components contributing to the total standard deviation of the ZWD (σ_{ZWD}) and integrated water vapor (σ_{IWV}) are assessed for average situations.

mm seems to be feasible in (near) real-time using the IGP orbits. However, the new ultra-rapid orbits (*IGU/ULT*) are an alternative since the ZWD accuracy obtained using this orbit product is only 2 mm worse than the solution using final orbits. Nevertheless, final orbits remain the best choice if highest precision is required. An orbit accuracy of 1 dm that is typical for IGS orbits may cause an error in ZWD of 1 to 4 mm for 500 km baselines and a minimum satellite constellation (\rightarrow 3.3.4.2). For average situations (6 satellites in view, orbits accurate to 1 to 2 dm), the expected ZWD uncertainty is in the range of 2 to 6 mm for baselines up to 1000 km. Consequently, the orbit error can be considered as one of the major error contributors to the overall error budget.

The *convergence error* (\rightarrow 3.3.4.3) is of very minor concern. All results presented in this thesis are based on absolute ZWD estimates (\rightarrow 3.3.4.3.1) without applying any constraints on the wet delays of particular stations. The relative method (\rightarrow 3.3.4.3.2) has never been applied. Nevertheless, the biases of the results are within reasonable limits and cannot be traced back to convergence errors at all.

Antenna phase center variations (PCV) are always taken into consideration. The current implementation (\rightarrow 2.3.6) applies the antenna phase center offset as well as elevation-dependent corrections. However, small differences between different

antennas of the same type may occur and azimuth-dependent variations that are currently omitted can cause remaining errors.

Multipath (→ 3.3.4.4) is a significant error source. The multipath error depends on several circumstances, e. g. the environment (no nearby buildings and conductors) and the kind of antenna in use (choke ring is recommended). The multipath experiment (→ 6.5) showed a mean RMS of 4 mm. One of the antennas in use was not a choke ring antenna, but had only a ground plane, so in normal operation with choke ring antennas, the multipath contribution is expected to be smaller, in the range of 2 to 4 mm.

The *hydrostatic delay* must be precisely determined in order to separate the wet from the neutral delay. The Saastamoinen hydrostatic model (→ 3.2.1.1.2) is recommended for this purpose. Its modeling errors are negligible and the main error source is the accuracy of surface total pressure. An uncertainty of 0.5 hPa causes a ZHD error of no more than 1.5 mm. This precision level can be reached with help of standard quality meteorological packages. However, the availability of such instruments is very unsatisfactory (→ 8.1.2).

Uncertainties of the *tropospheric mapping functions* (→ 3.3.4.6) are only minor contributors to the ZWD error budget. The results of all tested mapping functions (→ 6.2.3) only showed marginal discrepancies for a recommended minimum elevation angle of 15° (→ 6.2.6) and the stochastic modeling approach (→ 3.3.4.6) is obviously suitable to supply proper weights of the phase measurements depending on the zenith angle. A minimum elevation of 15° will also attenuate the impact of horizontal gradients and will exclude most observations that suffer from poor signal-to-noise ratios. It is not recommended to estimate *horizontal gradients* as additional parameters since an improvement in the accuracy of the analysis could not be confirmed (→ 6.6.3). The input of horizontal gradients determined with help of numerical weather models (→ 4.3.2) could not improve the solution either (→ 6.2.4) during the test period.

The *conversion error* to transform zenith wet delays into precipitable water vapor is worth to mention. Several ways are possible to provide the conversion factor. One method is to derive the humidity weighted mean temperature of the troposphere (→ 3.5.1) with help of 3-D numerical weather models (→ 4.4.4.1). Comparisons with radiosonde data agree at a RMS level of 2 to 3 K (→ 5.3). The other methods using surface temperature to predict the mean atmospheric temperature deviate at a RMS level of 0.15 to 0.20 kg/m² in comparison to the conversion factors from numerical weather models (→ 6.4.2). Consequently, these approaches can also be considered as suitable and would allow the GPS integrated water vapor estimation with a maximum degree of independence from weather models. An integrated water vapor uncertainty of 0.1 to 0.3 kg/m² due to the conversion uncertainty can be expected.

8.1.2 Meteorological Inputs

GPS alone is only able to provide zenith neutral delays, but not wet delays nor integrated water vapor. Two meteorological quantities are needed to turn ground-

based GPS receivers into tropospheric sounders: Surface pressure is needed to model the hydrostatic delay and, as a consequence, to allow zenith wet delay estimation. Surface temperature or the mean temperature of the atmosphere is needed to convert zenith wet delays into integrated water vapor. Unfortunately, meteorological sensor packages providing these necessary data are only available for very few stations of the IGS tracking network and the situation for many other permanent arrays is not better.

To overcome this shortcoming, the needed data can be extracted from numerical weather models (\rightarrow 4.2). Results show (\rightarrow 5.1, \rightarrow 5.3) that the chosen GDAS weather model meets the requirements. The most important quantity - surface pressure - can be extracted with a standard deviation of 0.5 to 0.6 hPa (global mean), and the long-term biases are in the same range for most stations. Surface temperature and the mean temperature of the troposphere can also be determined with the requested accuracy of 2 K (standard deviation). Generally speaking, results obtained using high-resolution weather models (\rightarrow 5.1.4) show only a marginally higher accuracy level.

However, the successful application of numerical weather models for the needs of ground-based GPS water vapor estimation should not hide the fact that in situ measurements would enhance the value of GPS for meteorology and climate research. Measurements of meteorological sensors at the antenna site would turn GPS receivers into true and independent atmospheric sounders. Using numerical weather models is, of course, a suitable way to go, but as the overall goal of GPS meteorology is to improve existing weather models, this causes the problem of inducing correlations: We must take into account that especially surface pressure, i. e. hydrostatic delay, and zenith wet delays are directly coupled with each other, so biases in the pressure of the weather model would directly lead to biases in the wet delays. Such correlations between the states of a numerical weather model are generally not wanted. For this reason, GPS tracking stations should better be equipped with meteorological sensor packages.

8.2 Gridded Tropospheric Correction Data

GPS tracking stations provide irregularly distributed tropospheric estimates. For many applications, it would be advisable to provide regularly gridded data sets. Efforts were made to use the contents of numerical weather models and to develop the TROPEX file format (\rightarrow 4.4) that supplies data layers for all necessary components for hydrostatic and wet delay computation at any place on the globe. Other interesting quantities like the temperature lapse rate, the height of the tropopause and the mean temperature of the troposphere can be extracted from these files as well.

8.2.1 NWM-derived Zenith Neutral Delays

TROPEX files initially carry data from the GDAS numerical weather fields. Zenith neutral delays derived from these tropospheric data files agreed to the GPS-derived neutral delays at a RMS level of 1.8 cm (\rightarrow 7.2). The standard deviation was 1.1 cm, i. e. significantly lower than the RMS which includes biases. Hence, systematic errors are obviously an important kind of uncertainty of numerical weather models what emphasizes the importance of GPS meteorology. From the water vapor analysis of

high-resolution weather models (→ 6.4.4) one may conclude that the zenith wet delay can be determined with an accuracy of slightly better than 1.5 cm.

8.2.2 Combination of NWM and GPS Data Sets

The integration or assimilation of GPS results into numerical weather models can be performed following two methods: Either zenith neutral delays or integrated water vapor is assimilated into the models. The first method is to be applied if it is impossible to separate the hydrostatic and wet component from each other and/or the conversion of wet delays into water vapor cannot be performed, i. e. in situ measurements of pressure and/or temperature are not available. The second method can be applied if surface meteorological measurements are present and strengthens the independence of the GPS estimates. A different approach is performed in this thesis that can be considered as an intermediate product focusing on tropospheric delay determination: The GPS delays are not assimilated into a weather model. Instead, both NWM and GPS delay data sets are combined. The TROPEX files are an ideal data carrier for such a combination of the regular NWM data sets and the irregularly distributed GPS data sets (→ 4.5).

Without any combination with GPS data, a zenith neutral delay of better than 2 cm can be reached in average (→ 7.2). This error budget can be reduced by assimilation of GPS wet delays and performing a combined adjustment of the NWM- and GPS-derived delays. The mean post-fit residuals have a RMS level of better than 1 cm (→ 7.3). One problem during the combined adjustment of NWM and GPS data is the definition of the stochastic model. This problem can be addressed using several approaches (→ 4.5.4) including variance component estimation. The tested configurations show similar results and can be considered to be usable in operational mode. A remaining problem seems to be related to the height reduction (→ 7.1), especially as far as possible extrapolation scenarios are concerned (→ 7.3). A few IGS tracking stations suffer from such effects that could likely be reduced by using a higher horizontal resolution of the weather fields. Generally speaking, it would be desirable to assimilate more GPS data.

8.3 Economical and Technical Aspects

All results presented in this thesis show that ground-based GPS wet delay and water vapor estimation has its place in meteorology and climate research. The accuracy level of GPS receivers and high-precision GPS data analysis is that promising that only a few water vapor sensors can compete with this technology. Two such instruments are ground-based water vapor radiometers and LIDAR.

From the *economical point of view*, GPS sensors have the clear advantage of being very inexpensive in comparison to water vapor radiometers and LIDAR. Dual-band GPS receivers with choke ring antennas can be purchased for less than 15,000 EUR and these prices are expected to drop considerably in the near future. This is 10 times cheaper than the price of water vapor radiometers (approximately 150,000 EUR) and LIDAR is a very expensive technology as well.

From the *technical point of view*, GPS sensors have the advantage of being easy to operate and they do not need any calibration because the analysis software is able to compensate instrumental errors by proper modeling - self-calibration is possible. Both factors are also important in terms of economical considerations because the non-existing need to calibrate the devices reduces costs as well as the fact that less skilled operators can be employed. Moreover, GPS results can be considered as more reliable than water vapor radiometer measurements. Radiometers cannot measure during periods of rainfall and the detection of the beginning rainfall is not always correctly reported.

Albeit being a reliable technique, certain GPS validation experiments showed that some stations suffer from a lack of availability (\rightarrow 6.1.1). This situation should - and can - be improved.

8.4 Summary and Outlook

Without any doubt, ground-based GPS water vapor estimation can be considered as a valuable method for meteorology and climatology. The integrated water vapor can be determined with an accuracy of better than 2 kg/m^2 in almost all cases. A comparison with measurements of a water vapor radiometer (\rightarrow 6.6) showed that this statement is true for Potsdam where more than 95% of all samples agreed to better than 2 kg/m^2 with the WVR samples and 68% were better than 1 kg/m^2 . The importance of ground-based GPS has meanwhile been recognized by meteorologists and climatologists and efforts are underway all over the world to assimilate GPS troposphere estimates into numerical weather models and to extend GPS capabilities to near real-time what has become convenient due to the increased orbit accuracy of the predicted and especially the ultra-rapid orbits of the IGS.

The goal of this study was to exploit the capabilities of permanent GPS arrays, i. e. static networks, for tropospheric delay and water vapor estimation and to make the methods developed ready for their application in both disciplines, meteorology/climatology and GPS processing. As far as meteorology and climatology are concerned, this goal could be reached by separating hydrostatic and wet component and supplying the conversion of wet delays into integrated water vapor with help of in situ meteorological measurements and - if unavailable - with help of numerical weather fields. The GPS society can take advantages from this work by making use of the tropospheric delays from numerical weather models contained in gridded troposphere correction files that allow to derive tropospheric delays conveniently. In this way, it is possible to reduce the tropospheric error in kinematic applications, for instance, and this may also allow a more reliable integer ambiguity fixing with increased baseline lengths.

Nevertheless, water vapor estimation on moving platforms like cars, ships and aircraft is an interesting and outstanding research objective for the future. Kinematic water vapor estimation is more challenging than it is in static networks, but enhanced algorithms may allow to obtain these target values with sufficient accuracy and thereby extend GPS meteorology considerably: Ships navigate through regions that usually suffer from a lack of meteorological information and aircraft may reach

regions of interest very quickly and, moreover, can provide vertical profiles of water vapor at least during start and landing.

The second interesting perspective for GPS meteorology can be seen in the radio occultation technique (→ 1.3.1): A low-earth orbiting satellite receives GPS signals during an occultation event and can determine the atmospheric bending angle that can be used to derive the vertical refractivity profile in the stratosphere and the upper troposphere and may thereby improve the numerical weather models. Quite a number of such LEO missions are planned and some have already been realized, so that even an operational use of the radio occultation method may become reality in the near future.

9. References

- ANTHES, R. A. [1974], *Data Assimilation and Initialization of Hurricane Prediction Models*, Journal of the Atmospheric Sciences, 31, pp. 702-719
- BAR-SEVER, Y., P. M. KROGER, and J. A. BORJESSON [1998], *Estimating Horizontal Gradients of Tropospheric Path Delay with a Single GPS Receiver*, Journal of Geophysical Research, Vol. 103, No. B3, pp. 5019-5035, March 10, 1998
- BASSIRI, S., and G. A. HAJJ [1993], *Higher-order Ionospheric Effects on the Global Positioning System Observables and Means of Modeling Them*, Manuscripta Geodaetica (1993) 18:280-289, Springer Verlag
- BEUTLER, G., I. BAUERSIMA, S. BOTTON, W. GURTNER, M. ROTHACHER, and T. SCHILDKNECHT [1989], *Accuracy and Biases in the Geodetic Application of the Global Positioning System*, Manuscripta Geodaetica (1989) 14:28-35, Springer-Verlag
- BEVIS, M., ST. BUSINGER, TH. A. HERRING et al [1992], *GPS Meteorology: Remote Sensing of Atmospheric Water Vapor Using the Global Positioning System*, Journal of Geophysical Research, Volume 97, pp. 15,787-15,801
- BEVIS, M., ST. BUSINGER, ST. CHRISWELL et al. [1994], *GPS Meteorology: Mapping Zenith Wet Delays onto Precipitable Water*, Journal of Applied Meteorology, Vol. 33, pp. 379-386, March 1994
- BLACK, H. D. [1978], *An Easily Implemented Algorithm for the Tropospheric Range Correction*, Journal of Geophysical Research, Vol. 83, No. B4, pp. 1825-1823, 1978
- BLACK, TH. L. [1994], *The New NMC Mesoscale Eta Model: Description and Forecast Examples*, Weather and Forecasting, Vol. 9, pp. 265-278, June 1994
- BRAASCH, M. S. [1996], *Multipath Effects*, in: SPILKER and PARKINSON (eds.), *GPS Theory and Applications*, Vol. I, Progress in Astronautics and Aeronautics, Vol. 163, pp. 547-568, 1996
- BROWN, R. G. and P. Y. C. HWANG [1997], *Introduction to Random Signals and Applied Kalman Filtering*, 3rd Edition, John Wiley & Sons, ISBN 0-471-12839-2
- CARTER, J. H. [1997], *Spaceborne Water Vapor Measurements*, ASE 389P - Remote Sensing from Space, University of Texas at Austin, Spring 1997 mid-term project; <http://www.ae.utexas.edu/courses/ase389/midterm/carter/carter.html>
- CHAO, C. C. [1972], *A Model for Tropospheric Calibration from Daily Surface and Radiosonde Balloon Measurements*, Technical Memorandum 391-350, Jet Propulsion Laboratory, Pasadena, California, USA, 1972

CHEN, G. and T. A. HERRING [1997], *Effects of Atmospheric Azimuthal Asymmetry on the Analysis of Space Geodetic Data*, J. of Geophys. Res., Vol 102, No B9, pp. 20,489-20,502, 1997-09-10

DEY, C. H. [1998], *GRIB (Edition 1) - The WMO Format for the Storage of Weather Product Information and the Exchange of Weather Product Messages in Gridded Binary Form*, Office Note 388, unreviewed manuscript, primarily intended for informal exchange of information among NCEP staff members, National Oceanic and Atmospheric Administration, National Weather Service, National Centers for Environmental Prediction, NCEP Central Operations, March 10, 1998

DABBERDT, W. F., H. L. COLE, N. CHAMBERLAIN, T. HOCK, E. KORN, D. LAURTISEN, K. NORRIS, and S. STENSLUND [1995], *A Reference Radiosonde*, in: Preprints, *Ninth Symposium on Meteorological Observations and Instrument*, pp. 55-59, American Meteorological Society, Boston, Mass., 1995

DANA, P. H. [1995], *Global Positioning System Overview*, Department of Geography, University of Texas at Austin, The Geographer's Craft Project; http://www.colorado.edu/geography/gcraft/notes/gps/gps_f.html

DAVIS, J. L., T. A. HERRING, I. I. SHAPIRO, A. E. E. ROGERS, and G. ELGERED [1985], *Geodesy by Radio Interferometry: Effects of Atmospheric Modeling Errors on Estimates of Baseline Length*, Radio Science, Vol. 20, No. 6, pp. 1593-1607, Nov.-Dec. 1985

DAVIS J. L., G. ELGERED, A. E. NIELL, and C. E. KUEHN [1993], *Ground-Based Measurement of Gradients in the "Wet" Radio Refractivity of Air*, Radio Science, Vol. 28, No. 6, pp. 1003-1018, Nov.-Dec. 1993

DOODSON, A. T. [1928], *The Analysis of Tidal Observations*, Phil. Trans. Roy. Soc. Lond., 227, pp. 223-279

DUAN, J., M. BEVIS, P. FANG, Y. BOCK, ST. CHISWELL, ST. BUSINGER et al. [1996], *GPS Meteorology: Direct Estimation of the Absolute Value of Precipitable Water*, Journal of Applied Meteorology, Volume 35, pp. 830-838, June 1996

EISSFELLER, B. [1998], *Stochastic Processes*, in: *Lecture Notes on Signal Processing*, Chapter 6, University FAF Munich, Germany

ELGERED, G., J. L. DAVIS, T. A. HERRING, and I. I. SHAPIRO [1991], *Geodesy by Radio Interferometry: Water Vapor Radiometry for Estimation of Wet Delay*, Journal of Geophysical Research, Vol. 96, No. B4, pp. 6541-6555, April 10, 1991

ELGERED, G. [1993], *Tropospheric Radio-Path Delay From Ground-Based Microwave Radiometry*, in: A. JANSSEN (ed.) [1993], *Atmospheric Remote Sensing by Microwave Radiometry*, Wiley-Interscience, pp. 215-258

ELLIOTT, W. P., and D. J. GAFFEN [1991], *On the Utility of Radiosonde Humidity Archives for Climate Studies*, Bull. Am. Meteorol. Soc., 72, 1507, 1991

- EMARDSON, T. R. [1998], *Studies of Atmospheric Water Vapor Using the Global Positioning System*, Chalmers University of Technology, Sweden, Technical Report No. 339
- ENGLAND M. N., R. A. FERRARE, S. H. MELFI, D. N. WHITEMAN, and T. A. CLARK [1992], *Atmospheric Water Vapor Measurements: Comparison of Microwave Radiometry and Lidar*, Journal of Geophysical Research, Vol 97, pp. 899-916, Jan. 20, 1992
- FEIGL, K. L., R. W. KING, TH. A. HERRING and M. ROTHACHER [1991], *A Scheme for Reducing the Effect of Selective Availability on Precise Geodetic Measurements from the Global Positioning System*, Geophysical Research Letters, 18, pp. 1289-1292, July 1991
- FLIEGEL, H. F., T. E. GALLINI, and E. R. SWIFT [1992], *Global Positioning System Radiation Force Model for Geodetic Applications*, Journal of Geophysical Research, Vol. 97, No. B1, pp. 559-568, January 10, 1992
- GABOR, M. [1997], *Remote Sensing of Water Vapor From GPS Receivers*, ASE 389P - Remote Sensing from Space, University of Texas at Austin, Spring 1997 mid-term project; <http://www.ae.utexas.edu/courses/ase389/midterm/gabor/gabor.html>
- GELB, A. [1992], *Applied Optimal Estimation*, The MIT Press, 1992, ISBN 0-262-200279
- GENDT, G. [1997], *SINEX_TRO - Solution (Software/technique) INdependent EXchange Format for combination of TROpospheric estimates Version 0.01* (March 01, 1997), ftp://cddisa.gsfc.nasa.gov/pub/formats/zpd_sinex.format
- GOAD, C. C. and A. MUELLER [1998], *An Automated Procedure for Generating an Optimum Set of Independent Double Difference Observables using GPS Carrier Phase Measurements*, Manuscripta Geodaetica (1998) 13:365-369
- GEORGIADOU, Y. and A. KLEUSBERG [1988], *On Carrier Signal Multipath Effects in Relative GPS Positioning*, Manuscripta Geodaetica (1988) 13:173-179, Springer-Verlag
- GURTNER, W. [1998], *RINEX: The Receiver Independent Exchange Format Version 2*, Astronomical Institute, University of Berne; <ftp://cddisa.gsfc.nasa.gov/pub/formats/rinex2.format>
- HAAS, R. [1996], *Untersuchungen zu Erddeformationsmodellen für die Auswertung von geodätischen VLBI-Messungen*, Dissertationen - Heft Nr. 466, Verlag des Instituts für Angewandte Geodäsie, Frankfurt am Main
- HANSSEN, R. [1998], *Atmospheric Heterogeneities in ERS Tandem SAR Interferometry, Chapter 2*, page 8-24, DEOS Report no. 98.1, Delft University Press

HEISKANEN, W. A., and H. MORITZ [1993], *Physical Geodesy*, Reprint, Institute of Physical Geodesy, Technical University of Graz, Steyrergasse 17, A-8010 Graz, Austria, 1993

HERRING, TH. A., J. L. DAVIS, and I. I. SHAPIRO [1990], *Geodesy by Radio Interferometry: The Application of Kalman Filtering to the Analysis of Very Long Baseline Interferometry Data*, Journal of Geophysical Research, Vol. 95, No. B8, pp. 12,561-12,581, August 10, 1990

HERRING, T. A. [1992], *Modeling Atmospheric Delays in the Analysis of Space Geodetic Data*, in: DE MUNCK, J. C and SPOELSTRA, T. A. TH (eds.), *Refraction of Transatmospheric Signals in Geodesy*, Proceedings of the Symposium, Netherlands Geodetic Commission, Publications on Geodesy, New Series, Number 36, The Hague, The Netherlands, May 19-22, 1992

HOFFMANN-WELLENHOF, B., H. LICHTENEGGER, and J. COLLINS [1993], *GPS - Theory and Practice*, 2nd Edition, Springer-Verlag Wien, New York, ISBN 3-211-82364-6

HOHL, R. (ed.) [1981], *Die Entwicklungsgeschichte der Erde*, Brockhaus Nachschlagewerke Geologie, 7. Auflage, VEB F. A. Brockhaus Verlag, Leipzig, DDR, 1981, ISBN 3-325-00100-9

HOKE, J. E., and R. A. ANTHES [1976], *The Initialization of Numerical Models by a Dynamic-Initialization Technique*, Monthly Weather Review, 104, pp. 1551-1556

HONEYWELL [1999], *Honeywell Hvac - Moisture Tutorial*, http://content.honeywell.com/building/components/Hycal_Html/moist.asp

HÖPCKE, W. [1980], *Fehlerlehre und Ausgleichsrechnung*, De Gruyter, Berlin, ISBN 3-11-007514-8, 1980

ICD-GPS-200 [1997], *ICD-GPS-200 - Navstar GPS Space Segment/Navigation User Interfaces*, Revision C, Initial Release, ARINC Research Corporation, El Segundo, CA , USA, 25 September 1997

IFADIS, I. [1986], *The Atmospheric Delay of Radio Waves: Modeling the Elevation Dependence on a Global Scale*, Technical Report no. 38L, School of Electrical and Computer Engineering, Chalmers University of Technology, Göteborg, Sweden, 1986

IGS [1997], *IGS Annual Report 1997*, International GPS Service for Geodynamics, JPL 400-786 10/98, also accessible via WWW, see URL <http://igscb.jpl.nasa.gov>

KANAMITSU, M., J. C. ALPERT, K. A. CAMPANA, P. M. CAPLAN, D. G. DEAVEN, M. IREDELL, B. KATZ, H.-L. PAN, J. SELA, AND G. H. WHITE [1991], *Recent Changes Implemented into the Global Forecast System at NMC*, Weather and Forecasting, Vol. 6, pp. 425-435, 1991

- KANIUTH, K., D. KLEUREN, and W. SCHLUETER [1998], *Elevationsabhaengige Phasenzentrumsvariationen geodaetischer GPS-Antennen*, Zeitschrift für Vermessungswesen (ZfV) 10/1998, pp. 319-325, Dt. Verein für Vermessungswesen e.V.
- KING, R. [2000], *SVNAV.DAT - Satellite Information Table of GAMIT/GLOBK (GAMIT Release 10.0 from December 2000)*, MIT, USA
- KLOBUCHAR, J. A. [1996], *Ionospheric Effects on GPS*, in: SPILKER and PARKINSON, *GPS Theory and Applications*; Vol. I, Progress in Astronautics and Aeronautics, Vol. 163, pp. 485-546, 1996
- KUO, Y.-H., Y.-R. GUO and E. R. WESTWATER [1993], *Assimilation of Precipitable Water Measurements into a Mesoscale Numerical Model*, Monthly Weather Review, pp. 1215-1238
- LANDAU, H. [1988], *Zur Nutzung des Global Positioning Systems in Geodäsie und Geodynamik: Modellbildung, Software-Entwicklung und Analyse*, Schriftenreihe Studiengang Vermessungswesen, Universität der Bundeswehr München
- LANGLEY, R. B. [1993], *The GPS Observables*, GPS World, April 1993, pp. 52-59
- LEINEN, ST. [1997], *Hochpräzise Positionierung über große Entfernungen und in Echtzeit mit dem Global Positioning System*, Deutsche Geodätische Kommission, ISBN 3 7696 9512 7
- LEONARD Jr., R. B. [1998], *NOAA/NGS Analysis Strategy Summary - International GPS Service*, National Geodetic Survey, NGS, USA, http://www.ngs.noaa.gov/GPS/noaa_acn.html
- MADER, G. L. [1999], *GPS Antenna Calibration at the National Geodetic Survey*, GPS Solutions, Vol. 3, No. 1, Summer 1999, Wiley & Sons
- MANIATIS, A. [1989], *Auswertung von GPS-Phasenbeobachtungen*, Mitteilungen aus den Geodät. Instituten der RFW Universität Bonn, ISSN 0723-4325
- MARINI, J. W. [1972], *Correction of Satellite Tracking Data for an Arbitrary Tropospheric Profile*, Radio Science, Volume 7, Number 2, pp. 223-231, February 1972
- MARINI, J. W., and C. W. MURRAY [1973], *Correction of Laser Range Tracking Data for Atmospheric Refraction at Elevations above 10 Degrees*, NASA report X-591-73-351, Goddard Space Flight Center, 1973
- MCCARTHY, D. D. [1996], *IERS Technical Note 21, IERS Conventions*, U.S. Naval Observatory, <http://maia.usno.navy.mil/conventions.html>
- MELBOURNE, W. et al [1983], *Project Merit Standards*, U. S. Naval Observatory, Washington D. C., Dec. 27, 1983

MELBOURNE, W. G. ET AL [1994], *The Application of Spaceborne GPS to Atmospheric Limb Sounding and Global Change Monitoring*, JPL Publication 94-18, NASA/JPL, Pasadena, CA, April 1994

MENDES, V. B. and R. B. LANGLEY [1998a], *Optimization of Tropospheric Delay Mapping Function Performance for High-Precision Geodetic Applications*, Proceedings of DORIS Days, 27-29 April 1998, Toulouse, France

MENDES, V. B. and R. B. LANGLEY [1998b], *Tropospheric Zenith Delay Prediction Accuracy for Airborne GPS High-Precision Positioning*, Proceedings of The Institute of Navigation 54th Annual Meeting, Denver, CO, U.S.A., 1-3 June; pp. 337-347

MENDES, V. B., G. PRATES, L. SANTOS, and R. B. LANGLEY [2000], *An Evaluation of the Accuracy of Models of the Determination of the Weighted Mean Temperature of the Atmosphere*, Proceedings of ION, 2000 National Technical Meeting, January 26-28, 2000, Pacific Hotel Disneyland, Anaheim, CA

MERVART L., G. BEUTLER, M. ROTHACHER, and U. WILD [1994], *Ambiguity resolution strategies using the results of the International GPS Geodynamics Service (IGS)*, Bulletin Géodésique, Springer-Verlag, (1994) 68:29-38

MIDDLETON, W. E. K., and A. F. SPILHAUS [1953], *Meteorological Instruments*, University of Toronto Press, Toronto, Ont., Canada, 1953.

MITTON, S. (ed.) [1977], *The Cambridge Encyclopaedia of Astronomy*, Jonathan Cape Ltd., London 1977

MOCKLER, S. B. [1995], *Water Vapor in the Climate System*, Special Report, American Geophysical Union (AGU), 2000 Florida Ave., N.W., Washington, DC 20009, ISBN 0-87590-865-9, December 1995; WWW: http://www.agu.org/sci_soc/mockler.html

MOPS [1998], *Minimum Operational Performance Standards for Global Positioning System/Wide Area Augmentation System Airborne Equipment*, Document No. RTCA/DO-229A, June 8, 1998, prepared by SC-159

NAITO, I., Y. HATANAKA, N. MANNOJI, R. ICHIKAWA, S. SHIMADA et al [1998], *Global Positioning System Project to Improve Japanese Weather, Earthquake Predictions*, in: EOS, Transactions, American Geophysical Union, Vol. 79, No. 26, June, 1998

NASA, NIMA [1998], *EGM96 - The NASA GSFC and NIMA Joint Geopotential Model*, <http://cddis.gsfc.nasa.gov/926/egm96/contents.html>

VAN NEE, R. D. J. [1992], *Multipath Effects on GPS Code Phase Measurements*, Navigation: Journal of the Institute of Navigation, Vol. 39, No. 2, Summer 1992, 177-190

- OLTMANS, S. J., and D. J. HOFMANN [1995], *Increase in Lower-Stratospheric Water Vapour at a Mid-Latitude Northern Hemisphere Site from 1981 to 1994*, *Nature*, 374, 146, 1995
- OWENS, J. C. [1967], *Optical Refractive Index of Air: Dependence on Pressure, Temperature and Composition*, *Applied Optics*, 6, 51-58, 1967
- PARRISH, D. F., and J. C. DERBER [1992], *The National Meteorological Center's Spectral Statistical-Interpolation Analysis System*, *Monthly Weather Review*, Vol. 120, pp. 1747-1763, August, 1992
- PELZER, H. (ed.) [1985], *Geodätische Netze in der Landes- und Ingenieurvermessung, Vermessungswesen bei K. Wittwer*, Stuttgart, 1985, out of print
- PELZER, H. [1996], *Analysis of Stochastic Processes*, Lecture Notes, Geodetic Institute, University of Hannover, Germany, 1996/97
- PRABHAKARA, C., D. A. SHORT, and B. E. VOLMER [1985], *El Niño and Atmospheric Water Vapor: Observations from Nimbus 7 SMMR*, *J. Climatol. Appl. Meteorol.*, 24, 1311, 1985
- PRESS, W. H., S. A. TEUKOLSKY, W. T. VETTERLING, and B. P. FLANNERY [1992], *Numerical Recipes in C : The Art of Scientific Computing*, Second Edition, Cambridge University Press, ISBN 0-521-43108-5
- RAY, J. K. and M. E. CANNON [1999], *Mitigation of Static Carrier-Phase Multipath Effects Using Multiple Closely Spaced Antennas*, *Navigation: Journal of the Institute of Navigation*, Vol. 46, No. 2, pp. 193-201, Summer 1999
- REMONDI, B. W. [1985], *Modeling the GPS Carrier Phase for Geodetic Applications*, in: GOAD, C. (ed.), *Proceedings of the First International Symposium on Precise Positioning with the Global Positioning System*, Vol. 1, National Geodetic Survey, Rockville, Maryland, pp. 357-361
- REMONDI, B. W. [1989], *Extending the National Geodetic Survey Standard GPS Orbit Formats*, NOAA Technical Report NOS 133 NGS 46; Rockville, MD, see also ftp://igscb.jpl.nasa.gov/igscb/data/format/sp3_docu.txt
- REMONDI, B. W. [1991], *The NGS GPS Orbital Formats*, NOAA, National Geodetic Survey, Coast and Geodetic Survey, August 1991, <ftp://igscb.jpl.nasa.gov/igscb/data/format/sp3.format>
- RIND, D., E.-W. CHIOU, W. CHU, S. OLTMANS, J. LERNER, J. LARSEN, M. P. MCCORMICK, and L. MCMASTER [1993], *Overview of the Stratospheric Aerosol and Gas Experiment II Water Vapor Observations: Method, Validation, and Data Characteristics*, *J. Geophys. Res.*, 98, 4835, 1993

ROCKEN C., F. S. SOLHEIM, R. H. WARE, M. EXNER, D. MARTIN, and M. ROTHACHER [1997], *Application of IGS Data to GPS Sensing of the Atmosphere for Weather and Climate Research*, found in WWW under http://www.unavco.ucar.edu/docs/science/pos_pap/ (apparently removed/not found on 03 Oct 2000)

ROTHACHER, M. and L. MERVART (editors) [1996], *Documentation of the Bernese GPS Software Version 4.0*, User Guide, Astronomical Institute, University of Berne, Sidlerstrasse 5, CH-3012 Berne, Switzerland, September 1996

ROTHACHER, M. [2000], *Personal E-Mail Communication, Response to Subject "GPS Orbits"*, 29.03.2000, 18.04.2000, Munich University of Technology, Germany

SAASTAMOINEN, J. [1972], *Atmospheric Correction for the Troposphere and Stratosphere in Radio Ranging of Satellites*, in: HENRIKSEN, *The Use of Artificial Satellites for Geodesy*, Geophys. Monogr. Ser., vol. 15, pp. 247-251, AGU, Washington, D.C., 1972

SCHAER, ST., W. GURTNER, and J. FELTENS [1998], *IONEX: The IONosphere Map Exchange Format Version 1*, <ftp://cddis.gsfc.nasa.gov/pub/formats/ionex1.pdf>

SCHENEWERK, M. [2000], *Personal e-mail communication, subject "Reference for Satellite Positions"*, response on 2000/04/17, National Geodetic Survey, NGS, USA, see also: LEONARD Jr. [1998]

SCHERNECK, H. G. [1983], *Crustal Loading Affecting VLBI Sites*, University of Uppsala, Institute of Geophysics, Dept. of Geodesy, Report No. 20, Uppsala, Sweden

SCHUELER, T. [1998a], *On the Interpolation of SP3 Orbit Files*, Technical Report IFEN-TropAC-TN-002-01 (internal, not published), Institute of Geodesy and Navigation, University FAF Munich, Germany, October 1998, <http://137.193.32.1/Forschung/TropAC/docs/ORB.PDF>

SCHUELER, T. [1998b], *On the Impact of Solid Earth Tides and Ocean Loading on Station Displacements*, Technical Report IFEN-TropAC-TN-003-01 (internal, not published), Institute of Geodesy and Navigation, University FAF Munich, Germany, October 1998, <http://137.193.32.1/Forschung/TropAC/docs/TIDES.PDF>

SCHUELER, T. [1998c], *Preliminary Analysis of Stochastic Properties of Tropospheric Zenith Path Delay Time Series*, Technical Report IFEN-TropAC-TN-004-02, Institute of Geodesy and Navigation, University FAF Munich, Germany, November 1998, available via <http://ifn.bauv.unibw-muenchen.de/Forschung/TropAC/docs/TN004.PDF>

SCHUELER, T., G. W. HEIN, and B. EISSFELLER [1999a], *GNSS Zenith Wet Delay Estimation Considering Their Stochastic Properties*, Proceedings of GNSS '99, 3rd European Symposium, Genua, Italy, Oct. 5-8, 1999, <http://ifn.bauv.unibw-muenchen.de/Forschung/TropAC/docs/gnss99/index.html>

SCHUELER, T., G. W. HEIN, and B. EISSFELLER [2000a], *On the Use of Numerical Weather Fields for Troposphere Delay Estimation in Wide Area Augmentation Systems*,

Proceedings of GNSS 2000, Royal Institute of Navigation, Edinburgh, Scotland, May 1-4, 2000, <http://ifn.bauw.unibw-muenchen.de/Forschung/TropAC/docs/GNSS2000.PDF>

SCHUELER, T., G. W. HEIN, and B. EISSFELLER [2000b], *Towards an Optimal Strategy for GPS Wet Delay Kalman Filtering*, Proceedings of IAIN 2000/ION Annual Meeting, San Diego, Catamaran Hotel, 26-28 June 2000

SCHUELER, T., G. W. HEIN, and B. EISSFELLER [2000c], *Improved Tropospheric Delay Modeling Using an Integrated Approach of Numerical Weather Models and GPS*, Proceedings of ION GPS 2000, The Institute of Navigation, Salt Lake City, Utah, USA, 19-22 September 2000

SEEBER, G. [1989]; *Satellitengeodäsie*, Verlag de Gruyter, Berlin - New York, 1993

SEEBER, G. [1993], *Satellite Geodesy - Foundations, Methods, and Applications*, Berlin; New York: de Gruyter, 1993, ISBN 3-11-012753-9

SELA, J. G. [1980], *Spectral Modeling at the National Meteorological Center*, Monthly Weather Review, Vol. 108, pp. 1279-1292, September 1980

SOLBRIG, P. [2000], *Untersuchungen über die Nutzung numerischer Wettermodelle zur Wasserdampfbestimmung mit Hilfe des Global Positioning Systems*, Diploma Thesis, Institute of Geodesy and Navigation, University FAF Munich, Germany, Feb. 2000

SPILKER, J. J. [1996], *Tropospheric Effects on GPS*, in: SPILKER and PARKINSON (eds.), *GPS Theory and Applications*; Vol. I, Progress in Astronautics and Aeronautics, Vol. 163, pp. 517-546, 1996

STARR, D. O., and S. H. MELFI (eds.) [1991], *The Role of Water Vapor in Climate: A Strategic Research Plan for the Proposed GEWEX Water Vapor Project (GVaP)*, NASA Conf. Publ., CP-3120, 50 pp., 1991

STAUFFER, D. R., and N. L. SEAMAN [1990], *Use of Four-Dimensional Data Assimilation in a Limited-Area Mesoscale Model. Part I: Experiments with Synoptic-Scale Data*, Monthly Weather Review, 118, pp. 1250-1277

STELZER, D. and H. B. PAPO [1994], *Kalman Filter, Smoothing and Datum of Dynamic Reference Systems*, manuscripta geodaetica (1994) 19:172-179, Springer-Verlag

SUSSKIND, J., J. ROSENFELD, D. REUTER, and M. T. CHAHINE [1984], *Remote Sensing of Weather and Climate Parameters from HIRS2/MSU on TIROS-N*, J. Geophys. Res., 89, 4677, 1984

THAYER, G. D. [1974], *An Improved Equation for the Radio Refractive Index of Air*, Radio Science, Vol. 9, pp. 803-807, 1974

THORNTON, C. L. and G. J. BIERMANN [1978], *Filtering and Error Analysis via the UDU^T Covariance Factorization*, IEEE Transactions of Automatic Control, Vol. AC-23, No. 5, pp. 901-907

TRANQUILLA, J. M. and J. P. CARR [1990], *GPS Multipath Field Observations at Land and Water Sites*, Navigation: Journal of the Institute of Navigation, Vol. 37, No. 4, Winter 1990-91, 393-414

UMWELTBUNDESAMT [1998], *Treibhauseffekt*, online resources, Federal Secretary of the Environment, <http://umweltbundesamt.de/uba-info-daten/daten/treibhauseffekt.htm>

WITTE, B. and H. SCHMIDT [1991], *Vermessungskunde und Grundlagen der Statistik für das Bauwesen*, 2., erweiterte Auflage, Konrad Wittwer Verlag, ISBN 3-87919-149-2

WU, J. T., S. C. WU, G. A. HAJJ, W. I. BERTIGER, and S. M. LICHTEN [1993], *Effects of Antenna Orientation on GPS Carrier Phase*, Manuscripta Geodaetica (1993) 18:91-98, Springer-Verlag

WÜBBENA, G. [1991], *Zur Modellierung von GPS-Beobachtungen für die hochgenaue Positionsbestimmung*, Wissenschaftliche Arbeiten der Fachrichtung Vermessungswesen der Universität Hannover, Nr. 168, Hannover 1991

Appendices

Appendix I: Process Noise Parameters

The following table gives zenith wet delay random walk process noise parameters for selected IGS tracking stations. The results are based on an analysis of the TropAC database using zenith neutral delays provided by the IGS analysis centers. The wet delay was derived by separating the hydrostatic component from the total value. The needed pressure records were either taken from available surface measurements if available or extracted from the NCEP GDAS 1° x 1° numerical weather model if not. The process noise value given in the table is processed by a linear fit to the first day of the auto-covariance function of the zenith wet delay time series. The standard deviation indicated by " $\pm x.x$ " describes the precision of this fit. The analyzed time interval depends on the availability of both IGS troposphere products and surface pressure. For some sites records beginning at 03/1997 were used and the final records come from 03/2000.

STOCHASTIC PROPERTIES OF ZENITH WET DELAY TIME SERIES

SITE	POSITION OF SITE			MEAN	SIGMA	SAMPLES		PRO.-NOISE
ALBH	48.4,	-123.5,	51	113.5	35.2	19224/	18	4.8 \pm 0.4
ALGO	46.0,	-78.1,	237	135.4	66.9	18360/	11	3.8 \pm 0.3
ALIC	-23.7,	133.9,	588	138.0	77.1	6696/	12	5.3 \pm 0.5
AMC2	38.8,	-104.5,	1930	80.4	48.7	6672/	6	3.1 \pm 0.2
ANKR	39.9,	32.8,	939	93.1	43.7	5880/	10	4.6 \pm 0.4
AOML	25.7,	-80.2,	28	211.4	78.8	17976/	12	6.5 \pm 0.5
ARTU	56.4,	58.6,	254	61.8	34.5	4776/	9	3.7 \pm 0.3
AUCK	-36.6,	174.8,	98	128.3	45.6	23016/	41	4.0 \pm 0.3
BAHR	26.2,	50.6,	11	131.4	44.4	23040/	36	5.7 \pm 0.5
BOGO	52.5,	21.0,	119	112.7	56.8	6696/	9	6.6 \pm 0.5
BOR1	52.3,	17.1,	89	109.1	54.1	6696/	10	6.1 \pm 0.5
BRMU	32.4,	-64.7,	23	195.4	77.7	6696/	8	6.0 \pm 0.5
BRUS	50.8,	4.4,	104	111.1	49.5	6696/	10	5.2 \pm 0.4
CAGL	39.1,	9.0,	192	118.8	49.3	6672/	9	5.8 \pm 0.5
CEDU	-31.9,	133.8,	154	116.7	53.2	6696/	15	3.9 \pm 0.3
CHAT	-44.0,	-176.6,	48	113.3	41.5	23040/	36	3.6 \pm 0.3
CHUR	58.8,	-94.1,	29	71.2	48.2	6696/	8	4.3 \pm 0.3
DRAO	49.3,	-119.6,	558	88.3	36.0	6696/	10	3.6 \pm 0.3
DUBO	50.3,	-95.9,	275	88.2	50.4	6696/	8	6.3 \pm 0.5
FLIN	54.7,	-102.0,	343	76.9	48.2	6696/	8	6.2 \pm 0.5
GILB	32.5,	35.4,	485	91.3	29.5	6696/	16	4.2 \pm 0.3
GLSV	50.4,	30.5,	201	102.7	60.3	6696/	8	5.2 \pm 0.4
GOPE	49.9,	14.8,	547	105.3	46.5	6696/	10	6.1 \pm 0.5
GOL2	35.4,	-116.9,	1018	68.1	43.8	5880/	22	3.1 \pm 0.3
Goug	-40.3,	-9.9,	58	100.8	36.9	4560/	48	4.8 \pm 0.3
GRAS	43.8,	6.9,	1269	74.2	44.0	5904/	8	4.0 \pm 0.3
GRAZ	47.1,	15.5,	491	105.3	57.2	6624/	7	6.0 \pm 0.5
HARK	-25.9,	27.7,	1530	110.8	58.3	5688/	8	2.6 \pm 0.2
HFLK	47.3,	11.4,	2336	49.7	28.5	6696/	9	4.0 \pm 0.3
HOB2	-42.8,	147.4,	45	106.7	35.2	6696/	27	4.4 \pm 0.4
HOFN	64.3,	-15.2,	18	89.2	39.2	6432/	10	4.6 \pm 0.4
HRAO	-25.9,	27.7,	1389	116.3	62.2	6576/	8	2.0 \pm 0.2
IRKT	52.2,	104.3,	541	76.8	63.4	6696/	7	4.9 \pm 0.4
JOZE	52.1,	21.0,	110	107.8	56.0	6696/	10	6.5 \pm 0.5
JPLM	34.2,	-118.2,	458	92.1	44.5	6696/	22	4.3 \pm 0.4
KABR	33.0,	35.1,	82	115.4	39.7	6696/	10	5.1 \pm 0.4

SITE	POSITION OF SITE			MEAN	SIGMA	SAMPLES		PRO. - NOISE
KARR	-21.0,	117.1,	117	170.8	89.9	6696/	9	5.0 ± 0.4
KATZ	33.0,	35.7,	324	109.8	31.7	4920/	22	4.3 ± 0.3
KELY	67.0,	-50.9,	198	59.6	33.4	6600/	8	3.6 ± 0.3
KERG	-49.4,	70.3,	33	69.5	30.8	5952/	20	3.5 ± 0.3
KOSG	52.2,	5.8,	54	111.5	46.2	6696/	10	5.4 ± 0.4
LAMA	53.9,	20.7,	158	102.9	53.4	6696/	10	6.3 ± 0.5
LPGS	-34.9,	-57.9,	14	135.6	52.3	6696/	16	4.1 ± 0.3
MAC1	-54.5,	158.9,	14	75.0	25.8	6696/	67	4.3 ± 0.4
MAD2	40.4,	-4.2,	777	85.6	35.4	6024/	11	4.8 ± 0.4
MAG0	59.6,	150.8,	345	57.3	46.7	6624/	7	2.7 ± 0.2
MAS1	27.8,	-15.6,	155	111.7	43.5	5016/	10	6.4 ± 0.5
MATE	40.6,	16.7,	490	107.1	46.7	6696/	9	5.9 ± 0.5
MAW1	-67.6,	62.9,	30	18.4	14.1	6624/	8	0.6 ± 0.0
MCM4	-77.8,	166.7,	151	17.7	9.0	6696/	12	1.5 ± 0.1
MDVO	56.0,	37.2,	239	104.7	53.9	6696/	7	5.0 ± 0.4
MEDI	44.5,	11.6,	10	129.5	63.3	6696/	7	6.3 ± 0.5
NICO	35.1,	33.4,	162	102.9	42.8	4896/	14	6.2 ± 0.5
NLIB	41.8,	-91.6,	240	119.0	72.4	6600/	8	5.6 ± 0.5
NOTO	36.9,	15.0,	85	134.0	50.9	6696/	8	6.0 ± 0.5
NRC1	45.5,	-75.6,	116	129.9	71.1	19224/	11	2.4 ± 0.2
NRC2	45.5,	-75.6,	116	104.9	63.1	4464/	13	7.1 ± 0.6
NYA1	78.9,	11.9,	48	52.1	33.6	6696/	8	3.5 ± 0.3
NYAL	78.9,	11.9,	42	51.6	31.7	6696/	8	4.1 ± 0.3
ONSA	57.4,	11.9,	9	100.0	48.4	6672/	10	5.9 ± 0.4
PENC	47.8,	19.3,	248	109.6	58.0	6696/	8	6.1 ± 0.5
PERT	-31.8,	115.9,	45	113.2	48.3	6696/	19	5.0 ± 0.4
PETP	53.1,	158.6,	188	76.9	54.0	6696/	7	3.9 ± 0.3
PIE1	34.3,	-108.1,	2370	66.0	46.4	6528/	7	2.2 ± 0.2
POL2	42.7,	74.7,	1755	59.0	37.3	5808/	8	5.0 ± 0.4
POTS	52.4,	13.1,	104	98.6	46.8	27192/	23	2.9 ± 0.2
RAMO	30.6,	34.8,	869	70.3	26.0	6696/	13	3.5 ± 0.3
RIOG	-53.8,	-67.8,	20	86.7	33.2	6696/	18	4.4 ± 0.4
SCH2	54.8,	-66.8,	518	72.0	48.8	6696/	8	4.3 ± 0.4
SELE	43.2,	77.0,	1385	73.9	47.1	6648/	7	5.5 ± 0.4
SFER	36.5,	-6.2,	40	120.1	43.9	6696/	11	5.5 ± 0.4
STJO	47.6,	-52.7,	143	97.0	52.7	19224/	17	2.4 ± 0.2
SUTH	-32.4,	20.8,	1763	64.7	35.7	6576/	14	2.5 ± 0.2
TELA	32.1,	34.8,	39	125.3	34.2	4920/	13	5.1 ± 0.4
THU1	76.5,	-68.8,	38	45.9	27.4	6696/	7	3.5 ± 0.3
TID2	-35.4,	149.0,	646	103.8	45.7	6048/	15	2.3 ± 0.2
TOUL	43.6,	1.5,	158	127.0	56.5	6312/	8	5.3 ± 0.4
TIXI	71.6,	128.9,	54	49.9	42.3	6696/	7	4.2 ± 0.3
TRO1	69.7,	18.9,	107	80.8	39.9	6696/	8	3.7 ± 0.3
TOW2	-19.3,	147.1,	30	217.0	85.4	6696/	9	6.6 ± 0.5
TROM	69.7,	18.9,	101	88.8	35.9	5448/	10	3.6 ± 0.3
USNO	38.9,	-77.1,	82	129.3	75.3	19368/	15	4.8 ± 0.4
VESL	-71.7,	-2.8,	850	15.3	9.0	4632/	29	1.5 ± 0.1
VILL	40.4,	-4.0,	595	97.9	41.1	6696/	10	4.4 ± 0.4
WHIT	60.8,	-135.2,	1420	48.3	29.2	6696/	8	2.7 ± 0.2
WILL	52.2,	-122.2,	1110	67.0	34.7	6696/	8	3.3 ± 0.3
WSRT	52.9,	6.6,	41	113.2	47.2	6696/	10	5.4 ± 0.4
WTZR	49.1,	12.9,	619	98.0	42.3	26040/	17	3.7 ± 0.3
WUHN	30.5,	114.4,	40	202.1	121.1	6528/	7	9.1 ± 0.7
YAKZ	62.0,	129.7,	105	67.1	55.8	6696/	7	3.8 ± 0.3
YAR1	-29.0,	115.3,	267	122.6	57.2	6696/	14	3.1 ± 0.2
YELL	62.5,	-114.5,	208	75.3	38.9	19224/	11	0.5 ± 0.0
ZIMM	46.9,	7.5,	908	89.6	41.2	25152/	16	4.4 ± 0.4
DAEJ	36.4,	127.4,	92	140.9	109.8	6696/	6	5.0 ± 0.4
KIRU	67.9,	21.0,	362	71.4	39.1	6696/	8	3.8 ± 0.3
OBER	48.1,	11.3,	596	92.7	45.1	19440/	12	3.7 ± 0.3
UPAD	45.4,	11.9,	39	127.6	70.4	6624/	7	6.6 ± 0.5

SITE	POSITION OF SITE			MEAN	SIGMA	SAMPLES	PRO.-NOISE
URUM	43.8,	87.6,	923	81.1	56.3	6696/ 7	5.0 ± 0.4
USUD	36.1,	138.4,	1466	93.3	73.9	6672/ 7	3.6 ± 0.3
WES2	42.6,	-71.5,	114	118.4	71.3	16008/ 13	5.0 ± 0.4
BSHM	32.8,	35.0,	205	110.2	33.4	5088/ 15	4.3 ± 0.3
NOUM	-22.3,	166.4,	23	215.2	66.5	6696/ 17	5.0 ± 0.4
PIMO	14.6,	121.1,	52	324.7	49.8	6600/ 17	8.6 ± 0.7
BISH	42.9,	74.6,	775	86.7	47.8	6696/ 8	5.4 ± 0.4
DARW	-12.8,	131.1,	75	249.6	100.7	6696/ 6	8.4 ± 0.7
JAMA	17.9,	-76.8,	13	181.0	36.2	2664/ 31	6.5 ± 0.5
NSSP	40.2,	44.5,	1173	137.4	24.1	1080/ 19	5.6 ± 0.4
SOL1	38.3,	-76.5,	17	154.1	83.5	11496/ 11	6.8 ± 0.5
USNA	39.0,	-76.5,	7	217.8	63.8	2328/121	6.9 ± 0.5
WSLR	50.1,	-122.9,	926	108.6	25.3	2328/ 21	3.6 ± 0.3
AMUN	-90.0,	139.2,	2846	12.8	5.5	456/ 14	0.8 ± 0.1
PALM	-64.8,	-64.1,	15	50.5	17.3	480/ 12	3.0 ± 0.2
GOLD	35.4,	-116.9,	1018	60.2	15.7	648/ 14	2.9 ± 0.2
MADR	40.4,	-4.2,	777	108.4	25.2	624/ 17	4.0 ± 0.3
TIDB	-35.4,	149.0,	646	66.5	22.8	648/ 32	3.3 ± 0.3
AMCT	38.8,	-104.5,	1930	117.7	21.9	600/ 28	3.7 ± 0.3

MEAN SIGNAL.....: 104.0 mm

MEAN PROCESS NOISE: 4.8 mm/√h

Table A-1 - Mean zenith wet delays (MEAN), their variability (SIGMA, standard deviation) and random walk parameters (PRO.-NOISE) with precision of fit in unit of [mm/√h]. The ZWD time series is treated as random walk stochastic process. The position of the IGS tracking stations is given by latitude, longitude [°, decimal] and orthometric height [m]. The number of original samples as well as the effective number are given. The effective number of samples takes auto-correlation into account. The smaller this number is in comparison to the original number, the higher the time series is auto-correlated. (last update: 2000/03/15)

The reader may also refer to section 3.3.3.2 for further background information and an approximation function for the derivation of process noise values for an arbitrary site.

Appendix II: Conversion Coefficients for Mean Temperature

Linear regression coefficients for the conversion of surface temperature T_s [°C] into mean atmospheric temperature T_M [°C] for selected stations of the IGS tracking network are given below. The theory is discussed in section → 3.5.

RELATION BETWEEN SURFACE AND MEAN TEMPERATURE
- RESULTS FROM LINEAR REGRESSION ANALYSIS -

CONVERSION FUNCTION: $T_m = a + b \cdot T_s$ with temperature in [°C]

T R O P I C A L B E L T								
SITE	a [°C]	b [/]	sigma [°C]	f	r	Ts(min)	Ts(max)	Ts(mean)
BARB	9.6	0.185	1.5	513	0.13	24.7 ...	29.6	27.5
COCO	7.0	0.285	1.5	633	0.13	24.3 ...	28.5	26.5
CRO1	6.4	0.310	1.3	532	0.40	22.0 ...	29.7	26.4
DGAR	-4.9	0.651	0.9	340	0.45	24.7 ...	31.0	27.3
MKEA	-10.2	0.115	3.8	390	0.06	0.4 ...	9.6	6.2
RIOP	-7.4	0.748	0.9	345	0.65	8.3 ...	14.1	10.6
THTI	12.9	0.020	1.8	570	0.01	22.1 ...	28.5	25.8
TOW2	0.9	0.505	1.9	813	0.52	17.9 ...	31.2	24.5
YKRO	2.4	0.411	0.8	172	0.79	21.6 ...	32.6	25.4
ASC1	8.3	0.241	0.9	624	0.25	20.9 ...	26.8	24.1
BAKO	-2.9	0.582	0.7	262	0.71	23.2 ...	30.3	26.1
PIMO	-2.5	0.581	0.8	680	0.76	21.6 ...	30.8	26.4
JAB1	6.3	0.335	1.7	254	0.53	21.1 ...	36.4	27.8
BOGT	-5.8	0.639	0.8	304	0.56	9.0 ...	13.9	11.5
FORT	7.0	0.289	1.4	265	0.30	24.7 ...	31.2	27.8
KOUR	-4.0	0.648	0.9	118	0.70	24.2 ...	31.1	27.0
IISC	6.0	0.182	1.2	183	0.41	15.4 ...	30.4	22.5
AREQ	-3.5	0.366	1.8	398	0.33	9.5 ...	19.8	14.0
NTUS	-0.8	0.501	0.6	382	0.75	24.3 ...	30.6	26.5
DARW	2.4	0.442	2.1	718	0.52	17.6 ...	35.0	26.8
GUAM	36.2	-0.824	1.4	115	-0.32	25.5 ...	28.2	27.2
JAMA	1.7	0.509	1.4	350	0.38	22.8 ...	28.1	25.9
MALI	-0.4	0.536	1.3	267	0.63	22.9 ...	33.0	26.4
GALA	6.1	0.293	1.0	226	0.58	20.3 ...	29.0	23.8

TROPICAL BELT 0°-20° LAT MEAN VALUES: $r = 0.43$, $\sigma = 1.3$, $a = 2.9$, $b = 0.356$

S U B T R O P I C S								
SITE	a [°C]	b [/]	sigma [°C]	f	r	Ts(min)	Ts(max)	Ts(mean)
ALIC	-0.6	0.408	2.7	858	0.75	5.4 ...	39.0	22.3
AMC2	-10.5	0.737	2.5	897	0.94	-8.8 ...	30.8	12.0
ANKR	-8.9	0.800	2.5	692	0.96	-13.0 ...	35.6	13.2
AOML	-2.3	0.581	1.8	942	0.75	8.6 ...	33.2	25.4
AUCK	-5.8	0.667	1.9	849	0.77	7.0 ...	24.0	14.9
BAHR	-5.4	0.767	2.6	963	0.92	11.4 ...	45.3	27.8
BRMU	-8.8	0.847	1.7	821	0.90	10.3 ...	29.0	22.5
CAGL	-10.7	0.971	1.9	903	0.95	7.9 ...	33.4	18.0
CEDU	-1.1	0.407	2.9	851	0.71	6.2 ...	40.0	19.4
GILB	-10.3	1.048	3.2	922	0.92	3.3 ...	35.9	18.1
GOL2	-8.7	0.711	2.9	767	0.90	1.6 ...	36.0	18.9
HARK	-2.5	0.470	2.0	602	0.75	1.9 ...	27.4	16.6
HRAO	-2.8	0.512	1.9	725	0.78	2.9 ...	29.7	17.2
JPLM	-8.6	0.857	3.4	938	0.85	3.2 ...	35.2	19.8
KABR	-13.7	1.199	2.7	908	0.94	6.8 ...	35.6	20.9
KARR	2.3	0.428	2.4	801	0.65	13.8 ...	40.0	26.1
KATZ	-8.2	0.944	3.5	574	0.84	6.6 ...	37.1	23.5
KOKB	3.0	0.242	2.4	659	0.31	0.0 ...	26.2	15.2
LPGS	-6.2	0.738	2.6	663	0.89	1.2 ...	35.5	17.6
MAS1	-12.5	1.145	2.2	611	0.78	13.0 ...	23.7	18.9
MDO1	-9.4	0.737	3.3	843	0.84	-2.3 ...	31.0	15.2
MONP	-10.0	0.741	3.7	931	0.83	-3.8 ...	28.0	14.1
NICO	-13.1	1.091	1.7	655	0.97	4.2 ...	30.7	17.9
NOTO	-9.6	0.886	2.1	948	0.95	6.9 ...	39.3	20.1
PERT	-3.1	0.605	2.2	801	0.84	8.6 ...	35.7	18.9
PIE1	-10.9	0.760	2.8	897	0.91	-10.3 ...	29.3	12.2
RAMO	-8.7	0.970	3.2	847	0.91	0.5 ...	33.4	16.2
SANT	-10.9	0.992	2.0	636	0.94	-0.6 ...	28.7	14.8
SFER	-8.6	0.896	2.2	805	0.91	6.7 ...	32.7	18.6
SUTH	-7.6	0.617	3.1	642	0.78	-4.7 ...	24.9	12.1
SUWN	-10.3	0.919	2.2	476	0.98	-11.6 ...	32.4	13.1
TELA	-12.0	1.125	3.0	654	0.84	11.1 ...	37.6	24.2
TID2	-5.5	0.603	2.3	803	0.86	1.7 ...	32.6	14.3
USNO	-7.9	0.831	3.0	880	0.95	-13.1 ...	37.1	14.4

SITE	a [°C]	b [/]	sigma [°C]	f	r	Ts(min)	Ts(max)	Ts(mean)
WUHN	-9.2	0.848	2.6	727	0.96	-5.1 ...	34.5	16.5
YAR1	-1.5	0.553	2.3	799	0.83	7.2 ...	37.9	19.2
DAEJ	-10.3	0.917	2.3	717	0.98	-9.9 ...	31.7	13.1
USUD	-9.3	0.883	1.7	659	0.98	-14.0 ...	22.2	6.4
BSHM	-14.1	1.225	3.0	661	0.87	9.5 ...	35.6	23.0
ELAT	-4.6	0.760	3.1	486	0.86	10.3 ...	41.9	27.7
GODE	-8.1	0.846	2.7	623	0.96	-12.8 ...	39.2	15.1
LHAS	-12.4	0.818	2.5	492	0.95	-12.1 ...	22.9	4.2
NOUM	-8.5	0.857	2.2	790	0.62	18.2 ...	27.5	23.0
TSKB	-11.0	0.921	1.7	505	0.98	-3.0 ...	31.2	15.7
CIC1	-8.7	0.825	2.5	122	0.84	9.4 ...	31.3	17.2
CORD	-4.7	0.611	2.7	309	0.70	9.2 ...	32.1	22.1
XIAN	-4.6	0.640	2.2	316	0.81	6.1 ...	36.2	26.0
BJFS	-11.2	0.807	2.5	149	0.91	-15.8 ...	17.9	-0.0
INEG	-0.6	0.344	1.2	264	0.77	4.8 ...	28.4	18.8
STR1	-3.1	0.536	2.7	176	0.71	5.7 ...	31.3	17.6
KUNM	-6.3	0.670	1.8	384	0.92	-1.5 ...	27.6	13.3
SHAO	-9.8	0.907	2.2	282	0.97	-6.0 ...	30.3	10.0
QUIN	-7.3	0.691	3.0	262	0.87	0.7 ...	36.2	18.5
EISL	-7.6	0.824	1.6	233	0.77	14.5 ...	25.6	19.2
KIT3	-6.1	0.627	3.0	287	0.87	-2.2 ...	38.5	25.2
SOL1	-4.2	0.682	2.2	364	0.77	14.6 ...	36.8	25.1
USNA	-3.7	0.684	2.2	355	0.78	13.8 ...	34.1	24.3

SUBTROPICS 20°-40° LAT MEAN VALUES: r = 0.85, sigma = 2.5, a = -7.3, b = 0.767

T E M P E R A T E Z O N E								
SITE	a [°C]	b [/]	sigma [°C]	f	r	Ts(min)	Ts(max)	Ts(mean)
ALBH	-9.8	0.885	1.8	848	0.95	0.6 ...	29.3	11.4
ALGO	-9.2	0.849	2.4	903	0.98	-29.7 ...	29.0	6.7
ARTU	-9.7	0.792	1.8	596	0.97	-23.0 ...	21.8	-1.9
BOGO	-9.1	0.812	1.9	809	0.97	-12.6 ...	31.0	9.4
BOR1	-8.6	0.748	1.9	871	0.97	-11.2 ...	32.1	10.3
BRUS	-8.0	0.771	1.7	873	0.95	-4.4 ...	28.8	11.6
CHAT	-9.3	0.863	1.8	847	0.83	3.0 ...	23.0	11.9
CHUR	-9.6	0.815	2.2	885	0.98	-30.6 ...	28.4	-2.0
DRAO	-9.6	0.753	1.5	865	0.98	-6.7 ...	32.0	10.2
DUBO	-9.0	0.767	2.3	740	0.98	-25.4 ...	31.8	3.8
FLIN	-9.3	0.720	2.1	910	0.98	-28.9 ...	30.6	3.1
GLSV	-8.5	0.806	2.2	965	0.97	-16.4 ...	30.4	9.2
GOPE	-9.0	0.807	1.8	853	0.97	-12.5 ...	28.5	8.4
GOUG	-11.5	1.017	1.7	439	0.83	2.7 ...	16.2	10.3
GRAS	-9.5	0.881	1.8	739	0.96	-6.4 ...	21.8	9.4
GRAZ	-9.4	0.835	1.6	843	0.98	-11.3 ...	28.9	10.2
HERS	-7.1	0.733	1.9	955	0.91	-5.1 ...	26.5	11.1
HFLK	-9.8	0.935	2.2	922	0.95	-19.8 ...	14.1	1.0
HOB2	-6.9	0.689	1.8	896	0.83	5.3 ...	28.4	12.9
HOLB	-10.2	1.005	1.9	465	0.88	-1.0 ...	17.8	9.3
IRKT	-11.5	0.791	2.0	922	0.99	-32.2 ...	37.6	4.4
JOZE	-9.0	0.798	2.0	906	0.97	-12.4 ...	31.9	10.3
KERG	-11.8	1.266	1.8	571	0.87	-3.2 ...	11.3	3.4
KOSG	-8.5	0.789	1.6	812	0.96	-5.1 ...	28.7	11.5
LAMA	-9.4	0.824	1.7	836	0.97	-7.6 ...	29.6	9.5
MAC1	-12.0	1.194	1.8	644	0.83	-4.3 ...	9.9	5.0
MAD2	-6.8	0.689	2.3	781	0.93	-5.1 ...	33.3	13.8
MAG0	-11.1	0.861	1.8	802	0.99	-30.1 ...	23.4	-1.8
MATE	-7.8	0.777	2.4	880	0.94	-4.7 ...	32.5	14.7
MDVO	-9.5	0.800	1.8	784	0.98	-21.2 ...	30.5	7.3
MEDI	-8.7	0.826	1.8	934	0.97	-2.9 ...	32.5	16.0
NLIB	-7.7	0.831	2.4	812	0.97	-18.7 ...	34.6	10.7
NRC1	-9.4	0.868	2.3	885	0.98	-25.6 ...	30.1	7.9
NRC2	-9.5	0.871	2.2	488	0.98	-25.6 ...	30.1	8.2
ONSA	-10.3	0.874	1.6	879	0.97	-4.2 ...	26.0	10.5
PENC	-8.3	0.781	2.2	708	0.96	-11.2 ...	29.7	10.5
PETP	-11.0	0.906	1.6	712	0.99	-25.2 ...	25.7	1.0
POL2	-11.8	0.767	1.5	688	0.98	-16.5 ...	27.4	6.1
POTS	-8.7	0.750	1.9	806	0.96	-9.2 ...	32.6	10.3
PRDS	-10.7	0.772	1.9	612	0.96	-16.2 ...	27.5	5.2
RIOG	-9.9	0.659	1.4	698	0.87	-1.9 ...	20.1	7.4
SCH2	-10.0	0.847	1.8	891	0.99	-34.0 ...	27.5	-2.6
SELE	-11.7	0.683	1.6	672	0.98	-16.1 ...	31.5	9.9
SJDV	-7.6	0.753	1.8	374	0.95	-5.6 ...	29.1	14.1
STJO	-9.1	0.983	2.3	825	0.96	-13.9 ...	21.3	6.0
TOUL	-7.0	0.756	1.9	748	0.95	-3.0 ...	33.8	15.1
VILL	-6.7	0.694	2.3	810	0.93	-4.1 ...	36.3	15.8
WILL	-10.6	0.762	1.5	854	0.97	-13.5 ...	26.9	5.0
WSRT	-9.1	0.819	1.6	880	0.96	-3.0 ...	27.3	11.5
WTZR	-9.1	0.800	1.7	882	0.97	-11.8 ...	30.0	9.2
YSSK	-11.9	0.926	1.3	420	0.99	-14.7 ...	19.6	-0.7
ZECK	-10.5	0.890	1.7	608	0.98	-11.9 ...	25.2	5.6
ZIMM	-8.6	0.806	1.8	913	0.96	-11.5 ...	25.2	8.0

SITE	a [°C]	b [/]	sigma [°C]	f	r	Ts(min)	Ts(max)	Ts(mean)
NANO	-9.1	0.838	1.8	337	0.89	1.6 ...	28.0	16.3
OBER	-9.4	0.797	1.7	865	0.97	-11.8 ...	34.2	10.1
UPAD	-9.4	0.856	1.7	737	0.97	-4.1 ...	31.2	15.7
URUM	-10.8	0.653	2.1	706	0.97	-14.6 ...	36.1	11.1
WES2	-9.0	0.847	3.0	850	0.96	-19.4 ...	34.9	10.0
KSTU	-11.6	0.700	2.0	260	0.97	-20.1 ...	28.8	0.4
BISH	-10.8	0.704	1.5	601	0.98	-8.7 ...	34.5	11.1
ZWEN	-9.6	0.807	1.8	768	0.98	-21.5 ...	31.0	6.4
UCLU	-10.7	0.994	1.9	379	0.87	2.3 ...	22.4	14.6
NSSP	-1.8	0.425	1.7	170	0.72	12.8 ...	30.1	20.8
WSLR	-8.8	0.775	1.6	345	0.92	2.2 ...	24.8	12.2

TEMPERATE ZONE 40°-60° LAT MEAN VALUES: r = 0.95, sigma = 1.9, a = -9.4, b = 0.817

P O L A R Z O N E

SITE	a [°C]	b [/]	sigma [°C]	f	r	Ts(min)	Ts(max)	Ts(mean)
BILI	-10.8	0.783	1.5	189	0.98	-30.9 ...	-0.6	-16.3
DAV1	-12.9	0.814	1.3	545	0.97	-24.3 ...	1.7	-9.0
HOFN	-12.2	1.058	1.3	656	0.97	-9.3 ...	18.4	6.6
KELY	-11.1	0.952	1.4	679	0.99	-25.8 ...	13.3	-2.6
MAW1	-12.3	0.866	1.2	716	0.98	-26.4 ...	0.7	-11.7
MCM4	-12.5	0.823	1.2	693	0.98	-29.6 ...	-1.4	-14.4
NYA1	-10.6	1.057	1.3	735	0.98	-20.2 ...	13.9	-2.9
NYAL	-10.8	1.047	1.3	731	0.98	-20.1 ...	13.9	-2.8
REYK	-11.7	0.980	1.3	812	0.97	-8.7 ...	19.6	6.0
THU1	-11.2	0.902	1.3	882	0.99	-28.1 ...	11.3	-6.7
TIXI	-9.7	0.806	2.2	891	0.99	-36.9 ...	25.3	-8.1
TRO1	-11.8	1.011	1.3	773	0.98	-11.3 ...	24.4	4.8
TROM	-11.9	1.036	1.3	644	0.97	-7.8 ...	23.1	6.5
VESL	-13.9	0.758	1.5	448	0.91	-26.1 ...	-6.1	-16.8
WHIT	-11.1	0.814	1.5	848	0.98	-31.6 ...	21.7	-1.3
YAKZ	-10.1	0.733	2.3	881	0.99	-40.9 ...	33.0	-4.5
YELL	-9.6	0.659	2.3	901	0.98	-38.1 ...	30.1	-0.8
FAIR	-10.5	0.607	4.2	775	0.90	-33.1 ...	26.6	-1.2
KIRU	-9.8	0.807	1.5	803	0.98	-19.8 ...	23.3	1.3
METS	-9.3	0.782	1.8	668	0.97	-19.7 ...	27.5	7.7
OHIG	-11.9	1.417	1.7	205	0.80	-1.9 ...	6.7	2.2
CAS1	-12.6	0.674	1.3	428	0.95	-22.8 ...	4.6	-5.9
SYOG	-13.4	0.794	1.2	161	0.95	-25.4 ...	-2.1	-13.1

POLAR ZONE 40°-60° LAT MEAN VALUES: r = 0.96, sigma = 1.6, a = -11.4, b = 0.877

Table A-2 - Analysis of the TropAC database for linear conversion coefficients of surface into mean atmospheric temperature separated into 4 major climatic zones. The function coefficients are denoted as a and b, respectively, and require the surface temperature to be input in units of degrees centigrade. The number of statistical degrees of freedom of the linear fit is given by "f" and the regression coefficient is denoted as "r". The last three columns give the minimum and maximum surface temperature that were present in the analyzed data set as well as the mean surface temperature of the ensemble. (last update: 2000/03/15)

The tables printed are results of a routine analysis on the TropAC database carried out quarterly. The values given here only cover a time period of about $\frac{3}{4}$ years.

The following notes on usage shall be considered by the reader: First, a regression function listed in the tables should only be applied if the number of statistical degrees of freedom f is sufficiently large, i. e. the results can be considered to be representative. Results with less than 500 degrees of freedom are not recommended to be used. Second, the user shall confirm that the surface temperature range of the analysis given by $T_s(\min)$ and $T_s(\max)$ really covers the temperatures which are actually to be converted. If this is not the case, the conversion result will be an extrapolation and might be of inferior accuracy.

Appendix III: Comparison of IWV Conversion Uncertainties

The following table gives a detailed, site-specific comparison of the ZWD to IWV conversion uncertainties discussed in section → 6.4.3. The reference data are Q-factors from high-resolution numerical weather models (14 km resolution in Germany and 55 km outside). The first column is the station identifier (4 characters) followed by the number of samples used for the comparison. The minimum and maximum difference between model and reference data follow as well as the bias, standard deviation (bias-reduced) and the RMS. The acronyms can be deciphered as follows: *mod-bev* = linear regression of Bevis, *mod-ema* = Q-function of Emardson, *mod-tro* = individual, site-specific linear regression functions of the TropAC database/GDAS weather model (the entry 0.00 indicates that no site-specific function could be found in the database) and *mod-sol* = linear regression after Solbrig. See also section → 3.5 for further information.

ANKR	720	-0.49	0.35	-0.06	0.15	0.17	mod-bev
		-0.28	0.52	0.08	0.14	0.16	mod-ema
		-0.62	0.24	-0.14	0.17	0.22	mod-tro
		-0.63	0.23	-0.15	0.17	0.23	mod-sol
AURI	720	-0.43	0.43	-0.04	0.16	0.17	mod-bev
		-0.21	0.61	0.09	0.19	0.21	mod-ema
		0.00	0.00	0.00	0.00	0.00	mod-tro
		-0.60	0.34	-0.12	0.16	0.20	mod-sol
BRUS	720	-0.44	0.53	0.00	0.17	0.17	mod-bev
		-0.25	0.67	0.14	0.18	0.22	mod-ema
		-0.63	0.42	-0.09	0.18	0.20	mod-tro
		-0.62	0.43	-0.09	0.18	0.20	mod-sol
ERLA	600	-0.45	0.55	-0.03	0.20	0.21	mod-bev
		-0.21	0.73	0.11	0.21	0.23	mod-ema
		0.00	0.00	0.00	0.00	0.00	mod-tro
		-0.68	0.48	-0.11	0.22	0.24	mod-sol
GRAZ	744	-0.35	0.54	0.01	0.17	0.17	mod-bev
		-0.20	0.71	0.13	0.19	0.23	mod-ema
		-0.52	0.48	-0.05	0.18	0.19	mod-tro
		-0.53	0.46	-0.06	0.18	0.19	mod-sol
HERS	670	-0.40	0.67	0.04	0.17	0.17	mod-bev
		-0.21	0.87	0.19	0.18	0.26	mod-ema
		-0.69	0.50	-0.08	0.18	0.20	mod-tro
		-0.63	0.54	-0.05	0.18	0.18	mod-sol
HFLK	552	-0.30	0.00	-0.09	0.05	0.10	mod-bev
		-0.20	0.10	-0.03	0.04	0.05	mod-ema
		-0.40	0.00	-0.09	0.07	0.12	mod-tro
		-0.39	-0.02	-0.12	0.07	0.13	mod-sol
HOBV	720	-0.54	0.37	-0.06	0.15	0.16	mod-bev
		-0.29	0.52	0.06	0.17	0.18	mod-ema
		0.00	0.00	0.00	0.00	0.00	mod-tro
		-0.71	0.26	-0.14	0.15	0.20	mod-sol

HOFN	696	-0.29	0.18	-0.10	0.09	0.13	mod-bev
		-0.15	0.31	0.01	0.09	0.09	mod-ema
		-0.28	0.27	-0.03	0.09	0.10	mod-tro
		-0.37	0.13	-0.15	0.10	0.18	mod-sol
KARL	720	-0.55	0.83	-0.01	0.22	0.22	mod-bev
		-0.27	0.97	0.14	0.22	0.26	mod-ema
		0.00	0.00	0.00	0.00	0.00	mod-tro
		-0.77	0.73	-0.11	0.25	0.27	mod-sol
KIRU	744	-0.21	0.27	-0.08	0.06	0.10	mod-bev
		-0.14	0.36	-0.03	0.07	0.07	mod-ema
		-0.19	0.28	-0.06	0.07	0.09	mod-tro
		-0.24	0.21	-0.10	0.07	0.12	mod-sol
KOSG	744	-0.39	0.51	-0.00	0.18	0.18	mod-bev
		-0.23	0.68	0.14	0.20	0.24	mod-ema
		-0.52	0.40	-0.09	0.18	0.20	mod-tro
		-0.52	0.41	-0.09	0.18	0.20	mod-sol
LEIP	696	-0.52	0.40	-0.08	0.16	0.18	mod-bev
		-0.26	0.58	0.05	0.16	0.17	mod-ema
		0.00	0.00	0.00	0.00	0.00	mod-tro
		-0.69	0.31	-0.16	0.18	0.24	mod-sol
MATE	744	-0.55	0.40	-0.07	0.15	0.16	mod-bev
		-0.31	0.69	0.11	0.16	0.20	mod-ema
		-0.79	0.07	-0.25	0.15	0.29	mod-tro
		-0.72	0.15	-0.19	0.15	0.24	mod-sol
METS	696	-0.32	0.15	-0.13	0.07	0.14	mod-bev
		-0.19	0.28	-0.04	0.07	0.08	mod-ema
		-0.36	0.13	-0.14	0.07	0.16	mod-tro
		-0.41	0.09	-0.17	0.08	0.19	mod-sol
NICO	720	-0.54	0.50	0.03	0.23	0.23	mod-bev
		-0.29	0.75	0.25	0.22	0.33	mod-ema
		-1.22	0.39	-0.27	0.36	0.45	mod-tro
		-0.81	0.34	-0.14	0.26	0.30	mod-sol
ONSA	744	-0.41	0.28	-0.07	0.10	0.13	mod-bev
		-0.22	0.41	0.03	0.11	0.11	mod-ema
		-0.47	0.32	-0.08	0.12	0.14	mod-tro
		-0.54	0.24	-0.13	0.12	0.18	mod-sol
PFAN	720	-0.37	0.13	-0.06	0.09	0.11	mod-bev
		-0.17	0.24	0.02	0.08	0.08	mod-ema
		0.00	0.00	0.00	0.00	0.00	mod-tro
		-0.49	0.07	-0.12	0.10	0.16	mod-sol
POTS	744	-0.56	0.38	-0.08	0.14	0.16	mod-bev
		-0.26	0.59	0.05	0.16	0.17	mod-ema
		-0.67	0.28	-0.14	0.15	0.20	mod-tro
		-0.72	0.27	-0.15	0.16	0.22	mod-sol
REYK	744	-0.39	0.15	-0.14	0.10	0.17	mod-bev
		-0.25	0.33	-0.01	0.11	0.11	mod-ema
		-0.35	0.18	-0.10	0.10	0.14	mod-tro

		-0.48	0.08	-0.20	0.11	0.23	mod-sol
SOFI	720	-0.42	0.10	-0.09	0.08	0.12	mod-bev
		-0.25	0.22	0.01	0.07	0.07	mod-ema
		0.00	0.00	0.00	0.00	0.00	mod-tro
		-0.53	0.04	-0.15	0.11	0.18	mod-sol
WROC	600	-0.51	0.44	-0.06	0.16	0.17	mod-bev
		-0.25	0.59	0.06	0.17	0.18	mod-ema
		0.00	0.00	0.00	0.00	0.00	mod-tro
		-0.70	0.36	-0.13	0.17	0.21	mod-sol
WTZR	648	-0.33	0.26	-0.05	0.11	0.13	mod-bev
		-0.16	0.38	0.05	0.12	0.13	mod-ema
		-0.48	0.22	-0.10	0.12	0.16	mod-tro
		-0.52	0.21	-0.11	0.13	0.17	mod-sol
WTZT	624	-0.37	0.28	-0.06	0.11	0.13	mod-bev
		-0.16	0.41	0.04	0.12	0.12	mod-ema
		0.00	0.00	0.00	0.00	0.00	mod-tro
		-0.55	0.22	-0.12	0.13	0.18	mod-sol
ZECK	720	-0.26	0.19	-0.05	0.09	0.10	mod-bev
		-0.13	0.35	0.04	0.09	0.10	mod-ema
		-0.34	0.14	-0.08	0.10	0.12	mod-tro
		-0.36	0.11	-0.10	0.10	0.14	mod-sol
ZIMM	744	-0.43	0.25	-0.06	0.12	0.14	mod-bev
		-0.22	0.38	0.06	0.11	0.13	mod-ema
		-0.63	0.18	-0.13	0.15	0.20	mod-tro
		-0.61	0.18	-0.13	0.15	0.19	mod-sol
ZWEN	648	-0.33	0.29	-0.11	0.09	0.14	mod-bev
		-0.22	0.46	-0.02	0.11	0.11	mod-ema
		-0.36	0.27	-0.13	0.09	0.16	mod-tro
		-0.42	0.22	-0.16	0.10	0.19	mod-sol

Appendix IV: Mean Values for Water Vapor

Results of the harmonic analysis of integrated water vapor time series from the TropAC database are listed in this section. The least-squares fit to the harmonic function

$$IWV = mean + amp \cdot \sin(\omega \cdot t + phase)$$

includes the estimation of the mean water vapor (*mean*), the amplitude (*amp*) and the phase angle (*phase*). The period of the function is fixed to 1 year.

Note that the phase angle is uncertain for all those time series that only cover less than one year. The mean water vapor is the constant offset from the sine curve and can be slightly negative for certain sites, but should not deviate significantly from zero in such cases.

Two tables are provided: the first shows the water vapor time series at the antenna site and the second supplies the values reduced to mean sea level (0 m) with help of the water vapor scale heights listed in → Appendix V. Figure A-1, Figure A-2 and Figure A-3 serve for your orientation and show the climate zones and the IGS network stations used in this analysis. Figure A-4 to Figure A-7 graphically illustrate the time series as well as the adjusted harmonic functions for 4 selected stations.

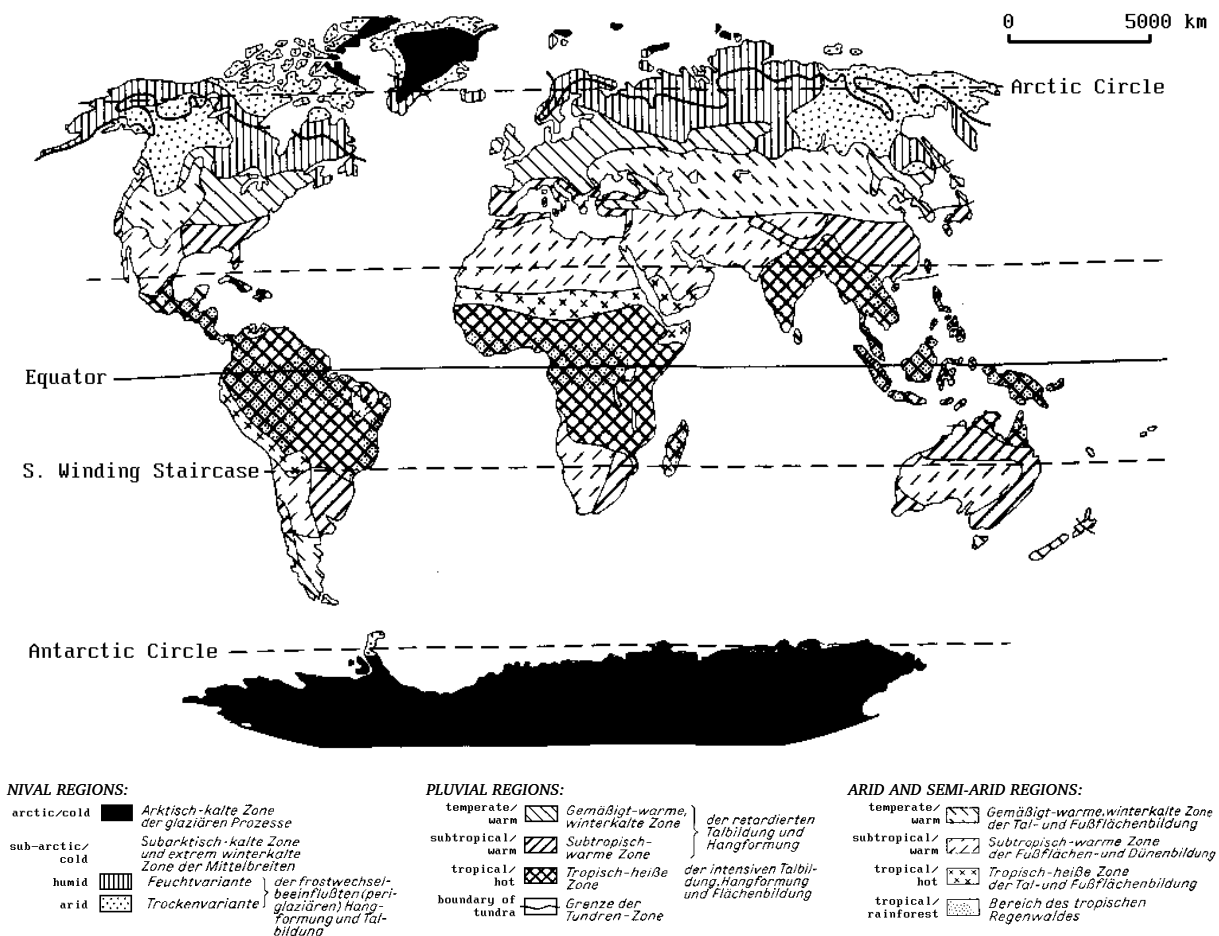


Figure A-1 - Classification of climate zones of the earth from HOHL [1981, p. 142].

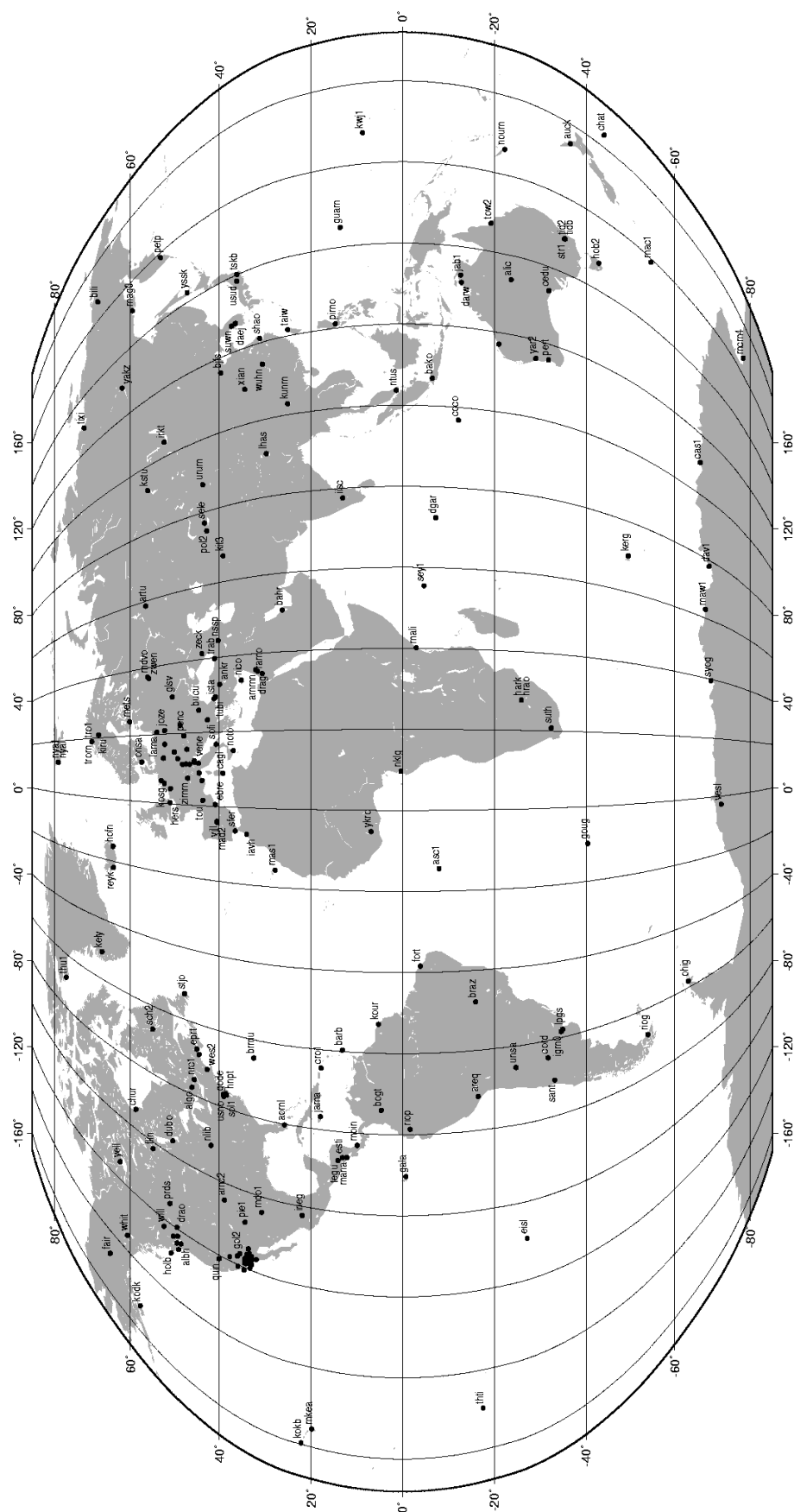
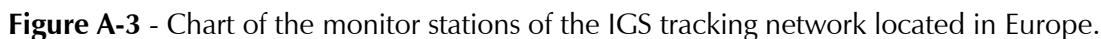


Figure A-2 - Global chart of the monitor stations of the IGS tracking network. A zoomed map for those sites located at the European continent is given on the following page.



SITE	station ID, 4 characters	amp	amplitude of IWW harmonic function in [kg/m ²]
LAT	latitude of site in [deg]	phase	phase angle of IWW harmonic function in [rad]
LON	longitude of site in [deg]	mean	mean offset of IWW harmonic function in [kg/m ²]
HEI	orthometric height in [m]	f	statistical degrees of freedom

Table A-3 - Description of the columns of the following result tables.

Harmonic Analysis of Integrated Water Vapor Referenced to the Antenna Height:

T R O P I C A L B E L T									
SITE	LAT	LON	HEI	amp [kg/m ²]	phase [rad]	mean [kg/m ²]	f		
BARB	13.09	-59.61	10	-9.5 ± 0.2	4.940 ± 0.021	40.4 ± 0.2	3168		
COCO	-12.19	96.83	5	10.1 ± 0.2	-196.354 ± 0.019	45.6 ± 0.1	3840		
CRO1	17.76	-64.58	13	-12.9 ± 0.2	11.220 ± 0.015	36.5 ± 0.1	3216		
DGAR	-7.27	72.37	10	4.5 ± 0.2	-0.342 ± 0.055	50.5 ± 0.2	2376		
MKEA	19.80	-155.46	3730	0.6 ± 0.1	0.104 ± 0.151	2.9 ± 0.1	2352		
RIOP	-1.65	-78.65	2790	1.6 ± 0.1	-0.648 ± 0.086	17.8 ± 0.1	2160		
THTI	-17.58	-149.61	92	7.8 ± 0.1	-0.526 ± 0.028	39.5 ± 0.1	3576		
TOW2	-19.27	147.06	30	13.6 ± 0.2	-0.540 ± 0.018	36.4 ± 0.2	4944		
YKRO	6.87	-5.24	242	-13.3 ± 0.6	5.114 ± 0.065	35.3 ± 0.8	1200		
ASC1	-7.95	-14.41	92	4.9 ± 0.1	-1.072 ± 0.029	31.4 ± 0.1	3816		
KWJ1	8.72	167.73	9	-2.2 ± 0.3	-0.065 ± 0.231	53.9 ± 0.3	480		
BAKO	-6.49	106.85	140	8.8 ± 0.2	-0.529 ± 0.030	50.1 ± 0.2	2136		
PIMO	14.64	121.08	52	-6.8 ± 0.1	-6.872 ± 0.028	52.5 ± 0.1	4896		
JAB1	-12.66	132.89	28	-25.8 ± 0.3	-3.491 ± 0.012	43.3 ± 0.2	1536		
BOGT	4.64	-74.08	2555	0.4 ± 0.2	-1.122 ± 0.198	20.5 ± 0.1	1920		
SEY1	-4.67	55.48	578	6.8 ± 1.6	-0.325 ± 0.167	34.0 ± 1.5	480		
FORT	-3.88	-38.43	28	5.2 ± 0.4	-1.308 ± 0.046	42.8 ± 0.2	1632		
KOUR	5.25	-52.81	8	5.9 ± 0.3	4.255 ± 0.053	51.3 ± 0.2	768		
IISC	13.02	77.57	930	13.8 ± 0.3	2.380 ± 0.027	31.4 ± 0.2	1320		
AREQ	-16.47	-71.49	2447	8.9 ± 0.1	-0.624 ± 0.017	14.0 ± 0.1	2448		
NTUS	1.35	103.68	68	5.9 ± 0.2	0.723 ± 0.028	50.7 ± 0.2	2520		
DARW	-12.84	131.13	75	-19.1 ± 0.1	-3.674 ± 0.010	41.7 ± 0.1	4344		
GUAM	13.59	144.87	147	9.0 ± 0.3	2.129 ± 0.036	45.3 ± 0.2	792		
JAMA	17.94	-76.78	13	5.0 ± 1.0	0.102 ± 0.089	25.9 ± 0.9	2112		
MALI	-3.00	40.19	7	3.2 ± 0.3	0.816 ± 0.055	40.8 ± 0.1	1728		
GALA	-0.42	-90.30	-350	-2.6 ± 0.2	-0.478 ± 0.356	37.6 ± 0.4	1368		
TROPICAL BELT		0°-20° LAT		MEAN: 37.4 ± 0.3 mm (amp: 0.9 ± 0.3 mm)					

S U B T R O P I C S								
SITE	LAT	LON	HEI	amp [kg/m ²]	phase [rad]	mean [kg/m ²]	f	
ALIC	-23.67	133.89	588	11.7 ± 0.2	-0.537 ± 0.021	23.8 ± 0.1	5256	
AMC2	38.80	-104.52	1930	-9.3 ± 0.1	-0.043 ± 0.010	13.9 ± 0.1	5664	
ANKR	39.89	32.76	939	-7.0 ± 0.1	-0.105 ± 0.022	14.5 ± 0.1	4368	
AOML	25.73	-80.16	28	14.4 ± 0.1	2.391 ± 0.007	34.9 ± 0.1	14304	
AUCK	-36.60	174.83	98	5.1 ± 0.1	-0.712 ± 0.016	20.2 ± 0.1	15528	
BAHR	26.21	50.61	11	-3.9 ± 0.1	-20.141 ± 0.022	20.2 ± 0.1	15600	
BRMU	32.37	-64.70	23	13.0 ± 0.1	2.533 ± 0.016	31.5 ± 0.1	5136	
CAGL	39.14	8.97	192	-8.4 ± 0.1	-0.784 ± 0.015	18.7 ± 0.1	5712	
CEDU	-31.87	133.81	154	7.3 ± 0.1	-0.827 ± 0.026	20.0 ± 0.1	5280	
GILB	32.48	35.42	485	-4.1 ± 0.1	-0.901 ± 0.022	14.3 ± 0.1	5568	
GOL2	35.43	-116.89	1018	-6.5 ± 0.2	0.528 ± 0.021	13.1 ± 0.1	4752	
HARK	-25.89	27.71	1530	10.9 ± 0.1	-0.660 ± 0.017	18.7 ± 0.1	3720	
HRAO	-25.89	27.69	1389	11.0 ± 0.1	-0.431 ± 0.015	19.3 ± 0.1	4488	
JPLM	34.20	-118.17	458	-4.9 ± 0.1	0.396 ± 0.026	16.0 ± 0.1	5808	
KABR	33.02	35.15	82	-6.4 ± 0.1	-13.187 ± 0.017	18.6 ± 0.1	5472	
KARR	-20.98	117.10	117	16.4 ± 0.2	30.528 ± 0.014	31.1 ± 0.1	4872	
KATZ	33.00	35.69	324	-7.1 ± 0.2	-0.829 ± 0.021	14.2 ± 0.1	3456	
KOKB	22.13	-159.66	1153	2.9 ± 0.1	-4.577 ± 0.034	15.6 ± 0.1	7368	
LPGS	-34.91	-57.93	14	6.4 ± 0.1	-0.440 ± 0.034	21.6 ± 0.1	4128	
MAS1	27.76	-15.63	155	6.7 ± 0.1	2.261 ± 0.033	18.7 ± 0.1	3744	
MDO1	30.68	-104.01	2027	8.1 ± 0.1	-3.628 ± 0.008	10.7 ± 0.0	10104	
MONP	32.89	-116.42	1875	-4.1 ± 0.1	-0.289 ± 0.026	9.2 ± 0.1	7608	
NICO	35.14	33.40	162	-8.1 ± 0.2	-0.372 ± 0.023	19.4 ± 0.1	4032	
NOTO	36.88	14.99	85	9.5 ± 0.1	2.244 ± 0.012	20.8 ± 0.1	5880	
PERT	-31.80	115.89	45	5.6 ± 0.1	-0.851 ± 0.029	18.8 ± 0.1	4896	
PIE1	34.30	-108.12	2370	-7.9 ± 0.1	-0.090 ± 0.014	11.1 ± 0.1	5472	
RAMO	30.60	34.76	869	-3.8 ± 0.1	-1.068 ± 0.019	10.7 ± 0.0	5112	
SANT	-33.15	-70.67	696	4.4 ± 0.1	-0.394 ± 0.028	13.1 ± 0.1	3864	
SFER	36.46	-6.21	40	7.0 ± 0.1	2.269 ± 0.020	18.9 ± 0.1	5112	
SUTH	-32.38	20.81	1763	4.6 ± 0.1	-0.248 ± 0.029	10.1 ± 0.1	3960	
SUWN	37.28	127.05	59	24.8 ± 0.2	-3.397 ± 0.012	24.8 ± 0.2	2952	
TELA	32.07	34.78	39	-8.0 ± 0.2	-26.056 ± 0.015	16.5 ± 0.1	3936	
TID2	-35.40	148.98	646	5.7 ± 0.1	-0.647 ± 0.031	16.8 ± 0.1	5064	
USNO	38.92	-77.07	82	-11.5 ± 0.1	-0.455 ± 0.009	21.4 ± 0.1	17064	
WUHN	30.53	114.36	40	23.6 ± 0.2	2.871 ± 0.011	34.4 ± 0.1	4464	
YAR1	-29.05	115.35	267	8.0 ± 0.2	-0.996 ± 0.023	21.2 ± 0.1	4944	
DAEJ	36.40	127.37	92	21.2 ± 0.2	2.719 ± 0.012	22.1 ± 0.2	4416	
USUD	36.13	138.36	1466	13.8 ± 0.1	2.668 ± 0.013	15.1 ± 0.1	4176	
BSHM	32.78	35.02	205	-6.6 ± 0.2	-0.845 ± 0.020	15.1 ± 0.1	3984	
ELAT	29.51	34.92	15	10.1 ± 0.2	2.175 ± 0.013	14.0 ± 0.1	2928	
GODE	39.02	-76.83	48	13.5 ± 0.1	9.024 ± 0.015	22.7 ± 0.1	6720	
LHAS	29.66	91.10	3659	-10.4 ± 0.1	-0.335 ± 0.005	10.1 ± 0.0	9312	
NOUM	-22.27	166.41	23	9.3 ± 0.2	-0.956 ± 0.023	35.7 ± 0.1	4800	
TSKB	36.11	140.09	28	24.2 ± 0.2	2.644 ± 0.011	27.8 ± 0.2	3216	
CIC1	31.87	-116.67	99	-10.3 ± 0.4	0.185 ± 0.030	20.0 ± 0.3	792	
CORD	-31.53	-64.47	720	8.9 ± 1.0	-0.423 ± 0.064	20.6 ± 0.9	1872	
XIAN	34.37	109.22	498	21.6 ± 1.0	-3.416 ± 0.025	21.9 ± 0.9	1944	
BJFS	39.61	115.89	98	-12.3 ± 0.9	-0.259 ± 0.019	16.7 ± 0.8	936	
INEG	21.86	-102.28	1902	-8.3 ± 0.2	0.351 ± 0.051	16.3 ± 0.2	1632	
STR1	-35.32	149.01	781	-5.3 ± 1.1	0.518 ± 0.296	23.3 ± 1.7	1080	
KUNM	25.03	102.80	2019	-12.8 ± 0.1	-0.333 ± 0.014	21.8 ± 0.1	2400	
SHAO	31.10	121.20	12	-21.6 ± 0.3	-0.367 ± 0.032	33.9 ± 0.3	1752	
QUIN	39.97	-120.94	1129	-1.6 ± 0.2	-0.229 ± 0.198	12.9 ± 0.2	1608	
EISL	-27.15	-109.38	120	6.7 ± 0.3	-0.766 ± 0.055	28.4 ± 0.2	1464	
CASC	38.69	-9.42	23	-39.8 ± 2.1	5.600 ± 0.015	-9.3 ± 1.8	552	
KIT3	39.13	66.89	659	-5.6 ± 0.1	-0.030 ± 0.014	14.0 ± 0.1	9624	
SOL1	38.32	-76.45	17	14.1 ± 0.1	2.669 ± 0.011	22.7 ± 0.1	10344	
USNA	38.98	-76.48	7	17.4 ± 2.2	2.670 ± 0.029	20.5 ± 2.0	2184	
GOLD	35.43	-116.89	1018	-25.5 ±12.7	-0.067 ± 0.132	-14.6 ±13.0	600	
TIDB	-35.40	148.98	646	-99.4 ±18.1	3.304 ± 0.012	108.9 ±18.0	600	
AMCT	38.80	-104.52	1930	104.7 ±21.0	-3.042 ± 0.019	-85.2 ±20.9	408	
SUBTROPICS 20°-40° LAT MEAN: 18.2 ± 1.1 mm (amp: 1.8 ± 1.1 mm)								

=====								
T E M P E R A T E			Z O N E					
=====								
SITE	LAT	LON	HEI	amp [kg/m²]	phase [rad]		mean [kg/m²]	f
=====								
ALBH	48.39	-123.49	51	-5.6 ± 0.1	-0.452 ±	0.012	17.3 ± 0.0	12648
ALGO	45.96	-78.07	237	-10.2 ± 0.1	-0.282 ±	0.010	16.9 ± 0.1	11880
ARTU	56.43	58.56	254	-7.2 ± 0.1	-0.293 ±	0.018	12.7 ± 0.1	3936
BOGO	52.48	21.04	119	-9.9 ± 0.1	-0.100 ±	0.014	18.7 ± 0.1	5328
BOR1	52.28	17.07	89	-9.1 ± 0.1	-0.199 ±	0.015	17.9 ± 0.1	5784
BRUS	50.80	4.36	104	-7.4 ± 0.1	-0.497 ±	0.018	17.8 ± 0.1	5832
CHAT	-43.96	-176.57	48	3.6 ± 0.1	-0.701 ±	0.019	17.4 ± 0.0	17112
CHUR	58.76	-94.09	29	-8.4 ± 0.1	-0.167 ±	0.013	11.5 ± 0.1	5856
DRAO	49.32	-119.63	558	-5.4 ± 0.1	-0.350 ±	0.018	14.0 ± 0.1	5976
DUBO	50.26	-95.87	275	-9.4 ± 0.1	-0.192 ±	0.014	14.7 ± 0.1	4896
FLIN	54.73	-101.98	343	-8.5 ± 0.1	-0.187 ±	0.013	12.5 ± 0.1	5952
GLSV	50.36	30.50	201	-10.8 ± 0.1	-0.151 ±	0.012	17.2 ± 0.1	5928
GOPE	49.91	14.79	547	-7.2 ± 0.1	-0.360 ±	0.017	16.7 ± 0.1	5928
GOUG	-40.35	-9.88	58	3.5 ± 0.3	-0.387 ±	0.078	17.3 ± 0.2	2784
GRAS	43.75	6.92	1269	-7.3 ± 0.1	30.837 ±	0.017	11.8 ± 0.1	4536
GRAZ	47.07	15.49	491	10.3 ± 0.1	-3.562 ±	0.011	16.8 ± 0.1	5880
HERS	50.87	0.34	32	-6.6 ± 0.1	-0.481 ±	0.011	17.5 ± 0.1	12936
HFLK	47.31	11.39	2336	-4.4 ± 0.1	-0.380 ±	0.017	7.8 ± 0.0	5568
HOB2	-42.80	147.44	45	3.3 ± 0.1	-0.317 ±	0.038	17.1 ± 0.1	5640
HOLB	50.64	-128.13	576	-5.7 ± 0.2	5.578 ±	0.031	12.8 ± 0.2	2880
IRKT	52.22	104.32	541	-11.8 ± 0.1	-0.103 ±	0.011	13.2 ± 0.1	5880
JOZE	52.10	21.03	110	-9.3 ± 0.1	-0.110 ±	0.015	17.8 ± 0.1	5904
KERG	-49.35	70.26	33	3.2 ± 0.1	-0.972 ±	0.042	11.0 ± 0.1	3672
KOSG	52.18	5.81	53	7.2 ± 0.1	15.116 ±	0.017	17.4 ± 0.1	5424
LAMA	53.89	20.67	158	-8.7 ± 0.1	-0.125 ±	0.015	16.8 ± 0.1	5568
MAC1	-54.50	158.94	14	1.8 ± 0.1	-0.984 ±	0.063	11.7 ± 0.1	4104
MAD2	40.43	-4.25	777	-5.3 ± 0.1	-0.394 ±	0.023	14.2 ± 0.1	4848
MAGO	59.58	150.77	345	-8.7 ± 0.1	-0.172 ±	0.010	9.6 ± 0.1	5232
MATE	40.65	16.70	490	-8.0 ± 0.1	30.872 ±	0.013	16.7 ± 0.1	5664
MDVO	56.03	37.22	240	9.7 ± 0.1	-3.583 ±	0.013	16.2 ± 0.1	5160
MEDI	44.52	11.65	10	11.5 ± 0.1	2.621 ±	0.011	20.7 ± 0.1	5880
NLIB	41.77	-91.57	240	-12.3 ± 0.1	-0.072 ±	0.015	19.8 ± 0.1	5088
NRC1	45.45	-75.62	116	-10.7 ± 0.1	-0.328 ±	0.010	17.1 ± 0.1	12840
NRC2	45.45	-75.62	116	-11.2 ± 0.2	-0.228 ±	0.037	18.0 ± 0.3	3168
ONSA	57.40	11.93	9	-7.2 ± 0.1	-0.433 ±	0.018	16.0 ± 0.1	5616
PENC	47.79	19.28	248	-10.1 ± 0.1	-0.295 ±	0.014	17.9 ± 0.1	4440
PETP	53.07	158.61	188	-9.0 ± 0.1	-0.266 ±	0.013	12.0 ± 0.1	4728
POL2	42.68	74.69	1755	-7.5 ± 0.1	-0.210 ±	0.014	11.0 ± 0.1	4512
POTS	52.38	13.07	104	-7.7 ± 0.1	-0.446 ±	0.007	15.3 ± 0.0	20328
PRDS	50.87	-114.29	1264	-7.1 ± 0.1	-0.298 ±	0.007	10.8 ± 0.0	10008
RIOG	-53.79	-67.75	20	3.2 ± 0.1	-0.679 ±	0.036	13.4 ± 0.1	4656
SCH2	54.83	-66.83	518	-8.2 ± 0.1	-0.297 ±	0.014	11.5 ± 0.1	6024
SELE	43.18	77.02	1385	-8.7 ± 0.1	-0.213 ±	0.013	12.5 ± 0.1	4512
SJDV	45.88	4.68	382	12.8 ± 0.3	2.255 ±	0.013	14.1 ± 0.2	2352
STJO	47.60	-52.68	143	-8.2 ± 0.1	-0.360 ±	0.012	16.1 ± 0.1	12096
TOUL	43.56	1.48	158	-10.0 ± 0.1	-6.723 ±	0.017	20.7 ± 0.1	4656
VILL	40.44	-3.95	595	-6.4 ± 0.1	-0.602 ±	0.017	15.5 ± 0.1	5064
WILL	52.24	-122.17	1110	-5.7 ± 0.1	-0.354 ±	0.014	10.5 ± 0.0	5952
WSRT	52.91	6.60	41	7.1 ± 0.1	-3.697 ±	0.018	17.9 ± 0.1	5784
WTZR	49.14	12.88	619	-7.3 ± 0.1	-0.278 ±	0.009	14.9 ± 0.0	15888
YSSK	47.03	142.72	66	-9.3 ± 0.2	-0.374 ±	0.016	12.8 ± 0.1	2736
ZECK	43.79	41.57	1145	-9.4 ± 0.1	-0.258 ±	0.010	13.7 ± 0.1	3888
ZIMM	46.88	7.47	908	-7.2 ± 0.0	-0.412 ±	0.006	13.8 ± 0.0	20520
NANO	49.29	-124.09	24	11.7 ± 0.5	-10.032 ±	0.020	13.0 ± 0.4	2112
OBER	48.09	11.28	596	-8.0 ± 0.0	-0.370 ±	0.007	14.9 ± 0.0	15312
UPAD	45.41	11.88	39	13.0 ± 0.1	2.677 ±	0.011	20.6 ± 0.1	4608
URUM	43.81	87.60	923	-10.6 ± 0.1	-0.254 ±	0.016	14.2 ± 0.1	4392
WES2	42.61	-71.49	114	-10.7 ± 0.1	5.822 ±	0.010	17.9 ± 0.1	12888
KSTU	55.99	92.79	249	-8.0 ± 0.1	-0.349 ±	0.017	11.4 ± 0.1	1776
BISH	42.88	74.59	775	-9.3 ± 0.1	-0.317 ±	0.014	15.5 ± 0.1	4032
ZWEN	55.70	36.76	190	5.4 ± 0.2	-3.804 ±	0.040	19.2 ± 0.1	9960
UCLU	48.93	-125.54	29	7.1 ± 0.3	2.482 ±	0.035	16.8 ± 0.3	2400
NSSP	40.23	44.50	1173	6.0 ± 4.6	0.647 ±	0.543	27.1 ± 5.4	1056
WSLR	50.13	-122.92	926	15.9 ± 0.8	2.589 ±	0.013	3.2 ± 0.7	2232
MADR	40.43	-4.25	777	-72.9 ± 25.9	-5.943 ±	0.050	-54.8 ± 25.9	432

TEMPERATE ZONE 40°-60° LAT MEAN: 14.1 ± 0.6 mm (amp: -4.9 ± 0.6 mm)

P O L A R Z O N E								
SITE	LAT	LON	HEI	amp [kg/m ²]	phase [rad]	mean [kg/m ²]	f	
BILI	68.08	166.44	448	-2.9 ± 0.2	-0.336 ± 0.049	4.5 ± 0.2	1272	
DAV1	-68.58	77.97	27	1.7 ± 0.0	-0.520 ± 0.029	5.1 ± 0.0	3528	
HOFN	64.27	-15.20	18	-6.4 ± 0.1	-0.424 ± 0.021	13.7 ± 0.1	4296	
KELY	66.99	-50.94	198	-5.6 ± 0.1	-0.266 ± 0.018	9.3 ± 0.1	4560	
MAW1	-67.60	62.87	30	1.9 ± 0.0	-0.619 ± 0.020	3.1 ± 0.0	4560	
MCM4	-77.84	166.67	151	1.0 ± 0.0	-0.387 ± 0.029	2.6 ± 0.0	4464	
NYA1	78.93	11.87	48	-5.6 ± 0.1	-0.195 ± 0.015	8.2 ± 0.1	4728	
NYAL	78.93	11.87	42	-5.3 ± 0.1	-0.147 ± 0.016	8.2 ± 0.1	4824	
REYK	64.14	-21.96	27	-5.6 ± 0.1	-0.593 ± 0.012	12.3 ± 0.0	12912	
THU1	76.54	-68.79	38	-5.0 ± 0.0	-0.142 ± 0.010	7.4 ± 0.0	5760	
TIXI	71.63	128.87	54	-8.1 ± 0.1	-0.028 ± 0.009	8.7 ± 0.0	5880	
TRO1	69.66	18.94	107	-6.9 ± 0.1	-0.311 ± 0.015	12.8 ± 0.1	4920	
TROM	69.66	18.94	101	-5.7 ± 0.1	-0.182 ± 0.025	13.2 ± 0.1	4080	
VESL	-71.67	-2.84	850	1.3 ± 0.1	-0.741 ± 0.033	3.0 ± 0.0	2880	
WHIT	60.75	-135.22	1420	-5.0 ± 0.0	-0.084 ± 0.013	8.0 ± 0.0	5664	
YAKZ	62.03	129.68	105	-10.9 ± 0.1	-0.037 ± 0.009	11.5 ± 0.1	5856	
YELL	62.48	-114.48	208	-7.5 ± 0.0	-0.431 ± 0.007	11.1 ± 0.0	13200	
FAIR	64.98	-147.50	308	-8.3 ± 0.1	-0.241 ± 0.007	9.9 ± 0.0	10272	
KIRU	67.86	20.97	362	-6.4 ± 0.1	-0.309 ± 0.014	11.2 ± 0.1	5256	
METS	60.22	24.40	76	-7.8 ± 0.1	-0.187 ± 0.011	13.9 ± 0.1	9960	
OHIG	-63.32	-57.90	8	3.6 ± 1.0	-0.533 ± 0.067	6.9 ± 0.9	1296	
CAS1	-66.28	110.52	39	2.0 ± 0.1	0.037 ± 0.039	5.8 ± 0.0	2688	
SYOG	-69.01	39.58	28	13.7 ± 0.9	-0.306 ± 0.011	14.5 ± 0.8	1032	
AMUN	-90.00	139.19	2846	5.1 ± 6.4	0.953 ± 1.203	-1.9 ± 8.8	336	
PALM	-64.78	-64.05	15	25.0 ± 28.3	4.574 ± 0.321	31.5 ± 29.2	432	
POLAR ZONE		40°-60° LAT		MEAN: 9.4 ± 1.6 mm (amp: -1.9 ± 1.5 mm)				

Table A-4 - Harmonic IWW analysis of the TropAC database separated into 4 major climatic zones and referenced to the station/antenna height. Last day analyzed: 2000/03/15

Harmonic Analysis of Integrated Water Vapor Referenced to the Mean Sea Level:

T R O P I C A L B E L T								
SITE	LAT	LON	HEI	amp [kg/m ²]	phase [rad]	mean [kg/m ²]	f	
BARB	13.09	-59.61	0	-9.5 ± 0.2	4.940 ± 0.021	40.6 ± 0.2	3168	
COCO	-12.19	96.83	0	10.2 ± 0.2	-196.354 ± 0.019	45.7 ± 0.1	3840	
CRO1	17.76	-64.58	0	-13.0 ± 0.2	11.220 ± 0.015	36.8 ± 0.1	3216	
DGAR	-7.27	72.37	0	4.5 ± 0.2	-0.342 ± 0.055	50.8 ± 0.2	2376	
MKEA	19.80	-155.46	0	2.6 ± 0.3	0.104 ± 0.151	13.2 ± 0.3	2352	
RIOP	-1.65	-78.65	0	7.2 ± 0.4	-0.648 ± 0.086	81.8 ± 0.5	2160	
THTI	-17.58	-149.61	0	8.2 ± 0.1	-0.526 ± 0.028	41.4 ± 0.1	3576	
TOW2	-19.27	147.06	0	13.8 ± 0.2	-0.540 ± 0.018	37.0 ± 0.2	4944	
YKRO	6.87	-5.24	0	-14.9 ± 0.7	5.114 ± 0.065	39.5 ± 0.9	1200	
ASC1	-7.95	-14.41	0	5.2 ± 0.1	-1.072 ± 0.029	33.1 ± 0.1	3816	
KWJ1	8.72	167.73	0	-2.2 ± 0.3	-0.065 ± 0.231	54.1 ± 0.3	480	
BAKO	-6.49	106.85	0	9.4 ± 0.2	-0.529 ± 0.030	53.2 ± 0.2	2136	
PIMO	14.64	121.08	0	-6.9 ± 0.1	-6.872 ± 0.028	53.7 ± 0.1	4896	
JAB1	-12.66	132.89	0	-26.1 ± 0.3	-3.491 ± 0.012	43.9 ± 0.2	1536	
BOGT	4.64	-74.08	0	1.6 ± 0.7	-1.122 ± 0.198	80.9 ± 0.5	1920	
SEY1	-4.67	55.48	0	9.3 ± 2.1	-0.325 ± 0.167	46.8 ± 2.0	480	
FORT	-3.88	-38.43	0	5.2 ± 0.4	-1.308 ± 0.046	43.4 ± 0.2	1632	
KOUR	5.25	-52.81	0	5.9 ± 0.3	4.255 ± 0.053	51.5 ± 0.3	768	
IISC	13.02	77.57	0	22.0 ± 0.5	2.380 ± 0.027	50.1 ± 0.3	1320	
AREQ	-16.47	-71.49	0	29.2 ± 0.3	-0.624 ± 0.017	46.1 ± 0.3	2448	
NTUS	1.35	103.68	0	6.1 ± 0.2	0.723 ± 0.028	52.2 ± 0.2	2520	
DARW	-12.84	131.13	0	-19.8 ± 0.1	-3.674 ± 0.010	43.1 ± 0.1	4344	
GUAM	13.59	144.87	0	9.7 ± 0.3	2.129 ± 0.036	48.5 ± 0.2	792	
JAMA	17.94	-76.78	0	5.0 ± 1.0	0.102 ± 0.089	26.1 ± 0.9	2112	
MALI	-3.00	40.19	0	3.2 ± 0.3	0.816 ± 0.055	40.9 ± 0.1	1728	
GALA	-0.42	-90.30	0	-2.2 ± 0.2	-0.478 ± 0.356	32.2 ± 0.4	1368	
TROPICAL BELT		0°-20° LAT		MEAN: 45.6 ± 0.3 mm (amp: 2.5 ± 0.4 mm)				

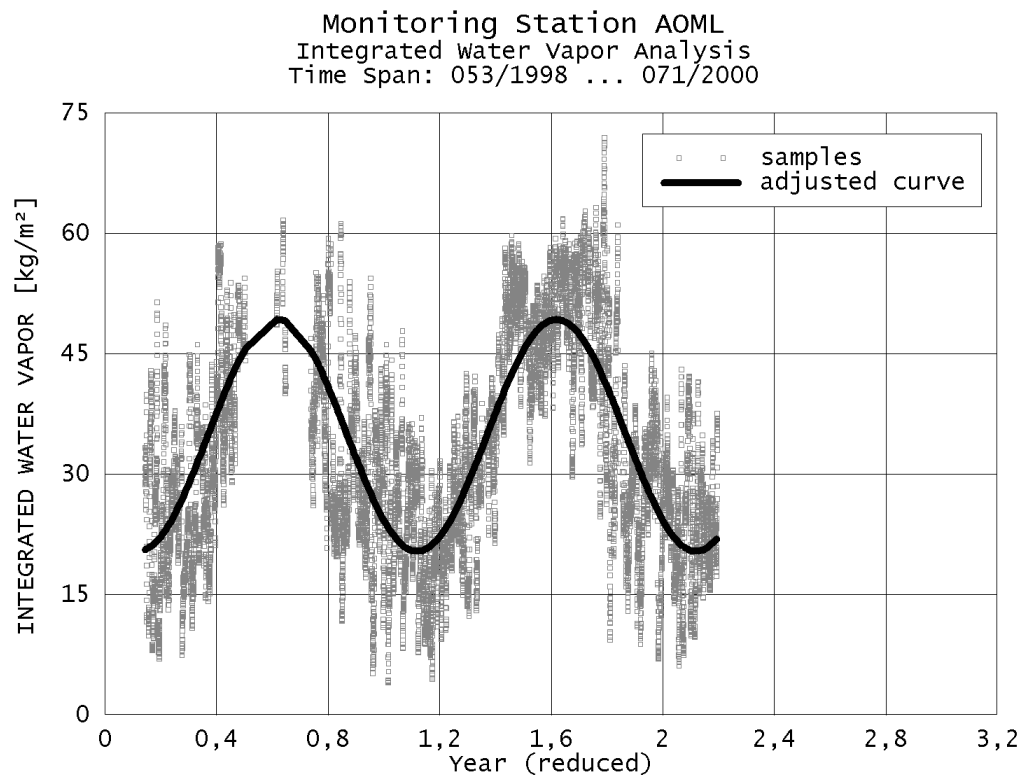


Figure A-4 - IWV samples (gray) and the harmonic function (black) for tracking station AOML at a latitude of 25.73°.

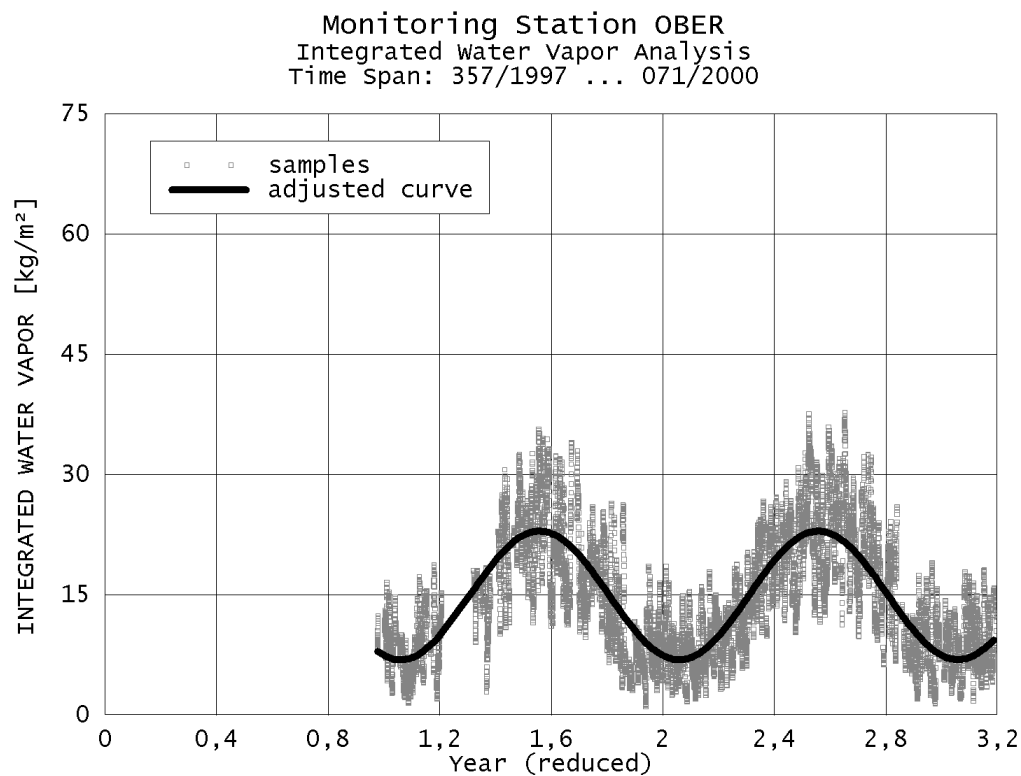


Figure A-5 - IWV samples (gray) and the harmonic function (black) for tracking station OBER at a latitude of 48.09°.

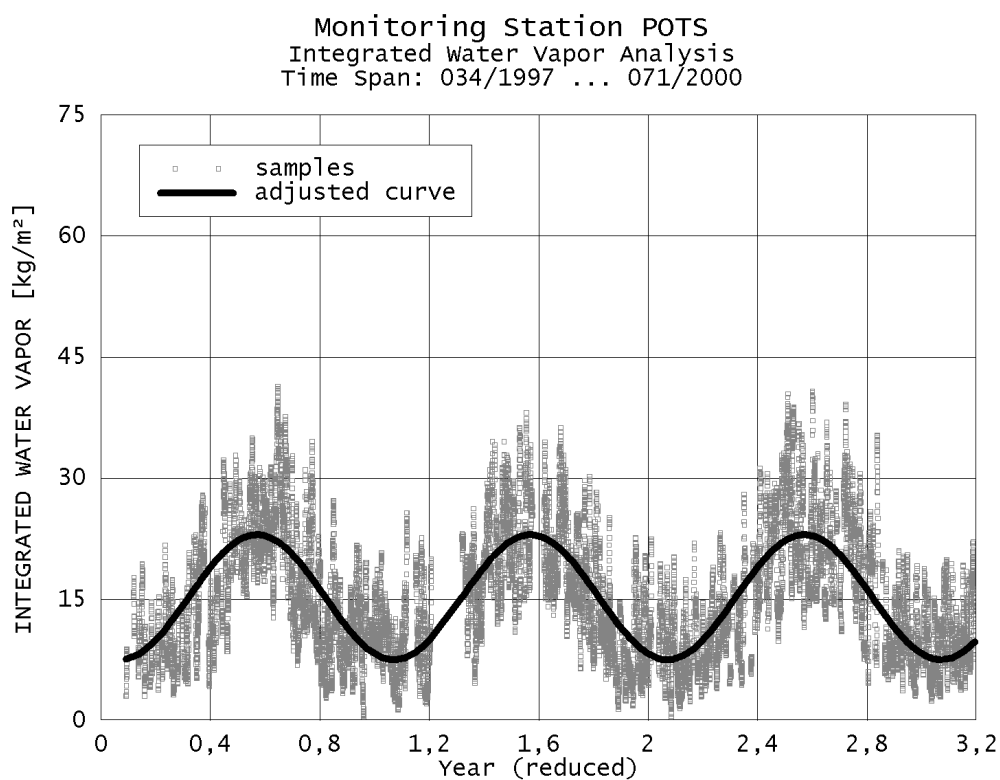


Figure A-6 - IWV samples (gray) and the harmonic function (black) for tracking station OBER at a latitude of 52.38°.

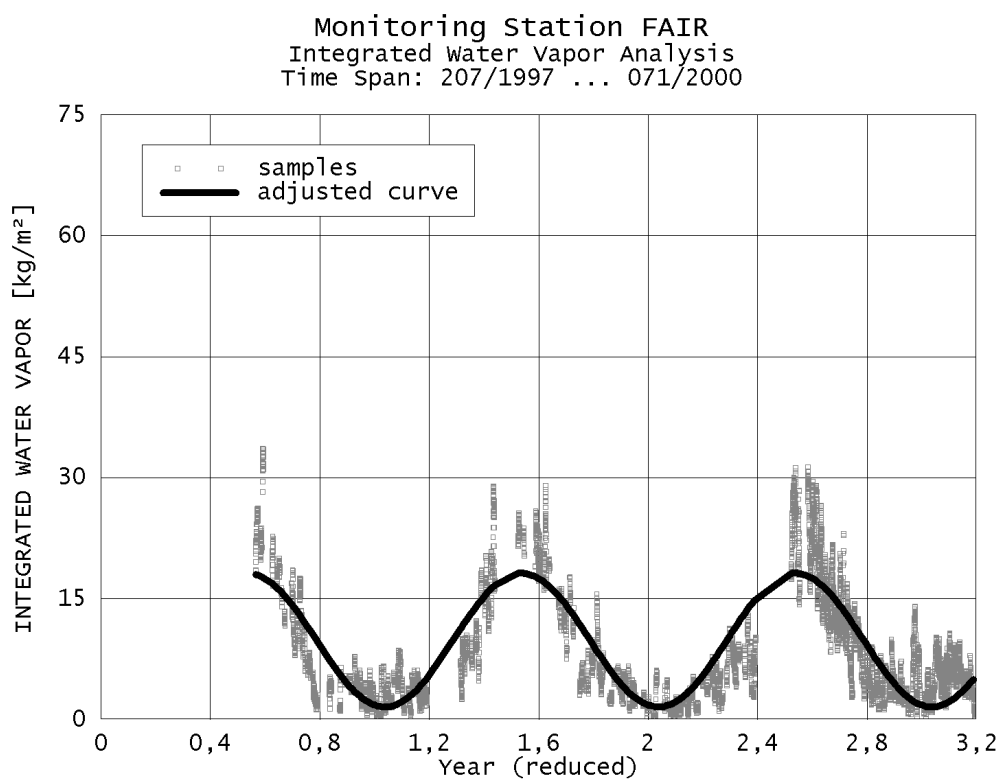


Figure A-7 - IWV samples (gray) and the harmonic function (black) for tracking station OBER at a latitude of 64.98°.

SUBTROPICS 20°-40° LAT MEAN: 24.2 ± 1.9 mm (amp: 2.0 ± 1.9 mm)

T E M P E R A T E Z O N E							
SITE	LAT	LON	HEI	amp [kg/m ²]	phase [rad]	mean [kg/m ²]	f
ALBH	48.39	-123.49	0	-5.8 ± 0.1	-0.452 ± 0.012	17.8 ± 0.0	12648
ALGO	45.96	-78.07	0	-11.4 ± 0.1	-0.282 ± 0.010	18.9 ± 0.1	11880
ARTU	56.43	58.56	0	-8.1 ± 0.1	-0.293 ± 0.018	14.4 ± 0.1	3936
BOGO	52.48	21.04	0	-10.5 ± 0.1	-0.100 ± 0.014	19.8 ± 0.1	5328
BOR1	52.28	17.07	0	-9.5 ± 0.1	-0.199 ± 0.015	18.7 ± 0.1	5784
BRUS	50.80	4.36	0	-7.8 ± 0.1	-0.497 ± 0.018	18.8 ± 0.1	5832
CHAT	-43.96	-176.57	0	3.7 ± 0.1	-0.701 ± 0.019	17.9 ± 0.0	17112
CHUR	58.76	-94.09	0	-8.5 ± 0.1	-0.167 ± 0.013	11.7 ± 0.1	5856
DRAO	49.32	-119.63	0	-7.1 ± 0.1	-0.350 ± 0.018	18.5 ± 0.1	5976
DUBO	50.26	-95.87	0	-10.7 ± 0.1	-0.192 ± 0.014	16.6 ± 0.1	4896
FLIN	54.73	-101.98	0	-10.0 ± 0.1	-0.187 ± 0.013	14.6 ± 0.1	5952
GLSV	50.36	30.50	0	-11.9 ± 0.1	-0.151 ± 0.012	19.0 ± 0.1	5928
GOPE	49.91	14.79	0	-9.7 ± 0.1	-0.360 ± 0.017	22.4 ± 0.1	5928
Goug	-40.35	-9.88	0	3.6 ± 0.3	-0.387 ± 0.078	17.9 ± 0.2	2784
GRAS	43.75	6.92	0	-14.7 ± 0.2	30.837 ± 0.017	23.6 ± 0.1	4536
GRAZ	47.07	15.49	0	13.3 ± 0.1	-3.562 ± 0.011	21.7 ± 0.1	5880
HERS	50.87	0.34	0	-6.7 ± 0.1	-0.481 ± 0.011	17.8 ± 0.1	12936
HFLK	47.31	11.39	0	-17.0 ± 0.2	-0.380 ± 0.017	30.4 ± 0.2	5568
HOB2	-42.80	147.44	0	3.4 ± 0.1	-0.317 ± 0.038	17.6 ± 0.1	5640
HOLB	50.64	-128.13	0	-7.5 ± 0.3	5.578 ± 0.031	16.7 ± 0.2	2880
IRKT	52.22	104.32	0	-15.2 ± 0.1	-0.103 ± 0.011	16.9 ± 0.1	5880
JOZE	52.10	21.03	0	-9.8 ± 0.1	-0.110 ± 0.015	18.8 ± 0.1	5904
KERG	-49.35	70.26	0	3.3 ± 0.1	-0.972 ± 0.042	11.2 ± 0.1	3672
KOSG	52.18	5.81	0	7.4 ± 0.1	15.116 ± 0.017	17.9 ± 0.1	5424
LAMA	53.89	20.67	0	-9.4 ± 0.1	-0.125 ± 0.015	18.2 ± 0.1	5568
MAC1	-54.50	158.94	0	1.8 ± 0.1	-0.984 ± 0.063	11.8 ± 0.1	4104
MAD2	40.43	-4.25	0	-8.1 ± 0.1	-0.394 ± 0.023	21.7 ± 0.1	4848
MAG0	59.58	150.77	0	-10.1 ± 0.1	-0.172 ± 0.010	11.2 ± 0.1	5232
MATE	40.65	16.70	0	-10.5 ± 0.1	30.872 ± 0.013	21.8 ± 0.1	5664
MDVO	56.03	37.22	0	10.9 ± 0.1	-3.583 ± 0.013	18.2 ± 0.1	5160
MEDI	44.52	11.65	0	11.5 ± 0.1	2.621 ± 0.011	20.8 ± 0.1	5880
NLIB	41.77	-91.57	0	-13.8 ± 0.2	-0.072 ± 0.015	22.2 ± 0.1	5088
NRC1	45.45	-75.62	0	-11.3 ± 0.1	-0.328 ± 0.010	18.1 ± 0.1	12840
NRC2	45.45	-75.62	0	-11.9 ± 0.2	-0.228 ± 0.037	19.0 ± 0.3	3168
ONSA	57.40	11.93	0	-7.3 ± 0.1	-0.433 ± 0.018	16.0 ± 0.1	5616
PENC	47.79	19.28	0	-11.5 ± 0.1	-0.295 ± 0.014	20.4 ± 0.1	4440
PETP	53.07	158.61	0	-9.9 ± 0.1	-0.266 ± 0.013	13.2 ± 0.1	4728
POL2	42.68	74.69	0	-17.7 ± 0.2	-0.210 ± 0.014	26.0 ± 0.2	4512
POTS	52.38	13.07	0	-8.1 ± 0.1	-0.446 ± 0.007	16.0 ± 0.0	20328
PRDS	50.87	-114.29	0	-13.1 ± 0.1	-0.298 ± 0.007	19.9 ± 0.1	10008
RIOG	-53.79	-67.75	0	3.2 ± 0.1	-0.679 ± 0.036	13.5 ± 0.1	4656
SCH2	54.83	-66.83	0	-10.3 ± 0.1	-0.297 ± 0.014	14.5 ± 0.1	6024
SELE	43.18	77.02	0	-16.4 ± 0.1	-0.213 ± 0.013	23.5 ± 0.1	4512
SJDV	45.88	4.68	0	15.6 ± 0.3	2.255 ± 0.013	17.3 ± 0.2	2352
STJO	47.60	-52.68	0	-8.7 ± 0.1	-0.360 ± 0.012	17.2 ± 0.1	12096
TOUL	43.56	1.48	0	-10.8 ± 0.1	-6.723 ± 0.017	22.5 ± 0.1	4656
VILL	40.44	-3.95	0	-8.8 ± 0.1	-0.602 ± 0.017	21.2 ± 0.1	5064
WILL	52.24	-122.17	0	-10.0 ± 0.1	-0.354 ± 0.014	18.4 ± 0.1	5952
WSRT	52.91	6.60	0	7.2 ± 0.1	-3.697 ± 0.018	18.3 ± 0.1	5784
WTZR	49.14	12.88	0	-9.7 ± 0.1	-0.278 ± 0.009	19.9 ± 0.1	15888
YSSK	47.03	142.72	0	-9.7 ± 0.2	-0.374 ± 0.016	13.2 ± 0.2	2736
ZECK	43.79	41.57	0	-17.3 ± 0.1	-0.258 ± 0.010	25.1 ± 0.1	3888
ZIMM	46.88	7.47	0	-10.9 ± 0.1	-0.412 ± 0.006	21.1 ± 0.0	20520
NANO	49.29	-124.09	0	11.9 ± 0.5	-10.032 ± 0.020	13.1 ± 0.4	2112
OBER	48.09	11.28	0	-10.6 ± 0.1	-0.370 ± 0.007	19.7 ± 0.0	15312
UPAD	45.41	11.88	0	13.2 ± 0.1	2.677 ± 0.011	21.0 ± 0.1	4608
URUM	43.81	87.60	0	-15.5 ± 0.2	-0.254 ± 0.016	20.7 ± 0.1	4392
WES2	42.61	-71.49	0	-11.3 ± 0.1	5.822 ± 0.010	18.8 ± 0.1	12888
KSTU	55.99	92.79	0	-8.9 ± 0.1	-0.349 ± 0.017	12.8 ± 0.1	1776
BISH	42.88	74.59	0	-13.3 ± 0.1	-0.317 ± 0.014	22.1 ± 0.1	4032
ZWEN	55.70	36.76	0	6.0 ± 0.2	-3.804 ± 0.040	21.1 ± 0.1	9960
UCLU	48.93	-125.54	0	7.2 ± 0.3	2.482 ± 0.035	17.1 ± 0.3	2400
NSSP	40.23	44.50	0	10.3 ± 7.9	0.647 ± 0.543	46.7 ± 9.4	1056
WSLR	50.13	-122.92	0	25.5 ± 1.2	2.589 ± 0.013	5.1 ± 1.1	2232
MADR	40.43	-4.25	0	-113.7 ± 40.4	-5.943 ± 0.050	-85.5 ± 40.4	432

TEMPERATE ZONE 40°-60° LAT MEAN: 17.1 ± 0.9 mm (amp: -6.9 ± 0.9 mm)

P O L A R Z O N E								
SITE	LAT	Lon	HEI	amp [kg/m ²]	phase [rad]		mean [kg/m ²]	f
BILI	68.08	166.44	0	-3.5 ± 0.2	-0.336 ±	0.049	5.4 ± 0.2	1272
DAV1	-68.58	77.97	0	1.7 ± 0.0	-0.520 ±	0.029	5.2 ± 0.0	3528
HOFN	64.27	-15.20	0	-6.4 ± 0.1	-0.424 ±	0.021	13.8 ± 0.1	4296
KELY	66.99	-50.94	0	-6.1 ± 0.1	-0.266 ±	0.018	10.2 ± 0.1	4560
MAW1	-67.60	62.87	0	1.9 ± 0.0	-0.619 ±	0.020	3.2 ± 0.0	4560
MCM4	-77.84	166.67	0	1.1 ± 0.0	-0.387 ±	0.029	2.8 ± 0.0	4464
NYA1	78.93	11.87	0	-5.7 ± 0.1	-0.195 ±	0.015	8.4 ± 0.1	4728
NYAL	78.93	11.87	0	-5.5 ± 0.1	-0.147 ±	0.016	8.4 ± 0.1	4824
REYK	64.14	-21.96	0	-5.7 ± 0.1	-0.593 ±	0.012	12.5 ± 0.0	12912
THU1	76.54	-68.79	0	-5.1 ± 0.0	-0.142 ±	0.010	7.5 ± 0.0	5760
TIXI	71.63	128.87	0	-8.2 ± 0.1	-0.028 ±	0.009	8.9 ± 0.0	5880
TRO1	69.66	18.94	0	-7.3 ± 0.1	-0.311 ±	0.015	13.5 ± 0.1	4920
TROM	69.66	18.94	0	-6.0 ± 0.1	-0.182 ±	0.025	13.9 ± 0.1	4080
VESL	-71.67	-2.84	0	1.9 ± 0.1	-0.741 ±	0.033	4.5 ± 0.1	2880
WHIT	60.75	-135.22	0	-10.4 ± 0.1	-0.084 ±	0.013	16.7 ± 0.1	5664
YAKZ	62.03	129.68	0	-11.3 ± 0.1	-0.037 ±	0.009	12.1 ± 0.1	5856
YELL	62.48	-114.48	0	-8.2 ± 0.1	-0.431 ±	0.007	12.1 ± 0.0	13200
FAIR	64.98	-147.50	0	-9.5 ± 0.1	-0.241 ±	0.007	11.3 ± 0.0	10272
KIRU	67.86	20.97	0	-7.7 ± 0.1	-0.309 ±	0.014	13.5 ± 0.1	5256
METS	60.22	24.40	0	-8.1 ± 0.1	-0.187 ±	0.011	14.5 ± 0.1	9960
OHIG	-63.32	-57.90	0	3.6 ± 1.0	-0.533 ±	0.067	6.9 ± 0.9	1296
CAS1	-66.28	110.52	0	2.1 ± 0.1	0.037 ±	0.039	5.9 ± 0.0	2688
SYOG	-69.01	39.58	0	13.8 ± 0.9	-0.306 ±	0.011	14.7 ± 0.8	1032
AMUN	-90.00	139.19	0	18.4 ± 23.1	0.953 ±	1.203	-6.7 ± 31.8	336
PALM	-64.78	-64.05	0	25.2 ± 28.5	4.574 ±	0.321	31.7 ± 29.4	432
POLAR ZONE 40°-60° LAT				MEAN: 10.0 ± 2.6 mm (amp: -1.8 ± 2.2 mm)				

Table A-5 - Harmonic IWV analysis of the TropAC database separated into 4 major climatic zones and referenced to the mean sea level (0 m). Last day analyzed: 2000/03/15

Appendix IV: Mean Values for Water Vapor Scale Heights

The water vapor (or zenith wet delay) scale height q_{ZWD} is needed to perform the height reduction of wet delays or integrated water vapor (\rightarrow 4.4.3.2). The following table gives the mean scale heights for a number of IGS tracking stations that were analyzed with help of the TropAC database:

NO.	SITE	SAMPLES	q_{ZWD} [m]	SIG	NO.	SITE	SAMPLES	q_{ZWD} [m]	SIG
1	ALBH	242	2048	26	62	MEDI	243	1945	18
2	ALGO	247	2147	29	63	MKEA	96	2460	69
3	ALIC	218	2156	37	64	MONP	240	2241	35
4	AMC2	235	2059	21	65	NICO	166	1641	22
5	ANKR	181	1901	21	66	NLIB	211	2128	32
6	AOML	585	2162	14	67	NOTO	244	1844	22
7	ARTU	161	2124	29	68	NRC1	239	2181	30
8	AUCK	225	1669	25	69	NRC2	129	2194	43
9	BAHR	633	2217	13	70	NYA1	195	2091	27
10	BARB	131	1993	32	71	NYAL	201	2097	26
11	BILI	53	2437	66	72	ONSA	234	1910	19
12	BOGO	221	1959	21	73	PENC	185	1950	25
13	BOR1	240	1973	21	74	PERT	202	1705	31
14	BRMU	212	1932	25	75	PETP	195	2011	28
15	BRUS	243	1868	19	76	PIE1	225	2026	24
16	CAGL	238	1852	25	77	POL2	187	2038	22
17	CEDU	218	2056	46	78	POTS	842	2202	8
18	CHAT	231	1823	22	79	PRDS	164	2060	25
19	CHUR	243	2345	27	80	RAMO	212	1589	30
20	COCO	160	1971	31	81	REYK	221	1984	23
21	CRO1	133	1813	33	82	RIOG	192	1984	26
22	DAV1	145	2023	26	83	RIOP	90	1830	17
23	DGAR	98	2351	29	84	SANT	160	1864	26
24	DRAO	245	2047	22	85	SCH2	250	2253	30
25	DUBO	202	2261	31	86	SELE	188	2196	29
26	FLIN	248	2226	26	87	SFER	212	1813	24
27	GILB	230	1623	28	88	SJDV	98	1913	31
28	GLSV	246	2004	19	89	STJO	224	2196	33
29	GOPE	247	1868	20	90	SUTH	165	1894	36
30	GOL2	197	2270	30	91	SUWN	123	2125	42
31	GOUG	115	1856	35	92	TELA	162	1565	33
32	GRAS	187	1835	23	93	THTI	148	1949	33
33	GRAZ	243	1929	21	94	THU1	238	2188	21
34	HARK	154	1728	30	95	TID2	211	1755	30
35	HERS	528	2089	13	96	TOUL	194	1923	25
36	HFLK	232	1711	24	97	TIXI	245	2436	26
37	HOB2	233	1795	24	98	TRO1	205	1960	22
38	HOFN	177	2068	26	99	TOW2	205	1921	33
39	HOLB	119	2144	35	100	TROM	170	1988	22
40	HRAO	187	1762	27	101	USNO	701	2233	11
41	IRKT	243	2149	21	102	VESL	120	2034	29
42	JOZE	244	1959	20	103	VILL	210	1878	24
43	JPLM	238	2128	29	104	WHIT	234	1931	21
44	KABR	227	1566	26	105	WILL	248	1975	23
45	KARR	202	2171	31	106	WSRT	241	1894	17
46	KATZ	144	1657	40	107	WTZR	661	2144	11
47	KELY	190	2159	26	108	WUHN	185	2587	30
48	KERG	153	1989	29	109	YAKZ	244	2410	25
49	KOKB	163	1633	39	110	YAR1	205	1702	35
50	KOSG	224	1872	19	111	YELL	245	2332	26
51	LAMA	232	1940	22	112	YKRO	49	2153	24
52	LPGS	172	1994	29	113	YSSK	114	1844	24
53	MAC1	170	1969	25	114	ZECK	160	1881	24
54	MAD2	200	1853	25	115	ZIMM	843	2155	9
55	MAG0	218	2226	26	116	ASC1	156	1715	21
56	MAS1	155	1678	34	117	DAEJ	184	2169	35
57	MATE	227	1836	20	118	FAIR	421	2227	11
58	MAW1	190	2225	35	119	KIRU	216	1914	20
59	MCM4	185	2151	32	120	KWJ1	20	2345	53
60	MDVO	213	2042	22	121	METS	182	1916	25
61	MDO1	214	1913	25	122	NANO	87	2125	36

NO.	SITE	SAMPLES	q_{ZWD} [m]	SIG	NO.	SITE	SAMPLES	q_{ZWD} [m]	SIG
123	OBER	635	2148	11	157	AOA1	2	1827	88
124	UPAD	191	1965	19	158	INEG	68	1966	29
125	URUM	183	2416	40	159	STR1	45	1902	70
126	USUD	174	1930	35	160	KUNM	98	1892	35
127	WES2	525	2255	12	161	OHIG	53	2176	60
128	BAKO	89	2305	31	162	CAS1	112	2061	43
129	BSHM	163	1540	34	163	SHAO	72	2612	53
130	ELAT	120	1857	36	164	EBRE	2	2616	68
131	GODE	169	2143	36	165	EPRT	1	1828	999
132	KSTU	74	2143	40	166	QUIN	67	2024	45
133	LHAS	123	2025	20	167	UCLU	100	2158	34
134	NOUM	198	1955	36	168	EISL	61	1805	43
135	PIMO	204	2393	21	169	TUBI	1	1947	999
136	JAB1	64	2029	47	170	CASC	23	1866	65
137	BOGT	80	1862	18	171	GALA	56	2268	30
138	SEY1	20	1823	69	172	KIT3	74	2325	49
139	BISH	165	2182	28	173	NSSP	44	2156	29
140	FORT	68	1972	29	174	SOL1	92	2052	35
141	KOUR	32	2304	36	175	USNA	91	2047	33
142	ZWEN	208	2064	22	176	WSLR	93	1964	35
143	IISC	55	1993	58	177	BRAZ	2	1553	68
144	TSKB	133	2073	39	178	SYOG	43	2504	61
145	CIC1	32	2155	73	179	CIT1	2	2240	71
146	AREQ	102	2058	30	180	BUCU	1	1736	999
147	CORD	77	2095	39	181	AMUN	14	2203	63
148	NTUS	105	2463	12	182	PALM	18	2067	65
149	XIAN	80	2386	42	183	GOLD	24	2339	42
150	DARW	181	2238	35	184	MADR	17	1747	45
151	GUAM	33	2148	75	185	TIDB	25	1491	63
152	SNI1	1	2299	999	186	AMCT	17	2319	66
153	SIO3	1	1972	999	187	HART	3	1943	133
154	BJFS	39	2320	61	188	SCIP	1	1764	999
155	JAMA	87	1582	27					
156	MALI	70	2052	26					
					MEAN		2029		

Table A-6 - Mean zenith wet delays/water vapor scale heights for 188 stations of the IGS tracking network. The row "SITE" contains the 4-characters station ID, the number of samples denotes the number of days that were used for the derivation of the mean scale height and the scale height q_{ZWD} is given in meters as well as the associated empirical standard deviation "SIG". Only values obtained using a sufficiently large number of samples should be used. Some scale heights included in this table are based on very few observations. In such cases, it is recommended to use the mean scale height of about 2 km. Last day analyzed: 2000/03/15.

Appendix V: TROPEX Format Description

TROPEX correction files contain all necessary data for tropospheric delay computation which are primarily obtained by the analysis of 3-D numerical weather models. The default model is NOAA NCEP GDAS FNL with a resolution of $1^\circ \times 1^\circ$. The data are represented in equi-rectangular projection (matrix layout). A service area can be defined (by default, global maps are generated). Additionally, GPS-derived troposphere delays can be assimilated into the TROPEX model and thereby, conventional and new techniques can be combined. The following sections outline the file format and contents of TROPEX files.

1. Naming Convention

TROPEX data sets normally consist of two files, an index and a data file. The data file is named like <Analysis Center><DoY>0.<YY>a, e. g. IFEN1820.99a, where the analysis center code has exactly 4 characters, the DoY is the day of year and YY stands for the 2-digit year. The index file has the same name except for the "0" that is replaced by an "i" for *index*, e. g. IFEN182i.99a. Both files are usually packed in a zip archive named <DoY>_<YY>_a.zip, e. g. 182_99_a.zip, that will be uncompressed automatically by the TropAC analysis software.

2. File Identification and End

The very first line of a TROPEX file shall have the following form:

```
%=TRX 0.00 IFN 00:003 90.0000 0.0000 -90.0000 359.0000
```

In this case, "IFN" denotes the analysis center (3 characters maximum), "00:" is the shortened form of the year the model is computed for (00 = 2000) and ":003" is the day of year (DoY, i. e. 3 January). The last two pairs indicate the service area of the TROPEX file: 1st point = north/west = <latitude max.; longitude min.> (here: lat = $+90^\circ$ and lon = 0°), 2nd point = south/east = <latitude min.; longitude max.> (here: lat = -90° and lon = 359°). This means, there is a global coverage for a model with $1^\circ \times 1^\circ$ resolution. Note that longitude range is from 0 ... 360° (not -180° ... $+180^\circ$).

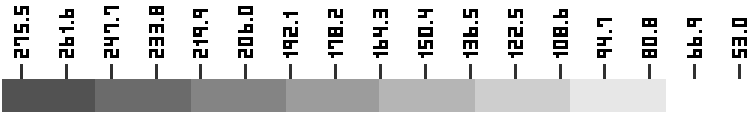
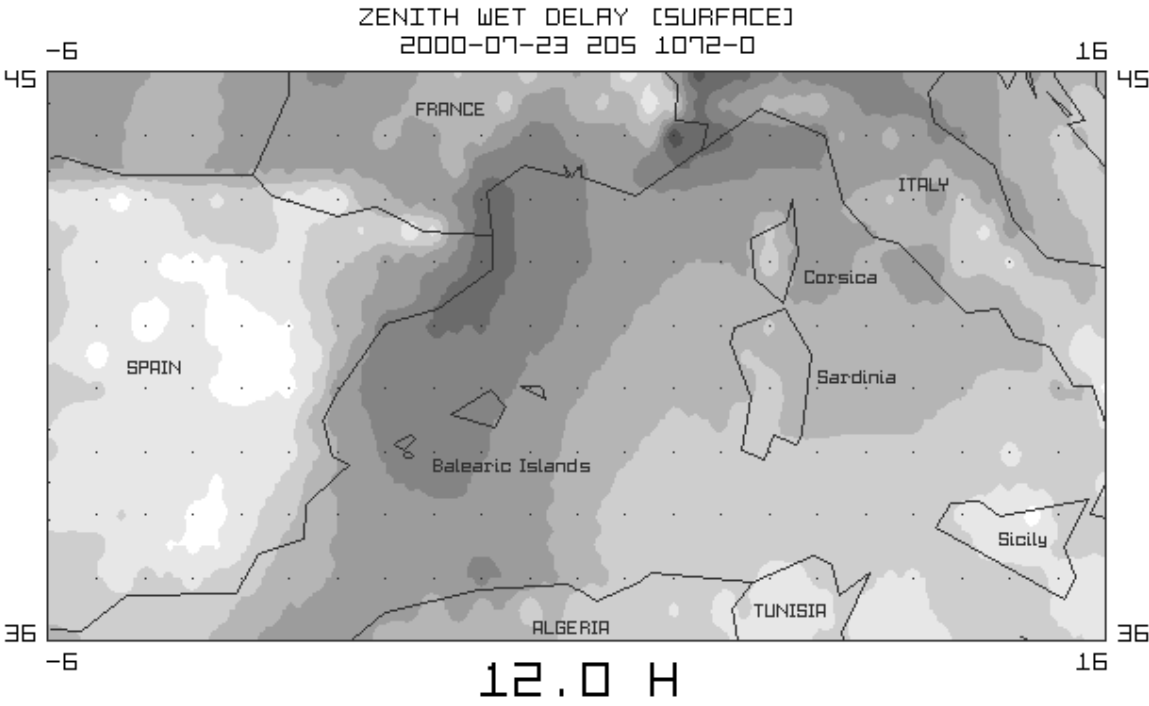
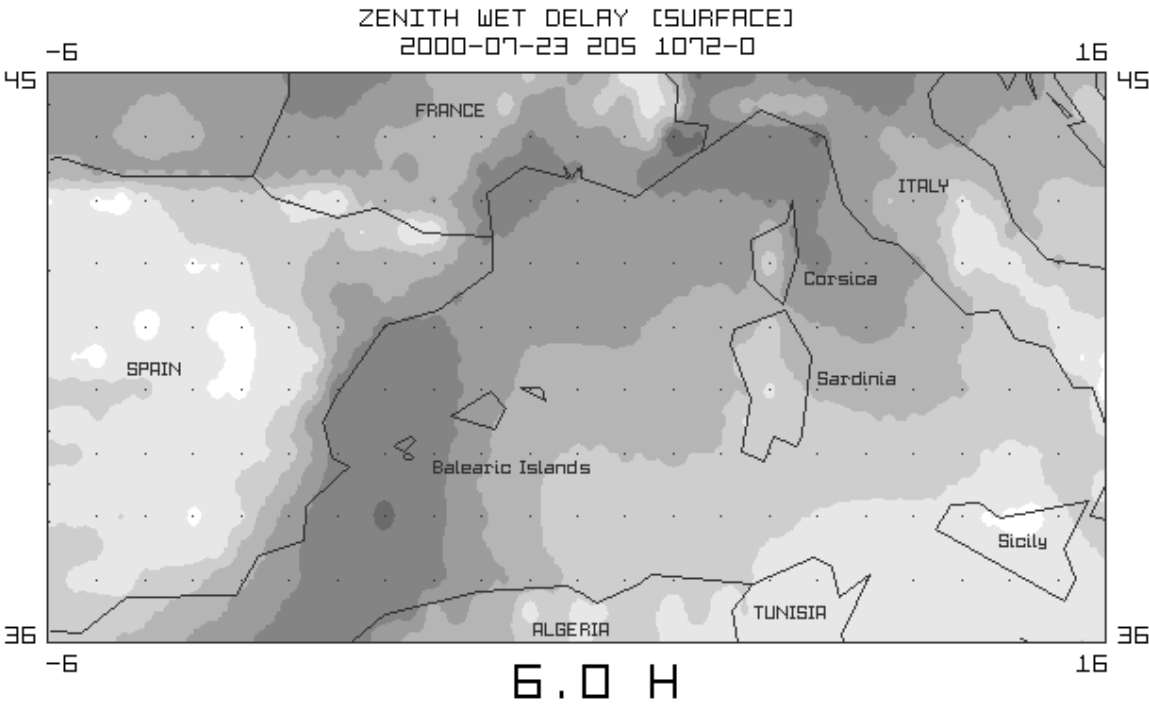
The last line of the TROPEX file should indicate its end by

```
%=ENDTRX
```

3. Reference Section of Index File

The index files simply consists of the reference section. Its purpose is to describe the data set. It usually consists of three lines listing the analysis center, the kind of output and the point of contact. Example:

```
+FILE/REFERENCE
ANALYSIS CENTER INSTITUTE OF GEODESY AND NAVIGATION, UNI FAF MUNICH
OUTPUT          TROPEX - TROPOSPHERE CORRECTION MODEL FROM GDAS FNL
CONTACT         TORBEN.SCHUELER@UNIBW-MUENCHEN.DE
-FILE/REFERENCE
```



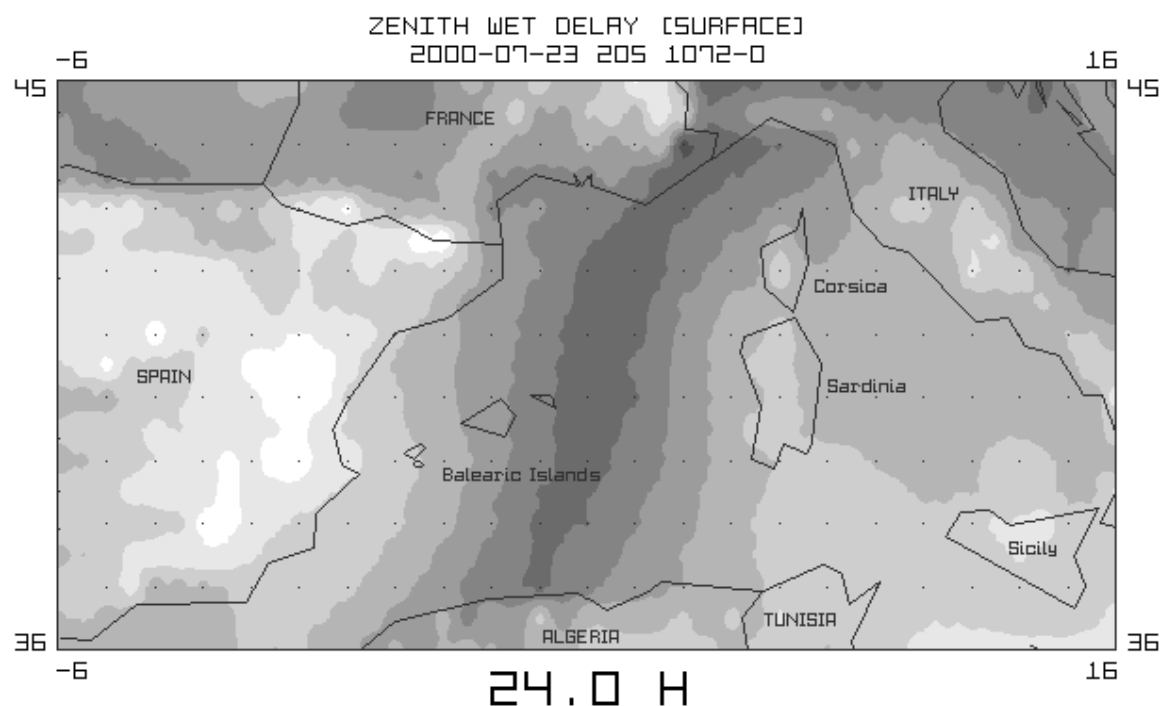
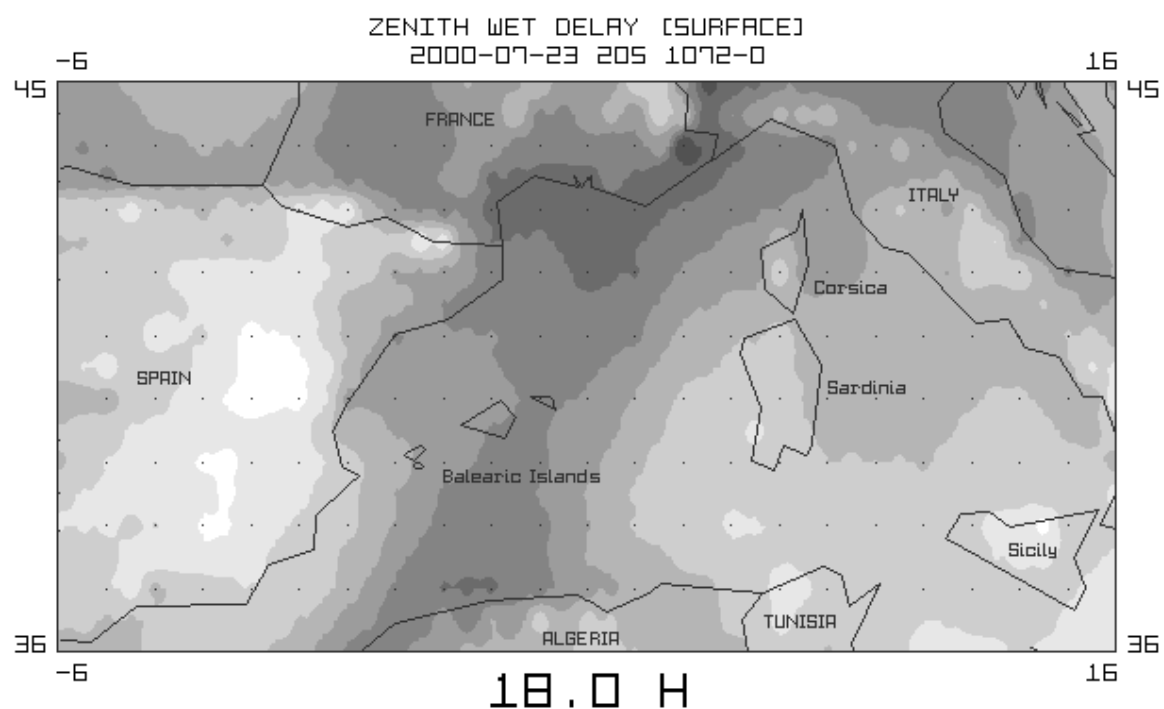


Figure A-8 - Sequence of zenith wet delay images for area of the Mediterranean Sea. The legend for the zenith wet delay values is given on the preceding page in units of millimeters. Blue colors indicate wet areas with a huge amount of humidity, red colors represent dry regions. The delays have been reduced to real topography using the standard 5' x 5' digital elevation model of the institute's tropospheric analysis system. The boundaries of the maps are 36° ... 45° (latitude) and - 6° ... 16° (longitude). Time is given in UTC.

4. Description Fields of Index File

This section is of highest importance in order to make use of TROPEX files afterwards as it contains all needed meta data. The following example is for gridded data sets:

```
+TRX/DESCRIPTION
* _____KEYWORD_____  _____VALUE(S)_____
DATE                        2000 01 03 003 1043 1
NUMBER OF EPOCHS           5
EPOCHS                     00 06 12 18 24
AREA: LEFT UP, LAT AND LON  90.0000  0.0000
AREA: RIGHT DOWN, LAT AND LON -90.0000 359.0000
AREA: NORTHWARD RESOLUTION 1
AREA: EASTWARD RESOLUTION  1
AREA: ROWS                 181
AREA: COLUMNS             360
AREA: VALUES PER LAYER    65160
MAX. HEIGHT FOR RED. COEFF. 12.000
MAX. HEIGHT FOR SCALE HEIGHT 20.000
MAX. HEIGHT FOR LAPSE RATE  TROPOPAUSE
PROJECTION                 EQUIRECTANGULAR (MATRIX LAYOUT)
COMPRESSION               DIFFERENTIAL (FIRST ORDER)
LAYER UNIQUE 01           GEOID HEIGHT EGM96
LAYER UNIQUE 02           GEOPOTENTIAL HEIGHT
LAYER PER EPOCH 01        SURFACE PRESSURE
LAYER PER EPOCH 02        PRECISION OF SURFACE PRESSURE
LAYER PER EPOCH 03        PRESSURE REDUCTION COEFF. A
LAYER PER EPOCH 04        PRESSURE REDUCTION COEFF. B
LAYER PER EPOCH 05        PRESSURE REDUCTION COEFF. C
LAYER PER EPOCH 06        ZENITH WET DELAY
LAYER PER EPOCH 07        PRECISION OF ZENITH WET DELAY
LAYER PER EPOCH 08        WATER VAPOR SCALE HEIGHT
LAYER PER EPOCH 09        MEAN TEMPERATURE OF TROPOSPHERE
LAYER PER EPOCH 10        TEMPERATURE LAPSE RATE
LAYER PER EPOCH 11        HEIGHT OF TROPOPAUSE
LAYER PER EPOCH 12        SURFACE TEMPERATURE
LAYER PER EPOCH 13        SURFACE WATER VAPOR PRESSURE
-TRX/DESCRIPTION
```

Explanation:

Keyword	Value(s), Format, Remarks
date	YYYY MM DD DOY WEEK DOW year, month, day of month, day of year, GPS-week (not reduced), day of week (0: Sunday)
no. of epochs	usually 5 as final analyses take place each 6 hours and the first analysis of the following day is also included in the TROPEX file to allow interpolation all the time (extrapolation is prohibited)
epochs	UTC hours for the analysis times contained in the TROPEX file
area: left up	the north/west corner of the service area (latitude, longitude in degrees)
area: right down	the south/east corner of the service area (latitude, longitude in degrees)
area: northward resolution	resolution in northward direction in degrees (decimal)
area: eastward resolution	resolution in eastward direction in degrees (decimal)
area: rows	number of rows per layer
area: columns	number of columns per layer

Keyword	Value(s), Format, Remarks
area: values per layer	total number of points per layer
maximum height for pressure reduction coefficients	pressure is reduced using 3 reduction coefficients which are computed individually for each grid point; the maximum height for this adjustment is given here; usually about 12 km (i.e. TROPEX file allow to be used for aviation)
maximum height for scale height of water vapor column	wet delays are reduced using the scale height which is computed individually for each grid point; the maximum height for this adjustment is given here; usually about 12 km
maximum height for temperature lapse rate	computation the maximum height for temperature lapse rate computation should be no higher than the height of the tropopause
projection	equi-rectangular map projection is always used for gridded data
compression	differential ASCII-compression is used by default leading to global 1° x 1° files with a size of about 9.5 MB per day; additionally, binary gzip-compression can be applied reducing the storage load down to about 3.5 MB (ASCII-compression is a very well preparation for effective binary compression afterwards); note: temporal resolution has been doubled in April 2000 increasing the daily file from 3.5 to 5.7 MB
layer unique	these layers appear once in the file as they do not change with time; these are for gridded data: geoid heights and geopotential heights for all grid-points.
layer per epoch	these layers appear each epoch, i.e. they contain time-varying information: surface pressure and corresponding reduction coefficients, zenith wet delays and corresponding scale heights; mean temperature of the atmosphere, temperature lapse rate, height of tropopause

Non-gridded data sets

Alternatively, TROPEX files may also contain non-gridded data sets, e. g. if only GPS-results from the IGS are used. In this case, the following two unique layers are added: latitude and longitude of point. Note that all unique layers are mandatory as well as the layers per epoch 01 to 08.

5. Input Files Section of Index File

Optionally, the input files used can be listed for each epoch:

```
+TRX/FILES
*_EPOCH_ _INPUT_FILE_____
00      /hdd3/ncep/2000-01-03/gdas1.T00Z.PGrbF00
06      /hdd3/ncep/2000-01-03/gdas1.T06Z.PGrbF00
12      /hdd3/ncep/2000-01-03/gdas1.T12Z.PGrbF00
18      /hdd3/ncep/2000-01-03/gdas1.T18Z.PGrbF00
24      /hdd3/ncep/2000-01-04/gdas1.T00Z.PGrbF00
-TRX/FILES
```

6. Data Section/Data Files

The data section first contains the unique layers and then all time-dependent ones sorted by time. Differential ASCII-compression is always applied.

```
+TRX/SOLUTION
*unique
*epoch 00
...
-TRX/SOLUTION
```

7. Implementation

All TROPEX functions like input/output as well as the interpolation and height reduction models are implemented in the class CTropex of the tropospheric analysis software TropAC TRIDENT (located in the source directory in subdirectory paf_tool).

Index of Keywords

A

absolute delay estimation 166
adjustment algorithm 93
ambiguities 102; 113
antenna eccentricity correction 74
antenna phase center correction (satellite) 86
antenna phase center corrections 74
antenna phase center offset 75
antenna phase center variations 76; 316
apparent zenith angle 150; 152
arithmetic weighted mean coordinates 112
atmosphere 129
auto-covariance function 175
availability 248

B

Baarda-type blunder detector 96
backward filtering 107
barometric height formula 200
base frequency 51
bending correction 150
best linear unbiased estimator 220
Black hydrostatic mapping function 153
Black wet mapping function 158
blunder detection 95; 108
body-fixed coordinate system (GPS spacecraft) 86
broadcast orbits 77

C

carbon dioxide 38
carrier beat phase 51
carrier phase measurements 51
centered networks 123
CfA 2.2 mapping function 154
Chao hydrostatic mapping function 153
Chao wet mapping function 158
check of innovations 109
check of stochastic model of the state vector 110
Clausius-Clapeyron equation 204
code ranges 50
colored noise 178
combination of NWM and GPS 221
combined GDAS/GPS solution 312
compressibility factors 134
convergence uncertainty of ZWD estimates 165; 189; 271; 316; 317; 339
conversion coefficients for mean temperature 336
conversion factor Q 186
conversion of wet delays into precipitable water 184
coordinate error 315
cosecant mapping function 149

covariance matrix of the innovations 105
covariance matrix of the state vector 102
cut-off elevation 172
cycle slip detection and repair 67

D

datum defects 119
datum transformation 120
Davis hydrostatic mapping function 154
design matrix 92; 104
dipole elements 57
dipole moment of water vapor 133
direct fixing of ambiguities 113
displacements 69
distance weighting 219
double differences 53
 δ -technique 55
dynamic tuning 180

E

eclipsing season 88
EDAS 193
effective dipole 57
EGM96 geopotential model 195
electron density 63
elevation mask 172
energy balance 37
epoch of signal transmission 81
equation of state for ideal gases 134
error budget of wet delay estimates 164; 315
estimation of tropospheric parameters 161
ETA 193
EUREF/GREF experiment 269

F

filter update 105
final orbits 76; 267
first order ionospheric effect 63
free network solution 121
functional matrix 92

G

gas laws of Boyle-Mariotte and Gay-Lussac 136
Gauss-Markov process 175
gain matrix 105
Gauss-Markov model 91
GDAS numerical weather model 193; 194
geodetic datum 119
geoid height 210
geomagnetic coordinates 64
geopotential heights 194
Global Data Assimilation System 194
global functions for ZWD conversion 187
global test 95
GPS radio occultation 41
gradient mapping functions 160

gradients 262; 285
 gravity acceleration 141
 greenhouse effect 37
 gridded tropospheric correction files (TROPEX)
 209

H

height dependency of mean temperature 188
 height of the dry atmosphere 139
 height of the ionosphere 64
 height of tropopause 146
 height systems 194
 Herring hydrostatic mapping function 156
 Herring wet mapping function 159
 high-resolution weather fields 238
 Hopfield hydrostatic delay model 136
 Hopfield wet delay model 146
 horizontal gradients 205; 262; 285
 horizontal gradient estimation 162
 horizontal interpolation (TROPEX) 218
 horizontal interpolation in weather fields 201
 horizontal tropospheric gradient model 132
 hourly process noise values 181
 humidity extraction 204
 hydrological cycle 37
 hydrostatic delay 132
 hydrostatic delay vs. ZWD error 169; 317
 hydrostatic mapping functions 151

I

Ifadis hydrostatic mapping function 155
 Ifadis wet delay model 147
 Ifadis wet mapping function 159
 index of refraction 133
 indirect fixing of ambiguities 115
 individual functions for ZWD conversion 188
 interpolation sequences in weather fields 197
 IONEX files 65
 IONEX maps 62
 ionosphere-free signal 61
 ionospheric amplification factor 61
 ionospheric delay 62
 ionospheric error 263
 ionospheric points 66
 iterating on a previous solution 95

J

jump detection 112

K

Kalman filtering 98

L

least-squares adjustment 91
 level-D check 109
 level-U check 110
 leveling networks 167
 LIDAR 40

linear combinations 60
 long-term experiment 248
 lower atmosphere 129

M

mapping function 149; 262
 mapping functions, NWM-derived 241
 mapping function coefficients 205
 mapping function coefficient estimation 163;
 285
 mapping function vs. ZWD error 170; 317
 Marini mapping function 151
 Matrix-Ricatti equation 175
 maximum process noise 181
 mean atmospheric temperature 184; 213; 241
 mean temperature, height dependency 188
 measurement noise vs. ZWD error 172
 median choice 112
 Mendes wet delay model 147
 methane 38
 microwave sensors 41
 MOPS hydrostatic delay model 142
 MOPS wet delay model 147
 multipath detection 68
 multipath experiment 276
 multipath vs. ZWD error 169; 317

N

narrow lane 61
 narrow lane fixing 117
 NAVSTAR GPS 38
 nearest neighbors 202
 network check 124
 network composition 123
 network partitioning 126
 network structure 167
 neutral slant path delay 132
 Niell hydrostatic mapping function 157
 Niell wet mapping function 160
 nominal ionosphere-free ambiguity 118
 normal equation matrix 93
 normalized weights 203
 numerical differentiation 104
 numerical weather fields 193
 numerical weather models 276
 NWM-derived zenith neutral delays 299

O

OBER-I experiment 256
 OBER-II experiment 267
 obliquity factor 149
 observation vector 92
 ocean loading 73
 orbit error vs. ZWD error 165; 315
 orbit accuracy 267
 orbit interpolation 79
 orientation problem 57
 orthometric height 195

P

parameter estimation techniques 91
partitioning of networks 126
penumbra 88
1-pillar-method 197
4-pillar-method 198
pole tide correction 73
Pope-type blunder detector 96
position error vs. ZWD error 164
post-fit residuals 94
predicted covariance matrix of the states 103
predicted orbits 76; 267
prediction of the state vector 103
pre-fit residuals 93
pressure 129
pressure (TROPEX) 211
pressure extraction 197
pressure scale height 200; 212; 291
process noise amplification 184
process noise definition 182
process noise parameters 177; 333
process noise values 178
pseudo-ranges 51

R

radiosonde 39
radiosonde data 266; 269
random walk 176
rapid orbits 76; 267
ray-tracing analysis 208
ray-tracing in weather fields 205
receiver clock error 83
receiver clock error behavior 85
redundancy matrix 94
refractivity formula 134
regional functions for ZWD conversion 187
relative humidity 234
residual analysis 111
residual-type blunder detector 96
relative delay estimation 167
relative humidity 131

S

Saastamoinen hydrostatic delay model 140
Saastamoinen mapping function 152
saturation water vapor pressure 204
sea level pressure 129
second order ionospheric effect 64
selective availability 55
shortest baseline networks 123
similarity system 119
similarity transformation 121
single differences 53
site displacements 69
site isolation logic 124
Snell's law of refraction 150
solar occultation 41

solid earth tides 71
Square Root Information Filter (SRIF) 106
stabilized filter 106
state vector 101
stochastic filtering 173
stochastic model 92
stochastic optimization 225
stochastic processes 174
stochastic properties of wet delays 172
stratopause 129
stratosphere 129
summarizing coordinates 111
surface data extraction 197
surface pressure 230
surface temperature 232
synchronization 55

T

temperature 131
temperature extraction 203
temperature lapse rate 131; 139; 155; 214; 240
temporal interpolation in weather fields 203
time series analysis 177
tides 69
time of signal transmission 82
time of signal travel 82
total clock error 82
transition matrix 102
TROPEX data 291
TROPEX-derived zenith neutral delays 299
TROPEX files 209
TROPEX format description 355
tropopause 129
tropopause height 146; 155; 214
troposphere 129

U

ultra-rapid orbits 267
umbra 88

V

validation experiments 247
variance component estimation 225
vector of innovations 105
vertical interpolation of pressure 199
vertical profile modeling of pressure 212
vertical profile modeling of wet delays 213
vertical stability 37
virtual wavelength 60

W

water vapor 37; 131
water vapor observing systems 39
water vapor pressure 204
water vapor radiometer 42
water vapor radiometer experiment 280
water vapor scale height 213; 297; 353

water vapor time series analysis 342
weighted mean gravity acceleration 141
wet delay 132
wet mapping functions 158
white noise 175; 177
wide lane 61
wide lane fixing 115

Z

zenith hydrostatic delay 39; 136; 211
zenith wet delay 39; 145
zenith wet delay (TROPEX) 212
zenith wet delay estimation 161
zenith wet delay scale height 213

Acknowledgements

Without any doubt, the successful completion of this research would not have been possible without the advice and support of many individuals and organizations.

First of all, I want to express my deep gratitude towards the maintainers of the IGS network for the availability and supply of GPS data and to all those analysts of the IGS processing centers who provide GPS satellite orbits of unprecedented accuracy. The provision of GPS data of the German Reference Network (GREF) by the Federal Agency of Cartography and Geodesy (BKG, Bundesamt für Kartographie und Geodäsie) is appreciated as well as the supply of radiosonde data by the Federal Armed Office of Geophysics (Amt für Wehrgeophysik). Special thanks are devoted to Dr. Christina Köpcken and Dr. Acker from the German Weather Service (DWD, Deutscher Wetterdienst) for providing several kinds of weather model data, water vapor radiometer samples and radiosonde profiles that were vital for the validation of the GPS results.

The invaluable help of my colleagues is highly appreciated. In particular, I offer my thanks to Robert Wolf for his support on ephemeris computation, Wolfgang Werner, Udo Rossbach and Bernhard Riedl for their invaluable advice throughout these studies, and Jón Ólafur Winkel for his patience. Moreover, I would like to honor the aid of Prof. Dr. Rothacher (Munich Technical University) and Dr. Mark Schenewerk (NGS, National Geodetic Survey, USA) with respect to the clarification of GPS satellite orbit issues.

Last but not least, the support of my supervisors, Prof. Dr. Guenter W. Hein, Prof. Dr. Bernd Eissfeller, and Prof. Dr. Guenter Seeber is gratefully acknowledged, and I want to thank the Department of Education and Research (BMBF, Bundesministerium für Bildung und Forschung) for partial funding of these studies.

Schriftenreihe des Studiengangs Geodäsie und Geoinformation der Universität der Bundeswehr München

Bisher erschienene Hefte:

Heft 1/1978 (*vergriffen*)

A. Schödlbauer (*Bearb.*): Curriculum für den wissenschaftlichen Studiengang Vermessungswesen der Hochschule der Bundeswehr München. 53 S.

Heft 2/1978

A. Chrzanowski and E. Dorrer (*Eds.*): Proceedings „Standards and Specifications for Integrated Surveying and Mapping Systems“. Workshop held in Munich, Federal Republic of Germany, 1-2 June, 1977. Assisted by J. McLaughlin. VII, 181 S.

Heft 3/1978

W. Caspary und A. Geiger: Untersuchungen zur Leistungsfähigkeit elektronischer Neigungsmesser. 62 S.

Heft 4/1979

E. Baumann, W. Caspary, H. Dupraz, W. Niemeier, H. Pelzer, E. Kuntz, G. Schmitt und W. Welsch: Seminar über Deformationsanalysen, gehalten an der Hochschule der Bundeswehr München. 106 S.

Heft 5/1981

K. Torlegård: Accuracy Improvement in Close Range Photogrammetry. 68 S.

Heft 6/1982

W. Caspary und W. Welsch (*Hrsg.*): Beiträge zur großräumigen Neutrassierung. 271 S.

Heft 7/1982

K. Borre and W. M. Welsch (*Eds.*): International Federation of Surveyors - FIG. Proceedings „Survey Control Networks“. Meeting of Study Group 5B, 7th-9th July, 1982, Aalborg University Centre, Denmark. 431 S.

Heft 8/1982

A. Geiger: Entwicklung und Erprobung eines Präzisionsneigungstisches zur Kalibrierung geodätischer Instrumente. Dissertation. 125 S.

Heft 9/1983

W. Welsch (*Hrsg.*): Deformationsanalysen '83. Geometrische Analyse und Interpretation von Deformationen Geodätischer Netze. Beiträge zum Geodätischen Seminar 22. April 1983. 339 S.

Heft 10/1984

W. Caspary, A. Schödlbauer und W. Welsch (*Hrsg.*): 10 Jahre Hochschule der Bundeswehr München. Beiträge aus dem Institut für Geodäsie. 244 S.

Heft 11/1984 (*vergriffen*)

W. Caspary und H. Heister (*Hrsg.*): Elektrooptische Präzisionsstreckenmessung. Beiträge zum Geodätischen Seminar 23. September 1983. 270 S.

Heft 12/1984

P. Schwintzer: Analyse geodätisch gemessener Punktlageänderungen mit gemischten Modellen. Dissertation. 159 S.

Heft 13/1984

G. Oberholzer: Landespflege in der Flurbereinigung. 81 S.

Heft 14/1984

G. Neukum: Fernerkundung der Planeten und kartographische Ergebnisse. Mit Beiträgen von G. Neugebauer. Herausgegeben von G. Neugebauer. 102 S.

Heft 15/1984

A. Schödlbauer und W. Welsch (*Hrsg.*): Satelliten-Doppler-Messungen. Beiträge zum Geodätischen Seminar 24./25. September 1984. 396 S.

Heft 16/1985 (*vergriffen*)

M. K. Szacherska, W. M. Welsch: Geodetic Education in Europe. 234 S.

Heft 17/1986

B. Eissfeller, G. W. Hein: A Contribution to 3d-Operational Geodesy. Part 4: The Observation Equations of Satellite Geodesy in the Model of Integrated Geodesy. 190 S.

Heft 18/1985

G. Oberholzer: Landespflege in der Flurbereinigung, Teil II. 116 S.

Heft 19/1986 (*vergriffen*)

H. Landau, B. Eissfeller and G. W. Hein: GPS Research 1985 at the Institute of Astronomical and Physical Geodesy. 210 S.

Heft 20/1985

Heft 20-1

W. Welsch and L. A. Lapine (Eds.): International Federation of Surveyors - FIG. Proceedings „Inertial, Doppler and GPS Measurements for National and Engineering Surveys“. Joint Meeting of Study Groups 5B and 5C, July 1-3, 1985. Volume 1. 310 S.

Heft 20-2

W. Welsch and L. A. Lapine (Eds.): International Federation of Surveyors - FIG. Proceedings „Inertial, Doppler and GPS Measurements for National and Engineering Surveys“. Joint Meeting of Study Groups 5B and 5C, July 1-3, 1985. Volume 2. S. 311 - 634

Heft 21/1986

G. Oberholzer: Landespflege in der Flurbereinigung, Teil III. 100 S.

Heft 22/1987

W. Caspary, G. Hein, A. Schödlbauer (Hrsg.): Beiträge zur Inertialgeodäsie. Geodätisches Seminar 25./26. September 1986. 386 S.

Heft 23/1987

E. Dorrer und J. Peipe (Hrsg.): Motografie. Symposium 11./12. März 1986. 285 S.

Heft 24/1987

G. Neugebauer (Hrsg.): Brenta-Monographie – Grundlagenforschung auf dem Gebiet der Hochgebirgskartographie. Mit Beiträgen von *D. Beineke, H. C. Berann, W. de Concini, G. Hell, D. Herm, H. Immel, U. Kleim, G. Neugebauer und K. Ringle.* 187 S.

Heft 25/1987

A. Perelmutter: Beiträge zur Ausgleichung geodätischer Netze. 75 S.

Heft 26/1987

W. Ellmer: Untersuchung temperaturinduzierter Höhenänderungen eines Großturbinentisches. Dissertation. 109 S.

Heft 27/1988

H. Heister: Zur automatischen Kalibrierung geodätischer Längenmeßinstrumente. Habilitationsschrift. 213 S.

Heft 28/1987

E. H. Paßberger: Systemstudie zur Sicherung ökologischer Vorrangflächen mittels Bodenordnung in Bayern / System study for the protection of ecological priority areas by means of Land rearrangement in Bavaria. Dissertation. 186 S.

Heft 29/1987

H. Glasmacher: Die Gaußsche Ellipsoid–Abbildung mit komplexer Arithmetik und numerischen Näherungsverfahren. Dissertation. 131 S.

Heft 30/1987

Y. Zhang: Beiträge zum Entwurf von optimalen Beobachtungsplänen für tektonische Überwachungsnetze. Dissertation. 151 S.

Heft 31/1988

W. Lechner: Untersuchung einer kreiselorientierten Landfahrzeug-Navigationsanlage im Hinblick auf geodätische Anwendungen und Möglichkeiten der Höhenübertragung. Dissertation. 165 S.

Heft 32/1988

R. König: Zur Fehlertheorie und Ausgleichung inertialer Positionsbestimmungen. Dissertation. 143 S.

Heft 33/1988

H. Borutta: Robuste Schätzverfahren für geodätische Anwendungen. Dissertation. 161 S.

Heft 34/1988

H. Landau, K. Hehl, B. Eissfeller, G. W. Hein and I. W. Reilly: Operational Geodesy Software Packages. 325 S.

Heft 35/1988

G. Oberholzer, E. Paßberger: Landespflege in der Flurbereinigung, Teil IV. 153 S.

Heft 36/1988

H. Landau: Zur Nutzung des Global Positioning Systems in Geodäsie und Geodynamik: Modellbildung, Softwareentwicklung und Analyse. Dissertation. 287 S.

Heft 37/1989

B. Eissfeller: Analyse einer geodätischen raumstabilisierten Inertialplattform und Integration mit GPS. Dissertation. 327 S.

Heft 38/1990 (*vergriffen*)

Heft 38-1

A. Schödlbauer (Hrsg.): Moderne Verfahren der Landesvermessung. Beiträge zum 22. DVW-Seminar 12.-14. April 1989. Teil I: Global Positioning System. 352 S.

Heft 38-2

A. Schödlbauer (Hrsg.): Moderne Verfahren der Landesvermessung. Beiträge zum 22. DVW-Seminar 12.-14. April 1989. Teil II: Nivellement. Teil III: Vermessungskreisel. S. 353 - 551

Heft 39/1989

N. Kersting, W. Welsch (Hrsg.): Rezente Krustenbewegungen. Seminar 8./9. Juni 1989. 307 S.

Heft 40/1989

G. Oberholzer: Ländliche Kulturgeschichte und Landentwicklung. 214 S.

Heft 41/1990

G. W. Hein, K. Hehl, B. Eissfeller, M. Ertel, W. Jacoby, D. Czerek: On Gravity Prediction Using Density and Seismic Data. 148 S.

Heft 42/1992

N. Kersting: Zur Analyse rezenter Krustenbewegungen bei Vorliegen seismotektonischer Dislokationen. Dissertation. V, 246 S.

Heft 43/1992

K. Hehl: Bestimmung von Beschleunigungen auf einem bewegten Träger durch GPS und digitale Filterung. Dissertation. XII, 206 S.

Heft 44/1992

W. Oswald: Zur kombinierten Ausgleichung heterogener Beobachtungen in hybriden Netzen. Dissertation. 128 S.

Heft 45/1993

Institut für Geodäsie (Hrsg.): Das Global Positioning System im praktischen Einsatz der Landes- und Ingenieurvermessung. Beiträge zum Geo-dätischen Seminar 12.-14. Mai 1993. 314 S.

Heft 46/1994

K. Brunner und J. Peipe (Hrsg.): Festschrift für Prof. Dr.-Ing. Egon Dorrer zum 60. Geburtstag. 254 S.

Heft 47/1994

Heft 47-1

K.-H. Thiemann: Die Renaturierung strukturarmer Intensivagrargebiete in der Flurbereinigung aus ökologischer und rechtlicher Sicht. Dissertation. Teil I: Renaturierungsleitbild, Naturschutzverfahren. XXXVI, 384 S.

Heft 47-2

K.-H. Thiemann: Die Renaturierung strukturarmer Intensivagrargebiete in der Flurbereinigung aus ökologischer und rechtlicher Sicht. Dissertation. Teil II: Planungsrechtliche Aspekte. XXXVI, S. 385 - 572

Heft 48/1994

C. Schwietz: Experimente zur GPS-gestützten Aerotriangulation unter besonderer Berücksichtigung systematischer Einflüsse. Dissertation. VIII, 192 S.

Heft 49/1995

R. Scheuring: Zur Qualität der Basisdaten von Landinformationssystemen. Dissertation. 126 S.

Heft 50/1997

W. M. Welsch, M. Lang, M. M. Miller (Eds.): Geodetic Activities, Juneau Icefield, Alaska, 1981 - 1996. 268 S.

Heft 51/1996

H. Blumenhofer: Untersuchungen zu hochpräzisen kinematischen DGPS-Echtzeitverfahren mit besonderer Berücksichtigung atmosphärischer Fehlereinflüsse. Dissertation. X, 168 S.

Heft 52/1997

J. G. Wang: Filtermethoden zur fehlertoleranten kinematischen Positionsbestimmung. Dissertation. XV, 138 S.

Heft 53/1996

G. Chen: Robuste Verfahren zur Analyse linearer stochastischer Prozesse im Zeitbereich. Dissertation. III, 128 S.

Heft 54/1997

J. Dold: Ein hybrides photogrammetrisches Industriemeßsystem höchster Genauigkeit und seine Überprüfung. Dissertation. 140 S.

Heft 55/1997

B. Eissfeller: Ein dynamisches Fehlermodell für GPS Autokorrelationsempfänger. Habilitationsschrift. XII, 182 S.

Heft 56/1997

T. Sutor: Robuste Verfahren zur Analyse linearer stochastischer Prozesse im Spektralbereich. Dissertation. 123 S.

Heft 57/1997

G. Oberholzer: Ländliche Kulturgeschichte und Landentwicklung, Teil II. 186 S.

Heft 58/1997

D. Zhong: Datumsprobleme und stochastische Aspekte beim GPS-Nivellement für lokale Ingenieurnetze. Dissertation. 160 S.

Heft 59/1997

T. Jiang: Digitale Bildzuordnung mittels Wavelet-Transformation. Dissertation. II, 136 S.

Heft 60/2000

Heft 60-1

W. Caspary, H. Heister, A. Schödlbauer, W. Welsch (Hrsg.): 25 Jahre Institut für Geodäsie. Teil 1: Wissenschaftliche Beiträge und Berichte. 331 S.

Heft 60-2

W. Caspary, H. Heister, A. Schödlbauer, W. Welsch (Hrsg.): 25 Jahre Institut für Geodäsie. Teil 2: Forschungsarbeiten und Veröffentlichungen. 113 S.

Heft 60-3

W. Caspary, H. Heister, A. Schödlbauer, W. Welsch (Hrsg.): 25 Jahre Institut für Geodäsie. Teil 3: Aus dem Leben des Instituts. 149 S.

Heft 61/1998

T. Cui: Generierung hochwertiger Digitaler Geländemodelle aus analogen Karten mittels Mathematischer Morphologie. Dissertation. 188 S.

Heft 62/1999

K. Brunner, W. M. Welsch (Hrsg.): Hochgebirgs- und Gletscherforschung. Zum 100. Geburtstag von Richard Finsterwalder. 114 S.

Heft 63/1999

C. Fosu: Astrogeodetic Levelling by the Combination of GPS and CCD Zenith Camera. Dissertation. 155 S.

Heft 64/1999

W. Werner: Entwicklung eines hochpräzisen DGPS-DGLONASS Navigationssystems unter besonderer Berücksichtigung von Pseudolites. Dissertation. 226 S.

Heft 65/1999

K. Krack: Dreizehn Aufgaben aus der Landesvermessung im Geographischen Koordinatensystem. 84 S.

Heft 66/2000

G. Joos: Zur Qualität von objektstrukturierten Geodaten. Dissertation. 150 S.

Heft 67/2000

H. Sternberg: Zur Bestimmung der Trajektorie von Landfahrzeugen mit einem hybriden Meßsystem. Dissertation. 158 S.

Heft 68/2000

G. Oberholzer: Die Weiterentwicklung der Kulturlandschaft. Landespflge in der Flurbereinigung, Teil V. 150 S.

Heft 69/2000

R. Hollmann: Untersuchung von GPS-Beobachtungen für kleinräumige geodätische Netze. Dissertation. 350 S.

Heft 70/2001

U. Roßbach: Positioning and Navigation Using the Russian Satellite System GLONASS. Dissertation. 167 S.

Heft 71/2001

D. Beineke: Verfahren zur Genauigkeitsanalyse für Altkarten. Dissertation. 155 S.

Heft 72/2001

V. Oehler: Entwicklung eines „end-to-end“ Simulators zur Satellitennavigation unter besonderer Berücksichtigung von Pseudolite gestützten GNSS-Landesystemen. Dissertation. 212 S.

Heft 73/2001

T. Schüler: On Ground-Based GPS Tropospheric Delay Estimation. Dissertation. 370 S.

